

NATIONAL INSTITUTE FOR FUSION SCIENCE

**NIFS-SWJTU JOINT PROJECT FOR CFQS
-PHYSICS AND ENGINEERING DESIGN-
VER. 4.1 2022. JAN.**

CFQS Team

National Institute for Fusion Science, National Institutes of Natural Sciences
Institute of Fusion Science, School of Physical Science and Technology,
Southwest Jiaotong University
Hefei Keye Electro Physical Equipment Manufacturing Co. Ltd.

(Received - 2022.01.25)

NIFS-PROC-122

Feb. 10, 2022

This report was prepared as a preprint of work performed as a collaboration research of the National Institute for Fusion Science (NIFS) of Japan. The views presented here are solely those of the authors. This document is intended for information only and may be published in a journal after some rearrangement of its contents in the future.

Inquiries about copyright should be addressed to the NIFS Library, National Institute for Fusion Science, 322-6 Oroshi-cho, Toki-shi, Gifu-ken 509-5292 JAPAN.

E-mail: tosho@nifs.ac.jp

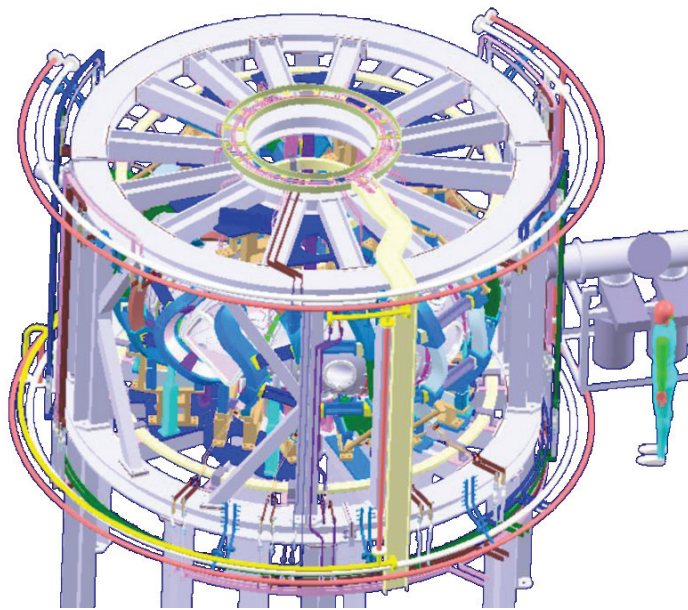
<Notice about copyright>

NIFS authorized Japan Academic Association For Copyright Clearance (JAC) to license our reproduction rights and reuse rights of copyrighted works. If you wish to obtain permissions of these rights, please refer to the homepage of JAC (<http://jaacc.org/eng/>) and confirm appropriate organizations to request permission.

NIFS-SWJTU JOINT PROJECT FOR CFQS

~PHYSICS AND ENGINEERING DESIGN~

VER. 4.1
2022. JAN.



CFQS Team

National Institute for Fusion Science, National Institutes of Natural Sciences

Institute of Fusion Science, School of Physical Science and Technology, Southwest Jiaotong University

Hefei Keye Electro Physical Equipment Manufacturing Co. Ltd.

NIFS-SWJTU Joint project for CFQS: Physics and engineering design Ver 4.1

CFQS Team

**National Institute for Fusion Science, National Institutes of Natural Sciences
Institute of Fusion Science, School of Physical Science and Technology, Southwest Jiaotong
University
Hefei Keye Electro Physical Equipment Manufacturing Co. Ltd.**

Abstract

The National Institute for Fusion Science (NIFS) and Southwest Jiaotong University (SWJTU) concluded an agreement for international academic cooperation to promote cooperative research in helical fusion plasma research on July 3, 2017. Since then, NIFS and SWJTU have continued the design study of the quasi-axisymmetric (QA) stellarator CFQS as a joint project. NIFS and SWJTU have organized the steering committee to manage this joint project. This document summarizes achievements of physical and engineering design study of the CFQS up to the 4th steering committee meeting, which was held on November 12, 2021 online, due to the effect of COVID-19.

Principal parameters of the CFQS is as follows: the major radius is 1 m, the magnetic field strength is 1 T, the aspect ratio is 4, and the number of toroidal period is 2. Magnetic field configuration is designed based on that of CHS-qa. Outstanding confinement property of CFQS in the context of neoclassical theory is achieved by its QA configuration. Appropriate feature of MHD stability is realized by its magnetic well characteristics. Magnetic field coil system is designed for the CFQS, which consists of 16 modular coils. Supporting system is designed to withstand strong electromagnetic force under 1 T operation, and it is improved to obtain wider space for heating and diagnostic systems. Analysis by using finite element method shows that the stress in the supporting structure is less than allowable level. Layout of main components, *e.g.* CFQS itself, diagnostic system, heating system, power supply in the torus hall is designed. For one of modular coils, mock up coil was constructed in the factory of Hefei Keye Electro Physical Equipment Manufacturing Co. Ltd., and various tests, such as heat run test and voltage isolation test were performed. Construction of actual modular coils has begun. Details of physics/engineering design, and current status of construction are reported in this document.

Keywords: quasi-axisymmetric stellarator, helical device, modular coil, CFQS, joint project, NIFS, SWJTU

Some figures and tables are in color only CD-ROM (PDF).

Documentation Contributors

(Alphabetical order of family name)

HIMURA	Haruhiko	Kyoto Institute of Technology (KIT)
HUANG	Jie	Southwest Jiaotong University (SWJTU)
INAGAKI	Shinichiro	Kyoto Institute of Technology (KIT)
ISOBE	Mitsutaka	National Institute for Fusion Science (NIFS)
KANDA	Motonari	National Institute for Fusion Science (NIFS)
KINOSHITA	Shigeyoshi	National Institute for Fusion Science (NIFS)
KOBAYASHI	Sakuji	National Institute for Fusion Science (NIFS)
LI	Yangbo	Southwest Jiaotong University (SWJTU)
LIU	Hai	Southwest Jiaotong University (SWJTU)
LIU	Haifeng	Southwest Jiaotong University (SWJTU)
MURASE	Takanori	National Institute for Fusion Science (NIFS)
NAGAOKA	Kenichi	National Institute for Fusion Science (NIFS)
NAKAGAWA	Sho	National Institute for Fusion Science (NIFS)
NAKATA	Motoki	National Institute for Fusion Science (NIFS)
OGAWA	Kunirhiro	National Institute for Fusion Science (NIFS)
OKAMURA	Shoichi	National Institute for Fusion Science (NIFS)
OISHI	Tetsutaro	National Institute for Fusion Science (NIFS)
SANPEI	Akio	Kyoto Institute of Technology (KIT)
SEKI	Ryohsuke	National Institute for Fusion Science (NIFS)
SHAO	Junren	Southwest Jiaotong University (SWJTU)
SHIMIZU	Akihiro	National Institute for Fusion Science (NIFS)
SUZUKI	Chihiro	National Institute for Fusion Science (NIFS)
TAKAHASHI	Hiromi	National Institute for Fusion Science (NIFS)
TANOUE	Hiroyuki	National Institute for Fusion Science (NIFS)
VARELA	Jacobo	Carlos III University of Madrid
WAN	Yi	Hefei Keye Electro Physical Equipment Manufacturing Co., Ltd. (Keye)
WANG	Hao	National Institute for Fusion Science (NIFS)
WANG	Xianqu	Southwest Jiaotong University (SWJTU)
XIONG	Guozhen	Southwest Jiaotong University (SWJTU)
XU	Yuhong	Southwest Jiaotong University (SWJTU)
YAMAGUCHI	Hiroyuki	National Institute for Fusion Science (NIFS)
YANG	Lang	Southwest Jiaotong University (SWJTU)

YIN	Dapeng	Hefei Keye Electro Physical Equipment Manufacturing Co., Ltd. (Keye)
YOSHIMURA	Yasuo	National Institute for Fusion Science (NIFS)
ZHU	Caoxiang	Princeton Plasma Physics Laboratory (PPPL)

Acknowledgements

During our work of making physics and engineering design of CFQS device and environmental utilities, we were given a lot of useful information from scientists and engineers in the experimental groups of various devices in the world. We are very grateful for their advices and supports.

Dr. Hutch Neilson, Dr. Tom Brown, and others from NCSX program in Princeton Plasma Physics Laboratory, Princeton, USA.

Prof. David Anderson, Prof. Simon Anderson, and others from HSX program in University of Wisconsin - Madison, USA.

Prof. Thomas Klinger, Dr. Lutz Wegener, Dr. Thomas Rummel, and others from W7-X program in Max Planck Institute for Plasma Physics, Greifswald, Germany.

Prof. Ge Zhuang, Tao Lan and others from KTX program in University of Science and Technology of China, People's Republic of China.

TABLE OF CONTENTS

1	Introduction.....	8
1.1	Overview.....	8
1.2	Steering committee meeting.....	11
2	Research target.....	13
3	Physics design.....	14
3.1	MHD equilibrium.....	14
3.1.1	MHD equilibrium with VMEC code.....	14
3.1.2	MHD equilibrium with HINT code.....	18
3.2	Confinement property.....	25
3.2.1	Neoclassical property.....	25
3.2.2	Plasma parameters expected from scaling law.....	29
3.3	MHD stability.....	32
3.3.1	Mercier stability/instability.....	32
3.3.2	Ballooning mode.....	36
3.3.3	Kink mode.....	38
3.3.4	Tearing mode.....	40
3.3.5	Alfvén mode.....	41
3.3.5.1	Alfvén mode analysis by MEGA code.....	41
3.3.5.2	Alfvén mode analysis by FAR3d code.....	47
3.4	Optimization approach of anomalous transport.....	52
3.4.1	Maximum- J	52
3.4.2	Micro instability.....	57
3.4.3	Plasma rotation.....	62
3.5	Energetic particle.....	67
3.5.1	NBI deposition analysis.....	67
3.5.2	Feasibility study of fast ion loss diagnostics.....	70
3.5.3	Preparative study for deuterium experiment for energetic ion confinement physics..	72
3.5.4	Predictive study of alpha particle confinement in a QAS-type reactor.....	75
3.6	ECRH deposition analysis.....	76
3.7	Modular coil design.....	79
3.7.1	Modular coil design by NESCOIL.....	79
3.7.2	Design of modular coils without torsions.....	85
3.7.3	Modular coil design by GOSPEL.....	92

3.7.4	Error evaluation using the Hessian matrix method	95
3.7.5	Influence of stellarator symmetric coil misalignment on magnetic field configuration 98	
3.7.6	Influence of general coil misalignment on magnetic surfaces	102
3.8	Divertor configuration	104
4	Engineering design.....	114
4.1	Whole assembly.....	114
4.1.1	Specification for engineering design.....	114
4.1.2	Overall Structure	116
4.1.4	Parts list for the CFQS	119
4.1.5	Overall production flow	120
4.2	Coil system	121
4.2.1	System configuration	121
4.2.2	Modular coil system (MC).....	125
4.2.2.1	Shape of the modular coil	125
4.2.2.2	Direction of the coil cross section.....	127
4.2.2.3	Support structure of the modular coil.....	128
4.2.3	Poloidal field coil system (PFC)	129
4.2.4	Toroidal field coil system (TFC).....	131
4.2.5	External current lead	133
4.2.6	Cooling water pipe.....	134
4.2.7	Cage type support structure.....	135
4.3	Vacuum vessel.....	137
4.3.1	Structure of main vessel.....	137
4.3.2	Port arrangement	139
4.4	Related equipment	142
4.4.1	Limiter system	142
4.4.2	Vacuum pumping system	142
4.4.3	Wall conditioning system.....	142
4.4.4	Fuel gas supply system (Gas puff system)	143
4.4.5	Vacuum management system	143
4.4.6	Shutter system to protect the glass windows.....	143
4.4.7	Vacuum test equipment	143
4.4.8	Compressed air supply system.....	144
4.4.9	Liquid nitrogen supply system.....	144
4.4.10	Pure water cooling system	144

4.5	Power supply.....	145
4.5.1	Requirement to power supply system with low voltage	145
4.5.2	Power supply system for the 1T operation.....	145
4.5.3	Power supply system for the 0.09T operation.....	147
4.6	Plasma heating system	149
4.6.1	Electron cyclotron resonance heating (ECRH) system	149
4.6.2	Neutral beam injection (NBI) heating system.....	151
4.7	Diagnostics system.....	152
4.7.1	Overview of diagnostic system	152
4.7.2	HIBP diagnostic	154
5	Research plan and schedule	158
5.1	Physics research plan	158
5.1.1	Research plan for 0.1 T operation	158
5.1.2	Research plan for 1.0 T operation	159
5.2	Construction schedule.....	159

APPENDIX-A1 (BD)	BASIC DESIGN
APPENDIX-A2 (RD)	RESEACH AND DEVELOPMENT
APPENDIX-A3 (DW)	DRAWING
APPENDIX-A4 (ST)	STANDARD INFORMATION
APPENDIX-A5 (PJ)	RELATED PROJECT

1 Introduction

1.1 Overview

The controlled nuclear fusion research is one of the most important issues for human beings because it is necessary to secure stable energy resources in order to enrich human life in the future. Fusion energy does not produce hydrocarbons and hence does not contribute to the global warming, which is one of the most serious environmental problems for Earth. The source of energy are isotopes of hydrogen, which are a common resource for the world because the hydrogen isotopes are obtained from seawater.

The development of technologies so far for making controlled nuclear fusion is based on two methods, namely, magnetic confinement of high temperature plasmas and the strong compression of high density plasmas with ultra-high intensity laser. For the magnetic confinement, high technology devices with strong magnetic field produced by large currents are used. This research started from the 1950s and varieties of different designs of magnetic confinement devices were proposed. After intensive research all over the world for more than a half century, two major magnetic confinement schemes have been established as candidates for the future fusion reactor design, namely, tokamak and stellarator.

These two designs have different advantages and disadvantages. Tokamak devices have better confinement property for high temperature plasmas because of their axisymmetric configuration of the magnetic field. However, tokamaks have essential problems of suffering current disruptions, which is very hazardous for the devices, and the high cost of current drive system because a large plasma current flowing in the plasma is a necessary element for the tokamak concept. On the other hand, stellarator does not have current disruption problems and does not need high cost current drive system because it does not require plasma current as a necessary element of a magnetic confinement concept. However, because of the lack of axisymmetry of the magnetic configuration, the confinement is degraded when the plasma temperature approaches the necessary conditions for the fusion reaction.

At present, large effort toward magnetic confinement of high temperature plasmas is focused on tokamak researches. In France, ITER, the largest facility of magnetic fusion research is now under construction as an international joint project. This device is a tokamak type and it is planned to produce 10 times larger fusion reaction energy than the electric energy consumed for maintaining high temperature plasmas in the device. This program is the final goal of the long way in making good plasma confinement using tokamak type devices. As a next step of fusion research toward the power reactor, we must solve many engineering problems. One of those significant issues is technology problems related to the plasma current (disruptions and current drive). It is strongly pointed out that we should have a multi-line research strategy for the future reactor design, namely, that we should

continue the stellarator research as a safe candidate for the fusion power plant free from the plasma current problems.

When the bright news of achieving high electron temperature in the tokamak device in Russia was distributed throughout the world fusion community in 1969, all plasma experimentalists began to work on tokamak experiments, thus giving up research with their own devices with different concepts from the tokamak. Since then, the main line of magnetic confinement fusion has been based on the tokamak concept. However, there were two continuous research activities for devices with the stellarator concept. In Kyoto University, in Japan, a series of devices with the names of Heliotron (A, B, C, D, DM, DR, E, and J) were built and the plasma parameters were improved continuously. In Germany, a series of devices with the name Wendelstein (1, 2, 3, ..., 6) were producing very promising data with stellarator configuration. In the final phase of these series, Wendelstein 7-A was built in Germany and started experiments in 1975. In Japan, Heliotron E was built and started experiments in 1980. Because the impact of experimental results from these devices were very large for the world fusion community, various types of stellarator programs were initiated in many countries in the 1980s.

In Japan, the designing work for Large Helical Device (LHD) started in 1985, and the construction of the device began in 1989. In Germany, the first design workshop for Wendelstein 7-X (W7-X) took place in 1987 and the first modular coil was ordered in 1998. These two world leading stellarator devices with super-conducting magnets are now in operation for experimental research in various topics of magnetic confinement with stellarator concept. In addition to these large devices, there were two medium size stellarators in operation from the 1980s to the 2000s both in Japan and in Germany. The roles of these devices were to conduct supporting experimental research in advance of the completion of construction and starting the experiments in larger-size major devices. Compact Helical System (CHS) was in operation from 1988 to 2006 and Wendelstein 7-AS was in operation from 1988 to 2002. The experimental results obtained in these devices before starting experiments in LHD and W7-X were very useful for planning experimental program in large devices. They also produced unique scientific results available only in the smaller size devices. In addition to these two experiments, many different types of stellarators were designed and built in other countries: in the United States, Advanced Toroidal Facility (ATF) with heliotron configuration and Helically Symmetric Experiment (HSX) with quasi-helical symmetric configuration started experiments in the 1980s. TJ-II in Spain and H-1 in Australia, both having the heliac configurations, started experiments in the 1980s. Among these devices, experiments in four devices are active at present, namely, LHD, W7-X, HSX, and TJ-II. Four other devices stopped experiments (ATF, W7-AS, CHS, and H-1).

The 1980s was an exciting period for stellarator research as many devices were designed and constructed. Fortunately, four devices continue in operation. However, we notice that it is too long for scientists in active research fields to keep running experiments in old devices designed and built more than 30 years ago even though the devices are in healthy condition for the experiments. In fact, there

were two research activities for the advanced design of stellarator concept in 1990s. In Japan, when CHS completed its initial phase of experimental program, the discussion for the next device after CHS was initiated in 1995. After making surveys for the possible candidates of the next devices, a plan for building a quasi-axisymmetric (QA) stellarator CHS-qa was chosen. Based on the physics and engineering design, a proposal of CHS-qa was completed in 2000 and submitted to the National Institute for Fusion Science (NIFS). Unfortunately, the proposal was not accepted because 2000 was just after the beginning of the LHD experiments and NIFS did not have financial and personnel capability to share in two large programs.

In Princeton Plasma Physics Laboratory (PPPL), a stellarator experiment program started in 1995 for building a medium size stellarator National Compact Stellarator Experiment (NCSX) in parallel to the existing spherical torus experiment, National Spherical Torus Experiment (NSTX). The design concept was a QA stellarator similar to CHS-qa. It had $N=3$ toroidal period number different from $N=2$ for CHS-qa. The proposal of the device construction was approved and PPPL started to build NCSX in 2000. Unfortunately, this program was cancelled in 2008 because of the rapid increase of the construction cost, which the United States government did not accept.

The advanced concept of QA stellarator is very attractive as it is a new scheme of stellarator configuration that had not been imagined by any scientists before 1994. A toroidal device of magnetic confinement must have rotating structures of magnetic field lines in a plasma toroid which can be produced either by a plasma current or by twisting of the plasma surface. Because a twisting shape is not axisymmetric, it is not naturally possible to make a twisting system as axisymmetric. A QA stellarator is not a hybrid device of tokamak and stellarator, either. When we design a hybrid system of two different concepts, all advantageous points and disadvantageous points are mixed together in general. However, the QA stellarator combines only advantageous points from both tokamak and stellarator, thus producing a new advantageous concept. Because such a new invention of the stellarator concept was not realized in the real experimental program in 2000, we now need to recover the lost 15 years by starting a new experiment with the quasi-axisymmetric stellarator CFQS.

The present design of the CFQS device incorporates numerous experiences we have learned in CHS-qa design work. In addition, we are adding many new design points that have been learned in theoretical and computational works during the past 15 years. The divertor configuration design, which is supposed be one of the most important research issues in advanced stellarator concept, was renewed from the CHS-qa design with a new concept of the island bundle divertor configuration. For the engineering design of the device and manufacturing, we will make use of new numerical technologies of mechanical design and of new engineering facilities in order to obtain very high accuracy of the three-dimensional shape of the device.

This program is a joint project conducted by NIFS in Japan and Southwest Jiaotong University (SWJTU) in China. We concluded the MoU in 2017 on NIFS and SWJTU Joint Project (NSJP) for

CFQS experiment. In addition, we are working together with Hefei Keye Electro Physical Equipment Manufacturing Co., Ltd. in Hefei with their contribution in engineering design and manufacture of the device. Thus, in fact, the program is a joint project by three organizations in Japan and China. We have been working together for the physics and engineering design of CFQS device. SWJTU and the Keye company are primarily responsible for the engineering design and for manufacturing the device. NIFS is primarily responsible to contribute in preparing plasma heating system and diagnostic system. The experiment in the device will be conducted as international collaborations by NIFS, SWJTU and other researchers in foreign countries who will be interested in the challenging advanced stellarator program in Chengdu, China.

1.2 Steering committee meeting

In order to decide the policy of the joint project in each year, the steering committee meeting is regularly held. On May 30 2018, 1st steering committee meeting was held in SWJTU in Chengdu, China. In this meeting, the basic CFQS physics design, which was designed based on CHS-qa, was confirmed. Main parameters of CFQS, major radius, $R = 1$ m, aspect ratio, $A_p = 4$, and toroidal magnetic field strength, $B_t = 1$ T were decided.

On May 29 2019, 2nd steering committee meeting was held in SWJTU in Chengdu, China. In this meeting, the site for experimental building was discussed. Emei campus was one of possible sites to construct the experimental building for CFQS. Progress of engineering design was checked. And the progress of mockup modular coil construction, which was built for check of manufacturing feasibility and achieved accuracy, was confirmed. Real scale 3-D plastic model of 1/4 toroidal section vacuum chamber was made, in order to check the workability in the inside of chamber, and accessibility to plasma.

On Nov. 12 2020, 3rd steering committee meeting was held by online. As the site of experiment building for CFQS, SWJTU suggested its new campus in Tianfu new district in Chengdu. The experimental building will be constructed in this site near future. The construction of mockup modular coil was completed. To check the performance of the mock up modular coil, various tests, such as heat run test, and voltage isolation test were done.

On Nov. 12 2021, 4th steering committee meeting was held by online. For the initial experimental phase for CFQS, SWJTU renovated the experimental hall in Jiuli campus. Based on the experience of mockup modular coil construction, construction of actual modular coils has begun by Keye. The construction of 1/4 toroidal section of vacuum vessel has also begun.

This report summarizes the achievement of physics, engineering research, and the construction of CFQS up to this meeting. In the following sections, important items in the physics and engineering designs of CFQS will be described. We hope this report will provide give sufficient information to all

researchers in the world about our CFQS program and motivate them to participate in the joint program of NSJP.

2 Research target

The CFQS is an international joint project between SWJTU in China and NIFS in Japan. It is the first stellarator to be manufactured and assembled by the Hefei Keye Electro Physical Equipment Manufacturing Co. Ltd. in China. Whereas in China there have been several tokamaks built by national institutions, there is no stellarator up to now. As the stellarator is technically much more complicated than the tokamak, our first target is to construct the CFQS device successfully and make it in good operation status in SWJTU. Secondly, we want to scientifically prove the major advantage of a QA stellarator in confining plasmas with reduced magnetic field ripple, and hence, neoclassical transport in comparison with previous conventional stellarators. Thirdly, for complementing the two-dimensional (2-D) tokamak physics, we will thoroughly study the intrinsic three-dimensional (3-D) physics in the CFQS stellarator to improve our understanding on related 3-D issues appeared in the tokamak, which has primarily 2-D magnetic configuration.

The main focus of the CFQS research activities is on basic physics studies under the advanced QA configuration. The scientific subjects include neoclassical transport, macro-scale magnetohydrodynamics (MHD) instabilities (interchange, ballooning, kink, and tearing modes, *etc.*), micro instabilities (electron drift wave, ion temperature gradient (ITG) and electron temperature gradient (ETG) modes, and trapped electron mode (TEM), *etc.*) and turbulence-induced transport, nonlinear interaction and energy cascading of multi-scale turbulence and zonal flows, confinement scaling and isotopic effects, plasma rotations, and edge and divertor physics. Special attention will also be paid on MHD activities arising from the neoclassical bootstrap current and the maximum- J issue in the QA configuration.

3 Physics design

3.1 MHD equilibrium

3.1.1 MHD equilibrium with VMEC code

The characteristics of three-dimensional (3-D) magnetic field configuration is uniquely determined, if the geometry of LCFS, the radial profile of pressure and the toroidal current as a function of flux are given [3.1.1-1]. The equilibrium of the magnetic field configuration is obtained by the VMEC code [3.1.1-2]. This code calculates the equilibrium from the given last closed flux surface (LCFS), the pressure and the toroidal current profile. The geometry of the torus LCFS can be parameterized by the Fourier series as follows,

$$\begin{aligned} R(\theta, \phi, s) &= \sum R_{mn}(s) \cos(m\theta - N_p n\phi), \\ Z(\theta, \phi, s) &= \sum Z_{mn}(s) \sin(m\theta - N_p n\phi). \end{aligned}$$

Here, θ , ϕ , and s are the poloidal angle, toroidal angle, and the radial flux coordinate, respectively. m , n , are the poloidal and toroidal mode, respectively, and N_p is the toroidal periodic number of the magnetic field configuration. In other words, the geometry of the LCFS, namely, the characteristics of the magnetic field configuration equilibrium, is expressed numerically by the dataset of R_{mn} and Z_{mn} . In stellarator optimization, we consider these parameters (R_{mn} , Z_{mn}) as control parameters, and some specific characters of magnetic field configuration are optimized. For numerical optimization, characters of magnetic field configuration are expressed numerically. For example, the sum of non-axisymmetric components of magnetic field in the Boozer coordinates [3.1.1-3], the Mercier criteria of D_I , and the effective helical ripple ε_{eff} etc. are used for the numerical evaluation of the magnetic configuration. These values that characterize the magnetic field configuration are optimized by changing the control parameters, *i.e.*, (R_{mn} , Z_{mn}) by using a non-linear optimization method. The guiding center orbits of charged particles in stellarators are determined by the absolute value of the magnetic field in the Boozer coordinates [3.1.1-3,4], therefore the spectrum of magnetic field strength B_{mn} in the Boozer coordinates are important. If the magnetic field strength in this coordinate system, B , is axisymmetric, *e.g.* it depends on only the θ , the guiding center orbits in this coordinates also become axisymmetric. This configuration is called as a QA system, because the geometry of plasma boundary is three dimensional, however, in the Boozer coordinates the particle orbit becomes axisymmetric and the good particle confinement property like tokamaks can be achieved.

As the post CHS project, the QA device, CHS-qa, was designed in NIFS [3.1.1-5]. The parameters of this device were as follows: The toroidal periodic number (N_p) is 2, the toroidal magnetic field strength (B_t) is 1.5 T, the major radius (R) is 1.5 m, and the aspect ratio (A_p) is 3.2, which is called as the 2b32 configuration. This configuration was designed to have a good QA property with good magnetic well and ballooning mode stability. Based on this configuration, new QA configuration is

designed for the CFQS. N_p of 2, B_t of 1.0 T, and R of 1.0 m are chosen for the CFQS. From the engineering point of view, the same low-aspect-ratio of the CHS-qa is not easy to realize, so the plasma size is shrunk and A_p of 4 is selected. In Fig. 3.1.1-1, the vacuum magnetic surfaces calculated by VMEC code are shown. The coefficients R_{mn} and Z_{mn} for the CFQS are shown in Table 3.1.1-1. The radial profile of the rotational transform and the magnetic well are shown in Fig. 3.1.1-2. The profile of rotational transform is characterized by low shear, and the magnetic well property is realized in the all radial region.

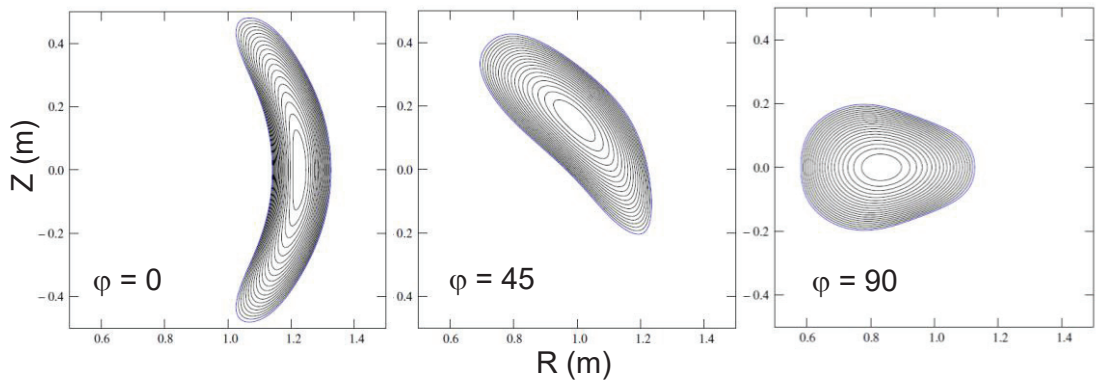


Fig. 3.1.1-1 CFQS magnetic flux surfaces in vacuum calculated by VMEC code at toroidal angles of 0, 45, and 90 degrees are shown.

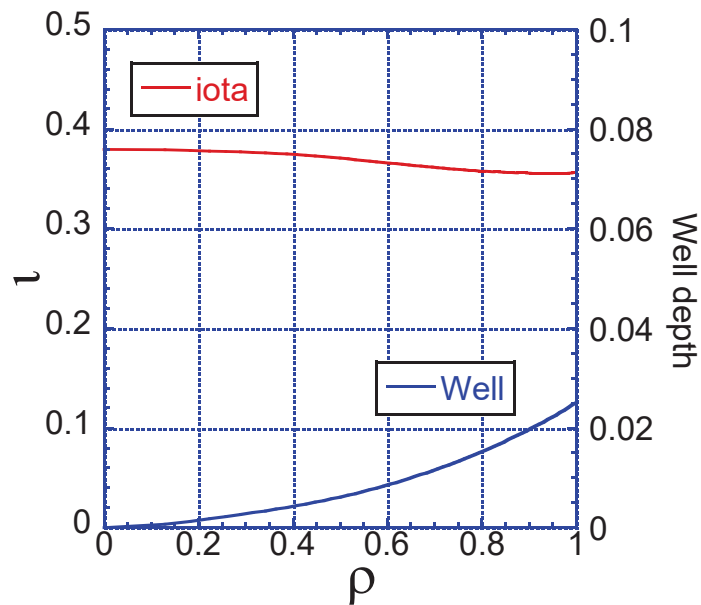


Fig. 3.1.1-2 Radial profiles of the rotational transform and magnetic well depth.

Table 3.1.1-1 Fourier components of R_{mn} , Z_{mn} for the CFQS boundary surface.

m	n	R_{mn}	Z_{mn}
0	0	1.000000E+00	0.000000E+00
0	1	1.391875E-01	-1.041401E-01
0	2	3.510066E-03	-2.047598E-03
0	3	-1.013876E-04	1.642899E-03
0	4	-9.175025E-05	1.845669E-05
1	-4	2.798909E-05	6.083008E-05
1	-3	-8.309604E-04	-1.061025E-03
1	-2	5.350281E-04	-1.240619E-03
1	-1	3.272968E-02	3.765426E-02
1	0	1.980512E-01	3.153157E-01
1	1	-1.190292E-01	1.059881E-01
1	2	-9.839016E-03	1.600162E-02
1	3	-1.036865E-04	-1.235699E-03
1	4	-1.774901E-04	-1.233294E-05
2	-4	-1.276662E-05	1.619552E-05
2	-3	-2.212222E-04	-1.655420E-04
2	-2	2.659139E-03	9.708512E-04
2	-1	5.392748E-03	3.943360E-03
2	0	2.368458E-02	5.220414E-03
2	1	4.800571E-02	1.879457E-02
2	2	1.418504E-02	-1.281654E-02
2	3	6.331471E-04	3.229137E-03
2	4	3.216150E-04	-3.067359E-05
3	-4	-2.244352E-05	-2.337868E-05
3	-3	2.247393E-06	7.071358E-05
3	-2	1.535243E-04	-7.055294E-05
3	-1	2.756543E-03	8.833038E-04
3	0	-3.334046E-03	3.224783E-03
3	1	-7.588701E-03	-6.650261E-03
3	2	-5.415940E-03	-2.327107E-03
3	3	-1.395157E-03	2.106916E-03
3	4	3.497018E-04	-6.340033E-04
4	-4	-1.132392E-05	4.601234E-06
4	-3	2.972533E-05	2.318047E-05
4	-2	-5.763365E-06	-6.467228E-05
4	-1	-8.356260E-05	-6.036524E-05
4	0	2.323114E-05	7.077580E-04
4	1	1.594329E-03	-9.755319E-04
4	2	-1.043988E-03	-2.935019E-03
4	3	-3.632249E-05	1.253345E-03
4	4	8.926982E-05	-2.034287E-04

5	-4	-1.660390E-06	-3.428524E-06
5	-3	2.634658E-06	4.226553E-06
5	-2	2.735705E-06	-5.476804E-07
5	-1	2.253818E-05	-1.345821E-05
5	0	-6.240069E-05	9.560246E-05
5	1	2.985376E-04	3.224349E-04
5	2	2.590860E-04	-7.446490E-05
5	3	2.474033E-04	2.527979E-04
5	4	9.280067E-05	-1.552233E-04
6	-4	1.525797E-05	-1.628272E-05
6	-3	-3.190926E-06	8.024808E-06
6	-2	7.765667E-06	-1.349779E-06
6	-1	-6.667636E-06	3.234683E-05
6	0	-4.959176E-05	-2.079634E-04
6	1	2.254973E-04	4.967132E-04
6	2	-1.654727E-04	-2.109075E-04
6	3	4.065117E-06	1.641132E-04
6	4	-1.144226E-05	-2.856708E-05
7	-4	-1.117052E-05	4.973842E-06
7	-3	-2.019870E-06	2.080768E-06
7	-2	1.753082E-06	9.119779E-07
7	-1	8.999813E-06	7.420079E-06
7	0	-2.983144E-05	-4.351131E-05
7	1	7.571942E-06	1.951069E-05
7	2	1.239090E-04	1.100027E-04
7	3	-4.699164E-05	-6.161755E-05
7	4	3.831545E-05	5.227709E-05

References

- [3.1.1-1] J. Nührenberg and R. Zille, Phys. Lett. **A 129** (1988) 113.
[3.1.1-2] S. P. Hirshman and J. C. Whitson, Phys. Fluids **26** (1983) 3553.
[3.1.1-3] A. H. Boozer, Phys. Fluids **23** (1980) 904.
[3.1.1-4] A. H. Boozer, Phys. Fluids **24** (1981) 1999.
[3.1.1-5] S. Okamura *et al.*, Nucl. Fusion **41** (2001) 1865.

3.1.2 MHD equilibrium with HINT code

The HINT code is a three-dimensional MHD equilibrium code based on the relaxation method without requiring the nested flux surface [3.1.2-1]. In this section, the typical configuration of the CFQS plasma is studied using the HINT code. A brief introduction of the code has been given here.

In the new version of the HINT code, the cylindrical coordinate (R, ϕ, Z) with the right-handed system is used with a high numerical accuracy. The steady-state solution based on the relaxation method is employed to solve single-fluid nonlinear MHD equations [3.1.2-2,3,4]. The relaxation consists of the following two steps, including (A) plasma pressure relaxation and (B) magnetic field relaxation. In step A, no pressure gradient along the magnetic field is satisfied with $\mathbf{B} \cdot \nabla p = 0$ for relaxation process of the plasma pressure (p), where the magnetic field \mathbf{B} is fixed. In step B, magnetic field is calculated with fixed p , which is updated in the step A. The reduced MHD equations are used as

$$\frac{\partial \mathbf{v}}{\partial t} = -\nabla p + (\mathbf{j} - \mathbf{j}_0) \times \mathbf{B},$$

$$\frac{\partial \mathbf{B}}{\partial t} = \nabla \times [(\mathbf{v} \times \mathbf{B}) - \eta(\mathbf{j} - \mathbf{j}_0 - \mathbf{j}_{\text{net}})],$$

where, t is time, \mathbf{v} is plasma velocity, \mathbf{j} is the total current density, \mathbf{j}_0 is the current density produced by vacuum magnetic field, \mathbf{j}_{net} corresponds to the net toroidal current like the neoclassical bootstrap current, η is dissipative parameter and constant plasma density is assumed. From the step B, a new magnetic field \mathbf{B} is obtained, then substituting it into step A that can yield new p . Both \mathbf{B} and p are updated via once iteration. After the multiple iteration process of the two steps, the final equilibrium is obtained when plasma velocity and magnetic field satisfy $dv/dt \rightarrow 0$ and $dB/dt \rightarrow 0$ simultaneously. The new version of HINT with the modified scheme of the pressure relaxation is efficient to calculate QAS and low shear stellarators [3.1.2-2].

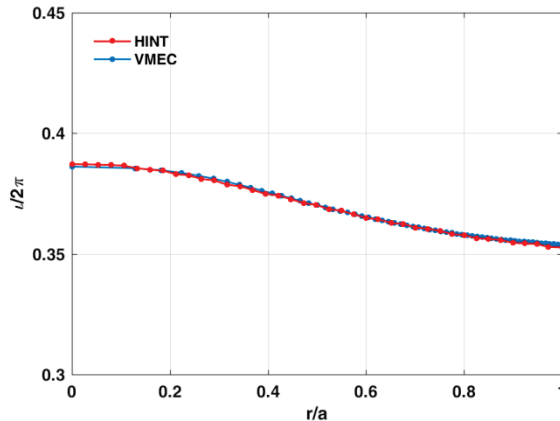


Fig. 3.1.2-1 Rotational transform ($t/2\pi$) in vacuum with normalized minor radius (r/a) for the HINT code and the VMEC code.

Fig. 3.1.2-1 shows a benchmark for CFQS equilibrium using the HINT and the VMEC code, where the rotational transform in vacuum for CFQS has been first given in previous work [3.1.2-5]. The VMEC free-boundary equilibrium result is in good agreement with the result of the HINT code for the zero pressure case. The typical rotational transform, $t/2\pi$, is smaller than 0.4, and this profile implies a weak shear comparing with other optimized stellarator configurations.

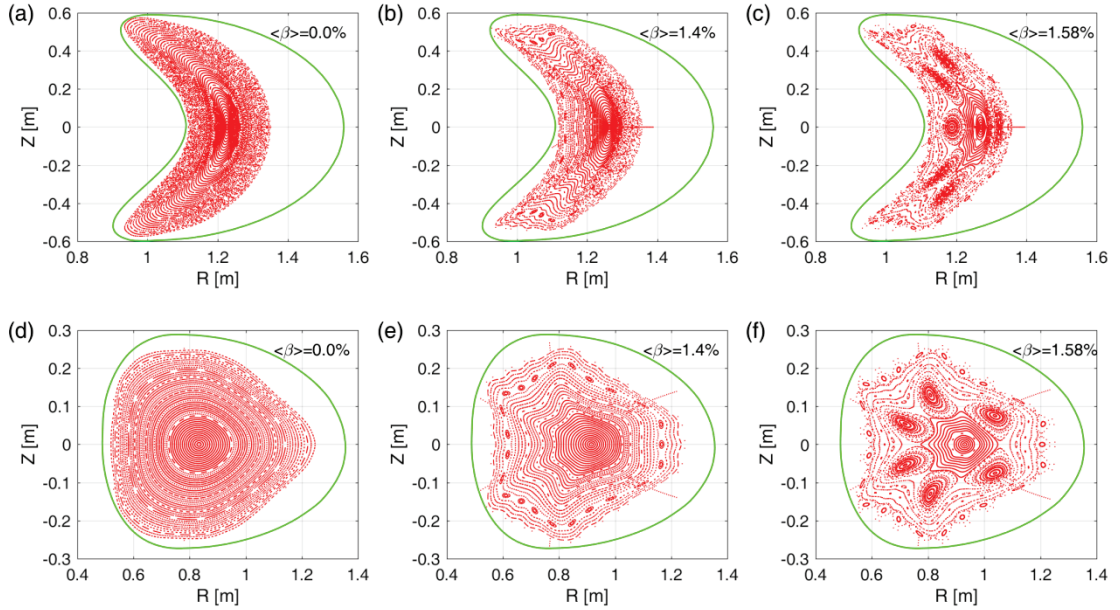


Fig. 3.1.2-2 Poincaré plots of magnetic flux surfaces calculated using HINT code for various volume averaged beta. (a)-(c) $\langle\beta\rangle = 0.0\%$, 1.4% , and 2.58% at $\phi = 0^\circ$. (d)-(f) $\langle\beta\rangle = 0.0\%$, 1.4% , and 2.58% at $\phi = 90^\circ$.

After the benchmark, we further calculate the finite beta equilibrium for the CFQS using the HINT code [3.1.2-6]. The Poincaré plots of magnetic surfaces are shown in Fig. 3.1.2-2, where the green line describes the vacuum vessel (VV) shape. The different volume-averaged beta $\langle\beta\rangle$ are considered. In this calculation, a reference configuration with a general pressure profile as $\propto (1-\psi)^2$ is employed, where ψ is the toroidal flux. Comparison of the difference $\langle\beta\rangle$ cases shows that an ergodization of magnetic surfaces expands with $\langle\beta\rangle$ increases in the boundary plasma ergodic region. When the plasma beta is sufficiently large, the large magnetic island generates not only on boundary but also on many low-order rational surfaces such as $m/n = 4/2$, $5/2$, and $6/2$, where m and n are the poloidal and toroidal mode number, respectively. The outer ergodic region expands towards plasma center, meanwhile, flux surfaces in high- β equilibrium tend to be more easily broken, which lead to plasma region shrinking. This suggests that the confinement of the edge plasma is significantly limited by the break of magnetic structure. On the other hand, however, $\langle\beta\rangle$ in Fig. 3.1.2-2(b) is larger than the design value of the CFQS regular operation as $\langle\beta\rangle = 1\%$ [3.1.2-5,7]. It is easily to predict that, in the low- β regime of $\langle\beta\rangle$ less than 1% , effective volume of the confinement region can be well retained

in the present equilibrium design. In order to reduce the outer magnetic surfaces loss caused by the outward shift of the surface position, an additional vertical field produced by external coils may be feasible for the CFQS to push the surface position back recovering the lost magnetic surfaces, as has been reported in reference [3.1.2-8,9].

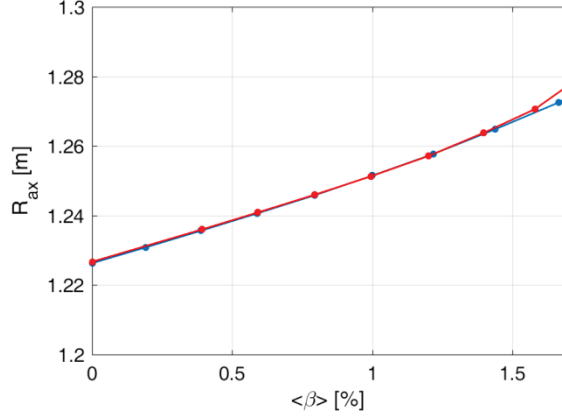


Fig. 3.1.2-3 The average position of the magnetic axis in major radius direction (R_{ax}) as a function of $\langle\beta\rangle$ calculated by the HINT (red line) and the VMEC code (blue line).

In fact, the finite beta effect not only on the edge, but also on every magnetic surfaces [3.1.2-2,10]. To explore the role of plasma beta and magnetic island in core region, we further calculate the magnetic axis shifts in the finite plasma beta cases by the HINT code and the VMEC code. The magnetic axis shift as a function of $\langle\beta\rangle$ is shown in Fig. 3.1.2-3, where the pressure profile is the same as that of Fig. 3.1.2-2. It is noted that when $\langle\beta\rangle < 1.4\%$, the result of the HINT code is quantitatively consistent with that of the VMEC code. The R_{ax} almost linearly depends on $\langle\beta\rangle$. In the high- β regimes of $\langle\beta\rangle$ larger than 1.5%, however, the shift is accelerated as a result of the $m/n = 6/2$ islands outward pushing. This point is confirmed in Fig. 3.1.2-2(c) and (f) in which many larger islands are produced on the left hand side of magnetic axis.

In CHS-qa, the estimated value of neoclassical bootstrap current reached to 100 kA for high- β discharges [3.1.2-11,12]. Since the CFQS is more compact QA system, substantial neoclassical bootstrap current is expected in high- β regime [3.1.2-7,13,14]. The HINT calculation of the equilibrium modified by neoclassical bootstrap current, therefore, is important to explore the configuration properties in detail. At first, the influence of neoclassical bootstrap current on MHD equilibrium of CFQS is investigated using the BOOTSJ code that calculates neoclassical bootstrap currents based on the drift kinetic model in non-axisymmetric magnetic configurations [3.1.2-15].

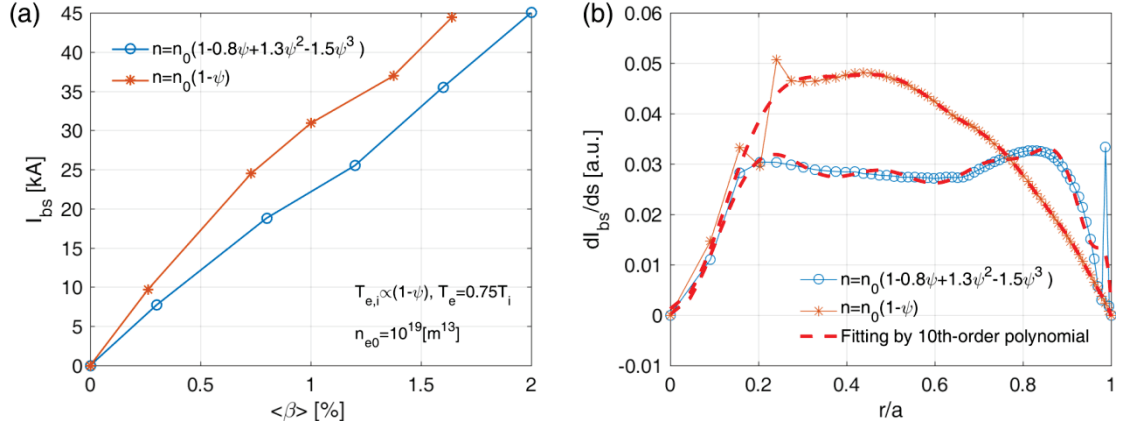


Fig. 3.1.2-4 (a) Neoclassical bootstrap current (I_{bs}) and (b) neoclassical bootstrap current density (dI_{bs}/ds) as a function of $\langle\beta\rangle$ for parabolic (Case 1) $n = n(0) \cdot (1 - \psi)$ and flat n_e profile (Case 2) $n = n(0) \cdot (1 - 0.8\psi + 1.3\psi^2 - 1.5\psi^3)$ calculated by the BOOTSJ code.

To study the effect of neoclassical bootstrap current, we consider two different density profiles with the fixed temperature profile of $T_{e,i} \propto (1 - \psi)$, corresponding to Case 1: parabolic profile ($n = n(0) \cdot (1 - \psi)$) and Case 2: flat density profile ($n = n(0) \cdot (1 - 0.8\psi + 1.3\psi^2 - 1.5\psi^3)$) as used in Fig. 3.1.2-4 (a) and (b), respectively. The parameters are the same as those used in Fig. 3.1.2-3 and then only the density profile is changed. From Fig. 3.1.2-4 (a) and (b), we can find the flattening of n_e profile can effectively reduce the neoclassical bootstrap current value and change the current density profile. The neoclassical bootstrap current almost linearly increases with $\langle\beta\rangle$ increases. For a general design of $\langle\beta\rangle \sim 1\%$, the amplitudes of neoclassical bootstrap current ~ 20 kA for Case 1 and ~ 30 kA for Case 2 are smaller than that in CHS-qa [3.1.2-8,9,13,14]. In Case 1, dI_{bs}/ds produced by the parabolic profile has a peak at $r/a = 0.4$ and results in the reversed magnetic shear, corresponding to advanced operation scenarios in tokamak. In Case2, dI_{bs}/ds rises toward the outer region and leads to a weak shear of $t/2\pi$ profile, which is similar to the result of reference [3.1.2-7].

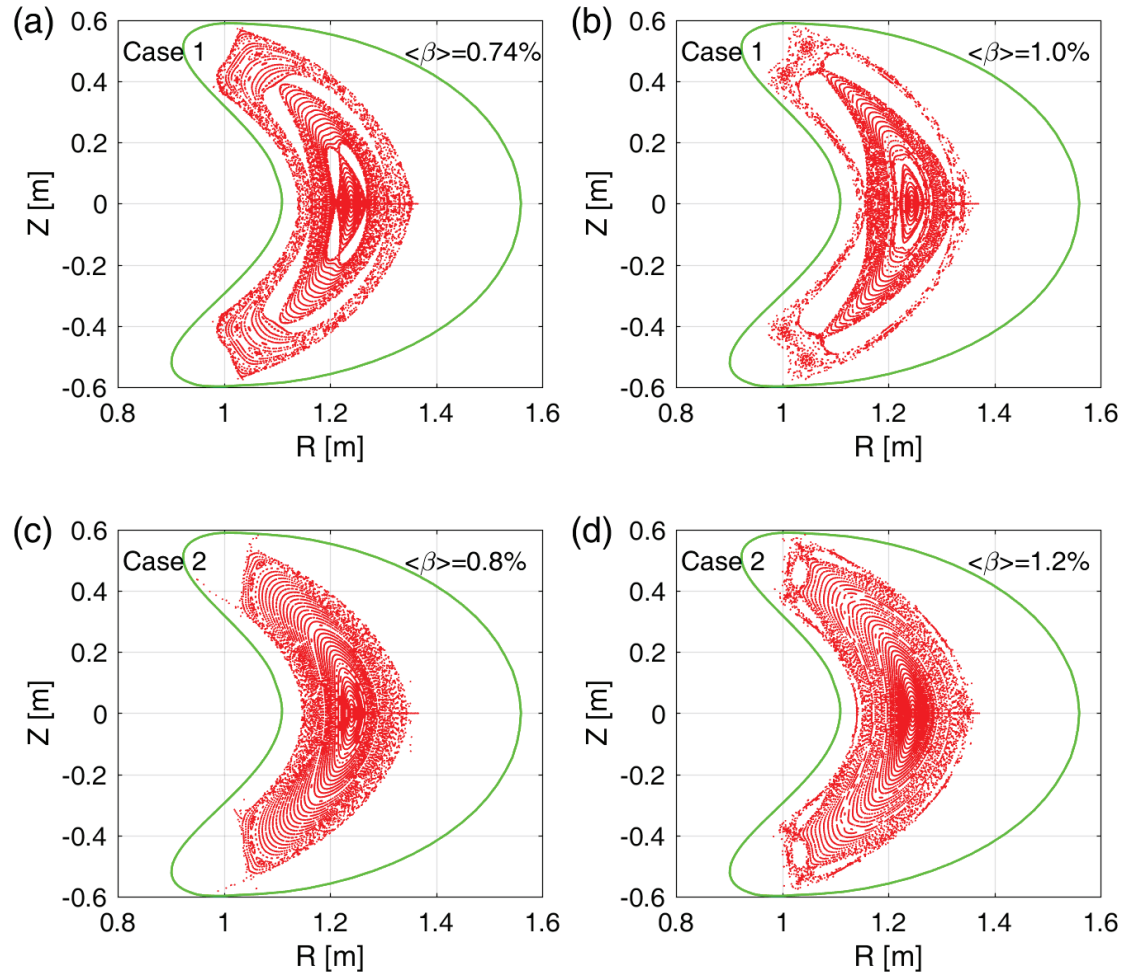


Fig. 3.1.2-5 Poincaré plots of magnetic surfaces for (a) Case 1 parabolic n_e profile with $\langle\beta\rangle = 0.74\%$, (b) Case 1 parabolic n_e profile with $\langle\beta\rangle = 1.0\%$, (c) Case 2 flat n_e profile with $\langle\beta\rangle = 0.8\%$, and (d) Case 2 flat n_e profile with $\langle\beta\rangle = 1.2\%$.

In general, in the 3-D MHD equilibrium, the magnetic island and stochasticization are driven by the nonlinear 3-D equilibrium response rather than the magnetic reconnection driven by the MHD instability [3.1.2-2,3,4,10]. It means that in the CFQS the neoclassical bootstrap current can enhance the rotational transform but does not have a direct contribution on the generation of equilibrium magnetic islands. To check the robustness of boundary magnetic structure and islands, we perform the HINT calculation for the CFQS including neoclassical bootstrap current and give the Poincaré plots of magnetic surfaces in Fig. 3.1.2-5 for the two different n_e profile cases, where the parameter setting is introduced in Fig. 3.1.2-4.

For Case 1, as is shown in Fig. 3.1.2-5 (a) and (b), with increasing of $\langle\beta\rangle$, the shape of the LCFS is opened clearly. The edge field is ergodized as a result of the finite pressure effects. The magnetic island forms at the rational surface corresponding to $\iota/2\pi = 2/4$. For the high- β equilibrium, the

increasing of stochastic region results in the effective volume of the confinement region shrinking to insides of islands. It implies that the force balance is not easy to maintain by residual plasma after the stochastization of magnetic field lines in the more peaked pressure configuration of Case 1.

For Case 2, as is shown in Fig. 3.1.2-5 (c) and (d), we can find in the moderate flattened pressure equilibrium with $\langle\beta\rangle \sim 1.2\%$, the magnetic island and stochastization are suppressed effectively. Although the boundary island remains due to increasing plasma beta, the relatively good flux surfaces are still kept over the entire plasma area. This offers the possibility to expect the high- β equilibrium for CFQS. Meanwhile, a high effective confinement volume in high- β operation scenarios can be realized if the density profile can be controlled by electron cyclotron resonance heating, pellet injection and so on.

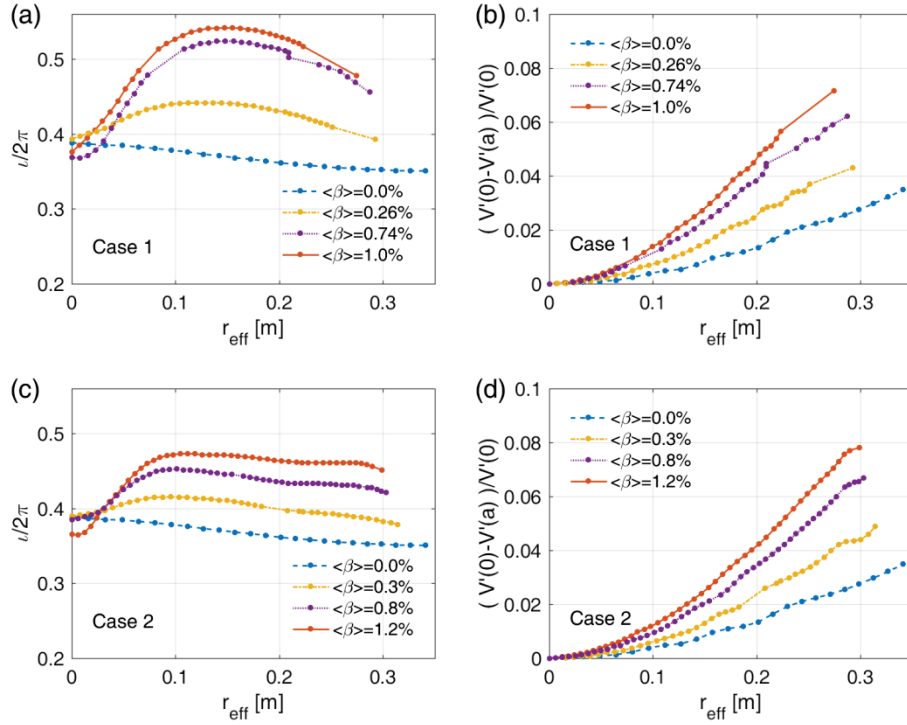


Fig. 3.1.2-6 (a) Rotational transform profiles and (b) magnetic well depth for different $\langle\beta\rangle$ in parabolic n_e profile. (c) Rotational transform profiles and (d) magnetic well depth for different $\langle\beta\rangle$ in flat n_e profile.

In previous works, it has been reported that the rotational transform can be enhanced by increasing the neoclassical bootstrap current in QAS [3.1.2-7,14]. Moreover, the enhanced rotational transform may play an important role in dynamics of the magnetic island. To explore the $\langle\beta\rangle$ dependence of rotational transform including neoclassical bootstrap current consistently, we present the results of $i/2\pi$ profile for various $\langle\beta\rangle$ in Fig. 3.1.2-6 (a) and (c). The magnetic well depth defined by $(V_p'(0) -$

$V_p'(a)/V_p'(0)$ to evaluate MHD property of QAS is shown in Fig. 3.1.2-6 (b) and (d), where V_p is the plasma volume with different effective radius and prime denotes the derivative of toroidal flux.

For Case 1, as $\langle\beta\rangle$ increased, the rotational transform crosses $\iota/2\pi=0.4, 0.5$, and the $\iota/2\pi$ profile is sensitive to the changes of $\langle\beta\rangle$ value, particularly in the small $\langle\beta\rangle$ regimes. On the rational surface, the modification of magnetic island near rational surface results in a vacancy region of iota profile in which the magnetic field line is closed insider islands rather than along its rotational transform. Moreover, it is also not possible to compute a $\iota/2\pi$ value further out due to the stochasticity of magnetic field lines in plasma edge region. Using the averaged effective radial position r_{eff} [m], we can easily find the confinement plasma region shrinking which corresponds to magnetic surface plotting of Fig. 3.1.2-5 (a) and (b). Fig. 3.1.2-6 (b) shows the effect of finite $\langle\beta\rangle$ on magnetic well depth. The magnetic well gradually rises from 3.5% to 6.7% on the LCFS, which qualitatively accords with the result of CHS-qa [3.1.2-11].

For Case 2, the iota profile flats in the intermediate region of $r_{eff} > 0.1$ [m] due to the profile effect of neoclassical bootstrap current. In a finite beta case, the magnetic well becomes deeper than that in vacuum equilibrium. Because the modified rotational transform suppresses plasma region shrinking, the well depth ($\sim 8\%$) for $\langle\beta\rangle = 1.2\%$ is also larger than that in Case 1 even with the low $\langle\beta\rangle = 1.0\%$. Then the magnetic well property is achieved throughout the entire plasma region.

References

- [3.1.2-1] S. P. Hirshman and J. C. Whitson, Phys. Fluids **26** (1983) 3553.
- [3.1.2-2] Y. Suzuki *et al.*, Plasma Phys. Control. Fusion **59** (2017) 054008.
- [3.1.2-3] Y. Suzuki, J. Geiger, Plasma Phys. Control. Fusion **58** (2016) 064004.
- [3.1.2-4] Y. Suzuki *et al.*, Contrib. Plasma Phys. **50** (2010) 576.
- [3.1.2-5] H. F. Liu *et al.*, Plasma Fusion Res. **13** (2018) 3405067.
- [3.1.2-6] X. Q. Wang *et al.*, Nucl. Fusion **61** (2021) 036021.
- [3.1.2-7] A. Shimizu *et al.*, Plasma Fusion Res. **13** (2018) 3403123.
- [3.1.2-8] K. Matsuoka *et al.*, Fusion Sci. Technol. **46** (2004) 378.
- [3.1.2-9] S. Okamura *et al.*, Nucl. Fusion **44** (2004) 575.
- [3.1.2-10] Y. Suzuki *et al.*, Nucl. Fusion **46** (2006) L19.
- [3.1.2-11] M. Isobe *et al.*, J. Plasma Fusion Res. SERIES **5** (2002) 360.
- [3.1.2-12] M. Isobe *et al.*, 28th EPS Conference on Controlled Fusion and Plasma Physics, Funchal, Portugal, 18-22 June 2001 ECA Vol.25A 761.
- [3.1.2-13] Y. Xu *et al.*, 27th IAEA Fusion Energy Conference (FEC 2018) Ahmedabad, India, 22-27 October 2018 EX/P5-23.
- [3.1.2-14] M. Isobe *et al.*, Plasma Fusion Res. **14** (2019) 3402074.
- [3.1.2-15] K. C. Shaing *et al.*, Phys. Fluids **B1** (1989) 148.

3.2 Confinement property

3.2.1 Neoclassical property

As stated above, the guiding center drift orbit is determined by the absolute value of \mathbf{B} in the Boozer coordinates, because in the guiding orbit equation, only the absolute value of \mathbf{B} appears and the vector components of \mathbf{B} do not appear. The Fourier components of the CFQS magnetic field in the Boozer coordinates are shown in Fig. 3.2.1-1. The toroidal ripple component, B_{10} is dominant for the good QA property. The contour map of magnetic field strength in the toroidal and poloidal angle plane is shown in Fig. 3.2.1-2.

Due to the QA property, the neoclassical bootstrap current is driven by the neoclassical effect. The BOOTSJ code can give us the neoclassical bootstrap current in the collision less limit [3.2.1-1]. With the BOOTSJ code, the neoclassical bootstrap current is estimated for the CFQS. Fig. 3.2.1-3 shows the dependency of the neoclassical bootstrap current on the volume-averaged plasma beta $\langle\beta\rangle$. Here, low-density case ($n_{e0}=1.0 \times 10^{19} \text{ m}^{-3}$, $T_e = 10 T_i$), and high-density case ($n_{e0}=2.0 \times 10^{19} \text{ m}^{-3}$, $T_e = T_i$) are considered. Radial profiles for density and temperature are assumed to be parabolic, $n_e \propto (1-\rho^2)$ and $T_e, T_i \propto (1-\rho^2)$. For the beta scan, n_e is fixed, and T_e , and T_i are changed. When $\langle\beta\rangle$ reaches 1 %, the neoclassical bootstrap current of 30 kA is expected. For low-density case, the change of the rotational transform profile is shown in Fig. 3.2.1-4. The MHD instability, such as kink mode, will be studied in the future.

The neoclassical transport in the $1/\nu$ regime can be estimated by the NEO [3.2.1-2] code. By this code, so-called the effective helical ripple ε_{eff} is estimated in this work. The neoclassical diffusion coefficient D is proportional to $v_d \varepsilon_{eff}^{3/2}/\nu$. Here, v_d and ν are the drift velocity and the collision frequency, respectively. The radial profile of $\varepsilon_{eff}^{3/2}$ are shown in Fig.3.2.1-5. The magnetic configurations of the CFQS in this figure are calculated with VMEC on fixed boundary and free boundary condition. The $\varepsilon_{eff}^{3/2}$ of the CFQS are two or three order less than that of the CHS. Up to $\langle\beta\rangle$ of 1.5%, the good neoclassical confinement property is kept.

Fourier spectrum of B in Boozer coordinates

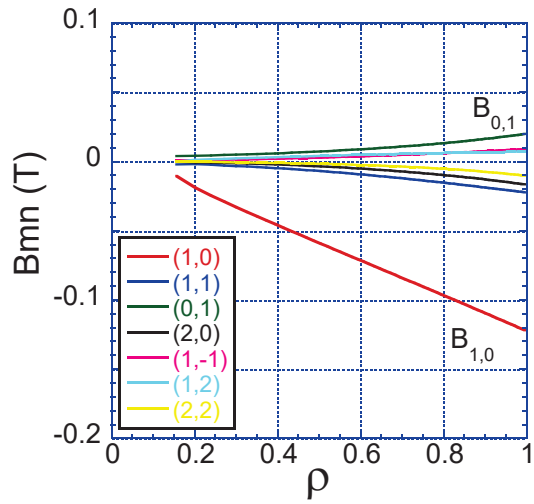


Fig. 3.2.1-1 Fourier spectrum of B in the Boozer coordinates.

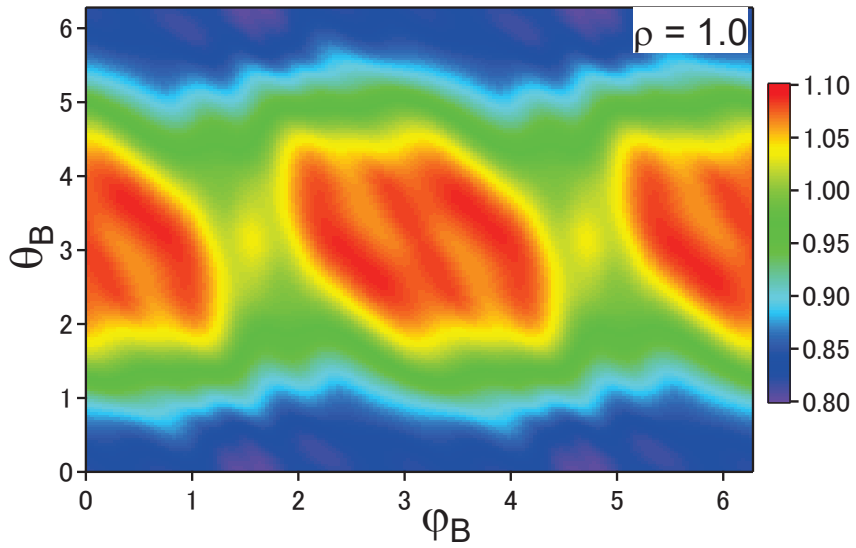


Fig. 3.2.1-2 Contour map of the magnetic field strength B in the Boozer coordinates on the LCFS of the CFQS.

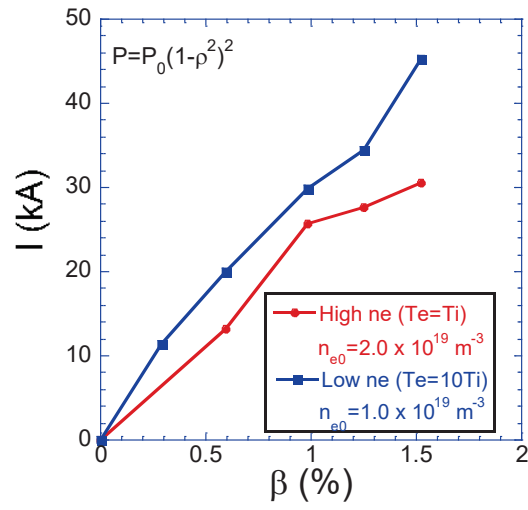


Fig. 3.2.1-3 Dependency of the neoclassical bootstrap current on the volume-averaged plasma beta.

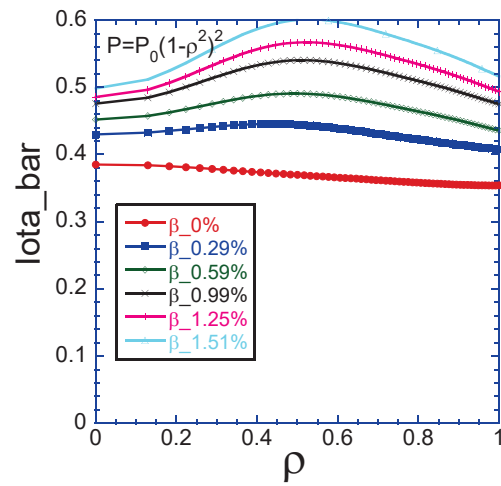


Fig. 3.2.1-4 Radial profile of the rotational transform considering the neoclassical bootstrap current.

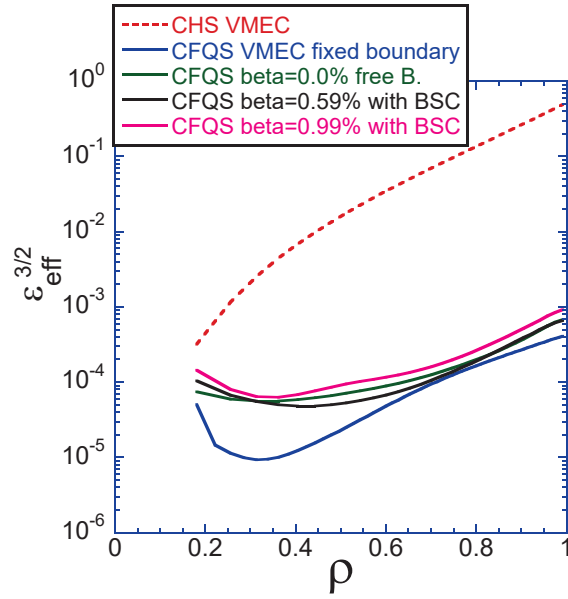


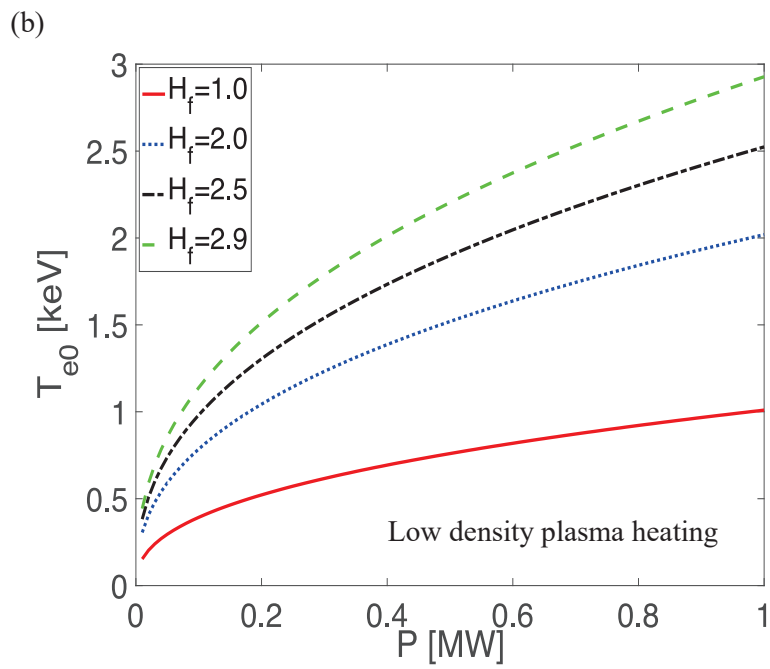
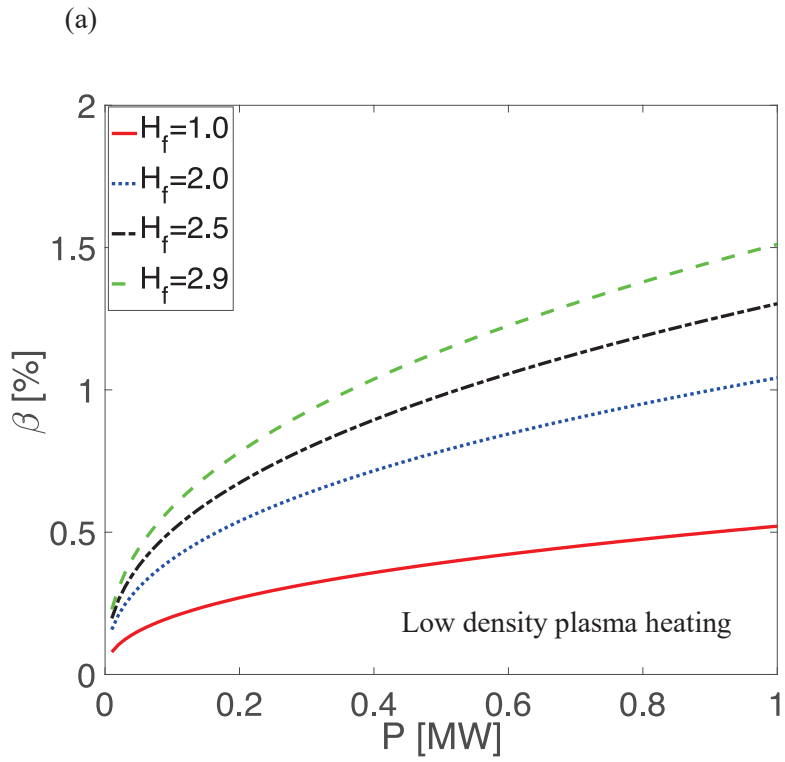
Fig. 3.2.1-5 Radial profiles of the effective helical ripple, $\epsilon_{\text{eff}}^{3/2}$. In the latter three cases, *i.e.*, green, black, and pink, the free-boundary calculation result of the VMEC are used to estimate $\epsilon_{\text{eff}}^{3/2}$.

References

- [3.2.1-1] K. C. Shaing *et al.*, Phys. Fluids **B 1** (1989) 148.
- [3.2.1-2] V. V. Nemov *et al.*, Phys. Plasmas **6** (1999) 4622.

3.2.2 Plasma parameters expected from scaling law

CFQS is expected to be operated in two different heating regimes. The facility will be equipped with 1.0 MW of ECRH (54.5 GHz, on axis heating). A low density, high electron temperature case could be achieved. To analyze plasma confinement and MHD behaviors in the second ballooning stable scenario, the impact of 1.0 MW of NBI (tangential injection with beam energy ~ 40 keV) and 2 MW of ICRH which is available in the 40–80 MHz range, has also been considered. This would allow access to higher density regimes than ECRH (density cut-off limited). The operational parameters of CFQS were estimated using the ISS95 scaling law [3.2.2-1]. The radial density and temperature profiles are assumed as $T = T_0(1-\rho^2)$ and $n_e = n_{e0} (1-0.8\rho^2+1.3\rho^4-1.5\rho^6)$, respectively. $T_{i0} = 2/3T_{e0}$. The enhancement factor $H_f = 1.0, 2.0, 2.5,$ and 2.9 are under consideration. The line-averaged density is $1 \times 10^{19} \text{ m}^{-3}$ for low-density plasma heating and $4 \times 10^{19} \text{ m}^{-3}$ for high-density plasma heating, respectively. The $H_f = 2.9$ is similar to that in the NCSX [3.2.2-2]. For the $B = 1.0$ T operation, the β and T_{e0} variations vs heating power in these two heating regimes are shown in Fig. 3.2.2-1. Concerning the low-density plasma heating, the expected β ranged from 0.5 % to 1.5 % at a heating power of 1.0 MW ECRH and the T_{e0} ranged from 1.0 to 3.0 keV as shown in Figs. 3.2.2-1 (a) and (b). With respect to the high-density plasma heating, the expected β ranged from 1.7 to 4.7 % with the range of T_{e0} from 0.7 to 2.3 keV at a heating power of 3.0 MW (1.0 MW NBI + 2.0 MW ICRH) as shown in Figs. 3.2.2-1 (c) and (d). There are numerous reasons to expect that the confinement may be enhanced in the CFQS configuration, compared with conventional stellarators and tokamaks. The robustness of quasi-symmetry should reduce neoclassical transport and suppress neoclassical toroidal viscosity, allowing development of persistent zonal flows. Furthermore, the shallow reversed/flat shear could stabilize trapped-particle modes, similar to reversed-shear advanced tokamak regimes.



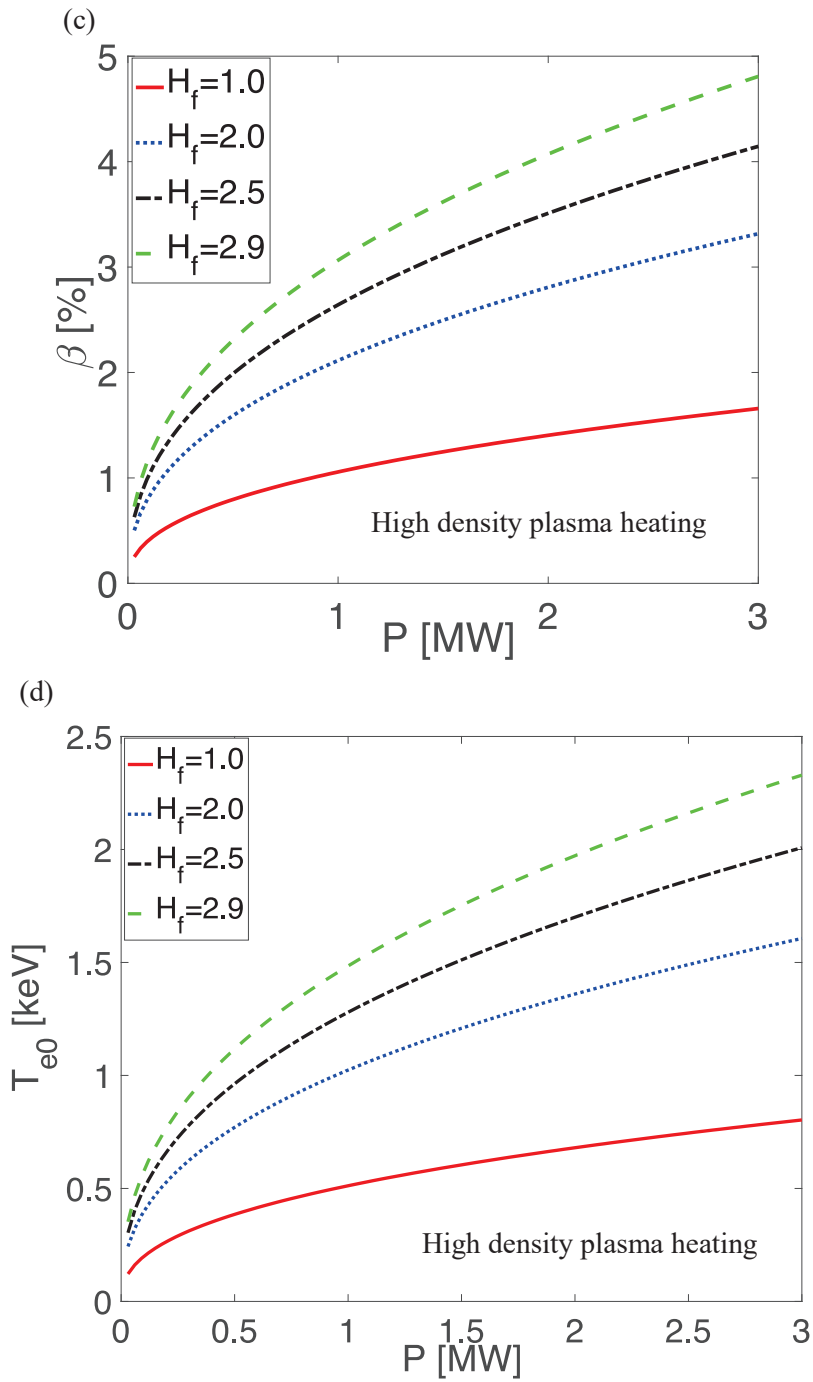


Fig. 3.2.2-1 Volume-averaged β (a) and electron temperature (b) for the low-density plasma heating, (c) and (d) for the high-density plasma heating estimated by the ISS95 scaling law in the $B = 1.0$ T operation.

References

- [3.2.2-1] U. Stroth, M. Murakami, R.A. Dory *et al.*, Nucl. Fusion **36** (1996) 1063.
[3.2.2-2] M.C. Zarnstorff *et al.*, Plasma Phys. Control. Fusion **43** (2001) A237.

3.3 MHD stability

Key MHD stabilities in the design of a finite- β QA stellarator configuration are discussed in this section. Mercier stability, ballooning mode, kink mode, and tearing mode are investigated to determination of β limit. These four issues are not independent. The VMEC, COBRAVMEC, BOOTSI, and TERPSICHORE codes are executed to estimate them [3.3-1~5].

References

- [3.3-1] S.P. Hirshman and J.C. Whitson, Phys. Fluids **26** (1983) 3353.
[3.3-2] A. H. Boozer, Phys. Fluids **24** (1981) 1999.
[3.3-3] K.C. Shaing *et al.*, Phys. Fluids **B1** (1989) 1663.
[3.3-4] R. Sanchez *et al.*, J. Comput. Phys. **161** (2000) 576.
[3.3-5] C. Mercier, Nucl. Fusion **1** (1960) 47.

3.3.1 Mercier stability/instability

The Mercier criterion is a necessary condition for the stability of localized interchange modes in a toroidal plasma, according to the ideal MHD model [3.3.1-1]. These modes are localized around mode-rational surfaces, where the parallel wave vector vanishes, so as to minimize the magnetic field line bending energy. The driving force for these modes is the pressure gradient across surfaces with average unfavorable curvature. The Mercier stability criterion involves competition between the driving force and the stabilizing effect of magnetic shear. The Mercier criterion can be written as summation of four terms, corresponding to the contributions coming from the shear, magnetic well, net currents, and geodesic curvature, respectively.

Once the magnetic field coils have been designed it needs to be established that these coils actually reproduce the desired MHD equilibrium and its relevant properties. For this purpose, free boundary equilibria were computed for volume averaged $\langle\beta\rangle=0$ and $\langle\beta\rangle=2\%$ [3.3.1-2]. The cross sections of the plasma boundary obtained from free boundary equilibrium calculations (*i.e.* using the external magnetic field generated by the modular coils described in Sec. 4.2) are obtained. A comparison of the flux surfaces of the vacuum field and the $\langle\beta\rangle=2\%$ solution (both VMEC) is presented in Fig. 3.3.1-1. It is observed that the Shafranov shift of the axis exists. The variation of Shafranov shift with $\langle\beta\rangle$ is displayed in the Fig. 3.3.1-2. When $\langle\beta\rangle$ equals to 1.7 %, the Shafranov shift is about the half of the minor radius.

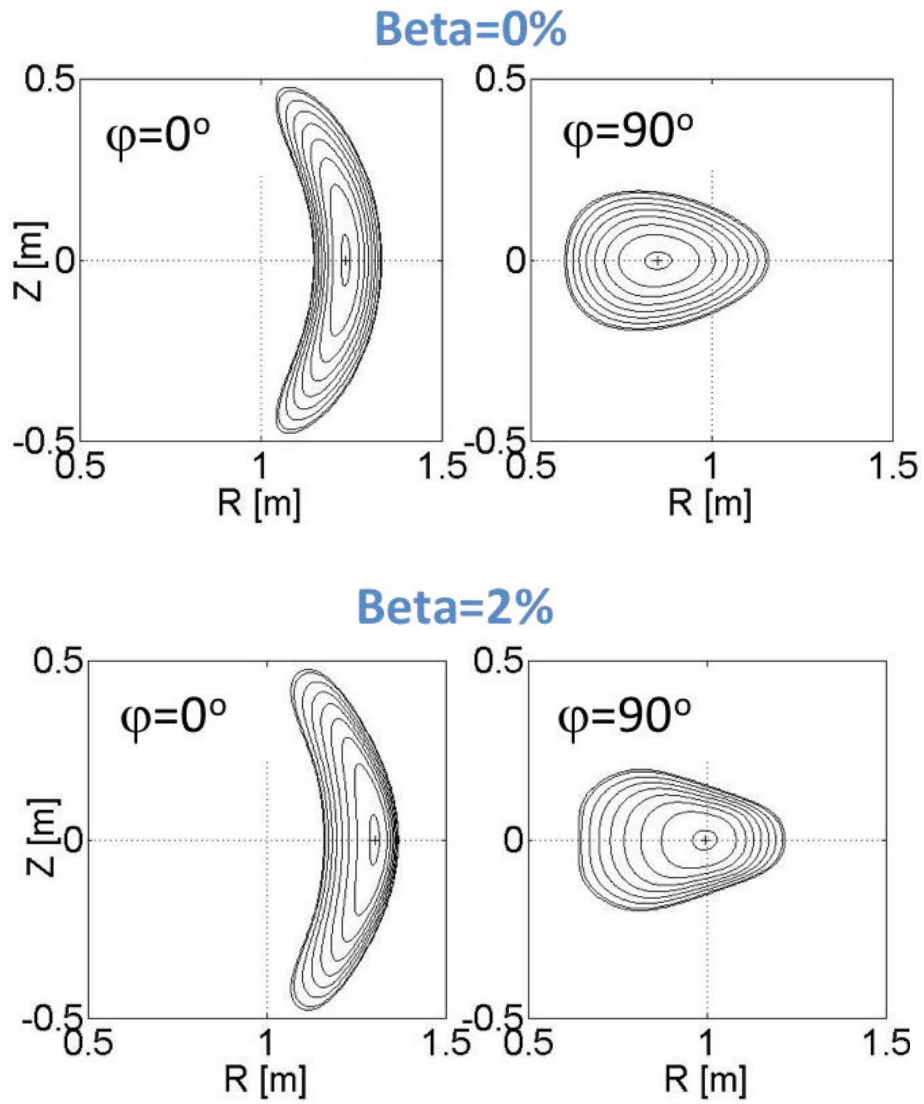


Fig. 3.3.1-1 Poloidal cross sections of the free-boundary equilibrium calculated by the VMEC code with the plasma pressure free (top panel) and $\langle\beta\rangle = 2\%$ (bottom panel).

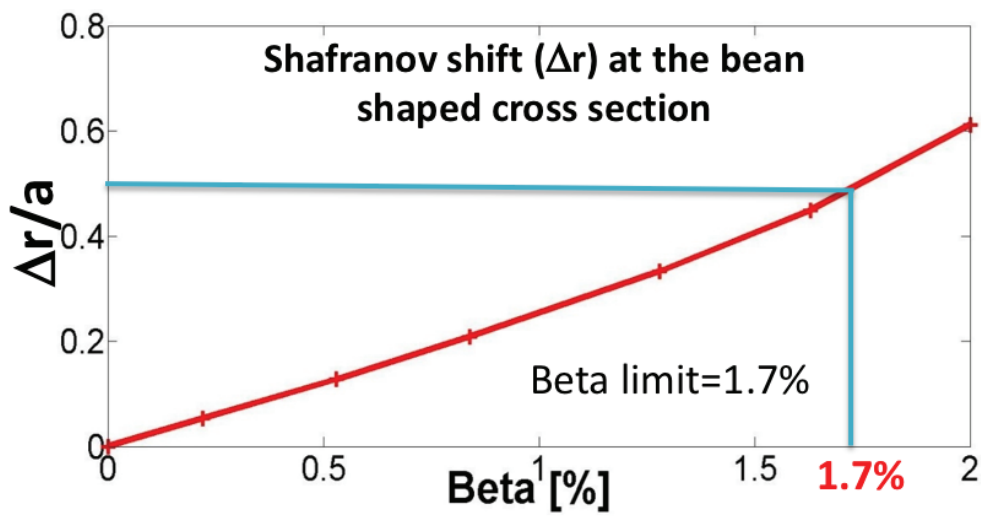


Fig. 3.3.1-2 Shafranov shift vs. $\langle \beta \rangle$ at the bean-shaped poloidal cross section.

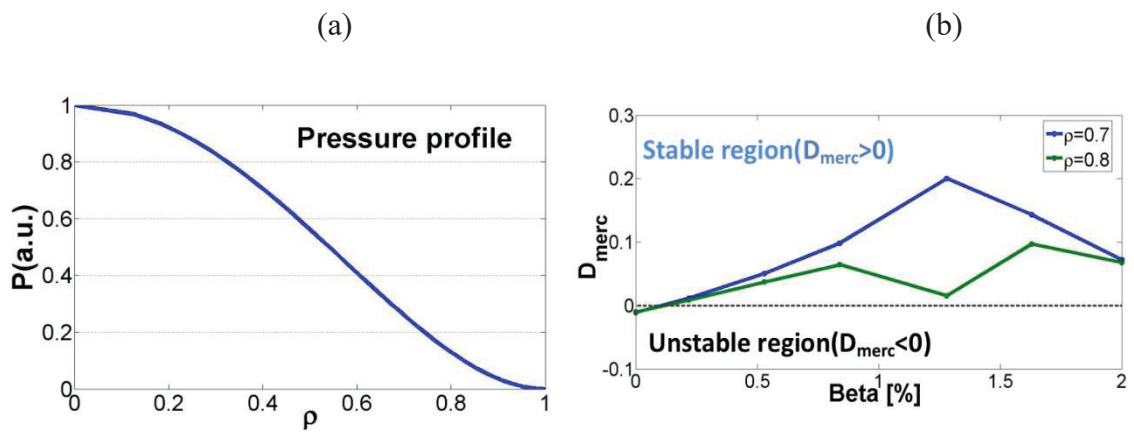


Fig. 3.3.1-3 (a) Assumed radial profile of plasma pressure (quadratic form) and (b) the variation of Mercier stability with $\langle \beta \rangle$ at two different radial position, *i.e.*, $\rho = 0.7$ and 0.8 .

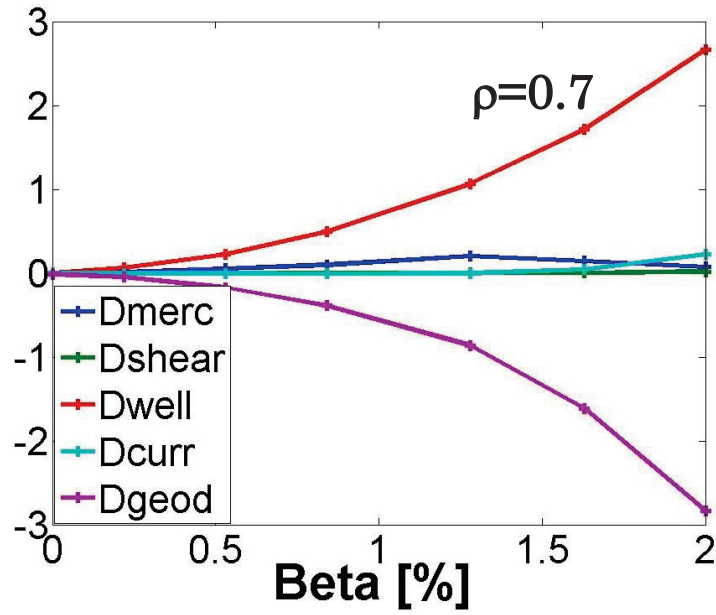


Fig. 3.3.1-4 Shear term, well term, current term and geodesic curvature term versus $\langle\beta\rangle$ at radial position $\rho = 0.7$, showing stabilization from the contribution of magnetic well.

The Fig. 3.3.1-3 (a) gives the input profile of plasma pressure $P(\rho) = P_0(1+\rho^2)^2$ for the VMEC calculation with the unfixed plasma boundary and Fig. 3.3.1-3 (b) displays the variation of Mercier stability with the volume-averaged beta at two different radial positions, *i.e.*, $\rho = 0.7$ and 0.8 . It shows that the interchange mode is stable up to $\langle\beta\rangle = 2\%$. The Mercier criterion can be expressed as $D_{merc} = D_{shear} + D_{well} + D_{curr} + D_{geod}$, where these terms correspond to the contributions coming from the shear, magnetic well, net currents, and geodesic curvature, respectively. In the Fig. 3.3.1-4, the variation of these four terms versus $\langle\beta\rangle$ at radial position $\rho = 0.7$ is shown, which depicts the stabilizing effect from the magnetic well ($D_{well} > 0$) is stronger than the destabilizing effect from the geodesic curvature term ($D_{geod} < 0$).

References

- [3.3.1-1] C. Mercier, Nucl. Fusion **1** (1960) 47.
- [3.3.1-2] H. Liu, *et al.*, Nucl. Fusion **61** (2021) 016014.

3.3.2 Ballooning mode

A principle aim of stellarator research is to understand the physical mechanisms that limit the plasma stored energy. The expectation is that pressure driven instabilities will be excited as the plasma energy increases relative to the magnetic energy. Since one of the advantages of stellarators is the avoidance of current driven instabilities, pressure driven instabilities may be critical in limiting stellarator operation. In theoretical studies of particular configurations, local criterion deduced from ideal MHD ballooning theory is often used to predict the plasma pressure limits of stellarators.

A feature related to second stability, which we call ‘self-stabilization’ for large pressure gradients after Ref. [3.3.2-1] has been observed in various stellarator experiments [3.3.2-2,3]. In these results, geometrical deformations associated with the Shafranov shift result in configurations which are stable with respect to Mercier modes as the plasma pressure increases. In this section, the COBRAVMEC code is utilized to calculate ideal ballooning stability for VMEC equilibria.

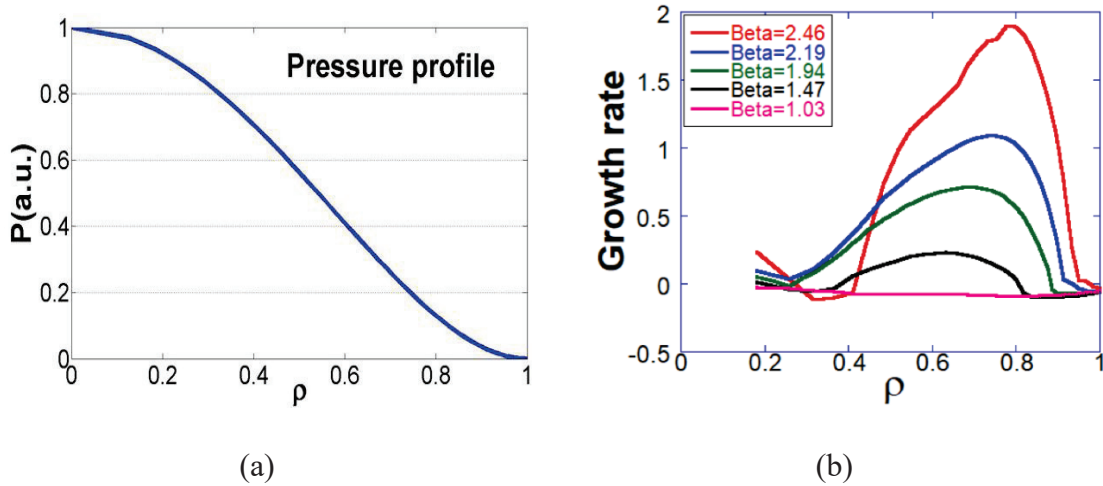


Fig. 3.3.2-1 (a) Assumed radial profile of plasma pressure (quadratic form), (b) Ballooning growth rates from COBRAVMEC as a function of the normalized flux for various volume-averaged beta, indicating the first stability boundary.

For the reference configuration, a quadratic pressure profile, $P(\rho) = P_0(1+\rho^2)^2$ was chosen. Ballooning growth rates as a function of the normalized flux label, ρ , are shown in Fig. 3.3.2-1 (a). As the plasma pressure increases, the plasma first becomes ballooning unstable at $\langle \beta \rangle$ of 1.03%, displayed in Fig. 3.3.2-1 (b). The region of instability grows until 3 %, where a region of second stability appears as shown in Fig. 3.3.2-2.

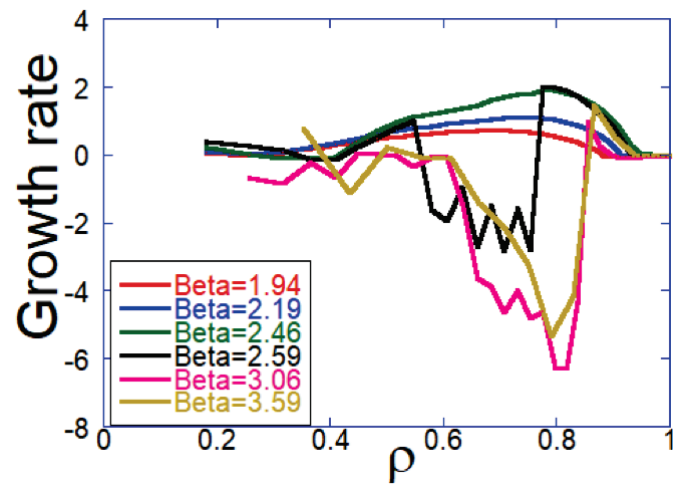


Fig. 3.3.2-2 Ballooning growth rates from COBRAVMEC as a function of the normalized flux for various volume-averaged beta, indicating the onset of second stability.

References

- [3.3.2-1] R. D. Hazeltine and J. D. Meiss, Plasma Confinement (Addison Wesley, Redwood City, 1992), pp. 309–312.
- [3.3.2-2] C. C. Hegna and S. R. Hudson, Phys. Plasmas **9** (2002) 2014.
- [3.3.2-3] R. Hudson and C. C. Hegna, Phys. Plasmas **10** (2003) 4716.

3.3.3 Kink mode

In a QA configuration, larger amount of neoclassical bootstrap current (BSC) flows and increases rotational transform due to its tokamak-like magnetic field structure. Therefore, the onset of an external kink mode should be carefully assessed in the ideal MHD stability analysis including plasma current. If a BSC profile is given, global low- n ideal MHD stability can be calculated with the TERPSICHORE code [3.3.3-1]. Since such a calculation for the CFQS configuration has not been performed yet, a typical example for the CHS-qa configuration [3.3.3-2] is described below.

A self-consistent BSC profile for a CHS-qa reference configuration has been calculated with SPBSC code [3.3.3-3]. We have solved finite beta equilibria including BSC assuming the fixed density and temperature profiles for three representative cases; (A) $n_e = 1.0 \times 10^{20} \text{ m}^{-3}$, $T_e = 1.04 \text{ keV}$, (B) $n_e = 0.2 \times 10^{20} \text{ m}^{-3}$, $T_e = 5.2 \text{ keV}$, (C) $n_e = 1.5 \times 10^{20} \text{ m}^{-3}$, $T_e = 1.04 \text{ keV}$ [3.3.3-4]. The resulting rotational transform is shown in Fig. 3.3.3-1 as a function of the normalized toroidal flux. Then the ideal global MHD stability has been analyzed with artificially changing the total parallel current while keeping its profile. The dependences of the most unstable eigenvalues on the total current are shown in Fig. 3.3.3-2 for the three representative cases. The onset of destabilization above 150 kA in the cases A and B clearly corresponds to the crossing of the edge rotational transform beyond 0.5 and 0.6. The associated amplitude of the dominant perturbation mode increases toward the edge, which clearly indicates the characteristics of an external kink instability. On the other hand, the global mode is kept stable up to 250 kA for the case C which has a different current profile. It indicates the possibility of stabilization of the external kink mode by controlling the current profile in a QA configuration.

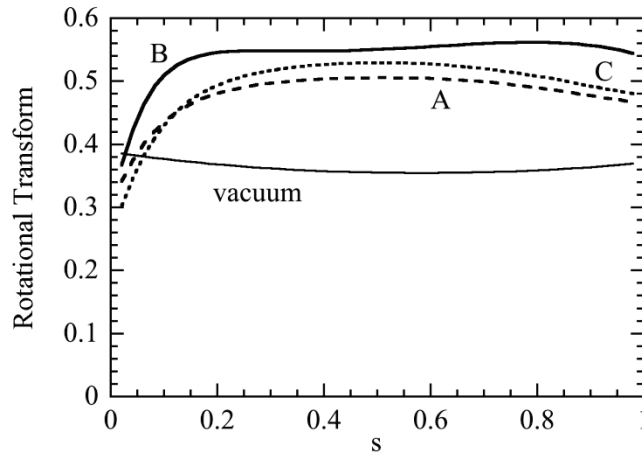


Fig. 3.3.3-1 Radial profiles of rotational transform for the three representative cases.

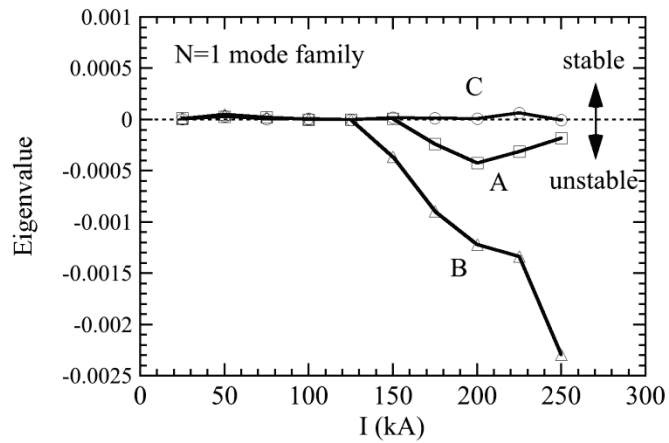


Fig. 3.3.3-2 Most unstable eigenvalues as functions of total current for the three representative cases.

References

- [3.3.3-1] D.V. Anderson *et al.*, *Int. J. Supercomput. Appl.* **4** (1990) 34.
- [3.3.3-2] C. Suzuki *et al.*, *J. Plasma Fusion Res. SERIES 6* (2004) 519.
- [3.3.3-3] K.Y. Watanabe *et al.*, *Nucl. Fusion* **35** (1995) 335.
- [3.3.3-4] M. Isobe *et al.*, *J. Plasma Fusion Res. SERIES 5* (2002) 360.

3.3.4 Tearing mode

The tearing mode stability, which is determined by Δ' , is analyzed for existing singular point in the plasma region with the same code described in Ref. 3.3.4-1 for the CHS-qa configuration [3.3.4-2]. Here, we consider a pressure less plasma in the cylindrical system with parabolic net toroidal current density J_z and check whether the tearing mode is stable or not at the rational surface of interest with increasing J_z . The tearing mode is stable for rational surfaces $n/m = 2/5, 3/7, 4/9$, and $1/2$ in the core domain (see Fig. 3.3.4-1) but the analyses indicate that it becomes unstable when singular point is in outer region ($r/a > 0.6$) for $n/m = 1/2$.

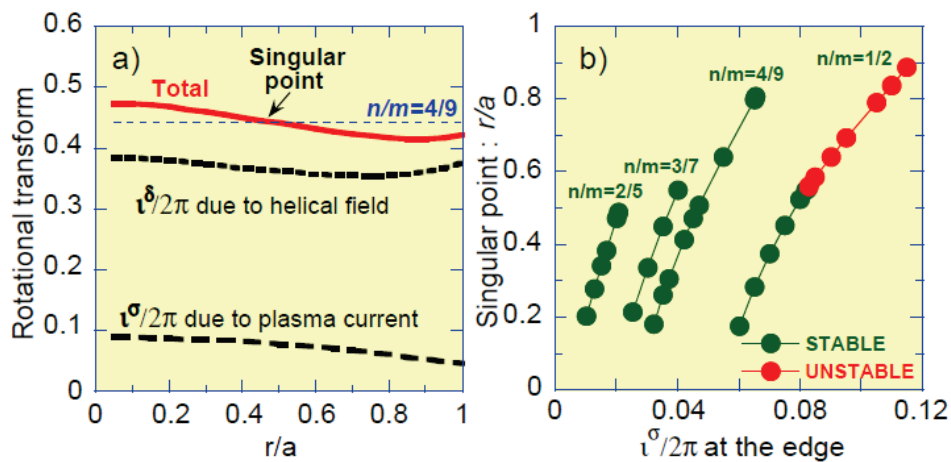


Fig. 3.3.4-1 (a) An example of rotational transform profile for tearing mode analysis for $n/m = 4/9$, and (b) Δ' analysis results are shown.

References

- [3.3.4-1] K. Matsuoka *et al.*, Nucl. Fusion **17** (1977) 1123.
- [3.3.4-2] M. Isobe *et al.*, 28th EPS Conference on Controlled Fusion and Plasma Physics, Funchal, Portugal, 18-22. June 2001, ECA Vol. **25A** (2001) 761.

3.3.5 Alfvén mode

3.3.5.1 Alfvén mode analysis by MEGA code

To further study the MHD stability in CFQS configuration, we perform the MHD simulation by MEGA code without energetic particles. The module and equations of this code are same as that of reference [3.3.5.1-1,2]. The MHD equilibrium is calculated by HINT2 code in Fig. 3.3.5.1-1 (b) with the core averaged pressure value being 3.7×10^{-3} [3.3.5.1-3]. The random initial perturbation and small normalized dissipation coefficients ($= 1 \times 10^{-8}$) are adopted. From the Fig. 3.3.5.1-2, we can find that in this configuration the MHD mode is stable with the negative growth rate defined by $\gamma = d(\ln E_k)/dt$.

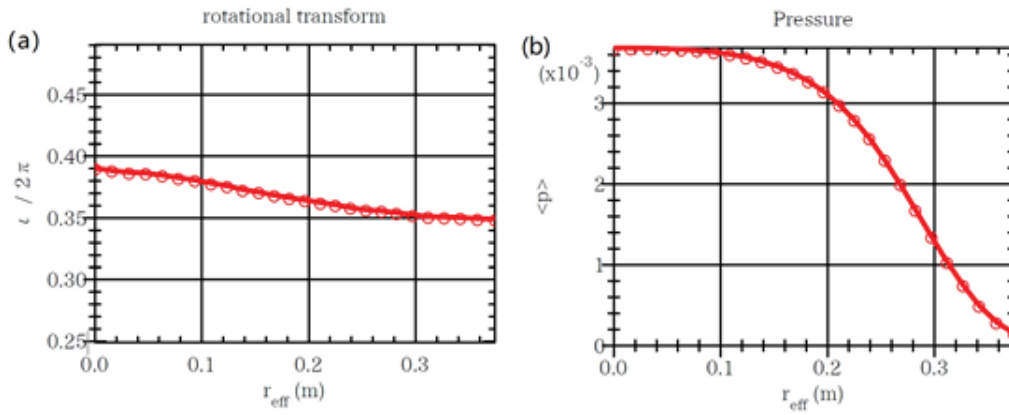


Fig. 3.3.5.1-1 MHD equilibrium profiles for (a) iota and (b) plasma pressure.

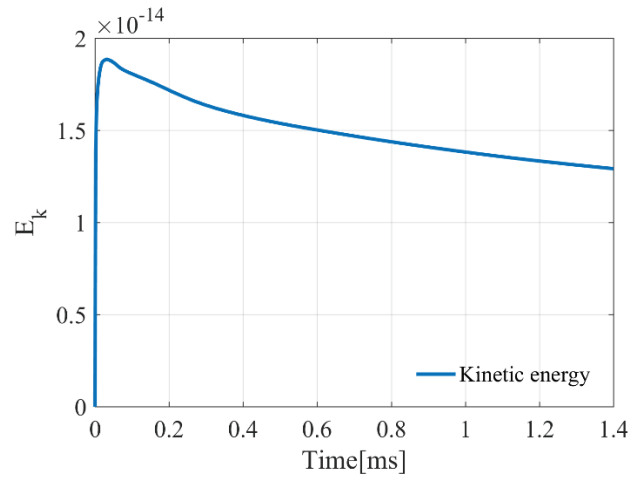


Fig. 3.3.5.1-2 Time evolution of kinetic energy.

MHD instability analysis is essential to evaluate the basic properties of QAS configuration [3.3.5.1-4~7]. Especially, the stability of external kink mode and ballooning mode has been paid close attention in the physical design and optimization of QAS. As an initial value MHD code, MEGA code is a powerful tool to study nonlinear MHD instabilities in 3-D tokamak and stellarator [3.3.5.1-2,8,9].

Therefore, the simulations of global MHD stability have been carried out for the optimized equilibrium (Case 2) given in section 3.1.2 using MEGA code. In the simulations, the potential MHD stabilities are considered self-consistently adopting of an initial random perturbation. The plasma viscosity and diffusion coefficients are set to 10^{-5} to maintain numerical stability, which are assumed to be equal to each other. The plasma resistivity are given as 5×10^{-5} or other values. The growth rate and mode frequency are normalized by Alfvén frequency for Case 2 equilibrium. Alfvén time is $\sim 1.4 \times 10^{-7}$ second with plasma density being $1 \times 10^{19} \text{ m}^{-3}$. A Boozer coordinate system of the MHD equilibrium was constructed for the spectral analysis of the simulation results [3.3.5.1-2].

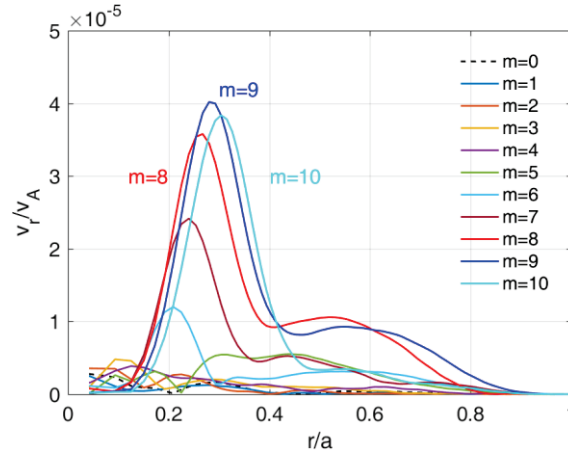


Fig. 3.3.5.1-3 The profiles of radial velocity for $m = 0 \sim 10$ and $n = -4$.

The radial eigenmode structures of the unstable mode with a dominated toroidal mode number $n = -4$ are shown in Fig. 3.3.5.1-3, where radial velocity v_r is normalized by Alfvén velocity v_A . The mode harmonics are dominated by $m = 8 \sim 10$. The peaking location is near the rational surface of $1/2\pi = 0.5$ and also close to the weak shear regions as shown in Fig. 3.1.2-6 (c). The mode structure with a strong coupling is compared with conventional resistive ballooning modes as reported in such publications [3.3.5.1-9,10].

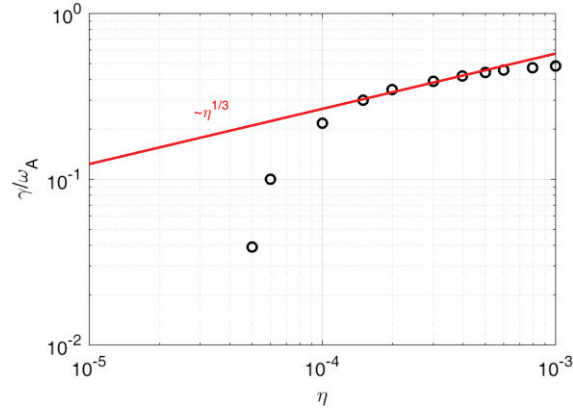


Fig. 3.3.5.1-4 The linear growth rate of the mode, $\gamma = d(\ln Ek)/dt$, as a function of plasma resistivity and the fitting by $\eta^{1/3}$ with $\langle\beta\rangle \sim 1.2\%$.

Considering the important role of resistivity in dynamics of the MHD mode, we show the resistivity dependence of mode growth rate in Fig. 3.3.5.1-4, where the linear growth rate $\gamma = d(\ln Ek)/dt$ is normalized by Alfvén frequency ω_A , η is plasma resistivity, and Ek is the kinetic energy. It is seen that, for the high- η regimes, the mode is unstable with a zero mode frequency. For the low- η regimes, the mode is stabilized in this equilibrium. In the resistivity-dominated region of $10^{-4} < \eta < 10^{-3}$, the $\eta^{1/3}$ scaling of growth rates obtained from the simulations is in agreement with the theoretical result of resistive ballooning modes in stellarator [3.3.5.1-11]. This suggests that the resistive MHD mode can be excited due to the finite plasma pressure in CFQS plasmas.

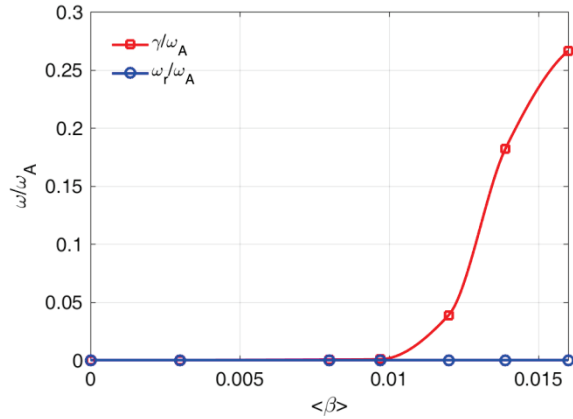


Fig. 3.3.5.1-5 Mode frequency and growth rate as a function of $\langle\beta\rangle$.

To clear the finite plasma pressure effects, we scan the growth rate and mode frequency as a function of $\langle\beta\rangle$ as shown in Fig. 3.3.5.1-5. A strong $\langle\beta\rangle$ dependence of the mode growth rate and zero mode frequency are found, corresponding to a pure MHD mode. On the other hand, the mode is stable when the $\langle\beta\rangle$ is smaller than $\sim 1\%$, which suggests a beta limit for the present design of CFQS. It has to be pointed out that the ideal external kink mode as one important MHD stability in QAS [3.3.5.1-5,12,13],

we have not discussed here, may be unstable when the boundary rotational transform exceeds 0.5 [3.3.5.1-5] and should be studied in future.

Next, two different equilibrium files generated using HINT2 code are used for the simulation. They correspond to the case with magnetic islands and the case without magnetic island, as shown in Fig. 3.3.5.1-6 (a) and (b). The rotational transform ι profile is slightly different in these two cases, as shown in Fig. 3.3.5.1-6 (c). For the case with magnetic islands, ι profile intersects $\iota = 1/3$ line near the plasma edge.

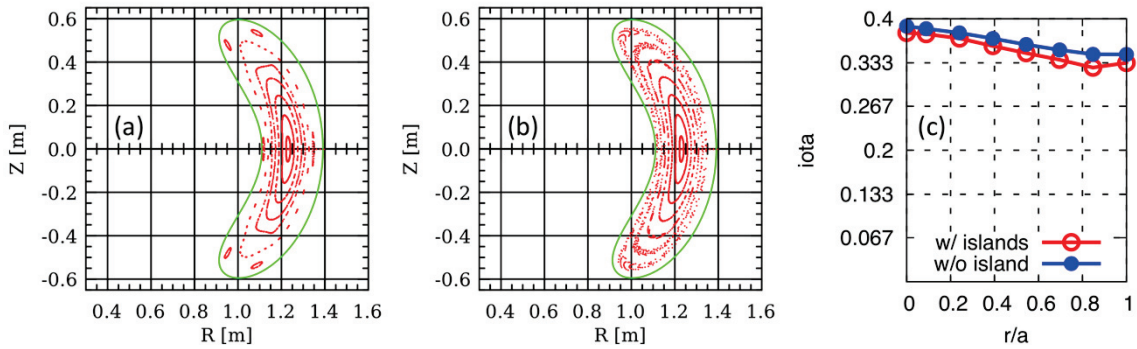


Fig. 3.3.5.1-6 Poloidal cross sections with Poincaré plots of the magnetic configurations of two cases (a) with magnetic islands and (b) without magnetic island. The ι profile is shown in panel (c).

The instability in CFQS in three-dimensional form is shown for the first time, as shown in Fig. 3.3.5.1-7. In the toroidal direction, only 3/4 tours are shown from $\varphi = 0$ to $\varphi = 1.5\pi$. The plasma from $\varphi = 1.5\pi$ to $\varphi = 2\pi$ is cut in order to better observe the poloidal cross section. The poloidal cross section on the left side is located at $\varphi = 0$, while the poloidal cross section on the right side is located at $\varphi = 1.5\pi$. They are bean-shaped and triangular-shaped, respectively.

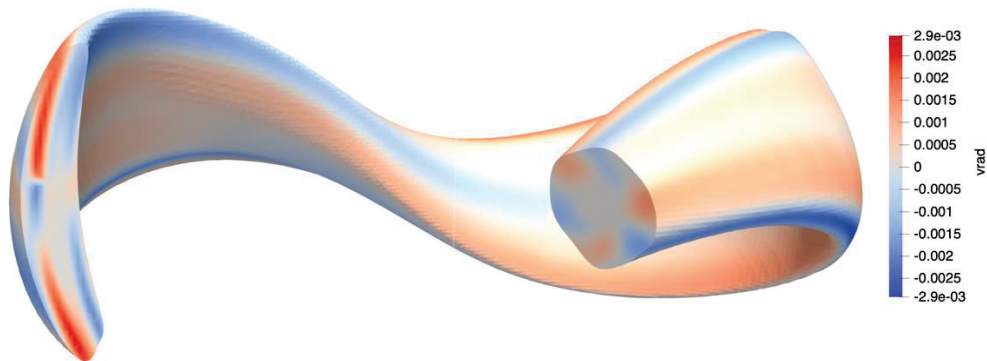


Fig. 3.3.5.1-7 Radial velocity v_{rad} of GAE in three-dimensional form.

Both global Alfvén eigenmode (GAE) and toroidal Alfvén eigenmode (TAE) are found in CFQS with and without magnetic island. The dominant mode numbers are $m/n = 3/1$ for GAE and $m/n = 5/2$ for TAE. Strong mode coupling is found under the condition of a very low number of field period N_{fp} value. This result is consistent with theoretical prediction [3.3.5.1-14], and it is similar to the simulation of FAR3d code [3.3.5.1-15]. For GAE, the mode frequency 79 kHz does not depend on energetic particle pressure or energetic particle beam velocity, while the growth rate increases with energetic particle pressure, as shown in the GAE case of Fig. 3.3.5.1-8. The growth rate is maximum for the energetic particle beam velocity of $0.5v_A$ where v_A is Alfvén velocity. For TAE, similarly, the mode frequency 125 kHz does not depend on energetic particle pressure, energetic particle beam velocity, or peak value of energetic particle pitch angle. The growth rate increases with energetic particle pressure, as shown in the TAE case of Fig. 3.3.5.1-8. The growth rate is maximum for the energetic particle beam velocity of $0.5v_A$. The resonant condition $f_{mode} = nf_\varphi - lf_\theta$ is confirmed. For GAE, $n = 1$ and $l = 2$, and for TAE, $n = 2$ and $l = 4$.

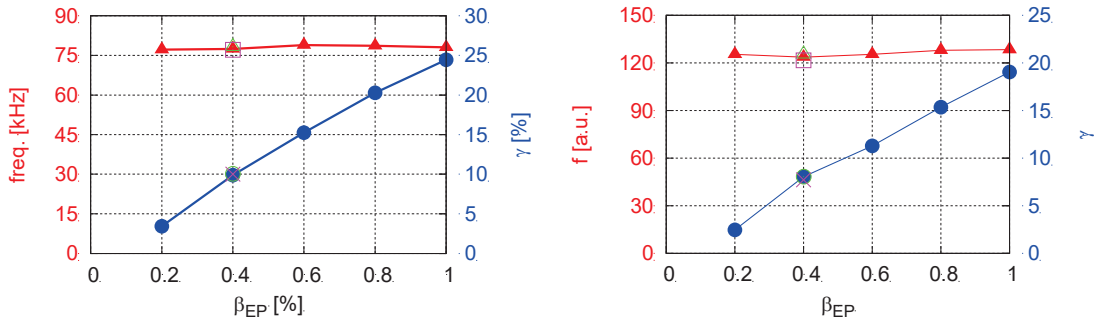


Fig. 3.3.5.1-8 The mode frequency and growth rate versus energetic particle pressure of (left) GAE and (right) TAE.

GAE frequency chirps in the nonlinear saturated phase, and TAE is similar to that, as shown in Fig. 3.3.5.1-9. Hole and clump structures are formed in the pitch angle and energy phase space. The particles comprising the hole and clump are kept resonant with the GAE or TAE during the mode frequency chirping. This is the first time to show nonlinear frequency chirping of Alfvén eigenmodes in CFQS.

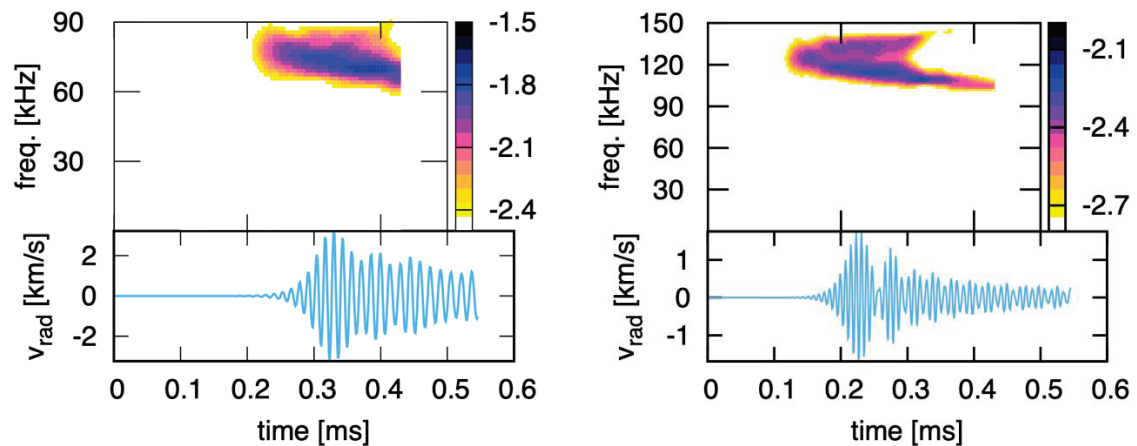


Fig. 3.3.5.1-9 The mode frequency spectrum and mode amplitude time evolution of (left) GAE and (right) TAE.

Finally, during the mode activities, energetic particles are lost from the core region. For the present simulation, the transport caused by GAE is stronger than that of TAE.

References

- [3.3.5.1-1] Y. Todo *et al.*, Plasma Fusion Res. **5** (2010) S2062.
- [3.3.5.1-2] Y. Todo *et al.*, Phys. Plasmas **24** (2017) 081203.
- [3.3.5.1-3] Y. Suzuki *et al.*, Nucl. Fusion **46** (2006) L19–L24.
- [3.3.5.1-4] S. Okamura *et al.*, Nucl. Fusion **41** (2001) 1865.
- [3.3.5.1-5] M. Isobe *et al.*, 28th EPS Conference on Controlled Fusion and Plasma Physics, Funchal, Portugal, 18-22 June 2001 ECA Vol.25A 761.
- [3.3.5.1-6] G. Y. Fu *et al.*, Phys. Fluids **B 4** (1992) 1401.
- [3.3.5.1-7] S. A. Henneberg *et al.*, Nucl. Fusion **59** (2019) 026014.
- [3.3.5.1-8] Y. Todo *et al.*, Nucl. Fusion **50** (2010) 084016.
- [3.3.5.1-9] Y. Todo *et al.*, Plasma Fusion Res. **5** (2010) S2062.
- [3.3.5.1-10] M. Sato *et al.*, Nucl. Fusion **57** (2017) 126023.
- [3.3.5.1-11] W. A. Cooper, Phys. Rev. **A 32** (1985) 3124
- [3.3.5.1-12] G. Y. Fu *et al.*, Fusion Sci. Technol. **51** (2007) 218.
- [3.3.5.1-13] C. Suzuki *et al.*, J. Plasma Fusion Res. SERIES **6** (2004) 519.
- [3.3.5.1-14] D. Spong *et al.*, Phys. Plasma **10** (2003) 3217.
- [3.3.5.1-15] J. Varela *et al.*, Nucl. Fusion **61** (2021) 026023.

3.3.5.2 Alfvén mode analysis by FAR3d code

We analyze the stability of the AE in CFQS using the code FAR3d [3.3.5.2-1]. A set of free boundary results from the VMEC equilibrium code is calculated for the vacuum CFQS configuration ($\beta_{th}=0$) and finite thermal β cases with $\beta_{th}=0.01, 0.02,$ and 0.03 . The effect of the bootstrap current is included in the equilibria, calculated using the BOOTSJ code [3.3.5.2-2]. The magnetic field at the magnetic axis is 1 T, the toroidal field period number is 2, the averaged inverse aspect ratio is $\iota = 0.25$ and the major radius $R_0 = 1$ m. The energy of the injected particles by the NBI is $T_{f0} = 30$ keV and the nominal energy of the EP resulting in an averaged Maxwellian energy equal to the average energy of a slowing-down distribution is 17 keV. Fig.3.3.5.2-1 shows the main profiles of the thermal plasma. The thermal β of the model increases because the thermal plasma density increases. Fig. 3.3.5.2-2 shows the EP density profiles used in the study. The energy of the EP is assumed constant, with no radial dependency, for simplicity.

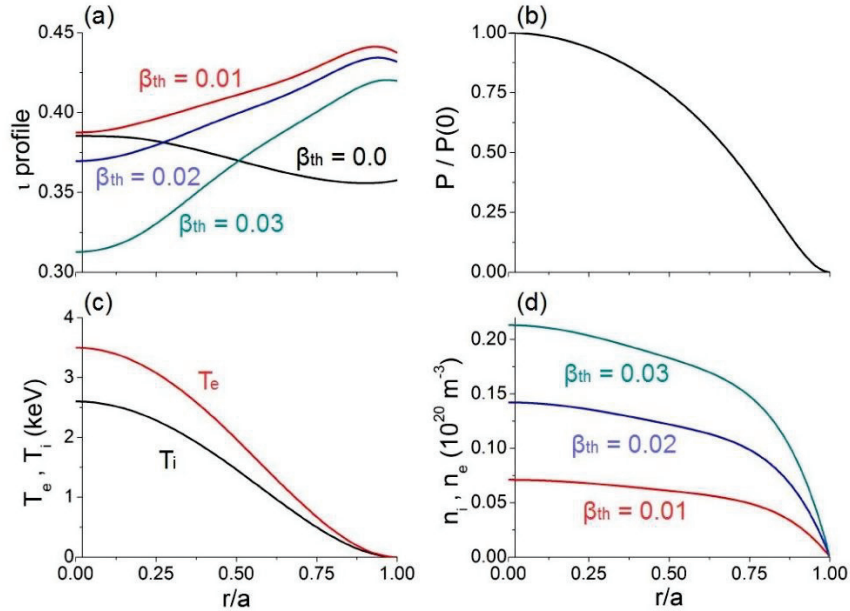


Fig. 3.3.5.2-1 (a) ι profile, (b) total pressure, (c) thermal plasma temperature and (d) thermal plasma density.

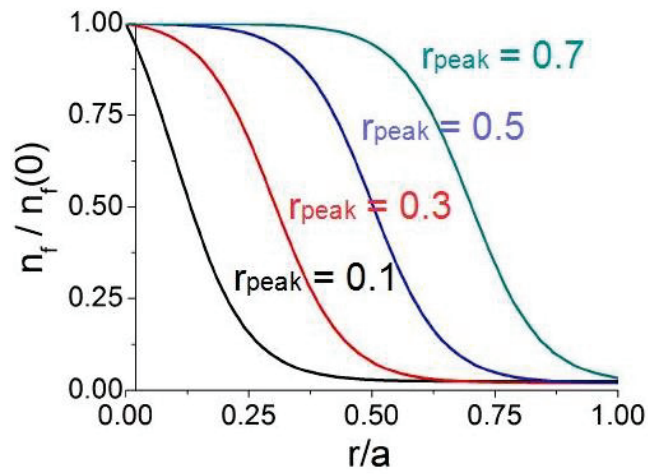


Fig. 3.3.5.2-2 EP density profiles.

Figure 3.3.5.2-3 shows the growth rate and frequency of the $n = 1$ to 4 toroidal families for different EP β and energies. Fig. 3.3.5.2-4 shows the same analysis for the helical families $n = 1, 3$ and $2, 4$.

The analysis of the simulations indicates the destabilization of $n = 1$ to 4 AEs as well as $n = 2, 4$ HAEs in NBI-heated CFQS plasma. The EP β threshold to destabilize AEs is calculated for EP during the slowing down process, that is to say, from weakly thermalized EP ($T_f \geq 25$ keV) to EP at the last stage of the slowing down process ($T_f \leq 15$ keV).

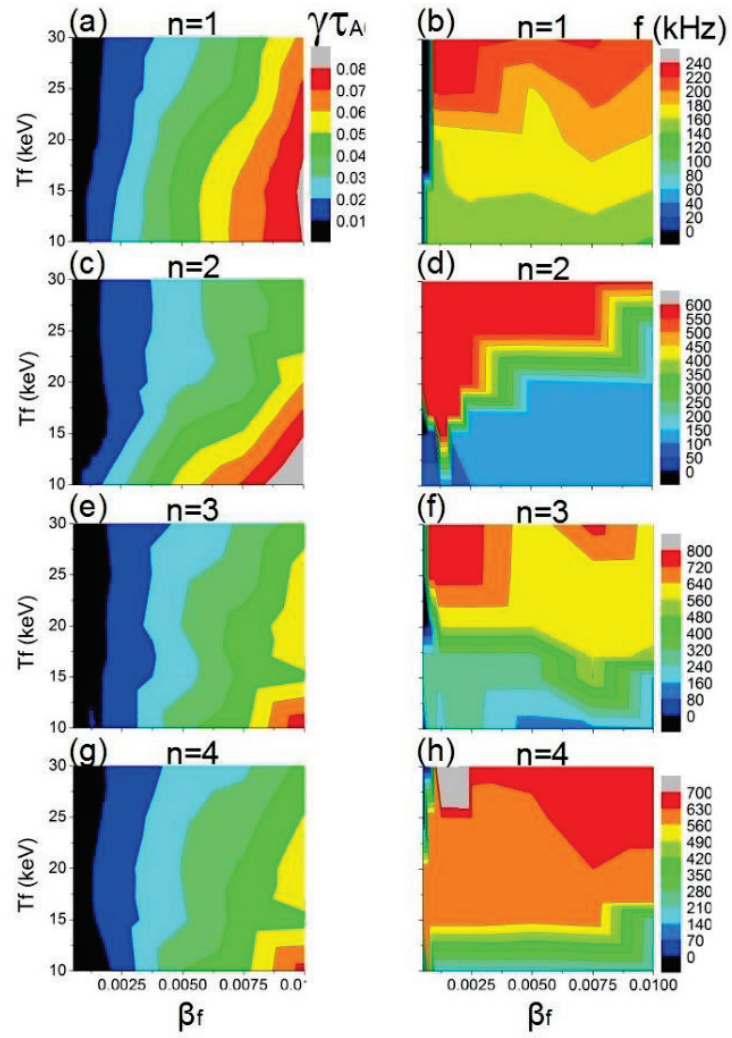


Fig. 3.3.5.1-3 Growth rate and frequency of the $n = 1$ to 4 toroidal mode families for different EP β and energies.

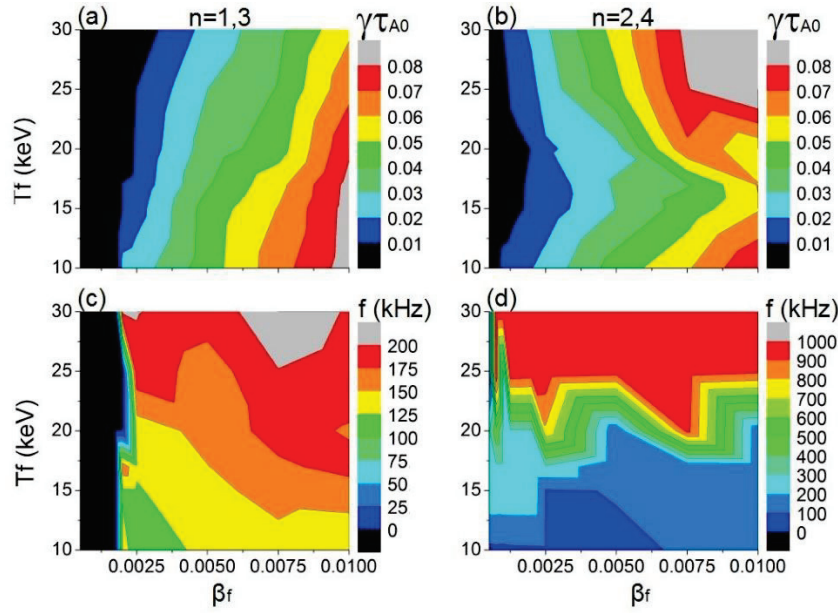


Fig. 3.3.5.1-4 Growth rate and frequency of the $n = 1,3$ and $2,4$ helical modes families for different EP β and energies.

The study of the AE destabilization threshold with respect to the EP β for different EP energies indicates that, an optimized operational regime of the NBI requires a power injection not exceeding EP $\beta = 0.001$ to avoid the destabilization of high frequency AEs (EAE and NAE) by weakly thermalized EP. In addition, TAEs and BAEs that can be triggered by EPs during the slowing down process ($T_f \leq 17$ keV) are stable if EP $\beta < 0.0005$. The simulations performed adding the effect of the helical couplings indicate the possible destabilization of $2/5$ and $2/6$ HAEs by EP with $T_f \geq 15$ keV if EP $\beta \geq 0.0005$. On the other hand, the simulations show stable $n = 1,3$ HAEs. The analysis of the Alfvén gaps indicates narrow $n = 1,3$ HAE gaps with respect to the $n = 2,4$ HAE gaps, thus the continuum damping is strong enough to stabilize the $n = 1,3$ HAE.

Fig. 3.3.5.2-3 indicates the analysis of off-axis NBI models, showing no evident optimization trend with respect to an on-axis NBI injection, because the growth rate of the $n = 1$ AE decreases although the growth rate of the $n = 2-4$ AE increase. On the other hand, there is a transition to lower frequency AEs if the beam is deposited in the middle plasma or the periphery. It should be noted that the effect of the Shafranov shift leads to the outward displacement of the magnetic axis as β_{th} increases, thus the NBI deposition region changes from on-axis in low β operations to off-axis in high β operations. Consequently, a detailed analysis of the AE stability for off-axis NBI depositions is required in high β operations.

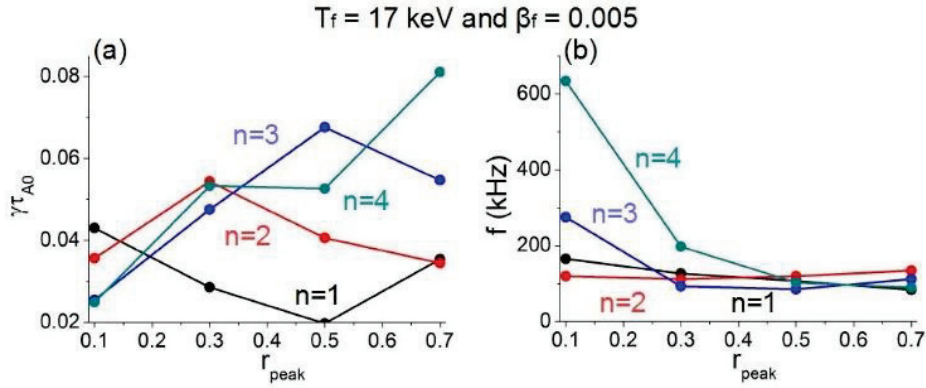


Fig. 3.3.5.2-5 (a) Growth rate and (b) frequency of the $n = 1$ to 4 modes for different locations of the EP radial density profile gradient.

The analysis of the AE stability in models with a finite β_{th} indicates that CFQS operation with high β should have an improved AE stability with respect to low β discharges. High β operations show slender Alfvén gaps, thus the continuum damping is enhanced increasing the EP β threshold required to destabilize the AEs. The simulations show a decrease of the growth rate of the $n = 1$ to 4 AEs as well as the $n = 1, 3$ and $2, 4$ helical families as β_{th} increases. It should be noted that the model assumes an increase of β_{th} caused by a larger thermal plasma density, thus the AE stability trend can be different if the β_{th} increases by a larger thermal plasma temperature. Future analysis will be dedicated to clarify the effect of the thermal plasma temperature on the AE stability in CFQS plasma.

The simulations including the effect of the thermal ion FLR, EP FLR and e-i Landau damping indicate the stabilization of the $n = 1$ to 4 EAE/NAEs triggered in the simulations without damping effects. Also, the $n = 1$ to 4 BAE/TAEs show a lower growth rate and frequency relative to the simulations without damping effects, as well as the improved AE stability of CFQS operational scenarios with a high thermal β .

In summary, the heating efficiency of CFQS plasma heated by a tangential NBI can decrease due to the destabilization of $n = 1$ to 4 BAE/TAEs and $n = 2, 4$ HAEs above a given injection intensity threshold, particularly if the thermal β of the discharge is low. Nevertheless, the heating efficiency can be improved by an optimized NBI operational regime with respect to the NBI voltage, injection intensity and deposition region as well as the thermal plasma parameters. The present analysis will be extended to stellarators that explore different quasi-symmetries, identifying the magnetic configurations that show an optimal AE stability, particularly for reactor-relevant plasma.

References

- [3.3.5.2-1] J. Varela *et al.*, Nucl. Fusion **61** (2021) 026023.
- [3.3.5.2-2] K. C. Shaing *et al.*, Phys. Fluids B **1** (1989) 1663.

3.4 Optimization approach of anomalous transport

3.4.1 Maximum- J

The turbulent fluctuation suppression in the CFQS has got emphasized considerably. The suppression of the turbulent transport due to the sheared flow induced fluctuation decorrelation has been widely investigated, theoretically, leading to the significant progress in the understanding of the improved confinement regime. The other possible mechanism for turbulent suppression has been proposed based on the stabilization of microinstabilities. Several kinds of microinstabilities appear when directions of the diamagnetic drift and ∇B drift (B is the magnetic field strength) are in the same direction for trapped particles [3.4.1-1, 2]. In an axisymmetric configuration, the relevant drift is in the toroidal direction (toroidal precession). The velocity of the toroidal precession can be expressed in terms of the second adiabatic invariance J [3.4.1-3]. Also, the stability condition for microinstabilities is derived [3.4.1-4] with a scalar plasma pressure P as

$$\nabla P \cdot \nabla J > 0,$$

which is frequently called the maximum- J condition; it reduces to $dJ/dr < 0$ for a usual pressure gradient with $dP/dr < 0$. This indicates that microinstabilities can be stabilized or suppressed if the toroidal precession of trapped particles is in a favorable ($dJ/dr < 0$) direction.

Orbits of blocked or helically trapped particles: These particles are located in the region of phase space near the locally trapped- passing boundary. These particles may be regarded as locally trapped for a few bounces but they are able to de-trap collisionlessly. A blocked particle's trajectory is not restricted to a single toroidal segment but extends to neighbouring sections. Such particles are also called transitioning [3.4.1-5]. An illustration of these three types of orbits and a comparison with particle orbits in an axisymmetric plasma is given in Fig. 3.4.1-1.

Without plasma the contour plot of J is shown as a function of the minor radius and the toroidal angle in the Fig. 3.4.1-2. The calculation of J is made by following the particle orbits starting from the outboard side of the torus with different toroidal angles. $\zeta_N = 0$ corresponds to the vertically elongated cross section and $\zeta_N = 0.5$ to the horizontally elongated cross section. When B_{ref} equals 0.95 T, there is no maximum- J region. Whereas B_{ref} equals 0.97 T, the maximum- J region comes up at the core area.

Radial profiles for density and temperature are assumed to be parabolic, $n_e \propto (1-\rho^2)$ and $T_e, T_i \propto (1-\rho^2)$. When $\langle \beta \rangle$ reaches 1 %, the neoclassical bootstrap current of 30 kA is expected. The change of the rotational transform profile with beta is shown in Fig. 3.4.1-3. As $\langle \beta \rangle$ increases the region of the reversal magnetic shear near the magnetic axis appears and increases. In these equilibria the contour plots of J are given with $B_{ref} = 0.91$ T in Fig. 3.4.1-4 and $B_{ref} = 0.93$ T in Fig. 3.4.1-5, respectively. It is found that as the beta increases the region of the maximum- J increases in the core region.

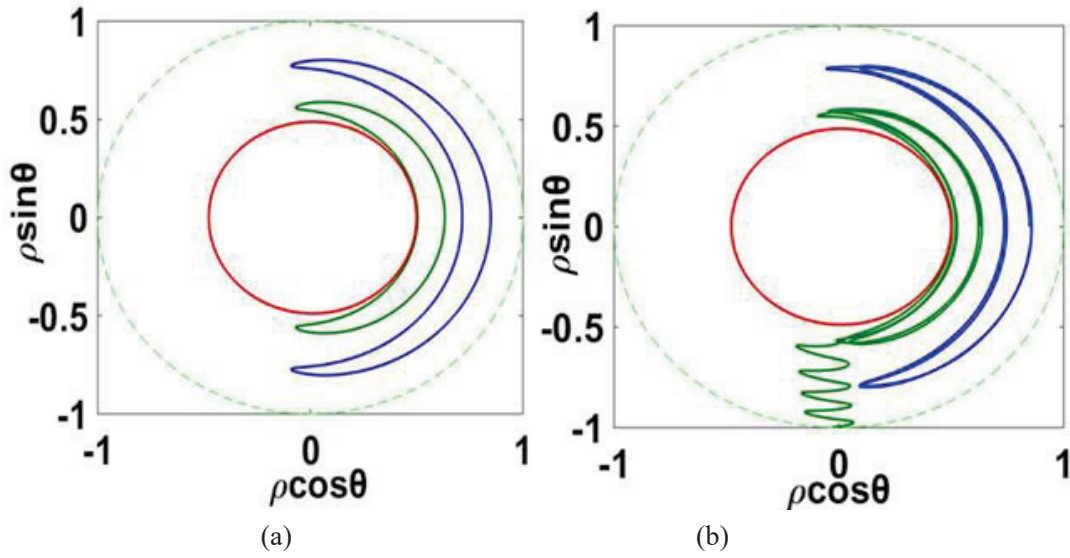


Fig. 3.4.1-1 Examples of the main orbit topologies in a perfect axisymmetric system and a CFQS. The dashed line represents the LCFS for each case. Guiding center (GC) orbits of (a) passing particle (red, $B_{ref} = 1.5$) and toroidally trapped particles (green, $B_{ref} = 0.94$ and blue, $B_{ref} = 0.98$) in axisymmetric equilibrium. GC orbits of (b) passing particle (red, $B_{ref} = 1.5$) and toroidally trapped particles (green, $B_{ref} = 0.94$ and blue, $B_{ref} = 0.98$) in the CFQS equilibrium. Particle (green) drifts radially due to ripple banana diffusion and is trapped in local ripple well, and is finally lost.

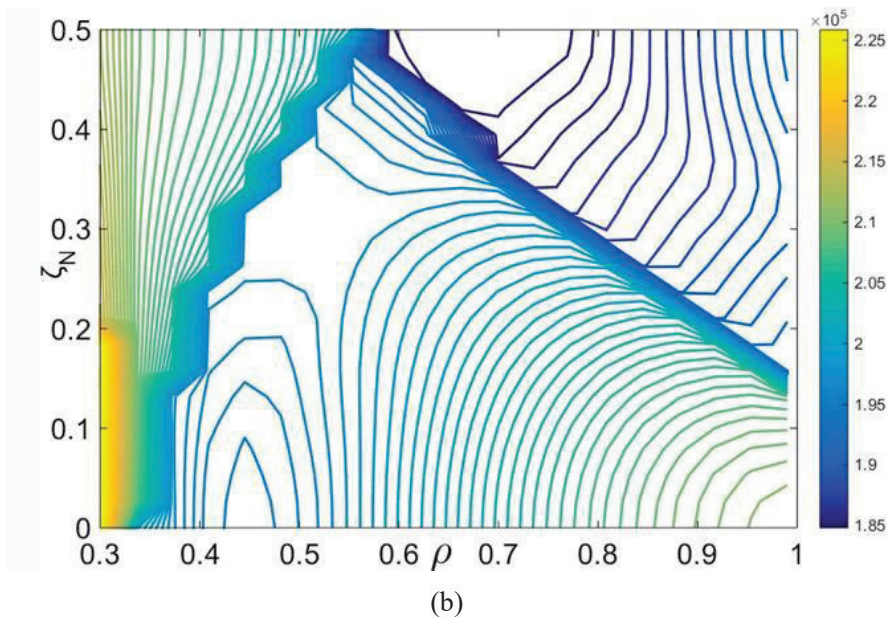
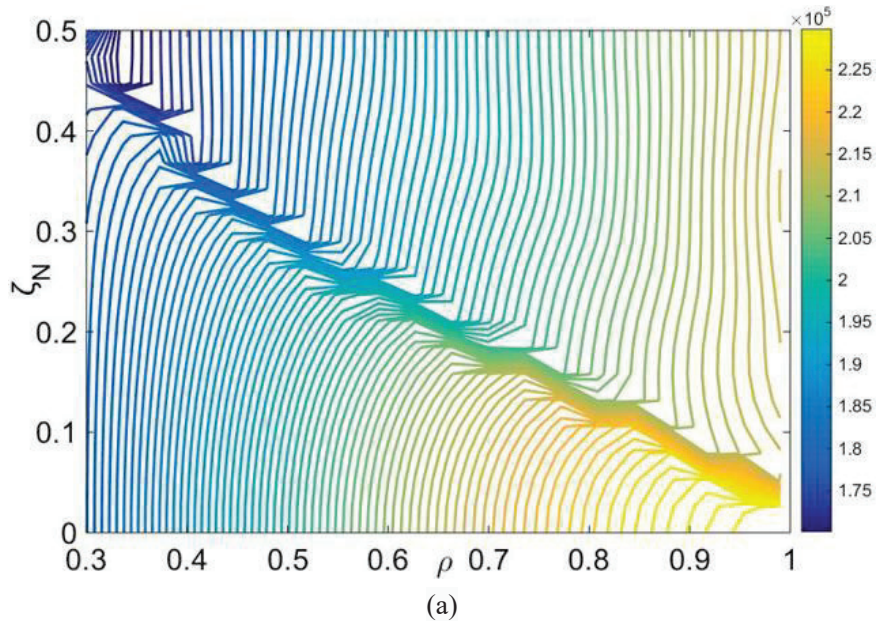


Fig. 3.4.1-2 Contour J on the (ρ, ζ_N) plane. (a) B_{ref} equal to 0.95 T, without maximum- J region (b) B_{ref} equal to 0.97 T, with maximum- J region.

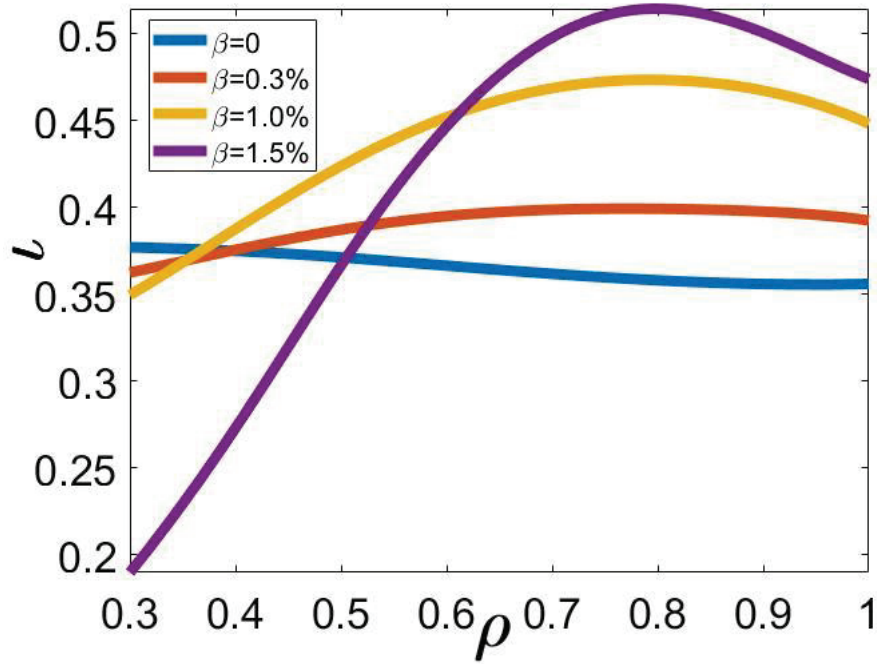


Fig. 3.4.1-3 Radial profiles of the rotational transform considering the neoclassical bootstrap current.

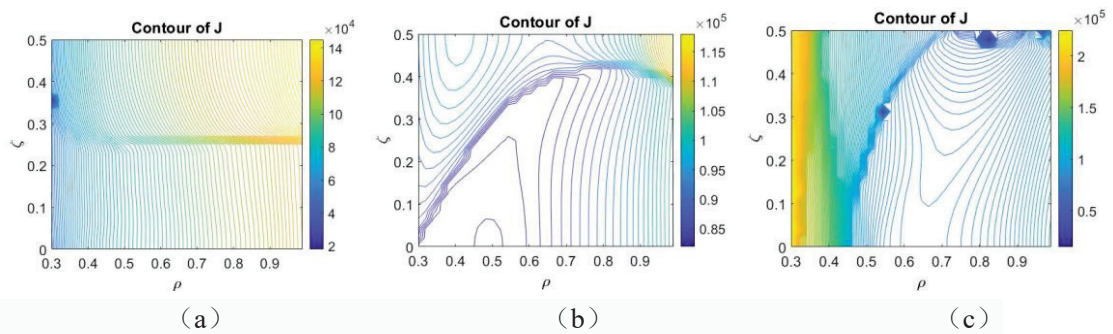


Fig. 3.4.1-4 Contour J on the (ρ, ζ) plane, B_{ref} equal to 0.91 T, $\langle \beta \rangle = 0.3\%$ for (a), $\langle \beta \rangle = 1.0\%$ for (b), and $\langle \beta \rangle = 1.5\%$ for (c).

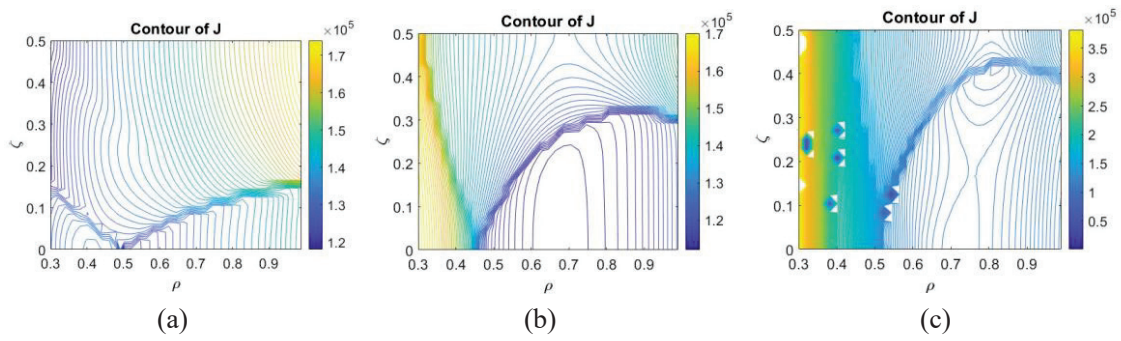


Fig. 3.4.1-5 Contour J on the (ρ, ζ) plane, B_{ref} equal to 0.93 T, $\langle \beta \rangle = 0.3\%$ for (a), $\langle \beta \rangle = 1.0\%$ for (b), and $\langle \beta \rangle = 1.5\%$ for (c).

References

- [3.4.1-1] H. P. Furth and M. N. Rosenbluth, 1969 Proc. Conf. 3rd Int. on Plasma Physics and Controlled Nuclear Fusion Research (Novosibirsk, 1968) vol. **1** (Vienna: IAEA) p 821.
- [3.4.1-2] B. B. Kadomtsev and O. P. Pogutse, 1970 Reviews of Plasma Physics vol. **5** (New York, London: Consultants Bureau) p 249.
- [3.4.1-3] B. B. Kadomtsev and O. P. Pogutse, Nucl. Fusion **11** (1971) 67.
- [3.4.1-4] R. J. Hastie *et al.*, Ann. Phys. **41** (1967) 302.
- [3.4.1-5] C. D. Beidler *et al.*, Phys. Plasmas **8** (2001) 2731.

3.4.2 Micro instability

The linear ion temperature gradient (ITG)-driven instability is examined by means of the electromagnetic gyrokinetic Vlasov simulations with GKV [3.4.2-1], where a local flux-tube at the mid-minor radius of $\rho = 0.5$ in the vacuum equilibrium is considered. An axisymmetric limit with the same rotational transform, the magnetic shear, and the aspect ratio is compared to identify the impact of non-axisymmetric geometry on the microinstability properties, where the circular poloidal cross section is assumed for the simplicity. The linear growth rate spectra of the ITG mode at $R_{ax}/L_n = 0$ is shown in Fig. 3.4.2-1, where the electrons are assumed to be adiabatic here. It is found that the CFQS has more unstable ITG modes with higher growth rate $\gamma R_{ax}/\nu_{ti}$ in a wider range of the wavenumber space $k_\theta \rho_{ti}$, compared with that in the axisymmetric limit [3.4.2-2]. The difference is mainly associated with the geometric structures appearing in the squared perpendicular wavenumber $(k_\perp \rho_{ti})^2$, which provides the finite Larmor radius (FLR) stabilization of the ITG modes. It is known that the density gradient can also affect ITG modes. The linear growth rate spectra of ITG modes at $R_{ax}/L_n = 8$ is shown in Fig. 3.4.2-2. From Fig. 3.4.2-1 and Fig. 3.4.2-2, there is a critical temperature gradient for ITG modes. If R_{ax}/L_{ti} exceeds this critical gradient, the ITG mode is unstable. As R_{ax}/L_{ti} increases, ITG modes become more unstable, and as density gradient R_{ax}/L_n increases, the $k_\theta \rho_{ti}$ of the most unstable mode shifts to a higher $k_\theta \rho_{ti}$. Fig. 3.4.2-3 shows the relationship between the maximum growth rate of ITG modes and R_{ax}/L_n . From the figure it is found a moderate R_{ax}/L_n can destabilize ITG modes but for a large R_{ax}/L_n the growth of ITG mode is strongly suppressed. If R_{ax}/L_n is negative, *i.e.* a hollow density profile, even if R_{ax}/L_n is small, ITG modes are suppressed. The growth rate of ITG modes almost increases linearly with R_{ax}/L_{ti} for any R_{ax}/L_n . By fitting these lines, the threshold of the critical temperature gradient for ITG modes can be gotten. A negative R_{ax}/L_n enhances this threshold, and a positive R_{ax}/L_n can reduce the threshold firstly and then enhances the threshold as R_{ax}/L_n increases. From Fig. 3.4.2-4, the relationship between growth rate and R_{ax}/L_n is very clear. As R_{ax}/L_n increases, the growth rate firstly increases and then decreases. For a negative R_{ax}/L_n , ITG modes are always suppressed and their growth rate decreases as the absolute value of R_{ax}/L_n increases. From the previous results, a large R_{ax}/L_n or density peaking can strongly stabilize ITG modes [3.4.2-3].

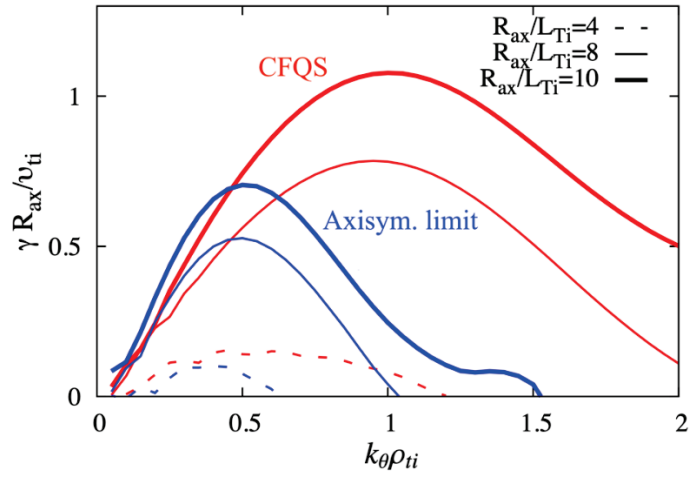


Fig. 3.4.2-1 Linear growth rate spectra for the ITG mode in CFQS and the axisymmetric limit (Axisym. limit) for several cases of the normalized ion temperature gradient parameters $R_{ax}/L_{Ti} = -R_{ax}d(\ln T_i)/dr$ at $R_{ax}/L_n = -R_{ax}d(\ln n)/dr = 0$.

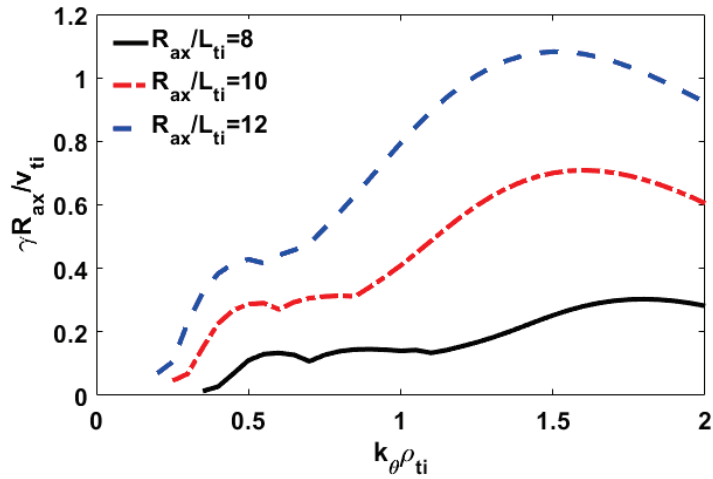


Fig. 3.4.2-2 Linear growth rate spectra for the ITG mode in CFQS for several cases of the normalized ion temperature gradient parameters R_{ax}/L_{Ti} at $R_{ax}/L_n = 8$.

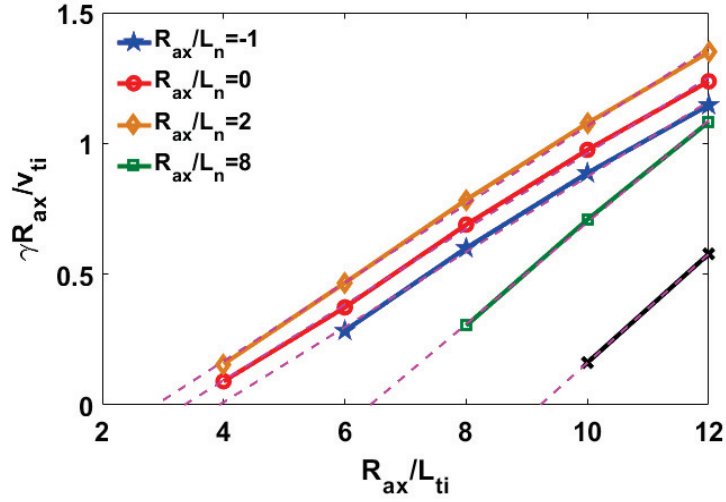


Fig. 3.4.2-3 The maximum growth rate of electrostatic ITG modes in CFQS vs. R_{ax}/L_{ti} for various R_{ax}/L_n . The dashed lines are the fitted lines of the corresponding lines of growth rate.

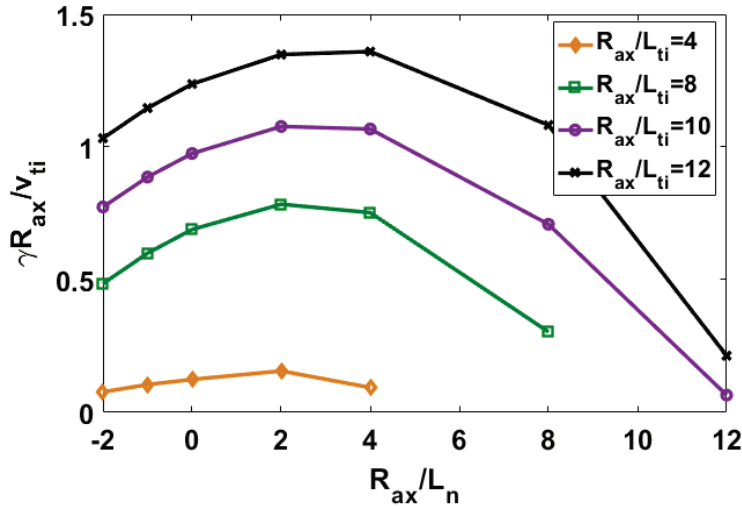


Fig. 3.4.2-4 The maximum growth rate of electrostatic ITG modes in CFQS vs. R_{ax}/L_n for various R_{ax}/L_{ti} .

To scan R_{ax}/L_n and R_{ax}/L_{ti} , the ITG growth rates vs. R_{ax}/L_n and R_{ax}/L_{ti} are shown in Fig. 3.4.2-5. The ITG mode with the largest growth rate is located at the region with the largest R_{ax}/L_{ti} and a moderate $R_{ax}/L_n \sim 4$. The growth of ITG mode depends on the competition between the driving of R_{ax}/L_{ti} and damping of R_{ax}/L_n . To compare with the NCSX results [3.4.2-4], the relationship between the growth rate of ITG modes and R_{ax}/L_{ti} and R_{ax}/L_n in CFQS and NCSX are very similar. It reveals that this relationship is rarely affected by the difference between the CFQS and NCSX magnetic configurations.

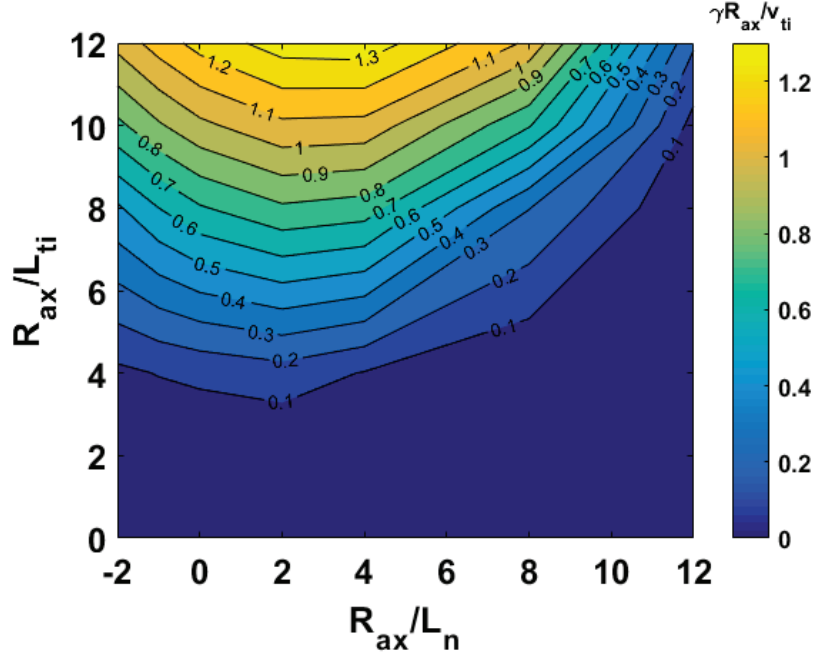


Fig. 3.4.2-5 The maximum growth rates of electrostatic ITG modes vs. R_{ax}/L_n and R_{ax}/L_{ti} .

The nonlinear ITG turbulence simulation has also been carried out. As shown in Fig. 3.4.2-6 (a), we observe that the saturated turbulent transport level Q_t/Q_{GB} in the CFQS is comparable or less than that in the axisymmetric limit. It is also found from Fig. 3.4.2-6 (b) that the CFQS indicates a relatively stronger zonal-flow generation W_{ZF}/W_{total} , in comparison to the axisymmetric limit. The magnetic fluctuations effects in the finite β cases, which can destabilize the kinetic ballooning modes (KBM) and micro tearing modes (MTM), will be investigated in the future works.

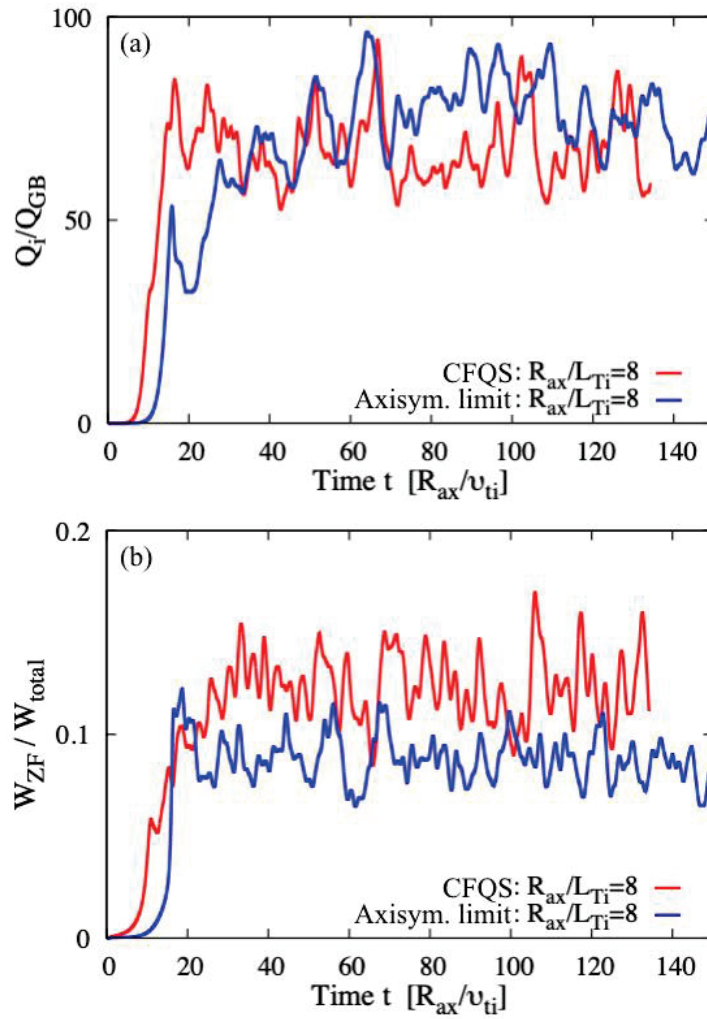


Fig. 3.4.2-6 Nonlinear GKV simulation results of (a) the ion turbulent heat flux Q_i / Q_{GB} and (b) the zonal flow energy normalized by the total energy W_{ZF} / W_{total} in the ITG-driven turbulence in the CFQS and the axisymmetric limit (Axisym. limit).

References

- [3.4.2-1] T. -H. Watanabe and H. Sugama, Nucl. Fusion **46** (2006) 24.
- [3.4.2-2] M. Nakata *et al.*, “Turbulent transport and zonal flow generation in quasi-axisymmetric stellarator”, The 27th International Toki Conference and the 13th Asia Pacific Plasma Theory Conference (2018) O-1.
- [3.4.2-3] M. Romanelli, C. Bourdelle, W. Dorland, Phys. Plasmas **11** (2004) 3845.
- [3.4.2-4] J. A. Baumgaertel *et al.*, Phys. Plasmas **19** (2012) 122306.

3.4.3 Plasma rotation

In conventional helical devices, an impact of radial electric field on plasma confinement has extensively been investigated so far. It is one of the major issues also in a QA device because plasma rotation, which is closely related to radial electric field, can be driven more easily, and because anomalous transport can be possibly reduced by controlling plasma rotation/flow. Since the discovery of H-mode in tokamaks, the roles of shear flow on an improved confinement have been widely understood also in helical systems; *e.g.*, high ion/electron temperature modes [3.4.3-1,2]. Consequently, the reduction of anomalous transport by shear flow has become a general issue in toroidal plasmas.

Unlike tokamaks, radial electric field or plasma rotation in helical devices are determined by a solution of an ambipolar condition according to the neoclassical theory. Also, toroidal plasma rotation tends to be dissipated in conventional helical systems because of larger toroidal viscosity which originates from larger toroidal ripple of magnetic field strength [3.4.3-3]. According to theoretical studies on tokamaks, transport barriers are established by a positive feedback mechanism that reduces the transport coefficients through the increase in local pressure gradient. Radial electric field (or plasma flow), which is strongly correlated with the local pressure gradient, is a key parameter for the mechanism mentioned above. In order to promote such spontaneous growths of shear flow and pressure gradient, plasma flow should be free from any constraints.

In conventional helical devices such as CHS, plasma mainly rotates poloidally because of larger toroidal viscosity. In this situation, Pfirsch-Schlüter-type return flow should exist so as to satisfy incompressibility, which can possibly be dissipated by helical ripple [3.4.3-4]. Therefore, it is quite difficult to drive high speed plasma rotation in conventional helical systems due to large parallel viscosity both in toroidal and poloidal directions. Indeed, the radial electric field strengths observed in CHS and Heliotron-E are around 100 V/cm at most. Furthermore, the scale length of the radial electric field tends to be longer, which leads to weaker shear. Consequently, tokamak-like transition phenomena relevant to edge transport barrier have never been observed so far in helical systems.

In order to establish transport barriers, a magnetic configuration should be free from any constraints of plasma flow due to parallel viscosity. This expanded parameter range of plasma rotation is one of the reasons why we adopt the QA configuration, which is ideal for reducing toroidal viscosity as well as achieving low aspect ratio and incompressible flow at the same time.

In QA configuration, ripple trapped particles can be suppressed by reducing residual ripple. In such a situation, according to the neoclassical theory, confinement property is similar to that in an axisymmetric system. That is to say, values of radial electric field are never restricted by the ambipolar condition, which is a characteristic feature not found in the other optimized stellarators. As described below, the residual ripple in a QA configuration is drastically reduced in comparison with CHS.

In the earlier experiments in tokamaks and helical devices, it has been found that the plasma current, plasma rotation (or radial electric field) are well explained by the neoclassical theory, while particle/heat transport is dominated by anomalous transport [3.4.3-5]. The plasma rotation interpreted by the neoclassical theory gives a good hint to study the anomalous transport. Also, it is important to study the neoclassical theory itself as it is still incomplete for non-axisymmetric systems. In addition, it would be also important to investigate whether the neoclassical theory can predict neoclassical bootstrap current, toroidal viscosity and radial electric field in a QA configuration with non-axisymmetric perturbation.

Neoclassical parallel viscosity is roughly proportional to the square of the magnetic field ripple strength defined by $\gamma^2 = \langle (\delta B / \delta s)^2 / B^2 \rangle$, where $\delta / \delta s$ is differential with respect to the flow direction and $\langle \rangle$ denotes averaging on a magnetic surface. This parameter should be quantitatively evaluated from the calculations including all of the Fourier components of the field strength B because higher order mode may largely contribute to the value of γ . Since the calculation of γ for the CFQS configuration has not been carried out yet, the results for the CHS-qa configuration [3.4.3-6] are shown hereafter. In principle, similar results are expected in the CFQS.

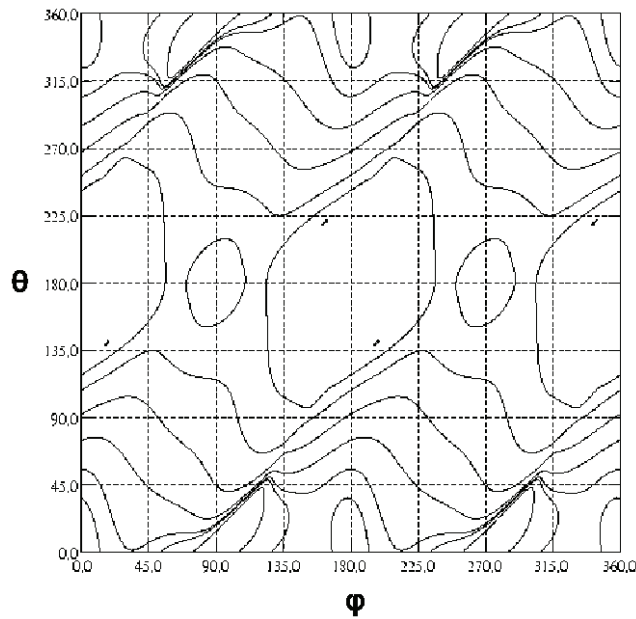


Fig. 3.4.3-1 Contour plot of B for the LCFS of CHS-qa (2w39) configuration.

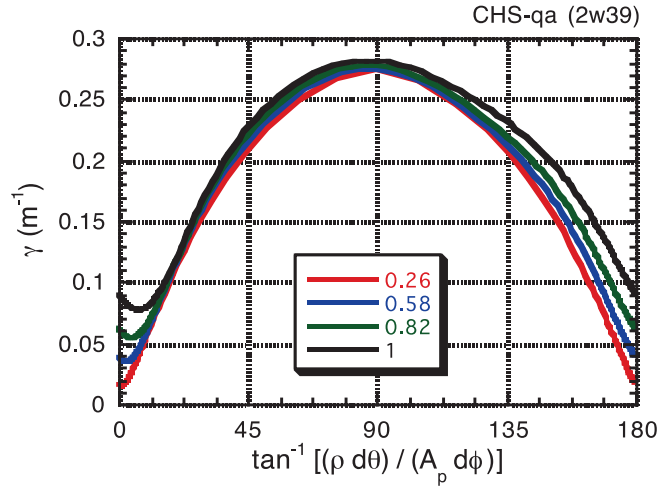


Fig. 3.4.3-2 Angle dependence of γ for CHS-qa (2w39) configuration.

Fig. 3.4.3-1 shows a contour plot of B on the LCFS of a reference configuration of CHS-qa (2w39). The grid data for B in cylindrical coordinates (R, Z, Φ) are constructed from the result of VMEC code calculation. Toroidal (ϕ) and poloidal (θ) angles are expressed in real coordinates, and $\theta = \tan^{-1}[(R - R_{ax}) / (Z - Z_{ax})]$, where R_{ax} and Z_{ax} are R and Z values at the magnetic axis in an equal ϕ plane, respectively. This means that the effect of the excursion of the magnetic axis is ignored in the calculation. We assumed a flow direction expressed by a straight line in this ϕ - θ plane. When averaging, we fixed the angle of $\delta/\delta s$ direction with respect to the toroidal direction ($=\tan^{-1}(r \theta / R \phi)$).

Fig. 3.4.3-2 shows the calculated dependence of γ for CHS-qa (2w39) on the flow direction at the four different flux surfaces (normalized minor radii of 0.26, 0.58, 0.82, and 1.0). As shown, the values of γ have peaks around 90 degrees in the QA configuration, which indicates larger parallel viscosity in the poloidal direction. In the toroidal direction, γ is less than 0.1 even in the LCFS, which implies that perpendicular/anomalous viscosity plays an important role for determining toroidal rotation speed in a similar way to tokamaks. Though the effect of coil ripples is not included in the present calculation, the angle minimizing γ is not zero but $1.1 \sim 6.8$ degrees unlike tokamaks, which is considered to be the effect of residual non-axisymmetric components.

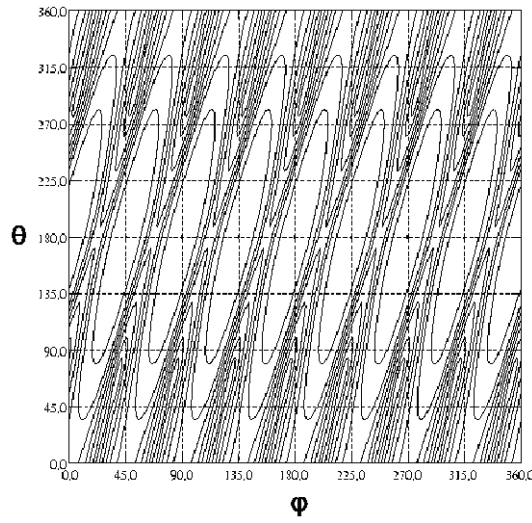


Fig. 3.4.3-3 Contour plot of B for the LCFS of CHS ($R_{ax} = 92.1$ cm) configuration.

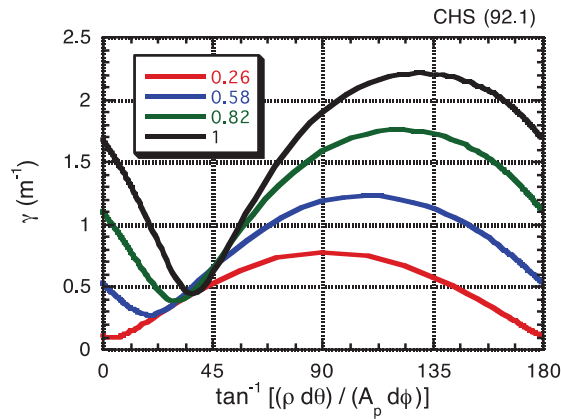


Fig. 3.4.3-4 Angle dependence of γ for CHS ($R_{ax} = 92.1$ cm) configuration.

For the comparison with a conventional helical device, the calculation of γ has been performed for a representative configuration of CHS. The contour of B on the LCFS and the results of the γ calculation are shown in Fig. 3.4.3-3 and Fig. 3.4.3-4, respectively, in a similar way to the CHS-qa. The angle minimizing γ is around 40 degrees, which indicates that the flow tends to be driven along the helical structure ($m = 2, n = 1$) of the CHS configuration. Nevertheless, this minimum value of γ in CHS is still larger than the maximum value of γ along the poloidal direction in CHS-qa. Therefore, high-speed toroidal rotation cannot be driven in CHS because of strong toroidal viscosity, as demonstrated in the previous CHS experiment.

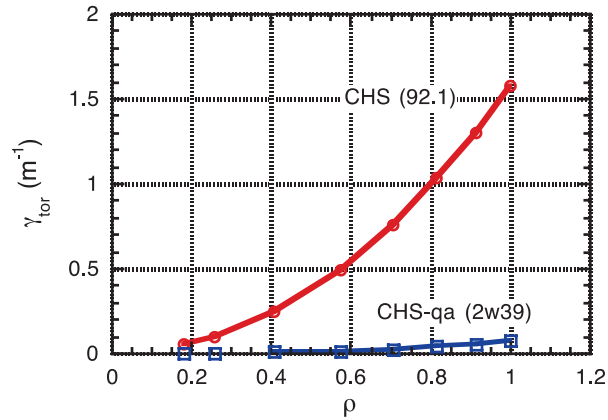


Fig. 3.4.3-5 Dependence of toroidal γ on minor radius for CHS-qa and CHS.

In reality, the direction of plasma flow cannot be expressed simply by a straight line in real coordinates. Experimental results in CHS suggests that the spontaneous rotation, which is driven without external momentum input (with NBI), tends to be driven along the direction minimizing parallel viscosity. In a QA configuration, this direction is the toroidal direction in the Boozer coordinates. Therefore, we have also calculated γ with the angle of $\delta/\delta s$ direction fixed in the Boozer coordinates. Fig. 3.4.3-5 shows γ in the toroidal direction as a function of normalized minor radius for CHS and CHS-qa. As shown, γ_{tor} in CHS-qa is much smaller than that in CHS, which implies tokamak-like nature of a QA configuration with respect to plasma rotation.

References

- [3.4.3-1] K. Ida *et al.*, Phys. Rev. Lett. **76** (1996) 1268.
- [3.4.3-2] A. Fujisawa *et al.*, Phys. Rev. Lett. **79** (1997) 1054.
- [3.4.3-3] K. Ida *et al.*, Phys. Rev. Lett. **67** (1991) 58.
- [3.4.3-4] S. Nishimura *et al.*, Phys. Plasmas **7** (2000) 437.
- [3.4.3-5] O. Okamoto, NIFS-PROC-**25** (1995).
- [3.4.3-6] C. Suzuki *et al.*, Plasma Phys. Control. Fusion **44** (2002) A225.

3.5 Energetic particle

Energetic alpha particles produced by the d-t reaction will play an essential role in sustaining a self-ignition condition in burning plasma in the future. When alpha particles are substantially lost from the plasma, the self-ignited state is easily terminated. Moreover, the localized heat load on the first wall due to the impact of the escaping alphas may seriously damage the device. Because of the reason above, a great deal of attention has to be paid to physics issues related to energetic ions such as the magnetic field ripple transport, anomalous transport and/or loss caused by MHD instabilities. Note that although neoclassical transport in CFQS is outstandingly reduced, it does not always guarantee good energetic-ion confinement. Since QAS is quite similar to tokamak in magnetic field structure, EP orbits in QAS is also quite similar to those in tokamak [3.5-1~5].

References

- [3.5-1] M.H. Redi *et al.*, Phys. Plasmas **6** (1999) 3509.
- [3.5-2] M. Isobe *et al.*, J. Plasma Fusion Res. SERIES **6** (2004) 622.
- [3.5-3] H.W. Kugel *et al.*, Fusion Sci. Technol. **51** (2007) 203.
- [3.5-4] S. Murakami *et al.*, Proceedings of 1997 International Symposium on Plasma Dynamics in Complex Electromagnetic Fields ~ for Comprehension of Physics in Advanced Toroidal Plasma Confinement ~, 8-11 December, 1997. **IAE-RR-98 054**, March 1998, pp. 137-140.
- [3.5-5] D. A. Spong *et al.*, Phys. Plasmas **18** (2011) 056109.

3.5.1 NBI deposition analysis

To obtain high plasma parameter and to study the beam ion confinement in QA configuration, the installation of neutral beam (NB) injector is planned with CFQS. Feasibility study of NB injection on CFQS is performed using the beam deposition calculation code and the guiding center orbit following code [3.5.1-1]. Fig. 3.5.1-1 shows the schematic drawing of the CFQS with NB injector. According to the CAD modeling including the coil case, the VV, and the coil supporting structure, the possible injection angle of NBI is from 44 degrees to 52 degrees [3.5.1-2]. Here, we considered to use an NB injector operated in the CHS [3.5.1-3] with injection energy and power of 30 keV and 0.9 MW.

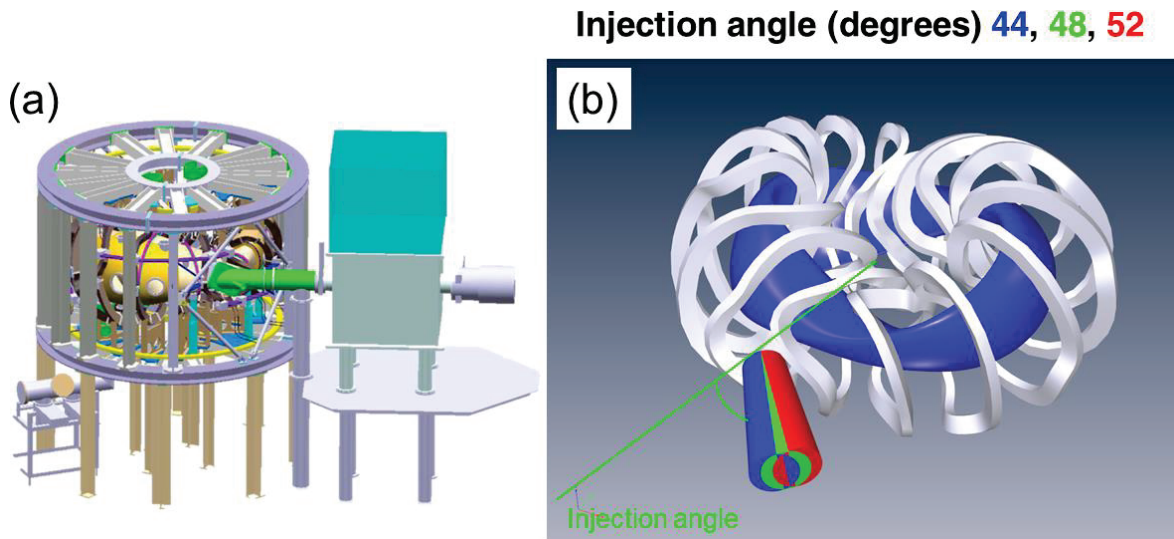


Fig. 3.5.1-1 (a) Schematic drawing of CFQS with NB injector, (b) Possible NB injection lines.

Deposition fraction on NB injection angle was surveyed by means of HFREYA code which is deposition calculation code using the Monte Carlo methods [3.5.1-4]. Here, the plasma parameter is assumed to be parabolic profile, *i.e.*, $\sim (1-(r/a)^2)^2$. The central electron temperature T_{e0} is given using central electron density n_{e0} with $T_{e0} = 2.0/n_{e0}$ (10^{19} m^{-3}) in order to maintain the plasma stored energy. We changed NB injection angle from 44 to 52 degrees with 2 degrees steps. Fig. 3.5.1-2 shows the deposition fraction of NB injection as a function of line-averaged electron density (n_{e_avg}). The deposition fraction rapidly increases with n_{e_avg} at n_{e_avg} of less than $4 \times 10^{19} \text{ m}^{-3}$. The maximum deposition fraction is obtained with NB injection angle of from 44 to 48 degrees.

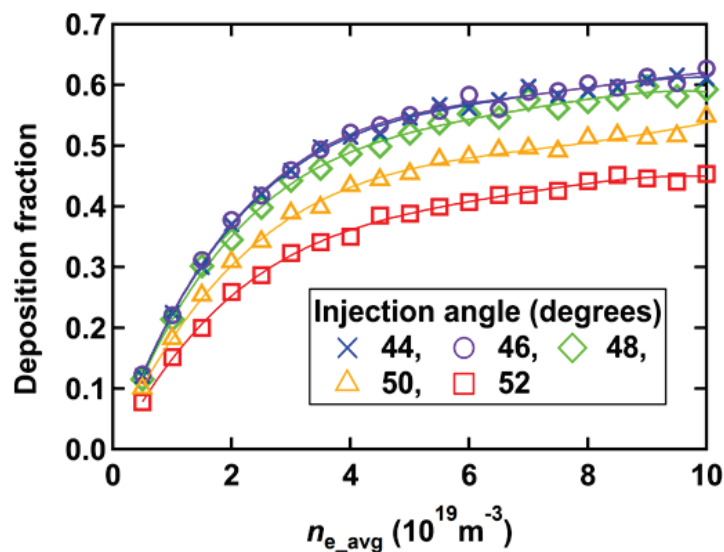


Fig. 3.5.1-2 Dependence of deposition fraction of NB on line-averaged electron density.

The beam ion orbit calculation is performed by the guiding center orbit following code in the Boozer coordinates DELTA5D [3.5-5] in order to evaluate the beam ion confinement. Fig. 3.5.1-3 shows the Poincaré plots of typical collisionless orbit of co-going transit ion (H^+) at B_t of 1 T in toroidal angles of 90 and 180 degrees. Here, beam ion energy and pitch angle are 30 keV and 22 degrees, respectively. The deviation of orbit from the magnetic flux surfaces is relatively large due to the relatively low magnetic field strength and the relatively low rotational transform. Beam ion confinement is evaluated using DELTA5D code including beam-plasma collision. Here, we randomly choose 1000 beam ions injected by co-inject NB and followed in thermalization time of beam ions (~ 50 ms). Time evolution of loss energy of beam ions as a function of time is plotted in Fig. 3.5.1-4 (a). Here, calculation is performed with n_{e_avg} of $2 \times 10^{19} \text{ m}^{-3}$. Loss energy gradually increases with time until t of 25 ms, and then is almost saturated. We obtained relatively low loss energy at the injection angle of 48 to 52 degrees. Fig. 3.5.1-4 (b) shows the loss energy at t of 50 ms as a function of n_{e_avg} . The loss energy slightly increase with the n_{e_avg} . The loss energy at 50 ms is relatively lower at the injection angle of 48 to 52 degrees when $n_{e_avg} < 4 \times 10^{19} \text{ m}^{-3}$. This is because the fraction of beam ions deposited in smaller R region, where the confinement of co-passing beam ion seems to be worse due to the large outward deviation of orbit becomes larger with the decrease of the injection angle. It seems that the injection angle of 48 degrees is more favorable regarding deposition and beam ion confinement.

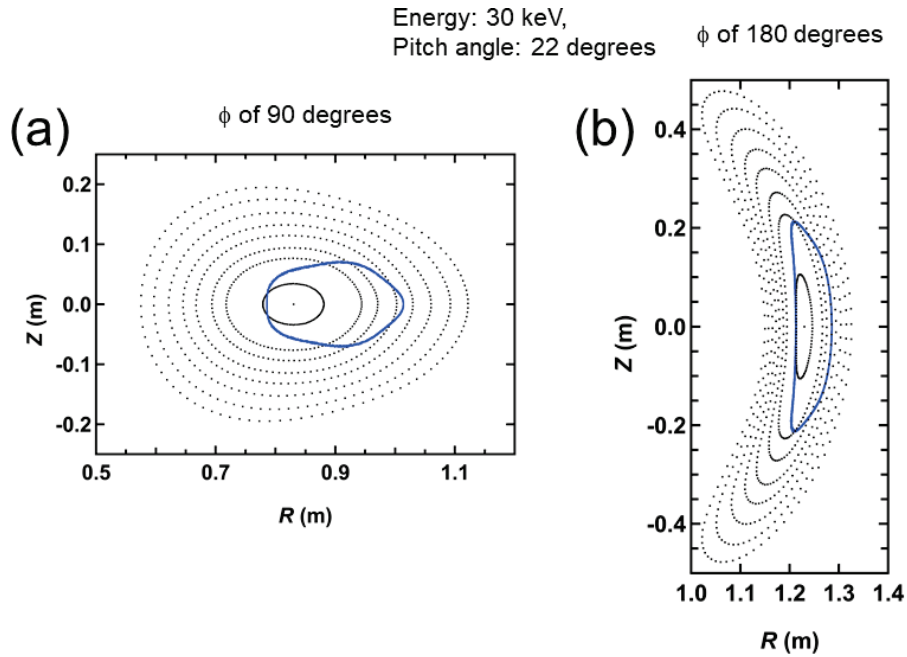


Fig. 3.5.1-3 Poincaré plots of typical co-going transit beam ion orbit at two different toroidal angles, (a) 90 degrees, and (b) 180 degrees.

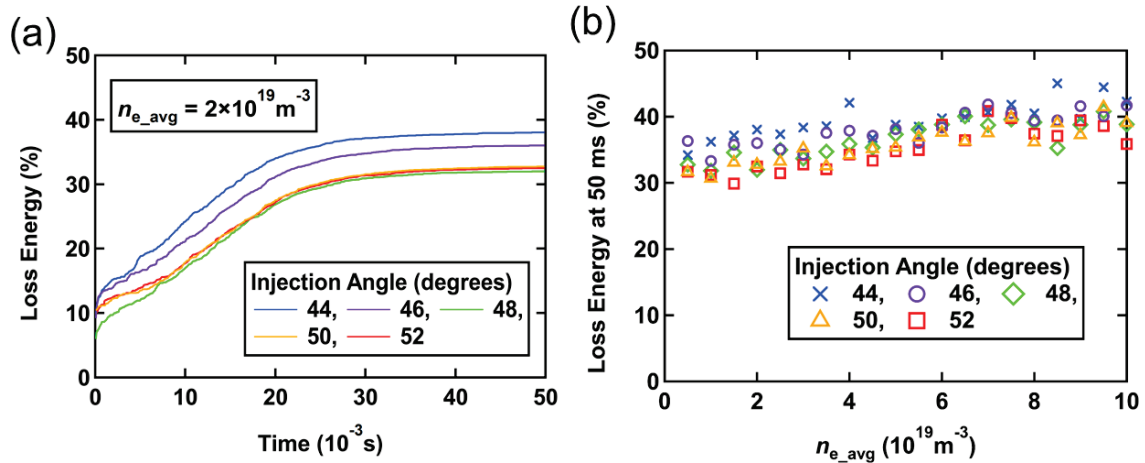


Fig. 3.5.1-4 (a) Time evolution of loss energy of beam ions. (b) Loss energy at 50 ms as a function of line-averaged electron density.

References

- [3.5.1-1] K. Ogawa *et al.*, Plasma Fusion Res. **14** (2019) 3402067.
- [3.5.1-2] S. Kinoshita *et al.*, Plasma Fusion Res. **14** (2019) 3405097.
- [3.5.1-3] K. Matsuoka *et al.*, Plasma Phys. Control. Fusion **42** (2000) 1145.
- [3.5.1-4] S. Murakami *et al.*, Trans. Fusion Technol. **27** (1995) 256.

3.5.2 Feasibility study of fast ion loss diagnostics

The velocity distribution of loss flux of escaping fast ion is essential information in understanding confinement-loss boundary and fast ion transport due to MHD instabilities. Fast ion loss detector (FILD) [3.5.2-1], which provide the energy and the pitch angle of escaping fast ion, has been employed in tokamaks and stellarator/helical devices. Feasibility study of fast ion loss diagnostics has been performed using DELTA5D and LORBIT codes [3.5.2-2]. DELTA5D code is used for calculating the guiding center orbit from the birth position of NB ion including the slowing down with bulk plasma in the Boozer Coordinates until the beam ion reaches the LCFS or is thermalized. Then, LORBIT code [3.5.2-3] is utilized to calculate the collisionless Larmor orbit from the LCFS position where the beam ion reached. Fig. 3.5.2-1 shows the distribution of loss points of beam ion on the vacuum vessel. The lost points mainly appear at the upper side of the vacuum vessel due to the gradient magnetic field drift.

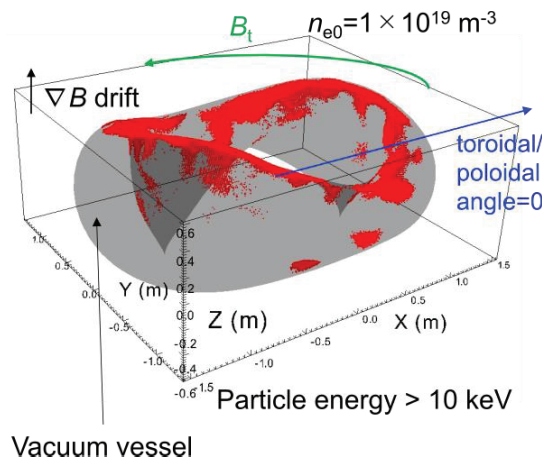


Fig. 3.5.2-1 Three-dimensional plot of beam ion loss point on the vacuum vessel at n_{e0} of $1 \times 10^{19} \text{ m}^{-3}$.

The candidate positions for a stacking-foil-type and scintillator-type FILDs were investigated regarding the beam ion loss distribution on the vacuum vessel. Fig. 3.5.2-2 shows the candidate location of FILDs considered in this analysis. A point at the upper side of the vacuum vessel, where relatively high beam loss flux is expected, is chosen as the candidate position for the stacking-foil-type FILD. Three different toroidal locations are selected for scintillator-based FILDs.

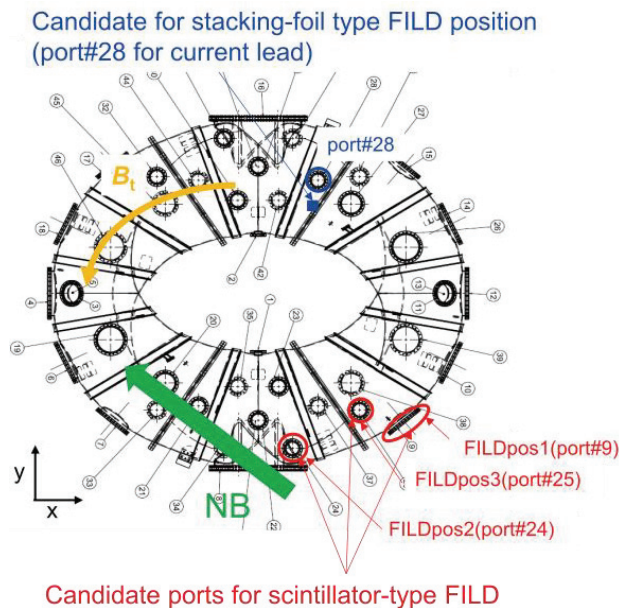


Fig. 3.5.2-2 The candidate location of FILDs.

The calculation shows that some energetic ions having an energy greater than 20 keV reaches stacking-foil-type FILD position. Fig. 3.5.2-3 shows the energy and pitch angle distributions of beam ions detected by the FILD at $R = 1.28 \text{ m}$ for FILDpos1, $Z = 0.02 \text{ m}$ for FILDpos2, and $Z = 0.25 \text{ m}$ for FILDpos3. In these cases, the three spots that exist for energy/pitch angle are $\sim 10 \text{ keV}/\sim 70 \text{ deg.}$, ~ 10

keV/100 deg., and ~ 25 keV/140 deg. The former two spots correspond to the barely-trapped ion, whereas the third spot corresponds to the co-going ions near the injection energy. An experimental study of energy/pitch angle resolved toroidal/poloidal distribution of beam ion losses due to magnetic field ripples as well as MHD instabilities becomes prospective for the first time in QA stellarator using the multiple fast ion loss diagnostics.

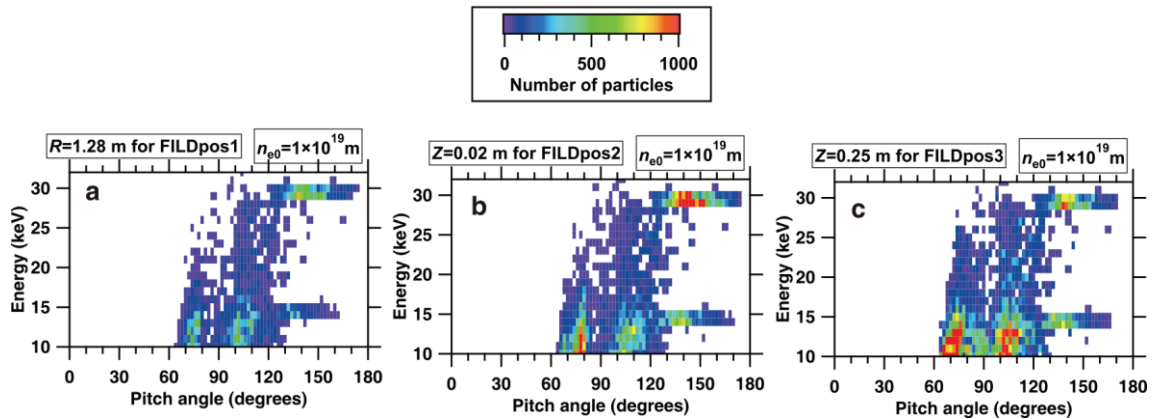


Fig. 3.5.2-3 Beam ion energy and pitch angle distribution at (a) FILDpos1, (b) FILDpos2, and (c) FILDpos3.

References

- [3.5.2-1] S. J. Zweben, Rev. Sci. Instrum. **60** (1989) 576.
- [3.5.2-2] K. Ogawa *et al.*, J. Instrum. **16** (2021) C09029.
- [3.5.2-3] M. Isobe *et al.*, J. Plasma Fusion Res. SERIES **8** (2009) 330.

3.5.3 Preparative study for deuterium experiment for energetic ion confinement physics

The deuterium experiment will be one of the strategic options to investigate the isotope effect and energetic particle physics. In the deuterium experiments, 2.45 MeV neutrons are generated by nuclear fusion reactions between thermal deuterons, beam deuteron-thermal deuteron, and beam deuterons. In NB-heated CFQS plasmas, the neutron emission due to beam-thermal reaction is expected to be the main component because the injection energy of NB is much higher than the expected ion temperature. In this case, the neutron emission rate (S_n) reflects the global confinement of beam ions. FIT3D-DD code [3.5.1-4, 3.5.3-1], which is based on a simple analytical solution for the Fokker-Planck equation, is applied to evaluate S_n and the heating efficiency in deuterium CFQS plasmas under the various temperature and density ranges [3.5.3-2]. In the FIT3D-DD code, the birth profile of beam ions is calculated by the HFREYA module, and then the beam ion orbit is traced for a short time in order to evaluate the prompt loss of beam ion using the MCNBI module. The neutron emission rate and heating profile are evaluated using the analytical Fokker-Planck equation based on the radial beam ion profile calculated by HFREYA and MCNBI modules. In this database, density and temperature profiles have

a parabolic profile. The ranges of the central electron temperature, the central ion temperature, and the central electron density are set to be 0.5-4.0 keV, 0.5-1.0 keV, and 0.5×10^{19} - $4.0 \times 10^{19} \text{ m}^{-3}$, respectively. Figure 3.5.3-1 shows S_n database with the central ion temperature of 1.0 keV. The neutron emission rate monotonically increases with the electron temperature and the electron density in this plasma parameter region. The expected S_n by calculation is 10^{12} (n/s) order.

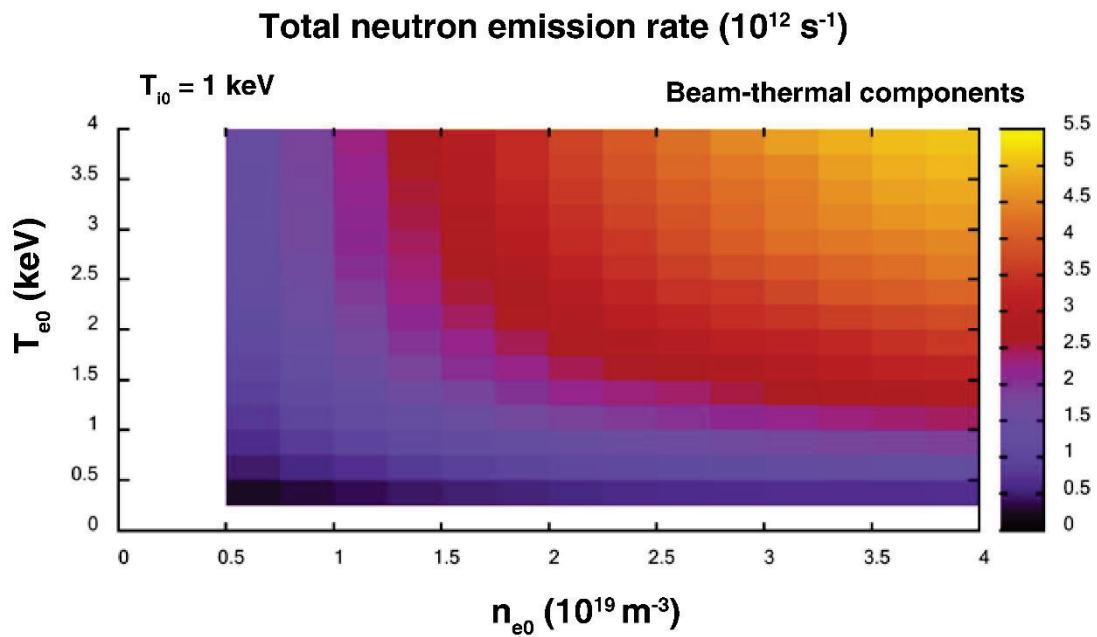


Fig. 3.5.3-1 Total neutron emission rate prediction by the FIT3D-DD code.

The comparison of neutron emissivity profiles in different densities is performed (Fig. 3.5.3-2). The peak of neutron emissivity shifts outwardly due to the increase in density. The possible reason for the shift is due to the beam ion deposition profile. In high-density cases, beam ion deposition points accumulate in the foreground, *e.g.*, outward, compared to low-density cases.

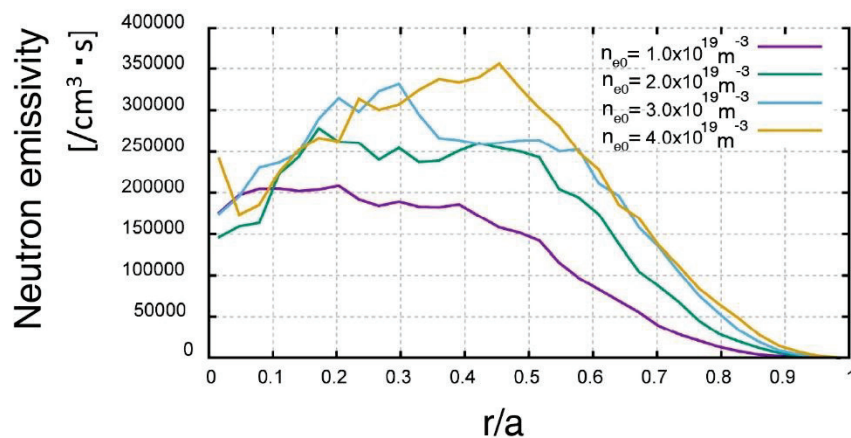


Fig. 3.5.3-2 Radial profile of neutron emissivity on different density cases.

In the deuterium experiment, 3 MeV protons are also produced with almost the same amount with 2.45 MeV neutrons. Therefore, the information of beam ions confined in a plasma core region can be obtained by 3 MeV protons. The energy Larmor radius of 3 MeV proton at the toroidal magnetic field strength of CFQS 1 T is 0.25 m, the same as the minor radius of a CFQS plasma. Therefore, the 3 MeV protons born in the plasma core region can be lost on the vacuum vessel before full gyro motion. Therefore, the inverse transformation of the deuterium-deuterium (D-D) fusion profile is feasible using the collimated proton detector array located on the vacuum vessel. For a feasibility study of D-D profile measurement, *e.g.*, possibility of D-D fusion profile inversion by D-D-born 3 MeV proton, was performed using the FIT3D-DD code and the LORBIT code [3.5.3-3]. Here, candidate detector position is set to be (x, y, z) of (1.46 m, 0.05 m, -0.34 m). The detector direction changes from 10 degrees to 50 degrees with 5 degrees steps. Here, the angle starts from the negative x -axis. Therefore, totally nine detectors are considered. We assumed that the length of the collimator is long enough, *e.g.*, the initial velocity of the proton is set to be parallel to the detector axis. Inversion of the D-D fusion profile was conducted by solving the linear matrix equation $\mathbf{b}=\mathbf{A}\mathbf{x}$, where \mathbf{b} , \mathbf{A} , and \mathbf{x} represent the signal of the detector array, weight function, and DD fusion profile, respectively. The weight function \mathbf{A} is obtained by making the dwell time of in each normalized minor radius position from the time-reversed 3 MeV proton orbit calculated by the LORBIT code (Fig. 3.5.3-3). Here, for the radial grid, r/a from 0.1 to 1.0 is divided into nine regions.

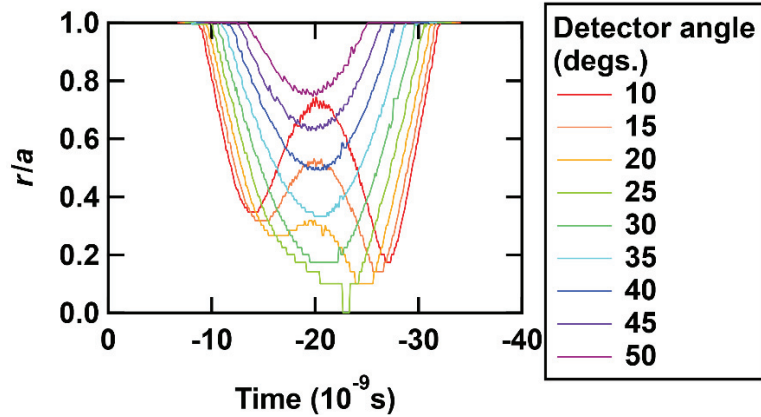


Fig. 3.5.3-3 Time trace of normalized minor radius position of 3 MeV protons. Time-reversed 3 MeV proton orbits are calculated from the candidate detector position.

The signal vector \mathbf{b} having nine components was calculated by integrating the 3 MeV proton emissivity profile obtained by the FIT3D-DD code along the proton orbit. The linear matrix equation $\mathbf{b}=\mathbf{A}\mathbf{x}$ was solved using the NumPy linear matrix solution library (linalg.solve 1.0.4) with python3.8.2. Figure 3.5.3-4 shows the comparison of inversed D-D fusion profile to the input D-D profile. It is found that the inversed profile almost matches with the input profile except for the edge region of the

plasma, *e.g.*, $r/a > 0.8$. The D-D fusion profile inverted by the calculated proton detector array signal shows the possibility of D-D fusion profile diagnostics by 3 MeV proton in CFQS.

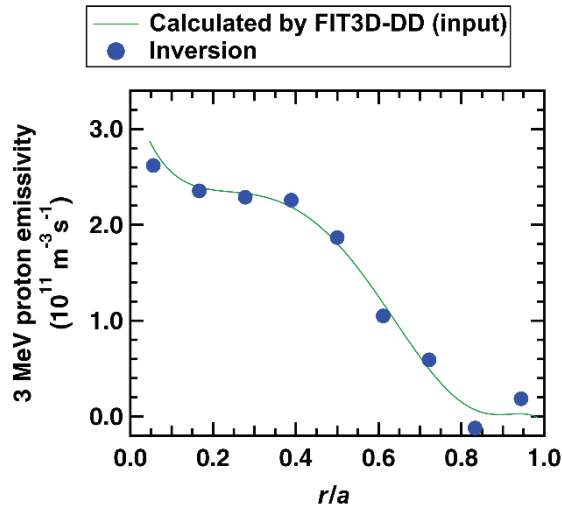


Fig. 3.5.3-4 3 MeV proton emissivity calculated by the FIT3D-DD code (input) and the inverted profile from the calculated detector signals. The inverted profile almost agrees with the input profile.

References

- [3.5.3-1] R. Seki *et al.*, Plasma Fusion Res. **14** (2019) 3402126.
- [3.5.3-2] R. Seki *et al.*, “Prediction of Neutron Emission Rate in Deuterium Neutral Beam heated CFQS plasmas using FIT3D-DD code.”, The 30th International Toki Conference (2021) 19Aa4.
- [3.5.3-3] K. Ogawa *et al.*, “Feasibility study of deuterium-deuterium fusion profile diagnostics using fusion born 3 MeV proton for CFQS”, The 30th International Toki Conference (2021) 17Am7.

3.5.4 Predictive study of alpha particle confinement in a QAS-type reactor

Collisionless alpha particle confinement in reactor-sized Stellarator based on W7-AS and W7-X [3.5.4-1], as well as QA configuration [3.5.4-2,3] had been investigated to show the way toward a future fusion reactor. A study of alpha particle confinement in a QAS-type reactor based on the CFQS magnetic field has been initiated using a guiding center orbit code in the Boozer coordinates [3.5.4-4].

References

- [3.5.4-1] W. Lotz *et al.*, Plasma Phys. Control. Fusion **34** (1992) 1037.
- [3.5.4-2] S. Gori *et al.*, Plasma Phys. Control. Fusion **43** (2001) 137.
- [3.5.4-3] S. Okamura *et al.*, J. Plasma Fusion Res. SERIES **3** (2000) 73.
- [3.5.4-4] Y. Zhang *et al.*, submitted to Phys. Plasmas.

3.6 ECRH deposition analysis

Electron cyclotron resonance heating (ECRH) power deposition and electron cyclotron current drive (ECCD) are analyzed using the ray-tracing code, TRAVIS [3.6-1]. For the analysis, a CFQS equilibrium file “wout.2b40R1mB01” was applied for the TRAVIS code. The frequency and the injected power of EC-wave in X-mode polarization are 54.5 GHz and 1 MW, respectively. As a test case, peaked electron temperature profile with T_{e0} of 3.5 keV and flat electron density profile with n_{e0} of $1.0 \times 10^{19} \text{ m}^{-3}$ were assumed. The T_e and n_e profiles are plotted in Fig. 3.6-1.

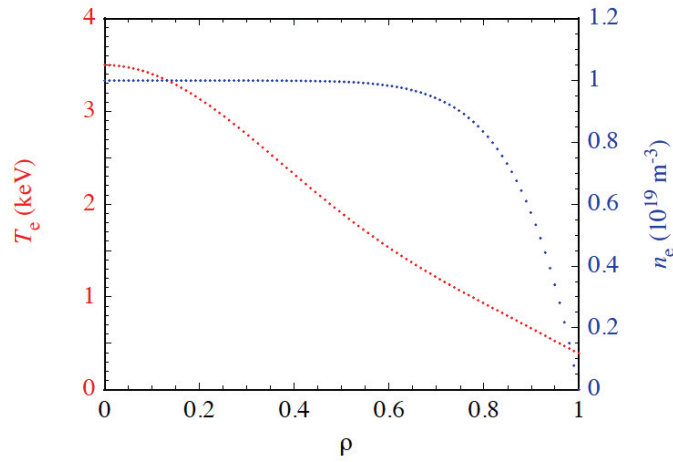


Fig. 3.6-1 Assumed electron temperature and density profiles for ECRH power deposition and ECCD analysis using the TRAVIS code.

Considering the dimension of the ECRH power injection port (CFQS O-8.5 port, ICF406), the size of 2-D steerable final plane mirror is determined as H134×W96 mm, the position of the center of the plane mirror is (R : major radial position = 1.55 m, T : toroidal position = 0 m, and Z : vertical position = -0.104 m) and the focused beam waist radius ($1/e$ radius of electric field amplitude) is 25 mm at the position ($R = 1.185$ m, $T = 0$ m, and $Z = 0$ m), in this analysis. Positive directions of T and Z are right side looking from outside of the torus and upper side, respectively. Using the 2-D steerable mirror, EC-wave power deposition control and ECCD can be realized.

Fig. 3.6-2 shows the controllability of power deposition position by scanning beam aiming position (R_f , T_f , Z_f). Here, R_f , T_f , and the magnetic field on axis at the bean-shape poloidal cross section, B , were fixed at 1.2 m, 0 m, and 0.975 T, respectively. Z_f was varied vertically as 0, -0.1, -0.2, and -0.25 m. The vertical axis of Fig. 3.6-2 is absorbed power density per volume, dP/dV (MW m^{-3}). By the variation of Z_f , the peak position of power deposition shifts toward outside as $\rho = 0$, ~ 0.2 , ~ 0.4 , and ~ 0.6 , respectively. Though the heating efficiency degrades with the outward shift of the power deposition position, high heating efficiency over 80 % can be expected in the wide range.

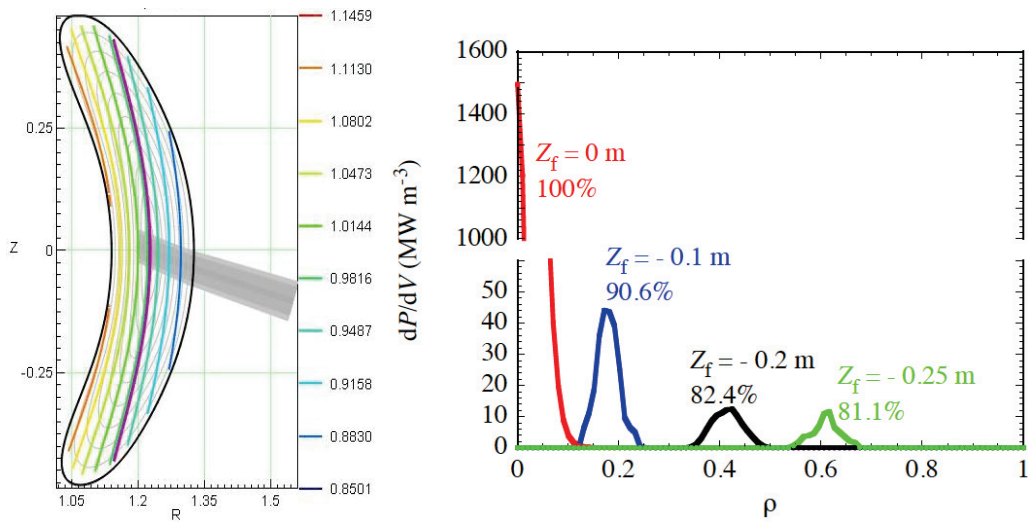


Fig. 3.6-2 Left: an example of a poloidal cross section plotted with an EC-wave beam path (here, $Z_f = 0$ m) and right: power deposition profiles with Z_f settings at 0, -0.1, -0.2, and -0.25 m.

Scanning EC-wave beam direction toroidally, dependence of EC-driven current I_{ECCD} against the parameter T_f is obtained as seen in Fig. 3.6-3. Here, R_f was fixed at 1.2 m. Z_f and B were slightly adjusted at each T_f , to keep on-axis heating and center-peaked current profile.

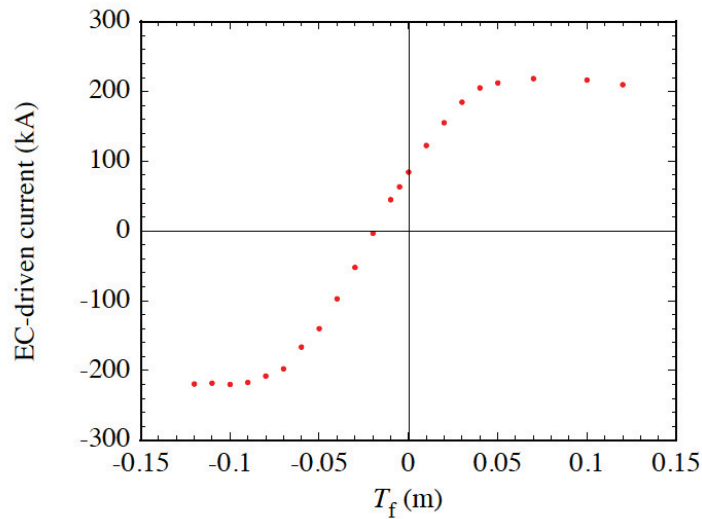


Fig. 3.6-3 EC-driven current as a function of T_f . Positive direction of current is clockwise looking from top side of the torus.

The magnitude of I_{ECCD} increases up to ~ 200 kA and then saturates with the magnitude of T_f . The asymmetry of I_{ECCD} about $T_f = 0$ m comes from the downward shift of the start position of the EC-wave beams (that is, center of the final plane mirror).

Thus, the 2-D steerable EC-wave beam injection system is expected to be available for a wealth of physical experiments in CFQS which require power deposition, current, and current profile controls.

References

[3.6-1] N.B. Marushchenko *et al.*, Phys. Plasmas **18** (2011) 032501.

3.7 Modular coil design

3.7.1 Modular coil design by NESCOIL

Vacuum equilibrium properties of a toroidal configuration are determined by the shape of the LCFS. Generally, considering the nested magnetic flux surfaces, the VMEC code enables to solve the three dimensional MHD equilibrium accurately and efficiently. In order to achieve the target magnetic configuration, a modular coil system is necessary to be designed to reproduce the plasma boundary. Due to the Neumann boundary condition, the accuracy of the magnetic configuration induced by the coil system is dependent on the normal component of the magnetic field on the plasma boundary, which is expressed as where B is the vacuum magnetic field generated from the coil system on the plasma boundary and n is the normal unit vector of this surface. Via the minimization of on the plasma boundary, the modular coil geometry is optimized. Meanwhile, the engineering constraints are taken into account which are the minimum interval between adjacent coils and maximum curvature. This optimization process is accomplished by the NESCOIL code [3.7.1-1]. In the design of the coil system for the CFQS, the coil numbers, major radii and aspect ratio have been scanned to achieve an optimum modular coil system. The corresponding parameters of coil systems are listed in the Table 3.7.1-1. We have designed 10 magnetic configurations and 19 coil systems in total. The N_p of all configurations is the same, 2.0. Making a comparison among them, the configuration with the major radius (R_0) = 1.0 m, aspect ratio (A_p) = 4.0, magnetic field strength (B_t) = 1.0 T and minor radius (a) = 0.25 m is advantageous. In our work, the 20-coil, 16-coil, and 12-coil systems are designed. The results of filament-coil optimization are listed in the Table 3.7.1-2. In comparison of the physics and engineering constraints among them, the table indicates that the 16-coils system is preferable, which shows that the minimum interval between adjacent filament coils is the widest; the minimum radius of curvature is the largest and the magnetic flux surface generated is the closest to the target surface.

Table 3.7.1-1 Parameters for 10 magnetic configurations designed, showing the configuration with the major radius $R_0 = 1.0$ m, aspect ratio $A_p = 4.0$, magnetic field strength $B_t = 1.0$ T, and minor radius $a = 0.25$ m.

R_0 (m)	A_p	a (m)	B_t (T)	Num of modular coils
1.5	3.2	0.47	1.0	20
1.5	3.9(2w39)	0.38	1.0	20
1.5	4.0	0.38	1.0	20
1.5	5.0	0.30	1.0	20
1.2	3.8	0.32	1.0	20
1.2	4.0	0.30	1.0	24, 20, 16, 12
1.2	5.0	0.24	1.0	20
1.0	3.2	0.31	1.0	20, 16, 12
1.0	3.6	0.28	1.0	20, 16, 12
1.0	4.0	0.25	1.0	20, 16, 12
Total	Number of configurations:10		Number of coil systems:19	

Table 3.7.1-2 Parameters of three different types of coil systems for CFQS-2b40.

A_p	R_0 (m)	a (m)	Number of coils	Minimum distance between coils (cm)	Minimum radius of curvature (cm)	$\mathbf{B} \cdot \mathbf{n} / \mathbf{B} $	Current per coil (MA)	Cross section of coils (cm ²)
4.0	1	0.25	20	17.0	18.2	1.11 %	0.2500	17×9
4.0	1	0.25	16	18.5	21.5	0.97 %	0.3125	18×10
4.0	1	0.25	12	14.2	14.7	1.21 %	0.4167	19×13

Fig. 3.7.1-1 gives the of 16-modular coil system. Due to $N_p = 2$ and stellarator symmetry, the whole torus consists of four symmetric sections. Therefore, the coils system possesses four different shaped modular coils. The centerline of each finite sized coil is assigned by the corresponding filament coil. The all 16 filament coils are from the results of the NESCOIL code. The coil cross section is rectangular and the area is $13.2 \times 6.9 \text{ cm}^2$ which includes copper conductor, and insulation.

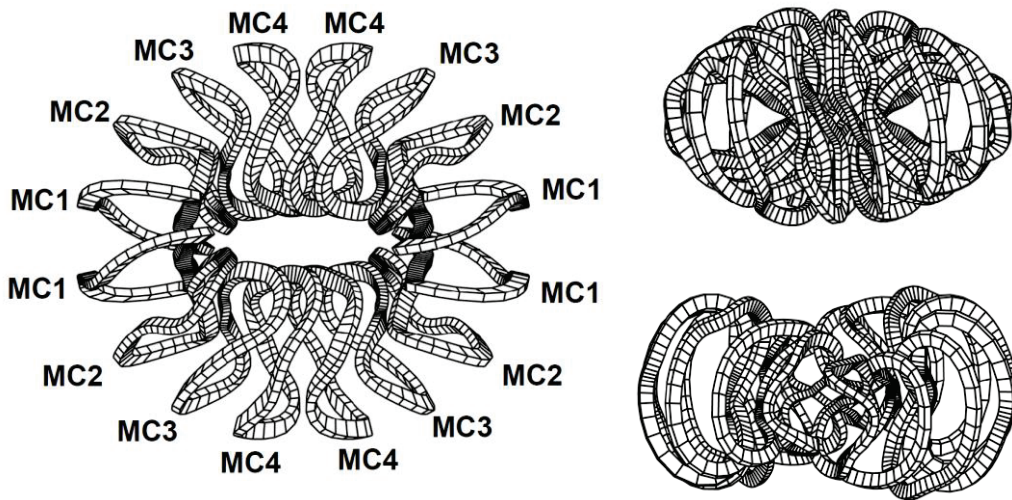


Fig. 3.7.1-1 Modular coils of the CFQS, the top view and side views at toroidal angle= 0° (vertical elongation), and 90° (horizontal elongation). The serial number of coils represents the various shapes of coils. The coil system comprises of four different shape coils.

In order to estimate the accuracy of the magnetic configuration induced by the 16-coil system, the coils generated magnetic flux surfaces, rotational transform and Fourier spectrum of the magnetic field strength are calculated. In Fig. 3.7.1-2, Poincaré plots of magnetic flux surfaces and rotational transform induced by the modular coils are analyzed, assuming the coils are filament ones. At the toroidal angle= 0° , 45° , and 90° , cross sections are displayed. The angle = 0° and 90° correspond to the vertically and horizontally elongated cross sections, respectively. The average of $\mathbf{B} \cdot \mathbf{n} / |\mathbf{B}|$ on the plasma boundary is below 1%, which cannot be reduced from the viewpoint of the engineering. The rotational transform profile and magnetic well induced by coils and target profile are compared in Fig. 3.7.1-2 (d). Horizontal axis ρ in this figure represents the normalized average minor radius. The figure shows a good agreement in rotational transform profile and magnetic well depth, between coils induced ones and target ones. From Fig. 3.7.1-2 (a)-(c), they depict a good coincidence in the shapes of a magnetic flux surface and that of target plasma boundary. It should be noted that the width of outmost flux

surface produced by modular coils is larger than that of target plasma boundary, which is beneficial to raise the plasma volume by movable limiters. In order to precisely estimate the QA property of the configuration, the magnetic field strength is decomposed into a Fourier spectrum in the Boozer coordinates. Fig. 3.7.1-3 (a) depicts the spectrum of the magnetic field strength based on the target magnetic configuration. To extinguish the small-amplitude components, the largest component B_{00} is omitted. In Fig. 3.7.1-3 (a), the magnetic field strength is 1.0 T. B_{10} is the dominant component resulting from the toroidicity. Other components, such as mirror ripple (B_{01}) and helical ripples (B_{11} , B_{12}), are much less than B_{10} , which indicates a tokamak-like QA configuration. In Fig. 3.7.1-3 (b), coil induced spectrum of magnetic field strength is given. On the basis of synthetical analyzation, the designed 16-coil system is well workable.

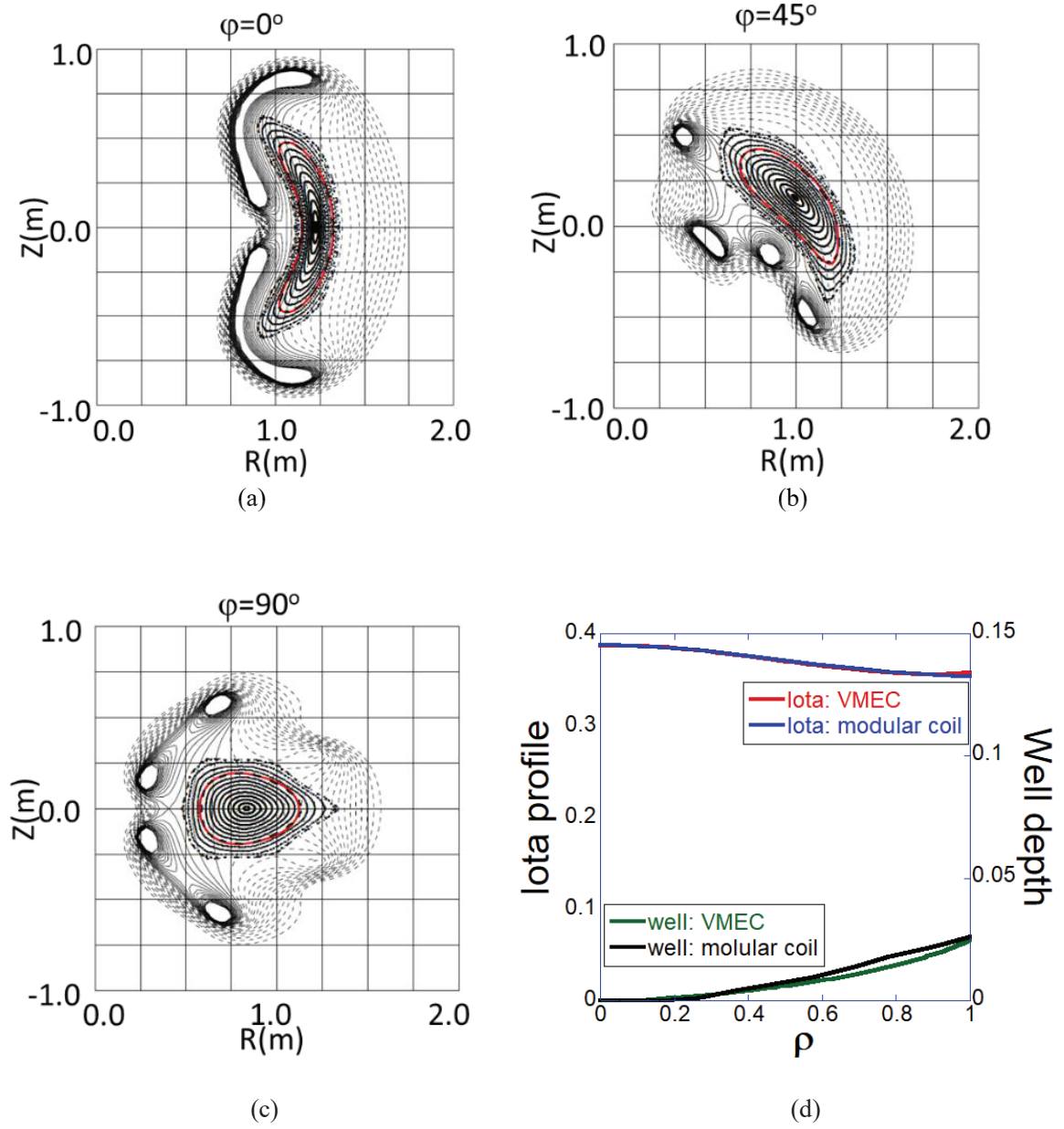


Fig. 3.7.1-2 Poincaré plots of magnetic flux surfaces at the toroidal angle $=0^\circ$, 45° , and 90° for (a)-(c) respectively. The red curve represents the target plasma boundary. (d) shows the comparison of the rotational transform and magnetic well between the configuration produced by modular coils and target one.

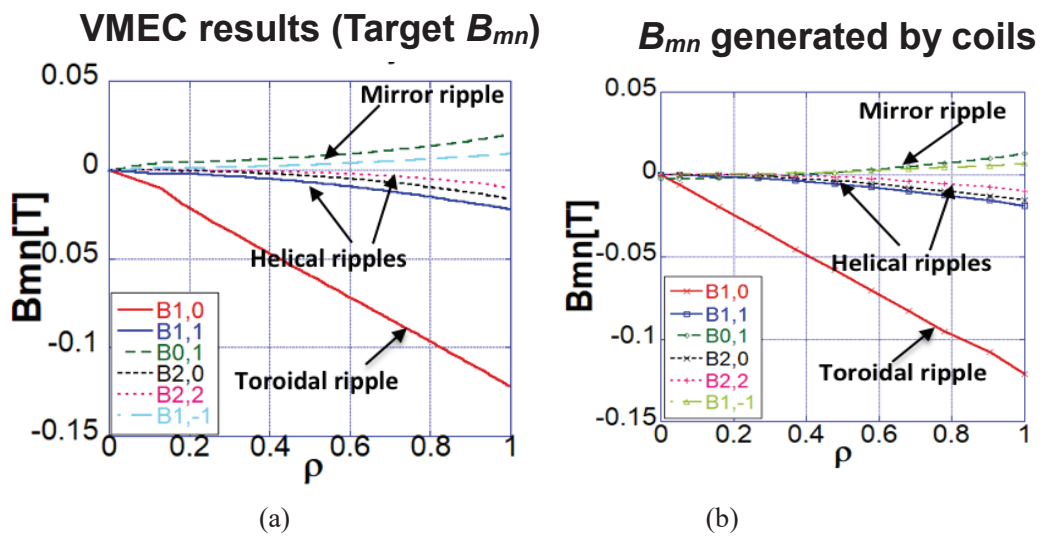


Fig. 3.7.1-3 Fourier spectrum of the magnetic field strength for the CFQS configuration in the Boozer coordinates. (a) B_{mn} from VMEC results (target spectrum), (b) B_{mn} generated by modular coils.

References

[3.7.1-1] M. Drevlak, Fusion Technol. **33** (1998) 106.

3.7.2 Design of modular coils without torsions

In the fabrication of coils, the coil's torsion has a great influence on the difficulty of manufacture. The greater the torsion, the coil is more complex. So, we have optimized the coil system by reducing the torsion.

We compute the torsion by these equations as follows:

For arbitrary point r_c in the modular coil cross section,

$$\mathbf{r}_c(l, \xi, \eta) = \mathbf{r}_G(l) + \xi \mathbf{u}(l) + \eta \mathbf{v}(l). \quad (3.7.2-1)$$

Tangential vector is as follows,

$$\mathbf{t}_c \equiv \frac{d\mathbf{r}_c}{dl_c} = \left(\frac{d\mathbf{r}_G(l)}{dl} + \xi \frac{d\mathbf{u}(l)}{dl} + \eta \frac{d\mathbf{v}(l)}{dl} \right) / \frac{dl_c}{dl}. \quad (3.7.2-2)$$

Here, $-x_w \leq \xi \leq x_w$ and $-y_w \leq \eta \leq y_w$.

We define vector,

$$\mathbf{b} = \mathbf{t}_c \times \mathbf{u} \quad \mathbf{n} = \mathbf{b} \times \mathbf{t}_c. \quad (3.7.2-3)$$

Torsion,

$$\tau(l) = -\mathbf{n} \cdot \frac{d\mathbf{b}}{dl_c}. \quad (3.7.2-4)$$

We rotate the cross section of coils and calculate the torsion after each rotation. Next, we can find the minimum torsion in our calculated result. When we get the minimum in all cross section, we finish the optimization of the coil [3.7.2-1].

The following figures (Fig. 3.7.2-1~8) show the torsion of the coil without optimization and with optimization, respectively.

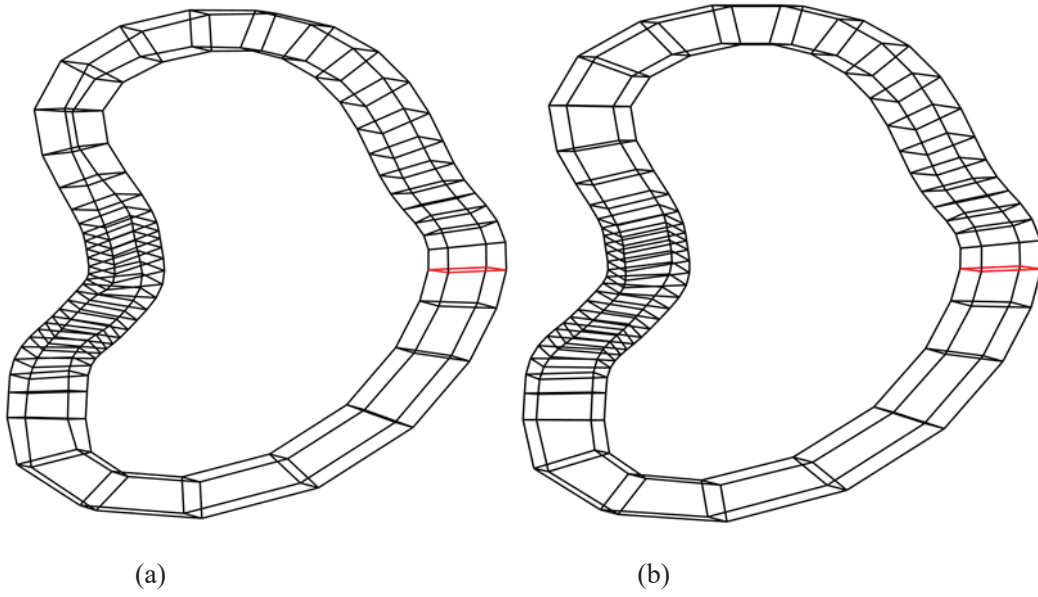


Fig.3.7.2-1 MC1 coil without optimization (a) and with optimization (b). The red line is the first cross section.

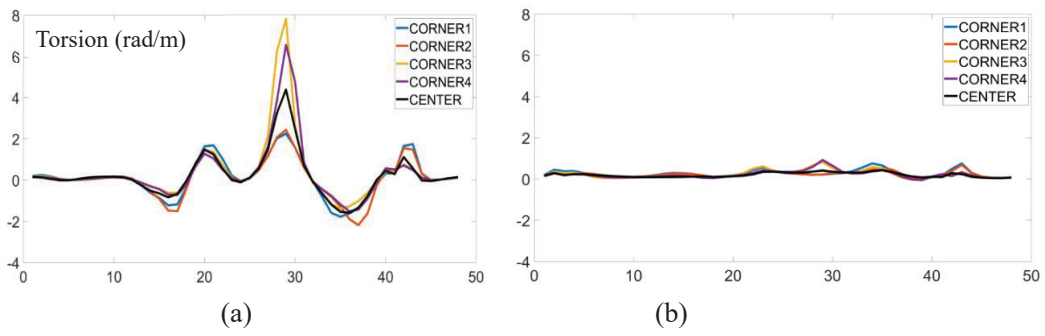


Fig. 3.7.2-2 Torsion of MC1 coil without optimization (a) and with optimization (b).

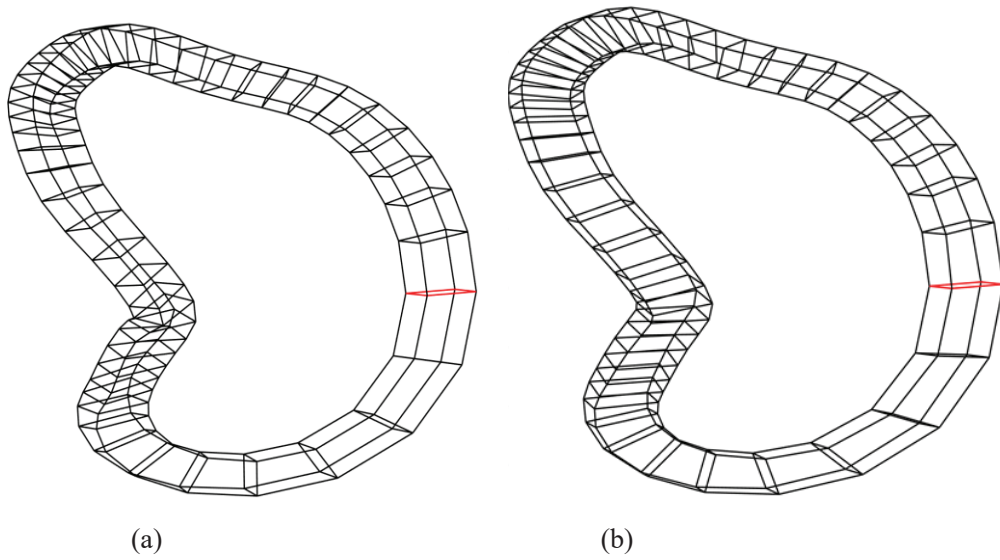


Fig. 3.7.2-3 MC2 coil without optimization (a) and with optimization (b).

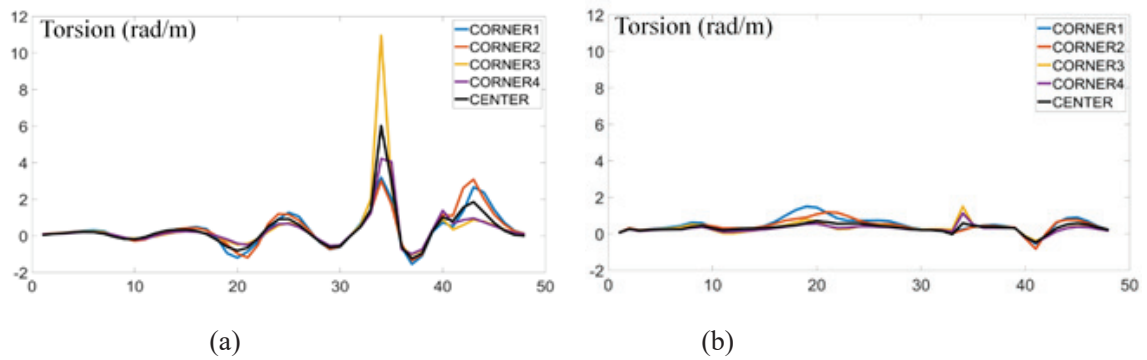


Fig. 3.7.2-4 Torsion of MC2 coil without optimization (a) and with optimization (b).

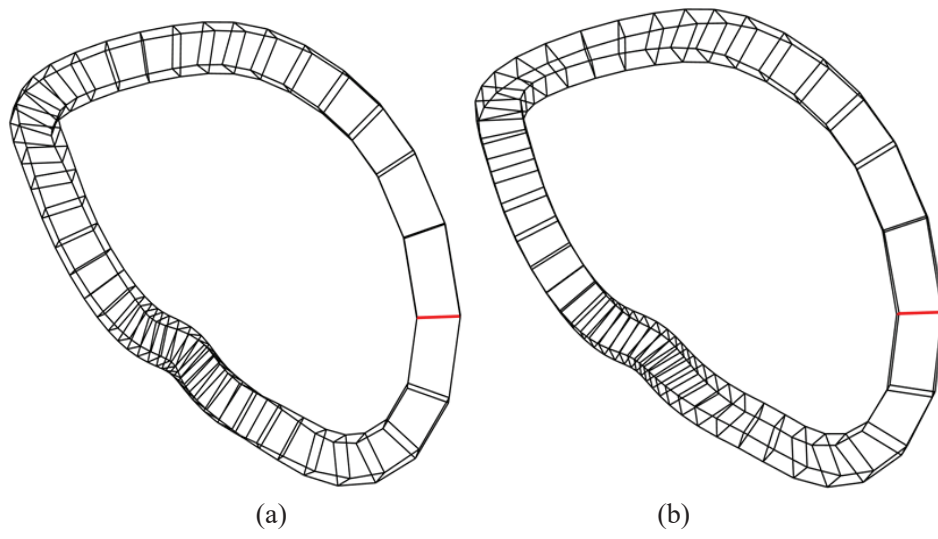


Fig. 3.7.2-5 MC3 coil without optimization (a) and with optimization (b).

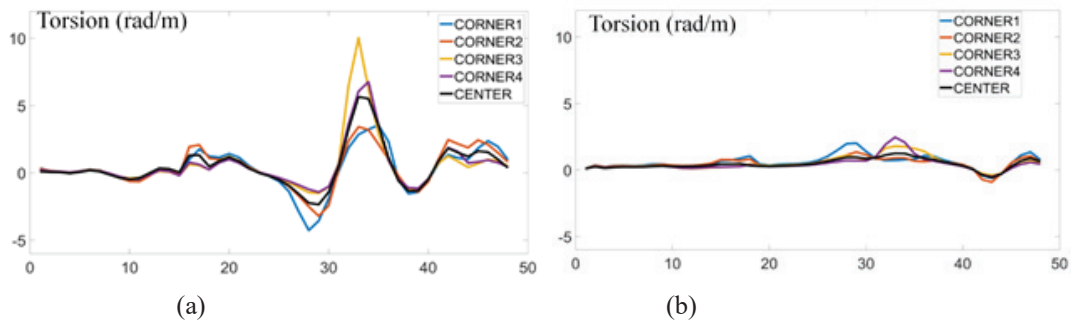


Fig. 3.7.2-6 Torsion of MC3 coil without optimization (a) and with optimization (b).

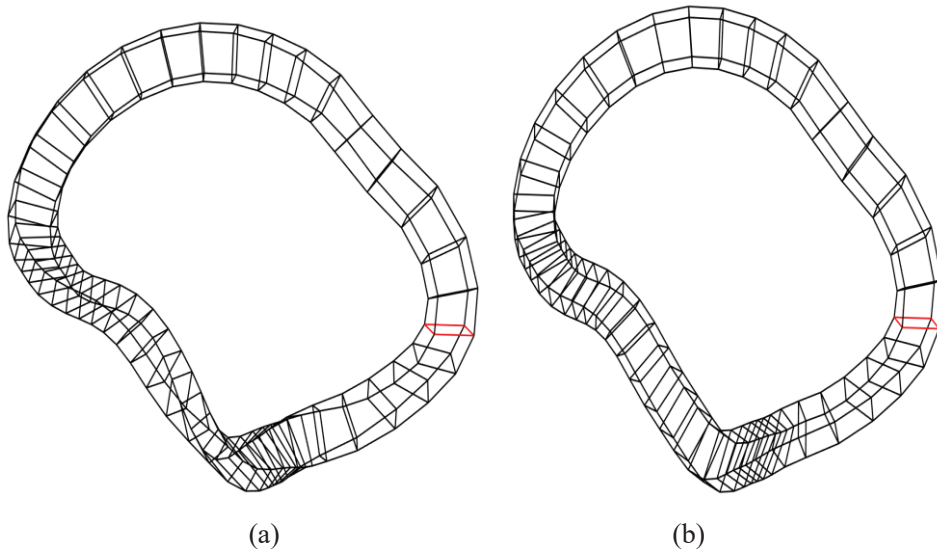


Fig. 3.7.2-7 MC4 coil without optimization (a) and with optimization (b).

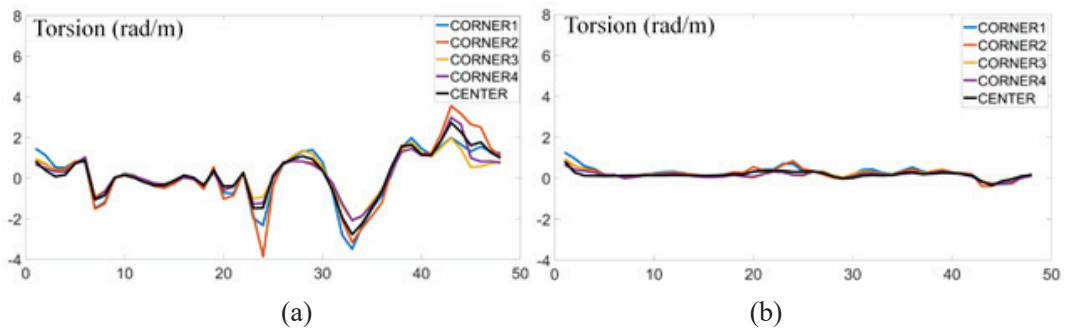


Fig. 3.7.2-8 Torsion of MC4 coil without optimization (a) and with optimization (b).

Through the figures above, it's clearly shown that the torsion has been well optimized.

In addition, curvature is also an important parameter for the coil system, of course, it is not a good parameter for the coil, the equations of curvature as follows:

$$k = \frac{|d\mathbf{t}_c|}{|dl_c|} = \left| \frac{d^2\mathbf{r}_c}{dl_c^2} \right|.$$

\mathbf{t}_c is calculated in equation (3.7.2-2) and \mathbf{r}_c is calculated in equation (3.7.2-1).

Then, we compare the curvature of coils without optimization and with optimization, respectively.

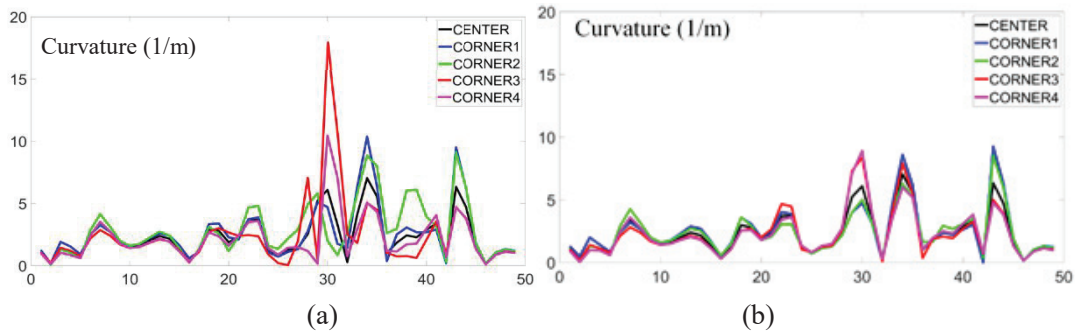


Fig. 3.7.2-9 Curvature of MC1 coil without optimization (a) and with optimization (b).

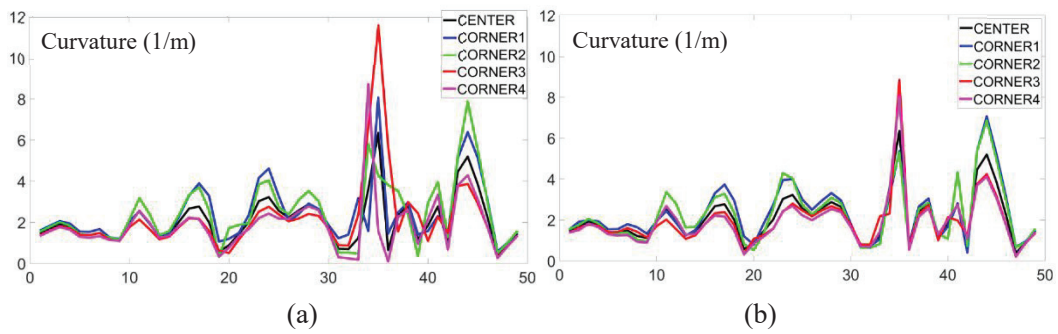


Fig. 3.7.2-10 Curvature of MC2 coil without optimization (a) and with optimization (b).

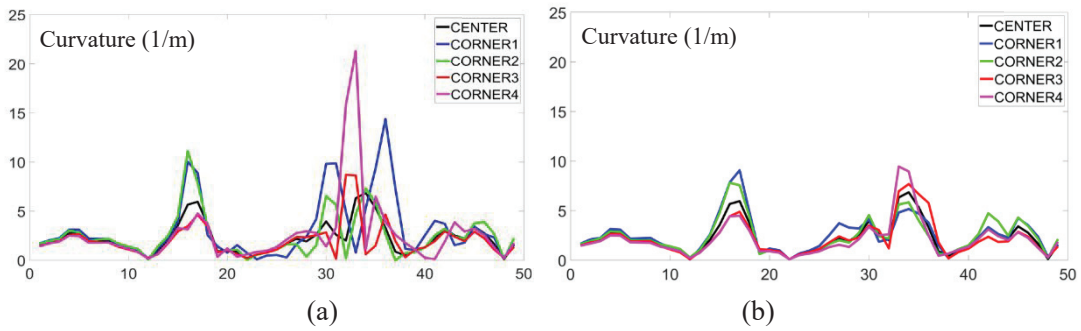


Fig. 3.7.2-11 Curvature of MC3 coil without optimization (a) and with optimization (b).

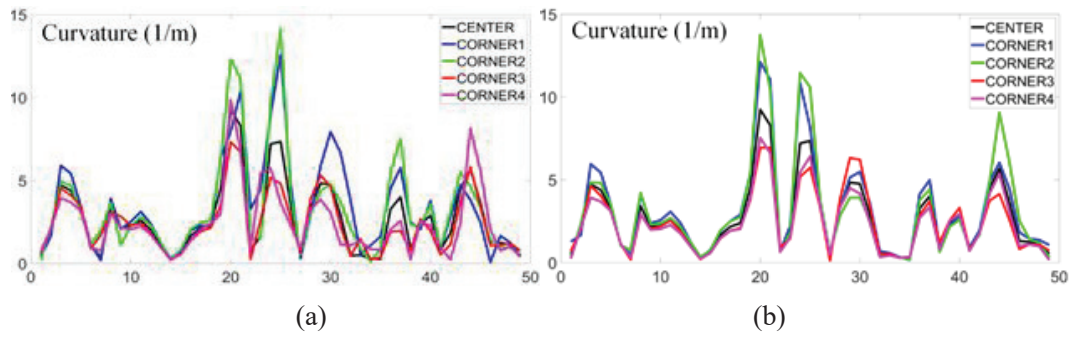


Fig. 3.7.2-12 Curvature of MC4 coil without optimization (a) and with optimization (b).

The above figures (Fig. 3.7.2-9~12) show that the coil optimization for torsion also have a good improvement in curvature. Fig. 3.7.2-13 shows the final results of modular coils with plasma boundary.

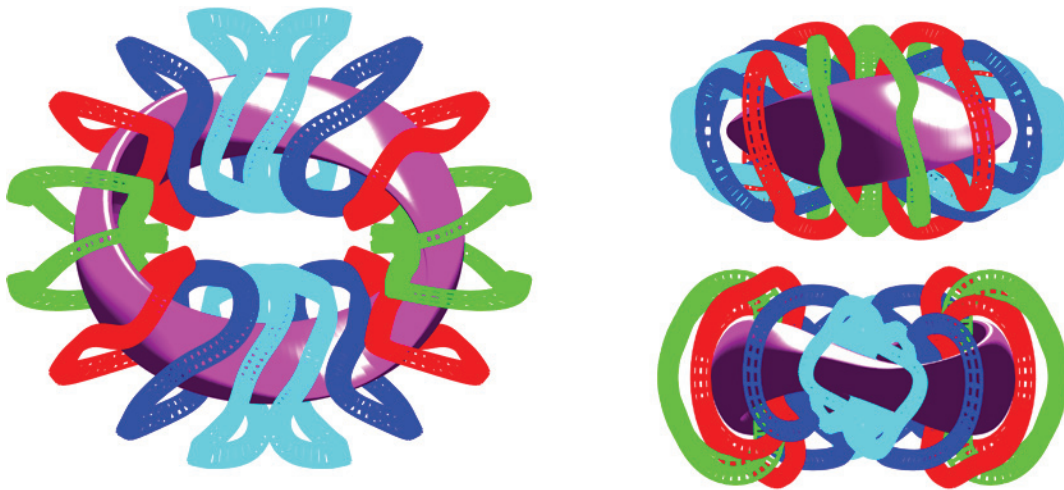


Fig. 3.7.2-13 Modular coils and plasma boundary of CFQS.

References

[3.7.2-1] Y. Li *et al.*, Plasma Phys. Control. Fusion **62** (2020) 125004.

3.7.3 Modular coil design by GOSPEL

Modular and helical coil optimization for CFQS applying the newly-developed coil optimization code GOSPEL [3.7.3-1] has been done. The GOSPEL code has been developed for efficient designing of modular and helical coils using free-form curves without assuming a winding surface, neither giving a specific initial guess of the coil shape from other codes. In the GOSPEL code, a filamentary coil is assumed and expressed using cubic B-spline curve in the three-dimensional real space. The position of the control points of B-spline curve and the current for each of the coils are optimized using the algorithm based on genetic algorithm to minimize the objective function, f . The objective function includes the normal field component generated by the coils on the target magnetic surface as the primary component. In the calculations shown here, the normal field component of the objective function was defined as $f_{bn} = (\frac{1}{M} \sum_{j=1}^M |\mathbf{b}_j \cdot \mathbf{n}_j|^2)^{1/2}$, where \mathbf{b}_j and \mathbf{n}_j are unit vector along the magnetic field and the normal vector on the target surface, respectively, and the subscript j ($j=1, \dots, M$) denotes reference points on the target surface. The engineering components regarding the coil curvature, torsion, distances between coils and target boundary *etc.* can be added to f .

The boundary magnetic surface of CFQS was chosen as one of the first targets for GOSPEL. First, coil optimization was done assuming modular coils with and without the engineering components. The number of coils, the minimum curvature radius, the minimum distance between coil center, and the maximum coil length assumed in the optimization were imported from the original coil design [3.7.3-2]. Fig. 3.7.3-1 shows the modular coils obtained by GOSPEL with 16 control points per coil considering the engineering components. Note that the coils are drawn as volume coil with square cross section just to enhance the readability of three-dimensional geometry. The coil shape by GOSPEL shows less winding sections compared to the original design by NESCOIL [3.7.3-3] although both designs have almost the same minimum coil curvature. This difference may come from the presence/absence of winding surface and different expressions of coil shape (B-spline/Fourier) employed in these two codes. The Poincare plots of the vacuum magnetic field produced by the modular coils by GOSPEL reproduced the target boundary and VMEC equilibrium well as seen in the right view graph in Fig. 3.7.3-1. The normal field component of this coil configuration was $f_{bn} = 0.92\%$.

Next, the optimization of continuous helical coils was done applying GOSPEL. The pattern of the coil arrangement using three helical coils and two poloidal field coils was found to reproduce the optimized stellarator configuration of the Wendelstein 7-X [4] well in the preliminary calculation. Fig. 3.7.3-2 (left) shows the optimized helical coil configuration for CFQS together with the last-closed magnetic surface (LCFS) generated by these coils. One of the helical coils has up-down symmetry and the remaining two helical coils creates up-down symmetry as a pair. For this helical coil configuration, the normal field component was $f_{bn} = 1.9\%$. Fig 3.7.3-2 (right) shows the comparison of the Poincare plots including the edge region for this helical coil configuration and the modular coils of Fig. 3.7.3-1. The field lines outside of the LCFS were traced until they reach to the virtual wall drawn as a gray

curve. The modular coils create closed magnetic surface outside of the target boundary while the helical coil create broken magnetic surfaces and divertor-leg-like structure in this region.

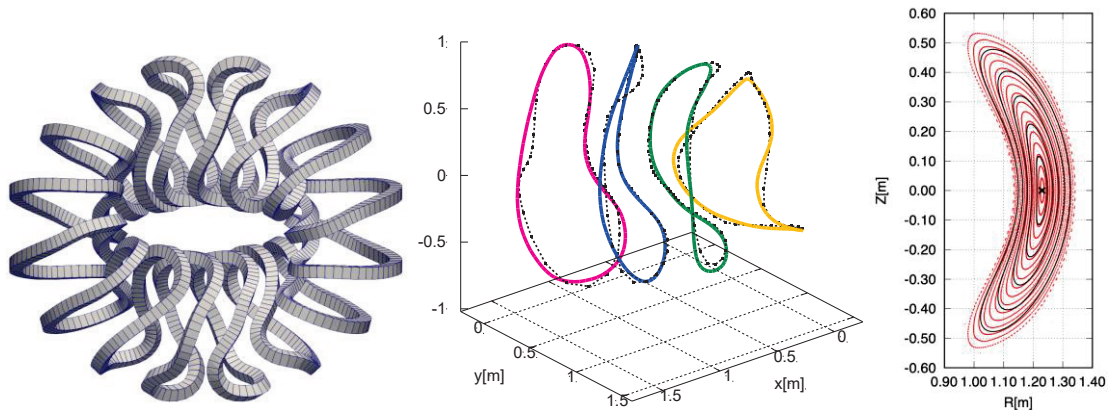


Fig. 3.7.3-1 (Left) Modular coils obtained under the engineering constraints with GOSPEL, (middle) comparison of four unique coils with the original design (symbols connected by dotted lines) in [3.7.3-2], (right) the Poincaré plot of the vacuum magnetic field generated by the obtained coils (red) and the target boundary and equilibrium (black curve, magnetic axis is denoted by x).

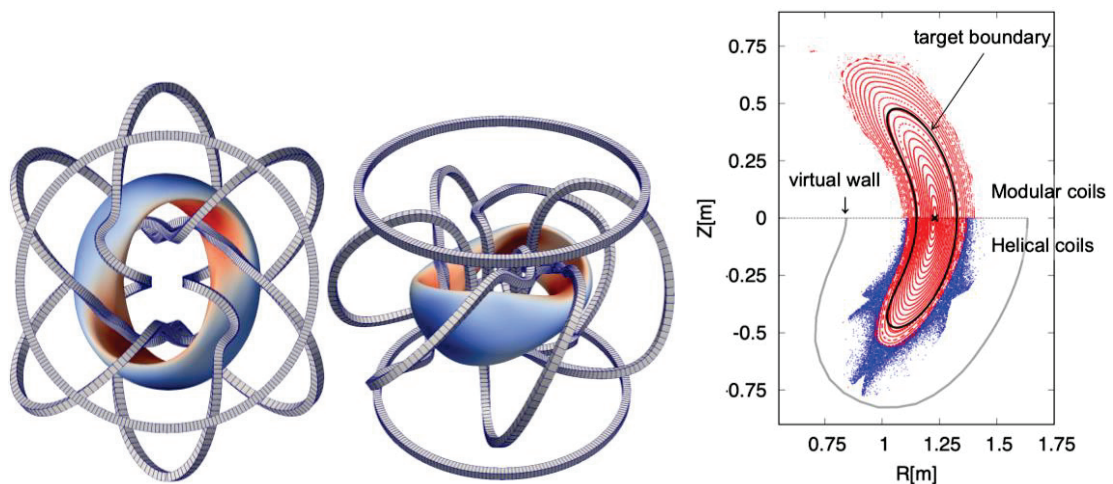


Fig. 3.7.3-2 (Left) Top and perspective views of helical coil configuration for CFQS obtained with GOSPEL. The last-closed magnetic surface generated by these coils is also drawn. (Right) The Poincaré plots for the modular (top half) and the helical coil (bottom half) configurations with the target boundary and the virtual wall assumed for helical coil configuration.

References

- [3.7.3-1] H. Yamaguchi *et al.*, Nucl. Fusion **61** (2021) 2106004.
- [3.7.3-2] H. Liu *et al.*, Plasma Fusion Res. **13** (2018) 3405067.

[3.7.3-3] P. Merkel, Nucl. Fusion **27** (1987) 867.

[3.7.3-4] T. Klinger *et al.*, Fusion Eng. Des. **88** (2013) 461.

3.7.4 Error evaluation using the Hessian matrix method

Plasma performance in magnetically confined fusion devices depends on the quality of the magnetic field. Magnetic field irregularities, namely ‘error fields’, can lead to the destruction of magnetic surfaces and locked modes. One of the main sources of error field is inevitable coil deviations. The stellarator generally has more complicated coils than axisymmetric devices (like tokamaks) and the confining magnetic field predominantly arises from carefully shaped external coils. Therefore, controlling error fields during coil fabrication and assembly is crucial for stellarator construction. As-built coil geometries might differ from designed models in location, orientation or even shape. Coil deviations, as measured between designed models and final built shapes, have different effects on plasma performance. The cost and complexity of a device can increase dramatically with tight construction tolerance. Thus, it is necessary to carry out an error field sensitivity analysis for identifying important coil deviations and determining acceptable tolerance prior to machine construction.

The Hessian matrix can be used for sensitivity analysis. In [3.7.4-1], a Hessian matrix method was described to determine error field sensitivity to coil deviations. The figure of merit used was the root-mean-squared (RMS) normal field error on the target plasma boundary, which comes from the coil design code FOCUS [3.7.4-2]. A quadratic approximation indicates coil perturbation in the direction of the eigenvector corresponding to the largest eigenvalue has the most significant effect on the figure of merit. The Hessian matrix method was then applied to a CNT-like configuration as a proof of principle and the results were consistent with previous observations. The RMS normal field error represents the discrepancy between the desired magnetic field and the one produced by coils, but it does not have any particular physics meaning. In practical situations, what should be considered when evaluating the error field is plasma confinement performance. In this paper, we will implement the Hessian matrix method over the magnetic island size, which is used in most error field studies. Additionally, we would also evaluate the so-called ‘quasi-symmetry’ of the magnetic field, which is the symmetry of magnetic field strength $|B|$. Quasi-symmetry has been both theoretically predicted and experimentally confirmed to reduce neoclassical transport and is one of the key qualities used in today’s stellarator optimizations.

Coil optimization consists of varying coil parameters, in whatever representation, and minimizing an objective function which is the weighted summation of multiple penalty functions. Once optimal coils are found, a small change in coil shapes (and currents), which can be described as $\delta\mathbf{x}$ in parameter space, will cause a departure in the figure of merit away from the optimum. This change can be approximated by

$$\delta F \approx \frac{1}{2} \delta\mathbf{x}^T \cdot \mathbf{H}_0 \cdot \delta\mathbf{x} , \quad (3.7.4-1)$$

where the matrix \mathbf{H} is known as the Hessian matrix (second-order derivatives). In equation (3.7.4-1), only the quadratic term is left since the linear term is zero at the optimum (stationary point) and we

are only considering a small perturbation (neglecting higher-order terms). The Hessian matrix is symmetric and its eigenvalues are positive. By perturbing coils in the direction of eigenvector, $\delta x = \zeta v_i$, the change of the figure of merit is

$$\delta F \approx \frac{1}{2} \lambda_i \zeta^2 \quad . \quad (3.7.4-2)$$

Its eigenvectors can be ordered by the magnitude of associated eigenvalues λ_i . The first principal eigenvector, which is the one corresponding to the largest eigenvalue, describes the most sensitive perturbation. With the information in eigenvectors and eigenvalues of the Hessian matrix, we can easily identify the sensitivity of the error field to coil deviations.

The Hessian matrix method is applied to CFQS to calculate the sensitivity of quasi-symmetry and magnetic islands to coil deviations [3.7.4-3]. The quality of quasi-symmetry (on one flux surface) can be evaluated using

$$F_{QS} = \sum_{n \neq 0} \left(\frac{B_{mn}}{B_{00}} \right)^2 \quad . \quad (3.7.5-3)$$

Note that $F_{QS} = 0$ indicates perfect quasi-symmetry of the magnetic field on the reference flux surface. The Fourier component of magnetic field strength, $B_{m,n}$, is then decomposed in Boozer angles (θ_B, ζ_B) . The magnetic island width is proportional to the resonant perturbation on a particular rational surface,

$$w = 4 \sqrt{\frac{b_{mn}}{m \iota_{mn}}} \quad . \quad (3.7.5-4)$$

Both quantities are analytically differentiated in FOCUS and thus the Hessian matrix can be computed. Fig. 3.7.4-1 show how the $n/m = 4/11$ magnetic island chain changes when the coils are perturbed in the direction of the first principal eigenvector. The magnetic islands are either reduced or enlarged when the external coils are perturbed, which are both deviated from the original state. The corresponding coil perturbation can be viewed in Fig 3.7.4-2(a), where the inboard side of MC1 and MC2 coils is significantly more sensitive than other parts. Similar results can be seen in Fig 3.7.4-2(b) in which the first principal eigenvector of the quasi-symmetry with respect to coil perturbations are shown.

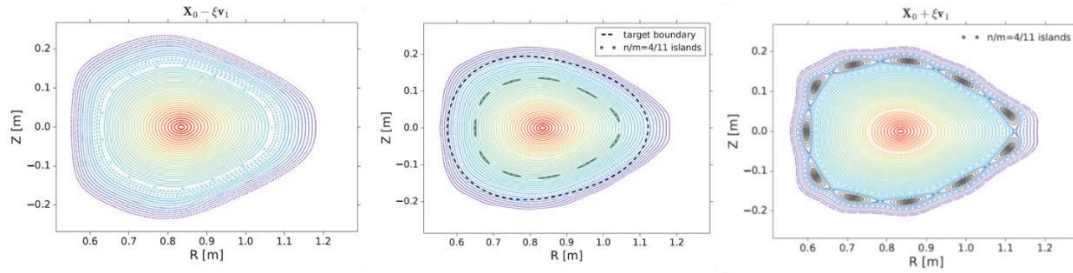


Fig. 3.7.4-1 The $n/m = 4/11$ magnetic island chain changes with different coil deviations in the direction of the first principal eigenvector, left: negative perturbation; middle: unperturbed coils; right: positive perturbation.

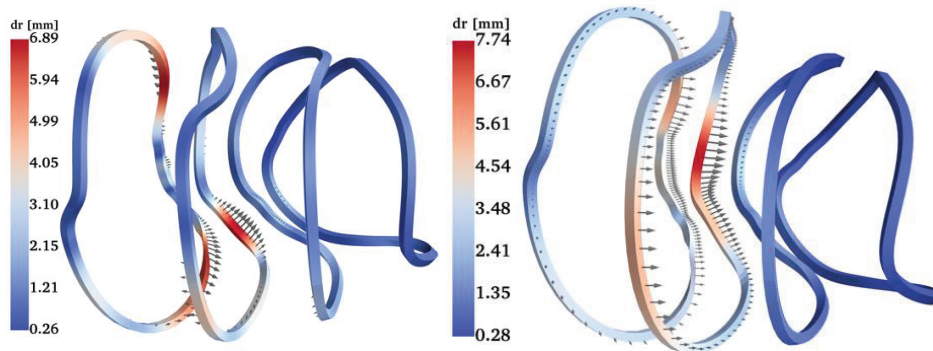


Fig 3.7.4-2 Coil deformations under the first principal eigenvector for (a) 4/11 islands; (b) QA quality on the half-toroidal-flux surface. Colors on coils imply the departure distance of data points in each coil and arrows demonstrate the deforming direction.

With the two new figures of merit for quantifying error fields, we have applied the Hessian matrix method to the CFQS device which is under construction. We have successfully found the most effective coil perturbation scheme that will enlarge the 4/11 islands. In addition, the important coil perturbations deteriorating the QA on the half-toroidal-flux surface are also identified. These results will provide insights for the upcoming coil manufacture and assembly: avoiding critical coil deformations and relaxing coil tolerance at insensitive parts. A simple estimation indicates that the maximum allowable coil deviation is about 5 mm if 10 % of QA quality deterioration is acceptable. We have also demonstrated the ability to improve coil designs towards better QA quality. This could be used in future coil optimization studies.

References

- [3.7.4-1] C. Zhu *et al.*, Plasma Phys. Control. Fusion **60** (2018) 054016.
- [3.7.4-2] C. Zhu *et al.*, Nucl. Fusion **58** (2018) 016008.
- [3.7.4-3] C. Zhu *et al.*, Nucl. Fusion **59** (2019) 126007.

3.7.5 Influence of stellarator symmetric coil misalignment on magnetic field configuration

To consider the effects of misalignment of modular coils, the following three cases are considered [3.7.5-1]: Case A, where the coils move to radial direction; Case B, where the coils move to the vertical (Z) direction; and Case C, where the coils tilt around the cylindrical R coordinate. Assumptions of these three cases are shown in Fig. 3.7.5-1. The displacement structure has stellarator symmetry for the simplicity of calculation. Herein, stellarator symmetry means that for the radial deformation, $\Delta R(\varphi, \theta) = \Delta R(-\varphi, -\theta)$, and for the vertical deformation, $\Delta Z(\varphi, \theta) = -\Delta Z(-\varphi, -\theta)$ are considered. Here, φ and θ are the toroidal and poloidal angles, respectively. Moreover, a toroidal periodicity of two is assumed. Hence, in Case A, eight modular coils move to the radially outward direction and another eight modular coils move to the radially inward direction. The situation in Cases B and C is similar to this. Therefore, eight modular coils move in the same direction. For the deformation, the toroidal mode number of eight is considered to investigate the effect of main highest mode. The low mode will be included in future analyses for a more comprehensive understanding of the deformation effect on magnetic field properties.

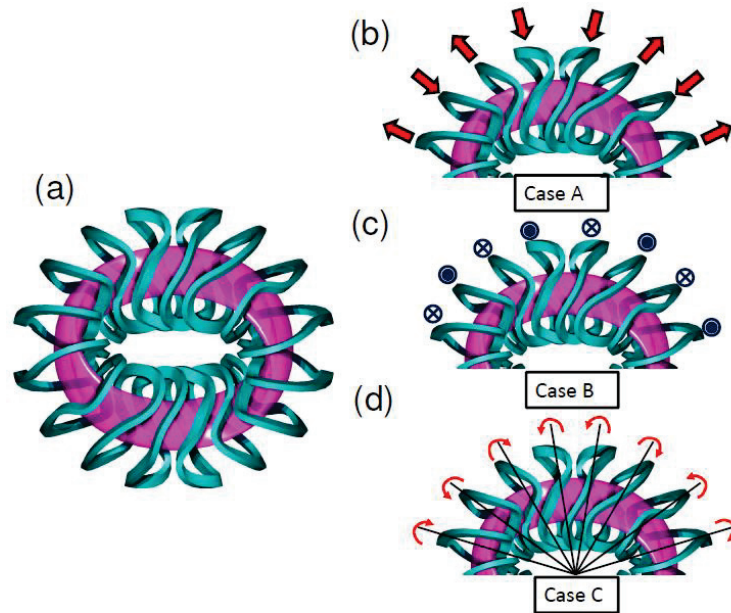


Fig. 3.7.5-1 (a) the top view of modular coil system of the CFQS. (b) assumed coil displacement of Case A, with coils moved to the radial direction. (c) Case B, with coils moved to the vertical direction, and (d) Case C, with coils tilting around the cylindrical R coordinates.

Magnetic surfaces are considered for these three types of displacements, as shown in Fig. 3.7.5-2. The displacement magnitudes are illustrated as follows: Fig. 3.7.5-2(a) depicts magnetic surfaces for the case where no displacement is considered. Fig. 3.7.5-2(b) is for $\Delta R = 10$ mm in Case A, Fig. 3.7.5-2(c) is for $\Delta Z = 10$ mm in Case B and Fig. 3.7.5-2(d) is for $\Delta\theta = 0.6$ degrees in Case C. The red line depicts the originally designed plasma boundary surface of the CFQS. Magnetic surfaces exist outside

the red line, so that the limiter in the actual experiment will determine the outermost magnetic surface. Generally, good magnetic surfaces are maintained in all cases of displacement are considered. We checked the good magnetic surfaces up to the displacement of $\Delta R = 50$ mm, $\Delta Z = 50$ mm, and $\Delta\theta = 3.0$ degrees. Therefore, magnetic surfaces are very robust.

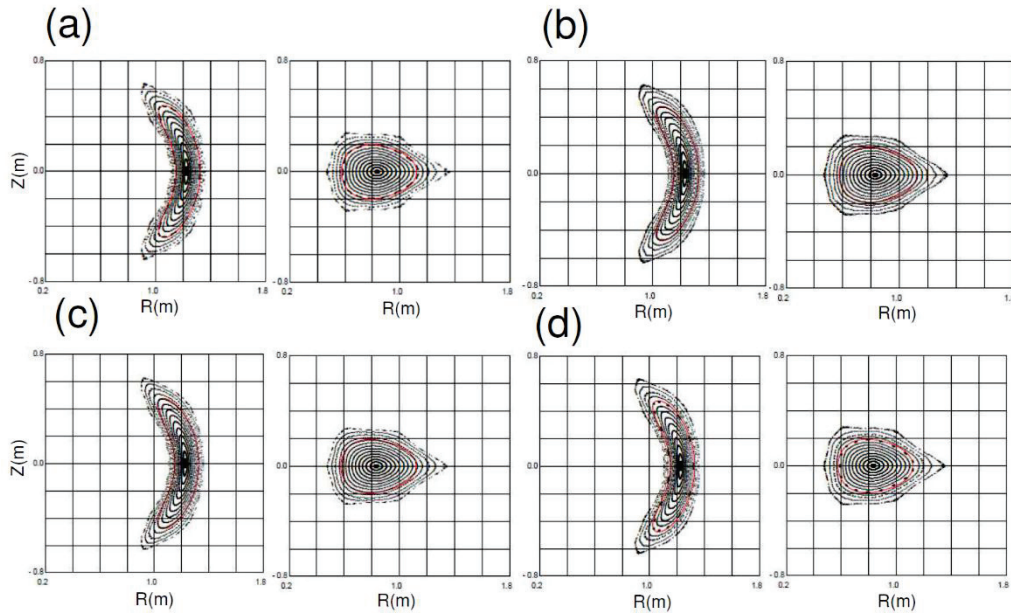


Fig. 3.7.5-2 Poincaré plots with (a) no displacement of coils, (b) $\Delta R = 10$ mm displacement in Case A, (c) $\Delta Z = 10$ mm in Case B, and (d) $\Delta\theta = 0.6$ degree in Case C.

Fig. 3.7.5-3 shows changes in the radial profile of rotational transform in Case A, B, and C. ΔR and ΔZ are scanned from 5 to 50 mm, and $\Delta\theta$ is scanned from 0.3 to 3.0 degrees (these values of $\Delta\theta$ correspond to the change in the maximum displacement of coil position from 5 to 50 mm). As shown in these figures, the effect of the misalignment on the rotational transform is small; therefore, islands caused by the low mode rational surface do not appear in the magnetic field configuration. Fig. 3.7.5-4 shows the change in the radial profile of the magnetic well depth. In all cases, the magnitude of change is very small.

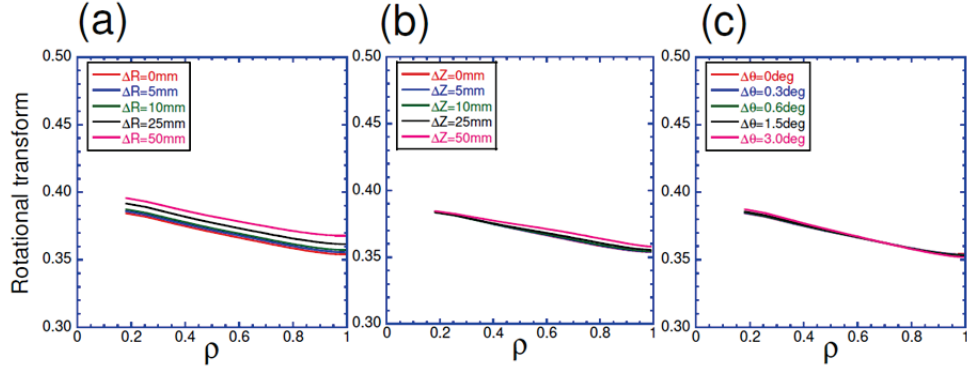


Fig. 3.7.5-3 Radial profile of rotational transform, with horizontal axis as the normalized minor radius. (a) change in the rotational transform for Case A, (b) Case B, and (c) Case C.

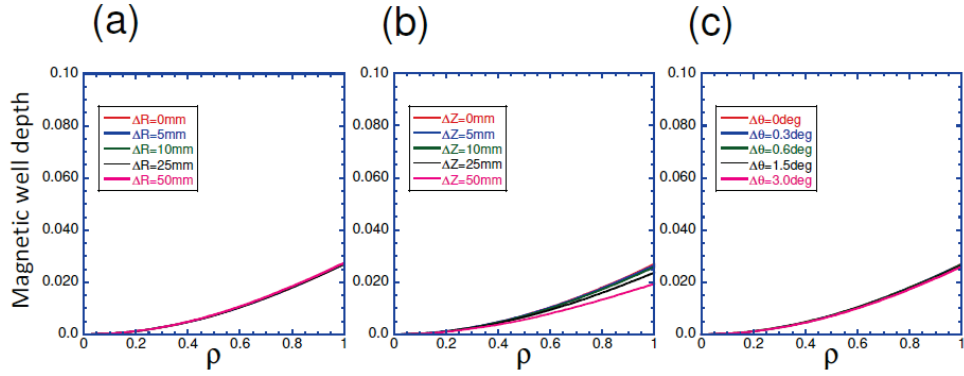


Fig. 3.7.5-4 Radial profile of magnetic well depth. (a) change in magnetic well depth for Case A, (b) Case B, and (c) Case C.

The effective helical ripple, ε_{eff} , is employed because the neoclassical diffusion coefficient in the $1/\nu$ regime, D_{NEO} , is proportional to $v_d \varepsilon_{eff}^{3/2} / \nu$. Here, v_d is the drift velocity, and ν is the collision frequency. Fig. 3.7.5-5 shows the radial profiles of the $\varepsilon_{eff}^{3/2}$ calculated from NEO code [3.7.5-2] for the displacement in Case A (Fig. 3.7.5-5 (a)), B (Fig. 3.7.5-5 (b)), and C (Fig. 3.7.5-5 (c)). The quantitative estimation of effects of the displacement of coils on neoclassical transport becomes directly possible from these figures.

If the displacement of modular coils is less than 10 mm, the physical properties such as magnetic surfaces, the profile of rotational transform, and magnetic well depth are not significantly changed according to the calculation results. For the neoclassical diffusion coefficient estimated from ε_{eff} , the magnitude does not change. Meanwhile, if the displacement reaches 25 mm, a few factors of D_{neo} will increase. Therefore, if the displacement of coils is less than 10 mm, main physical properties such as the rotational transport, magnetic well, and QA property do not change significantly. Naturally, this

conclusion is limited to the case where the displacement structure has stellarator symmetry (and toroidal periodic number is two).

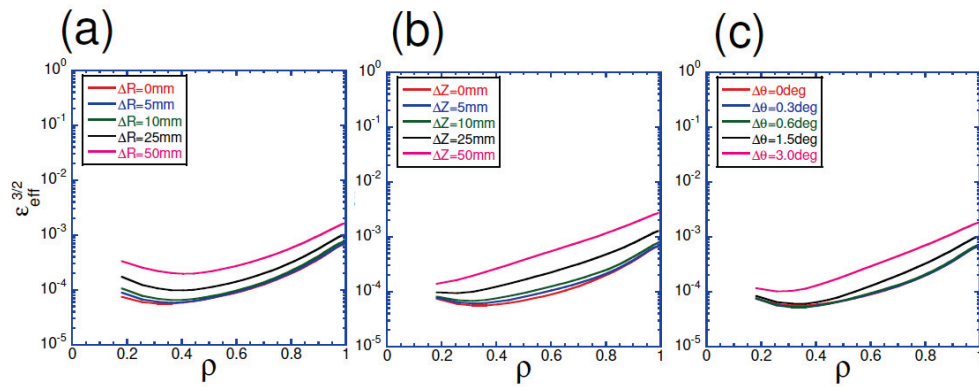


Fig. 3.7.5-5 Radial profile of effective helical ripple, $\epsilon_{\text{eff}}^{3/2}$ (a) change in effective helical ripple for displacement in Case A, (b) Case B, and (c) Case C.

References

- [3.7.5-1] A. Shimizu *et al.*, Plasma Fusion Res. **14** (2019) 3403151.
- [3.7.5-2] V. V. Nemov *et al.*, Phys. Plasmas **6** (1999) 4622.

3.7.6 Influence of general coil misalignment on magnetic surfaces

Coil misalignment will affect magnetic field configuration. Estimating these effects are important for determining an acceptable tolerance error in a process of constructing and assembling the modular coils. We have calculated magnetic field produced by the modular coils adding some displacement to the coils and evaluated differences in the results [3.7.6-1]. We consider three directions of the coil displacement as shown Fig. 3.7.6-1 and two types of combination of the coil displacement (Case A and Case B) as shown Fig. 3.7.6-2.

According to this calculation, we found that a change of rotational transform, *i.e.* ι with displacement in Z direction tends to be larger than the other directions. Fig. 3.7.6-3 shows the ι dependence on displacement in Z direction. These are values on a magnetic surface where its average minor radius is 0.05 m. A displacement of MC2 causes larger change of ι . Therefore, we should give a priority to an accuracy of MC2 during coil assembling process. In addition, Case B also causes a larger change of ι , and magnetic islands appears with 20 mm displacement as shown in Fig. 3.7.6-4. We think more than 20 mm misalignment is supposed to have significant effect from this result. Thus, we will set an acceptable displacement to be 5 mm for potential error of coil location, because coils will be adjusted by spacer with thickness of 5 mm. For assembling accuracy of positioning, we will set it to be 5 mm, therefore the final acceptable value of total misalignment to be 10 mm.

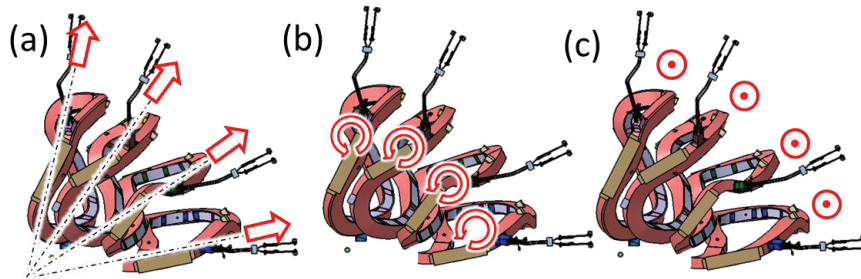


Fig. 3.7.6-1 Direction of MC displacement (a) major radius direction R (b) rotational direction around vertical axis of each coil α (c) vertical direction Z .

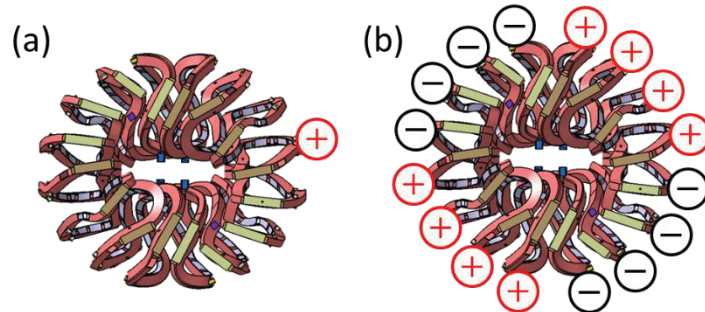


Fig. 3.7.6-2 Combination of MC displacements (a) Case A; One MC is moved (b) Case B; MCs in 90 deg. section are moved together and alternately in toroidal direction.

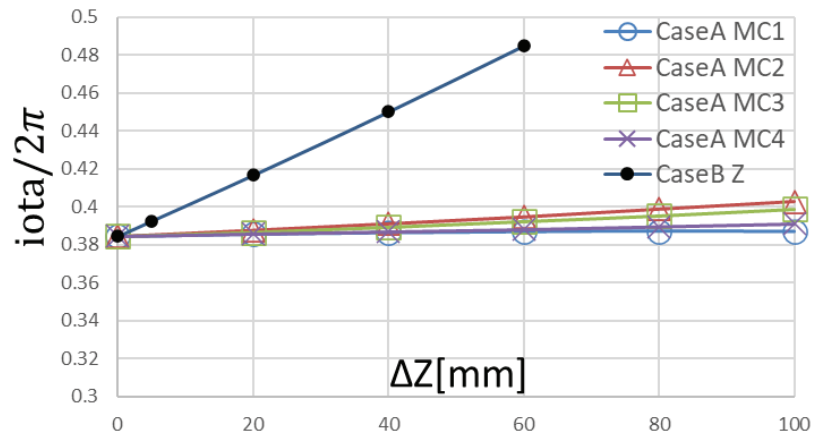


Fig. 3.7.6-3 A change of rotational transform, *i.e.* ι with displacement in Z direction.

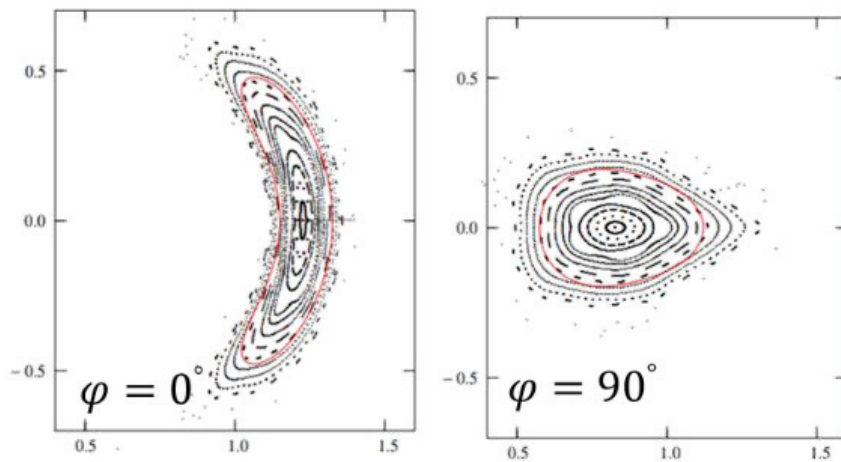


Fig. 3.7.6-4 A plot of magnetic surface in vacuum field with 20 mm displacement in Z direction in case B.

References

- [3.7.6-1] S. Nakagawa *et al.*, The 23rd IEEE Pulsed Power Conference (PPC) and the 29th IEEE Symposium on Fusion Engineering (SOFE), online, 12-26 December 2021, Poster 366.

3.8 Divertor configuration

In designing the magnetic configuration of an experimental device, the first priority is placed on designing the configuration of the core confinement region. However, it is well known that without a proper design of magnetic configuration of the peripheral region the concept is not useful for the fusion reactor. This is called “divertor design” because the most important physics issue related to the peripheral magnetic configuration is particle and heat removal.

In tokamak research, the concept of divertor is almost established and all existing tokamak devices in the world have similar divertor configuration (single null divertor) with the direct extension to the tokamak demo design. There are still discussions for the new ideas of advanced configurations (double null divertor and snow flake divertor) but they have not been adopted in real experimental devices. In stellarator research, we do not have one established concept of divertor partly because we have varieties of stellarator configurations and divertor concept strongly depends on the magnetic configuration of core confinement region. In fact, for the two largest stellarator experiments, LHD and W7-X, these devices have different divertor structures. In LHD, the intrinsic helical divertor has divertor magnetic field lines connecting the ergodic boundary layer of the core confinement region and the divertor plates on the wall [3.8-1, 2, 3]. In W7-X, the island divertor provides a sophisticated divertor structure combined with small islands created near the boundary of the core confinement region [3.8-4, 5, 6, 7]. For the new stellarator CFQS in China, we are designing a new divertor configuration which provides a sufficiently long connection length of magnetic field lines between the plasma boundary and the wall [3.8-8].

Three poloidal cross sections of the LCFS of CFQS are shown in Fig.3.8-1. These figures are VMEC output as a target configuration of the modular coil design. Modular coils were designed to realize such a magnetic configuration with a choice of the number of coils around the torus as 16 [3.8-9, 10]. The success of this coil design was the most important contribution to the finding of a new divertor concept for CFQS. Fig. 3.8-2 shows the punctual plots of the vacuum magnetic field lines (magnetic surfaces) produced with these modular coils (for the third cross section in Fig.3.8-1). Red line shows the LCFS of the target configuration in the modular coil design. The magnetic field produced by the modular coils has many closed magnetic surfaces with a larger area beyond the target LCFS. The result of the magnetic structure outside of the LCFS (defined by VMEC) does not come from the target configuration. In fact, another modular coil design with 20 coils with the same target configuration gave similar magnetic surfaces inside LCFS but the boundary configuration is very different. It has a stochastic layer just outside of the LCFS with small islands ($n = 2/m = 6$) surrounded by the stochastic layer.

The blue (lower) line in Fig. 3.8-3 shows the profile of the rotational transform of the vacuum magnetic configuration produced by the 16 modular coils. A very flat profile for the outer region is important for creating large islands for the divertor configuration. The rotational transform profile of

W7-X is also flat, but not as flat as that of CFQS. The polarities of the weak shear of both devices are different, namely, the CFQS has a weak negative shear (in the stellarator terminology) at the boundary while W7-X has a positive shear. A black arrow shows the position of the averaged minor radius of the LCFS of the target configuration. Although we decided upon an aspect ratio of 4.0 for the CFQS device, it is technically possible to create a larger confinement region if we design the vacuum chamber with a sufficiently large size to provide space for such larger closed magnetic surfaces. A control of plasma boundary with a movable limiter might be a possible choice for the plasma operation in experiments.

When we introduce the auxiliary toroidal coils to provide additional toroidal field to the stellarator field produced with modular coils, the magnetic configuration is changed to include large islands at the boundary of the core confinement region shown in Fig. 3.8-4. The QA property is conserved with the additional toroidal field. The strength of the additional toroidal field is -0.055 times averaged toroidal field produced by modular coils. The rotational transform is increased to change the boundary value to 0.4 (shown by red (upper) line in Fig. 3.8-3). This is a typical magnetic configuration for any type of stellarator that has a rational value of the rotational transform near the boundary. However, essential differences between the configuration shown in Fig. 3.8-3 from many other cases are 1) large size of islands and 2) the completeness of the island magnetic surfaces. It is shown in Fig. 3.8-4 that clearly formed island bundle flux surrounds the core confinement region with a clearly defined interface of the magnetic field separatrix. This is the reason why we call such a configuration as “island bundle divertor (IBD)”. The entire magnetic confinement area is clearly separated into two regions: hot plasma region in the core and cold plasma region in the periphery.

Fig. 3.8-5 shows the divertor field line tracing, which is created in the following calculation procedures. We found first the LCFS of the core confinement region. Then we distributed many field line tracing starting points with a small deviation (5 mm for $R = 1$ m torus) from the LCFS. Because the island magnetic surfaces are complete, there is no escaping field line in such a calculation. Fig. 3.8-5 shows blue line for one of the possible shapes of the vacuum chamber wall. If we install divertor plates at this wall position, the cold plasma in the island bundle flux can be absorbed at the divertor plates. Fig. 3.8-6 shows the divertor tracing with the wall target where the field line tracing is stopped. The pattern of the magnetic field line Poincaré plots is very similar to the tokamak divertor structure. In fact, the transport of the magnetic field lines is exactly the same as tokamak divertor, where the peripheral regions of the divertor are connected to the core confinement region with a clear magnetic separatrix, and magnetic field lines in divertor region have long connection length between the null point and the wall. Because the magnetic field lines go around through all five island bundle fluxes with very small incident angles to the wall, the distribution of the heat load on the divertor plates is determined by the precise geometric design of the shapes and the locations of divertor plates.

Fig. 3.8-7 shows the distribution of the connection lengths for magnetic field lines near the X point of inboard side at the toroidal angle ϕ of 90° . The horizontal axis corresponds to the major radius of the calculation point in the poloidal cross section and the vertical axis to the vertical positions (a major radius of the device is 1 m). Calculation was made at 500 points for both horizontal and vertical directions. Three areas are clearly separated by a sharp separatrix created by the islands. A yellow area on the right of X point is the core confinement region, two violet areas above and yellow X point are inside islands and almost black area on the left of X point is outside of islands. In the magnetic island areas, the connection lengths of magnetic field lines are in the range of 500 to 1000 m and there is no exceptional field line with shorter length. This is because the island magnetic surfaces are very regular and there is only little ergodic region between the core confinement region and the island divertor flux. This is a clear difference from the LHD-type divertor structure where there are some field lines with shorter length between the core region and the divertor plate because of the ergodicity of the boundary layer of the core confinement region.

The magnetic field lines located on the separatrix lines (with red color) are parts of the field lines escaping from the core confinement region (yellow color) through the separatrix interface between core and island region. These field lines finally hit the wall (shown by the boundary of the black color area) at the left side of the figure. The position of this strike point moves as the position of the island changes. When the rotational transform value is shifted with the change of the current in the auxiliary toroidal coils by 2%, the position of the strike point moves about 1.5 cm along the wall. This sensitivity of the island position is within the controllability of the rotational transform with the auxiliary toroidal coil.

Because the rotational transform of IBD region is 0.4, island bundles shown in Fig. 3.8-4 are connected together. In other words, this bundle flux is a single flux. Thus particles and heat flux transferred from the core confinement region to the IBD can be removed at any position in the torus. Because the space between the plasma and the wall is very narrow in the toroidal position of the crescent shape of plasma (the leftmost LCFS in Fig. 3.8-1), we can avoid installing divertor structure at this region and take advantage of installing it where the space is larger. As shown in Fig. 3.8-6, the number of divertor feet is as many as ten. Thus it is possible to reduce the maximum heat load at the divertor compared with the tokamak case, where the number of feet is two (in the case of a single null). On the other hand, because the divertor fields are all connected into a single structure, it is not necessary to install as many as ten divertor plates.

We have discussed so far the island divertor concept for CFQS based on the vacuum magnetic field produced by the external coils. Because the neoclassical bootstrap current is larger for the QA stellarator compared to other types of stellarator, it is necessary to find the operation scenario of the island divertor for the plasmas with finite beta. An example of the neoclassical bootstrap current calculation for CFQS is reported in the previous paper with planned experimental parameters [3.8-10].

Fig. 3.8-8 shows an example of the calculated profiles of the rotational transform in the operation with finite beta value. The calculation is based on the VMEC code which is widely used for the calculation of three dimensional equilibria with given plasma current profile. The black line shows the profile for the vacuum equilibrium with zero beta. It is equivalent to the blue line in Fig. 3.8-3 plotted from the magnetic field line tracing for the vacuum field. The red line shows the rotational transform profile with the averaged beta value of 0.35 %. The neoclassical bootstrap current is calculated using BOOTSJ code [3.8-11] for the pressure profile shown by the blue curve in the Pascal unit. This shape of the pressure profile is assumed based on the typical density and temperature profiles observed in many stellarator experiments [3.8-10]. When these codes are used for calculating the rotational transform profile with neoclassical bootstrap current, the reliability of the profile data in the vicinity of the magnetic axis is not good. Therefore these line are shown by dots for that area. It passes the value of 0.4 ($n/m = 2/5$) at the edge, which is expected to form islands. However, because the VMEC code assumes the existence of clear magnetic surfaces, the discussions of island structure need more advanced theoretical work using HINT, which is beyond the scope of this paper.

The green dotted line shows an example of controllability for the rotational transform profile using auxiliary toroidal coil. This profile is an example of applying the additional toroidal field to shift up the profile from the one with neoclassical bootstrap current. Actually the expected operation would be either shifting up or shifting down the rotational transform profile to match to the value of 0.4 in order to create island divertor configuration for the plasma with beta value different from 0.35 %.

For such finite beta plasmas, it is necessary to make two different controls in order to create good island divertor configuration. The first one is to adjust the rotational transform value near plasma edge at 0.4, which is resonant to the $n/m = 2/5$ islands. This control is relatively easy using an adjustable power supply for the auxiliary toroidal coils. The second one is to control plasma pressure profile for obtaining a suitable neoclassical bootstrap current profile, which produces the rotational transform profile with very low negative shear. This control would be technically difficult but could be achievable with proper heating control, which will be an important research topic in the experiments. The duration of the plasma discharge planned in the CFQS program is 100 ms due to the limitation of the heating devices. The estimated rising time of the neoclassical bootstrap current is between 20 to 100 ms depending on the collisionality. Even if the fully developed equilibria with neoclassical bootstrap current is not possible for collisionless plasmas in the strict sense, the experimental analysis for this scientific topic will be possible.

Because theoretical analysis of the island divertor configuration needs the equilibrium calculation including island structure, the model calculation using HINT code [3.8-12] is now in progress and will be reported in the succeeding paper. The equilibrium calculations using VMEC for the rotational transform profiles with auxiliary toroidal coils were made for different volume-averaged beta values

up to 1.5 %. For higher beta than 0.35 %, the auxiliary toroidal field must be positive (same polarity as the basic toroidal field) in order to decrease the rotational transform at the plasma edge down to 0.4.

Since the island structure is in general very sensitive to the control of the rotational transform, the control of neoclassical bootstrap current in the stellarator operation will be essential to keep the IBD concept stable. However, we know that any plasma parameters and engineering parameters must be controlled extremely accurately in the future fusion reactor. The control of neoclassical bootstrap current would be within available control knobs in the fusion reactors.

References

- [3.8-1] Y. Takeiri *et al.*, Nucl. Fusion **57** (2017) 102023.
- [3.8-2] S. Masuzaki *et al.*, Fusion Sci. Technol. **50** (2006) 361.
- [3.8-3] M. Kobayashi *et al.*, Fusion Sci. Technol. **58** (2010) 220.
- [3.8-4] R. C. Wolf *et al.*, Nucl. Fusion **47** (2017) 102020.
- [3.8-5] H. Renner *et al.*, Plasma Phys. Control. Fusion **44** (2002) 1005.
- [3.8-6] Y. Suzuki, J. Geiger, Plasma Phys. Control. Fusion **58** (2016) 064004.
- [3.8-7] Y. Feng *et al.*, Nucl. Fusion **56** (2016) 126001.
- [3.8-8] S. Okamura *et al.*, J. Plasma Phys. **86** (2020) 815860402.
- [3.8-9] H. Liu *et al.*, Plasma Fusion Res. **13** (2018) 3405067.
- [3.8-10] A. Shimizu *et al.*, Plasma Fusion Res. **13** (2018) 3403123.
- [3.8-11] K. C. Shaing *et al.*, Phys. Plasma **B1** (1989) 148.
- [3.8-12] Y. Suzuki *et al.*, Nucl. Fusion **46** (2006) L19.

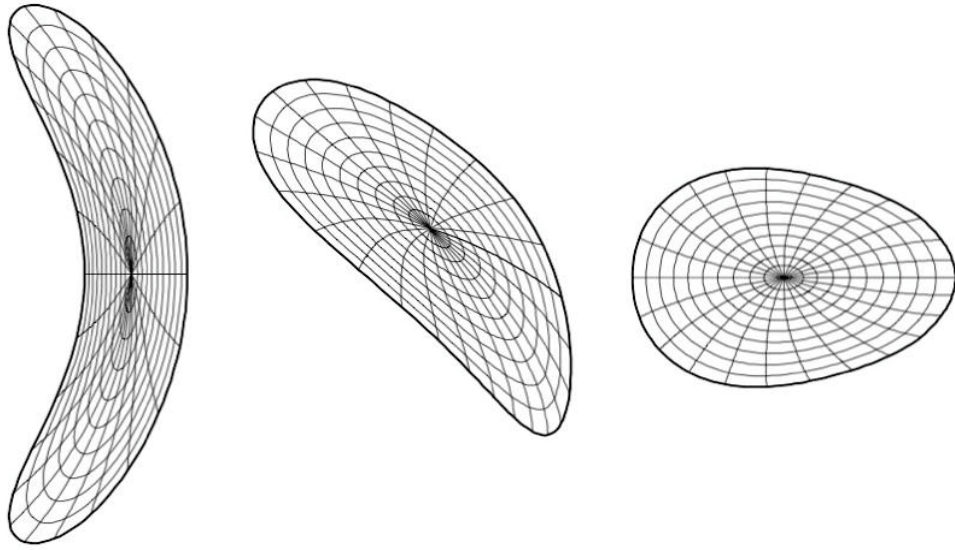


Fig. 3.8-1 LCFS for CFQS advanced stellarator design. Cross sections for three toroidal positions are shown.

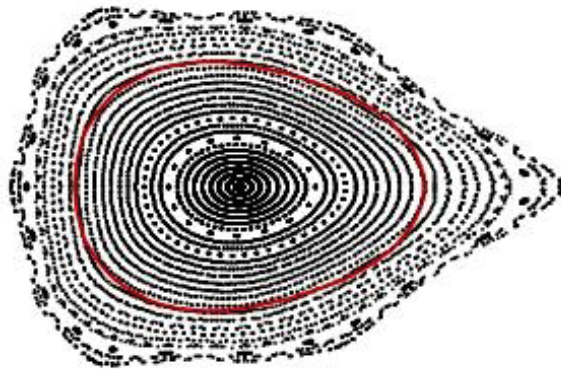


Fig. 3.8-2 Punctual plots of magnetic surfaces for CFQS configuration produced by 16 modular coils. Red line corresponds to the LCFS of the 3rd plot in Fig. 3.8-1.

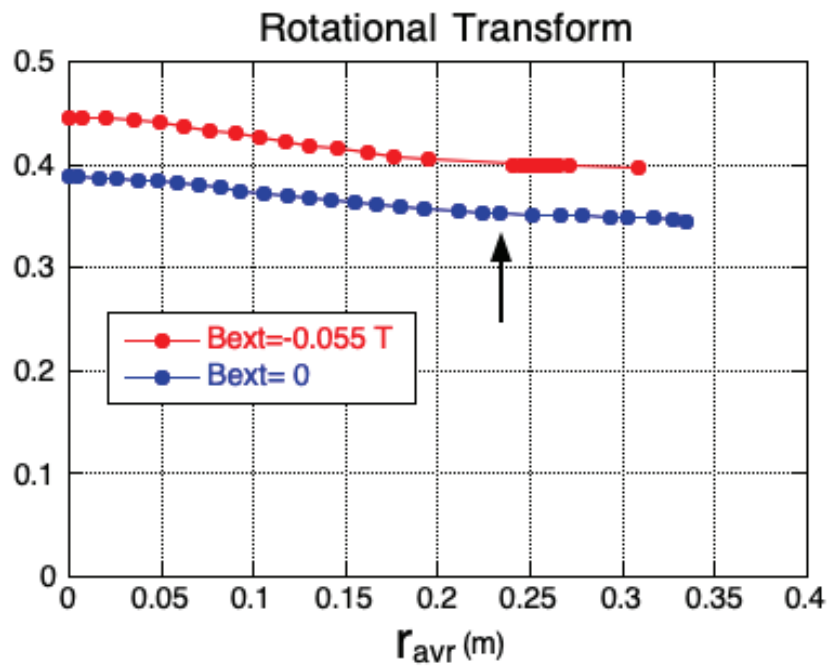


Fig. 3.8-3 Blue [lower] line: Rotational transform profile of vacuum field of CFQS. Arrow indicates the position of LCFS of target configuration. Red [upper] line: Rotational transform profile of island divertor configuration ($n/m = 2/5$) with additional toroidal field.

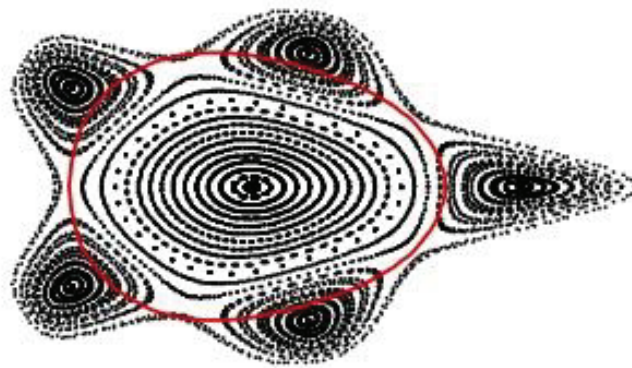


Fig. 3.8-4 Magnetic configuration of island bundle divertor.

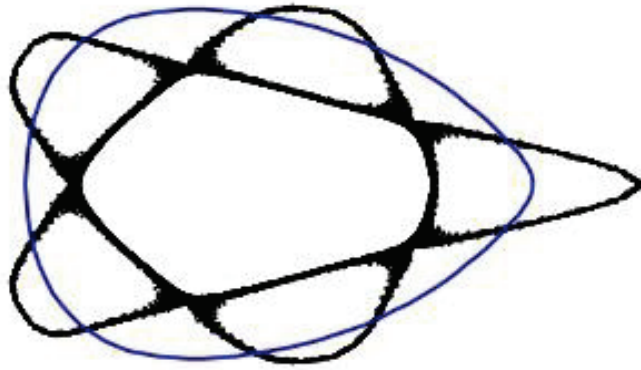


Fig. 3.8-5 Divertor field line tracing for island bundle divertor. Blue line shows one example of vacuum chamber wall position for locating divertor plates.

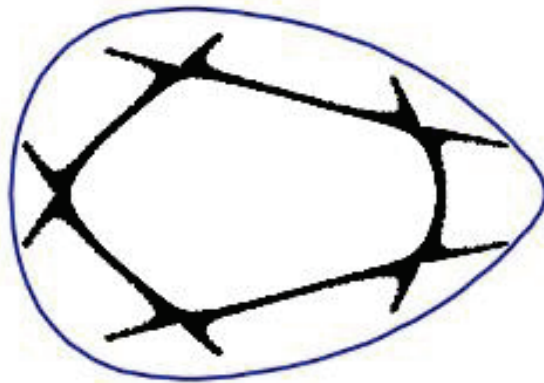


Fig. 3.8-6 Divertor field line tracing with assumed existence of divertor targets.

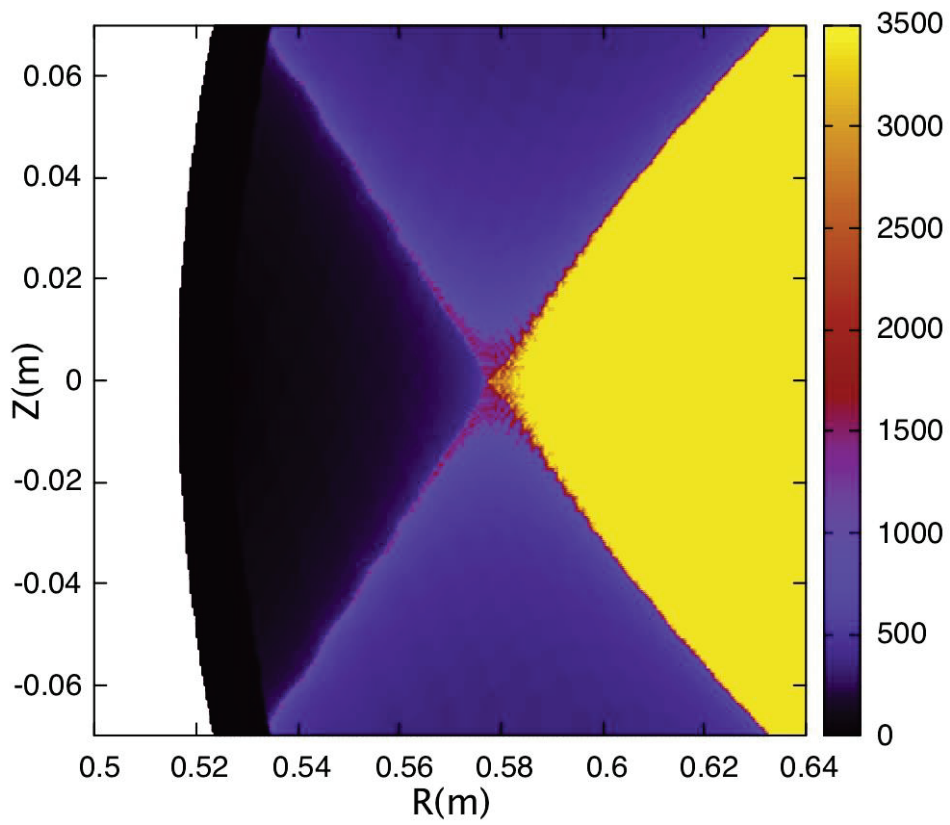


Fig. 3.8-7 Distribution of connection length near one of X-points in the island divertor of CFQS.

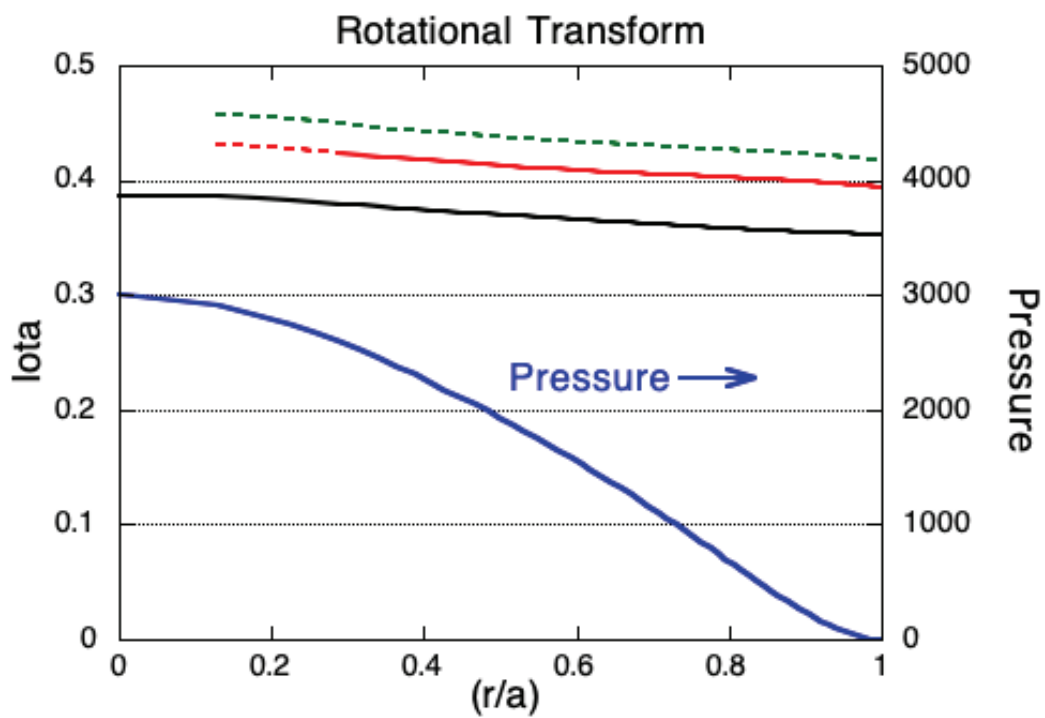


Fig. 3.8-8 Rotational transform profiles calculated by VMEC code. Black line shows the profile for the vacuum field (zero beta). Red line shows the profile with neoclassical bootstrap current calculated for beta value of 0.35 % and the pressure profile shown by blue curve. Green line shows an example of profile control using auxiliary toroidal field to shift up the red profile by reducing the toroidal field produced by modular coils.

4 Engineering design

Only an overview of engineering design is given in this chapter. If you want to see the details, please refer to the appendix.

4.1 Whole assembly

4.1.1 Specification for engineering design

The CFQS design is based on 2b32 CHS-qa configuration, and reduces the major radius, increases the aspect ratio, and reduces the magnetic field slightly to reduce costs and make it easier to manufacture. Table 4.1.1-1 shows physical main parameters of the CFQS. We can achieve low magnetic shear and a shallow well structure throughout the entire region as mentioned in the chapter for the equilibrium. The dominant ripple is the toroidal mode $B_{1,0}$, which indicates a tokamak-like or QA configuration. The CFQS project aims to confirm the effectiveness of this equilibrium. The aspect ratio of CFQS is the smallest in helical devices and the coil shape is very complicated. They are the disadvantages that make engineering is relatively harder than other devices. For example, the work area in the central region is very narrow and special structural idea is necessary for assembling the CFQS. The electromagnetic force will be locally large although the magnetic field in the plasma is not so large and only 1T. Therefore, a strong reinforcement structure is required. They are engineering disadvantages for cost reduction. As described later, the direction of the electromagnetic force is unlike the tokamak. Special design is required because vertical and toroidal components are generated in the electromagnetic force. Table 4.1.1-2 gives technical data of the CFQS. A basic QA configuration can be produced by four types of modular coils (for total of 16). However, to allow flexible configuration, we will install four poloidal field coils (to move the magnetic axis horizontally) and twelve toroidal field coils (to change the rotational transform).

Table 4.1.1-1 Comparison of physical specifications for stellarator.

No	Parameter	CFQS	W7-X	HSX
1	Type	QA	QI	QH
2	Major radius (m)	1.0	5.5	1.2
3	Minor radius (m)	0.25	0.5	0.15
4	Aspect ratio	4	11	8
5	Magnetic field (T)	1	3	1
6	Toroidal periodic number	2	5	4
7	Rotational transform	0.35-0.38	0.85-1.0	1.0-1.1
8	Magnetic well depth	0-0.025		

QA; Quasi-axisymmetric configuration

QI; Quasi-isodynamic configuration

QH; Quasi-helical symmetric configuration

Table 4.1.1-2 Facilities of the CFQS.

Facility	Parameter	Value			
Plasma	Pulse width (s)	0.1 s for pulse, 120 s for steady			
	Magnetic field	1 T for pulse, 0.09T for steady			
	Heating	450 kW (54.5GHz ECH 0.1s pulse)			
		20 kW (2.45GHz RF)			
	Diagnostics	1,000 kW (NBI 40kV 0.1s pulse)			
Thomson scattering, micro wave interferometer Magnetic surface, Langmuir probe, HIBP, CXRS et al.					
Coil	Name	MC	PFC(IV)	PFC(OV)	TFC
	Cross section (mm ²)	69 x 132	48 x 100.5	100.5 x 48	66 x 7
	Number of types	4	1	1	3
	Number of coils	16	2	2	12
	Number of turns per one coil	12 x 3 x 2	8 x 4	8 x 2 x 2	8 x 2
	Winding method	Pancake, 3 conductors simultaneously	Solenoid	Pancake, 2 conductors simultaneously	Solenoid
	Conductor (mm ²)	58.83	58.83	58.83	20
	Maximum current (kA)	4.34	4.34	4.34	2.0 (TFC10) 3.0 (TFC32) 3.0 (TFC70)
	Dielectric strength against the ground	2.4 kV DC	0.5 kV DC	1.6 kV DC	0.6 kV DC
	Test voltage against the ground	5.8 kV DC	5.8 kV DC	5.8 kV DC	2.2 kV DC
	Dielectric strength between layers	0.4 kV DC	0.125 kV DC	0.4 kV DC	0.15 kV DC
	Test voltage between layers	0.8 kV DC	0.8 kV DC	0.8 kV DC	0.3 kV DC
	EM force support	Reinforced with clamps or cases	Rigidity of the coil itself	Rigidity of the coil itself	Fixed on the vacuum vessel
	Heat resistance class	B (<130°C)	A (<105°C)	A (<105°C)	B (<130°C)
Cooling method	Water cooling			Natural air	
Coil PS for pulses	Total operation power (MW)	32	5.7	4.4	
	Energy consumption (MJ)	35.3	2.2	0.82	
	Pulse width (s)	1.11	0.38	0.19	
	Power source	A motor generator with 10kV AC			
Coil PS for steady	Total operation power (MW)	0.257	0.046	0.035	
	Power source	Mobile energy storage stations with 380V AC			
Vacuum vessel	Cross-sectional shape	Bean shape with 0.45 m x 1.2 m at vertically elongated section			
	Load support	8 leaf spring type legs			
	Material	SUS316 with thickness of 6mm			
	Number of ports	Over 46			
	One turn break	Nothing			
	One turn resistance	0.4mΩ (By ANSYS/Maxwell)			
	Baking temperature	130 °C or less			
	Vacuum pumping	1500 ℓ/s TMP x 2			

4.1.2 Overall Structure

Fig. 4.1.2-1 to Fig. 4.1.2-5 show schematics of the CFQS with power supplies. The CFQS body is approximately 2800 mm high between a top frame and a bottom frame and has an outer diameter of 4300 mm. The electromagnetic force applied to the modular coils is supported by a cage-type support structure, with diagonal beams to absorb the overturning force and two central pillars to absorb the centripetal force. The mass of the device body is about 30 tons. These devices will be installed in a torus hall with power supplies, as shown in Fig. 4.1.2-3. Fig. 4.1.2-4 and Fig. 4.1.2-5 indicate main dimension of the CFQS. To install various equipment's around the CFQS body, Stages with a height of approximately 2.3m and a width of 10m will be installed. The center height of the body is planned to be 3.5m from the floor, and we are going to create large space under the device to install measuring instruments and related equipment.

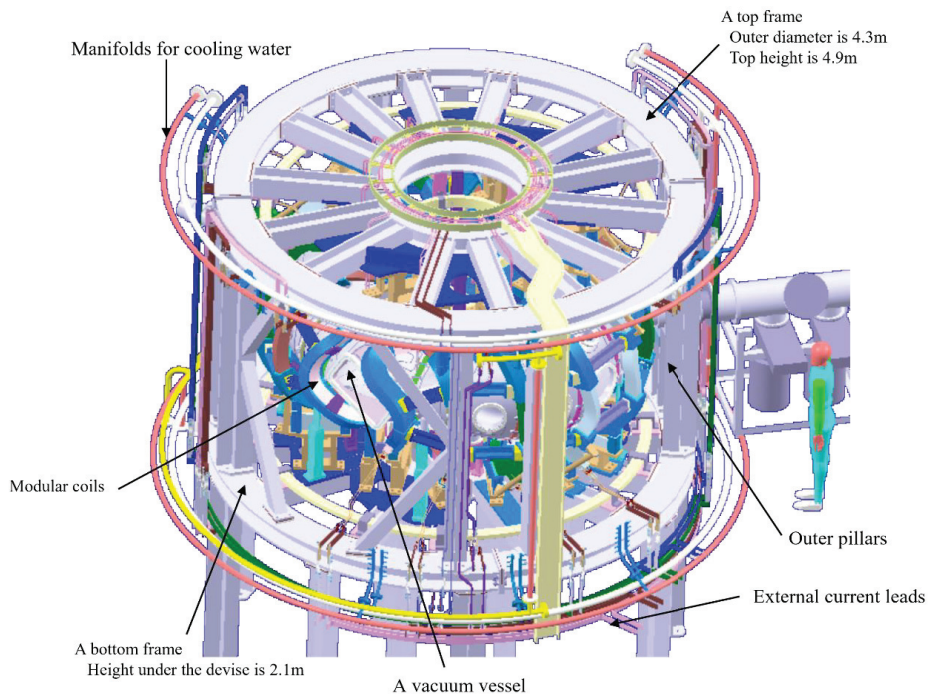


Fig. 4.1.2-1 Schematic drawing of the CFQS.

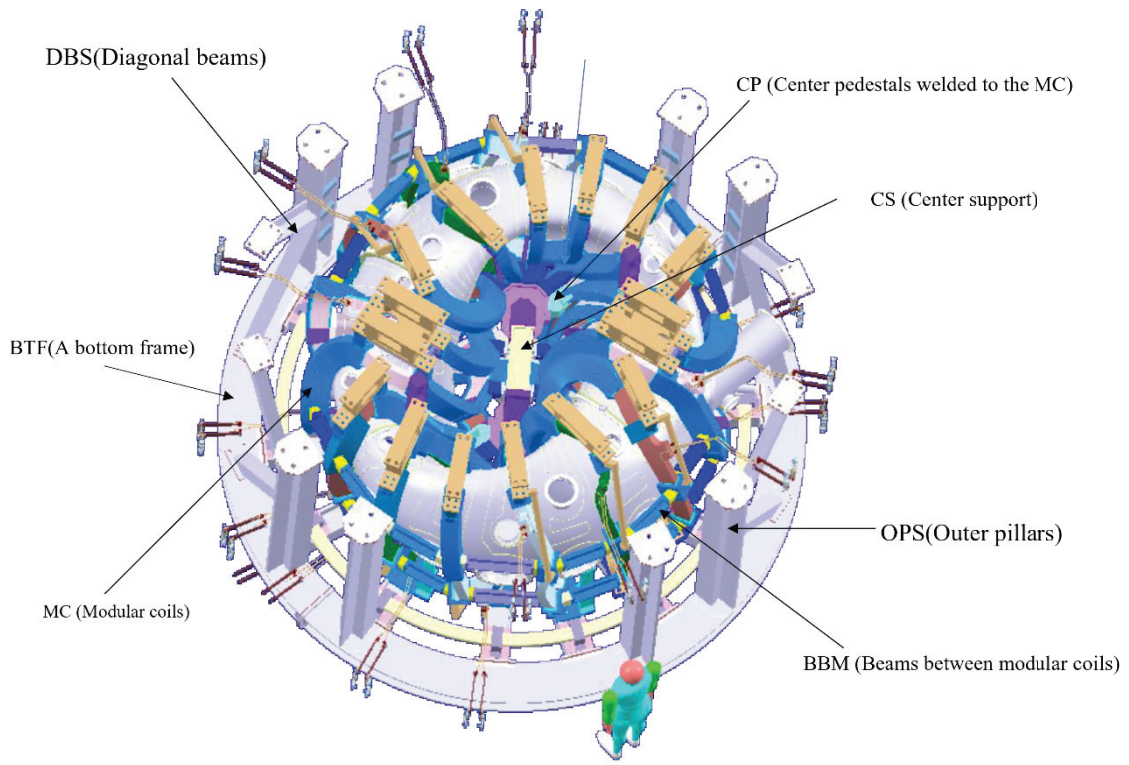


Fig. 4.1.2-2 Schematic drawing in the cage-type support structure.

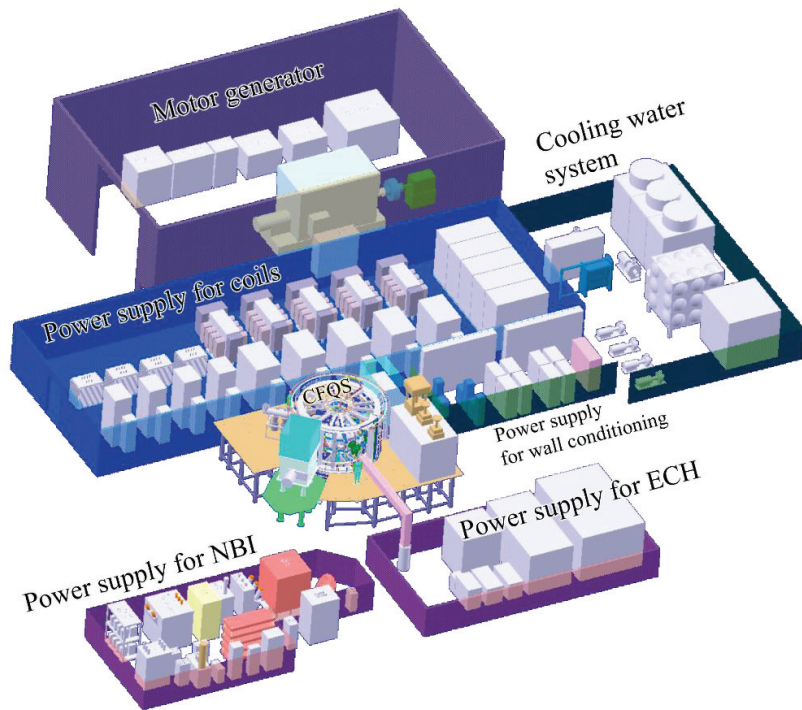


Fig. 4.1.2-3 Layout of the research laboratory.

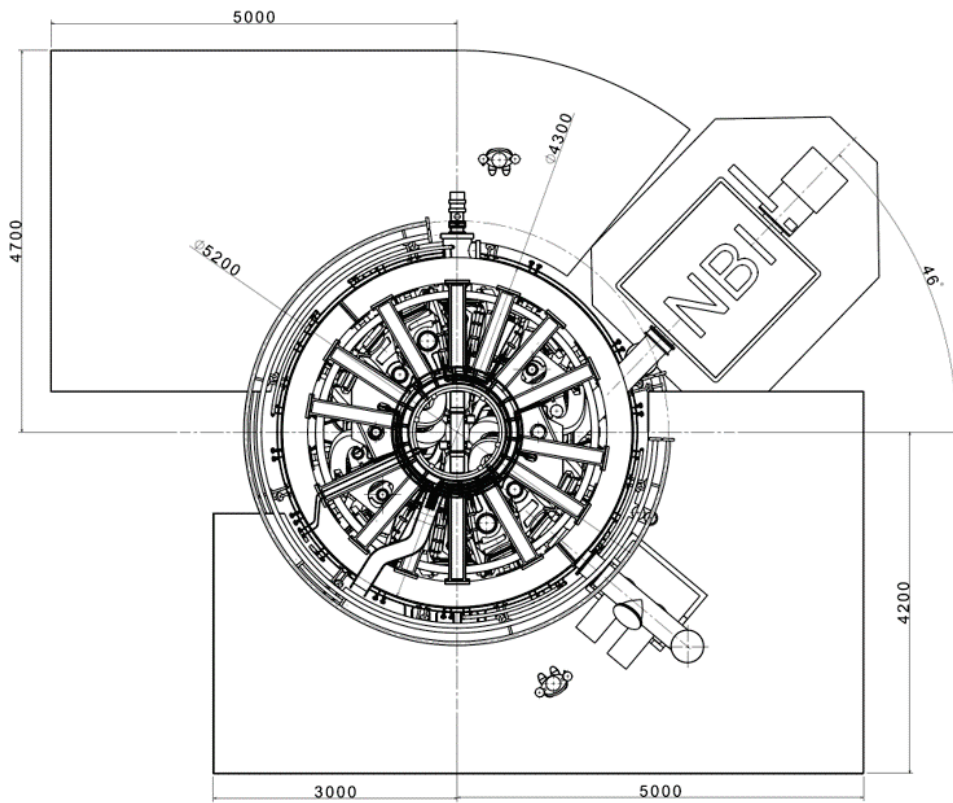


Fig. 4.1.2-4 Top view of the CFQS.

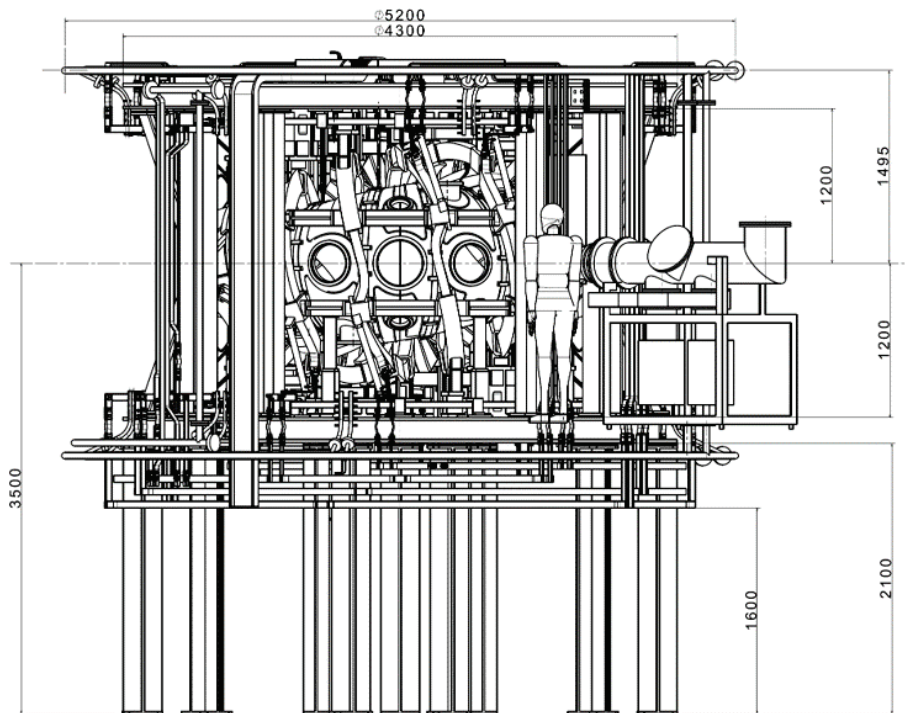


Fig. 4.1.2-5 Front view of the CFQS.

4.1.4 Parts list for the CFQS

The part list is shown in the table below. The total weight is about 32 tons, and the heaviest part is the top and bottom frame.

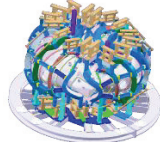
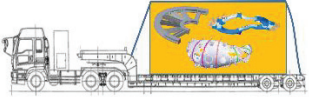
Table 4.1.4-1 Parts list of the CFQS

No	Product	Part	Mass(kg)	Quantity	Total(kg)	Picture
1	Vacuum vessel with TFC's and legs	Type A	400	2	2,160	
		Type B	680	2		
2	NBI port flange		60	2	120	
3	Modular coils	MC1	540	4	10,200	
		MC2	520	4		
		MC3	680	4		
		MC4	810	4		
4	Beams between the MCs	Long	16	28	480	
		Short	4	8		
5	Top and bottom frames	Top	2200	2	8,800	
		Bottom	2200	2		
6	Base plates for the MC	Upper	360	2	1,500	
		Bottom	390	2		
7	Pillars with diagonal beam	Pillar	310	4	2,600	
		Pillar with beams	340	4		
8	Legs	out	210	8	2,400	
		in	180	4		
9	Center support		400	1	400	
10	Manifolds	Upper	103	1	250	
		Lower	147	1		
11	PFC	IV	130	2	1,100	
		OV	420	2		
12	External current leads		400	1	400	
13	Others (extra)		1590	1	1590	
Sum					32,000	

4.1.5 Overall production flow

The table below shows the overall production flow for the CFQS. Although it depends on the installation location and road conditions along the way, it is considered difficult to transport about 30 tons all at once. After verifying the quality of individual parts in the factory, it is planned to disassemble and transport the individual parts and reassemble them in the laboratory.

Table 4.1.5-1 Rough production flow

STEP	Contents	Illustration
1	Purchase materials and standard products.	
2	Product parts and sub-assemblies in a factory.	
3	Pre-assemble the modular coil and vacuum vessel in a factory.	
4	Assemble the main parts, test them, and verify quality of each sub assembly in a factory, such as the vacuum vessel, the coil, and the bottom frame.	
5	Disassemble it for the transportation.	
6	Transport sub assembling products and parts in a research laboratory.	
7	Pre-assemble the modular coils and vacuum vessel in the laboratory.	
8	Assemble major products, such as the bottom frame, vacuum vessel, modular coil, and lower PFC.	
9	Individually test the major products on the way, such as the vacuum leak test and accuracy measurement of the coil position.	
10	Assemble other many parts.	
11	Validate the CFQS by overall operation test.	

4.2 Coil system

4.2.1 System configuration

Schematic of the coil system is shown in Fig. 4.2.1-1. It shows 16 modular coils (brown), 4 poloidal field coils (yellow) and 12 toroidal field coils (pink). The last closed magnetic flux surface (LCFS) is shown in beige. Table 4.2.1-1 to Table 4.2.1-3 show the operation parameters for each coil system. Here, the MC and TFC currents are the values that generate the required magnetic field obtained by the equilibrium calculation. The required vertical magnetic field, which is generated by the PFC, for plasma control is not clear. We assume 10% of total modular coil current as a design specification for the PFC.

A basic QA configuration can be produced by four types of modular coils (for total of 16). However, to allow flexible configuration, we will install four poloidal field coils (to move the magnetic axis horizontally) and twelve toroidal field coils (to change the rotational transform). The coil currents are driven by nine power supplies. The power supplies, the diagnostics and the heating apparatus are different in the experimental phase, but the coil system is common. It will be constructed under the rated operation conditions.

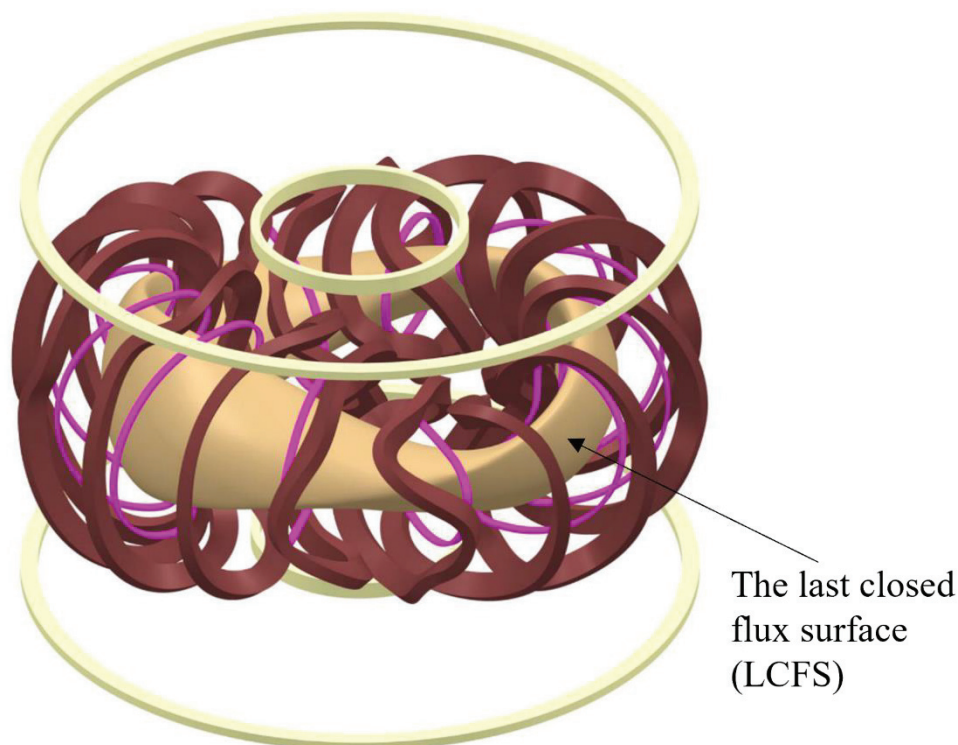


Fig. 4.2.1-1 Schematic drawing of the three coil systems. The brown shows the modular coil, the pink the toroidal field coil, and the yellow the poloidal coil.

Table 4.2.1-1 Operation parameters of the modular coil system (MC).

Category	Parameters	unit	MC1	MC2	MC3	MC4	Remarks	
Electrical design	DH	mm		132			Including earth isolation and cooling hall	
	DW	mm		69				
	Number of coils			4				
	Cross-section of a conductor	mm ²		58.83				
	Number of turns	1/coil		72			12 x 3 x 2	
	Winding method		Pancake, 3 conductors simultaneously					
	Length of one turn conductor	m/turn	4.390	4.330	4.200	4.126	By CATIA	
	Resistance	mΩ	435.7	429.5	415.6	401.2	By Maxwell for 4 coils adding margin of 5%	
	Inductance	mH	82.5	81.1	78.7	76.0		
	Time constant	s	0.1894	0.1889	0.1895	0.1893		
	Dielectric strength against the ground	kV		2.4			110% of the start-up	
	Test voltage against the ground	kV		5.8			2E+1000	
	Dielectric strength between layers	kV		0.4				
	Test voltage between layers	kV		0.8			2E, Impulse	
Heat resistance class			B			< 130°C		
Cooling design	Number of cooling circuits	1/coil		3				
	Length of cooling pipe	m	105.4	103.9	100.8	96.2	Average 102	
	Flow velocity	m/s		1.9				
	Flow rate	m ³ /s		2.39E-05				
	Loss head	m	185.1	182.5	177.0	168.9	Hazen Williams'	
Pulse operation (1T)	Current in a conductor	kA		4.34				
	Total current in a coil	kAT		312.5				
	Current density (Conductor only)	A/mm ²		73.8				
	Current density (With isolator)	A/mm ²		34.3				
	Start-up voltage	kV	2.151	2.119	2.052	1.981	Current wave form Startup exponential Flat top constant Damping exponential	
	Flat-top voltage	kV	1.891	1.864	1.804	1.741		
	Decay voltage	kV	0.997	0.985	0.950	0.918		
	Current rise time	s		0.4				
	Flat top time	s		0.6				
	Discharge period	s		300				
	Stored magnetic energy	kJ	777	764	742	715	Total 2,998	
	Energy consumption	MJ	9.1	9.0	8.7	8.4	Total 35.3	
	RWET	s		1.11			Equivalent time	
	PS power at a flat top	MW	8.2	8.1	7.8	7.6	Total 31.7	
Adiabatic temperature rise	k		35.8			In a short pulse		
Time averaged current	kA		0.264			In a conductor		
Steady operation (0.09T)	Current in a conductor	kA		0.391				
	Current density (Conductor only)	A/mm ²		6.64				
	Voltage	V	170.2	167.8	162.3	156.7		
	Stored magnetic energy	kJ	6.29	6.19	6.01	5.80	Total 24.3	
	PS power at a flat top	kW	66.5	65.5	63.4	61.2	Total 257	
	Average temperature rise	k	55.6	54.9	53.1	51.2		
Start-up voltage	V	204.2	201.3	194.8	188.1	120% of the flat top.		

Table 4.2.1-2 Operation parameters of the poloidal field coil system (PFC).

Category	Parameters	unit	IV	OV	Remarks	
Electrical design	R0	mm	536	1695		
	Z0	mm	±900	±1100		
	DR	mm	48	100.5	Including earth isolation and cooling hall	
	DZ	mm	100.5	48		
	Number of coils		2	2		
	Cross-section of a conductor	mm ²	58.83	58.83		
	Number of turns	1/coil	32	32	8 x 4 (IV), 8 x 2 x 2(OV)	
	Winding method		Solenoid	Pancake, 2 con.s simultaneously		
	Length of one turn conductor	m/turn	3.4	10.6		
	Resistance	mΩ	73.0	230.6	By Maxwell for 2 coils adding margin of 5%	
	Inductance	mH	5.00	18.85		
	Time constant	s	0.068	0.082		
	Dielectric strength against the ground	kV	0.5	1.6	110% of the start-up	
	Test voltage against the ground	kV	5.8	5.8	Same as for the MC	
Dielectric strength between layers	kV	0.125	0.4			
Test voltage between layers	kV	0.8	0.8	Same as for the MC		
Heat resistance class		A	A	< 90°C		
Cooling design	Number of cooling circuits	1/coil	1	2		
	Length of cooling pipe	m	108.8	169.6		
	Flow velocity	m/s	1.9	1.5		
	Flow rate	m ³ /s	2.39E-05	1.88E-05		
	Loss head	m	191.1	192.3	Hazen Williams' equation	
Pulse operation (1T)	Current in a conductor	kA	4.34			
	Total current in a coil	kAT	139			
	Current density (Conductor only)	A/mm	73.8			
	Current density (With isolator)	A/mm	28.8			
	Start-up voltage	kV	0.413	1.418	Current wave form Startup exponential Flat top constant Damping exponential	
	Flat-top voltage	kV	0.317	1.001		
	Decay voltage	kV	0	0		
	Current rise time	s	0.1			
	Flat top time	s	0.3			
	Discharge period	s	300			
	Stored magnetic energy	kJ	47.1	177.5	Total	224.6
	Energy consumption	MJ	0.523	1.671	Total	2.2
	RWET	s	0.38		Equivalent time	
	PS power at a flat top	MW	1.4	4.3	Total	5.7
Adiabatic temperature rise	k	12.2		In a short pulse		
Time averaged current	kA	0.16		In a conductor		
Steady operation (0.09T)	Current in a conductor	kA	0.39			
	Current density (Conductor only)	A/mm	6.6			
	Voltage	V	28.5	90.1		
	Stored magnetic energy	kJ	0.38	1.44	Total	1.8
	PS power at a flat top	kW	11.1	35.2	Total	46.3
	Average temperature rise	k	55.9	111.9		
Start-up voltage	V	34.2	108.1	120% of the flat top.		

Table 4.2.1-3 Operation parameters of the toroidal field coil system (TFC)

Category	Parameters	unit	TFC10	TFC32	TFC70	Remarks
Electrical design	DH	mm	7			Including earth isolation and cooling hall
	DW	mm	66			
	Number of coils		4			
	Cross-section of a conductor	mm ²	20			3 x 7-R0.5
	Number of turns	1/coil	16			8 x 2
	Winding method		Solenoid			
	Length of one turn conductor	m/turn	3.390	3.150	2.588	By CATIA
	Resistance	mΩ	228.1	210.0	173.6	By Maxwell for 4 coils adding margin of 5%
	Inductance	mH	3.00	2.70	2.16	
	Time constant	s	0.013	0.013	0.012	
	Dielectric strength against the ground	kV	0.6			110% of the start-up
	Test voltage against the ground	kV	2.2			2E+1000
	Dielectric strength between layers	kV	0.15			
	Test voltage between layers	kV	0.3			2E, Impulse
Heat resistance class		B			< 130°C	
Cooling	Cooling method		Natural air flow and heat conduction			
Pulse operation (1T)	Current in a conductor	kA	2	3	3	
	Total current in a coil	kAT	32	48	48	
	Current density (Conductor only)	A/mm ²	100	150	150	
	Current density (With isolator)	A/mm ²	69	104	104	
	Start-up voltage	kV	0.467	0.643	0.530	Current wave form Startup exponential Flat top constant Damping exponential
	Flat-top voltage	kV	0.456	0.630	0.520	
	Decay voltage	kV	0	0	0	
	Current rise time	s	0.05			
	Flat top time	s	0.15			
	Discharge period	s	300			
	Stored magnetic energy	kJ	6.0	12.2	9.7	Total 27.9
	Energy consumption	MJ	0.172	0.357	0.295	Total 0.8
	RWET	s	0.19			Equivalent time
	PS power at a flat top	MW	0.9	1.9	1.6	Total 4.4
	Adiabatic temperature rise	k	11	25	25	In a short pulse
Time averaged current	A	50.0	75.0	75.0	In a conductor	
Steady operation (0.09T)	Current in a conductor	kA	0.180	0.270	0.270	
	Current density (Conductor only)	A/mm ²	9.00	13.50	13.50	
	Voltage	V	41.1	56.7	46.9	
	Stored magnetic energy	kJ	0.05	0.10	0.08	Total 0.2
	PS power at a flat top	kW	7.4	15.3	12.7	Total 35.4
	Average temperature rise	k	not clear	not clear	not clear	Because air cooling
Start-up voltage	V	49.3	68.0	56.2	120% of the flat top.	

4.2.2 Modular coil system (MC)

4.2.2.1 Shape of the modular coil

Fig. 4.2.2.1-1 shows the shape of the modular coil. Shape of the coil lead is not easy to decide properly in a desk study, because it is necessary to bend intricately considering interference with peripheral parts and fixing place. Therefore, the conductor shape will be adjusted according to the surrounding structure during installation. To prepare for this, leave 500 mm to 800 mm as an extra length and cut the conductor at an appropriate place during installation. After adjusting the length and bending them, the go and return conductors are wrapped with glass tape and fixed with a resin.

The cross section is shown in Fig. 4.2.2.1-2. Since the current density is very high, the conductor temperature rises about 20 degrees per second of operation. To absorb this heat before next shot, the coils are cooled by pure water. Fig. 4.2.2.1-3 shows joint of conductors. To reduce the number of power supplies, the three conductors are electrically connected in series outside the coil by the copper blocks of joint_1 and the joint_2. And in order not to increase the head loss of cooling water, the inlet and outlet of cooling water will be provided for each conductor. Therefore, the number of electric circuits is 1 per coil, and the number of cooling water flow paths is 3 per coil.

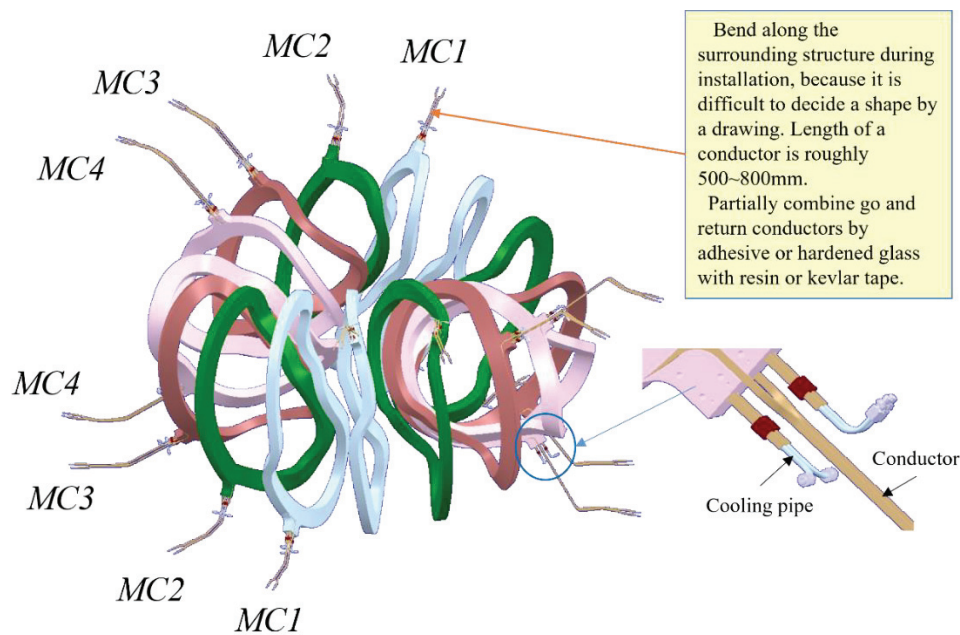


Fig. 4.2.2.1-1 Modular coil system, showing the current leads and the cooling pipes.

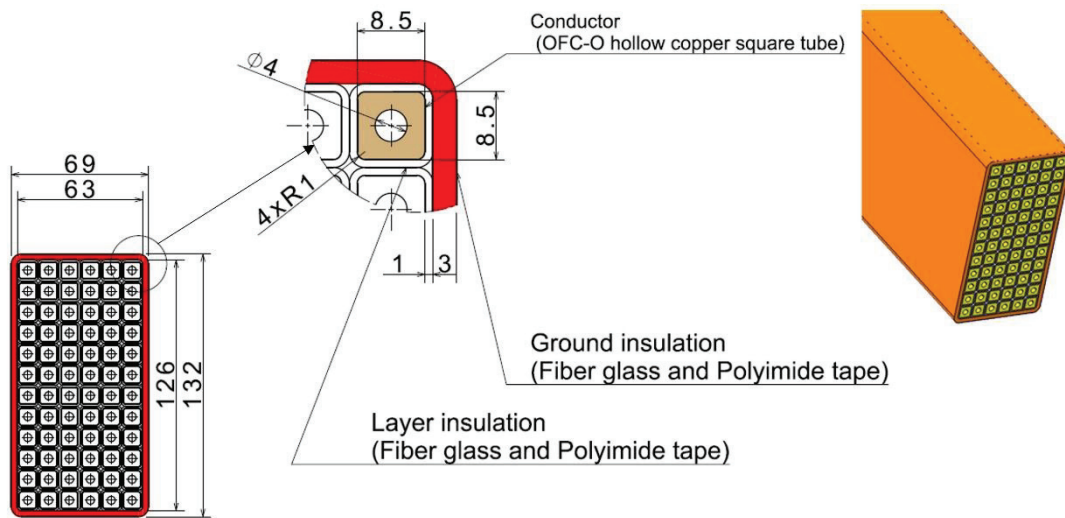


Fig. 4.2.2.1-2 Cross section of the modular coil.

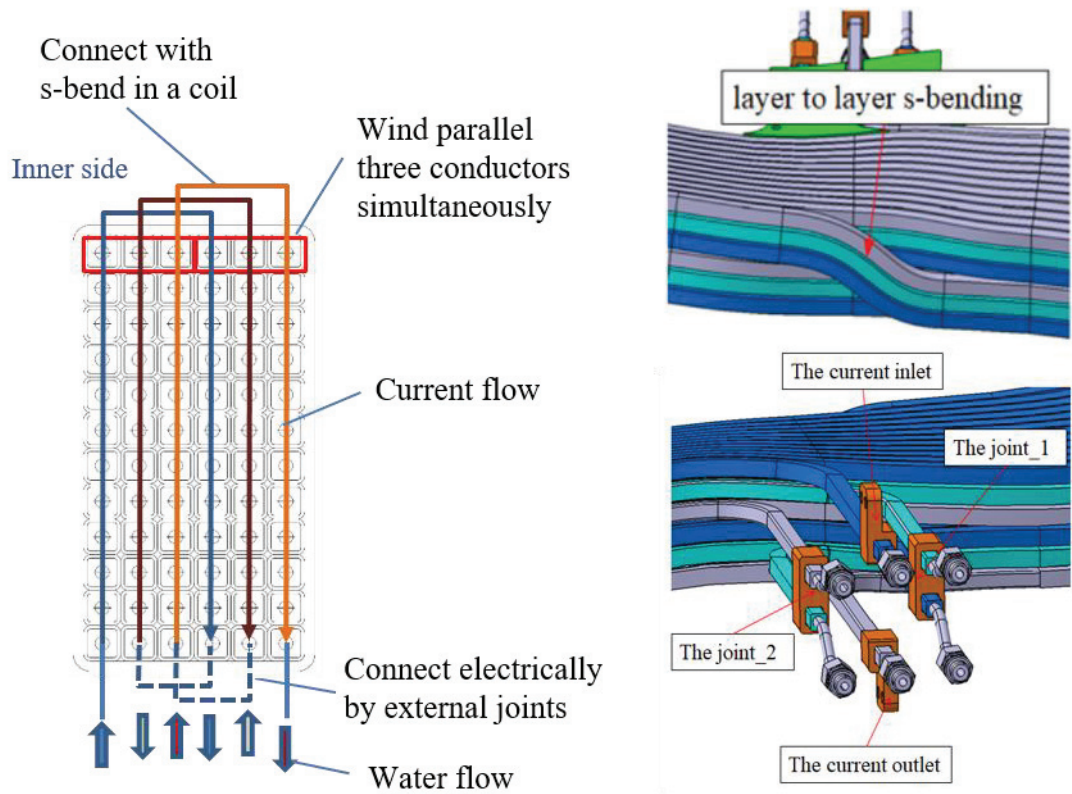


Fig. 4.2.2.1-3 Joint and cooling pipes of the modular coil.

4.2.2.2 Direction of the coil cross section

The MHD equilibrium created by the modular coil is almost determined by the center trajectory and the total current, which are calculated with the NESCOIL system. The cross-sectional area is defined in consideration of the limit of current density.

It is also necessary to determine the direction of the coil cross section for winding. The NESCOIL system optimizes the center trajectory assuming the longer axis (the normal vector) is perpendicular to the current carrying surface (CCS) as shown in Fig. 4.2.2.2-1, but it was found that the twisting angle (θ) has little effect on the equilibrium. Therefore, the twisting angle was adjusted from the viewpoint of manufacturability. Its result is shown in Fig. 4.2.2.2-2. Please see the appendix-A for details.

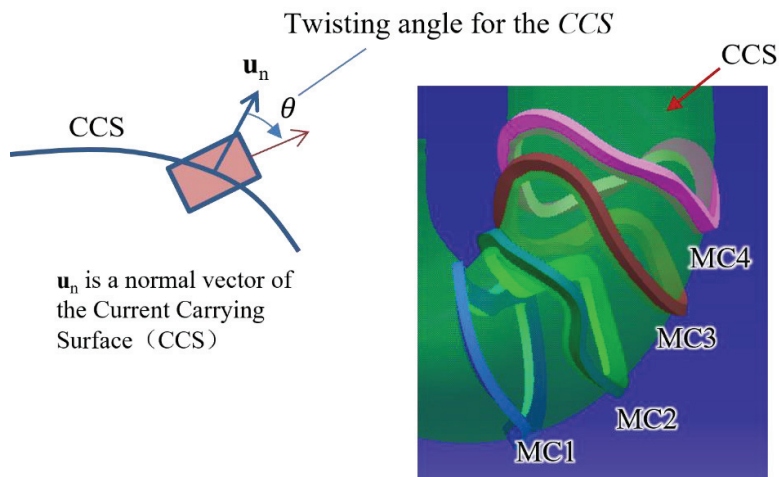


Fig. 4.2.2.2-1 Normal direction of the cross section.

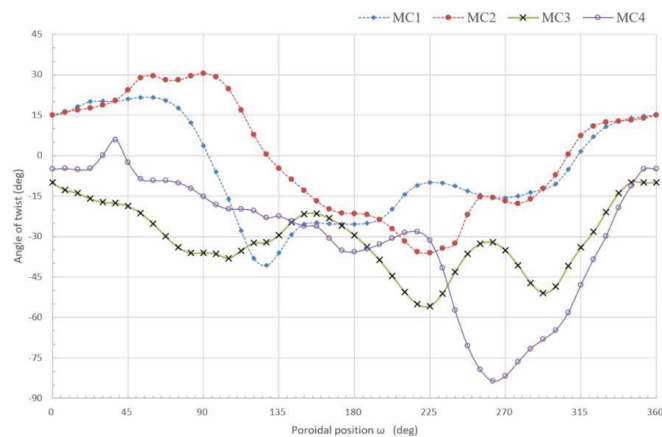


Fig. 4.2.2.2-2 Tilting angle of the cross-section.

4.2.2.3 Support structure of the modular coil

Very large magnetic forces are applied to the modular coils. The forces' magnitude and direction may be very complicated, and their characteristics are not easy to describe. They are like those of a tokamak's toroidal field coil, but the modular coils are more difficult to analyze and operated under more severe conditions because even the components that are negligible for tokamaks cannot be ignored. The strength of the coil conductor is not expected to be sufficient for large forces, the modular coil must be reinforced with the metal cases like the tokamak's toroidal field coil.

Fig. 4.2.2.3-1 and Fig. 4.2.2.3-2 show the coil support with the partial clamping type coil case. The shape of the clamp is roughly classified into 3 types of A, B and C. The type-A is the u-shaped clamp with one side open, the type-B is the u-shaped clamp made of flat plates, and the type-C is the u-shaped clamp with open inside. The two Type B clamps are connected by a connecting bar to prevent movement along the coil.

Pedestals for transmitting electromagnetic force to other support structure are welded on the coil case. It is necessary to strictly control the accuracy of the pedestal to contact other support structures, but it is difficult to secure that accuracy by assembly adjustment. Therefore, the policy is to manufacture pedestals with some extra length left, assemble the coil and the case, and then machine to ensure the accuracy of the pedestal surface.

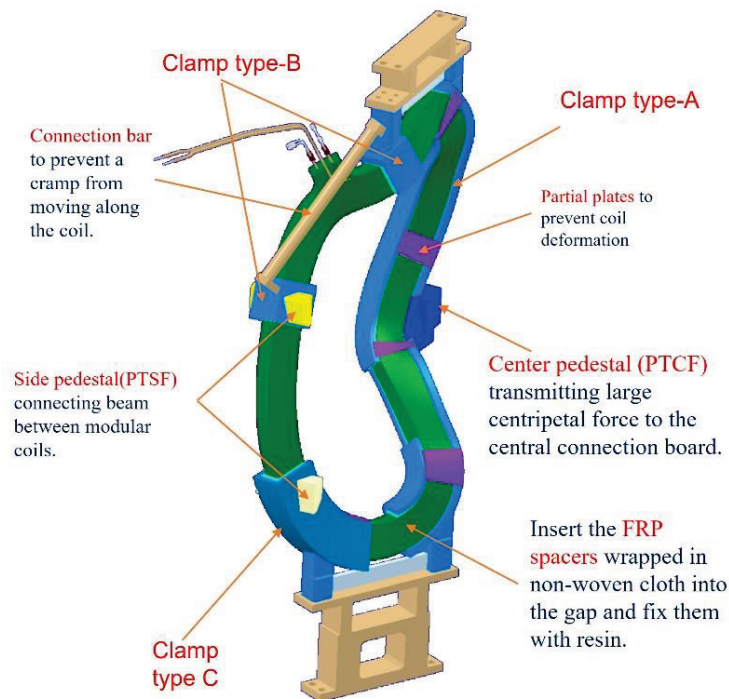


Fig. 4.2.2.3-1 Structure of the partial clamping type coil case.

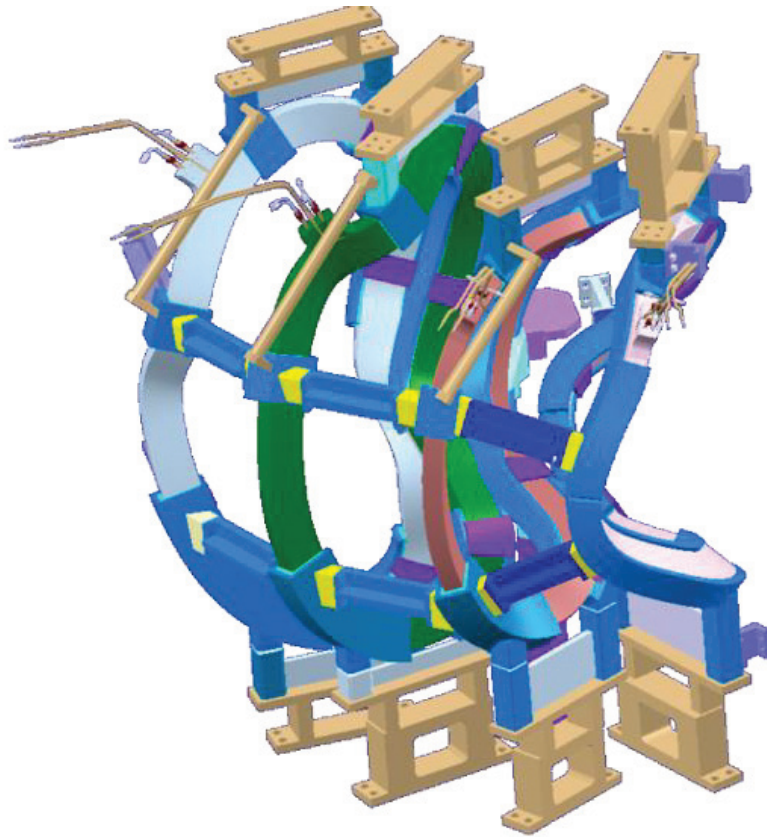


Fig. 4.2.2.3-2 Modular coil system, showing coils, legs, coil cases as a supporting structure, beams between the modular coils and the coil leads.

4.2.3 Poloidal field coil system (PFC)

Two pairs of PFCs will be installed in the CFQS. Main purpose of poloidal field coils is to apply vertical field to change the position of magnetic axis. Layout and cross section of the PFC's are shown in Fig. 4.2.3-1 and Fig. 4.2.3-2. As shown in the figures, the PFC is 32-turn water cooled coil, the IV is solenoid wound and the OV is double pancake with two simultaneous windings. The PFCs will be fixed to the upper and lower frames. The vertical magnetic field necessary for plasma control is not clear. We temporarily defined 10% of total modular coil current as a design specification for the PFC.

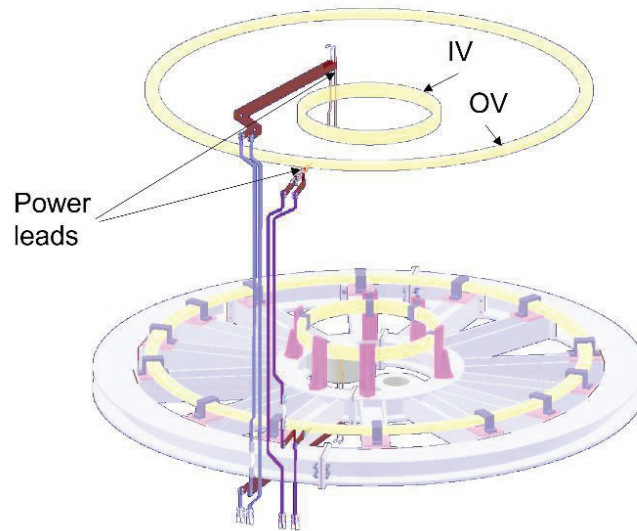


Fig. 4.2.3-1 Layout of the poloidal field coil system. Showing the coils, the current leads, the coil supports and the bottom frame.

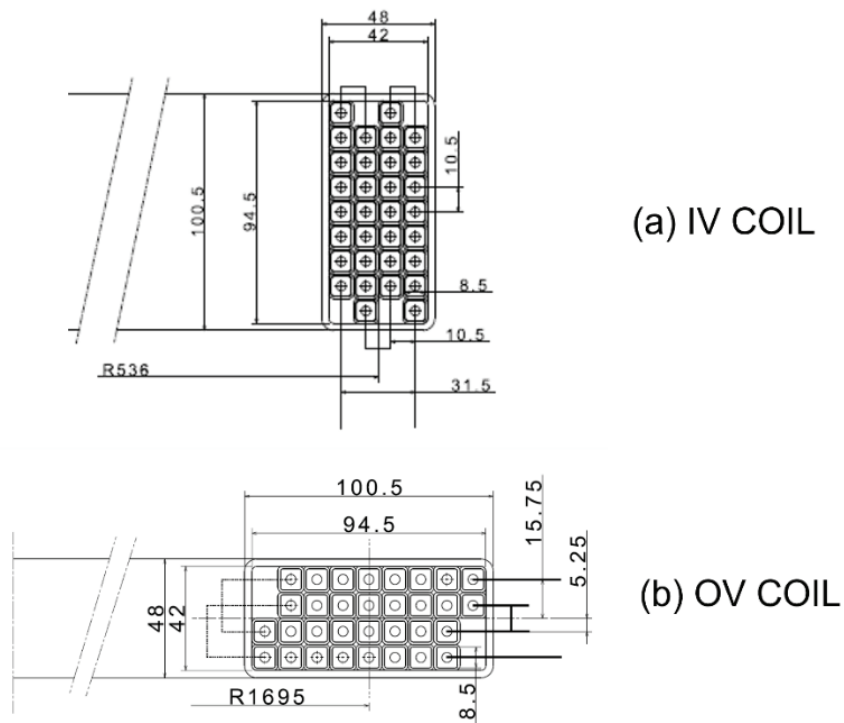


Fig. 4.2.3-2 Cross section of the poloidal field coils. The winding method is a solenoid winding for the IV and a double pancake with two simultaneous winding. The number of turns is 32 with 8 turns and 4 layers. The insulation process is vacuum pressure impregnation (VPI). The material of the conductor is hollow copper square tube of the Oxygen free copper annealed (OFC-O, equivalent JIS C1020).

4.2.4 Toroidal field coil system (TFC)

Auxiliary toroidal field coils will be installed in the CFQS to control the rotational transform. At present design, we have designed total of 12 TFCs with three types. The shape of the coil are shown in Fig. 4.2.4-1 and Fig. 4.2.4-2.

The TFC has been designed according to the basic design policy in Table 4.2.4-1. It is obvious that the water-cooled coil is desirable to realize the low magnetic field long-time operation. For that purpose, it is necessary to increase the coil cross-sectional area, which makes winding difficult and there is a concern that the TFC may interfere with the MC. In addition, the development of a water-cooled current lead, which should be thin and flexible as in the current design, is not easy. Originally, the TFC is supposed to be an experiment with a short pulse, so it is judged that the experiment can be performed with natural air cooling. However, we want to expect cooling due to heat conduction from the vacuum vessel, so we design the TFC insulation as thin as possible.

The wiring path should be adjustable according to the actual product because it must pass through a complicated and narrow gap, and it is difficult to strictly design the route only by desk study.

Table 4.2.4-1 Design policy of the TFC

No	Basic design goal
1	The wiring route should be adjustable according to the actual product, because it must pass through a complicated and narrow gap between the modular coils, and it is difficult to strictly design the route only by desk study.
2	Increasing the number of turns and reducing the current to make the leads thinner because there is no space to thick current leads.
3	Winding a solid conductor with insulation directly on the vacuum vessel by the solenoid wind method. The conductor will be cooled by natural air and heat conduction from the vacuum vessel without cooling water.
4	Shortening the pulse width reduces the temperature rise in a shot.
5	If the temperature rise is large, the experiment on that day will be stopped when the maximum temperature exceeds 90 °C.
6	The insulated wire as the current lead and the coil may be connected by solderless terminals.

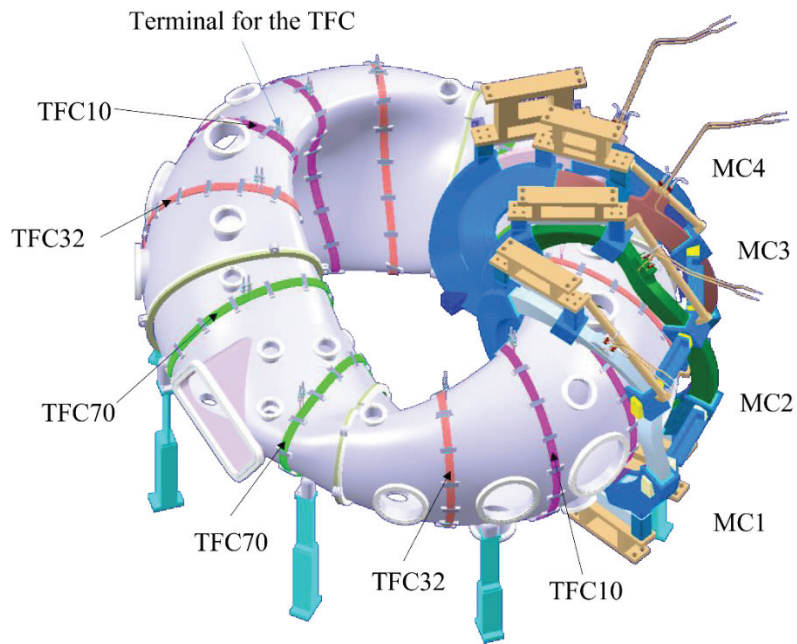


Fig. 4.2.4-1 Schematic drawing of the TFC. Solid conductors with insulation are directly wound on the vacuum vessel. The conductors are cooled by natural air and heat conduction from the vacuum vessel.

Solenoid winding
 8 turns x 2 solenoids
 Natural air flow

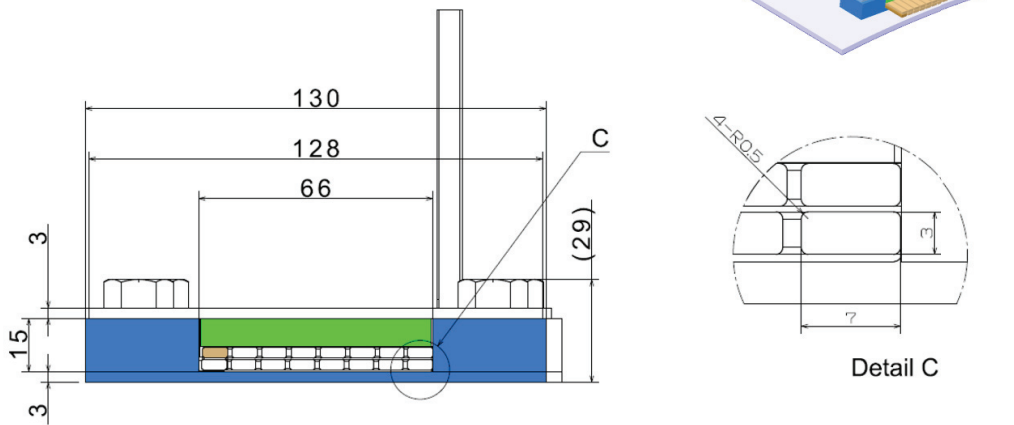


Fig. 4.2.4-2 Cross section of the TFC. A conductor with no cooling channel coated by insulator is clamped to the bobbin on the vacuum vessel. The SUS bobbins are fixed on the vacuum vessel by the arc spot welding. Winding structure is two solenoids.

4.2.5 External current lead

The 32 coils are installed in the CFQS, but it is not realistic to wire all those current leads to a control power supply room because very large space is necessary. We think that it is preferable to connect the coils with copper bus bar near the CFQS body to minimize space of the wiring and to reduce cost. The busbar system saves space but is difficult to design because it is inflexible.

Fig. 4.2.5-1 shows wiring plan of the current lead. The water-cooling coils of PFC and MC are connected by copper busbars and flat braid flexible terminals which may absorb thermal displacement and assembly error. The TFCs with complicated wiring routes are connected by flexible electric wires covered with insulation coating.

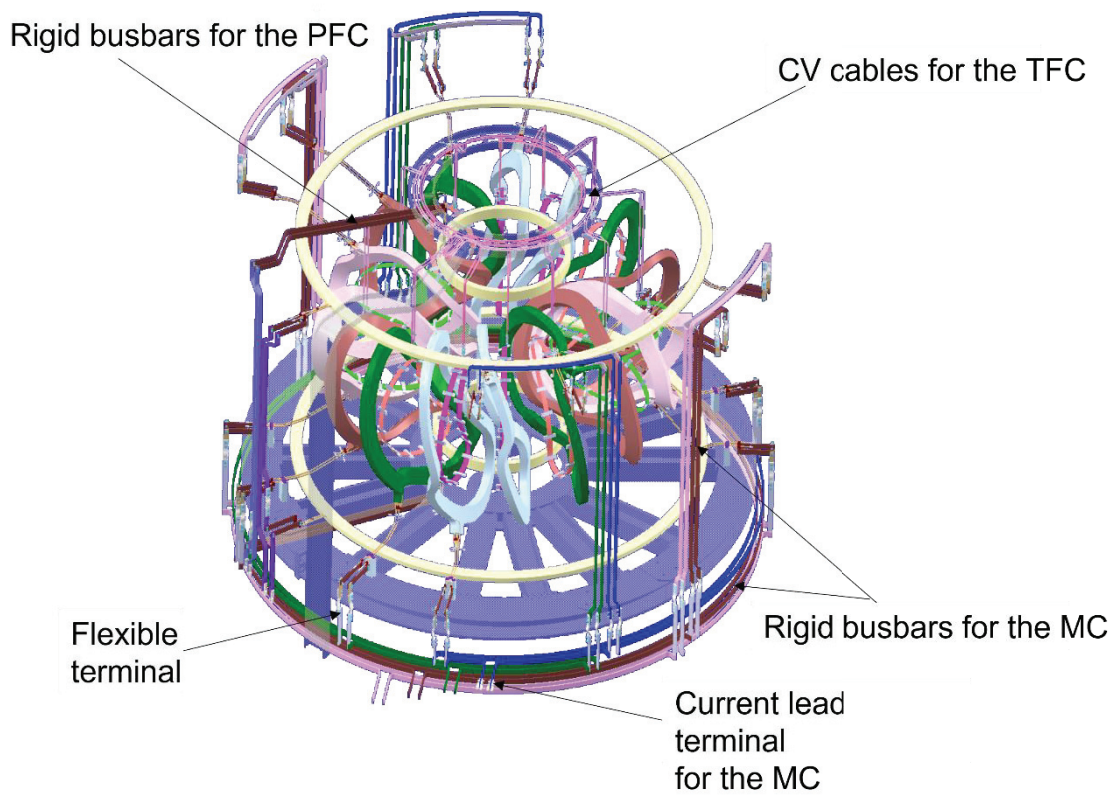


Fig. 4.2.5-1 External current leads for the coil system.

4.2.6 Cooling water pipe

To cool the coils, it is necessary to disperse 108 cooling pipes (hoses) around the CFQS. The size and arrangement of a manifold (an assembly of branch pipes) for connecting them to the cooling water device are determined as shown in Fig. 4.2.6-1. It was designed according to the basic design policy in Table 4.2.6-1.

Table 4.2.6-1 Design policy of the cooling water pipe.

No	Basic design goal
1	Flow rate in a manifold is 5 m ³ /hr for the MC and 1 m ³ /hr for the PFC, and loss head in a manifold is 10m or less.
2	SUS304 or SUS316 pipe with Sch20 (Maximum pressure=2MPa or more).
3	A welding flange with gasket seal is used to improve reliability. Do not use screw-in flange.
4	Provide a function to adjust the flow rate and monitor flow rate for each type of coil. It is not necessary to adjust the flow rate for each channel for cost reduction. The flow rate in each channel will be measured by a portable ultrasonic flow meter, and the flow balance between channels is adjusted by an orifice or the like
5	Fix c-shaped manifold extended in the toroidal direction on the support frame.
6	Connect the manifold and coil with insulated nylon or PFA hose with a heat resistance of 100 °C or higher. Applying metal reinforced hose is prohibited because high voltage is applied to the coil.

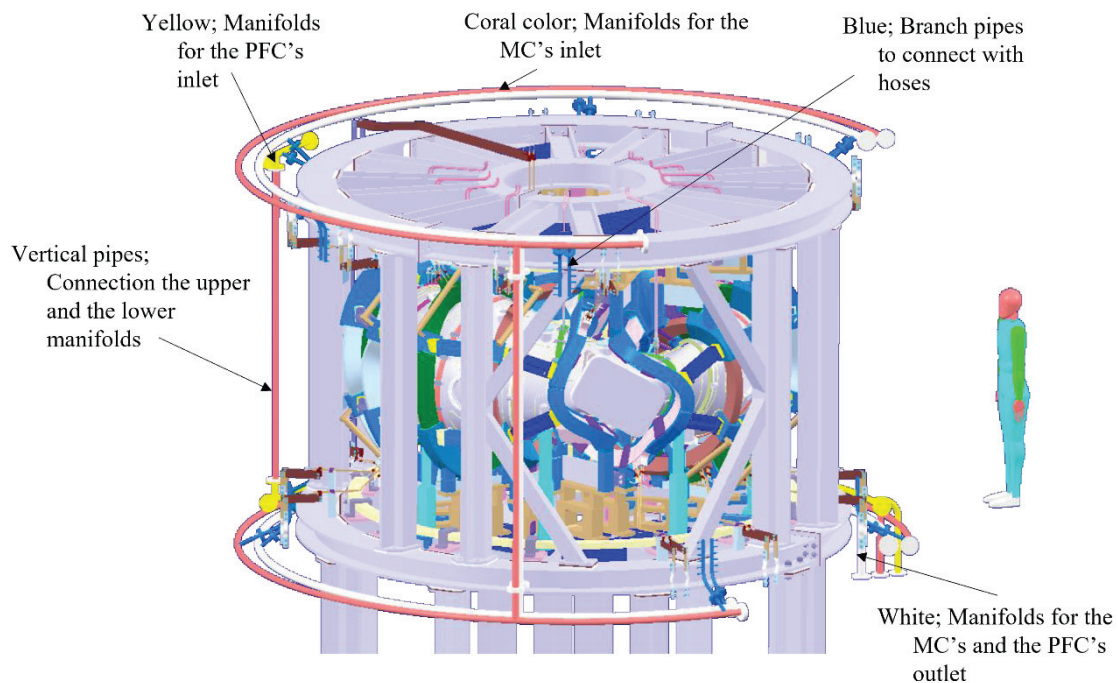


Fig. 4.2.6-1 Cooling water pipe.

4.2.7 Cage type support structure

The cage type support structure is shown in Fig. 4.2.7-1 and Fig. 4.2.7-2. Its main role is to prevent deformation of the modular coil. It also has, among other components, a vacuum vessel, other coils, and a diagnostic system attached on it.

Large tokamaks are typically designed with TFC wedges to support the centripetal forces. However, the CFQS cannot take this approach due to shape of constraints. Instead, it is designed to absorb such a large force, whose main component is the centripetal force, with central connection boards (CCB) and some pedestals (PRF). Central pillars (CPS) are installed to support the PRF's during assembly work. There is a big rectangular free area to access the inside port on the vacuum vessel.

The cage type structure with diagonal beams (DBS) that prevents deformation of the modular coils by the overturning moments or vertical forces and handle the entire load. For use in future NBI experiments, we adopted a design with high-rigidity DBS instead of providing the outer pillars (OPS) around the large rectangular ports.

Intermediate base plates (IBP) are flat on which the vacuum vessel and the modular coils are installed. Their upper surface becomes the installation reference for other parts, so it should be strictly controlled, such as improving flatness by machining and marking reference points for coil placement.

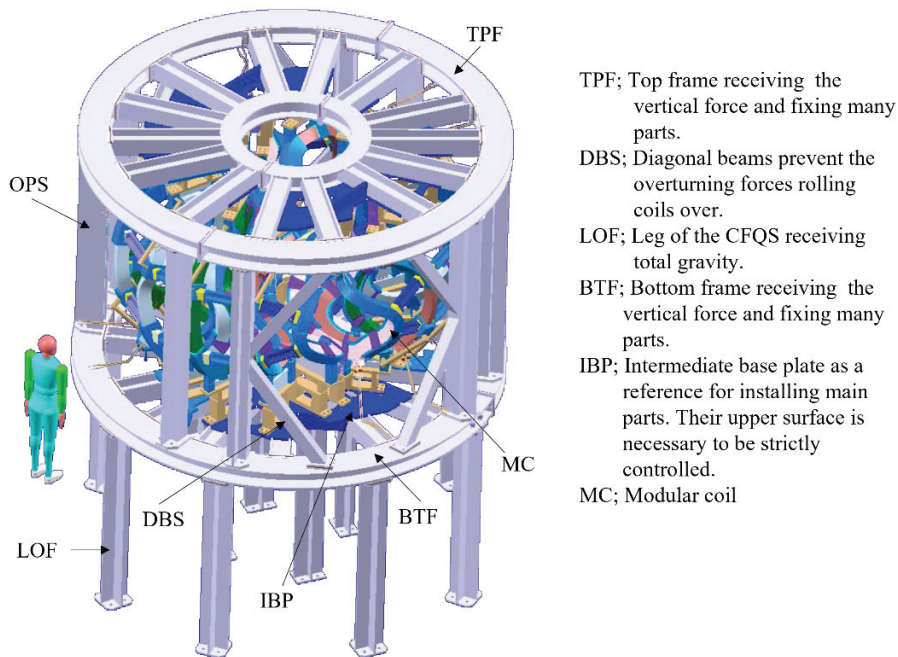


Fig. 4.2.7-1 Cage type support structure.

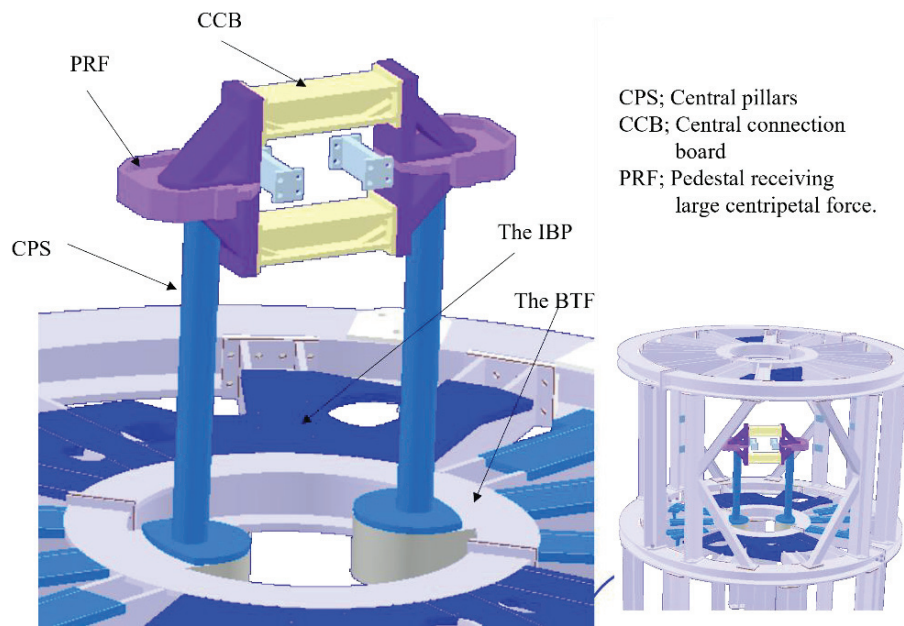


Fig. 4.2.7-2 Center support of the modular coil system.

4.3 Vacuum vessel

4.3.1 Structure of main vessel

The design goal of the vacuum vessel is summarized in the following table.

Table 4.3.1-1 Design policy of the vacuum vessel.

No	Basic design goal
1	Minimize field work for cost saving and reduce lead-time on the laboratory.
2	Provide inspection process in the middle of the production and reduce the risk of backtracking work.
3	Think about how to respond to problems and design a structure that can be repaired or modified.
4	Make it possible to utilize the space inside the vacuum vessel. It is difficult to access the vacuum vessel from the outside because many parts, mainly coils, are installed nearby.
5	Provide large ports for entering the inside of the vacuum vessel and ensuring a workable cross-sectional area. The purpose is as follows. <ul style="list-style-type: none"> · To weld together split places in the vacuum vessel. · To install measurement equipment like magnetic probes. · To install some plates to protect vacuum vessel from heat.
6	Simplify the structure without one turn break since there will be no plasma current. Instead, priority is given to increasing the internal volume of the vacuum vessel to increase the degree of freedom in the experiment.
7	Install as many large ports as possible to enhance plasma measurement and make the experiment more flexible.
8	The structure should be such that a tangential NBI can be installed for high beta experiments with high power plasma heating.
9	Assemble the main parts in a factory and make sure there will be no interferences or vacuum leaks. If a defect will be found during on-site work, it will take a lot of time and cost to deal with it. Since it is difficult to transport the entire vacuum vessel, repairing defects found on the site may be very difficult and will take a lot of time.
10	Make it possible to divert as many CHS assets as possible.

Fig. 4.3.1-1 shows a schematic of the main vacuum vessel, which will be manufactured by welding together four sections of two types in the toroidal direction. The flanges used for welding are also shown in the figure. Since the electromagnetic forces on the vessel are expected to be small, it will be fabricated from SUS316L with relatively thin walls of 6 mm. As a result, the one-turn resistance is roughly 0.3 mΩ which we believe to be sufficiently large while not producing significant joule heating. The wall will be conditioned by baking them at 130-150°C via baking sheath heaters. The main vessel is fixed by eight leaf-type legs, added to allow for the vessel's thermal expansion during baking.

The shape of inner surface is shown in Fig. 4.3.1-2. The cross-sectional area is much larger than that of the 2b32 reference surface that is defined for the island bundle divertor experiment, and minimum space required from a physical point of view. The last closed magnetic surface (outer most magnetic surface) of the standard 2b40 equilibrium is narrower than the 2b32 surface. The minimum

gap between the 2b32 plane and the inner surface of main vessel is about 30 mm. The width and height of the inner surface are both at least 450 mm, which is sufficient for people to work inside. Using such a large vessel also helps to make the experiment more flexible.

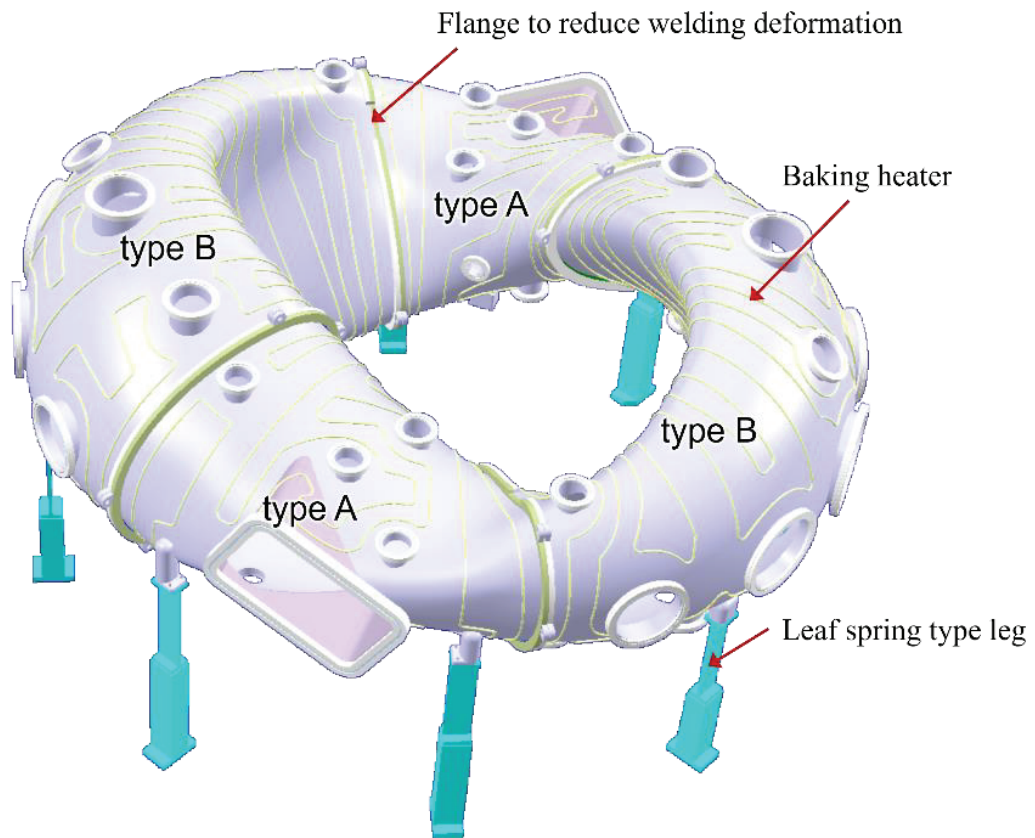
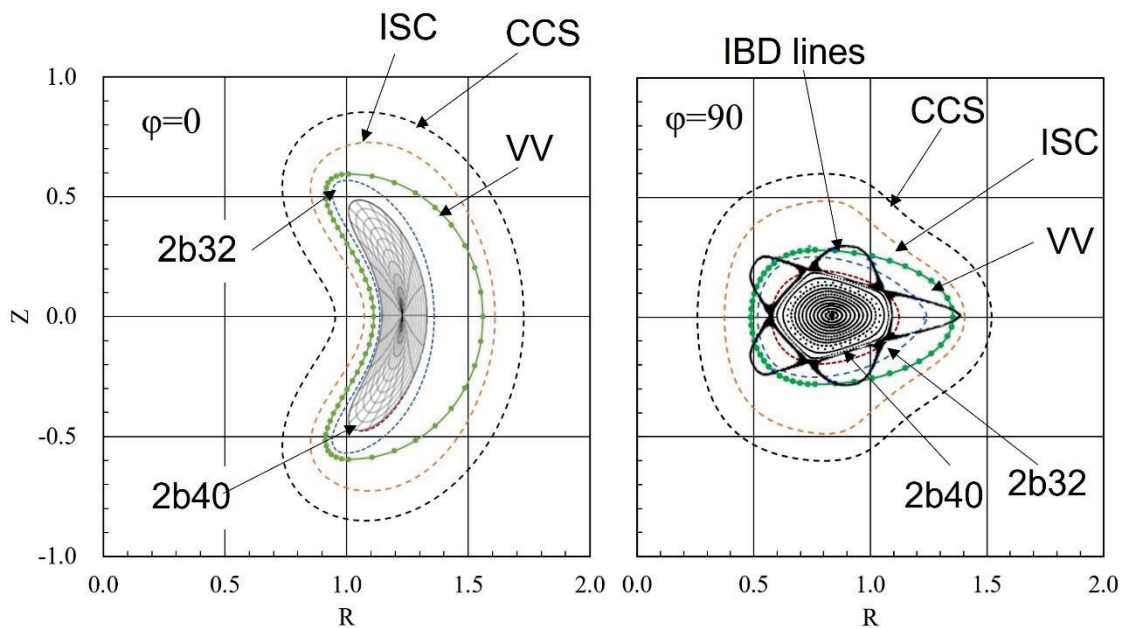


Fig. 4.3.1-1 Schematic of the vacuum vessel.



- 2b40 shows a last closed magnetic surface of the standard equilibrium,
- 2b32 shows a reference surface of the IBD configuration (aspect ratio =3.2),
- CCS shows the current carrying surface on which the center of modular coil is placed,
- ISC shows an innermost peripheral surface of the modular coil,
- VV shows the inner surface of the vacuum vessel.

Fig. 4.3.1-2 Cross section of the main vessel inner surface.

4.3.2 Port arrangement

More than 46 large ports with a diameter of at least 114 mm, are provided for heating and measurement. Two of them are large rectangular ports both for a worker to enter and for use in NBI and Thomson scattering.

We examined the location and size of the ports to get many large ports. However, small ports with a diameter of 70 or less may not be considered and may be increased further if it will be necessary for the experiment. Table 4.3.2-1 and Fig. 4.3.2-1 show the purpose and location of the port.

Table 4.3.2-1 Port list.

No	name	Flange Size	Center Position				Use
			Φ	Height (Z)	Radius (R)	Section	
1	I-090	Φ 114	90	0	450	S05-I	150GHz interferometer
2	I-270	Φ 114	270	0	450	S13-I	Beam dump for Thomson scattering
3	O-000U	Φ 203	0	(55°)	((1424))	S01-U	A spectroscope observing visible light
4	O-000	Φ 420	0	0	1600	S01-O	FIR with mirror
5	O-000L	Φ 203	0	(-55°)	((1424))	S01-L	Mirnov-TA S2,S16
6	O-026	Φ 356	26(150)	0	1570	S02-O	NPA, Tangential view port with CCD camera
7	O-050	Φ 305	50(200)	0	1500	S03-O	Main vacuum pump
8	O-090S	440x680	90	0	1400	S05-O	150GHz interferometer, CCD and NBI
9	O-130	Φ 305	130(200)	0	1500	S07-O	FILD(Sci-type)
10	O-154	Φ 356	154(150)	0	1570	S08-O	Movable limiter
11	O-180U	Φ 203	180	(55°)	((1424))	S09-U	Ti-getter
12	O-180	Φ 420	180	0	1600	S09-O	54.5GHz ECH
13	O-180L	Φ 203	180	(-55°)	((1424))	S09-L	Mirnov-TA S8,S10
14	O-206	Φ 356	206(150)	0	1570	S10-O	2.45GHz ECH
15	O-230	Φ 305	230(200)	0	1500	S11-O	HIBP
16	O-270S	440x680	270	0	1400	S13-O	Thomson,Fluorescent mesh for mapping
17	O-310	Φ 305	310(200)	0	1500	S15-O	VUV, μ -wave reflectometer, camera for mapping
18	O-334	Φ 356	334(150)	0	1570	S16-O	Tangential view port with CCD camera, Ti-getter
19	U-018	Φ 253	18	630	1180	S02-U	Langmuir probe(Center)
20	U-045	Φ 203	45	560	1000	S03-U	CXS & MSE
21	U-063	Φ 152	63	440	1000	S04-U	
22	U-090	Φ 152	90	320	1000	S05-U	
23	U-102IN	Φ 152	102	280	750	S05-U	Ti-getter
24	U-102	Φ 152	102	220	1250	S06-U	FILD(Sci-type)
25	U-130	Φ 152	130	390	1200	S07-U	FILD(Sci-type)
26	U-198	Φ 253	198	630	1180	S10-U	Langmuir probe(Center)
27	U-225	Φ 203	225	560	1000	S11-U	HIBP
28	U-243	Φ 152	243	440	1000	S12-U	FILD(Foil-type)
29	U-270	Φ 152	270	320	1000	S13-U	
30	U-282IN	Φ 152	282	280	750	S13-U	Ti-getter
31	U-282	Φ 152	282	220	1250	S14-U	Nude and B-A ionization vacuum gauge
32	U-310	Φ 152	310	390	1200	S15-U	Langmuir probe(Edge)
33	L-050	Φ 152	50	-390	1200	S03-L	Visible light (Edge)
34	L-078	Φ 152	78	-220	1250	S04-L	Grow discharge electrode
35	L-078IN	Φ 152	78	-280	750	S05-L	Mirnov-TA (S4,S6)
36	L-090	Φ 152	90	-320	1000	S05-L	Movable limiter
37	L-117	Φ 152	117	-440	1000	S06-L	Gas puff
38	L-135	Φ 203	135	-560	1000	S07-L	CXRS(ref)
39	L-162	Φ 253	162	-630	1180	S08-L	Radiation detectors.E-gun for mapping exp.
40	L-230	Φ 152	230	-390	1200	S11-L	Mirnov-PA
41	L-258	Φ 152	258	-220	1250	S12-L	
42	L-258IN	Φ 152	258	-280	750	S13-L	Mirnov-TA (S12,S14)
43	L-270	Φ 152	270	-320	1000	S13-L	Gas puff
44	L-297	Φ 152	297	-440	1000	S14-L	Rogowski, Diamagnetic
45	L-315	Φ 203	315	-560	1000	S15-L	μ -wave reflectometer
46	L-342	Φ 253	342	-630	1180	S16-L	SX and ECE

In parentheses in the Φ column ; Movement from the center

FILD;Fast Ion Loss Detector

ECE;Electron Cyclotron Emission

Mirnov-TA;Toroidal Array of Mirnov probes

Mirnov-PA;Poloidal Array of Mirnov probes

E-gun;Electron gun

CXS;Charge exchange spectroscopy

MSE;Motional stark effect

HIBP;Heavy Ion Beam Probe

NPA;Neutral particle analyzer

SX;Soft X-ray detector

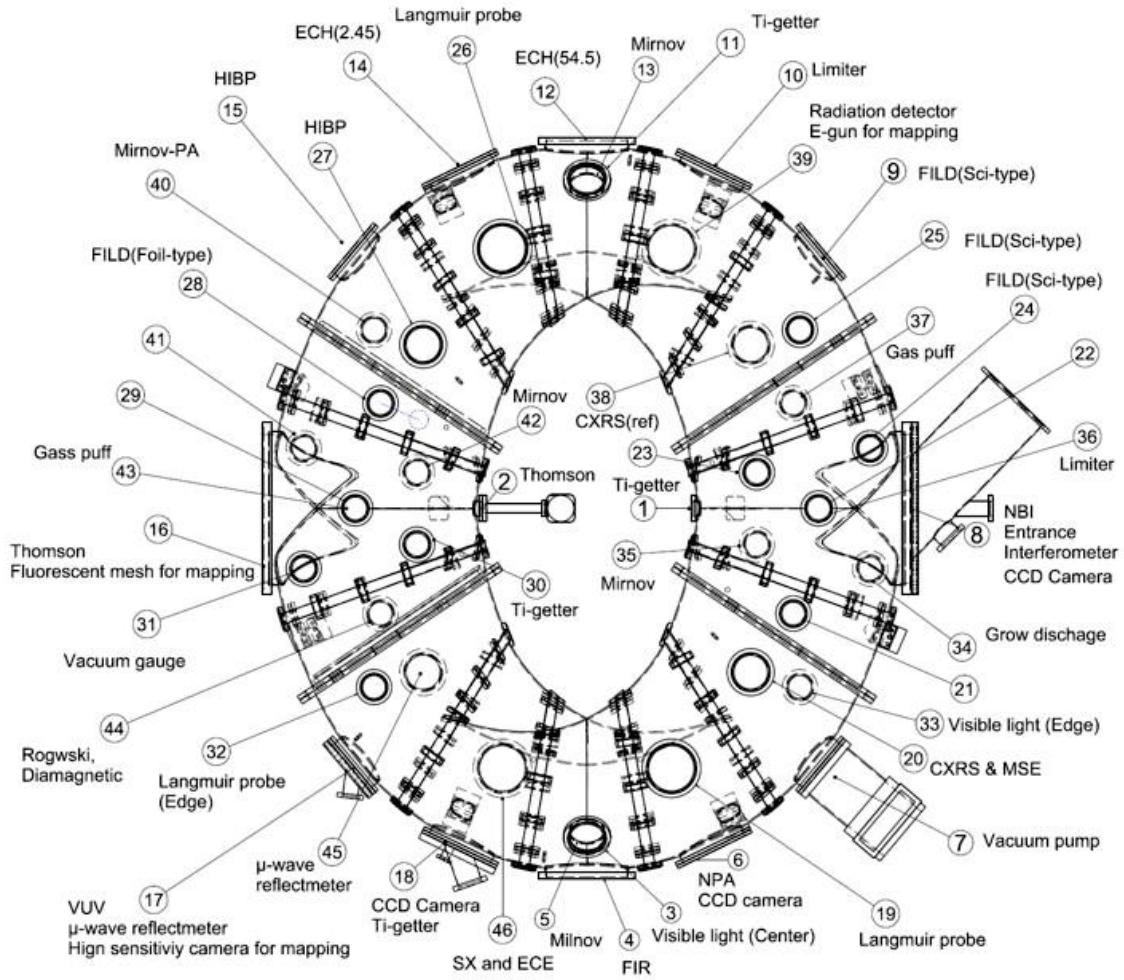


Fig. 4.3.2-1 Port arrangement, it shows the usage of each port.

4.4 Related equipment

4.4.1 Limiter system

As in other magnetically confined fusion devices, the plasma in the CFQS is confined within last closed magnetic flux surfaces and a boundary exists between plasmas and the machine-wall components. This boundary is generally called the scrape-off layer (SOL), which is determined by a solid surface (limiter) or topologically by magnetic field perturbations (divertor). In the SOL the impurities originated from plasma-facing components may cause a lot of problems, such as huge radiative power loss and dilution of fuel particles.

The limiter configuration is to use a solid surface to define the edge of the plasma. Depending on the shape and the positioning of the solid diaphragm, the limiters are generally divided into (a) poloidal limiter; (b) rail limiter and (c) toroidal limiter, as depicted in the below figure (Fig. 4.4.1-1). In the CFQS, we intend to put four sets of the poloidal or rail limiter inside the vacuum vessel for defining the plasma and protecting the wall. These four limiters will be installed at two approximately opposite toroidal locations of the torus. The limiter primarily serves to protect the wall from erosion by plasma heat loads. For withstanding heavy heat load, the limiter itself is usually made of a refractory material, such as carbon, tungsten, or molybdenum. Because the CFQS is free of major plasma disruptions, there is little thermal shock occurred during the operation. Thus, the sputtering and arcing rates from limiters are expected to be very low.

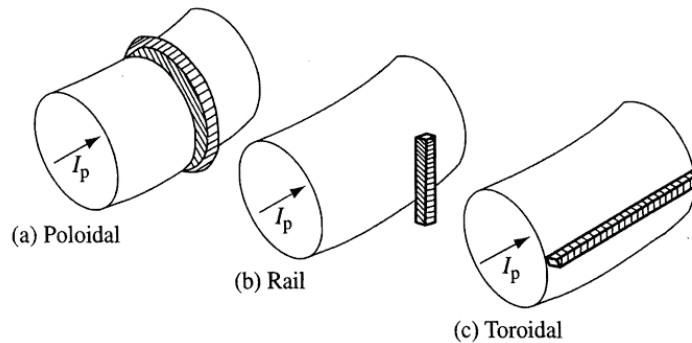


Fig. 4.4.1-1 Schematic of different types of the limiter.

4.4.2 Vacuum pumping system

Pumping system in CHS will be transferred to the CFQS. The rotary pump will be used for rough pumping, then two turbo molecular pumps will get involved. The ultimate vacuum pressure will be 1×10^{-7} Pa.

4.4.3 Wall conditioning system

Wall conditioning is important to produce plasma after the maintenance of vacuum vessel. Typical methods are glow discharge with helium or hydrogen, and titanium getter.

For other conditioning, the discharge cleaning may be applied. The plasma may be created by 2.45 GHz microwave heating. The resonance magnetic field strength of this frequency is 0.0875 T, and steady state magnetic field is favorable for this purpose. Microwave is generated by magnetron and transferred by wave guide.

4.4.4 Fuel gas supply system (Gas puff system)

Various kinds of gases will be injected for various purposes, it is likely that an equipment for performing them is required.

To generate plasma, it is necessary to control the supply amount of high purity gas. To do that, high-speed control valve system to adjust gas injection rate with gas purification function to remove impurities from the injected gas is required. The equipment that does them is commonly called a gas puff system.

Normally, hydrogen gas is injected for plasma generation, but noble gas such as helium or argon may be injected. Nitrogen gas may be injected to calibrate the measuring instrument. Argon gas may be used for magnetic surface measurements. In addition, a large amount of nitrogen gas or dry air may be injected to open the inside of the vacuum vessel to the atmosphere.

4.4.5 Vacuum management system

Vacuum management is very important to produce high-performance plasma, and instruments for that purpose and protective functions in case of trouble are required.

Typical instrument is high speed ionization vacuum gauge, quadrupole mass spectrometer, helium leak detector, and so on. As a vacuum protection device, a gate valve system for interrupting the vacuum in an emergency is essential. Detail will be designed in the future.

4.4.6 Shutter system to protect the glass windows

Glass windows may be attached for plasma measurements. The plasma may cause the glass window to be coated with some film, making it difficult for light to pass through. To prevent such a problem, it is preferable to add a movable shutter on the vacuum side of the glass window and close the shutter when the glass window is not used. Since there is a high possibility that the glass window will be coated at the time of the wall conditioning with titanium getter or glow discharge, the shutter should be closed in such a case.

4.4.7 Vacuum test equipment

As the experiment progresses, various equipment will be added to the vacuum vessel port. To reduce the risk of vacuum leaks causing damage to working equipment, it is essential to confirm that newly added equipment has no leak in a unit test. The vacuum vessel with a vacuum pumping unit should be prepared separately from the CFQS body for a unit leak test.

4.4.8 Compressed air supply system

Compressed air supply system is mainly used to control the gate valve. Detail will be designed in the future.

4.4.9 Liquid nitrogen supply system

Liquid nitrogen is often used for various purposes in fusion devices. They are nitrogen trap for removing impurities, pre-cooling of superconducting device, cooling of heat shields and so on. If desired, liquid nitrogen can be purchased in a Dewar bottle, but when the amount used is large, there are many cases where a liquid nitrogen production device is prepared. The need for such equipment will be considered separately.

4.4.10 Pure water cooling system

Pure water-cooling system is required to cool magnetic coil system, heating system, diagnostic system, and pumping system. And industrial water system to cool the motor generator may be also required.

4.5 Power supply

4.5.1 Requirement to power supply system with low voltage

Chinese power environment is different from Japan as shown in Table 4.5.1-1. To relocate some equipment's of the CHS for CFQS experiments, it is reasonable to prepare converters, mainly transformers, for solving the difference in voltage. Although it is possible to install individual transformers for each used device, it is considered that cost reduction can be achieved by putting them together as there are many devices scheduled to be used. Table 4.5.1-2 shows summary of required power with the low voltage power board for the CFQS.

Table 4.5.1-1 Comparison of power environment.

	Frequency	HV	LV 1 ϕ	LV 3 ϕ
NIFS in Japan	60(West Japan)	6.6 kV	100 V	200 V
SWJTU in China	50	10 kV	220 V	380 V

HV; High voltage LV; Low Voltage

Table 4.5.1-2 Total electric power to be required.

No	Power board	Voltage	Phase	Total capacity	Use
1	HV	10kV	3 ϕ	5MVA	MG
2	LV	380 V	3 ϕ	1MVA	ECH, baking, cooling etc.
3	LV	220 V	1 ϕ	Not clear	Diagnostic, control etc.
4	LV	200 V	3 ϕ	Not clear	For equipment from Japan
5	LV	100 V	1 ϕ	Not clear	For equipment from Japan

4.5.2 Power supply system for the 1T operation

To apply large currents to the CFQS coils, a short pulse large capacity power supply of about 70 MVA and 1s of a pulse length is required. Since it is difficult to supply this power from the commercial power source, a current source with energy storage function is required. The power supply with an induction motor (IM) and a synchronous generator (SG) may be most suitable type for 1.0 T operation because it can store large amount of electrical energy and supply power with good controllability.

Fig. 4.5.2-1 shows the preliminary one line diagram of power supply system with the generator with a flywheel type energy storage driven by the induction motor [4.5.2-1]. The circuit mainly consists of an induction motor (IM), a synchronous generator with a flywheel (SG), an inverter for the IM, an exciter for the SG, and nine 6-phase thyristor converter units. The typical SG with two poles will

generate 50 MJ of short pulse AC power every 5 minutes with pulse length of about 1 s, 10 kV, 50 Hz and 50 MW.

Where, the parts surrounded by the red broken line indicate the equipment's for the NBI.A high-power electron cyclotron heating (ECH) system is required to generate high temperature plasma. Since the ECH system will be able to use a capacitor bank power supply and the instantaneous power can be designed small, we believe that it will receive from a low voltage power board. The coil power for 0.09T and the 2.45GHz ECH will be used for discharge cleaning.

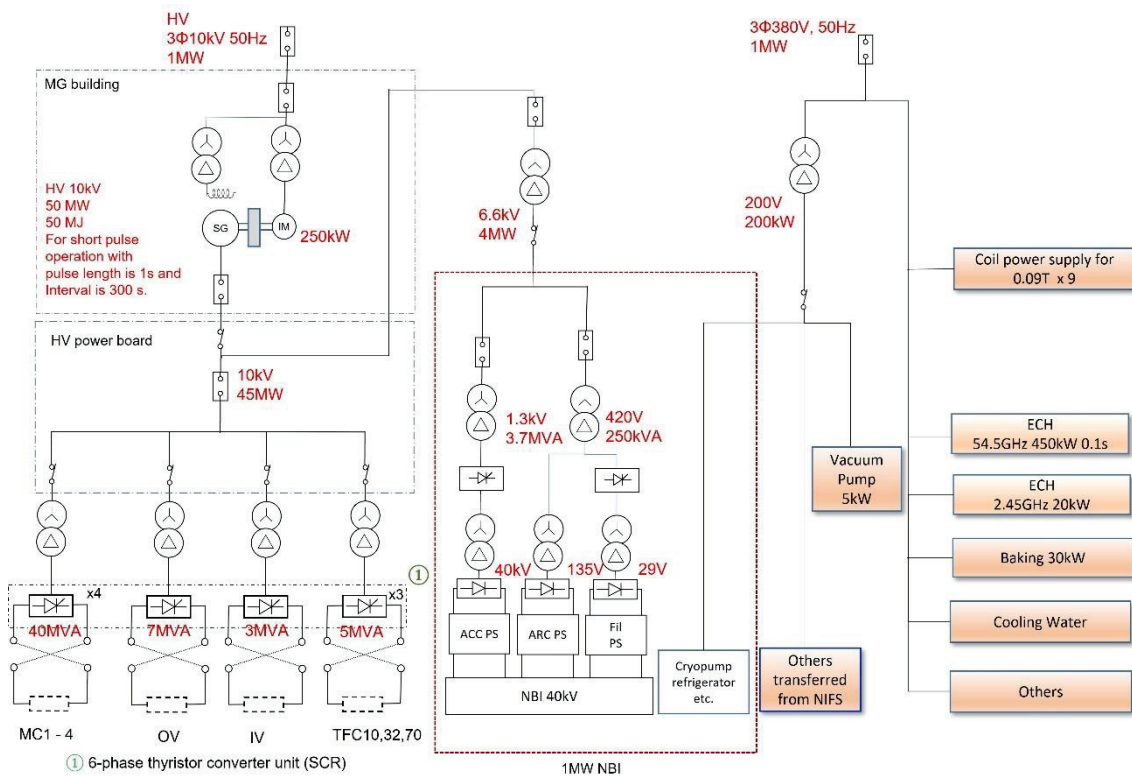


Fig. 4.5.2-1 Power system with a flywheel type energy storage generator for the 1T operation.

Fig. 4.5.2-2 shows a layout of the power supply system for the CFQS. As can be seen from the figure, the installation space of the power supply system is much larger than that of the CFQS itself, and a laboratory with about 60m times 40m that can store them is required. A new experimental building to store these will be built on another site within the SWJTU.

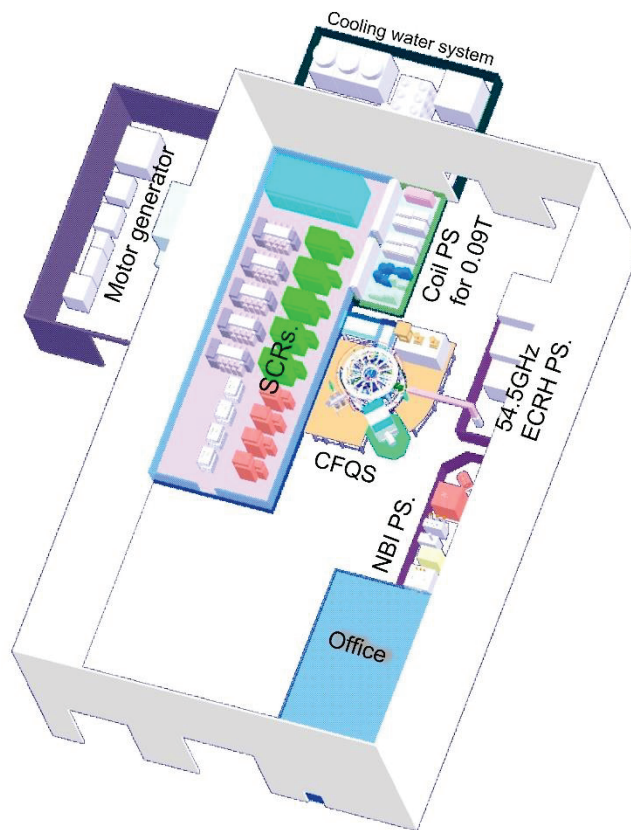


Fig. 4.5.2-2 Layout of the power system for the 1T operation.

References

- [4.5.2-1] H. Tanoue *et al.*, The 23rd IEEE Pulsed Power Conference (PPC) and the 29th IEEE Symposium on Fusion Engineering (SOFE), online, 12-26 December 2021, Poster 65.

4.5.3 Power supply system for the 0.09T operation

In the initial experiments after the CFQS will be completed, we have a plan to carry out the measurement of plasma shape with low magnetic field and longtime discharge. At that stage, the coil power system for the 0.09T operation and the ECH system with 2.45GHz may be required.

At that stage, we think the power supply shown in Fig. 4.5.3-1 is enough. It mainly consists of four voltage adjusters and four diode rectifiers for the modular coil (MC), and five 6-phase thyristor converter units for the toroidal field coil (TFC) and the poloidal field coil (PFC). Two energy storage stations with 0.5 MVh each will be installed to supply these with a large amount of power equivalent to 600 kVA during the experiment. The charging power will be reduced to 100kW, and the charging time will be 10 hours per one day at night.

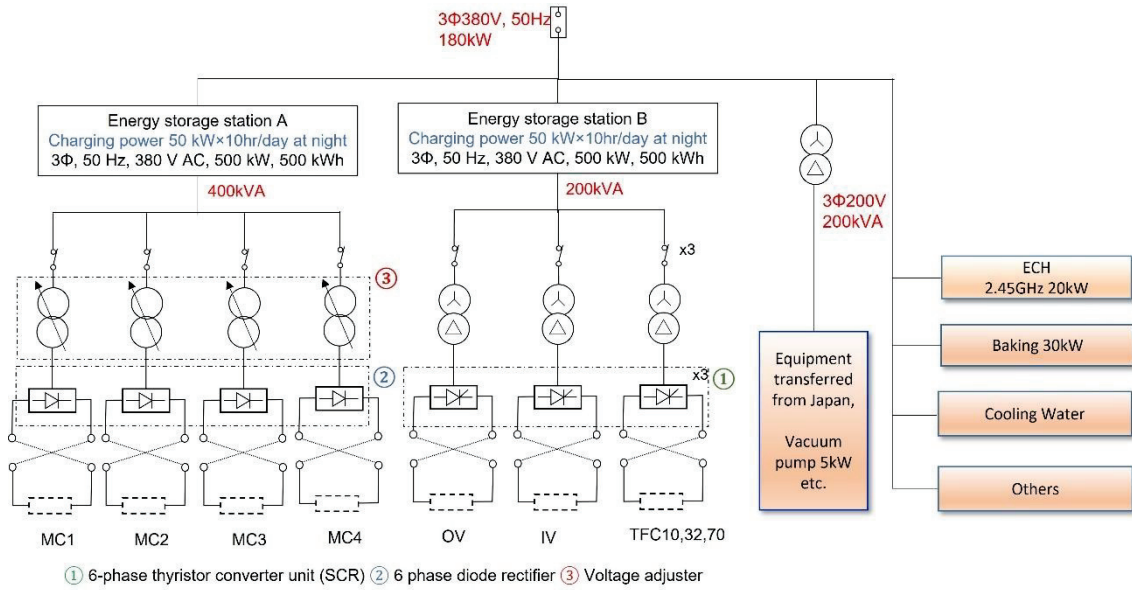


Fig. 4.5.3-1 Power supply system for the 0.09T operation.

Fig. 4.5.3-2 shows a layout of the power supply system for the 0.09 T operation. As can be seen from the figure, the installation space of the power supply system is not so large. It is thought that the experiment with 0.09T will be started in the current experiment building in Jiuli campus in SWJTU, which has a space with about 20 m times 30 m.



Fig. 4.5.3-2 Layout of the power system for the 0.09 T operation

4.6 Plasma heating system

4.6.1 Electron cyclotron resonance heating (ECRH) system

The main component of the electron cyclotron resonance heating (ECRH) system is gyrotron. The gyrotron which was used for CHS experiment and will be used in CFQS experiment has an oscillation frequency of 54.5 GHz and the maximum output power of up to 450 kW. The maximum pulse length is 100ms. Fig. 4.6.1-1 shows the single line diagram of ECH system, and Fig. 4.6.1-2 shows a preliminary layout of the ECRH system, and Fig. 4.6.1-3 shows the ECH power injection antenna. It is necessary to secure a large area (100 m² for the power supply) near CFQS to install the ECRH system.

The EC-waves generated by the gyrotron effectively and locally heat the electrons at a position on the EC-wave beam path where the resonance condition ($n\omega_{ce} = \omega - k_{\parallel}v_{\parallel}$ and $\omega_{ce} \equiv eB/m_e$) is satisfied. Here, integer n denotes harmonic number, ω_{ce} is electron cyclotron angular frequency, e is a unit charge of an electron, B is the strength of magnetic field, m_e is the mass of an electron with relativistic effect, ω is angular frequency of EC-waves, and k_{\parallel} and v_{\parallel} are the components of wave number and electron velocity parallel to the magnetic field line, respectively. Applying the frequency of 54.5 GHz, the resonance condition for $n = 2$ (second harmonic resonance) is satisfied with $B = 0.97$ T.

In the case of the CHS experiment, the EC-wave power was transmitted from the gyrotron to the CHS vacuum vessel by a quasi-optical transmission line. The transmission line was furnished with focusing and plane mirrors, polarizer mirrors to control transmitted wave's polarization arbitrarily, and vacuum window to keep the vacuum condition in CHS.

By use of the power transmission and injection systems, effective and localized ECRH with power deposition control, electron cyclotron current drive (ECCD), and electron Bernstein wave heating (EBH) may be realized. For that purpose, two dimensionally steerable power injection system with beam focusing is necessary. To realize the power injection system, at least, two mirror antenna system (one is plasma facing 2-D steerable plane mirror, and the other is beam focusing mirror) inside the vacuum vessel is required. The dimensions of the mirrors depend on the focused beam waist size at the plasma core region and the distance between the plasma and the mirrors. The antenna design should be optimized under the available circumstance of CFQS vacuum vessel design, to realize the beam waist size as small as possible in the plasmas.

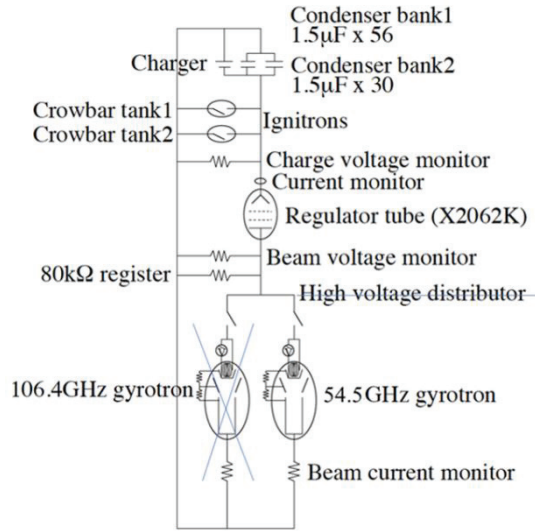


Fig. 4.6.1-1 Single line diagram of ECRH.

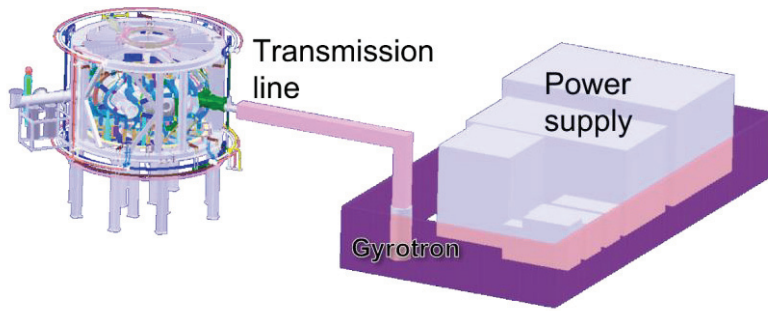


Fig. 4.6.1-2 Preliminary layout of ECRH system.

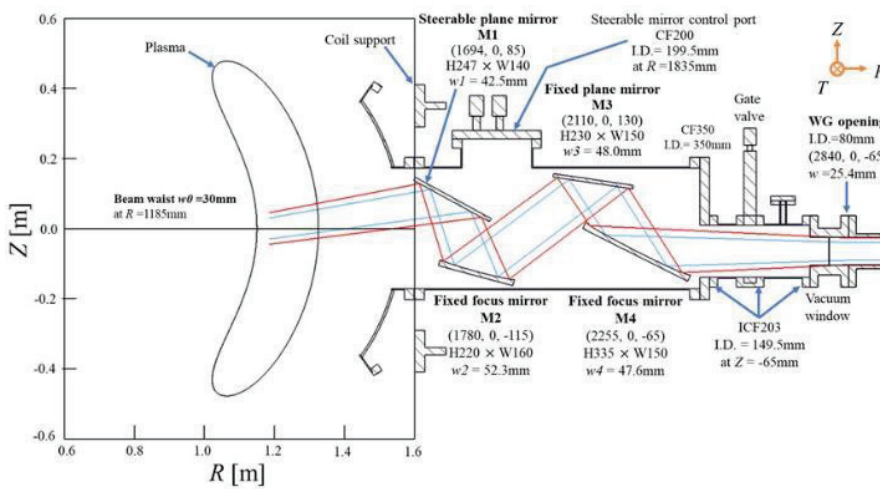


Fig. 4.6.1-3 Design of ECH power injection antenna.

4.6.2 Neutral beam injection (NBI) heating system

Neutral beam injection (NBI) is a powerful tool for plasma heating and drive of the plasma current and flow. To study energetic particle physics, tangential NBI is an inevitable device. Tangential port with diameter of 300 mm is recommended to install NBI. Fig. 4.6.2-1 shows a preliminary layout of the NBI system for the CFQS. It is necessary to secure a large area (100 m² for the power supply and 10 m² for the ion source) near CFQS to install the NBI system.

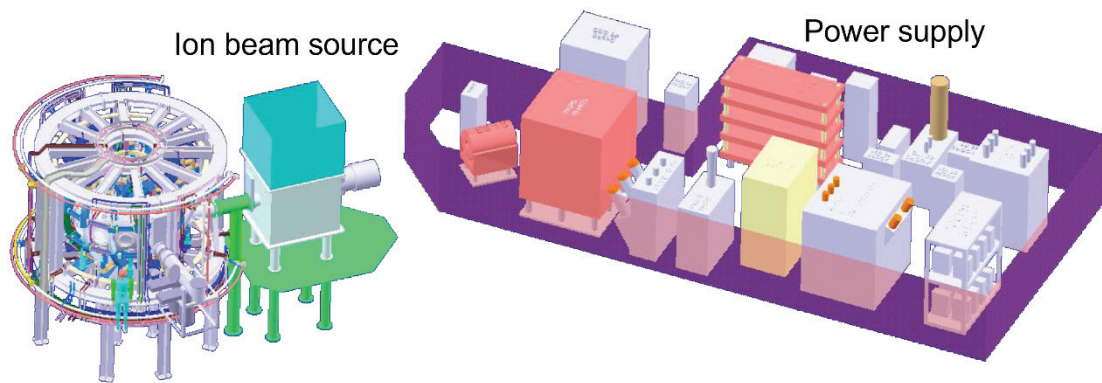


Fig. 4.6.2-1 Preliminary layout of NBI system.

4.7 Diagnostics system

4.7.1 Overview of diagnostic system

Diagnostics are indispensable for studying high temperature plasma physics in modern fusion research. There are a lot of interesting topics to be studied; transitions to improved confinement modes, formation of transport barriers, and their impact on plasma turbulence, etc. Roles of diagnostics are increasing in the studies on high temperature plasma properties, not only for fusion but also for basic physics.

CFQS is an innovatively designed device to achieve tokamak-like confinement properties and helical-like stability at the same time. Plasmas produced in the CFQS will become a good target for research which aim at achieving cost-effective stable burning plasmas. High-quality data based on detailed measurements should be obtained for comprehensive understanding of toroidal plasmas.

As mentioned above, anomalous transport and improved confinement modes are important issues for understanding toroidal plasmas. Based on the successful results of the advanced diagnostics in CHS and LHD, we will employ advanced diagnostic systems such as heavy ion beam probe (HIBP) and microwave reflectometry to study the Spatio-temporal turbulence structure and the structures of electric field and plasma flow. After the installation of NBI in the future, we will consider developing charge exchange spectroscopy (CXS) for the measurement of radial electric field and plasma flow velocity to study the relation between toroidal rotation and momentum input.

Also, physics of density limit is important in helical devices because confinement property of helical systems is improved as the density increases following the scaling law. Therefore, higher priorities are given for the diagnostics of edge plasma, MHD and radiation power, including magnetic probe, bolometer, etc.

For basic diagnostics, microwave interferometer should be firstly developed to measure the electron density. Thomson scattering is also important to study the physics of transport barriers. Multi-dimensional measurement is useful for studying internal structure of basic plasma parameters. Therefore, the development of two-dimensional or three-dimensional measurements will be performed as far as possible. So that the structure and non-linear development of plasmas can be observed in detail.

Diagnostics planned in the CFQS are listed in Table 4.7.1-1 and Table 4.7.1-2. Assignment of ports to these diagnostics is planned as shown in the section about the vacuum vessel. Some of the ports should be specifically designed for HIBP and Thomson scattering because these diagnostics require special geometries.

Table 4.7.1-1 Basic diagnostics.

Diagnostics	Target	Remark
Multichannel Thomson scattering	Electron temperature	
	Electron density	
150 GHz μ -wave interferometer	Electron density	
Electron cyclotron emission	Electron temperature	
Soft x-ray detector	Bremsstrahlung	Motion of electrons
Hard x-ray detector	Runaway electron	
Fast neutral particle analyzer (NPA)	Ion temperature	
Visible light spectroscope	Ion temperature	
H α detector	Edge plasma	
Langmuir probe	Edge plasma	
Vacuum ultraviolet spectroscope	Impurities	
Pyroelectric detector	Radiation power	
Mirnov probe (Magnetic probe)	MHD instability	
Diamagnetic loop	Stored energy	
Rogowski coil	Plasma current	
CCD camera	Shape of plasma	

Table 4.7.1-2 Advanced diagnostics.

Diagnostics	Target	Remark
Beam fluorescence	Magnetic surface	Mapping
Far infrared interferometer	Electron density	High density
Multichannel resistive bolometer	Radiation power	
AXUV photodiode array	Radiation power	
Heavy ion beam probe (HIBP)	Electric potential	
	Turbulence	
	Plasma flow velocity	Rotation
Charge exchange spectroscopy (CXS)	Electric field	
	Plasma flow velocity	Rotation
	Ion temperature	
Motional stark effect (MSE)	Magnetic field	q-profile
Fast-ion loss diagnostics (FAST)	Beam ion loss	
Microwave reflectometer	Turbulence	

4.7.2 HIBP diagnostic

Heavy ion beam probe (HIBP) [4.7.2-1] is a powerful diagnostic tool to study the physics related to E_r , because it can measure the potential, the density, the magnetic field, and their fluctuations in magnetically confined high temperature plasmas, with good temporal and spatial resolutions, without giving any disturbances to plasma. Up to now, utilizing these superior features, HIBPs have been used to investigate many fascinating phenomena related to E_r and flow in plasmas. To study these attractive physics in CFQS with HIBP, HIBP will be installed. In this section, the feasibility study of this diagnostic is reported.

The vacuum vessel design of CFQS is shown in Fig. 4.7.2-1, which has many ports for heating and diagnostic systems. We consider using two ports for HIBP, the top port with ICF203(CF150) size for probe beam injector, and the side port with ICF305(CF250) for energy analyzer and detector.

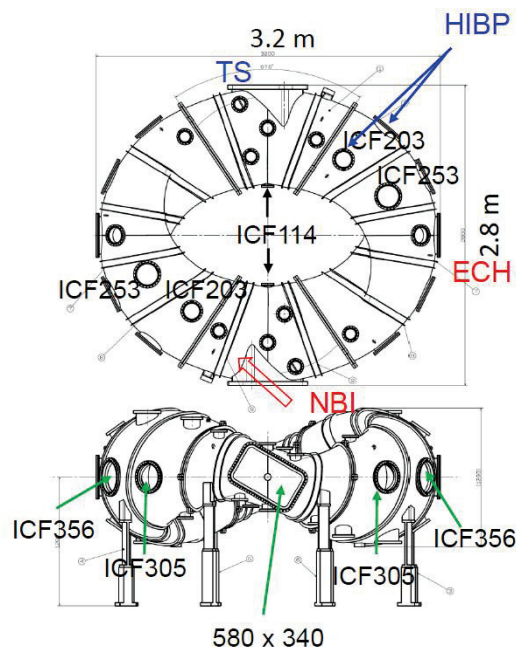


Fig. 4.7.2-1 Vacuum vessel design and port arrangement for HIBP.

For a probe beam of HIBP, the Larmor radius of beam particle should be larger than the averaged radius of plasma to inject the beam into the plasma center. The Larmor radii as a function of beam energy is shown in Fig. 4.7.2-2. Here, as beam particles, Li(7), Na(23), K(39), Rb(85), and Cs(133) with single charge are considered. Number means mass number of beam particles. Since, averaged minor radius of CFQS plasma is 0.25 m, at least the energy of 25 keV for Cs is required, however for Li the energy of 475 keV are required. We would like to reuse the high voltage power supply (< 200 kV) of HIBP in CHS [4.7.2-2,3], therefore, K, Rb, Cs are acceptable from the point of probe beam energy, however, Li and Na, the beam energy is too large. In the orbit calculation, Cs particles are assumed in this section, but we can transform the required energy for other species easily by multiplying the mass ratio between Cs and considered beam species.

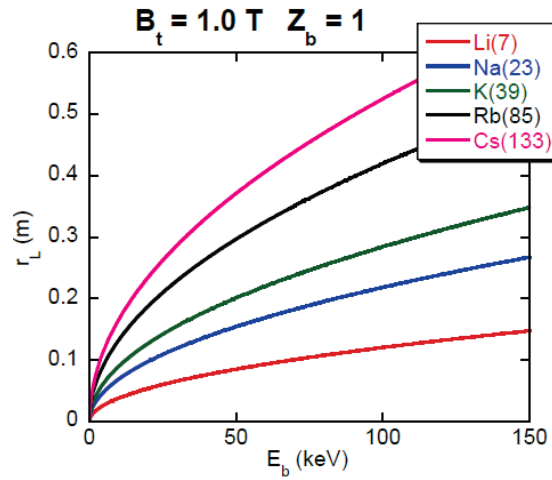


Fig. 4.7.2-2 Larmor radius, r_L , of various ion as a function of beam energy, E_b .

In the orbit calculation, the detailed structure of HIBP system, e.g., 8 pole electrostatic deflector and energy analyzer, is not included, however, results shown here are utilized to determine actual arrangement of those components. Injection/ejection point of probe beam are chosen to be the center of top (injection)/side (ejection) port, for simplicity of initial and boundary condition. To optimize the probe beam orbit so that the beam injected from the center of injection port should reach to the ejection point at the center of side port, injection angle in the toroidal and poloidal direction is scanned and determined. A typical obtained orbit with the beam energy of 40 keV is shown in Fig. 4.7.2-3. Projections of the orbit on top view plane (Fig. 4.7.2-3 (a)) and on the poloidal cross section plane at the toroidal angle of 45 deg (Fig. 4.7.2-3 (b)) are shown. In this case, primary beam are changed to be secondary beam near plasma center, so this means that observed region is plasma center.

By scanning the beam energy and the injection angle, E_b - θ grid map of observation region were calculated as shown in Fig. 4.7.2-4. For Cs, the beam energy of 30 ~ 50 keV are useful for HIBP, which corresponds to the energy of Li: 570 ~ 950 keV, Na: 173 ~ 289 KeV, K: 102 ~ 171 KeV, and Rb: 47 ~ 78 keV.

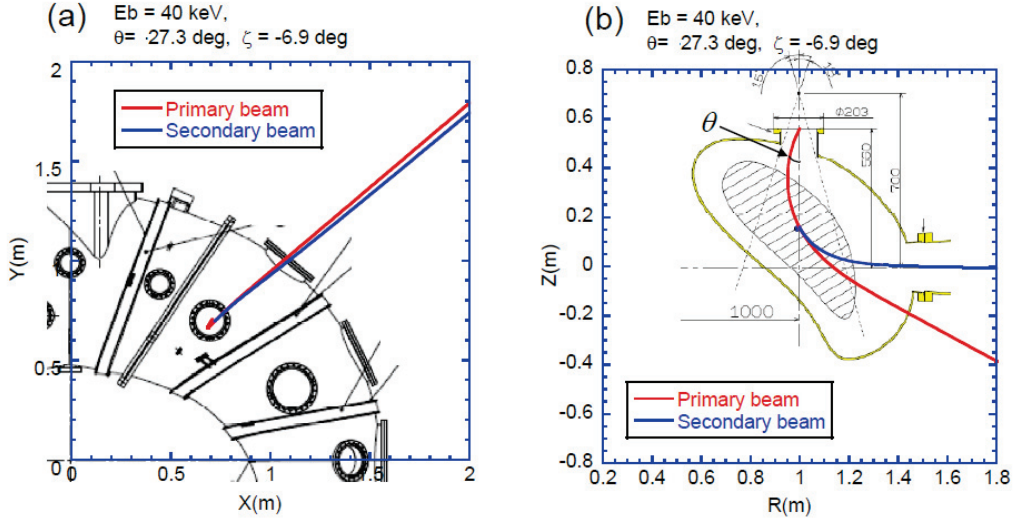


Fig. 4.7.2-3 Typical example of probe beam orbit. Projection on (a) top view and (b) poloidal cross section plane. Cs of which beam energy of 40 keV is assumed in this orbit calculation.

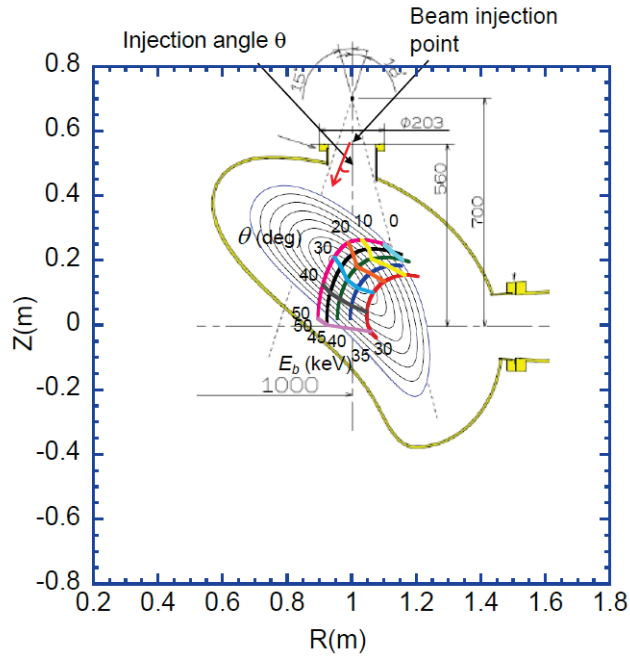


Fig. 4.7.2-4 E_b - θ grid map of observation region for HIBP are shown. Cs beam is assumed.

For HIBP, probe beam attenuation by the collision with plasma is an important factor to consider the appropriate density range in measurements. The probe beam is attenuated mainly by collisions with electrons. The detected beam current of the secondary beam at the detector can be expressed as,

$$I_D = 2I_0 n_e \langle \sigma_1 v_e \rangle w / v_B \times \exp[-\int n_e \langle \sigma_1 v_e \rangle / v_B d\ell - \int n_e \langle \sigma_2 v_e \rangle / v_B d\ell]. \quad (1)$$

Here, I_0 is the injected current as the primary beam, I_D the detected current as the secondary beam, $\langle \sigma_1 v_e \rangle$ rate coefficient of $A^+ \rightarrow A^{2+}$ with electron impact, $\langle \sigma_2 v_e \rangle$ rate coefficient of $A^{2+} \rightarrow A^{3+}$ with electron impact, n_e the electron density, w the sample volume length, v_B the beam velocity, and dl the path integral along beam orbit. The beam energy of 40 KeV for Cs, and orbit shown in Fig. 4.7.2-3, are chosen to estimate I_D . We use the rate coefficient from the Lotz's empirical formula [4.7.2-4]. Temperature and density profiles of plasma are assumed as, $T_{e0} (1 - \rho^2)$ and $n_{e0} (1 - 0.8 \rho^2 + 1.3 \rho^4 - 1.5 \rho^6)$, and $T_{e0} = 1$ keV. In this case, estimated value of I_D/I_0 as a function of the line averaged electron density, \bar{n}_e , is shown for Cs, Rb, K, Na in Fig. 4.7.2-5. When $\bar{n}_e < 1.0 \times 10^{19} \text{ m}^{-3}$, Cs is the best in these species, while in the range of $\bar{n}_e > 1.0 \times 10^{19} \text{ m}^{-3}$, Rb is a better choice. For much larger density, K is another possible choice. From CHS experiments, when I_D is larger than a few hundreds of nA, large signal to noise ratio can be expected to measure turbulence, zonal flow etc. in plasma. I_D/I_0 is $10^{-3} \sim 10^{-2}$, therefore, the primary beam current I_0 of a few hundreds of μA is required. This range of current is not difficult to achieve by zeolite ion source [4.7.2-5], therefore, HIBP in CFQS will provide good opportunity to study attractive physics related to E_r .

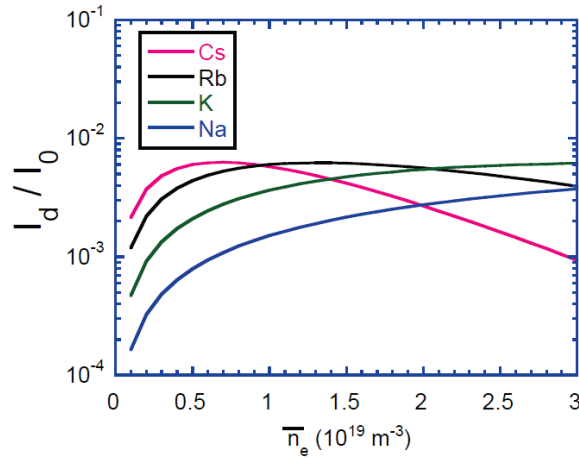


Fig. 4.7.2-5 The beam attenuation of I_D/I_0 as a function of line averaged electron density.

References

- [4.7.2-1] F. C. Jobes, and R. L. Hickok, Nucl. Fusion **10** (1970) 195.
- [4.7.2-2] A. Fujisawa, H. Iguchi *et al.*, Phys. Rev. Lett. **82** (1999) 2669.
- [4.7.2-3] A. Fujisawa *et al.*, Rev. Sci. Instrum. **67** (1996) 3099.
- [4.7.2-4] W. Lotz, Astrophys. J. Suppl. **14** (1967) 207.
- [4.7.2-5] S. Ohshima, A. Fujisawa, A. Shimizu *et al.*, Rev. Sci. Instrum. **77** (2006) 03B704.

5 Research plan and schedule

The CFQS manages to offer available solutions to critical challenges for toroidal confinement fusion: it provides a steady-state, disruption-free reactor concept as well as neoclassically optimized magnetic configurations. With respect to the magnetic configurations, the CFQS is designed and operated to achieve three types of advanced configurations, *i.e.*, QA, mirror linked, and divertor configurations. To guarantee the safety of the facility operation and accuracy of each magnetic configuration two steps are scheduled to operate CFQS, which are the low magnetic field operation and standard magnetic field operation.

5.1 Physics research plan

5.1.1 Research plan for 0.1 T operation

The research plan for the 0.1 T operation is as follows,

- i. Operate all the diagnostics and auxiliary systems, *e.g.*, electron gun, CCD camera, interferometer, probes, visible light, *etc.*
- ii. Achieve flexible magnetic configurations, *i.e.*, QA configuration, mirror linked configuration as well as divertor configuration; check the accuracy of magnetic field configurations in vacuum by mapping experiment.
- iii. Verify optimization of neoclassical transport and whether the tokamak-like fundamental transport properties are realized or not.

5.1.2 Research plan for 1.0 T operation

The research plan for the 1.0 T operation is as follows,

- i. Neoclassically optimized magnetic configurations.
- ii. Turbulence and transport research.
- iii. Island bundle divertor.
- iv. Plasma-materials interactions in 3-D systems.
- v. Energetic-particle confinement.
- vi. Equilibrium and stability at high- β .
- vii. Impurity confinement and accumulation.
- viii. Optimize the coil system for the next generation stellarator.

5.2 Construction schedule

- Phase I; Physics design and main machine design
 - Configuration
 - Neoclassical transport
 - MHD
 - Modular coils
 - Vacuum vessel
 - Supporting structure *etc.*
- Phase II; Fabrication of CFQS, transfer essential heating, and diagnostic systems from NIFS to SWJTU
 - NBI
 - Gyrotron
 - Interferometer
 - X-ray diagnostic *etc.*
- Phase III; Commissioning, verify construction accuracy, and obtain first plasma.
- Phase IV; Magnetic configuration studies and heating experiments in 0.1 T operation.
- Phase V; Magnetic configuration studies and heating experiments in 1.0 T operation.

For the experimental phase of 0.1 T operation, experiment building in Jiuli campus in SWJTU was renovated as China-Japan collaboration laboratory during 2020-2021. Following pictures, Fig. 5.1.2-1 and Fig.5.1.2-2, show entrance, torus hall, control room, and meeting room of China-Japan collaboration laboratory.



Fig. 5.1.2-1 China-Japan collaboration laboratory in Jiuli campus, left: entrance, right: torus hall.



Fig. 5.1.2-2 China-Japan collaboration laboratory in Jiuli campus, left: control room, right: meeting room.

During FY 2022, the first plasma of the CFQS will be achieved.

NIFS-SWJTU JOINT PROJECT FOR CFQS
~PHYSICS AND ENGINEERING DESIGN~

VER. 4.1

2022. JAN.

APPENDIX -A1 (BD)

~BASIC DESIGN~

CFQS Team



NIFS; National Institute for Fusion Science

SWJTU; Institute of Fusion Science, School of Physical Science and Technology Southwest Jiaotong University

Hefei Keye; Hefei Keye Electrical Physical Equipment Manufacturing Co., Ltd.

Table of Contents

1	General information.....	4
1.1	Abbreviation	4
1.2	Guideline of allowable limit value of stress and strain for the CFQS.....	6
2	Coil system	7
2.1	Modular coil (MC).....	7
2.1.1	Design of modular coil.....	7
2.1.2	Trajectory of the center the cross section.....	11
2.1.3	Optimization of the twisting angle of each modular coil	19
2.1.4	Resistance	29
2.1.5	Pressure loss of cooling water.....	30
2.1.6	Cage type support structure for the modular coil system.....	32
2.2	Poloidal field coil system (PFC)	39
2.3	Toroidal field coil system (TFC)	40
2.4	Inductance matrix for the coil system	42
2.5	Wiring of the coil system.....	44
2.6	Cooling of the coil system	46
3	Validation of the coil design.....	52
3.1	Validating the ANSYS/Maxwell result for inductance (MC).....	52
3.2	Electromagnetic force of the modular coil (MC).....	53
3.2.1	Coil system for the CFQS and analysis method	53
3.2.2	Magnetic field and EM force distribution on the modular coils	53
3.2.3	Characteristics of the EM force	54
3.3	Eddy current on the modular coil case (MC).....	63
3.4	Magnetic field distribution of the poloidal field coil (PFC)	64
3.5	Magnetic field distribution and electromagnetic force of the toroidal field coil (TFC).....	66
3.5.1	Magnetic field distribution.....	66
3.5.2	Estimation of the magnitude and direction of the EM force	66
3.5.3	Consideration related to support design.....	67
3.6	Stress analysis of the modular coil with the support structure.....	73
3.6.1	Summary.....	73
3.6.2	Model of the analysis	73
3.6.3	Results of the analysis.....	75
4	Vacuum vessel.....	78
4.1	Cross section of vacuum vessel	78
4.2	Shape of the vacuum vessel defined by the Fourier expansion	82
4.3	Port location and the cross-sectional shape of vacuum vessel at the port.....	84

4.4	Design of leaf-spring type leg.....	90
4.4.1	Summary.....	90
4.4.2	Design values.....	90
4.4.3	Buckling load and safety factor	91
4.4.4	Bending stress with the forced displacement.....	91
4.5	Eddy current analysis of vacuum vessel	93
4.5.1	Time constant of eddy current and its effect on plasma discharge.	93
4.5.2	EM force on the vacuum vessel.....	98
4.5.3	Inductive heating of the vacuum vessel	100
4.6	Structural analysis of vacuum vessel	102
4.6.1	Stress and displacement in various operating conditions.....	102
4.6.2	Effect of mesh size in the analysis for the vacuum vessel	108
4.7	Baking heater for vacuum vessel.....	110
4.7.1	Specification of the baking heaters	110
4.7.2	Required length of the baking heater	110
4.8	Preliminary layout of magnetic measuring elements	113
4.9	Preliminary layout of the view ports.....	114
4.10	Preliminary layout of the limiters	115
5	Preliminary production flow of the CFQS.....	116
5.1	Production flow of vacuum vessel in a factory.....	116
5.2	Pre-assembly procedure of modular coils and vacuum vessel on site	119
6	Power supply for coils	121
6.1	Current wave form to estimate required power capacity	121
6.2	Trial design of coil power supply for 0.09 T operation	126
6.3	Trial design of coil power supply for 1 T operation	127
6.3.1	Designed circuit diagram and the layout of MG building.....	127
6.3.2	Specifications of SG, IM, and a flywheel	129
7	Related equipment.....	131
7.1	ECH power injection antenna	131
7.2	Vacuum pumping system.....	133
7.3	Pure water cooling system	134
7.4	Baking power supply	135

1 General information

1.1 Abbreviation

This document includes various abbreviation words. The following table shows their meaning.

Table 1.1-1 Abbreviation

No	Abbreviation	Description
1	A/F	Arc and filament
2	ACC or ACL	Acceleration
3	ACR	Auto current regulator
4	ACSW	Acceleration Thyristor switch
5	APR	AC power regulator
6	AVP	Auxiliary vacuum pump
7	AXUV	Absolute extreme ultraviolet
8	AVR	Auto voltage regulator
9	BLA	Beam line auxiliary control board
10	BMAG or BNDMAG	Bending magnet
11	CB	Control board or Circuit breaker
12	COOL OIL	Cooling oil equipment
13	CRYOP	Cryogenic pump
14	CTRL or CP	Control panel
15	CXS	Charge exchange spectroscopy
16	DCC	DC capacitor
17	DCL	DC reactor, DC inductor or Deceleration
18	DCM	DC generator and motor
19	DS	Disconnecter
20	ECE	Electron cyclotron emission
21	ECH	Electron cyclotron heating
22	EMF	Electric magnetic force
23	EQ	Equipment
24	FAST	Fast ion loss diagnostics
25	FIR	Far infrared
26	GS	Grounding switch
27	GTO	Gate turnoff Thyristor
28	HIBP	Heavy ion beam probe
29	HSYG	Horizontal synchronous generator
30	HV	High voltage
31	HX	Hard x-ray
32	HX	Heat exchanger
33	IM	Induction motor
34	ι (Iota)	Rotational transform angle
35	IS	Ion source
36	ISO	Isolation
37	Keye	Hefei Keye Electro Physical Equipment Manufacturing Co.
38	LCFS	Last closed flux surface, Outermost magnetic surface
39	LHe	Liquid helium

No	Abbreviation	Description
40	LN2	Liquid nitrogen
41	LV	Low voltage
42	MC	Modular coil
43	MC	Magnet contactor
44	MCCB	Molded case circuit breaker
45	MG	Motor generator
46	MSE	Motional stark effect
47	NBI	Neutral beam injector
48	NIFS	National Institute for Fusion Science
49	NPA	Fast neutral particle analyzer
50	PFC	Poloidal field coil
51	PFC	Plasma facing component
52	PS	Power supply
53	PSC	Polarity switching circuit
54	q	Safety factor
55	QA	Quai-axisymmetric configuration
56	QH	Quasi-helical symmetric configuration
57	QI	Quasi-isodynamic configuration
58	RP	Rotary pump
59	REFCR	Refrigerator for cryogenic pump
60	RF	Radio frequency wave
61	RWET	Rectangular wave equivalent time
62	SA	Surge absorber
63	SB	Surge blocker
64	SCR	Thyristor
65	SG	Synchronous generator
66	SIM	Self-excited induction generator and motor
67	SW or SWB	Switch, switch board or power board
68	SWJTU	Southwest Jiaotong university
69	SX	Sort x-ray
70	TB	Table or Terminal box
71	TCB	Temperature converter board
72	TFC	Toroidal field coil
73	TMP	Turbo molecular pump
74	TRF	Transformer
75	VCB	Vacuum circuit breaker
76	VD	Voltage divider
77	VP or VPS	Vacuum pumping system
78	VSYG	Vertical synchronous generator
79	VUV	Vacuum ultraviolet
80	VV or VC	Vacuum vessel or Vacuum chamber

1.2 Guideline of allowable limit value of stress and strain for the CFQS

Although there is no publicly determined standard for fusion research, it is convenient to define something as guidelines. The stress component of the fusion device is complicated and its analysis not sufficient. So, it is not easy to step in detail on technical standards. We may only follow the basic idea, but we should think about the details flexibly. The fusion research often follows the ASME III. Even in the CFQS project, we will be better to follow the same guideline.

A design guideline in Table 1.2-1 may be used for the CFQS, that is a just guideline, not a necessary and sufficient condition. If it cannot be satisfied, it may be sometimes used on condition that the integrity is confirmed in the periodic inspections.

Table 1.2-1 Design guideline of typical materials for the CFQS.

Material			SUS316	C1020-O (Conductor)	Resin	Composite (Coil)	FRP
Young's Modulus	(GPa)	E	198	100	1~3	110	100
Design stress	(MPa)	S_m	137	50	-	30	50
Design strain		ε				<0.1%	
Tensile strength	(MPa)	σ_u	520	230	10~100	200	2000
Yield strength	(MPa)	σ_y	205	80	-	80	500
Elongation	(%)		40	50	1~2	1~2	5
Poisson's ratio		ν	0.3	0.34	-	0.3	0.3
Density	(kg/m ³)	ρ	7800	8960	1100	8000	1500
Thermal expansion		α	1.73×10^{-5}	1.65×10^{-5}	5×10^{-5}	1.65×10^{-5}	2.0×10^{-5}
Comments			300k	OFC	after curing	OFC + isolator	Varies

$S_m = \min(2/3 \sigma_y, 1/3 \sigma_u)$; ASME III criterion is changed according to operating temperature.
If possible, it is desirable that strain ratio ε is less than 0.1 % or 0.5 % at worst for the coil

Material properties of the coil (that is on copper and insulation composite) differ greatly from structural material. The ASME III should not be strictly applied for them. The strength of the coil is affected by the working method and the heat treatment conditions in addition to the selection of the material. As these data are not released to the public, they need to be acquired by developers themselves through element prototyping and inspection. It is difficult to decide the guidelines when it is not done,

Because it is inconvenient if we have no guidelines, we will temporarily extend the ASME III to the coil, but we also decided to consider its own properties.

- The conductor is very flexible and cannot be cut in a short time even if it exceeds the yield strength.
- The insulation (especially cured resin close to glass) is easy to crack and should be restricted by strain.
- It is more reliable to minimize the deformation of the coil within the measurable range.
- The target of the deformation is 1 mm or less.

2 Coil system

2.1 Modular coil (MC)

2.1.1 Design of modular coil

Fig 2.1-1 shows shape of the modular coil system. Shape of the coil lead is not easy to decide properly in a desk study, because it is necessary to bend intricately considering interference with peripheral parts and fixing place. Therefore, the conductor shape will be adjusted according to the surrounding structure during installation. To prepare for this, leave 500 mm to 800 mm as an extra length and cut the conductor at an appropriate place during installation. After adjusting the length and bending them, the go and return conductors are wrapped with glass tape and fixed with a resin. The system consists of 4 types of 16 coils. In the figure, for example, four white MC1s have the same shape, but half of them are installed upside down.

The cross section of the coil is shown in Fig 2.1-2. The winding method is a double pancake with three simultaneous windings. The structure of the conductors at the beginning and end of winding is shown in Fig 2.1-3. The function of the S-bending filler block is to fill the gap of the S-bending area to provide a smooth surface for wrapping the 3 mm ground insulation. The function of the joint filler block is to fix all conductors together to resist electromagnetic (EM) force, and to fill the gap of the joint area for wrapping the ground insulation.

Since the current density is very high, the conductor temperature rises about 20 degrees per second of operation. To absorb this heat before next shot, the coils are cooled by pure water. Fig 2.1-4 shows current and cooling water flow, and conductor connection. To reduce the number of power supplies, the three double pancakes are electrically connected in series outside the coil. And in order not to increase the head loss of cooling water, the inlet and outlet of cooling water will be provided for each conductor.

Detail of joints are shown in Fig 2.1-5. Two types of copper block are designed to connect conductors. One of them is for connection between pancakes and other is for current lead. The copper blocks of joint_1 and the joint_2 electrically connects the conductors in series. Location the copper blocks must be far from the coil main body to avoid damage of the insulation by the high temperature of the brazing. Two square holes are designed on the copper block and the conductor can be inserted from one side. After inserting of the conductor, the copper block will be welded with the conductors by silver brazing. Therefore, the number of electric circuits is one per one coil, and the number of cooling water flow paths is three per one coil. A $\Phi 6 \times \Phi 4$ pipe is designed for the water-cooling pipes as shown in the figure. The material of the pipes is stainless steel. The terminal of the conductors will be drilled a $\Phi 6$ mm hole for inserting of the pipe. A standard water pipe joint is selected for the cooling water and the material is also stainless steel. The pipes will also be welded with the conductors by silver brazing.

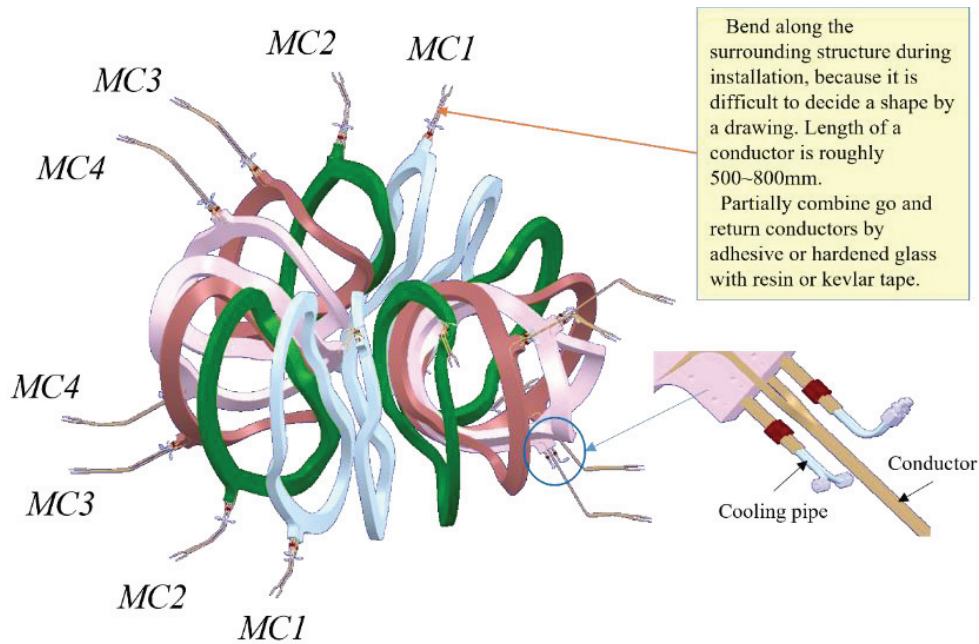


Fig 2.1-1 Modular coil system. Showing current leads and cooling pipes. The current leads is difficult to decide the wiring path in detail. The current lead conductors should be wind in a solenoid shape and temporary fix it at an appropriate place. It will be wired in its final position after installing the modular coil in the CFQS body.

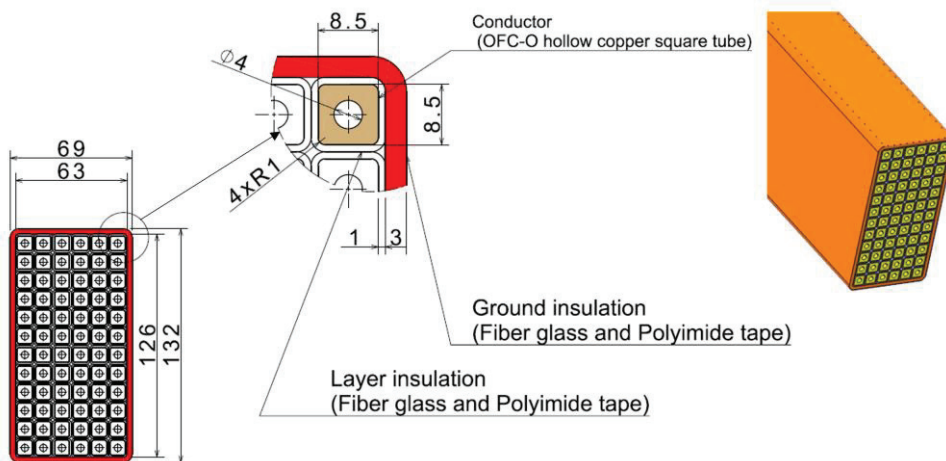


Fig 2.1-2 Cross section of the modular coil. The winding method is a double pancake with three simultaneous winding. The number of turns is 72 with 12 turns and 6 layers. The insulation process is vacuum pressure impregnation (VPI). The material of the conductor is hollow copper square tube of the Oxygen free copper annealed (OFC-O, equivalent JIS C1020). The layer and ground insulations are composites of Fiber glass tape with a thickness of 0.2 mm and Polyimide tape (Kapton) with a thickness of 0.05 mm.

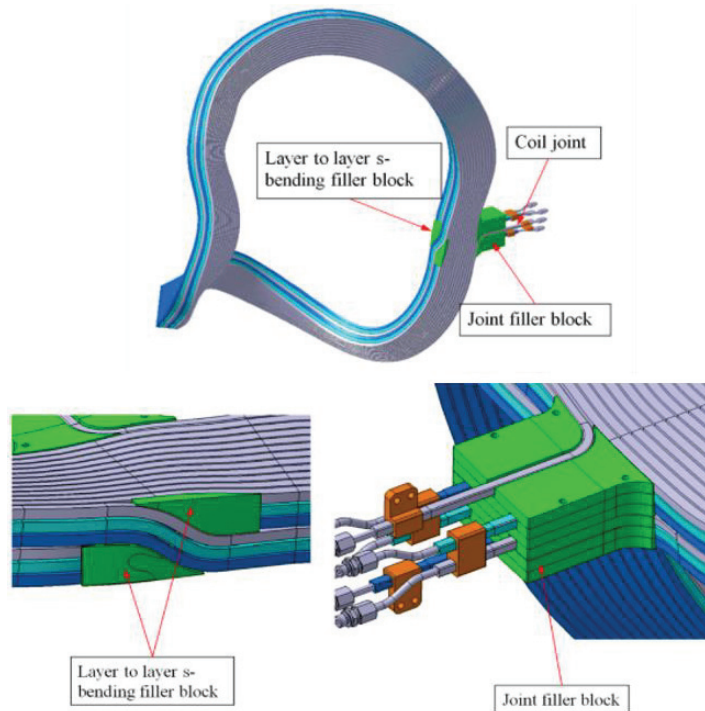


Fig 2.1-3 Structure of winding start and winding end. The winding start is the s-bending on the inner side of the coil, and the winding end is the terminal. At the beginning and end of winding, the filler blocks made of the FRP (Fiber Reinforced Plastics) are placed to fill the gap and fix conductors.

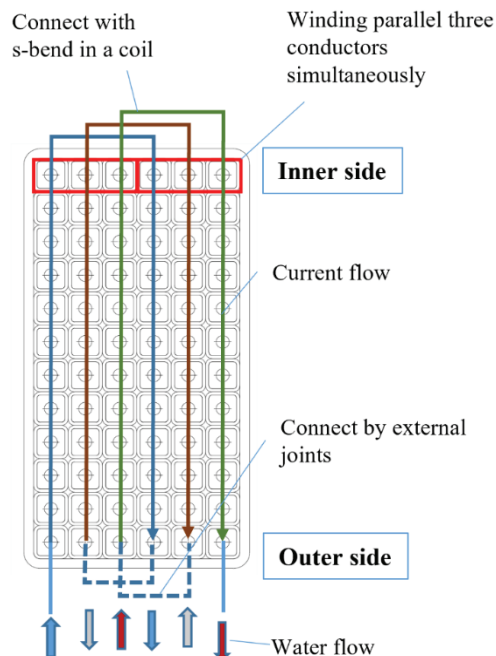


Fig 2.1-4 Current and cooling water flow. The three conductors are electrically connected in series outside the coil. The inlet and outlet of cooling water are provided for each conductor not to increase the head loss.

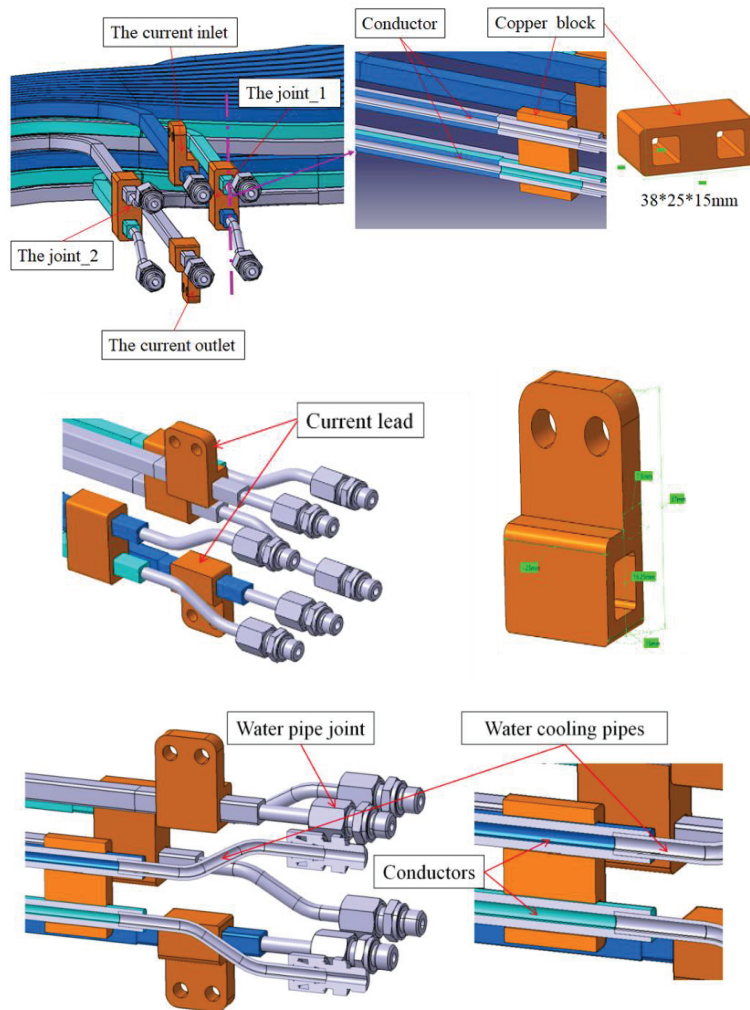


Fig 2.1-5 Detail of the conductor joint and the cooling water joint. Copper blocks of joint_1 and joint_2 are electrical connections. Insulated hoses are connected to the six water pipe joints (The tube fitting) at the ends of the cooling pipes.

2.1.2 Trajectory of the center the cross section

The current carrying surface (CCS), on which the coil current flows, will be defined by the optimization calculation. As a restriction condition of the optimization calculation, the area where the CCS can be arranged is defined.

$$\begin{aligned} R_{in}(\theta, \phi) &= \sum R_{in\ mn} \cos(m\theta - N_p n\phi) \\ Z_{in}(\theta, \phi) &= \sum Z_{in\ mn} \sin(m\theta - N_p n\phi) \\ R_{out}(\theta, \phi) &= \sum R_{out\ mn} \cos(m\theta - N_p n\phi) \\ Z_{out}(\theta, \phi) &= \sum Z_{out\ mn} \sin(m\theta - N_p n\phi) \end{aligned}$$

where θ and ϕ is the poloidal and the toroidal angle in the VMEC magnetic coordinate system, m and n is the poloidal and toroidal mode number. and N_p is the toroidal periodic number and equal 2 for the CFQS. Note that the angles in the magnetic coordinate system are normalized in one period.

$R_{in}(\theta, \phi)$ and $Z_{in}(\theta, \phi)$ is the coordinate of the inner limit surface, and $R_{out}(\theta, \phi)$ and $Z_{out}(\theta, \phi)$ is the coordinate the outer limit surface. $R_{in\ mn}$, $Z_{in\ mn}$, $R_{out\ mn}$ and $Z_{out\ mn}$ are the Fourier series expansion coefficients of the position coordinates. The Fourier coefficients are shown in Table 2.1-1.

The designer considers the situation around the coil and defines these limit surfaces. In the CFQS design, a surface 0.2 m outside the last closed flux surface (LCFS) was defined as the inner limit surface, and a surface 0.4 m outside the LCFS was defined as the outer limit surface. The LCFS coordinates are calculated by the VMEC and are described in the MHD equilibrium chapter.

$$\begin{aligned} R_{LCFS}(\theta, \phi) &= \sum R_{mn} \cos(m\theta - N_p n\phi) \\ Z_{LCFS}(\theta, \phi) &= \sum Z_{mn} \sin(m\theta - N_p n\phi) \end{aligned}$$

The Fourier coefficients of the LCFS are shown in the MHD equilibrium chapter and the shape of the LCFS and the limit surfaces are shown in Fig 2.1-6.

The current carrying surface (CCS) and the trajectory of the cross sectional center were determined by the NESCOIL system. The trajectory is defined by the following equations.

$$\begin{aligned} \phi &= 2\pi \sum \{C_m \cos(m\omega) + D_m \sin(m\omega)\} \\ \theta &= \omega + 2\pi \sum \{E_m \cos(m\omega) + F_m \sin(m\omega)\} \\ \omega &= 0 \sim 2\pi \end{aligned}$$

where θ and ϕ is the magnetic coordinate of the point on the trajectory of the cross sectional center. ω is the auxiliary variable. The angular coordinate (θ, ϕ) is calculated by the above equations for each variable ω divided at equal intervals. Fig 2.1-7 shows the magnetic coordinates of the trajectory. The position of the trajectory is obtained by substituting them into the following equations.

$$R_{CCS}(\theta, \phi) = (1 - A)R_{in}(\theta, \phi) + A R_{out}(\theta, \phi)$$

$$Z_{CCS}(\theta, \phi) = (1 - A)Z_{in}(\theta, \phi) + A Z_{out}(\theta, \phi)$$

$$A = \frac{1}{2}(1 + \tanh\{F(\theta, \phi)\})$$

$$F(\theta, \phi) = \sum F_{mn} \cos(m\theta - N_p n\phi)$$

where $F(\theta, \phi)$ is the function defining the CCS. The Fourier coefficients of C_m, D_m, E_m, F_m and F_{mn} are optimized numerically by the NESCOIL system. The result is shown in Table 2.1-2 and Table 2.1-3 and shape of the CCS is shown in Fig 2.1-8. Fig 2.1-9 shows the trajectory of the cross sectional center and Table 2.1-4 shows the coordinate of the trajectory in the real space.

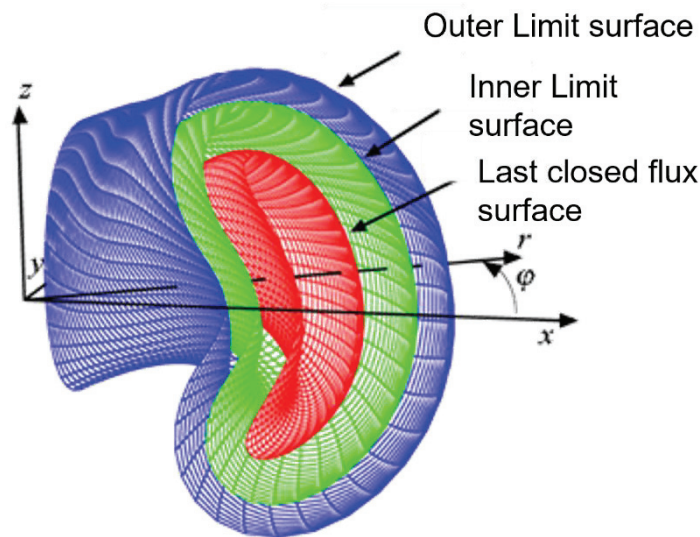


Fig 2.1-6 The last closed flux surface (LCFS) and the limit surfaces. By the optimization calculation, the current carrying surface (CCS) will be placed between the inner limit surface and the outer limit surface. In the CFQS design, the inner limit surface is 0.2 m outside of the LCFS, and the outer limit surface is 0.4 m outside the LCFS.

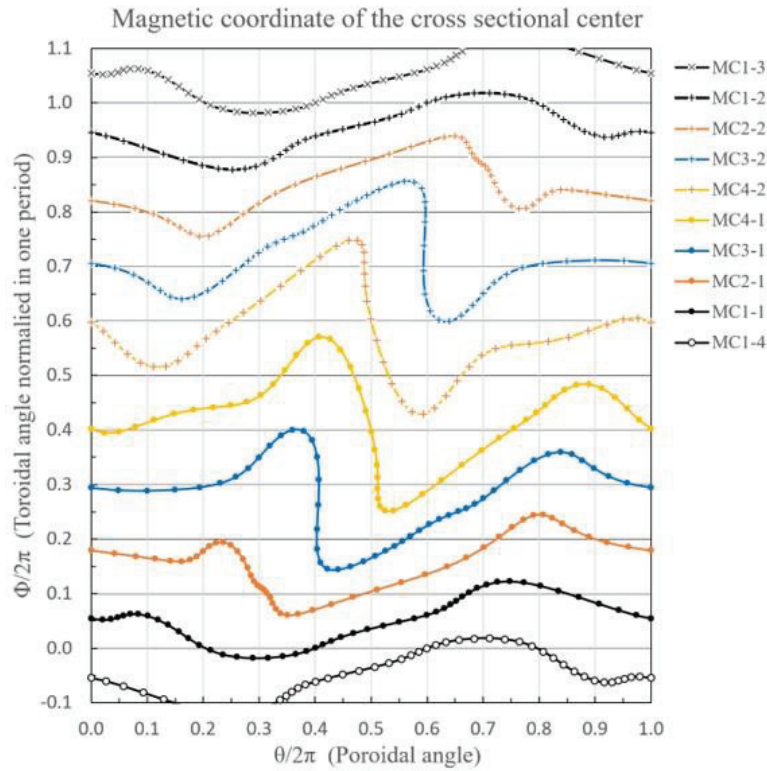


Fig 2.1-7 Cross sectional center of the modular coils in the magnetic coordinate system. The MC1-1, MC2-1, MC3-1, and MC4-1 show the reference trajectories, and others are parallel or inverted copies of them.

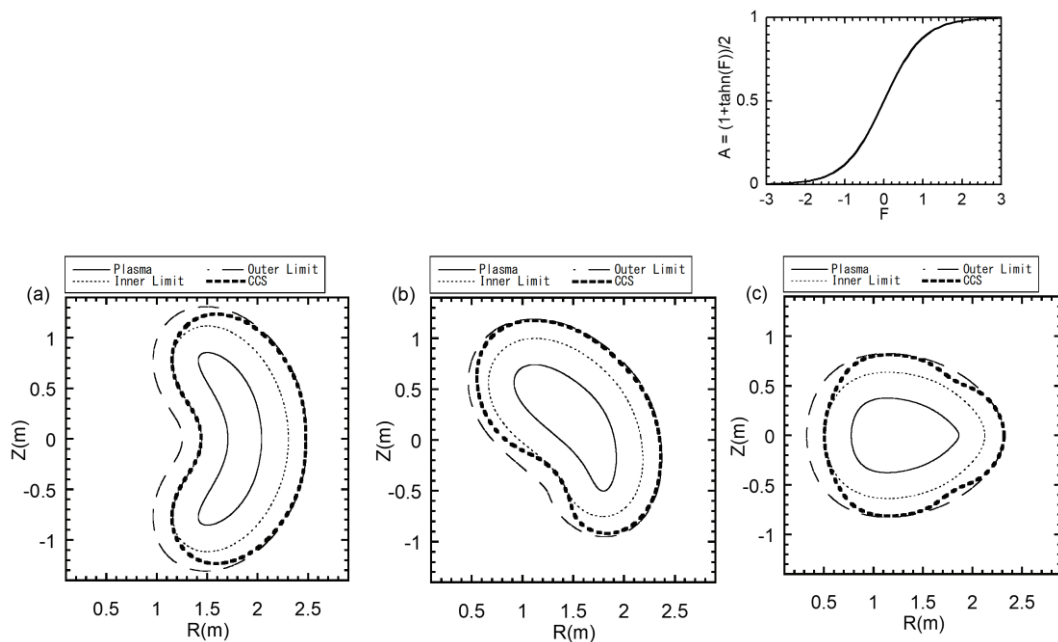


Fig 2.1-8 Current carrying surface for the CFQS on three toroidal angle planes in the real space coordinate system (Cartesian coordinate system). The LCFS of the CFQS-2b40, the inner limit surface and the outer limit surface are also shown in the figures.

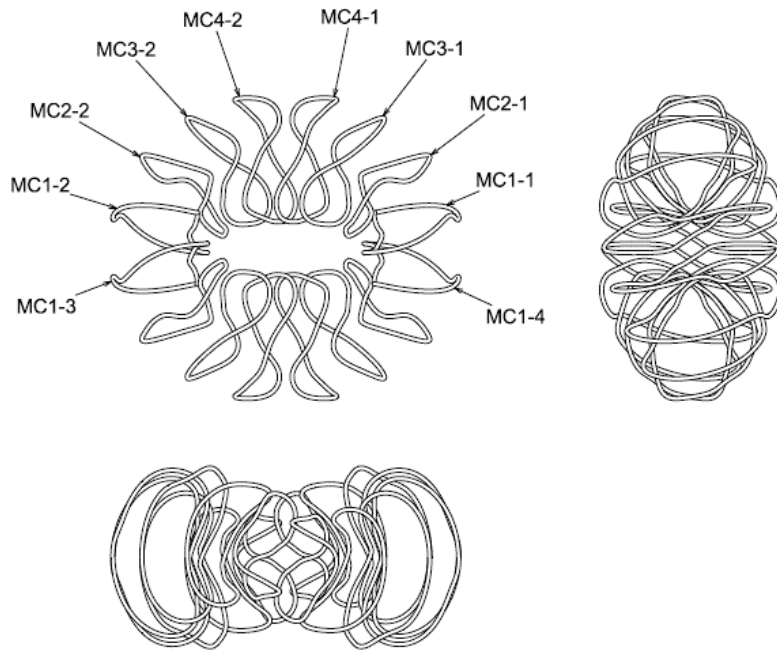


Fig 2.1-9 Center trajectory of the modular coil. The modular coil system consists of 16 coils of 4 types. For example, the MC1-3 is arranged 180 degrees rotational movement with respect to the z-axis, and the MC1-2 and the MC1-4 are arranged in reversal movement with respect to the x-axis and the y-axis.

Table 2.1-1 Fourier coefficients of the inner and outer limit surfaces with $N_p=-2$

No	m	n	$R_{in\ mn}$	$Z_{in\ mn}$	No	m	n	$R_{out\ mn}$	$Z_{out\ mn}$
1	0	-5	7.58893E-05	-1.23896E-04	1	0	-5	-7.24653E-05	-1.76900E-03
2	1	-5	5.88874E-04	-5.90320E-04	2	1	-5	-5.62472E-04	-2.38014E-03
3	2	-5	-9.93690E-04	-8.29019E-04	3	2	-5	-7.46116E-04	-1.05989E-03
4	3	-5	2.00471E-04	7.09052E-04	4	3	-5	-8.99424E-04	-1.27986E-03
5	4	-5	-2.89474E-05	-2.25925E-04	5	4	-5	5.36311E-04	-3.53406E-04
6	5	-5	4.60150E-04	9.86710E-05	6	5	-5	-1.10476E-04	-2.79005E-04
7	0	-4	-8.82758E-04	2.10849E-04	7	0	-4	-2.30944E-04	4.76685E-04
8	1	-4	-2.52390E-03	-3.72585E-03	8	1	-4	-7.99981E-04	1.07888E-04
9	2	-4	5.98392E-04	4.95277E-04	9	2	-4	4.06099E-04	6.04160E-04
10	3	-4	6.43471E-05	3.98781E-04	10	3	-4	1.01270E-03	1.78005E-03
11	4	-4	-9.14981E-04	-1.76857E-05	11	4	-4	-1.68382E-03	9.41983E-04
12	5	-4	6.60776E-04	-9.35607E-04	12	5	-4	1.77685E-03	-5.20256E-04
13	0	-3	2.67142E-04	1.64110E-03	13	0	-3	5.08546E-04	1.28775E-03
14	1	-3	9.69115E-04	1.66142E-03	14	1	-3	2.21033E-03	2.20875E-03
15	2	-3	3.78223E-04	6.89165E-04	15	2	-3	-2.62808E-03	8.16607E-04
16	3	-3	4.81043E-03	-1.90706E-03	16	3	-3	7.89832E-03	-2.00844E-03
17	4	-3	-4.01147E-03	-5.31294E-05	17	4	-3	-8.22716E-03	-7.76895E-04
18	5	-3	5.96518E-04	-1.75179E-04	18	5	-3	4.13703E-03	-1.20405E-03
19	0	-2	4.88553E-03	-4.54739E-03	19	0	-2	8.68554E-03	-4.60778E-03
20	1	-2	-1.91325E-02	7.90749E-03	20	1	-2	-2.33415E-02	-8.39923E-03
21	2	-2	1.53106E-02	7.38326E-03	21	2	-2	2.13368E-02	2.44986E-02
22	3	-2	-5.78966E-03	-2.13940E-02	22	3	-2	-8.84368E-03	-4.38617E-02
23	4	-2	-4.07759E-03	-3.21457E-03	23	4	-2	-9.87862E-03	-1.00593E-02
24	5	-2	2.16776E-03	1.15788E-03	24	5	-2	5.77898E-04	-6.75209E-05
25	0	-1	1.14085E-01	-8.90299E-02	25	0	-1	7.52536E-02	-7.12151E-02
26	1	-1	-6.07918E-02	8.64941E-02	26	1	-1	1.93247E-04	7.37886E-02
27	2	-1	7.79414E-02	6.66492E-02	27	2	-1	1.13775E-01	1.06531E-01
28	3	-1	-4.15514E-02	-4.57962E-02	28	3	-1	-7.67599E-02	-8.01721E-02
29	4	-1	-2.24503E-03	-2.67740E-03	29	4	-1	-4.55782E-03	-6.19579E-03
30	5	-1	9.10644E-04	4.07485E-04	30	5	-1	1.02690E-03	1.54877E-03
31	0	0	9.89838E-01	0.00000E+00	31	0	0	9.84164E-01	0.00000E+00
32	1	0	4.01667E-01	4.79762E-01	32	1	0	5.93841E-01	6.55724E-01
33	2	0	4.18809E-02	2.97421E-02	33	2	0	5.29714E-02	4.38610E-02
34	3	0	-5.06871E-03	-1.28982E-03	34	3	0	7.49001E-04	6.89802E-03
35	4	0	-2.59686E-03	-2.45049E-03	35	4	0	-7.30051E-03	-5.82146E-03
36	5	0	-1.61801E-04	-4.98495E-04	36	5	0	6.28137E-04	6.60517E-04
37	0	1	0.00000E+00	0.00000E+00	37	0	1	0.00000E+00	0.00000E+00
38	1	1	-2.71483E-03	1.53054E-03	38	1	1	-3.36202E-02	-3.42443E-02
39	2	1	1.21748E-02	1.21290E-02	39	2	1	2.11696E-02	2.46768E-02
40	3	1	4.50659E-03	3.18066E-03	40	3	1	3.58031E-03	7.14075E-04
41	4	1	-4.71928E-04	-1.01870E-03	41	4	1	2.52975E-03	6.92529E-04
42	5	1	4.39000E-04	6.64062E-04	42	5	1	-1.24835E-04	-2.82946E-04
43	0	2	0.00000E+00	0.00000E+00	43	0	2	0.00000E+00	0.00000E+00
44	1	2	5.64231E-03	3.45978E-03	44	1	2	1.13825E-02	1.31972E-02

No	m	n	R _{in mn}	Z _{in mn}	No	m	n	R _{out mn}	Z _{out mn}
45	2	2	1.92327E-03	-3.37713E-04	45	2	2	-4.92088E-05	-5.53134E-03
46	3	2	-1.49141E-04	-1.08491E-04	46	3	2	9.99323E-04	1.73881E-03
47	4	2	-3.95140E-04	-5.72319E-04	47	4	2	-1.97504E-03	-1.51006E-03
48	5	2	4.38081E-04	-3.16476E-04	48	5	2	1.04029E-06	1.35136E-04
49	0	3	0.00000E+00	0.00000E+00	49	0	3	0.00000E+00	0.00000E+00
50	1	3	-2.63734E-03	-2.40970E-03	50	1	3	-2.45286E-03	-4.84102E-03
51	2	3	2.90365E-04	2.60341E-04	51	2	3	-9.68455E-04	5.50127E-04
52	3	3	-3.45647E-04	-1.06698E-03	52	3	3	-8.91717E-04	-1.14382E-03
53	4	3	-4.72284E-04	-4.57068E-04	53	4	3	7.91674E-04	3.10660E-04
54	5	3	7.15537E-05	2.24636E-04	54	5	3	2.14578E-04	-1.45782E-04
55	0	4	0.00000E+00	0.00000E+00	55	0	4	0.00000E+00	0.00000E+00
56	1	4	3.06708E-03	3.10727E-03	56	1	4	5.64010E-04	9.25952E-04
57	2	4	5.33223E-04	6.82975E-04	57	2	4	6.44155E-04	-5.18989E-04
58	3	4	-2.25753E-04	-2.75855E-04	58	3	4	5.29607E-05	-6.69925E-05
59	4	4	-2.56868E-05	-2.83892E-04	59	4	4	-1.09624E-03	-1.03013E-03
60	5	4	1.34530E-04	3.80411E-05	60	5	4	-6.23919E-05	-5.44685E-06
61	0	5	0.00000E+00	0.00000E+00	61	0	5	0.00000E+00	0.00000E+00
62	1	5	-1.37126E-05	-4.32788E-04	62	1	5	9.03430E-04	1.13871E-03
63	2	5	4.49605E-04	2.83268E-04	63	2	5	1.01342E-03	6.98894E-04
64	3	5	-2.54177E-04	-2.30475E-04	64	3	5	2.43954E-04	8.65377E-05
65	4	5	-4.62391E-05	-1.40534E-04	65	4	5	8.72839E-05	-3.13013E-04
66	5	5	8.01961E-05	1.35227E-04	66	5	5	1.07874E-04	-7.81701E-05

Table 2.1-2 Fourier coefficients defining the trajectory of the cross-sectional center (CFQS-CCS) which were obtained by the NESCOIL system.

No	Coil	m	C _m	D _m	E _m	F _m
1	MC1	0	5.08238063E-02	0.00000000E+00	-4.46786279E-02	0.00000000E+00
2	MC1	1	3.17161288E-02	-4.67121323E-02	3.57121610E-03	8.97025268E-03
3	MC1	2	-8.50878306E-03	5.97887485E-03	1.96052598E-02	9.68120583E-03
4	MC1	3	-1.42922019E-02	1.40667751E-03	1.77332574E-02	7.30683970E-04
5	MC1	4	-4.95305439E-03	-1.79961895E-04	-1.72787726E-03	-3.94294552E-03
6	MC1	5	-3.19256196E-04	-2.62164294E-05	5.49677186E-03	5.94815068E-04
7	MC2	0	1.54442039E-01	0.00000000E+00	-5.67830447E-02	0.00000000E+00
8	MC2	1	6.06780744E-02	-8.72720177E-03	8.41699345E-02	4.42984135E-02
9	MC2	2	-3.06081594E-02	-2.48111140E-02	-3.02522546E-02	6.18334659E-03
10	MC2	3	-9.97758074E-03	-3.92713621E-03	3.23212753E-03	2.39406697E-02
11	MC2	4	1.85804822E-03	-2.09923315E-03	2.06865760E-03	3.06592036E-03
12	MC2	5	2.94826018E-03	6.96195525E-03	-2.43542004E-03	3.69679871E-03
13	MC3	0	2.77245336E-01	0.00000000E+00	2.39217568E-02	0.00000000E+00
14	MC3	1	7.80796685E-02	1.48474079E-02	1.39028660E-02	8.33803903E-02
15	MC3	2	-5.23875821E-02	-1.48848340E-04	-1.80686429E-02	2.97898452E-02
16	MC3	3	-1.04369860E-02	-3.89659092E-02	-8.98503055E-03	-1.55357504E-03
17	MC3	4	6.83482331E-03	3.26077377E-03	-2.04836764E-03	8.17832166E-03
18	MC3	5	-5.18198119E-03	8.05588182E-03	-8.72258156E-03	4.19837022E-03
19	MC4	0	4.15911850E-01	0.00000000E+00	2.35306646E-02	0.00000000E+00

No	Coil	m	C _m	D _m	E _m	F _m
20	MC4	1	4.75027013E-02	6.33649000E-02	1.34852253E-03	6.12024715E-02
21	MC4	2	-4.95492054E-02	-7.43992241E-02	-2.23766903E-02	-2.09709873E-02
22	MC4	3	9.77380093E-03	3.10392796E-03	-6.16152784E-03	1.24809127E-02
23	MC4	4	-8.68311865E-03	4.77923986E-03	4.84051215E-03	-7.75099870E-03
24	MC4	5	-1.23679439E-02	-6.94790762E-03	-1.18148146E-03	-3.11969834E-03

Table 2.1-3 Fourier coefficients defining the CCS position with Np=2 (CFQS-CCS) which were obtained by the NESCOIL system.

No	m	n	F _{mn}	No	m	n	F _{mn}	No	m	n	F _{mn}
1	0	-5	1.0451526E-02	22	2	-1	3.0167782E-02	43	4	-2	-3.0186636E-03
2	0	-4	-3.2246210E-02	23	2	0	1.1424471E-01	44	4	-1	-7.7384896E-03
3	0	-3	-5.5378747E-02	24	2	1	1.8902919E-01	45	4	0	5.3603370E-02
4	0	-2	-1.4575198E-01	25	2	2	-1.3637218E-01	46	4	1	-8.8244211E-03
5	0	-1	-4.2343833E-01	26	2	3	1.2191454E-01	47	4	2	2.8490246E-02
6	0	0	1.2111113E+00	27	2	4	-6.3524118E-03	48	4	3	5.1272386E-02
7	1	-5	2.1197255E-02	28	2	5	-2.8253809E-04	49	4	4	-4.0296114E-02
8	1	-4	4.7218044E-03	29	3	-5	2.9258881E-02	50	4	5	2.5810687E-02
9	1	-3	7.2852863E-02	30	3	-4	1.8245548E-02	51	5	-5	-4.8638491E-02
10	1	-2	-2.2770681E-01	31	3	-3	2.1531166E-02	52	5	-4	-4.8215517E-02
11	1	-1	1.5708038E+00	32	3	-2	4.5203975E-01	53	5	-3	-2.2685688E-02
12	1	0	1.3316260E+00	33	3	-1	-6.8609554E-01	54	5	-2	-1.1746071E-01
13	1	1	-1.3103095E-01	34	3	0	1.9339655E-01	55	5	-1	7.0528030E-04
14	1	2	-1.5026153E-01	35	3	1	-1.0553564E-01	56	5	0	9.1842103E-02
15	1	3	1.4170268E-02	36	3	2	1.5037399E-01	57	5	1	2.4884115E-02
16	1	4	2.6749029E-02	37	3	3	1.1815016E-01	58	5	2	1.4915268E-03
17	1	5	-2.3231334E-02	38	3	4	2.9072859E-03	59	5	3	-6.6864726E-03
18	2	-5	-3.2638846E-02	39	3	5	1.5208853E-02	60	5	4	-2.0354558E-03
19	2	-4	1.5357525E-02	40	4	-5	-2.2644707E-02	61	5	5	1.4333211E-02
20	2	-3	-2.8669915E-02	41	4	-4	-6.5898961E-03				
21	2	-2	-4.2796981E-01	42	4	-3	-1.1506971E-01				

Table 2.1-4 Trajectory of the cross-sectional center which were obtained by the NESCOIL system.

No	M1-N0			M2-N0			M3-N0			M4-N0		
	X	Y	Z	X	Y	Z	X	Y	Z	X	Y	Z
1	1695.5	293.0	20.7	1411.2	891.5	9.7	962.8	1275.3	-56.4	463.9	1468.2	-68.1
2	1689.9	279.6	103.7	1394.8	848.1	205.8	955.7	1230.0	191.4	497.3	1455.5	23.2
3	1678.3	282.8	164.5	1364.2	799.0	344.1	905.6	1158.6	384.0	480.4	1433.6	130.6
4	1663.3	296.8	212.9	1327.8	750.3	450.3	841.7	1089.4	503.8	422.0	1388.8	239.4
5	1646.0	313.2	257.9	1282.9	705.7	541.7	765.1	1018.5	589.3	345.3	1316.6	330.2
6	1626.2	323.0	307.5	1231.7	672.5	615.1	675.2	943.7	656.4	281.4	1253.0	422.1
7	1602.8	318.8	368.3	1178.9	656.7	666.6	580.8	876.8	698.6	235.2	1183.2	509.8
8	1573.1	296.2	444.3	1125.5	657.4	700.3	487.7	823.7	716.4	202.3	1095.0	565.0
9	1532.1	254.8	535.6	1069.3	666.2	724.7	396.1	776.5	717.2	174.9	1004.7	600.0
10	1474.1	198.5	635.7	1010.1	670.7	747.8	309.0	721.6	707.5	141.1	915.1	620.9
11	1395.4	135.2	731.1	950.2	659.2	774.7	235.1	651.1	689.7	94.5	826.9	625.4

No	M1-N0			M2-N0			M3-N0			M4-N0		
	X	Y	Z	X	Y	Z	X	Y	Z	X	Y	Z
12	1295.2	74.0	806.4	893.2	624.7	806.3	183.8	567.3	664.3	37.3	740.4	609.9
13	1176.4	23.0	848.4	840.7	567.7	838.8	158.8	480.1	633.5	-20.7	653.2	572.9
14	1046.7	-12.9	848.3	792.5	495.8	864.5	157.1	402.3	602.0	-66.8	565.7	516.1
15	919.5	-33.4	801.9	748.9	421.0	876.0	173.6	341.5	571.1	-91.5	482.8	446.4
16	816.9	-41.9	706.7	711.8	354.7	870.7	203.9	297.0	540.6	-91.9	407.4	371.3
17	769.0	-44.0	573.3	682.4	303.2	852.4	245.4	264.6	509.8	-73.0	343.1	294.9
18	782.6	-43.3	438.0	658.7	267.0	827.6	301.0	245.3	467.0	-44.9	299.8	222.6
19	819.6	-38.6	331.5	637.6	242.4	800.2	367.5	235.7	409.3	-13.5	276.6	168.5
20	851.4	-29.0	255.5	618.0	224.8	770.8	431.3	232.2	339.0	19.8	264.6	135.7
21	873.8	-15.6	203.2	601.3	209.5	738.6	486.0	238.7	259.6	53.8	260.6	110.5
22	888.6	0.6	166.8	590.0	193.3	703.0	531.0	258.1	178.1	87.1	259.8	84.2
23	899.3	18.6	138.3	585.9	175.1	664.0	565.7	288.0	102.1	119.5	262.4	58.1
24	908.9	38.0	111.0	588.6	155.6	621.1	590.1	322.6	37.9	153.6	271.9	36.1
25	919.4	58.6	80.7	596.1	137.3	572.4	605.8	356.3	-11.4	190.9	286.3	20.2
26	930.1	80.1	46.9	607.1	124.0	514.6	614.8	386.3	-46.7	231.3	302.4	8.4
27	938.8	102.1	12.5	622.9	120.1	443.7	619.0	413.0	-71.5	274.3	319.4	-5.1
28	942.5	123.6	-20.2	649.8	129.4	357.8	619.4	438.5	-90.4	318.0	338.6	-26.4
29	939.4	143.6	-51.7	693.0	154.3	261.2	617.5	465.8	-106.1	357.7	362.3	-60.2
30	930.1	161.7	-84.6	745.3	193.1	162.9	615.0	496.5	-119.6	387.4	393.7	-107.8
31	917.7	178.1	-118.5	791.8	240.2	71.6	612.9	529.3	-131.7	402.6	436.5	-166.1
32	905.8	193.9	-150.3	823.8	289.0	-1.2	610.4	560.3	-144.8	402.9	493.8	-227.5
33	896.2	210.2	-176.9	838.6	334.9	-50.3	607.7	586.3	-159.9	389.6	564.7	-284.8
34	888.5	227.8	-198.6	834.8	376.0	-89.6	605.1	607.5	-176.1	363.4	641.0	-337.6
35	881.8	247.1	-218.2	815.5	414.0	-135.2	601.3	626.7	-192.8	330.8	717.6	-381.6
36	875.3	268.1	-239.4	792.5	456.0	-188.5	593.7	648.2	-211.0	299.7	794.8	-403.5
37	869.5	290.2	-265.4	773.0	506.9	-242.5	579.4	676.7	-232.1	271.5	867.6	-401.7
38	865.7	312.2	-298.9	757.3	565.0	-291.0	557.3	715.5	-256.9	243.8	930.1	-391.3
39	865.6	332.4	-342.4	743.5	622.7	-334.5	528.8	765.4	-284.3	213.4	984.1	-383.0
40	868.7	347.6	-401.2	733.4	671.2	-381.1	498.6	824.3	-312.8	177.2	1035.6	-377.8
41	867.2	351.7	-492.1	734.9	707.1	-439.6	474.7	889.6	-341.5	136.0	1090.2	-372.7
42	882.5	351.0	-630.8	758.6	734.0	-508.8	466.5	957.0	-370.7	95.4	1151.0	-363.3
43	991.3	373.0	-743.8	812.8	759.2	-574.2	482.5	1021.6	-406.2	67.1	1218.9	-346.8
44	1180.2	405.4	-767.0	900.0	787.5	-619.3	528.2	1081.5	-445.2	65.5	1297.1	-326.1
45	1392.4	422.3	-674.5	1017.6	822.2	-628.6	602.2	1133.6	-468.3	103.0	1380.9	-298.3
46	1560.4	407.5	-484.7	1156.7	863.3	-577.6	698.2	1180.9	-461.4	180.4	1441.0	-252.4
47	1652.7	367.8	-271.3	1291.7	900.1	-441.7	806.4	1229.0	-406.7	282.8	1468.1	-197.5
48	1688.3	324.4	-99.0	1383.5	912.8	-227.6	906.0	1269.5	-274.4	386.0	1474.0	-139.2

2.1.3 Optimization of the twisting angle of each modular coil

The MHD equilibrium created by the modular coil is almost determined by the center trajectory and the total current, which are calculated with the NESCOIL system. The cross-sectional area is defined in consideration of the limit of current density.

It is also necessary to determine the direction of the coil cross section for winding. The NESCOIL system optimizes the center trajectory assuming the longer axis (the normal vector) is perpendicular to the current carrying surface (CCS) as shown in Fig 2.1-10, but it was found that the twisting angle (θ) has little effect on the equilibrium. Therefore, the twisting angle was adjusted from the viewpoint of manufacturability, the gap with other parts and curvature of the three-dimensional (3-D) surface.

The optimized result of the twisting angle is shown in Table 2.1-5 to Table 2.1-8 and Fig 2.1-11. For comparison, the orthogonal direction views after and before optimization are shown in Fig 2.1-12 and Fig 2.1-13. For comparison, the coil shapes before and after optimization are shown in Fig 2.1-14. It can be clearly seen that the twisting angle of the MC4 is changed significantly. The twisting angle was determined according to the following procedure.

- ❑ The angle was changed continuously so that the curvature and the torsion in the Frenet-Serret formular did not increase abruptly.
- ❑ The initial angle was selected so that they would not interfere when the coil is inserted into the case.
- ❑ The gap between the coils and the gap with the vacuum vessel were evaluated on 3-D CAD, and the solution with an appropriate size was manually selected.

Fig 2.1-12 shows that the coil dose not contact the case when the coil is inserted, and Fig 2.1-13 shows that it is difficult to pull out the coil from the coil case.

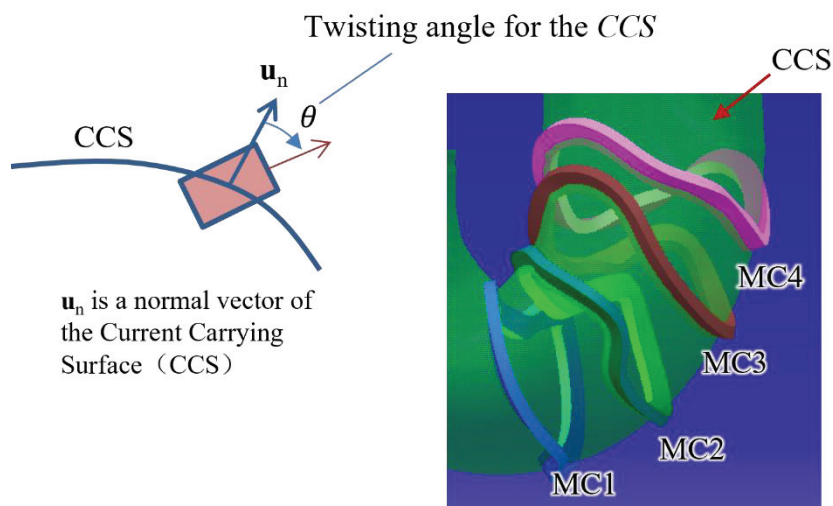


Fig 2.1-10 Normal direction of the rectangular cross section. The NESCOIL system gives us the optimized result with the long axis of the cross section orthogonal to the CCS ($\theta=0$).

Table 2.1-5 Coordinate of 4 corners of the MC1 (SWJTU-Type X)

No	M1-N1			M1-N2			M1-N3			M1-N4			Angle twisted
	X	Y	Z	X	Y	Z	X	Y	Z	X	Y	Z	
1	1630.3	328.7	24.6	1762.2	325.4	28.0	1628.8	260.6	13.5	1760.8	257.3	16.9	15.00
2	1626.9	317.1	91.1	1756.8	310.8	113.4	1623.0	248.3	94.1	1753.0	242.0	116.3	15.97
3	1620.4	320.5	136.7	1746.0	311.4	176.2	1610.5	254.1	152.8	1736.1	245.1	192.4	18.20
4	1608.9	334.7	179.0	1730.9	324.1	228.3	1595.7	269.5	197.6	1717.7	259.0	246.9	20.07
5	1589.7	352.3	228.6	1711.9	341.7	277.6	1580.1	284.6	238.2	1702.2	274.1	287.1	20.16
6	1565.8	362.2	288.4	1689.8	352.4	332.6	1562.5	293.6	282.4	1686.5	283.8	326.6	20.20
7	1539.7	356.6	357.0	1664.5	347.2	398.8	1541.1	290.4	337.8	1665.9	281.0	379.7	20.95
8	1508.9	332.9	435.2	1632.7	323.0	480.2	1513.6	269.4	408.5	1637.3	259.5	453.5	21.64
9	1468.3	291.2	523.7	1588.2	279.9	577.7	1476.0	229.6	493.5	1595.9	218.3	547.6	21.62
10	1412.4	235.6	616.6	1524.2	222.1	685.5	1424.0	174.9	585.9	1535.8	161.4	654.7	20.50
11	1339.4	173.9	700.8	1435.5	157.4	789.8	1355.2	113.0	672.4	1451.3	96.5	761.4	17.66
12	1251.5	115.0	762.1	1320.0	95.5	873.3	1270.4	52.6	739.6	1338.8	33.0	850.7	12.19
13	1153.6	66.2	792.1	1181.2	44.9	919.4	1171.6	1.2	777.3	1199.2	-20.1	904.6	3.71
14	1049.8	30.9	788.1	1029.7	10.3	917.0	1063.7	-36.2	779.6	1043.6	-56.7	908.4	-6.12
15	949.3	9.0	748.4	880.1	-7.6	859.6	958.9	-59.2	744.2	889.7	-75.8	855.3	-16.13
16	871.7	-3.3	674.2	757.4	-11.6	739.7	876.4	-72.1	673.6	762.1	-80.4	739.1	-27.88
17	835.6	-10.8	572.8	703.7	-8.3	574.2	834.3	-79.8	572.3	702.4	-77.3	573.7	-38.09
18	847.6	-13.3	458.6	721.2	-4.6	421.5	844.1	-82.0	454.4	717.7	-73.4	417.3	-40.76
19	882.3	-9.5	359.3	759.0	0.6	313.3	880.3	-77.8	349.8	756.9	-67.7	303.8	-36.13
20	912.8	-0.6	286.6	789.2	9.4	241.3	913.6	-67.5	269.8	790.0	-57.5	224.5	-29.25
21	934.2	11.5	237.2	809.3	20.9	195.7	938.3	-52.1	210.7	813.3	-42.7	169.1	-25.47
22	948.8	25.8	202.7	822.3	34.4	166.0	955.0	-33.3	167.5	828.5	-24.7	130.9	-24.91
23	959.5	43.0	174.7	832.4	51.3	140.2	966.2	-14.1	136.5	839.0	-5.8	102.0	-25.31
24	969.2	62.7	147.0	842.2	71.1	112.1	975.6	4.9	109.9	848.6	13.2	75.0	-25.44
25	980.2	83.9	115.4	852.8	92.0	81.7	985.9	25.1	79.7	858.5	33.3	45.9	-25.42
26	992.3	105.8	79.0	863.5	113.0	51.1	996.8	47.2	42.8	868.0	54.5	14.9	-25.08
27	1003.2	128.4	39.0	872.2	133.6	23.7	1005.3	70.6	1.3	874.3	75.8	-14.0	-23.69
28	1009.6	151.8	-4.6	877.7	153.6	1.0	1007.2	93.5	-41.4	875.3	95.3	-35.8	-19.93
29	1006.9	175.1	-50.5	878.2	173.0	-21.2	1000.7	114.2	-82.3	872.0	112.1	-53.0	-14.44
30	996.1	195.3	-92.5	871.6	190.8	-49.0	988.7	132.5	-120.2	864.2	128.0	-76.6	-11.04
31	983.4	211.9	-128.2	860.3	206.8	-80.8	975.2	149.4	-156.3	852.1	144.3	-108.9	-9.97
32	972.5	226.3	-157.2	849.2	221.2	-110.3	962.4	166.5	-190.2	839.2	161.5	-143.3	-10.17
33	964.4	240.1	-179.9	840.8	235.1	-133.9	951.7	185.3	-219.9	828.1	180.3	-173.8	-11.34
34	957.7	255.4	-198.7	833.7	250.7	-153.7	943.3	204.9	-243.5	819.4	200.2	-198.4	-13.14
35	951.1	274.2	-216.1	825.8	270.1	-174.7	937.7	224.1	-261.7	812.4	220.0	-220.2	-14.69
36	944.2	296.1	-234.8	816.6	293.3	-201.1	934.0	242.9	-277.6	806.4	240.1	-244.0	-15.52
37	937.5	319.5	-257.7	807.4	318.6	-235.8	931.6	261.7	-295.0	801.5	260.9	-273.1	-15.64
38	932.8	342.7	-288.1	801.0	344.2	-280.7	930.4	280.1	-317.1	798.6	281.7	-309.7	-15.03
39	932.0	363.9	-331.0	800.2	367.5	-336.4	930.9	297.2	-348.4	799.1	300.8	-353.8	-13.72
40	935.5	380.3	-397.2	803.7	383.9	-402.1	933.8	311.4	-400.2	801.9	314.9	-405.2	-12.42
41	933.7	385.2	-494.6	801.8	387.2	-489.8	932.6	316.2	-494.4	800.7	318.2	-489.6	-10.44
42	943.3	379.4	-598.6	822.0	390.2	-649.5	942.9	311.8	-612.2	821.6	322.6	-663.0	-5.15
43	1014.3	396.1	-676.8	958.8	416.5	-794.8	1023.7	329.6	-692.7	968.2	350.0	-810.7	1.69
44	1165.7	428.9	-697.8	1185.3	449.5	-826.7	1175.1	361.2	-707.2	1194.8	381.8	-836.1	6.98
45	1351.1	448.9	-618.5	1430.8	464.2	-722.6	1354.0	380.4	-626.3	1433.7	395.7	-730.5	10.73
46	1504.5	437.2	-445.5	1618.1	445.7	-512.1	1502.6	369.3	-457.3	1616.3	377.8	-523.9	12.75
47	1590.7	399.7	-245.0	1717.6	403.0	-281.3	1587.8	332.7	-261.3	1714.6	336.0	-297.6	13.83
48	1623.8	357.9	-82.7	1754.9	357.6	-97.9	1621.7	291.1	-100.1	1752.8	290.9	-115.2	14.56

Table 2.1-6 Coordinate of 4 corners of the MC2 (SWJTU-Type X)

No	M2-N1			M2-N2			M2-N3			M2-N4			Angle twisted
	X	Y	Z	X	Y	Z	X	Y	Z	X	Y	Z	
1	1336.8	895.0	10.5	1456.6	949.6	20.2	1365.8	833.4	-0.8	1485.6	888.0	9.0	15.00
2	1321.2	853.7	196.3	1438.8	902.9	230.2	1350.8	793.2	181.3	1468.4	842.4	215.3	16.18
3	1292.1	806.7	326.8	1405.5	850.7	378.2	1322.8	747.2	310.1	1436.2	791.2	361.4	16.96
4	1258.6	761.1	424.7	1366.4	799.8	490.3	1289.1	700.9	410.3	1396.9	739.6	475.9	17.68
5	1218.9	720.6	506.6	1319.3	753.5	585.8	1246.5	658.0	497.6	1346.9	690.9	576.7	18.72
6	1177.5	693.2	568.4	1266.7	718.1	662.5	1196.7	627.0	567.8	1285.9	651.8	661.8	20.52
7	1141.3	684.1	608.5	1213.3	698.0	718.2	1144.6	615.5	615.1	1216.6	629.4	724.8	24.28
8	1102.1	689.6	637.3	1156.9	693.5	757.3	1094.0	621.3	643.3	1148.8	625.3	763.3	28.80
9	1046.4	699.9	662.4	1096.5	701.3	784.5	1042.1	631.1	664.9	1092.3	632.5	787.0	29.65
10	976.1	702.3	689.5	1032.2	707.0	808.9	987.9	634.4	686.7	1044.0	639.1	806.0	28.14
11	903.3	685.1	723.1	967.0	694.1	838.3	933.5	624.2	711.1	997.2	633.2	826.4	28.01
12	838.6	644.6	759.7	905.5	655.4	873.1	881.0	594.0	739.6	947.9	604.9	852.9	29.49
13	784.6	584.4	792.7	847.3	592.8	908.6	834.1	542.7	768.9	896.8	551.1	884.8	30.48
14	740.1	512.9	814.3	789.8	514.0	936.6	795.1	477.5	792.3	844.8	478.6	914.6	29.16
15	705.9	442.4	819.1	732.6	431.5	947.9	765.2	410.4	804.1	791.9	399.5	932.9	24.64
16	684.2	384.2	808.1	679.1	358.3	937.5	744.6	351.1	803.9	739.5	325.2	933.2	16.90
17	673.3	343.0	790.1	635.3	303.3	910.1	729.5	303.2	794.7	691.5	263.5	914.7	7.81
18	665.5	315.6	771.6	603.3	267.0	877.4	714.1	266.9	777.8	651.9	218.4	883.6	0.41
19	655.1	296.2	751.7	577.7	242.9	844.5	697.5	242.0	756.0	620.2	188.7	848.7	-4.77
20	642.2	280.8	728.1	553.6	224.5	808.1	682.5	225.1	733.6	593.9	168.8	813.6	-8.91
21	630.8	266.1	700.2	531.6	207.6	764.9	671.0	211.3	712.3	571.8	152.9	777.0	-12.87
22	625.2	249.8	669.6	516.7	190.4	715.5	663.4	196.3	690.6	554.8	136.8	736.4	-16.80
23	626.6	231.6	637.5	511.5	172.6	663.9	660.3	177.6	664.1	545.2	118.7	690.5	-19.91
24	632.8	212.7	602.8	514.5	155.1	613.4	662.6	156.1	628.7	544.3	98.5	639.3	-21.28
25	642.0	195.3	563.8	522.4	139.4	561.9	669.8	135.1	582.9	550.3	79.2	581.0	-21.42
26	653.5	182.2	517.5	533.8	128.6	502.3	680.4	119.4	527.0	560.7	65.8	511.7	-21.94
27	668.7	176.7	459.5	550.8	127.2	426.6	695.1	113.0	460.8	577.2	63.5	428.0	-23.78
28	693.0	183.0	386.4	580.1	139.4	333.7	719.6	119.4	381.9	606.6	75.9	329.2	-27.07
29	732.6	204.6	299.2	625.2	166.2	232.8	760.8	142.3	289.6	653.4	103.9	223.2	-31.74
30	783.1	241.9	204.6	676.7	204.2	136.2	814.0	182.1	189.5	707.6	144.4	121.1	-35.68
31	829.0	287.7	115.3	720.9	248.6	50.4	862.7	231.8	92.8	754.6	192.8	27.8	-36.09
32	860.7	333.4	45.9	750.6	292.5	-14.5	897.0	285.5	12.0	786.9	244.6	-48.3	-34.44
33	879.6	378.0	-5.4	764.2	331.9	-50.0	913.0	338.0	-50.5	797.7	291.8	-95.1	-32.58
34	883.4	426.3	-63.9	763.7	370.8	-68.1	906.0	381.2	-111.1	786.3	325.7	-115.2	-21.89
35	865.2	467.1	-119.2	747.4	409.1	-105.3	883.5	418.9	-165.1	765.7	361.0	-151.2	-15.43
36	842.2	506.7	-165.9	723.1	449.9	-162.1	861.9	462.2	-214.8	742.8	405.4	-211.1	-15.59
37	821.6	553.0	-209.8	701.8	498.9	-222.3	844.3	514.9	-262.7	724.5	460.8	-275.2	-16.94
38	803.9	608.0	-251.9	684.8	556.4	-276.3	829.8	573.6	-305.8	710.7	522.0	-330.2	-17.77
39	788.8	668.5	-297.1	670.0	617.4	-323.7	817.0	628.0	-345.4	698.2	576.9	-371.9	-16.11
40	777.6	723.2	-351.1	659.0	672.5	-379.3	807.9	670.0	-382.9	689.3	619.3	-411.2	-12.24
41	777.8	760.6	-410.8	662.3	714.4	-454.9	807.4	699.8	-424.4	691.9	653.5	-468.5	-7.09
42	797.9	783.8	-469.8	694.4	748.5	-543.7	822.8	719.6	-473.9	719.2	684.3	-547.7	0.49
43	840.9	800.2	-518.8	765.3	784.2	-625.8	860.3	734.2	-522.6	784.7	718.1	-629.6	7.40
44	908.0	817.0	-551.5	873.1	823.7	-678.6	926.8	751.2	-560.1	891.9	757.9	-687.2	10.95
45	1000.0	839.6	-558.4	1011.9	868.6	-686.6	1023.3	775.8	-570.6	1035.2	804.8	-698.9	12.40
46	1112.6	870.3	-518.0	1172.3	918.0	-625.7	1141.1	808.6	-529.6	1200.7	856.3	-637.2	12.85
47	1228.4	901.8	-402.5	1324.8	959.7	-471.5	1258.6	840.4	-411.8	1355.0	898.4	-480.8	13.20
48	1311.0	914.1	-210.4	1426.4	973.1	-235.9	1340.6	852.4	-219.3	1455.9	911.4	-244.9	13.88

Table 2.1-7 Coordinate of 4 corners of the MC3 (SWJTU-Type H)

No	M3-N1			M3-N2			M3-N3			M3-N4			Angle twisted
	X	Y	Z	X	Y	Z	X	Y	Z	X	Y	Z	
1	909.1	1223.8	-58.1	951.2	1348.8	-52.5	974.4	1201.8	-60.3	1016.6	1326.8	-54.6	-10.00
2	906.2	1179.7	167.4	940.0	1301.2	206.2	971.3	1158.7	176.6	1005.1	1280.3	215.3	-12.68
3	862.8	1113.4	343.1	886.6	1227.3	405.4	924.6	1089.8	362.5	948.5	1203.7	424.8	-13.89
4	808.0	1050.8	449.7	818.6	1155.3	529.6	864.8	1023.5	477.9	875.3	1128.0	557.8	-15.94
5	740.6	985.2	527.4	738.3	1082.4	616.6	791.9	954.6	562.0	789.6	1051.9	651.3	-17.26
6	660.3	915.2	589.3	646.9	1007.3	682.9	703.4	880.0	630.0	690.1	972.1	723.6	-17.60
7	576.7	853.0	628.2	553.0	941.2	723.4	608.6	812.3	673.8	584.9	900.5	769.1	-18.70
8	493.8	803.2	645.0	458.5	888.1	739.7	516.9	759.3	693.0	481.6	844.2	787.7	-21.30
9	411.3	758.3	646.6	359.4	837.7	738.4	432.9	715.3	696.0	381.0	794.6	787.8	-25.20
10	333.8	707.0	638.7	259.8	774.8	724.5	358.2	668.3	690.4	284.3	736.1	776.2	-29.86
11	270.4	644.0	624.4	173.2	691.1	700.4	297.1	611.2	678.9	199.9	658.2	754.9	-34.05
12	227.8	571.3	604.3	113.3	591.1	667.0	254.3	543.4	661.5	139.9	563.2	724.3	-36.07
13	207.7	496.4	579.8	85.0	488.4	627.7	232.5	471.8	639.3	109.8	463.8	687.2	-36.02
14	207.3	432.2	556.0	84.2	396.9	587.7	229.9	407.6	616.3	106.8	372.3	648.1	-36.41
15	219.9	387.9	535.8	106.1	321.8	546.3	241.0	361.2	595.8	127.2	295.1	606.4	-38.04
16	243.0	355.2	515.5	144.1	268.2	506.9	263.7	325.8	574.4	164.9	238.8	565.7	-35.25
17	272.9	332.4	496.3	190.2	232.6	471.3	300.5	296.5	548.3	217.9	196.7	523.3	-32.41
18	316.3	318.2	465.7	251.7	211.4	422.6	350.2	279.2	511.4	285.7	172.4	468.3	-32.22
19	379.2	309.1	414.1	315.9	203.6	366.2	419.1	267.9	452.4	355.8	162.4	404.5	-29.50
20	441.1	305.3	349.3	375.4	201.8	300.4	487.3	262.6	377.6	421.6	159.1	328.7	-24.74
21	492.9	310.6	277.9	427.9	209.5	223.4	544.1	267.9	295.9	479.1	166.8	241.4	-21.64
22	535.7	327.4	205.0	471.7	230.3	142.6	590.2	286.0	213.6	526.2	188.9	151.2	-21.51
23	569.3	353.9	136.7	505.4	261.6	67.3	625.9	314.5	137.0	562.0	222.1	67.6	-23.23
24	593.7	384.6	79.0	528.8	297.6	3.9	651.5	347.6	72.0	586.5	260.5	-3.1	-25.96
25	609.8	413.9	35.6	543.4	332.7	-44.5	668.2	379.9	21.7	601.7	298.7	-58.4	-29.50
26	619.7	438.5	6.2	551.3	363.3	-78.0	678.4	409.3	-15.3	610.0	334.1	-99.6	-33.75
27	625.3	459.3	-13.6	554.5	389.2	-100.1	683.5	436.7	-42.9	612.7	366.6	-129.5	-38.76
28	627.9	478.7	-28.3	554.0	414.9	-117.0	684.8	462.2	-63.8	610.8	398.4	-152.5	-44.56
29	628.7	499.2	-40.5	550.9	445.4	-132.5	684.0	486.3	-79.7	606.2	432.5	-171.8	-50.54
30	628.8	524.9	-52.2	547.3	479.8	-145.7	682.7	513.2	-93.6	601.2	468.1	-187.1	-55.01
31	628.7	559.5	-65.6	544.2	512.8	-155.6	681.5	545.8	-107.9	597.0	499.1	-197.9	-55.79
32	628.0	598.1	-83.1	541.2	541.4	-164.7	679.6	579.3	-124.8	592.8	522.5	-206.5	-51.19
33	626.8	631.7	-104.0	538.0	565.4	-175.8	677.4	607.3	-144.1	588.6	541.0	-215.8	-43.10
34	625.8	657.2	-124.7	535.3	583.8	-186.7	674.9	631.2	-165.6	584.4	557.8	-227.6	-36.34
35	623.7	677.7	-143.4	532.7	598.0	-196.2	670.0	655.3	-189.5	579.0	575.6	-242.3	-32.64
36	618.2	698.5	-161.9	527.0	615.1	-208.3	660.4	681.2	-213.7	569.1	597.8	-260.1	-32.18
37	606.8	725.4	-182.9	513.9	641.9	-225.6	644.9	711.4	-238.7	552.0	628.0	-281.4	-35.09
38	588.0	761.9	-207.4	491.8	681.2	-248.1	622.8	749.8	-265.7	526.7	669.1	-306.4	-40.71
39	563.1	808.7	-234.3	461.9	734.1	-274.7	595.7	796.6	-293.9	494.6	722.0	-334.2	-47.22
40	536.8	862.3	-261.4	428.4	800.7	-304.7	568.8	847.9	-320.9	460.4	786.2	-364.2	-50.91
41	516.3	919.2	-287.3	400.8	880.9	-338.5	548.6	898.3	-344.6	433.1	860.0	-395.8	-48.47
42	507.9	978.9	-312.8	393.6	970.4	-378.3	539.3	943.6	-363.1	425.0	935.0	-428.5	-40.86
43	519.5	1035.7	-343.2	419.3	1055.3	-426.8	545.6	988.0	-385.6	445.4	1007.6	-469.3	-34.02
44	551.7	1082.1	-374.5	481.8	1131.5	-475.1	574.6	1031.4	-415.4	504.8	1080.9	-515.9	-28.24
45	605.1	1119.6	-395.2	572.9	1195.0	-498.6	631.6	1072.3	-437.9	599.3	1147.6	-541.3	-20.89
46	678.5	1152.5	-395.4	679.4	1248.7	-485.8	717.0	1113.1	-437.0	717.9	1209.3	-527.3	-13.92
47	765.1	1186.3	-361.8	793.8	1301.2	-420.1	818.9	1156.8	-393.3	847.7	1271.7	-451.6	-9.86
48	854.1	1218.2	-259.4	894.5	1343.1	-273.6	917.4	1195.9	-275.3	957.9	1320.8	-289.5	-10.00

Table 2.1-8 Coordinate of 4 corners of the MC4(SWJTU-Type G)

No	M4-N1			M4-N2			M4-N3			M4-N4			Angle twisted
	X	Y	Z	X	Y	Z	X	Y	Z	X	Y	Z	
1	423.9	1406.5	-56.4	439.8	1537.5	-55.4	487.9	1398.9	-80.9	503.9	1529.9	-79.8	-5.00
2	454.1	1396.3	10.0	472.9	1525.7	28.1	521.7	1385.3	18.3	540.5	1514.7	36.5	-4.80
3	442.6	1378.6	97.5	456.4	1503.8	137.0	504.3	1363.3	124.3	518.1	1488.5	163.8	-5.20
4	395.3	1341.7	188.2	391.3	1454.4	256.8	452.7	1323.2	221.9	448.6	1435.9	290.5	-4.80
5	322.1	1271.1	276.1	308.8	1377.3	353.3	381.8	1255.9	307.2	368.6	1362.2	384.4	0.17
6	253.6	1201.3	376.2	245.7	1315.0	442.9	317.0	1191.0	401.3	309.1	1304.7	468.0	5.88
7	215.8	1143.0	450.3	190.8	1231.8	544.6	279.7	1134.6	475.1	254.6	1223.5	569.4	-2.48
8	189.0	1068.3	496.8	152.4	1130.8	607.1	252.2	1059.2	522.9	215.6	1121.7	633.2	-8.61
9	165.7	987.7	528.0	123.6	1037.6	642.7	226.2	971.8	557.2	184.0	1021.6	671.9	-9.26
10	137.5	908.9	546.8	90.0	948.7	663.3	192.3	881.5	578.5	144.8	921.3	695.0	-9.29
11	98.1	832.0	551.2	42.5	859.5	667.7	146.4	794.4	583.1	90.8	821.9	699.6	-10.05
12	49.1	755.9	538.0	-18.8	767.6	650.6	93.4	713.2	569.2	25.5	724.9	681.8	-12.10
13	-1.1	678.7	505.7	-83.7	671.1	608.4	42.2	635.3	537.3	-40.3	627.7	640.1	-15.19
14	-40.9	601.0	455.9	-136.2	571.9	542.5	2.6	559.5	489.8	-92.7	530.4	576.4	-18.21
15	-61.8	527.1	394.4	-164.3	476.5	460.3	-18.6	489.0	432.4	-121.1	438.4	498.3	-19.82
16	-61.3	460.0	328.4	-164.6	391.2	373.4	-19.3	423.7	369.3	-122.5	354.9	414.3	-19.80
17	-44.3	404.0	263.0	-143.6	320.6	287.7	-2.4	365.7	302.2	-101.6	282.3	326.9	-20.44
18	-20.6	367.6	203.9	-109.9	270.5	201.0	20.1	329.0	244.1	-69.3	231.9	241.2	-23.03
19	7.3	347.5	158.4	-67.9	242.5	130.8	41.0	310.7	206.2	-34.2	205.8	178.5	-22.45
20	32.8	337.9	134.5	-24.9	228.6	88.3	64.5	300.6	183.1	6.8	191.3	136.9	-24.36
21	60.1	334.6	115.5	12.3	224.8	60.0	95.2	296.4	161.0	47.4	186.6	105.5	-26.09
22	92.0	333.8	91.7	44.7	225.0	33.8	129.5	294.7	134.5	82.2	185.9	76.6	-26.23
23	117.1	335.4	72.7	83.9	229.2	1.8	155.1	295.7	114.5	121.8	189.4	43.6	-30.58
24	140.6	341.6	58.7	132.2	243.7	-29.4	175.0	300.0	101.7	166.5	202.1	13.5	-35.07
25	172.6	353.6	46.2	178.9	262.9	-49.5	203.0	309.6	89.9	209.2	218.9	-5.8	-35.66
26	212.8	369.2	35.5	218.9	279.9	-61.6	243.7	324.8	78.3	249.9	235.5	-18.8	-34.59
27	257.7	386.5	22.6	253.2	294.6	-72.0	295.5	344.3	61.9	291.0	252.3	-32.7	-32.89
28	302.6	405.7	1.9	284.5	308.9	-85.9	351.5	368.3	33.1	333.3	271.4	-54.8	-30.69
29	341.5	428.1	-29.4	314.1	326.2	-108.7	401.3	398.4	-11.8	373.8	296.4	-91.1	-28.64
30	369.3	456.0	-71.3	339.5	351.7	-146.5	435.2	435.6	-69.1	405.4	331.3	-144.3	-28.17
31	383.5	492.1	-120.5	354.3	392.1	-201.5	450.8	480.8	-130.7	421.6	380.8	-211.7	-31.47
32	385.0	539.6	-171.6	354.6	450.9	-264.5	451.3	536.7	-190.5	420.8	448.0	-283.5	-41.69
33	374.1	603.3	-223.0	341.0	521.6	-321.3	438.1	607.7	-248.3	405.0	526.1	-346.6	-57.37
34	350.7	675.0	-272.5	314.5	597.7	-373.2	412.4	684.4	-301.9	376.2	607.0	-402.6	-70.53
35	324.8	738.4	-310.4	277.9	682.3	-420.3	383.8	753.0	-343.0	336.9	696.9	-452.9	-79.38
36	302.1	797.2	-329.1	241.8	770.1	-443.4	357.5	819.5	-363.6	297.3	792.4	-477.9	-83.52
37	278.3	861.5	-327.8	212.4	844.8	-441.0	330.5	890.3	-362.5	264.7	873.7	-475.6	-81.76
38	251.0	926.0	-317.3	187.4	901.0	-430.2	300.3	959.2	-352.3	236.7	934.3	-465.3	-76.55
39	219.4	984.1	-308.7	160.8	947.9	-421.3	265.9	1020.4	-344.6	207.3	984.1	-457.2	-71.59
40	183.8	1036.7	-303.6	125.7	997.1	-415.3	228.8	1074.1	-340.3	170.7	1034.4	-452.0	-68.18
41	146.2	1088.2	-299.0	80.5	1056.2	-408.9	191.5	1124.2	-336.6	125.8	1092.2	-446.5	-64.70
42	111.6	1141.5	-291.3	31.4	1130.8	-395.6	159.5	1171.2	-331.1	79.3	1160.5	-435.4	-58.18
43	87.4	1200.6	-277.5	-3.4	1224.1	-370.4	137.5	1213.7	-323.2	46.7	1237.2	-416.1	-47.97
44	85.7	1270.3	-259.6	-0.8	1327.5	-341.4	131.7	1266.7	-310.8	45.3	1323.9	-392.6	-38.48
45	114.1	1337.1	-239.1	51.5	1434.6	-302.3	154.4	1327.2	-294.3	91.9	1424.8	-357.4	-29.98
46	175.3	1385.1	-203.4	150.9	1508.7	-242.8	209.8	1373.3	-261.9	185.4	1496.8	-301.4	-19.19
47	266.5	1408.9	-155.3	265.1	1538.5	-180.6	300.5	1397.8	-214.4	299.0	1527.3	-239.6	-11.24
48	356.1	1414.0	-106.7	370.2	1544.5	-121.1	401.7	1403.5	-157.4	415.8	1534.0	-171.8	-5.00

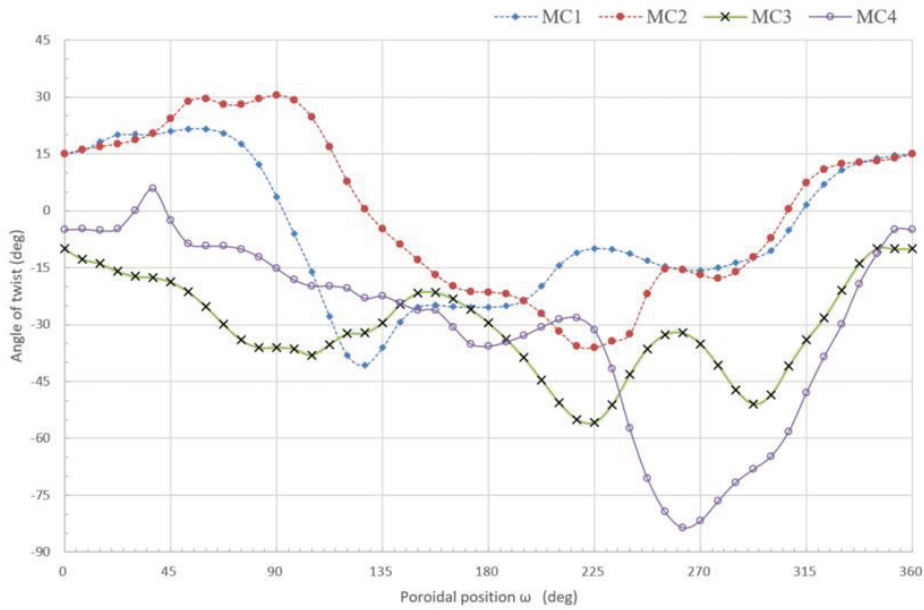
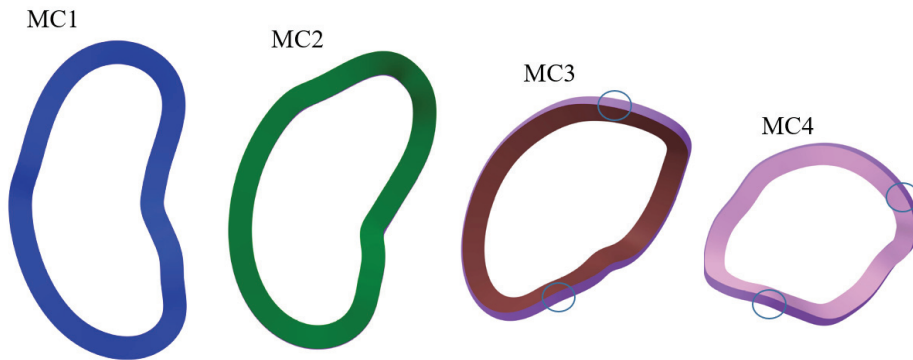


Fig 2.1-11 Optimized twisting angle of each modular coil. The angle of twist of 0 degree indicates that the long axis of the cross section is orthogonal to the CCS.



The inner and outer walls are not visible because they are parallel to view direction.

Only the outer walls (purple parts) are visible because they are open faces.

It shows that the coil does not contact the case when the coil is inserted.

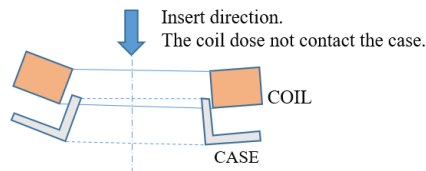
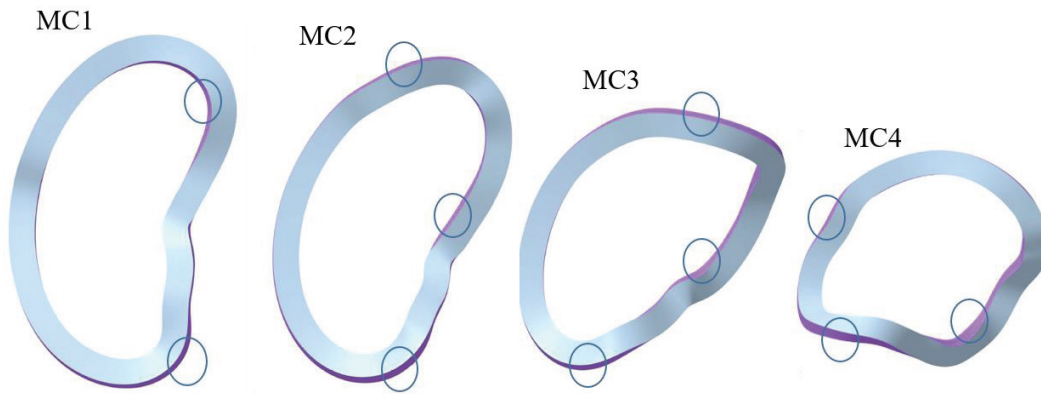


Fig 2.1-12 Orthogonal direction view of the optimized coils. All inner surface of the coil is behind the coil itself (invisible or parallel to the view)



The inner and outer walls (purple parts) are visible. It shows that the coil contacts the case when the coil is inserted.

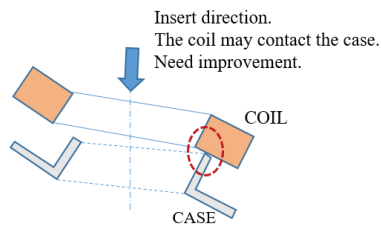
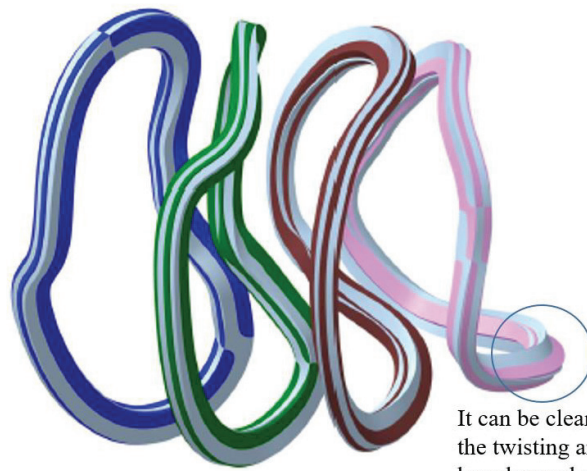


Fig 2.1-13 Orthogonal direction view of the unoptimized coils. Part of the inner surface of the coil is visible in the view.



It can be clearly seen that the twisting angle of MC4 has changed about 90 degrees from before optimization.

Fig 2.1-14 Comparison of coil shapes. The gray coils show the shape before optimization with the twisting angle of 0 degree, and others show shape after optimization.

The 3-D surface curvature on the ground insulation are shown in Table 2.1 5 and Table 2.1 6. The definition of the surface curvature is as follows by the differential geometry.

$$\text{Gaussian curvature } \sqrt{k} = \sqrt{k_1 k_2},$$

$$\text{Mean curvature } H = (k_1 + k_2)/2,$$

$$\text{Maximum curvature } \text{Max } (k_1, k_2),$$

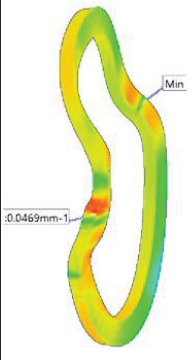
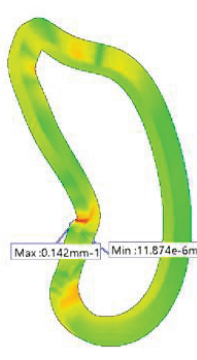
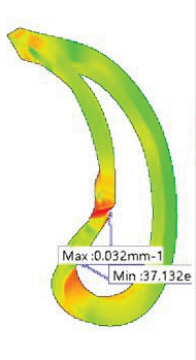
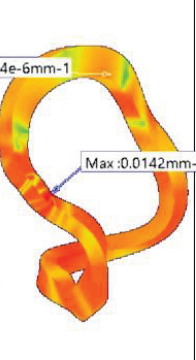
where, k_1 and k_2 are principal curvatures. $\text{Max } (k_1, k_2) \gg \text{Min } (k_1, k_2)$ indicates near cylindrical bending (single dimensional bending), and $\text{Max } (k_1, k_2) = \text{Min } (k_1, k_2)$ indicates bowl or saddle bending (two dimensional bending). It is better that the minimum curvature radius of $1/\text{Max } (k_1, k_2)$ is as large as possible, and it is desirable that it is 5 times or more the conductor diameter to prevent the conductor cross section from being deformed during winding.

Table 2.1-9 shows the coil without the optimization has small radius curvature, which indicates that winding is difficult, and Table 2.1-10 shows the coil after the optimization has larger curvature radius. In this way, the ease or difficulty of winding changes, so the twisting angle was optimized in consideration of these factors.

By changing the twist angle, the distance between the coil surface and the coil surface and the distance between the coil surface and the vacuum vessel change. Originally, the NESCOIL system determined the trajectory of the centerline on the condition that the coil cross section was orthogonal to a continuous plane called CCS, so it was unlikely that the coil would interfere with other coils or vacuum vessels. However, since the twist angle was corrected from the viewpoint of manufacturability, there was a concern that the coil would interfere with others. Therefore, the gap between the coil surface and others was also taken into consideration when considering optimization, and the design that made the gap extremely small was excluded. Table 2.1-11 and Table 2.1-12 show a comparison of the gaps. It was found that the change in the gap was not so large, and the gap became smaller after the twisting angle optimization in some places.

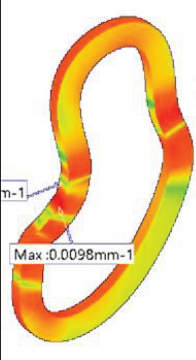
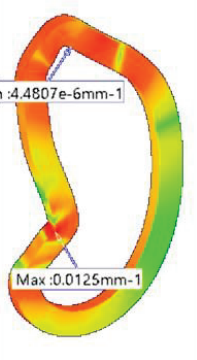
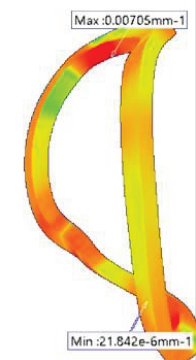
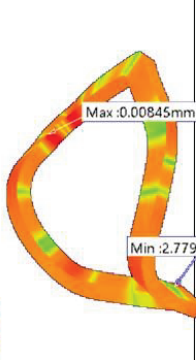
It seems that the optimized result may not be a logical optimum solution, but it is considered that the selection is an appropriate choice that is practically problem-free as can be seen by comparing with before optimization.

Table 2.1-9 3D surface curvature on the ground insulation before optimizing the twist angle.

Name of coil		MC1 (TypeB)	MC2 (TypeB)	MC3 (TypeB)	MC4 (TypeB)	Design Criterion
Feature		Normal vector orthogonal to the CCS				
Maximum curvature on the 3D surface of ground insulation (1/m)	√Gaussian	37.2 NG	15.8	9.6	5.1	Should be less than 23.5 1/m. (r>42.5mm)
	Mean	38.2 NG	72 NG	16.8	7.5	
	Max(k ₁ ,k ₂)	46.9 NG	142 NG	32 NG	14.2	
Profile of curvature Max (k ₁ ,k ₂)						

The curvature partially exceeds the design standard. Since the radius of curvature = 7 mm (curvature = 142 1 / m) is smaller than the conductor diameter of 8.5 mm, winding is considered very difficult.

Table 2.1-10 3D surface curvature on the ground insulation after optimizing the twist angle.

Name of coil		MC1 (TypeX)	MC2 (TypeX)	MC3 (TypeH)	MC4 (TypeG)	Design Criterion
Feature		Twisted to an angle where the inner wall can be seen				
Maximum curvature on the 3D surface of ground insulation (1/m)	√Gaussian	4.8	9.5	2.6	1.4	Should be less than 23.5 1/m. (r>42.5mm)
	Mean	5.2	9.7	3.6	4.3	
	Max(k ₁ ,k ₂)	9.8	12.5	7.1	8.5	
Profile of curvature Max (k ₁ ,k ₂)						

All curvatures are below the design criteria. Since the radius of curvature is more than 9 times the conductor diameter, there is no problem with winding.

Table 2.1-11 Minimum gap on the ground insulation before optimizing the twist angle.

Name of coil		MC1 (TypeB)	MC2 (TypeB)	MC3 (TypeB)	MC4 (TypeB)	Design guide
Feature		Normal vector orthogonal to the CCS				
Minimum gap between coils without case (mm)	MC1-MC1	64.1				Should be larger than 50mm.
	MC1-MC2	55.7				
	MC2-MC3		60			
	MC3-MC4			73.1		
	MC4-MC4				150.9	
Minimum gap between the coil without case and the vacuum vessel (mm)	With inner surface of the shell	27.7	57.5	57.8	82.1	Should be larger than 25mm.
	With a port	50(CF420)			22.6 (Rectangle OP)	

The gap is expected to be maximized because the twist angle orthogonal to the reference plane (CCS) is selected. It is estimated that the problem of interference will not occur even if it is assumed that a coil case of about 10 mm will be added.

Table 2.1-12 Minimum gap on the ground insulation after optimizing the twist angle.

Name of coil		MC1 (TypeX)	MC2 (TypeX)	MC3 (TypeH)	MC4 (TypeG)	Design guide
Feature		Twisted to an angle where the inner wall can be seen				
Minimum gap between the coils without case (mm)	MC1-MC1	106.7				Should be larger than 50mm.
	MC1-MC2	76.9				
	MC2-MC3		84.3			
	MC3-MC4			67.3		
	MC4-MC4				107.3	
Minimum gap between the coil without case and the vacuum vessel (mm)	With inner surface of the shell	25.2	54.9	53.8	83.9	Should be larger than 25mm.
	With a port	55.7(CF420)			43.6 (Rectangle OP)	

Since it is not orthogonal to the reference plane (CCS), there was a concern that the gap would become smaller. However, as a result of searching for an angle that does not cause this, it was designed so that the problem of interference does not occur.

2.1.4 Resistance

The resistance was obtained by the ANSYS/Maxwell system. The tables in this chapter show the results. The resistance of modular coil was calculated from the ohmic loss obtained by ANSYS/Maxwell with the condition of the cross section of 132 mm x 69 mm that was an average value including isolator and cooling hole. Since the actual conductor cross-section is smaller, the resistance value was evaluated by correcting the difference in cross-sectional area. Specifically, the above result shows the value obtained by multiplying the Maxwell result by $126.5/58.825=2.15$.

Table 2.1-13 Inductance and resistance of each coil.

Name of coil		MC1	MC2	MC3	MC4
Average arc length of a turn(m)		4.40	4.34	4.20	4.13
Number of turns		72	72	72	72
Ohmic loss with 312.5 kAT and $1.724E-8 \Omega m(kW)$		1,750	1,725	1,670	1,613
Resistance (m Ω) OFC 101%IACS $\alpha_{20}=0.00393$	0°C $\rho=1.573E-8 \Omega m$	84.8	83.6	80.9	78.1
	20°C $\rho=1.707E-8 \Omega m$	92.0	90.7	87.8	84.7
	22.5°C $\rho=1.724E-8 \Omega m$	92.9	91.6	88.7	85.6
	75°C $\rho=2.076E-8 \Omega m$	111.9	110.3	106.8	103.0

IACS; Conductivity of international annealed copper standard $\rho(T) = \rho_{20} [1 + \alpha_{20} (T - 20)]$

2.1.5 Pressure loss of cooling water

Fig 2.1-15 shows the design value of the flow rate dependence of the pressure loss (loss head), which is calculated by the Hazen Williams' equation below.

$$h_f = 10.67 \cdot L \frac{(Q/C)^{1.85}}{D^{4.87}}$$

$$\Delta P = \rho \times g \times h_f$$

$$Q = Au = u \times \frac{(\pi D^2)}{4}$$

where h_f is the loss head (m), L is the length of one cooling tube (m), Q is the flow rate in a tube (m^3/s), C is the roughness coefficient (Hazen-Williams-coefficient), and D is the inside tube diameter (m). g is the gravitational acceleration ($= 9.8 \text{ m/s}^2$), ρ is the density of water ($= 996 \text{ kg/m}^3$), ΔP is the pressure drop (P_a), A is the cross section of cooling hole (m^2), and u is the flow velocity (m/s).

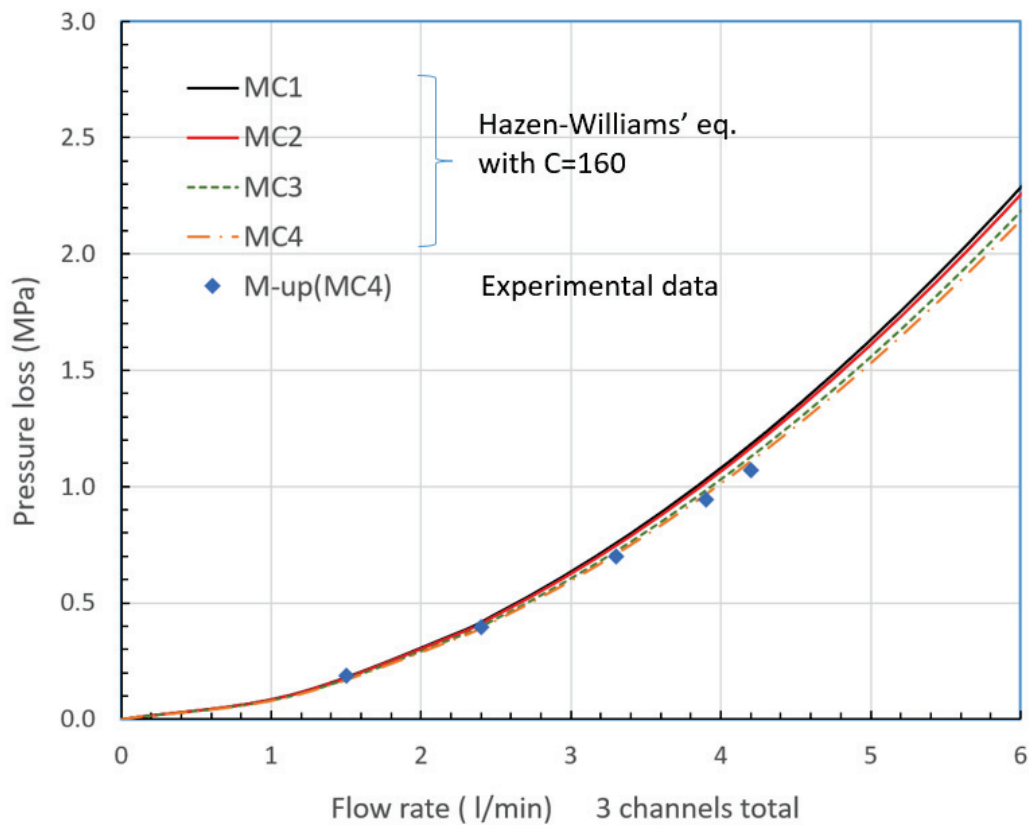


Fig 2.1-15 Flow rate dependence of the pressure loss. The Hazen-Williams coefficient C was adjusted according to the experimental data.

Table 2.1-14 shows the design parameters of the cooling channel for the modular coil. The pressure drop of the modular coil are shown in Table 2.1-15. Here the Hazen Williams coefficient C of 160 was adjusted according to the experimental data in Table 2.1-16.

Table 2.1-14 Design value of the cooling channel.

Item		MC1	MC2	MC3	MC4
Average arc length of one turn	Sone(m)	4.40	4.34	4.20	4.13
Number of turns for a cooling channel	NT	24	24	24	24
Cooling hole length	L(m)	105.6	104.2	100.8	99.2
Number of cooling channels	NC	3	3	3	3
Diameter of the cooling hole	d(m)	0.004	0.004	0.004	0.004

Table 2.1-15 Pressure drop of cooling water.

Flow velocity v (m/s)	Frow rate Q		Pressure drop (MPa)			
	(m ³ /s)	(l/min)	MC1	MC2	MC3	MC4
0	0.00E+00	0.0000	0.000	0.000	0.000	0.000
0.5	6.28E-06	1.1310	0.104	0.103	0.100	0.098
1	1.26E-05	2.2619	0.376	0.371	0.359	0.353
1.1	1.38E-05	2.4881	0.449	0.442	0.428	0.421
1.2	1.51E-05	2.7143	0.527	0.520	0.503	0.494
1.3	1.63E-05	2.9405	0.611	0.603	0.583	0.573
1.4	1.76E-05	3.1667	0.701	0.691	0.669	0.657
1.5	1.88E-05	3.3929	0.796	0.785	0.760	0.747
1.6	2.01E-05	3.6191	0.897	0.885	0.856	0.841
1.7	2.14E-05	3.8453	1.004	0.990	0.958	0.941
1.8	2.26E-05	4.0715	1.115	1.100	1.065	1.046
1.9	2.39E-05	4.2977	1.233	1.216	1.177	1.156
2	2.51E-05	4.5239	1.356	1.337	1.294	1.271
2.1	2.64E-05	4.7501	1.484	1.463	1.416	1.391
2.2	2.76E-05	4.9763	1.617	1.595	1.543	1.516
2.3	2.89E-05	5.2025	1.755	1.732	1.676	1.646
2.4	3.02E-05	5.4287	1.899	1.873	1.813	1.781
2.5	3.14E-05	5.6549	2.048	2.020	1.955	1.921
2.6	3.27E-05	5.8811	2.202	2.172	2.102	2.065
2.7	3.39E-05	6.1073	2.362	2.329	2.254	2.215

They were estimated by the Hazen Williams equation with C=160.

Table 2.1-16 Experimental data for the MC4 mockup coil.

Total flow rate (l/min)	Pressure (MPa)		
	Inlet	Outlet	Drop
1.5	0.204	0.017	0.187
2.4	0.432	0.038	0.394
3.3	0.764	0.066	0.698
3.9	1.042	0.099	0.943
4.2	1.185	0.113	1.072

2020/04/15 in Keye factory

2.1.6 Cage type support structure for the modular coil system

The cage type support structure is shown in Fig 2.1-16 to Fig 2.1-20. Fig 2.1-18 show the structure near the center of the device. Large tokamaks are typically designed with TFC wedges to support the centripetal forces. However, the CFQS cannot take this approach due to shape of constraints. Instead, it is designed to absorb such a large force, whose main component is the centripetal force, with central connection boards (CCB) and some pedestals (PRF). Central pillars (CPS) are installed to support the PRF's during assembly work. There is a big rectangular free area to access the inside port on the vacuum vessel.

Fig 2.1-19 and Fig 2.1-20 show the coil support with the partial clamping type coil case for the MC2 as an example. The main role is to prevent deformation of the modular coil (MC). It also has, among other components, a vacuum vessel, other coils, and a diagnostic system attached on it. Very large magnetic forces are applied to the modular coils. The forces' magnitude and direction may be very complicated, and their characteristics are not easy to describe. They are like those of a tokamak's toroidal field coil, but the modular coils are more difficult to analyze and operated under more severe conditions because even the components that are negligible for tokamaks cannot be ignored. For example, it is necessary to consider toroidal and vertical forces that can be ignored in tokamak. The strength of the coil conductor is not expected to be sufficient for large forces, the modular coil must be reinforced with the metal case.

The shape of the clamp is roughly classified into 3 types of A, B and C as shown in Fig 2.1-19. Their characteristics are shown in Fig 2.1-20. The type-A is a large u-shaped clamp. It is extended to reduce the deformation of the coil and the opening is provided on the side to facilitate the insertion of the coil. Since the MC3 and the MC4 is large and complicated, the clamp must be made in two pieces and weld both after inserting the coil. The type-B is the u-shaped clamp made of flat plates for cost reduction with open inside. The type-C is the u-shaped clamp made of thick block with open inside. The clamps are designed to be thick of 20 to 30mm to reduce deformation and reduce the amount of processing. Table 2.1-17 shows the minimum gap between the coil cases (cramps) and the vacuum vessel. It is considered that the coil case is about 20 mm away from the vacuum vessel and is within the adjustable range.

Pedestals of the PTCF, PTSF and PLEG are made machined into required shape at the same time as the clamp is made. All surfaces that contact with other parts are designed to be flat for easy assembly and adjustment. The pedestal is necessary to strictly control the accuracy to contact other structures, but it is difficult to secure that accuracy by assembly adjustment. Therefore, the policy is to manufacture pedestals with some extra length left, assemble the coil and the case, and then machine to ensure the accuracy of the pedestal surface. Diagonal beams (DBS) in Fig 2.1-16 mainly prevents deformation by the overturning moments, and others handle the vertical and horizontal forces. For use in future NBI experiments, we adopted a design with high-rigidity DBS instead of providing the outer pillars (OPS) around the large rectangular ports. Intermediate base plates (IBP) are flat on which the vacuum vessel and the modular coils are installed. Their upper surface becomes the installation reference for other parts, so it should be strictly controlled, such as improving flatness by machining and marking reference points for coil placement.

Fig 2.1-21 shows the other design example with a continuous coil case which was more effective in reinforcing the coil. At first, we examined the design with this shape, but gave up the adoption of this plan because it was

difficult to manufacture the case and insert the coil.

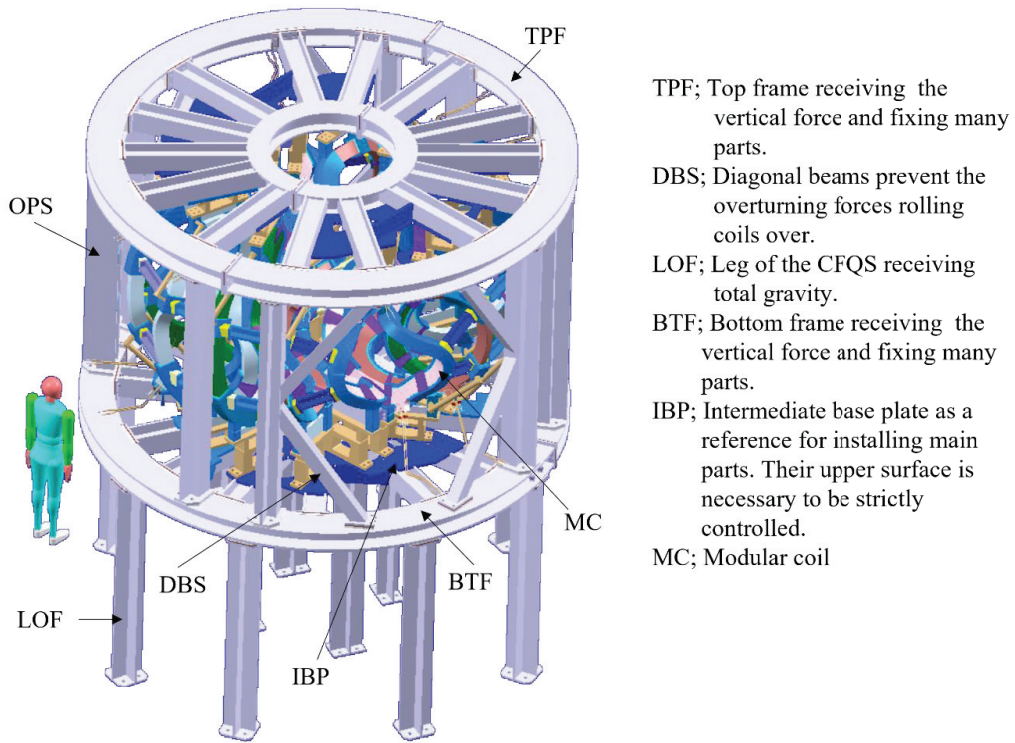


Fig 2.1-16 Cage type support structure and the modular coil system. The main role of the structure is to prevent deformation of the modular coil.

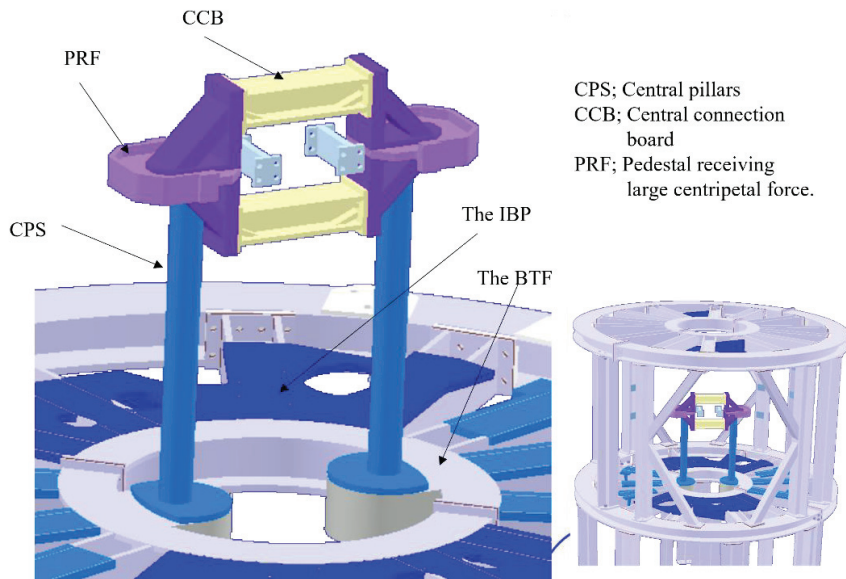


Fig 2.1-17 Structure near the center of the device. To support a large centripetal force of the modular coil, it is necessary to connect the MC on the inner side of the device. For that purpose, the pedestals receiving the large force PRF and the central connection boards CCB are placed.

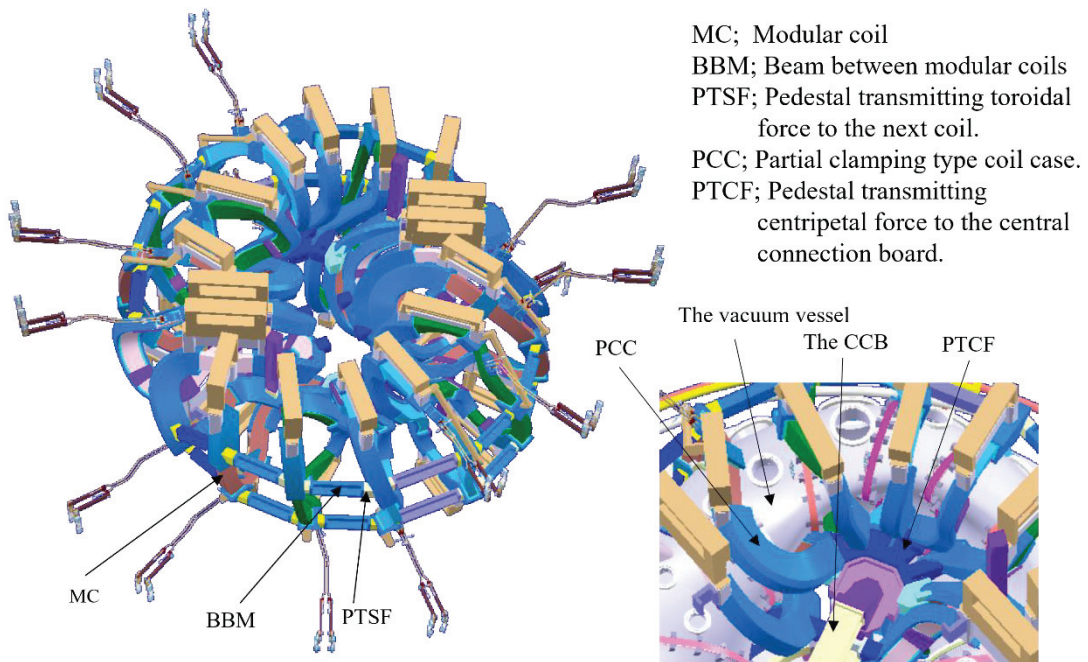


Fig 2.1-18 Support structure for the modular coils. Pedestals of the PTSF and the PTCF are placed to connect the modular coils on the outer and inner side of the device.

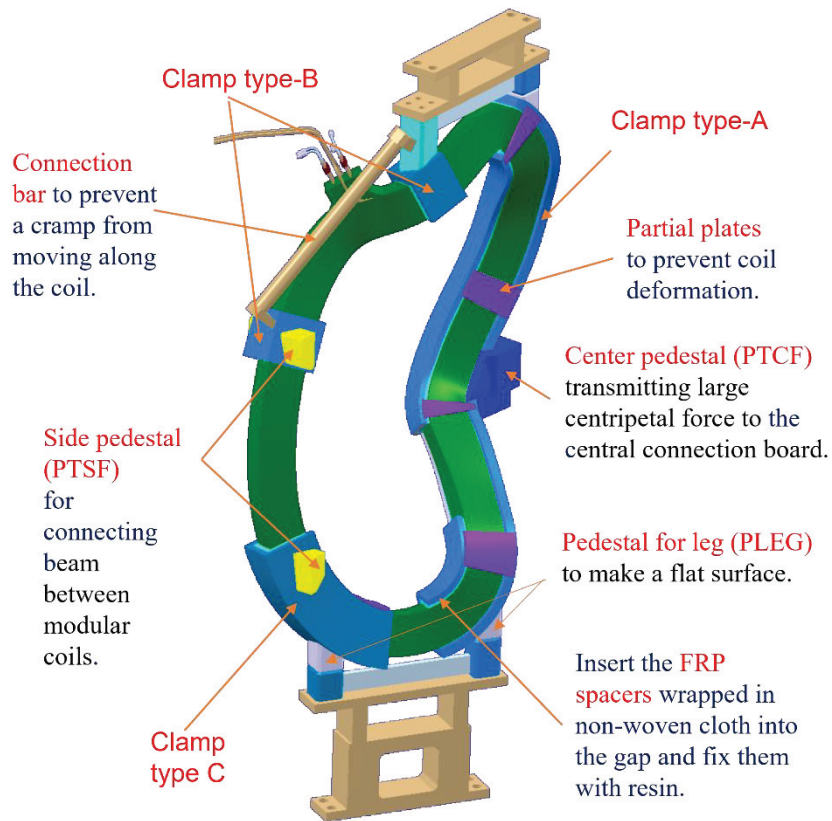
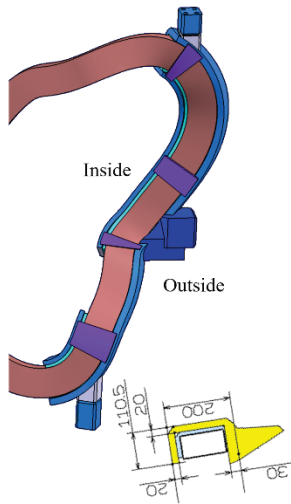
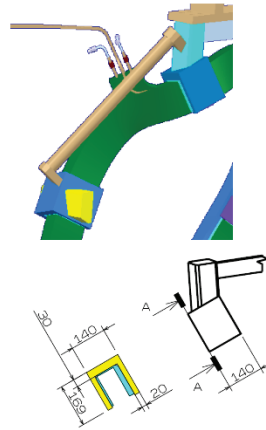


Fig 2.1-19 Structure of the partial clamping type coil case. Since a large EM force is applied to the coil, it is difficult to support it only with the coil conductor. To reinforce the coil, the coil is covered with three types of clamping coil cases.



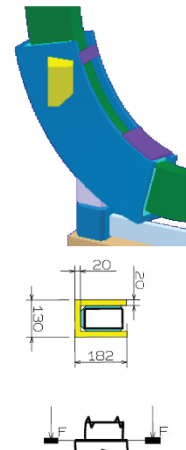
**Clamp type-A ;
U-shaped with one side open**

- The clamp is extended to reduce the coil deformation.
- An opening is provided on the side surface to facilitate the insertion of the coil.
- Since the MC3 and the MC4 is large and complicated, the clamp must be made in two pieces and weld both after inserting the coil.



**Clamp type-B ;
U-shaped made of flat plates**

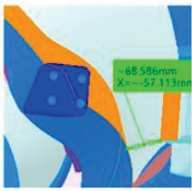
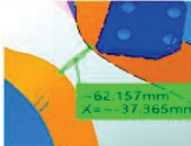
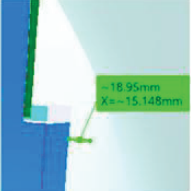
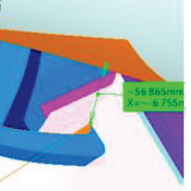
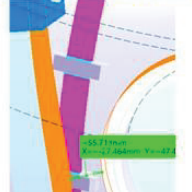
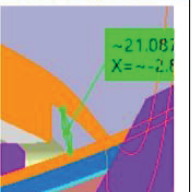
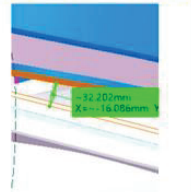
- A bar connects between two clamps.
- The clamp is a combination of simple flat plates to reduce cost.



**Clamp type-C ;
U-shaped with open inside**

Fig 2.1-20 Concept of the clamp design. Three types of clamps are used according to the required strength and coil shape for the purpose of reducing the manufacturing cost.

Table 2.1-17 Minimum gap with the coil case

Name of coil		MC1 (TypeX)	MC2 (TypeX)	MC3 (TypeH)	MC4 (TypeG)	Design guide
Feature		Twisted to an angle where the inner wall can be seen				
Minimum gap between coils with case (mm)	MC1-MC1	0(PEDE-PEDE)				Ideally there is no gap between cases to stop the movement of the cases.
	MC1-MC2	0(PEDE-PEDE)				
	MC2-MC3		0(PEDE-PEDE)			
	MC3-MC4			68.6(Case MC4-PEDE MC3)		
	MC4-MC4				62.2 (case-case)	
						
Minimum gap between the coil without case and the vacuum vessel (mm)	With inner surface of the shell	25.2 (coil)	19	27.7	56.9	Requires 5mm or more, which is a tolerance of the vacuum vessel. If possible, it should be 15 mm or more with the margin.
						
	With others	55.7(CF420)		21.1 (Split F)	32.2 (Rectangle OP)	
						

It is considered that the coil case is about 20 mm away from the vacuum vessel and is within the adjustable range.

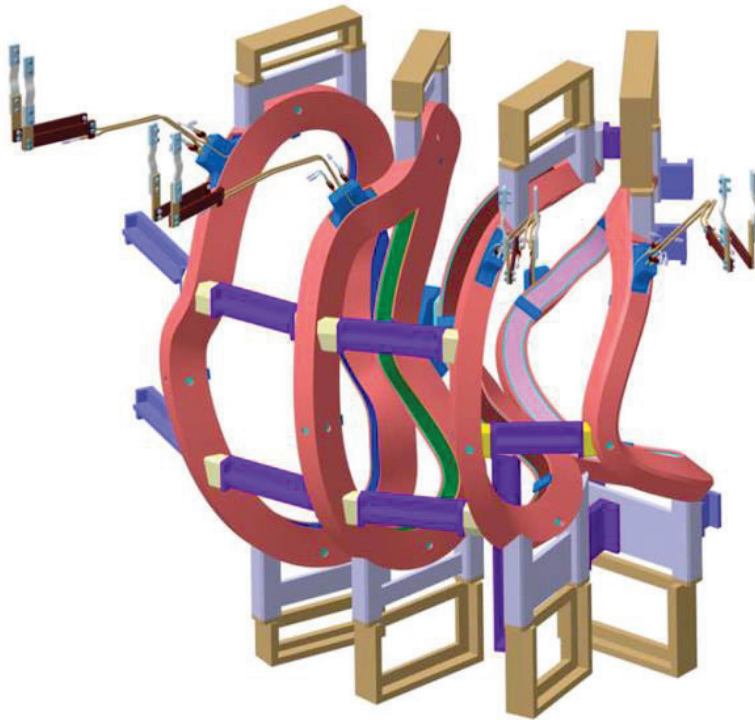


Fig 2.1-21 Design example of continuous C-type coil case. At first, we examined the design with this shape, but gave up the adoption of this plan because it was difficult to manufacture the case and insert the modular coil.

2.2 Poloidal field coil system (PFC)

The winding method is four solenoids winding for the IV coil and two double pancakes with winding parallel simultaneously for the OV coil. The structure of the conductors at the beginning and end of winding is conceptually shown in Fig 2.2-1 and Fig 2.2-2.

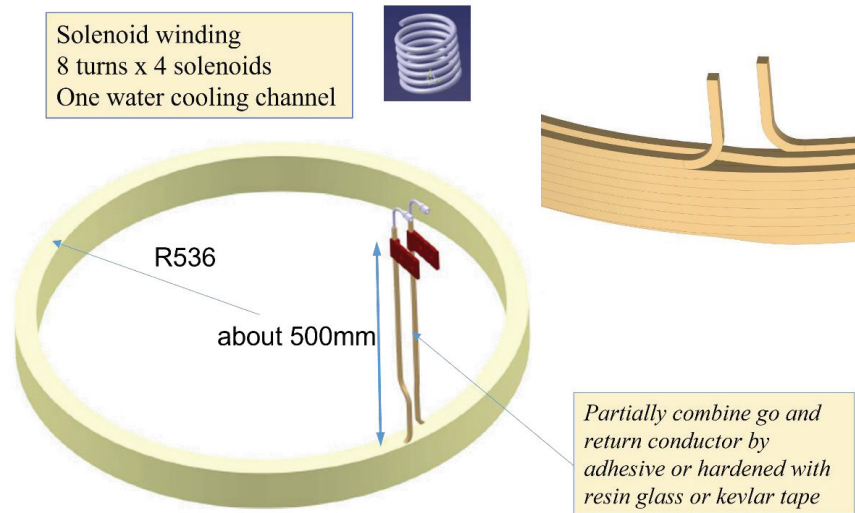


Fig 2.2-1 Structure of start and end of winding for the IV coil. The winding method is the solenoid.

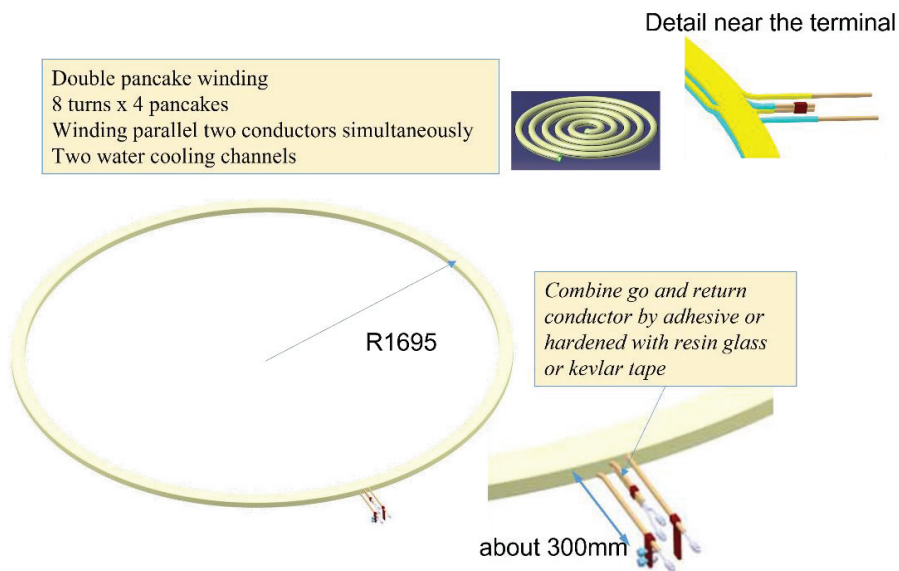


Fig 2.2-2 Structure of start and end of winding for the OV coil. The winding method is the double pancake.

2.3 Toroidal field coil system (TFC)

Layout of the TFC system is shown in Fig 2.3-1 and the position of its terminal is shown in Fig 2.3-2. All cables (power leads) that supply current to the TFC are designed to be pulled out from the opening of the top frame. There are 12 TFC bodies of 3 types, but half of them are installed upside down. There are 6 types including the terminal as shown in Fig 2.3-3. The coil and power supply are connected by a 2-core CV cable (CV-2C) (cross-linked polyethylene insulated vinyl sheath cable) that is easy to adjust the wiring route. As shown in Fig 2.3-4, the heat resistance class of the insulation is F for TFC body that touches the vacuum vessel to be baked, and A for the CV cable to be wired in the air.

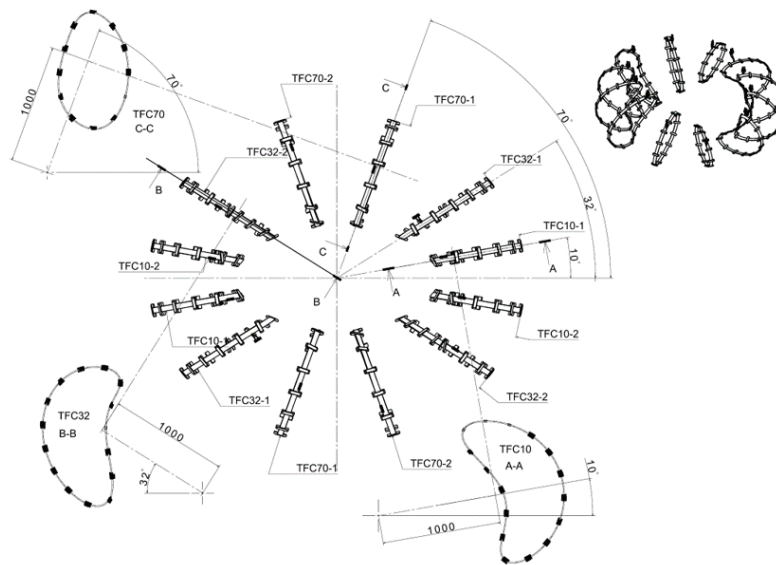


Fig 2.3-1 Layout of the TFC system. Twelve bean-shaped coils are arranged at approximately equal intervals.

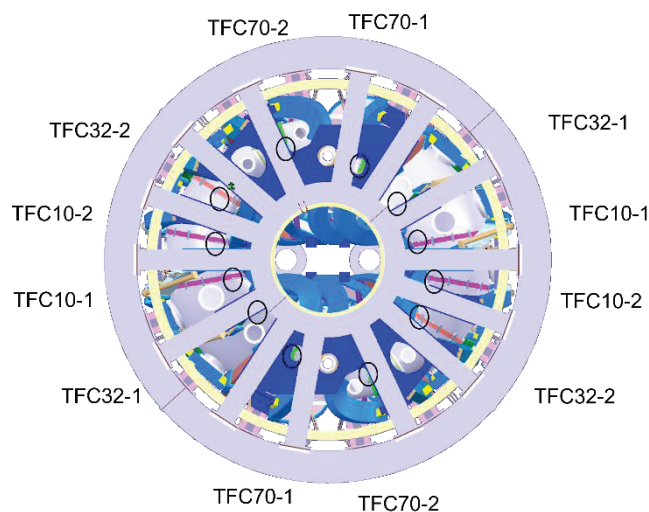
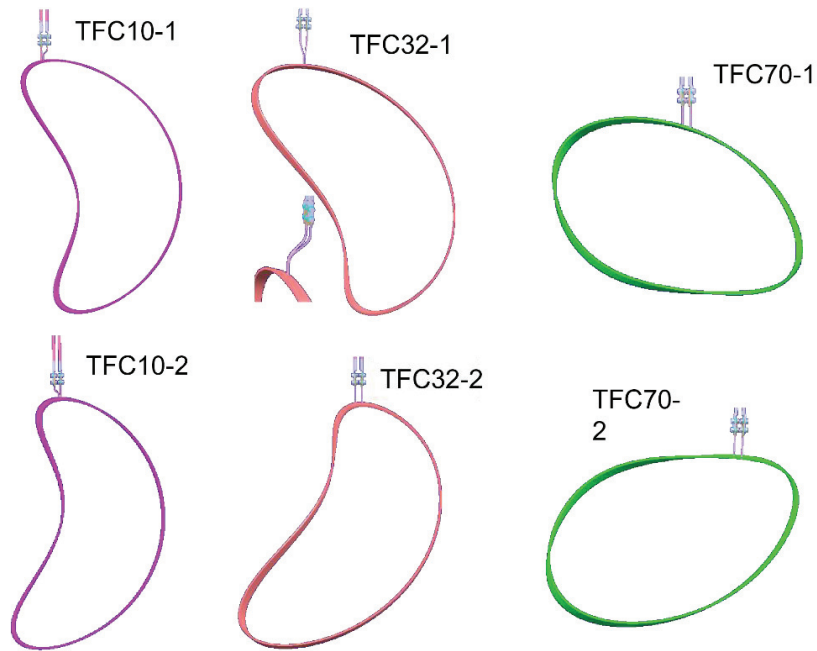


Fig 2.3-2 Position of current leads for the TFC. The current leads are pulled out through the gaps in the top frame.



TFC**-1 and TFC**-2 have the same shape and are placed upside down.
 All terminals are placed on the top, so the radial position is different.

Fig 2.3-3 The coil body and the terminal of each TFC. There are three types of coil bodies, but there are six types of coils including current leads.

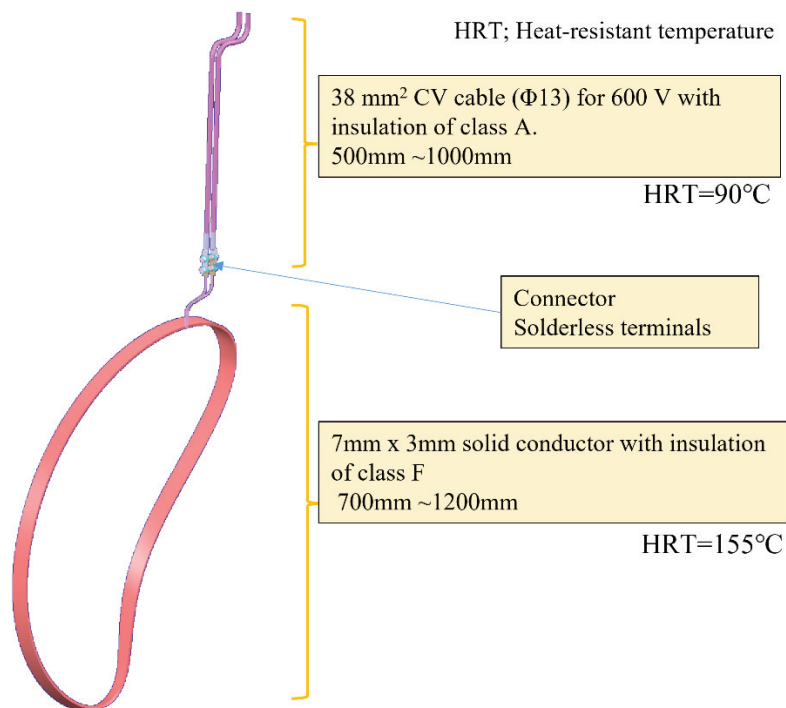


Fig 2.3-4 Example of current lead for the TFC. Flexible cables are wired because the route of the wire cannot be determined by the desk study.

2.4 Inductance matrix for the coil system

The inductance matrix was obtained by ANSYS/Maxwell. Table 2.4-1 and Table 2.4-2 show the result.

Table 2.4-1 Inductance matrix for each coil group.

Name	MC1	MC2	MC3	MC4	IV	OV	TFC10	TFC32	TFC70
Number of coils	4	4	4	4	2	2	4	4	4
Number of turns in a coil	72	72	72	72	32	32	16	16	16
MC1	58.87	14.15	5.77	3.72	0.07	0.85	-5.16	-1.73	-0.43
MC2	14.15	49.45	11.69	5.82	0.27	0.21	-2.00	-3.68	-0.72
MC3	5.77	11.69	47.41	13.86	-0.27	-0.48	-0.74	-1.68	-1.89
MC4	3.72	5.82	13.86	52.57	-0.60	-0.66	-0.45	-0.76	-3.32
IV	0.07	0.27	-0.27	-0.60	4.28	0.72	0.00	0.00	0.00
OV	0.85	0.21	-0.48	-0.66	0.72	18.13	0.00	0.00	0.00
TFC10	-5.16	-2.00	-0.74	-0.45	0.00	0.00	2.683	0.262	0.057
TFC32	-1.73	-3.68	-1.68	-0.76	0.00	0.00	0.262	2.335	0.108
TFC70	-0.43	-0.72	-1.89	-3.32	0.00	0.00	0.057	0.108	1.996

Obtained at May 2019 by NIFS after the design change of reducing the maximum curvature and tilting the normal direction to the current carrying surface. They were obtained by ANSYS/Maxwell. Each value includes margin of 5 %. Unit of inductance is mH.

Table 2.4-2 Inductance matrix for each coil obtained by the ANSYS/Maxwell. Each coil is composed of one turn. Unit of inductance is nH.

	MC1-1	MC1-2	MC1-3	MC1-4	MC2-1	MC2-2	MC2-3	MC2-4	MC3-1	MC3-2	MC3-3	MC3-4	MC4-1	MC4-2	MC4-3	MC4-4
MC1-1	2215	14	13	461												
MC1-2	14	2216	461	13												
MC1-3	13	461	2215	14												
MC1-4	461	13	14	2215												
MC2-1	462	15	14	160	2166	19	13	73								
MC2-2	15	462	160	14	19	2166	73	13								
MC2-3	14	160	462	15	13	73	2166	19								
MC2-4	160	14	15	462	73	13	19	2166								
MC3-1	157	21	17	71	451	31	14	41	2079	60	11	28				
MC3-2	21	157	71	17	31	451	41	14	60	2079	28	11				
MC3-3	17	71	157	21	14	41	451	31	11	28	2079	60				
MC3-4	71	17	21	157	41	14	31	451	28	11	60	2079				
MC4-1	70	36	26	39	158	62	21	27	463	140	16	18	1988	399	15	14
MC4-2	36	70	39	26	62	158	27	21	140	462	18	16	399	1986	14	15
MC4-3	25	39	70	36	21	27	158	62	16	18	462	140	15	14	1985	399
MC4-4	39	26	36	70	27	21	62	158	18	16	140	462	14	15	399	1987
IV-L	-1	8	-1	8	-8	35	-8	35	-17	-11	-17	-11	-27	-34	-27	-34
IV-U	8	-1	8	-1	35	-8	35	-8	-11	-17	-11	-17	-34	-27	-34	-27
OV-L	34	54	34	54	15	7	15	7	-7	-43	-7	-43	-24	-44	-24	-44
OV-U	54	34	54	34	7	15	7	15	-43	-7	-43	-7	-44	-24	-43	-24
T32-1	-254	-9	-9	-85	-702	-11	-9	-38	-301	-17	-9	-20	-95	-36	-12	-14
T32-2	-9	-254	-85	-9	-11	-702	-38	-9	-17	-301	-20	-9	-36	-95	-14	-12
T32-3	-9	-85	-254	-9	-9	-38	-702	-11	-9	-20	-301	-17	-12	-14	-95	-36
T32-4	-85	-9	-9	-254	-38	-9	-11	-702	-20	-9	-17	-301	-14	-12	-35	-95
T70-1	-41	-15	-11	-22	-100	-25	-10	-14	-313	-56	-9	-11	-502	-162	-11	-11
T70-2	-15	-41	-22	-11	-25	-100	-14	-10	-56	-313	-11	-9	-162	-502	-11	-11
T70-3	-11	-22	-41	-15	-10	-14	-100	-25	-9	-11	-313	-56	-11	-11	-502	-161
T70-4	-22	-11	-15	-41	-14	-10	-25	-100	-11	-9	-56	-313	-11	-11	-161	-502
T10-1	-754	-8	-8	-295	-300	-9	-8	-95	-92	-12	-10	-39	-37	-19	-14	-21
T10-2	-8	-754	-295	-8	-9	-300	-95	-8	-12	-92	-39	-10	-19	-37	-21	-14
T10-3	-8	-295	-754	-8	-8	-95	-300	-9	-10	-39	-92	-12	-14	-21	-37	-19
T10-4	-295	-8	-8	-754	-95	-8	-9	-300	-39	-10	-12	-92	-21	-14	-19	-37

	IV-L	IV-U	OV-L	OV-U	T32-1	T32-2	T32-3	T32-4	T70-1	T70-2	T70-3	T70-4	T10-1	T10-2	T10-3	T10-4
IV-L	1971	19														
IV-U	19	1971														
OV-L	275	59	8124	306												
OV-U	59	275	306	8125												
T32-1	0	0	0	0	2138	7	5	22								
T32-2	0	0	0	0	7	2138	22	5								
T32-3	0	0	0	0	5	22	2138	7								
T32-4	0	0	0	0	22	5	7	2137								
T70-1	0	0	0	0	69	16	6	9	1766	77	6	7				
T70-2	0	0	0	0	16	69	9	6	77	1766	7	6				
T70-3	0	0	0	0	6	9	69	16	6	7	1766	77				
T70-4	0	0	0	0	9	6	16	69	7	6	77	1767				
T10-1	0	0	0	0	180	5	5	53	24	9	7	13	2280	5	5	207
T10-2	0	0	0	0	5	180	53	5	9	24	13	7	5	2279	207	5
T10-3	0	0	0	0	5	53	180	5	7	13	24	9	5	207	2279	5
T10-4	0	0	0	0	53	5	5	180	13	7	9	24	207	5	5	2279

2.5 Wiring of the coil system

The 32 coils will be installed in the CFQS, but it is not realistic to wire all current leads to the power supply room. We think it is preferable to connect the coils with copper bus bar or the cables near the CFQS body to minimize space of the wiring and to reduce cost. Table 2.5-1 summarizes the requirement of the connection bar, cable, and flexible terminal. The wiring plan for each coil system are shown in Fig 2.5-1 to Fig 2.5-3.

Table 2.5-1 Requirement for solid bus bar and cable.

Part	Item	Requirement	Criteria	Notes	Target	
Solid Bus bar	Rigidity	Rigid		Does not easily deform	All	
	Displacement and stress	Within allowable range for the repulsive force between returning conductors	Stress <20 MPa	To prevent insulation breakdown		
			Deflection <2 mm	To prevent interference		
			Natural frequency >20 Hz	Seismic and stiffness evaluation criteria		
	Cross section	No excessive temperature rise without cooling	Adiabatic temperature rise <5k	In a shot for the pulse operation		
			Current density < 2A/mm ²	For continuous operation		
	Connection method	Multiple bolt fastening	Size of bolt ≥ M10		For one place	
			Number of bolts ≥ 2			
	Insulation	Allowable temperature is above the operating temperature.	≥ 90 °C		Class A	
	Cable and flexible terminal	Cross section	Current in steady operation is below the capacity except in special cases	S ≥ 200 mm ² for the MCs and PFCs	Current is 400A	MC, PFC
S ≥ 38 mm ² for the TFCs or 60 mm ² (desirable)				Current is 300A	TFC	
Connection method		Multiple bolt fastening	Size of bolt ≥ M10		For one place	
			Number of bolts ≥ 2			
Allowable voltage		Above the operating voltage	≥ 6000V	Operation voltage is 2400V	MC, PFC	
	≥ 600V		Operation voltage is 600V	TFC		
Insulation	Allowable temperature is above the operating temperature.	≥ 90 °C		Class A	All	

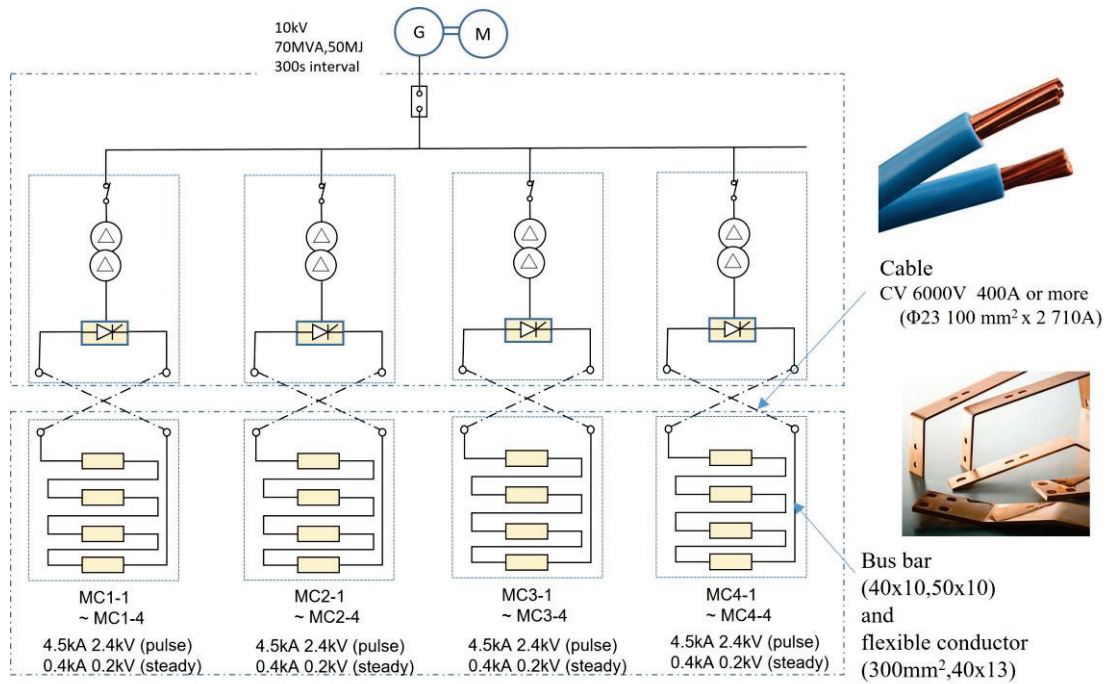


Fig 2.5-1 Wiring plan for the modular coil. Four coils are connected in series with bus bars around the main body, and cables are connected between the coil and the power supply.

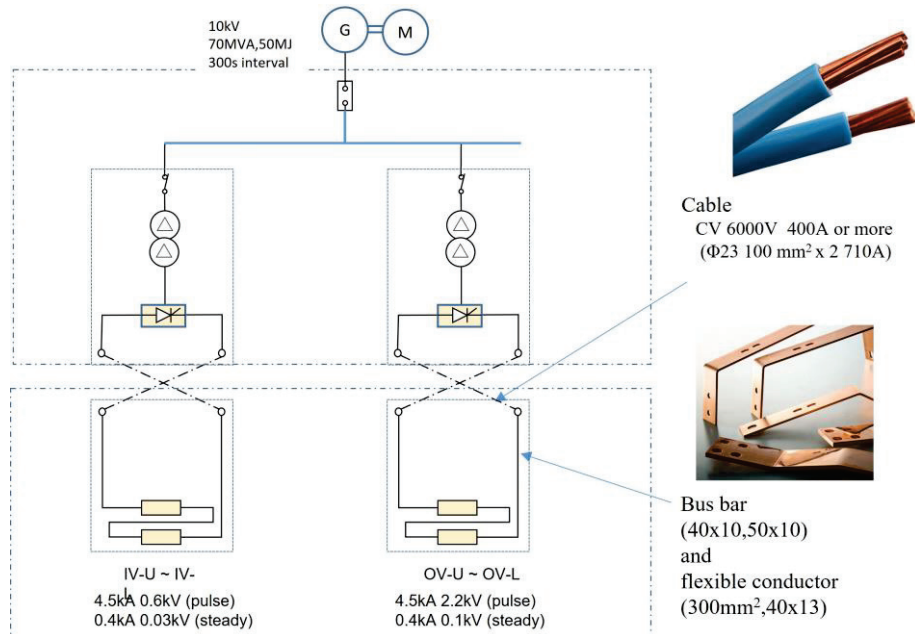


Fig 2.5-2 Wiring plan for the PFC. Two coils are connected in series with bus bars around the main body, and cables are connected between the coil and the power supply.

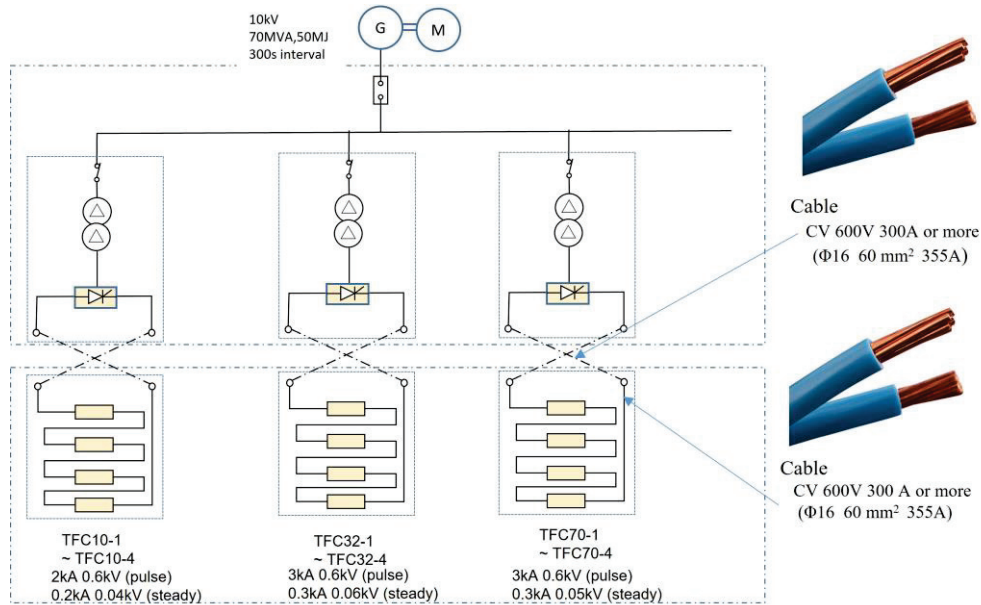


Fig 2.5-3 Wiring plan for the TFC. Four coils are connected in series with cables in the cable tray on the top frame, and cables are connected between the coil and the power supply.

2.6 Cooling of the coil system

The requirements of the cooling pipe and the design plan of cooling coil system are shown in Table 2.6-1 and Table 2.6-2. The time average current density is low enough to be cooled by natural air cooling. Since the temperature rise in one shot of the MC is very large, water cooling is used to shorten the cooling time constant. Although the current density of PFC is not high, it is also water cooled because the air-cooling efficiency seems to be poor due to the large cross section. To cool the coils, it is necessary to disperse 108 cooling pipes (hoses) around the CFQS. The size and arrangement of a manifold (an assembly of branch pipes) for connecting them to the cooling water device were determined as shown in Table 2.6-3 and the figures in this chapter.

Pressure drop (loss head) of the piping is calculated by the Hazen Williams' equation below.

$$h_f = 10.67 \cdot L \frac{(Q/C)^{1.85}}{D^{4.87}}$$

$$\Delta P = \rho \times g \times h_f$$

$$Q = Au = u \times \frac{(\pi D^2)}{4}$$

where h_f is the loss head (m), L is the length of one cooling tube (m), Q is the flow rate in a tube (m³/s), C is the roughness coefficient (Hazen-Williams-coefficient =100~200), and D is the inside tube diameter (m). g is the gravitational acceleration (=9.8 m/s²), ρ is the density of water(=996 kg/m³), ΔP is the pressure drop (P_a), A is the cross section of cooling hole (m²), and u is the flow velocity(m/s).

Average temperature rise of cooling water is calculated by the equation below.

$$\Delta T_{water} = \frac{\text{Average heat input}}{(\text{Flow rate})(\text{Density})(\text{Specific heat capacity})} = \frac{\Delta W}{t_{period}} \cdot \frac{1}{(Q_0 \rho C_h)}$$

where Q_0 is the flow rate in a tube(m^3/s), ΔW is the heat generation in one pulse(J), t_{period} is the discharge period(s) and C_h is the Specific heat capacity of water ($=4186 \text{ J/kg K}$).

Table 2.6-1 Requirement of the cooling pipe.

No	Design requirement
1	Flow rate in a manifold is 5 m ³ /hr for the MC's and 1 m ³ /hr for the PFC's. Minimum flow rate required was obtained by calculation is 4.57 m ³ /hr in total.
2	Length of a main pipe is 100 m or less, and maximum pressure is 20 atm or less. SUS304 pipe with Sch20 should be used.
3	A welding flange with gasket seal is used to improve reliability. Do not use screw-in flange (or threaded flange) as much as possible.
4	Inject pure water from below the CFQS body.
5	Provide a function to adjust the flow rate for each type of coil. It is not necessary to adjust the flow rate for each channel. If necessary, adjust the flow rate by the orifice.
6	Install a flow meter on the manifold so that the flow rate of the entire the MC's and the PFC's can be monitored. Monitoring for each channel is not required for cost reduction. The flow rate in each channel will be measured by a portable ultrasonic flow meter, and the flow balance between channels is adjusted by an orifice or the like.
7	Fix c-shaped manifold extended in the toroidal direction on the support frame.
8	Connect the manifold and coil with insulated nylon or PFA hose with a heat resistance of 100 °C or higher. Applying metal reinforced hose is prohibited because high voltage is applied to the coil

Table 2.6-2 Temperature rise in one shot and cooling method.

Item		unit	MC	PFC	TFC
Cross section of the coil		mm ²	69 × 132	100.5 × 48	66 × 7
Cooling method			Water	Water	Natural air
Pulse Operation (1T)	Pulse length (Square wave conversion time)	s	1.11	0.38	0.2
	Pulse period	s	300	300	300
	Maximum current	A	4,340	4,340	3,000
	Time average current	A	265	155	74
	Maximum current density	A/mm ²	74	74	150
	Temperature rise in a shot	k	36	12	25
	Typically cooling time (Expected empirical value)		10 minutes	10 minutes	1 hour
Steady operation (0.09T)	Maximum current	A	391	391	270
	Maximum current density	A/mm ²	6.6	6.6	13.5
	Average temperature rise	k	56	112	Not clear

Table 2.6-3 Pressure drop, and average temperature rise of the cooling water.

Parameters			unit	Inlet			Outlet
				MC	PFC(IV)	PFC(OV)	ALL
Coil	Length of one cooling tube	L	m	100	108.8	169.6	
	Size of cooling hole in a conductor	D	mm	4	4	4	
	Flow velocity of water	u	m/s	2.1	1.9	1.5	
	Number of cooling tubes for a coil	n		3	1	2	
	Flow rate in a hole	Q	m^3/s	2.64E-05	2.39E-05	1.88E-05	
			l/min	1.58	1.43	1.13	
	Loss head (Hazen Williams' equation)	h_f	m	143.93	130.13	130.99	
	Pressure drop $=\rho \times g \times h_f$	ΔP	MPa	1.40	1.27	1.28	
	Number of coils	m		16	2	2	
	Resistance of a coil at 75°C	R	Ω	0.105	0.036	0.116	
	Pulse operation						
	Current	I	kA	4.34	4.34	4.34	
	Pulse length (Square wave conversion)	Δt	s	1.11	0.38	0.38	
	Discharge period	t_{period}	s	300	300	300	
	Heat generation of a coil in one pulse	ΔW	MJ	2.20	0.26	0.83	
	Heat generation all in one pulse		MJ	35.12	0.52	1.66	
	Average temperature rise of the cooling water	ΔT_w	k	22.2	8.6	17.6	
	Steady operation						
	Current	I	kA	0.391	0.391	0.391	
	Average heat generation of a coil	P	kW	16.1	5.5	17.7	
Average temperature rise of the cooling water	ΔT_w	k	48.6	55.3	112.8		
Manifold	Spec of main pipe			40A Sch20	40A Sch20	50A Sch20	
	Inner diameter of pipe	D_0	mm	42.6	42.6	53.5	
	Length of main pipe (Preliminary)	L_0	m	200	200	200	
	Flow rate in a pipe $= \sum n \times m \times Q$	Q_0	m^3/s	1.27E-03	1.23E-04	1.39E-03	
			m^3/hr	4.56	0.44	5.00	
	Flow velocity of water	v_0	m/s	0.889	0.086	0.618	
	Loss head (Hazen Williams' equation)	h_f	m	3.684	0.049	1.442	
Pressure drop $=\rho \times g \times h_f$	ΔP	MPa	0.036	0.000	0.014		
Physical property	Roughness coefficient of hole	C		160	160	160	
	Density of water	ρ	kg/m^3	996	996	996	
	Gravitational acceleration	g	m/s^2	9.8	9.8	9.8	
	Specific heat capacity of water	C_h	$J/kg.k$	4186	4186	4186	

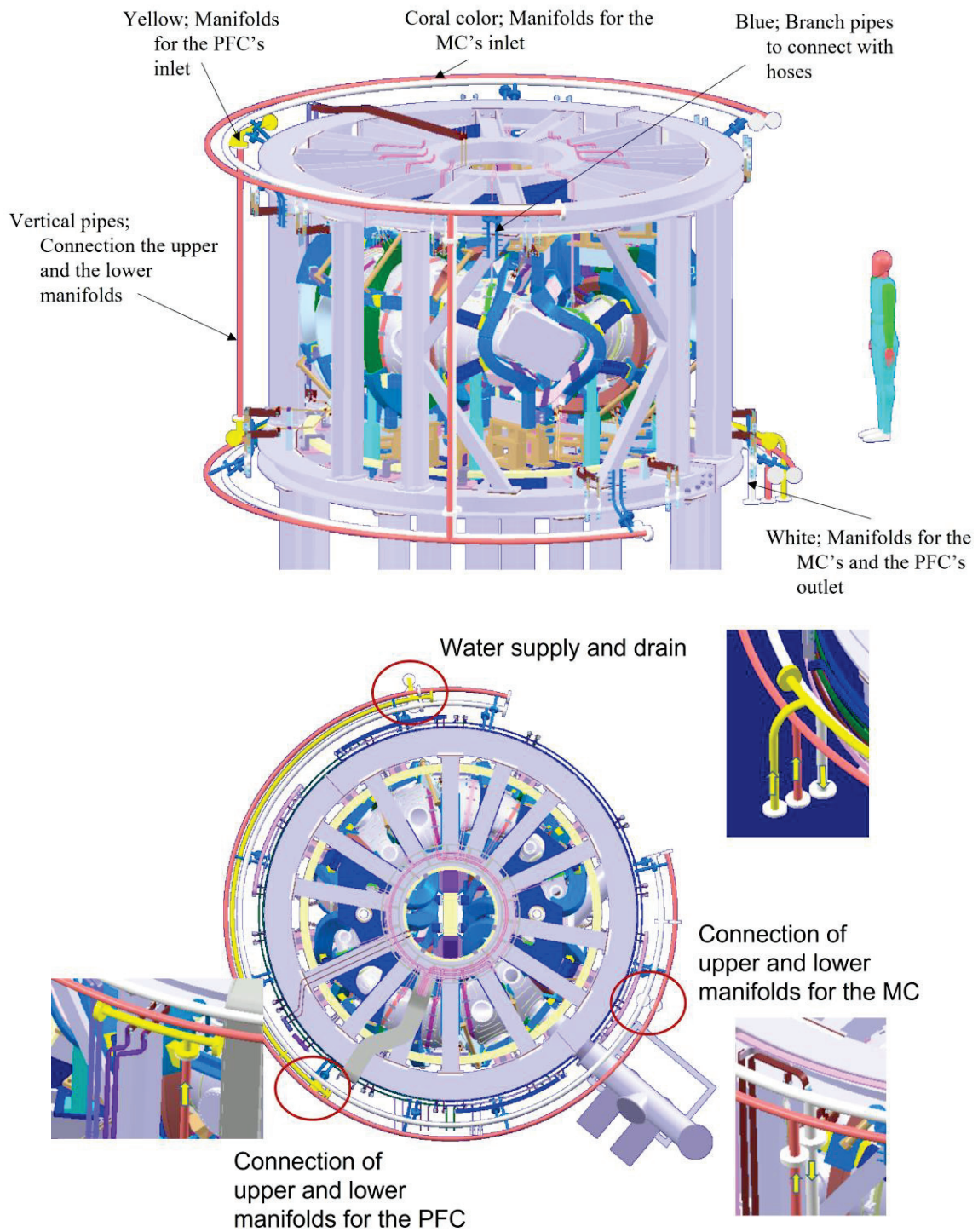


Fig 2.6-1 Placement of manifold for the cooling water. C-type manifolds made of pipes with a diameter of about 50 mm are installed in the upper and lower positions on the outer side of the device, and cooling water is supplied to the MC and PFC.

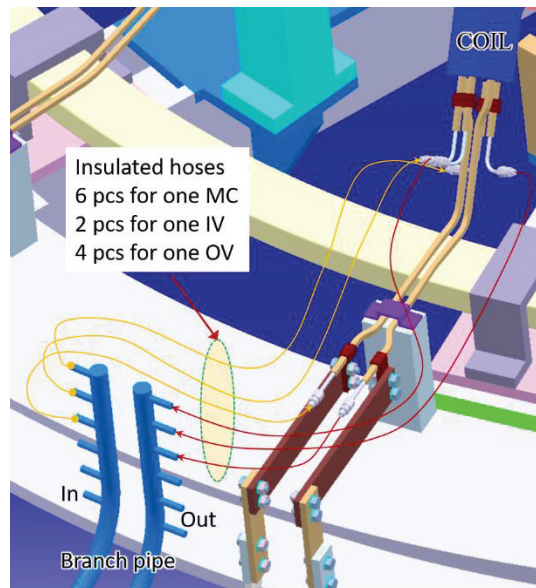


Fig 2.6-2 Connecting the cooling water hoses. Insulating hoses connect the manifold and the coil to supply the cooling water.

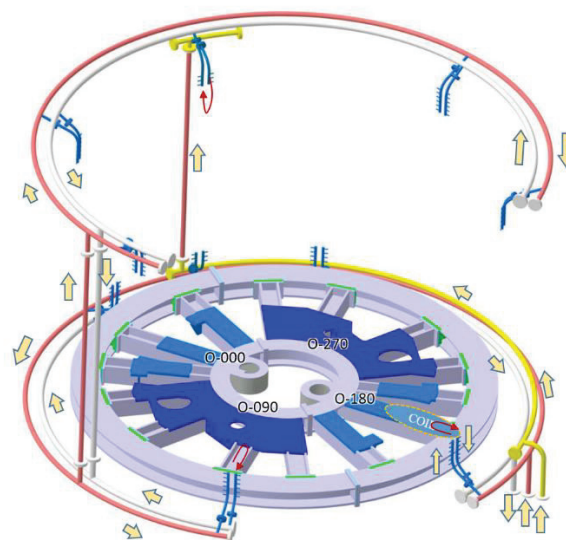


Fig 2.6-3 Cooling water flow direction in the manifold. There are two water injection manifolds, one for the MCs and one for the PFCs, and the drainage manifold is common.

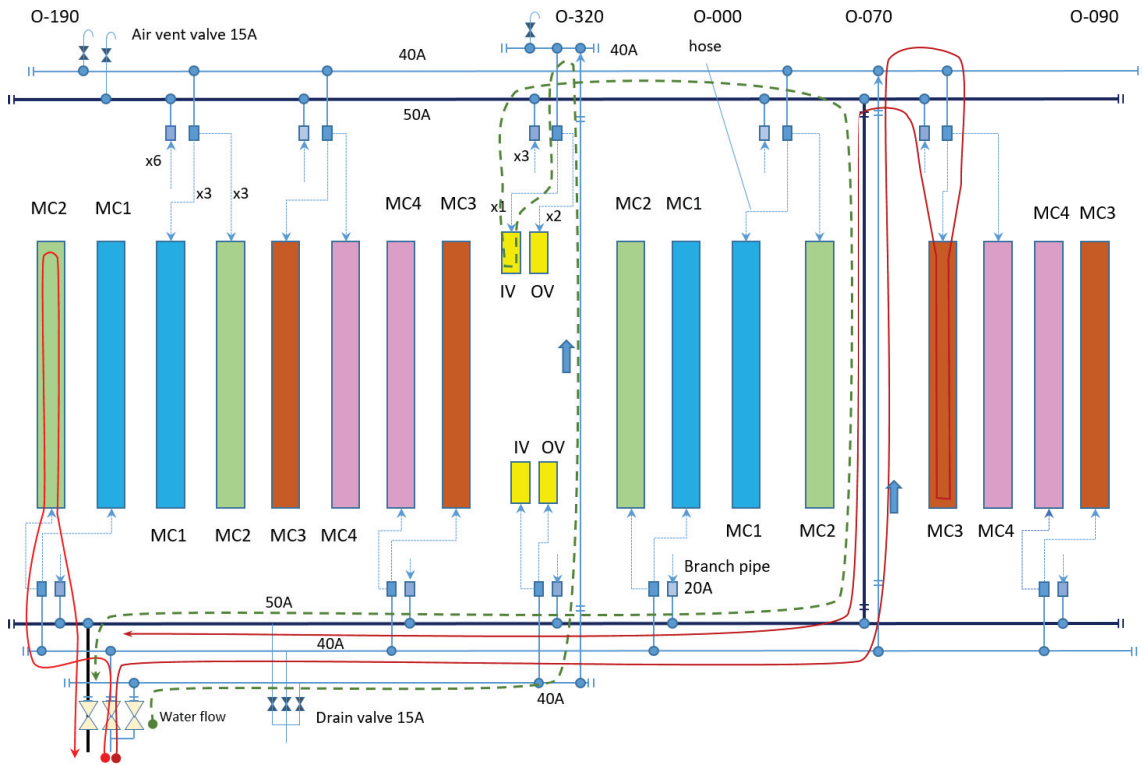


Fig 2.6-4 Cooling water flow path. Cooling water is supplied from the lower manifold to the MCs having the current lead on the lower side, and from the upper manifold to the MCs having the current lead on the upper side.

3 Validation of the coil design

3.1 Validating the ANSYS/Maxwell result for inductance (MC)

The inductance can be analytically estimated by the solenoid formula with the Nagaoka coefficient.

$$L = K \times 4\pi \times 10^{-7} \times \mu_r \times N^2 \times S / L_{length}$$

where K is a Nagaoka coefficient, μ_r is a relative permeability, N is the number of turns, S is a cross section of inside area of coil and L_{length} is a coil width.

□ MC1

$$S = \pi \times 0.92 \times \frac{1.62}{4} = 1.17$$

$$L_{length} = 0.069$$

$$\frac{D}{L_{length}} \sim \frac{0.61}{0.07} = 9$$

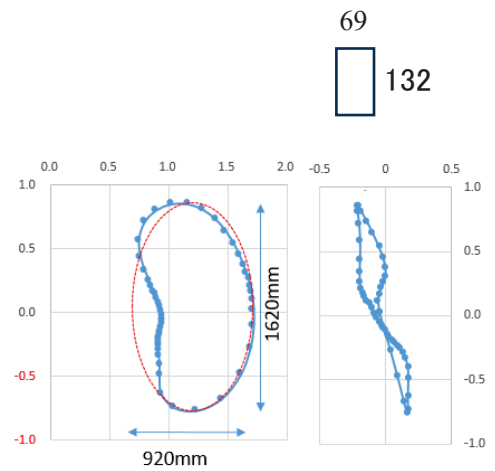
$$K = 0.2$$

$$L = \frac{0.2 \times 4\pi \times 10^{-7} \times 72^2 \times 1.17}{0.07} = 0.021[H]$$

Obtained by the formula

$$L = 2216 \times 10^{-9} \times 72^2 = 0.0115[H]$$

Obtained by the ANSYS/Maxwell



□ MC4

$$S = \pi \times 1.03 \times \frac{1.16}{4} = 0.94$$

$$L_{length} = 0.069$$

$$\frac{D}{L_{length}} \sim \frac{0.55}{0.07} = 7.9$$

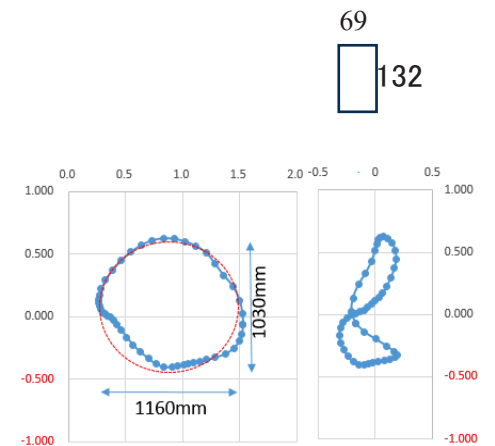
$$K = 0.2$$

$$L = \frac{0.2 \times 4\pi \times 10^{-7} \times 72^2 \times 0.94}{0.07} = 0.017[H]$$

Obtained by the formula

$$L = 1985 \times 10^{-9} \times 72^2 = 0.0103[H]$$

Obtained by the ANSYS/Maxwell



The results of the ANSYS/Maxwell are considered reasonable, which shows a value slightly larger than the roughly estimated value.

3.2 Electromagnetic force of the modular coil (MC)

A strong support structure is necessary for keeping device in a safety state when operating it. As for magnetic confinement fusion device, the EM force is the main load on coil system, which is the key component of whole device. Therefore, we need to understand the EM force on coil system and then design a reliable support structure.

3.2.1 Coil system for the CFQS and analysis method

There are MCs, PFCs and TFCs in the CFQS as shown in Fig 3.2-1. The modular coils are a major part of coil system, they have the most complicate shape and largest total current, so our analysis focus on them. Table 3.2-1 shows the total current of each coil system.

Each coil name in the modular coil system is shown in Fig 3.2-2. In our analysis, the ANSYS Maxwell system was used to get the magnetic field distribution in the 3D space and the electric magnetic force (EMF) on the coil.

To make it easy for predicting the behavior of coils, the EM forces on MCs are roughly divided into centripetal (radial), toroidal, and vertical components based on a cylindrical coordinate system of Fig 3.2-3. For designing support structure, detail of the force components applied on the coil is required. The characteristics of each component are as follows.

- ❑ The centripetal force ; It is a component that tends to move the coil toward the center of the device. The torus device has a strong magnetic field on the center side. The centripetal force is mainly generated by the difference in hoop force between the center side and the outer side. In the TFC design of a tokamak, the supportig structure that withstands this component is most important.
- ❑ The toroidal force ; Sum of toroidal components that is a vertically symmetry component. It is caused by the coil being pulled from the neighbor. The tokamak does not generate this component because the TFC is pulled with the same force from the left and right.
- ❑ The vertical force ; This is sum of vertical components that is a vertically asymmetry component. Since the normal tokamak TFC is designed to have a vertically symmetrical shape, this component is small. Since the CFQS uses vertically asymmetric modular coils, it is necessary to design it in consideration of supporting this component.
- ❑ Overturning force ; A component that turns (rotates) the coil in the toroidal direction. It is mainly caused by the interaction of the TFC current and the PFC field in the tokamak. Since this force does not disappear even when the total force of the TFC is added, a large rotational moment is generated. In the TFC design of a tokamak, the supporting structure that withstands this component is very important. It is caused by vertical asymmetry of the coil shape in the CFQS. There is this component when we look at each coil, but the whole is canceled, and the rotational moment is lost.

3.2.2 Magnetic field and EM force distribution on the modular coils

Fig 3.2-4 to Fig 3.2-7 show the magnetic field and the EM force distribution on each coil. Here, the EM force is displayed as a vector graph of body force. The magnetic field on each coil is not uniform, and the magnetic field

strength on the inboard side is larger than on the outboard side. The maximum magnetic strength reaches about 2.17 T, which is located on the inboard side of the MC4. It is clearly seen by the magnetic field distribution that the EM force will be irregular on MCs during the machine operation. The EM force are larger on the high-field side of the MCs as we expected, but it is difficult to grasp their characteristics such as the direction of the force that deforms the coil. The different force components on the different type of coil are shown in Fig 3.2-8 to Fig 3.2-11. We can see that the main components are different for each coil.

3.2.3 Characteristics of the EM force

As we all know, the CFQS is a tokamak-like device, we summarized the characteristics of the CFQS in comparison with tokamak in Table 3.2-2. A comparison of the total values of the force components for the entire coil is shown in Table 3.2-3. From these table, we can understand the EM force components applied each coil. It will be helpful for us to design and improve our support structure.

But we need further observation because they show only components applied on gravity center of each coil. In Table 3.2-4, the features of each coil are organized and shown. Since a very large force, whose strength is equivalent to that of a large truck, acts on each coil, it is necessary to reduce the deformation with strong support. The MC1 and the MC2 are like the tokamak's TFC with large centripetal force, and the supporting structure for the component is important. The MC3 and the MC4 are special coils with large vertical and toroidal components. The diagonal force with the vertical and centripetal components is big enough not to ignore in the MC3, which requests the strong support resists the diagonal force. The EM force to the MC4 is relatively smaller than others, but it is estimated that it will be difficult to install support due to the large port nearby. The overturning force is applied due to asymmetry. Since it can be easily canceled by connecting the coils, it does not pose a big problem.

Table 3.2-1 Currents in different coils.

Coil type	Total current in a coil (kA Turns)	Number of coils	Total current (kA Turns)
MC	312.5	16	5,000
PFC	139	4	556
TFC	48	12	512

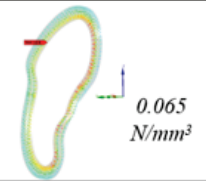
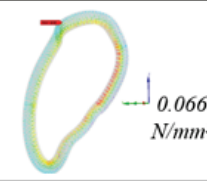
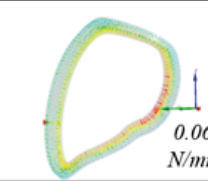
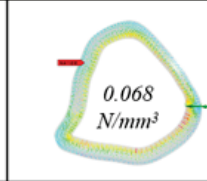
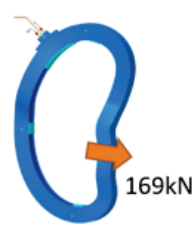
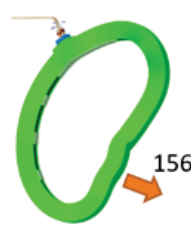
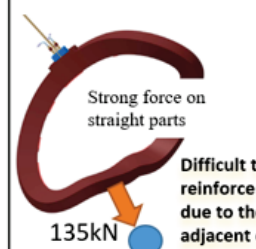
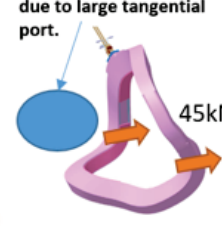
Table 3.2-2 Difference of EM force between tokamak and modular coil.

Force component	TFC for the Tokamak	MC for the CFQS
Vertical force	Small	Large on some coils (MC3)
Centripetal force	Very large	Large on some coils (MC1, MC2)
Toroidal force	Almost zero	Large on some coils (MC4)
Overturning force	Very large	Small (Canceled as all coils)

Table 3.2-3 Total EM force on the modular coil.

Coil name		MC1	MC2	MC3	MC4	Note	
Coil position	Cartesian coordinate	x(mm)	1202.9	973.4	593.3	207.0	
		y(mm)	215.1	582.5	801.3	891.5	
		z(mm)	52.5	146.1	165.5	75.9	
	Major radius	R(mm)	1222.0	1134.4	997.0	915.2	
	Toroidal angle	ϕ (degrees)	10.1	30.9	53.5	76.9	
EMF (N)		F_x	-162.46	-103.65	-29.39	34.56	
		F_y	-43.47	-106.26	-99.97	-49.27	
	Vertical	F_z	-18.70	-60.86	-93.46	-39.20	
	Horizontal	F_h	168.17	148.44	104.20	60.18	$\sqrt{F_x^2+F_y^2}$
	Centripetal	F_R	-167.57	-143.51	-97.84	-40.18	$F_x*\cos(\phi)+F_y*\sin(\phi)$
	Toroidal	F_T	-14.19	-37.95	-35.86	-44.81	$F_y*\cos(\phi)-F_x*\sin(\phi)$
	Total	F	169.21	160.43	139.97	71.83	$\sqrt{F_x^2+F_y^2+F_z^2}$
Proportion (%)	Vertical	P_z	11.1	37.9	66.8	54.6	$\text{abs}(F_z/F)$
	Centripetal	P_R	99.0	89.5	69.9	55.9	$\text{abs}(F_R/F)$
	Toroidal	P_T	8.4	23.7	25.6	62.4	$\text{abs}(F_T/F)$

Table 3.2-4 Characteristics of the EM force on the MCs.

		MC1	MC2	MC3	MC4
Maximum physical strength density					
	Total load	Absolute	169.2kN	160.1kN	140.0kN
Total load	Vertical	18.7kN	60.9kN	93.5kN	39.2kN
	Centripetal	167.6kN	143.5kN	97.8kN	40.2kN
	Toroidal	14.2kN	38.0kN	35.9kN	44.8kN
Features		Similar to D-type TFC Great centripetal force 	Similar to D-type TFC Great centripetal force 	Large diagonal force  Strong force on straight parts Difficult to reinforce due to the adjacent coil	Large toroidal force Difficult to reinforce due to large tangential port. 
		A large load equivalent to a large truck (10 to 20 tons) is applied to each coil.			
		Overturning force and vertical force are applied due to asymmetry. However, since it can be canceled by connecting the coils, it does not pose a big problem.			

The horizontal force that causes the centripetal force component is dominant in the MC1 and the MC2. The vertical force is big enough not to ignore in the MC3. The toroidal force of the MC4 is difficult to reinforce due to large tangential port.

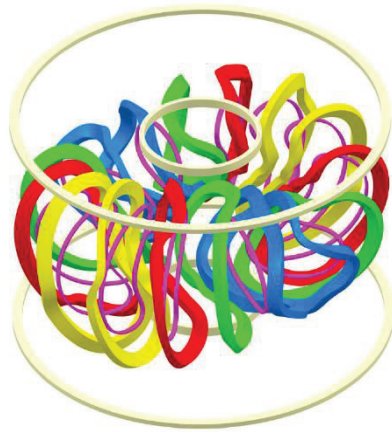


Fig 3.2-1 CFQS coil system. There are 4 types of the coil system. The light yellow indicates the PFC, the pink indicates the TFC, and others indicate the modular coil.

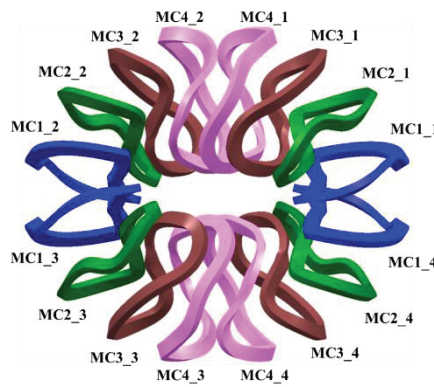


Fig 3.2-2 Top view of the modular coil system. The modular coil system consists of four types of coils, which are displayed with different colors.

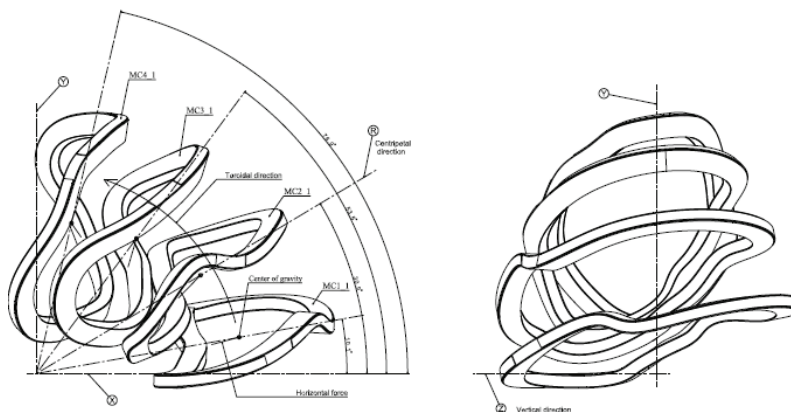


Fig 3.2-3 Definition of coordinate system.

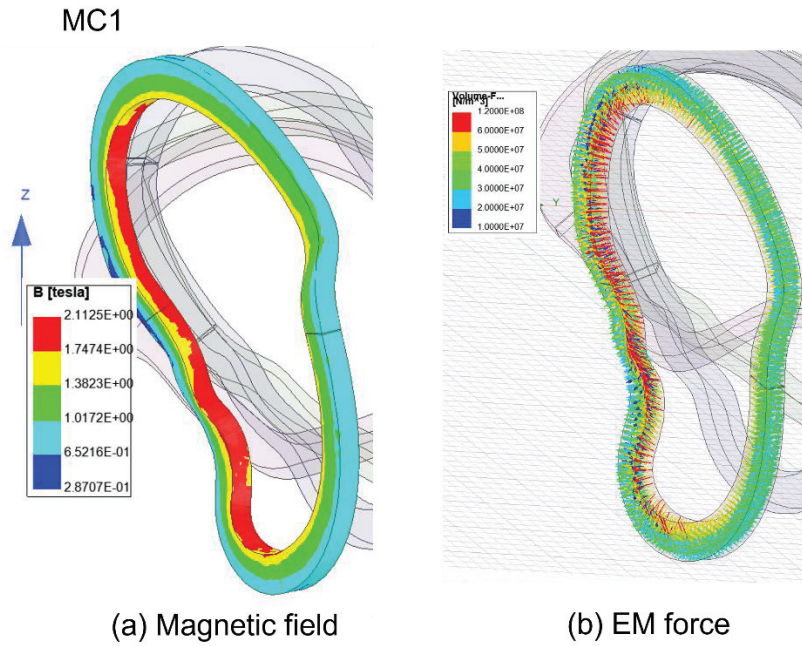


Fig 3.2-4 Distribution of the magnetic field and the EM force on the MC1 coil. The maximum magnetic strength reaches about 2.1 T, which is located on the inboard side. The EM force is large on the inboard side, but it is difficult to grasp its characteristics such as the direction of the force.

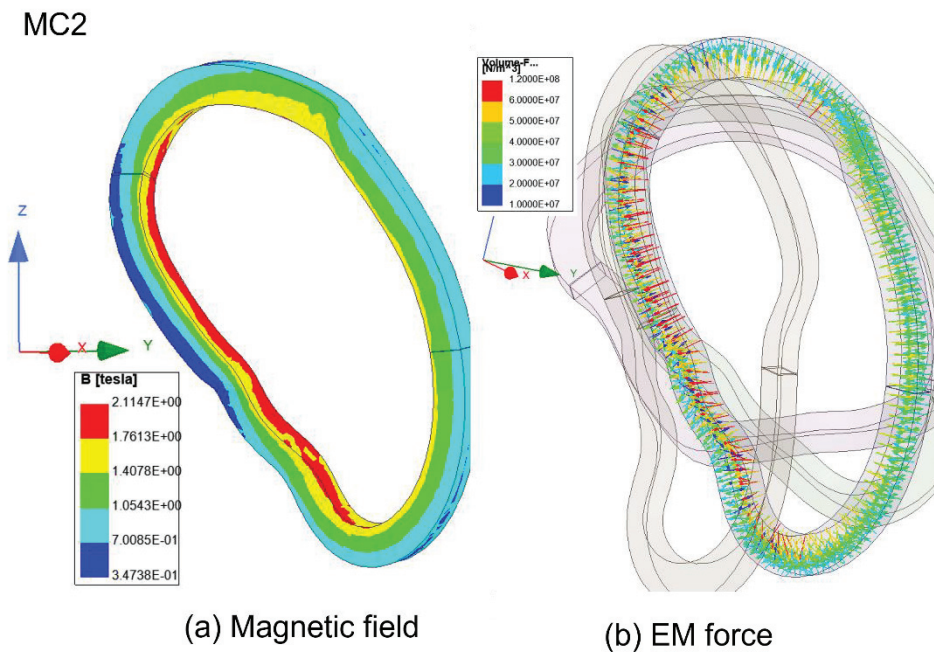


Fig 3.2-5 Distribution of the magnetic field and the EM force on the MC2 coil. The maximum magnetic strength reaches about 2.1 T, which is located on the inboard side. The EM force is large on the inboard side, but it is difficult to grasp its characteristics such as the direction of the force.

MC3

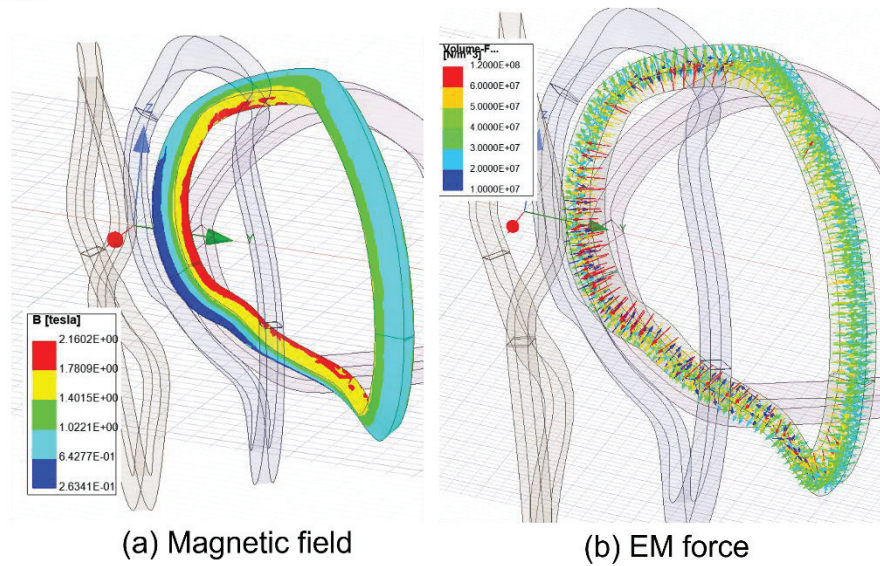


Fig 3.2-6 Distribution of the magnetic field and the EM force on the MC3 coil. The maximum magnetic strength reaches about 2.16 T, which is located on the inboard side. The EM force is large on the inboard side, but it is difficult to grasp its characteristics such as the direction of the force.

MC4

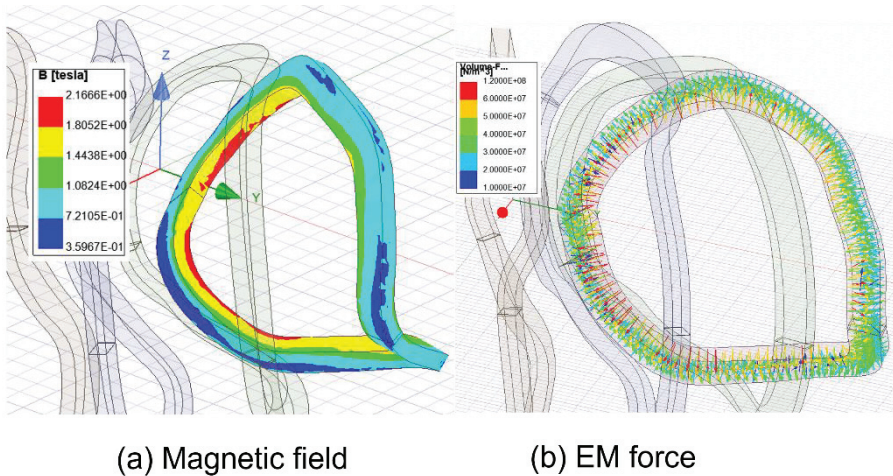
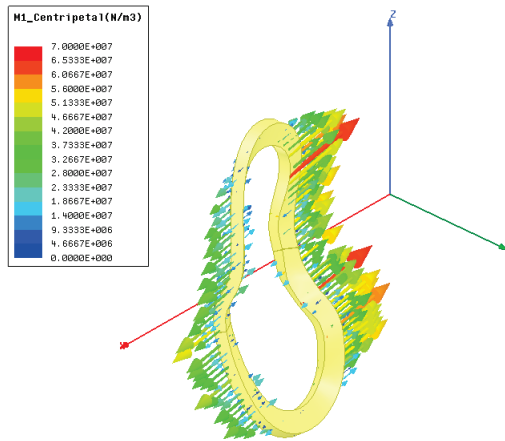
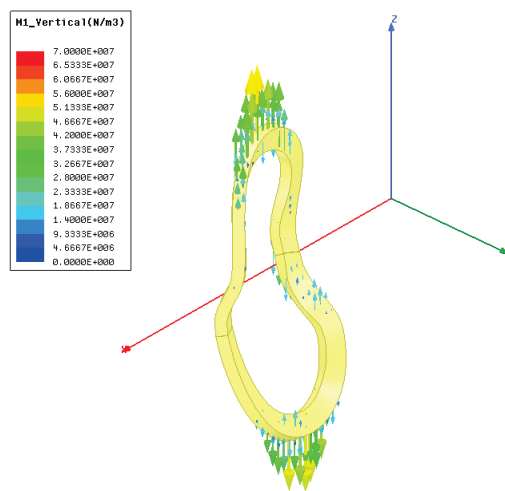


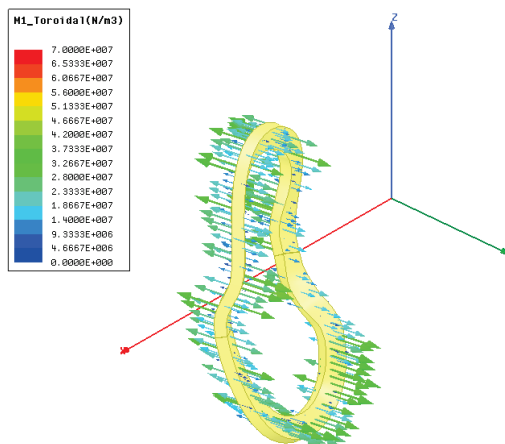
Fig 3.2-7 Distribution of the magnetic field and the EM force on the MC4 coil. The maximum magnetic strength reaches about 2.17 T, which is located on the inboard side. The EM force is large on the inboard side, but it is difficult to grasp its characteristics such as the direction of the force.



(a) Centripetal component.

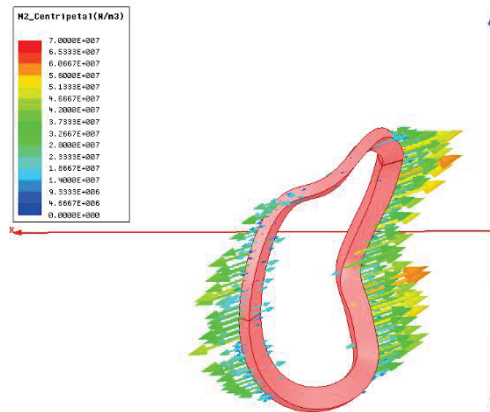


(b) Vertical component.

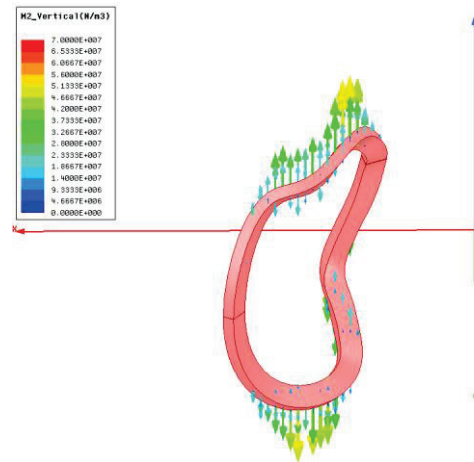


(c) Toroidal component.

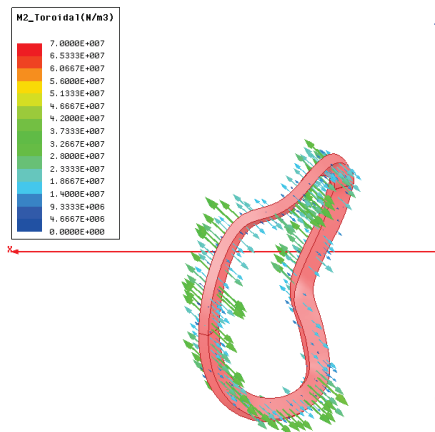
Fig 3.2-8 EM force on MC1. The centripetal component is dominant. The overturning component, which is generated by the vertical asymmetry of the toroidal component, is relatively small because of no PFC current.



(a) Centripetal component.

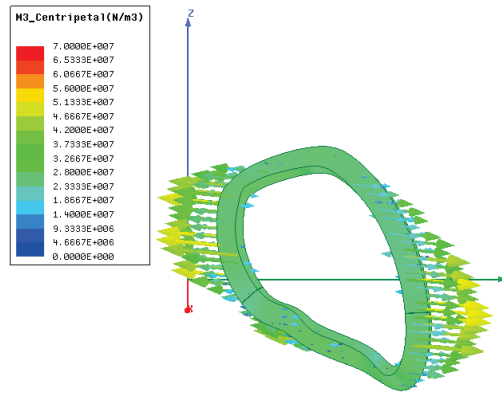


(b) Vertical component.

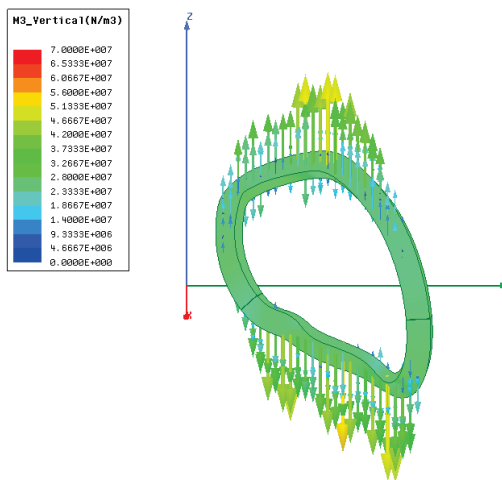


(c) Toroidal component.

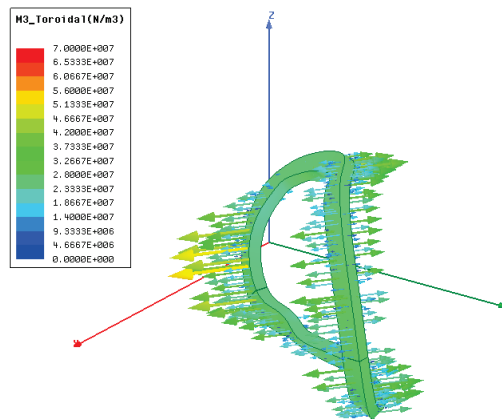
Fig 3.2-9 EM force on MC2. The centripetal component is dominant. The overturning component, which is generated by the vertical asymmetry of the toroidal component, is relatively small because of no PFC current.



(a) Centripetal component.

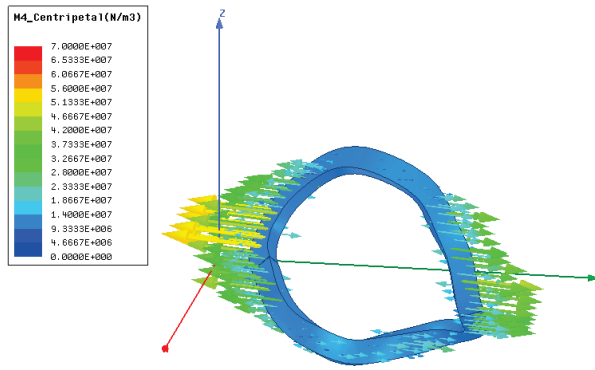


(b) Vertical component.

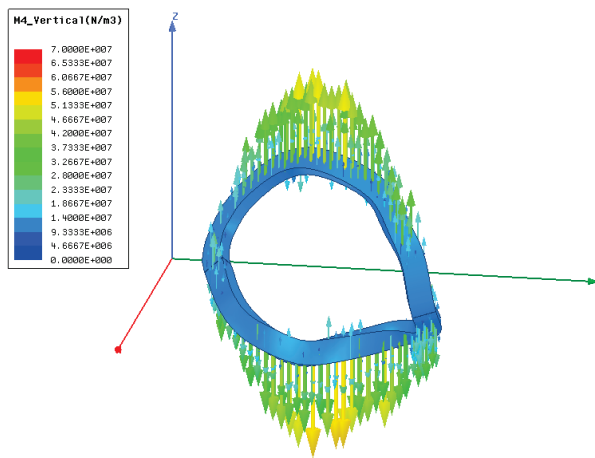


(c) Toroidal component.

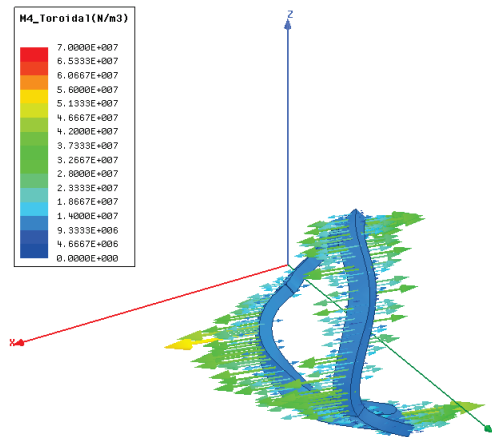
Fig 3.2-10 EM force on MC3. The vertical component is dominant. The overturning component, which is generated by the vertical asymmetry of the toroidal component, is relatively small because of no PFC current.



(a) Centripetal component.



(b) Vertical component.



(c) Toroidal component.

Fig 3.2-11 EM force on MC4. The toroidal component is dominant. The overturning component, which is generated by the vertical asymmetry of the toroidal component, is relatively small because of no PFC current.

3.3 Eddy current on the modular coil case (MC)

A time constant of an eddy current on a modular coil case was obtained. This analysis was performed preliminary for the design of continuous coil case. The time constant of the latest clamp type case is much shorter than the result of this analysis, so we would like to mention that it does not matter.

Fig 3.3-1 shows the MC4 for the eddy current analysis and its coil case. Thickness of the coil case is 13 mm and the material stainless steel. A current is applied in a cross section of the coil according to a waveform shown in Fig 3.3-2. The eddy current is obtained by integrating over a cross section. As a result, a time constant of the eddy current on coil case is estimated to be 2.5 ms, that is much shorter than the flat top length of the coil current. So, the effect of the coil case on the magnetic field is negligible.

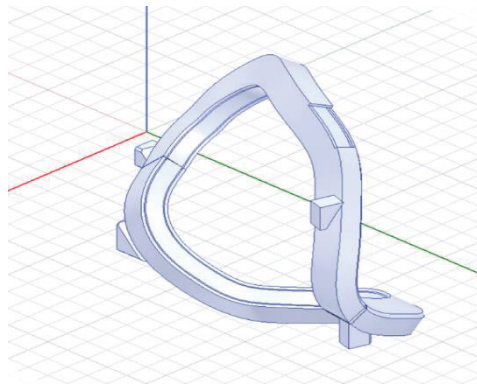


Fig 3.3-1 MC4 and its coil case. It is a C-type continuous shape of the coil case. Please note that this design is preliminary and is different from the latest design.

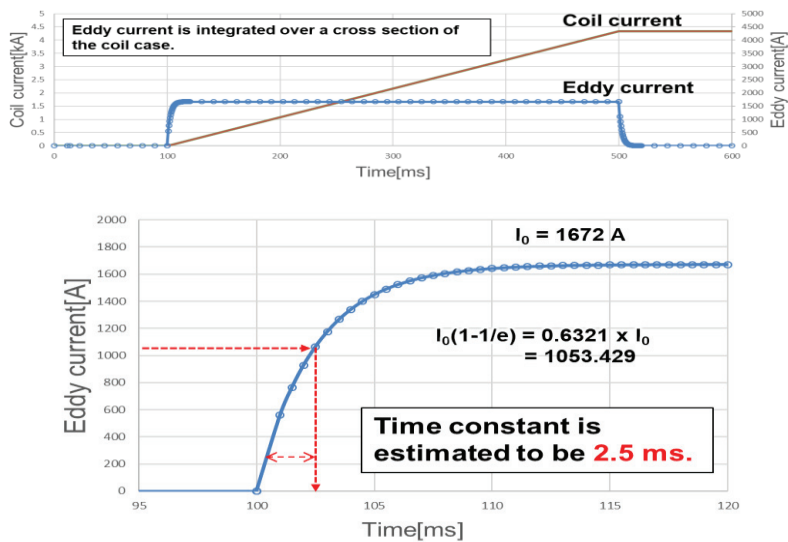


Fig 3.3-2 Time evolution of eddy current on the coil case. The time constant of 2.5 ms is much shorter than the flat top length of the coil current. The effect of the coil case on the magnetic field may be negligible.

3.4 Magnetic field distribution of the poloidal field coil (PFC)

The distribution of the magnetic field generated by PFC was calculated by the ANSYS/Maxwell. The results are shown in Fig 3.4-1 and Fig 3.4-2.

The magnetic field created by each coil varies from place to place. The IV generates a magnetic field of about 3 % (0.03 T) of the modular coil magnetic field and the OV of about 5 % (0.5 T) in the region where the equilibrium magnetic surface exists (about 0.5m around the magnetic axis $R = 1$ m). Originally, the toroidal ripple component ($B_{0,1}$ mode) which is the lowest order mode of the MC is up to 15 % of the toroidal magnetic field, and the other higher components are up to 3 %. Since the PFC can generate a magnetic field of the same magnitude as the higher-order mode, it is expected to be effective for deformation of the equilibrium magnetic surface.

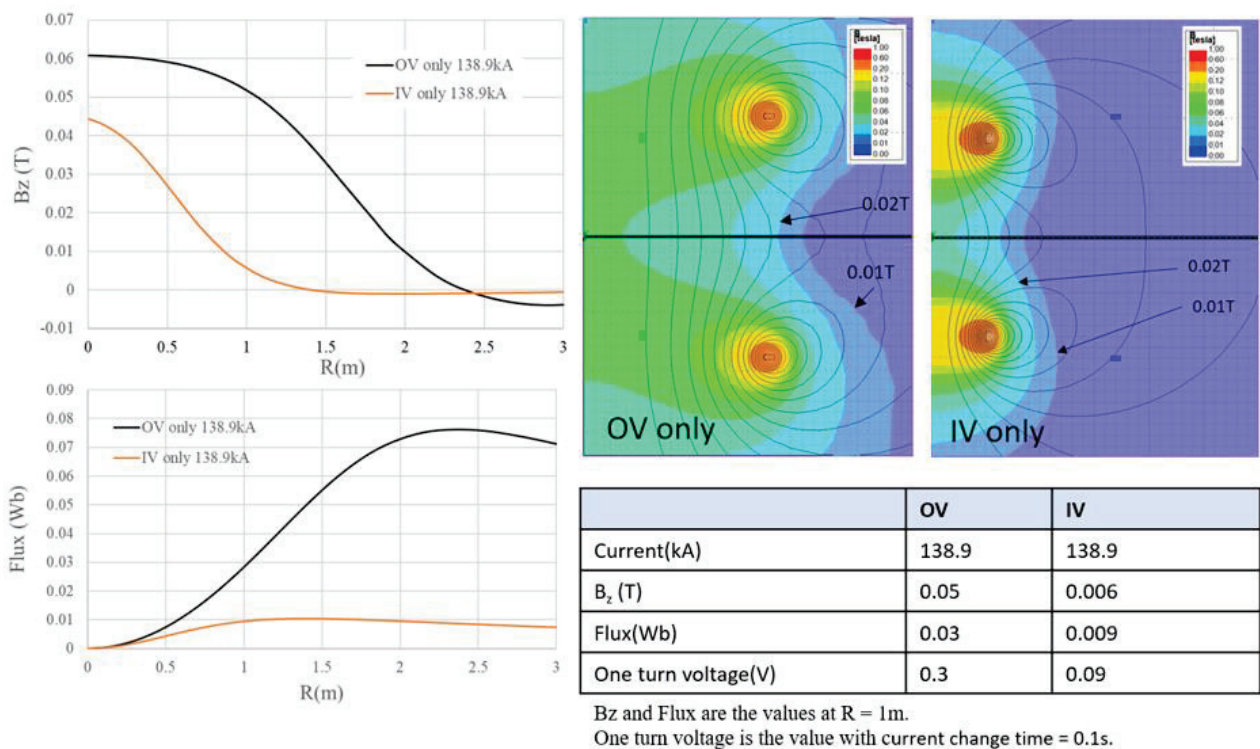


Fig 3.4-1 Magnetic field distribution of the IV and OV coil.

In the research field of tokamak fusion devices, the spatial distribution of the PFC magnetic field is represented by a set of typical magnetic field components called the functional magnetic fields, which often explains the effectiveness of equilibrium control. For example, the position of the magnetic axis is controlled by the uniform vertical magnetic field component B_V , and the ellipse of the plasma cross section is controlled by the quadruple vertical magnetic field component B_Q . In addition, if the induced voltage is calculated from the time change of the interlinkage flux, the influence on the plasma current can be evaluated.

The relationship between the functional magnetic field component of the PFC and the equilibrium of the modular coil device is not clear in theory, but it may be possible to expect the same effect as the tokamak device. Fig 3.4-2 shows the distribution of the functional magnetic field component. For example, if the B_V mode is changed to move the magnetic axis, a one-turn voltage is applied to the plasma. The magnitude of the voltage can be evaluated as

about 0.2 V when the coil current is changed at a high speed of about 0.1s. The effect of this voltage depends on the plasma temperature. It is difficult to evaluate the effect of the PFC on the plasma current when the rate of current change and the plasma temperature are not clear, but it seems that it cannot be ignored. In the case of CFQS, the B_V and B_Q components can be approximately controlled by adjusting the current ratio of the IV and OV currents. There is a mode in the tokamak that changes only the magnetic flux without the B_V and B_Q components (called OH mode), but the CFQS cannot control this component. Although the B_Q mode has a magnetic field distribution like that of the OH mode, the one-turn voltage may be small, so it is difficult to positively control the plasma current by the PFC.

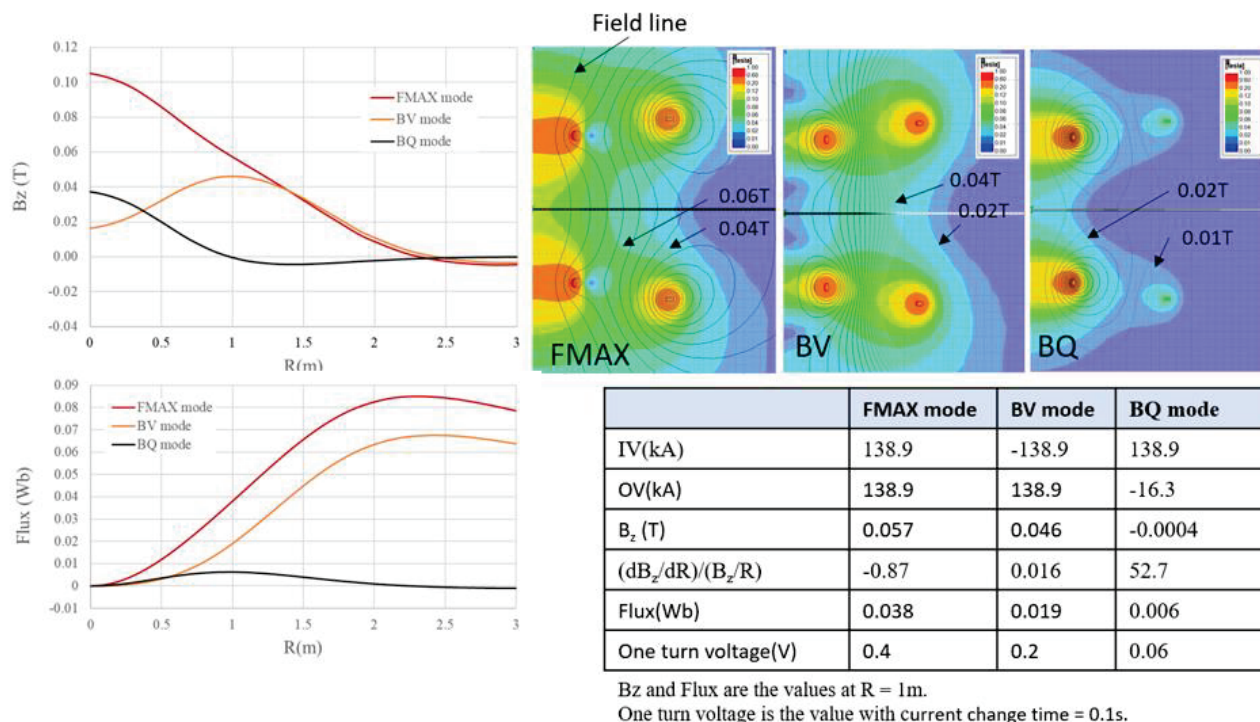


Fig 3.4-2 Magnetic field distribution of the control function produced by the PFC. FMAX is the mode with maximum magnetic flux, BV is the mode with small magnetic field change (the vertical magnetic field is uniform), and BQ is the mode with a large quadrupole component (the rate of spatial change in vertical magnetic field is large).

3.5 Magnetic field distribution and electromagnetic force of the toroidal field coil (TFC)

3.5.1 Magnetic field distribution

The distribution of the magnetic field generated by TFC was calculated by the ANSYS/Maxwell. The results is shown in Fig 3.5-1. The magnetic field created by each coil varies from place to place. The TFC system generates a magnetic field of about 10% (0.1T) of the modular coil magnetic field in the region where the equilibrium magnetic surface exists (about 0.5m around the magnetic axis $R = 1\text{m}$).

Name	Current
TFC10	32kA
TFC32	48kA
TFC70	48kA

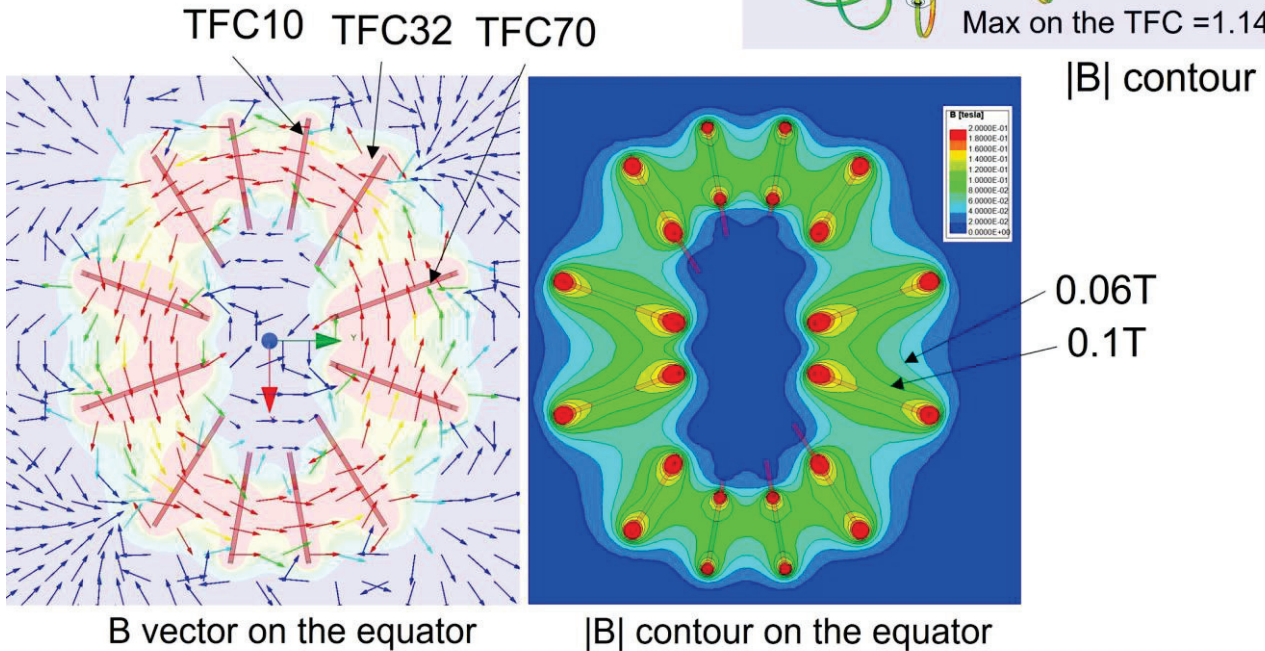
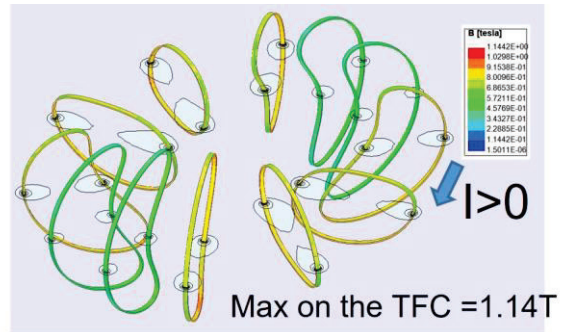


Fig 3.5-1 Magnetic field distribution of the TFC

3.5.2 Estimation of the magnitude and direction of the EM force

The EM force distribution of the toroidal filed coil system was obtained by the ANSYS/Maxwell to design the coil support. The analysis was performed on the following two cases.

- Case-1 ; Operation of the TFC alone for the heat run test etc. The hoop force may be mainly applied to the coil. It has a component in the direction of expanding the coil and is a self-load.
- Case-2 ; Operation in which the TFC and the MC current flows at the same time. The polarity of the TFC current is in the direction of increasing the rotational transform of the MC. Lorentz force ($I \times B$)

due to the TFC current and the MC magnetic field may act on the TFC. It has both the hoop force and the toroidal force, which has a component along the vacuum vessel surface.

The Ansys/Maxwell calculates the body force vector for the many and small elements, which are created by the automatic meshing function. Fig 3.5-2 shows the body force vectors for the case-1 as an example. Usually, the number of elements exceeds 10,000. By adding the body force vectors to the mesh element of structural analysis, it becomes possible to grasp the effect on the coil as a structure. However, since the body force vector has various directions and magnitudes for each small element, results with too many meshes do not help the designer.

Distribution of the force integrated over the coil cross section is required to derive the support requirements. Unfortunately, the ANSYS/Maxwell does not have the ability to integrate 3D vectors over a complex surface. Therefore, the coil was divided into suitable large parts, and the force was volume-integrated for each part. The shape of the model in which each TFC was divided into 10 parts are shown in Table 3.5-1 and Fig 3.5-3. These models were simplified to understand the characteristics of EM force distribution. The shape of the coil cross section was approximated by a circle with a diameter of 40 mm. The center line of a coil was a similar curve shifted by 20 mm from the vacuum vessel outer surface. In the structural analysis and the calculation of the EM force, other model with a rectangular cross section that reflects the actual shape will be developed.

The result of the EM force distribution is shown in Table 3.5-2, Table 3.5-3, and Fig 3.5-5. Here, the total force vector was obtained by the volume integral function of the ANSYS/Maxwell. The surface force density was calculated by the coordinate transformation. The f_n shows the normal component and the f_b shows the binormal component. The normal component is the hoop force of the planer coil and the binormal component is difference in force pulled from the left and right coils.

3.5.3 Consideration related to support design

The normal force f_n of 1500 to 4000 N/m for the case-1 is not much larger than the hoop force of a standard large circular coil. The polarity of f_n is positive, that is, the coils will be spread. The convex part of the coil (outboard side of TFC10 and TFC32, and all TFC72) may be supported only by the tensile stiffness of conductor. The concave part (inboard side of the TFC10 and TFC32) must be pressed against the vacuum vessel with clamps because the compressed force is applied to the conductor. Since the binormal force f_b of 500 N/m is not so large, deformation may be easily prevented by fixing the coil with clamps.

The polarity of f_n for the case-2 is negative, that is, the coils will be pressed against the vacuum vessel. The deformation of the coil due to this force may be supported by the vacuum vessel. Since the binormal force f_b of -20,000~40,000 N/m is very large, the coils may be displaced in the toroidal direction over the vacuum vessel. A reinforcing mechanism for toroidal displacement (referred to as a side stopper) is very important.

If the direction of the TFC current is reversed in the case-2, very large tensile force of 20,000 to 50,000 N/m will be applied to the coil. It is difficult to support this level of force solely by the rigidity of the conductor. To support this force, it is necessary to cover the entire coil with a case, but it seems difficult to realize because the structure is complicated.

Based on the above considerations, the support will be designed considering only the TFC only operation (the

case-1) and the TFC current in the direction of reducing rotational transform (the case-2).

Table 3.5-1 Coordinate of the nodes dividing the TFC.

Coil name	Node name	Coordinate (mm)		
		X	Y	Z
TFC10	N1	1559.8	275.0	0.0
	N2	1471.5	259.5	316.9
	N3	1239.5	218.6	548.1
	N4	928.6	163.7	641.0
	N5	837.3	147.6	402.7
	N6	1008.6	177.9	118.6
	N7	1033.5	182.2	-205.3
	N8	946.9	167.0	-522.2
	N9	1236.9	218.1	-543.4
	N10	1472.6	259.7	-317.1
TFC32	N1	1296.0	809.8	0.0
	N2	1202.7	751.5	284.8
	N3	1012.3	632.6	493.3
	N4	768.3	480.1	598.7
	N5	540.0	337.4	505.3
	N6	643.6	402.1	234.8
	N7	812.7	507.9	-0.3
	N8	891.7	557.2	-289.4
	N9	1035.6	647.1	-474.9
	N10	1240.9	775.4	-295.7
TFC70	N1	477.6	1312.2	0.0
	N2	431.5	1185.6	211.3
	N3	359.5	987.6	348.7
	N4	275.5	756.8	404.9
	N5	191.9	527.3	355.1
	N6	158.9	436.5	136.8
	N7	197.9	543.8	-83.7
	N8	274.6	754.5	-194.4
	N9	360.5	990.5	-223.3
	N10	446.4	1226.5	-204.6

The center line of the coil cross section is a similar curve shifted by 20 mm from the outer surface of the vacuum vessel.

Table 3.5-2 EMF distribution of the TFC in the TFC only operation.

Current of the MCs = 0 kA

Coil	Coil positoin ϕ (Deg)	Part name	Arc length Δs (m)	Total force for each part (N)			Avarage force density (N/m)					
				Fx	Fy	Fz	fx	fy	fz	fR	fn	fb
TFC10 (-2kA) (-32kAT)	10	P1	0.3334	434.6	84.1	127.5	1,303.6	252.3	382.3	1,327.6	1,381.5	22.1
		P2	0.3334	329.1	75.9	346.0	987.1	227.5	1,037.8	1,011.6	1,449.2	52.7
		P3	0.3334	134.6	89.5	539.5	403.6	268.5	1,618.3	444.1	1,678.1	194.3
		P4	0.3334	-652.9	-104.1	249.5	-1,958.3	-312.3	748.4	-1,982.8	2,119.3	32.5
		P5	0.3334	-558.4	-151.9	-353.7	-1,674.7	-455.7	-1,060.8	-1,728.4	2,028.0	-157.9
		P6	0.3334	-488.1	-111.0	-38.7	-1,464.1	-333.0	-116.1	-1,499.7	1,504.2	-73.7
		P7	0.3334	-685.3	-123.6	169.6	-2,055.4	-370.6	508.6	-2,088.6	2,149.6	-8.1
		P8	0.3334	-112.2	-38.0	-678.6	-336.5	-114.0	-2,035.5	-351.2	2,065.5	-53.8
		P9	0.3334	353.9	46.4	-382.3	1,061.3	139.1	-1,146.6	1,069.4	1,567.9	-47.3
		P10	0.3334	458.5	76.7	-127.3	1,375.2	230.0	-381.9	1,394.2	1,445.6	-12.3
TFC32 (-3kA) (-48kAT)	32	P1	0.3085	687.2	350.7	296.2	2,227.4	1,136.8	960.0	2,491.4	2,669.9	-216.3
		P2	0.3085	504.1	259.0	611.5	1,634.0	839.4	1,982.2	1,830.5	2,698.1	-154.0
		P3	0.3085	273.1	130.0	841.9	885.2	421.3	2,729.0	974.0	2,897.6	-111.8
		P4	0.3085	-386.5	-262.4	1,092.3	-1,252.9	-850.4	3,540.7	-1,513.2	3,850.5	-57.3
		P5	0.3085	-860.7	-723.0	-437.0	-2,790.0	-2,343.7	-1,416.4	-3,608.0	3,876.0	-509.1
		P6	0.3085	-402.5	-468.0	-501.0	-1,304.7	-1,516.9	-1,624.1	-1,910.3	2,507.4	-595.0
		P7	0.3085	-399.5	-413.3	-165.5	-1,294.9	-1,339.6	-536.4	-1,808.0	1,885.9	-449.9
		P8	0.3085	-682.9	-511.9	-881.1	-2,213.5	-1,659.4	-2,856.2	-2,756.5	3,969.4	-234.3
		P9	0.3085	552.3	277.9	-863.7	1,790.4	900.7	-2,799.8	1,995.6	3,438.2	-184.9
		P10	0.3085	779.6	413.7	-195.6	2,526.9	1,340.9	-634.2	2,853.5	2,923.2	-201.9
TFC70 (-3kA) (-48kAT)	70	P1	0.2531	213.2	621.0	410.4	842.2	2,453.5	1,621.3	2,593.6	3,058.7	47.7
		P2	0.2531	131.2	369.4	596.1	518.5	1,459.3	2,355.1	1,548.7	2,818.7	11.9
		P3	0.2531	13.5	171.6	732.7	53.5	678.1	2,894.7	655.5	2,968.0	181.6
		P4	0.2531	-100.2	-168.4	857.7	-395.7	-665.5	3,388.9	-760.7	3,473.3	144.2
		P5	0.2531	-323.9	-823.9	393.0	-1,279.8	-3,255.4	1,552.6	-3,496.8	3,826.0	89.2
		P6	0.2531	-254.6	-804.0	-439.2	-1,005.9	-3,176.5	-1,735.4	-3,329.0	3,754.2	-141.2
		P7	0.2531	-98.5	-394.6	-799.8	-389.0	-1,559.2	-3,160.2	-1,598.2	3,541.3	-167.8
		P8	0.2531	-2.2	-88.4	-710.3	-8.6	-349.2	-2,806.2	-331.1	2,825.7	-111.4
		P9	0.2531	42.4	56.1	-772.3	167.5	221.7	-3,051.3	265.6	3,062.9	-81.6
		P10	0.2531	314.9	878.8	-434.5	1,244.3	3,472.1	-1,716.8	3,688.3	4,068.3	18.2
Method of calculation		By CATIA	By ANSYS/MAXWELL			Fx/ Δs	Fy/ Δs	Fz/ Δs	By coordinate transformation			

Table 3.5-3 EMF distribution of the TFC with the MC field.

Current of the MCs = 4.34 kA (312.48kAT) $B_{\theta MC} = 1T$, $B_{\theta TC}/B_{\theta MC} < 0$

Coil	Coil positoin ϕ (Deg)	Part name	Arc length Δs (m)	Total force for each part (N)			Avarage force density (N/m)					
				Fx	Fy	Fz	fx	fy	fz	fR	fn	fb
TFC10 (-2kA) (-32kAT)	10	P1	0.3334	-8,581.0	-2,055.0	-2,493.6	-25,737.7	-6,163.6	-7,479.3	-26,417.0	-27,455.4	-1,600.7
		P2	0.3334	-5,653.8	-1,297.9	-5,824.0	-16,957.9	-3,892.9	-17,468.4	-17,376.3	-24,639.0	-889.0
		P3	0.3334	-2,244.3	240.9	-7,460.7	-6,731.4	722.6	-22,377.6	-6,503.7	-23,303.5	1,880.5
		P4	0.3334	6,110.7	5,485.8	-1,992.0	18,328.3	16,454.2	-5,974.9	20,907.1	-21,744.1	13,021.5
		P5	0.3334	8,251.1	6,113.9	5,619.1	24,748.5	18,338.1	16,854.0	27,556.9	-32,302.3	13,761.9
		P6	0.3334	11,466.4	3,566.3	794.1	34,392.4	10,696.8	2,381.7	35,727.4	-35,806.7	4,562.1
		P7	0.3334	10,248.9	-1,160.5	-2,742.2	30,740.6	-3,480.8	-8,225.0	29,669.1	-30,788.1	-8,766.0
		P8	0.3334	1,192.1	-2,209.9	7,421.8	3,575.7	-6,628.3	22,261.0	2,370.4	-22,386.9	-7,148.5
		P9	0.3334	-4,659.1	-2,336.9	5,329.5	-13,974.6	-7,009.4	15,985.2	-14,979.5	-21,906.9	-4,476.2
		P10	0.3334	-7,640.4	-2,631.3	2,110.3	-22,916.7	-7,892.4	6,329.7	-23,939.0	-24,761.7	-3,793.1
TFC32 (-3kA) (-48kAT)	32	P1	0.3085	-9,908.3	-5,867.7	-4,361.4	-32,117.7	-19,020.2	-14,137.4	-37,316.5	-39,904.8	889.8
		P2	0.3085	-6,682.4	-3,715.7	-8,181.3	-21,660.9	-12,044.3	-26,519.6	-24,752.0	-36,276.0	1,264.3
		P3	0.3085	-1,866.9	-4,336.1	-10,643.8	-6,051.4	-14,055.3	-34,501.6	-12,580.1	-36,723.6	-8,712.8
		P4	0.3085	2,895.4	1,353.1	-10,097.7	9,385.3	4,386.1	-32,731.6	10,283.5	-34,309.0	-1,253.8
		P5	0.3085	4,198.4	14,245.9	5,247.3	13,609.2	46,177.8	17,009.2	36,011.8	-39,826.6	31,949.2
		P6	0.3085	4,747.8	13,365.1	9,306.3	15,389.9	43,322.9	30,166.3	36,009.0	-46,975.0	28,584.5
		P7	0.3085	10,872.8	10,599.0	4,730.7	35,243.9	34,356.7	15,334.4	48,094.8	-50,480.2	10,459.7
		P8	0.3085	8,828.2	-254.5	5,830.4	28,616.5	-825.1	18,899.3	23,831.0	-30,415.4	-15,864.1
		P9	0.3085	-3,983.5	-6,358.8	8,951.1	-12,912.6	-20,611.9	29,014.8	-21,873.2	-36,335.8	-10,637.3
		P10	0.3085	-9,318.4	-7,956.4	2,554.5	-30,205.6	-25,790.5	8,280.5	-39,282.7	-40,145.9	-5,865.1
TFC70 (-3kA) (-48kAT)	70	P1	0.2531	-2,511.2	-8,051.2	-5,265.5	-9,921.7	-31,810.4	-20,803.9	-32,285.4	-39,252.0	-1,556.4
		P2	0.2531	370.2	-5,430.2	-7,608.8	1,462.8	-21,454.6	-30,062.6	-19,660.4	-35,920.6	-8,712.5
		P3	0.2531	2,197.3	-3,177.1	-9,969.0	8,681.5	-12,552.7	-39,387.8	-8,826.4	-40,364.6	-12,451.2
		P4	0.2531	5,510.2	213.9	-10,218.4	21,770.9	845.0	-40,373.0	8,240.1	-41,205.3	-20,169.0
		P5	0.2531	4,920.3	7,461.0	-3,862.0	19,440.3	29,478.5	-15,258.6	34,349.7	-37,586.2	-8,185.6
		P6	0.2531	-3,486.2	10,490.5	4,355.2	-13,774.1	41,448.2	17,207.3	34,237.5	-38,318.4	27,119.5
		P7	0.2531	-5,918.8	6,642.0	8,686.1	-23,385.1	26,242.6	34,318.6	16,661.8	-38,149.5	30,950.3
		P8	0.2531	-2,037.0	2,240.3	11,562.8	-8,048.1	8,851.6	45,684.9	5,565.1	-46,022.6	10,590.1
		P9	0.2531	1,573.8	-1,231.1	9,266.1	6,218.2	-4,864.0	36,610.4	-2,443.9	-36,691.8	-7,506.8
		P10	0.2531	-815.6	-6,903.8	2,518.1	-3,222.5	-27,276.8	9,948.8	-26,734.0	-28,525.2	-6,301.0
Method of calculation		By CATIA	By ANSYS/MAXWELL			Fx/ Δs	Fy/ Δs	Fz/ Δs	By coordinate transformation			

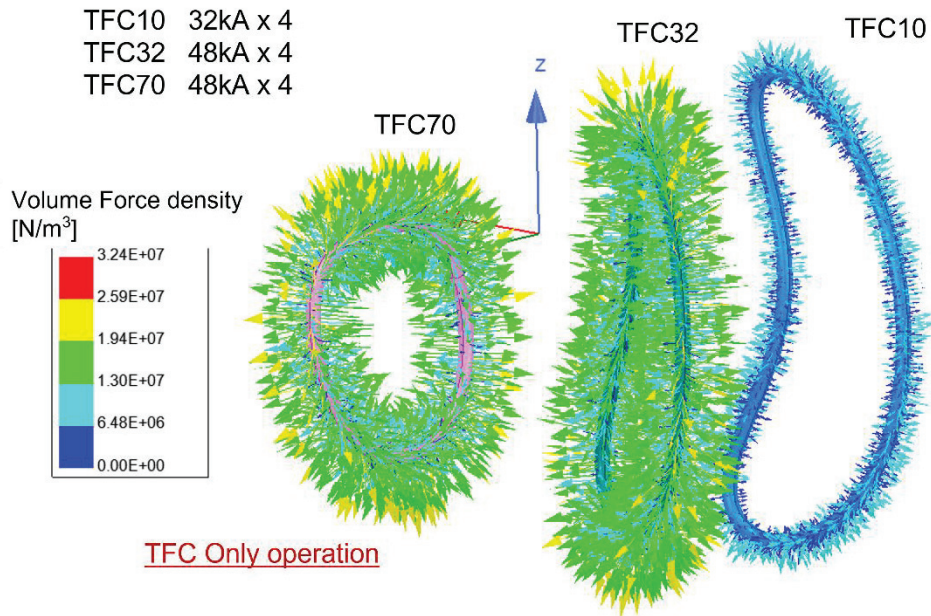


Fig 3.5-2 The body force vectors for the TFC only operation as an example. Since the body force vector has various directions and magnitudes for each small element, results with too many meshes do not help the designer.

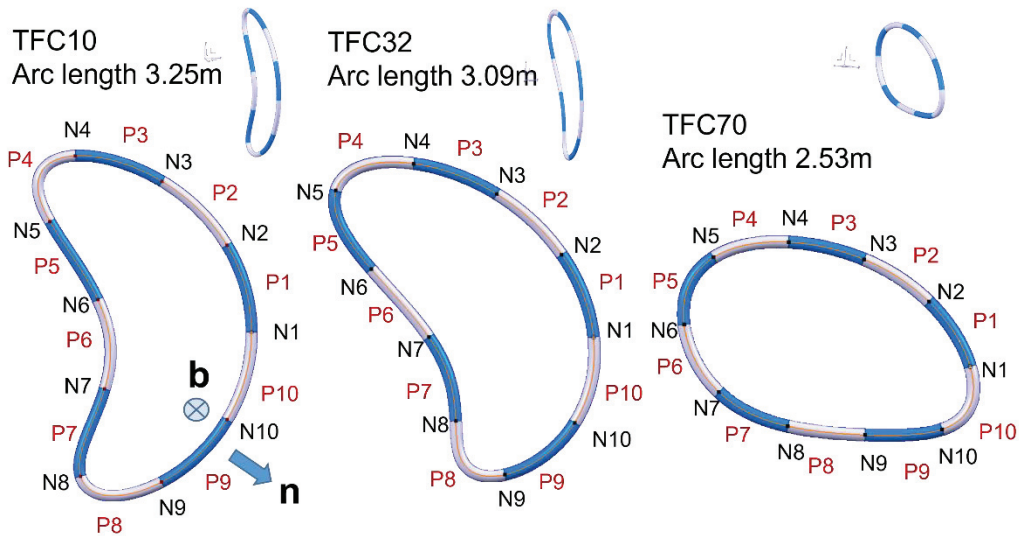


Fig 3.5-3 The shape of the model in which each TFC is divided into parts with appropriate size. The number of divisions is 10 each, and the cross section of the coil is approximately represented by a circle with a diameter of 40 mm. The center line of the coil cross section is a similar curve shifted by 20 mm from the outer surface of the vacuum vessel. The n is the normal vector which corresponds to the hoop force, and the b is the binormal vector which corresponds to the toroidal force. The N1~N10 is the name of the nodes and P1~P10 is the name of the parts by dividing the TFC.

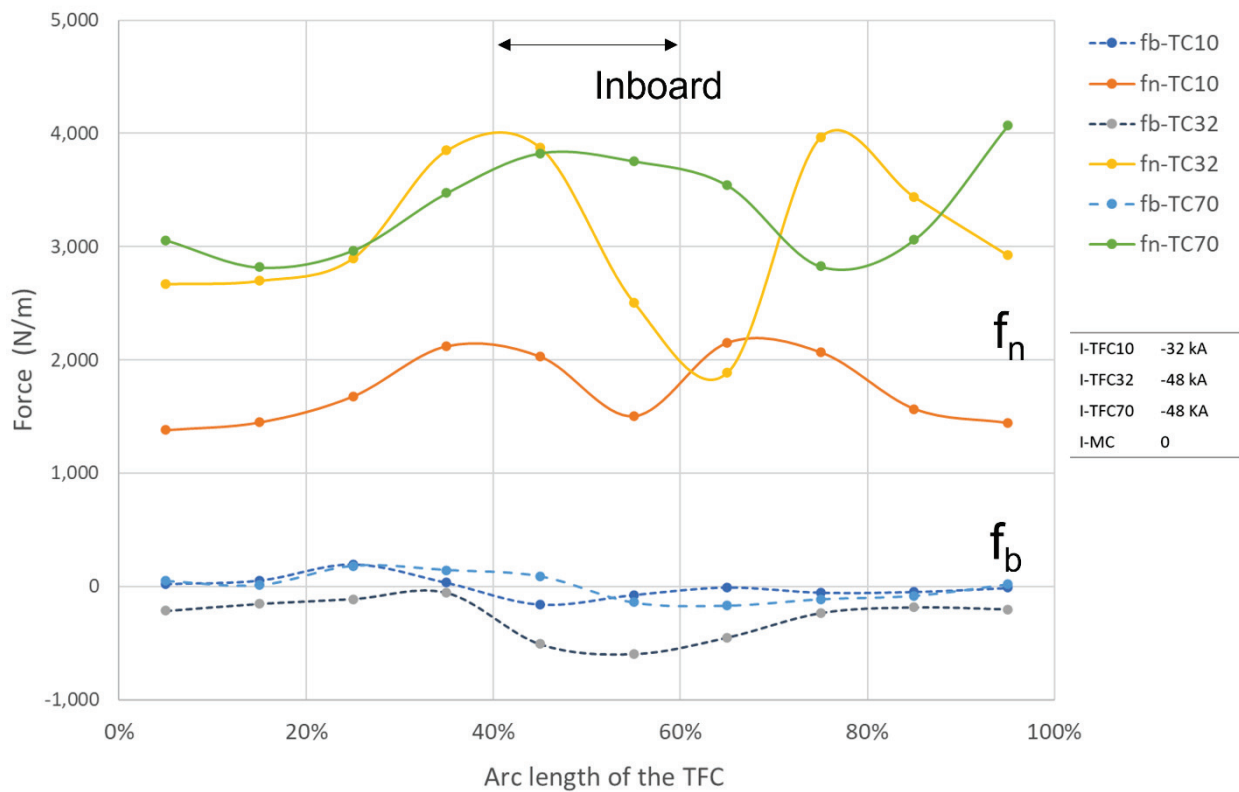


Fig 3.5-4 EMF distribution of the TFC in the TFC only operation which may be carried out for the heat run test. The f_n shows the normal component and the f_b shows the binormal component. The normal component is the hoop force of the planer coil and the binormal component is difference in force pulled from the left and right coils. Since the f_n of 1500 to 4000 N/m is not much larger than the hoop force of a standard large circular coil, the convex part (outboard side of TFC10 and TFC32 and TFC72) may be supported only by the tensile stiffness of conductor). It seems that the concave part (inboard side of the TFC10 and TFC32) needs to be pressed against the vacuum vessel with clamps. Since the f_b of 500 N/m is not so large, deformation may be easily prevented by fixing the coil with clamps.

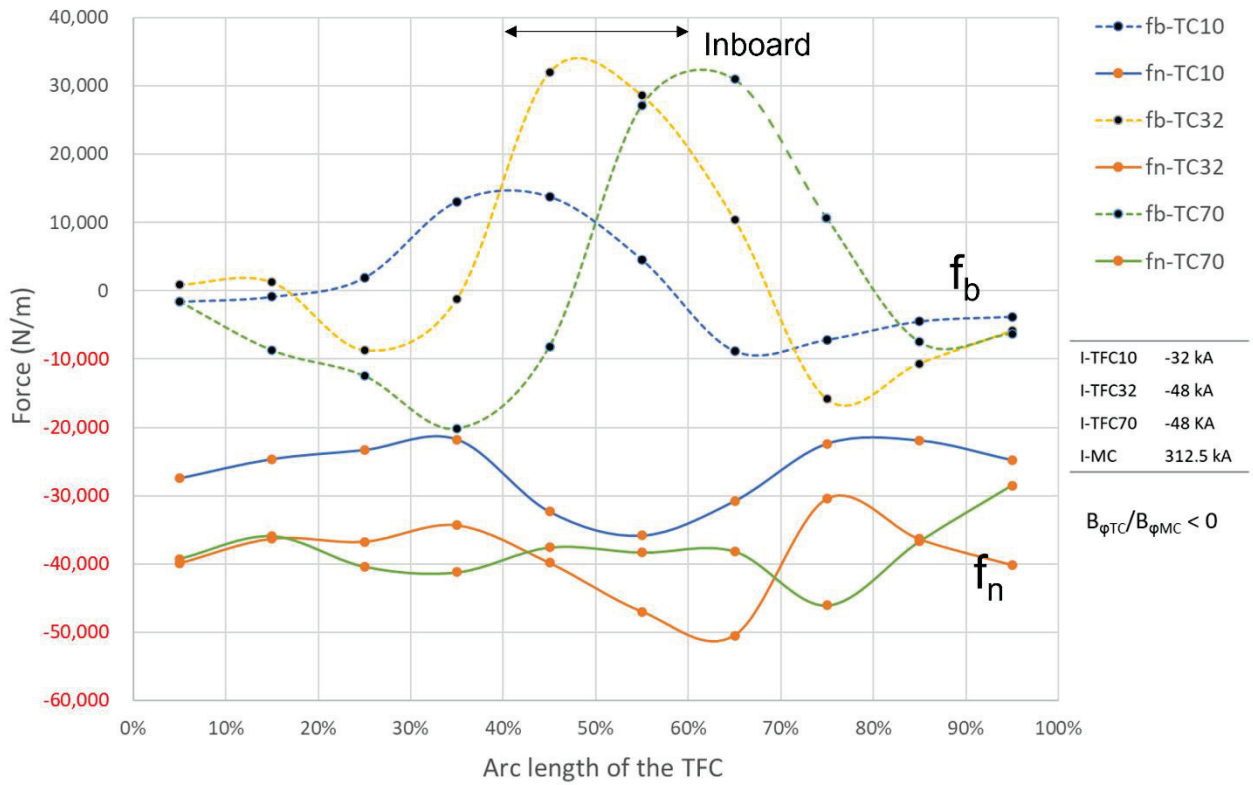


Fig 3.5-5 EMF distribution of the TFC with the MC magnetic field. The polarity of the TFC current is in the direction of increasing the rotational transform of the MC. The f_n shows the normal component and the f_b shows the binormal component. The polarity of f_n is negative, that is, the coils will be pressed against the vacuum vessel. Since the f_b of $-20,000 \sim 40,000$ N/m is very large, the coils may be displaced in the toroidal direction over the vacuum vessel. A reinforcing mechanism for toroidal displacement (referred to as a side stopper) is important.

3.6 Stress analysis of the modular coil with the support structure

3.6.1 Summary

A strong support structure is necessary for keeping device in a safety state when operating it. As for magnetic confinement fusion device, the EM force is the main load on coil system, which is the key component of whole device. Therefore, we need to understand the EM force on coil system and then design a reliable support structure. There are three types of coils in CFQS, MC, PFC and TFC. The MC is a major part of coil system. It has the most complicate shape and largest total current, so our analysis mainly focuses on them.

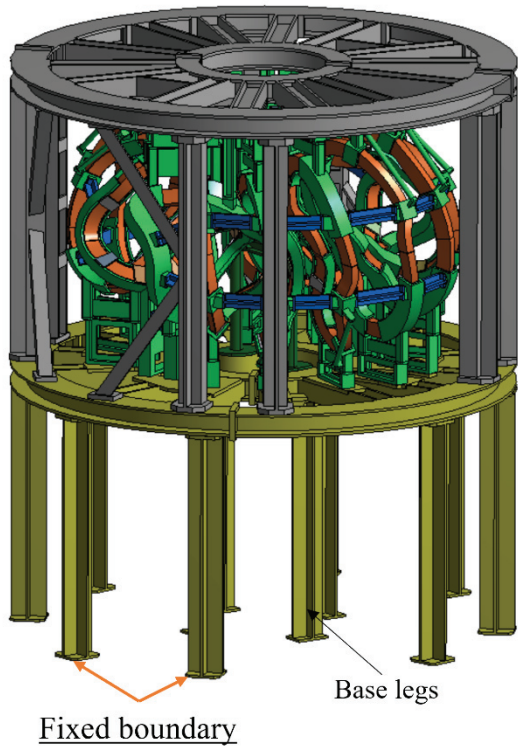
The finite element analysis has been widely used for structural analysis in many fusion devices. Usually, the analysis result is considered as a reference to estimate the quality of the supporting structure design and help designers to make optimization. Here, previous result of EM force analysis by the ANSYS/Maxwell was coupled into ANSYS mechanical, and deformation and von-Mises stress were evaluated. As a result, we have confirmed the design validity of the modular coil system with a mechanical support.

3.6.2 Model of the analysis

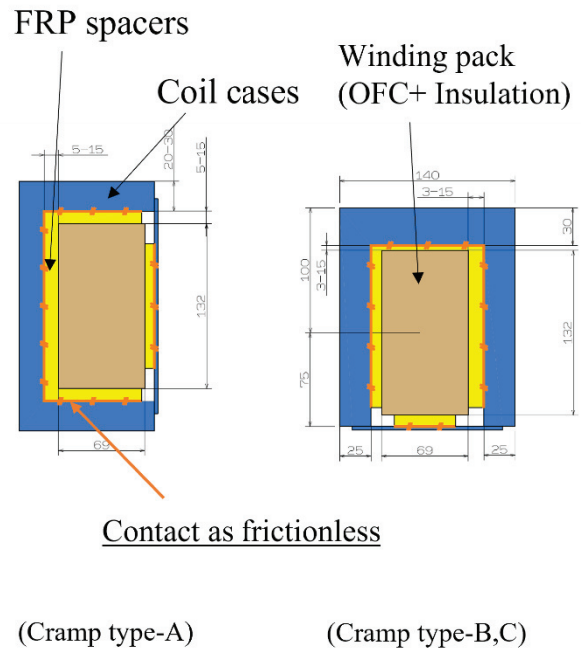
Fig 3.6-1 shows the model of the modular coil system with the supporting structure. The main points of modeling are shown below.

- The vacuum vessel is not included in this calculation.
- The bottom surface of twelve legs is set as fixed boundary.
- All parts are bonded together except for the coil case and the FRP spacer. Actually, the FRP spacer will be bonded to the coil case with resin, but it may peel off due to aging deterioration, so the contact condition with frictionless is assumed to get the property of the supporting structure in the worst situation.
- The Young's modulus of the winding packs is 110 GPa(OFC with isolation).
- The Young's modulus of others is 193 GPa (SUS).
- The Young's modulus of FRP is set to 1 GPa to eliminate the effect of higher rigidity, which is extremely smaller than the actual value of 100 GPa. In the real situation, the FRP spacer will be divided into small pieces and inserted, but in our simulation, the FPR spacers have to be a simplified continuous model. Since the continuous spacer may have higher rigidity than the splitted spacers, the Young's modulus is reduced so that a large displacement could be obtained.

In our design, lots of small parts are used in supporting coil system. To analyze the result, we divided whole structure into three major parts, a) support frame, b) center support, c) coil support. Fig 3.6-2 shows the three major parts. According to previous result of EM force analysis, these three parts support different force components. The support frame is mainly used for supporting vertical force and whole device. The center support resists the large centripetal force. The coil support resists the toroidal force, overturning force, and coil's bending.

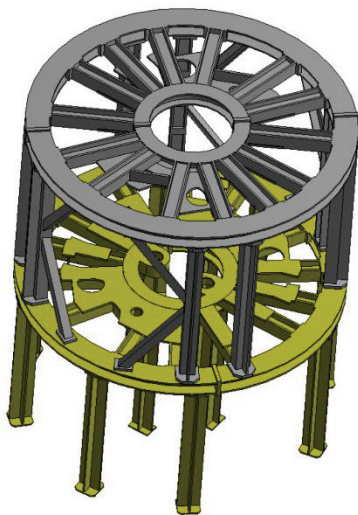


(a) Simplified global model



(b) Simplified winding pack

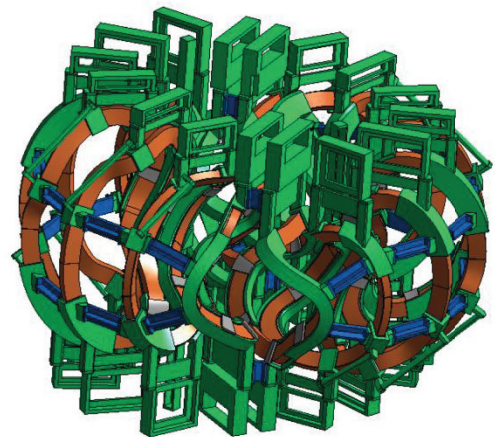
Fig 3.6-1 Model of the modular coil with supporting for the stress analysis. (a) Simplified global model, (b) Simplified winding pack and coil case. A bottom surface of twelve base legs is set as fixed boundary. A contact surface of the coil cases and the FRP spacers is set as the contact condition with frictionless.



(a) Support frame



(b) Center support



(c) Coil support and modular coils

Fig 3.6-2 Three major parts of the supporting structure. (a) Support frame, (b) Center support, (c) Coil support.

3.6.3 Results of the analysis

The two contour plots in Fig 3.6-3 show the relevant result about the winding pack. The distribution of deformation on winding pack indicates that the maximum deformation is about 1.477 mm, which occurs on the MC2. The maximum deformation is about 1.148 mm on the coil support. They are a little larger than the design target of 1mm, but it is not extreme, so we consider that the deformation will not affect the property of the entire MC system significantly. The maximum stress on the winding pack is about 63 MPa. It is located on the MC3, and less than the yield strength of 80 MPa. In the winding pack, the coils are formed by two parts, *i.e.*, OFC and resin insulation. But in this simulation the coils are replaced by one composite material. The design value for stress of 30 MPa should be satisfied if possible. The distribution of the stress indicates that it seems difficult to achieve it, but the value is in the tolerable range.

To make sure the support structure is reliable, we need to check the stress of the device. Fig 3.6-4 to Fig 3.6-7 show the stress distribution on the supporting structure. It is obvious that the maximum stress on the supporting structure is 133 MPa in the coil support. The maximum stress is located near the edge of the coil case for the MC3. The results indicate that the property of the supporting structure satisfies our design guideline for the SUS316 of 137 MPa or less.

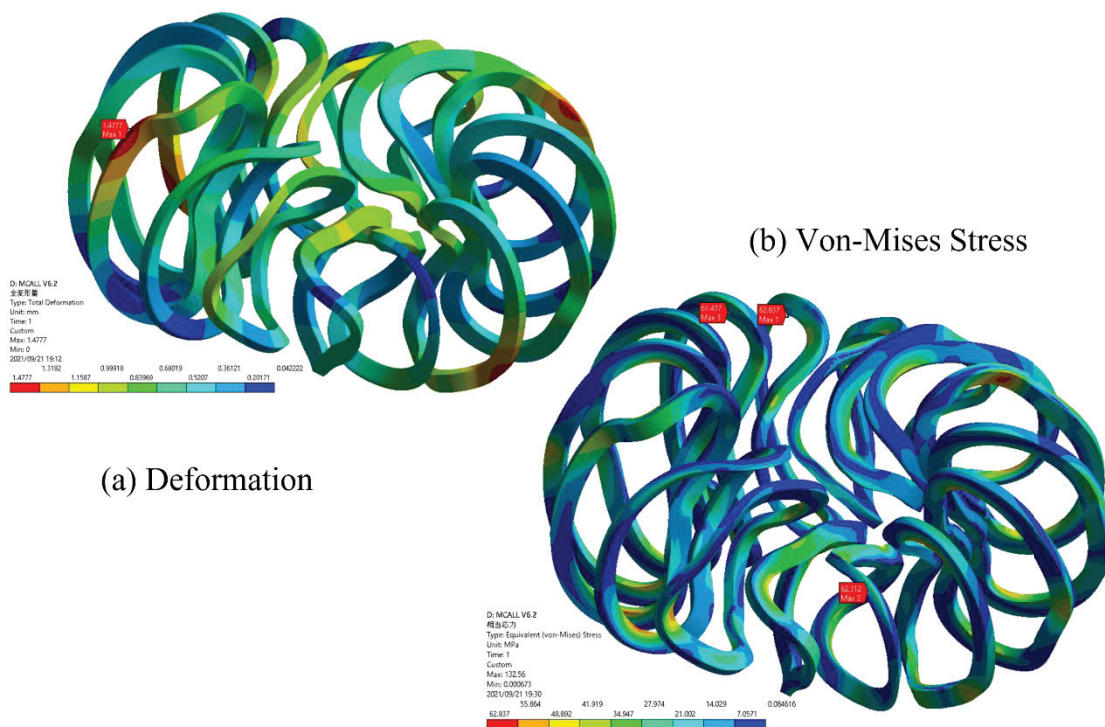
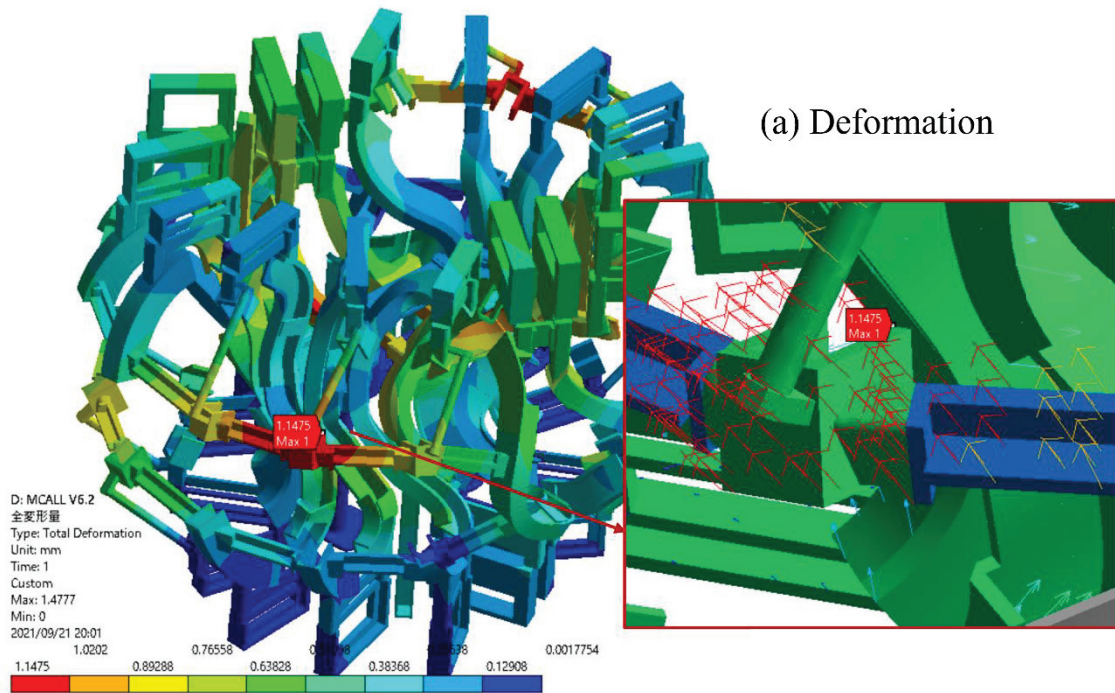
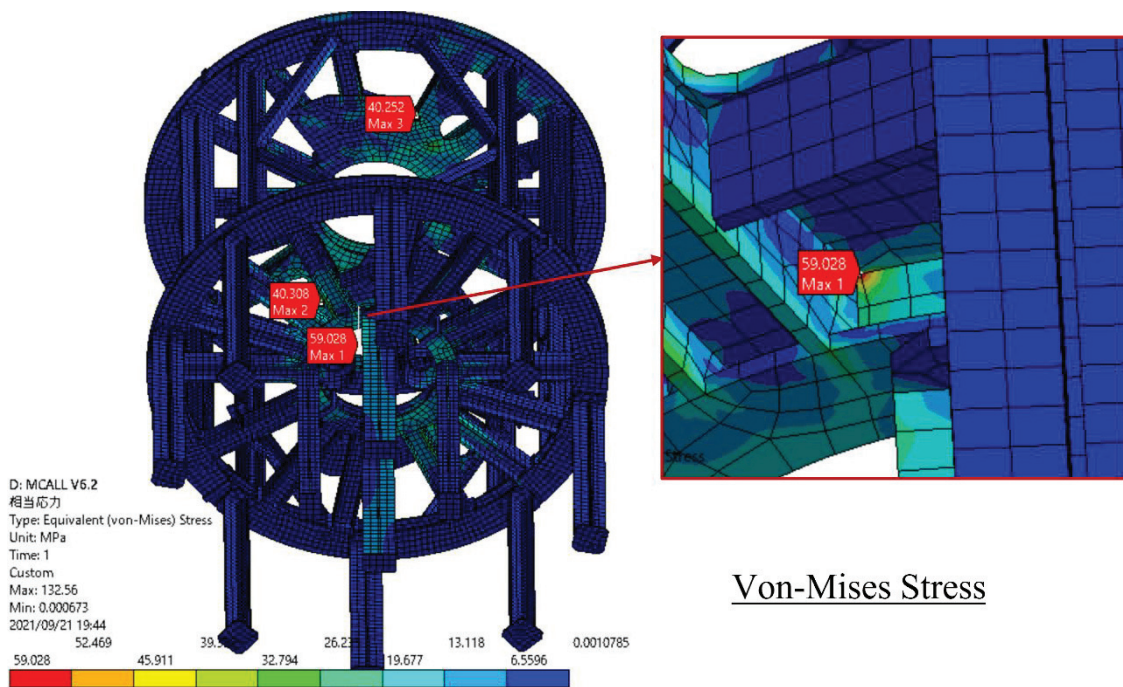


Fig 3.6-3 Deformation and stress of the winding packs. The deformation in the MC2 is 1.48 mm and the maximum in the winding pack. The Von-Mises stress in the MC3 is 63 MPa and the maximum in the winding pack. They slightly exceeds the design target, but in the acceptable range.



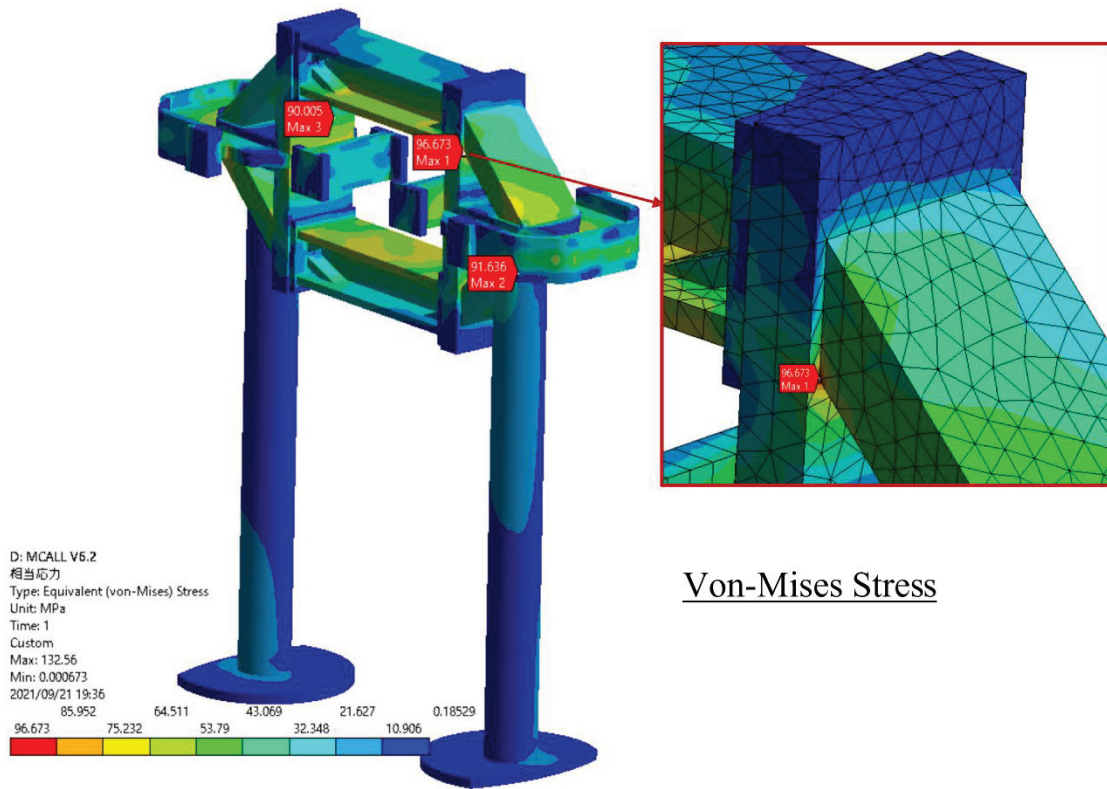
(a) Deformation

Fig 3.6-4 Deformation of the coil support. The deformation of 1.148 mm is maximum at the upper clamp type-B of the MC2 and is in the acceptable range.



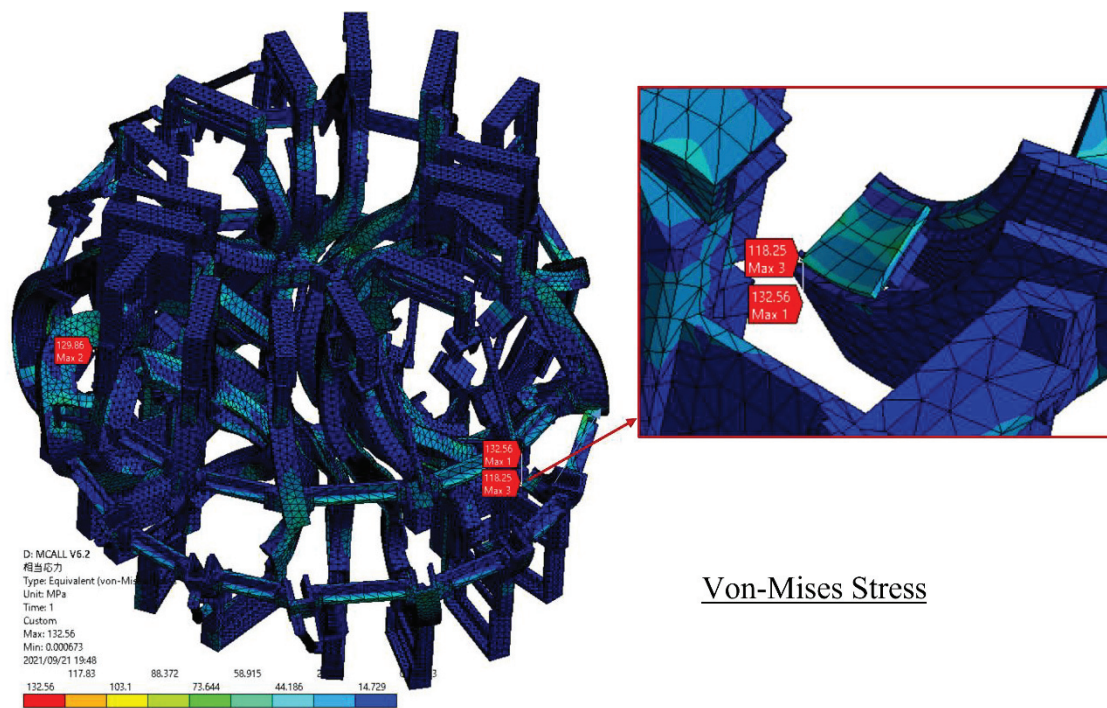
Von-Mises Stress

Fig 3.6-5 Stress of the support frame. The maximum of the stress is 59 MPa at the lower support frame, and there is no problem because it is below the permissible value of 137 MPa.



Von-Mises Stress

Fig 3.6-6 Stress of the center support. The maximum of the stress is 97 MPa, and there is no problem because it is below the permissible value of 137 MPa.



Von-Mises Stress

Fig 3.6-7 Stress of the coil support. The maximum of the stress is 133 MPa at the edge of the coil case, and there is no problem because it is below the permissible value of 137 MPa.

4 Vacuum vessel

4.1 Cross section of vacuum vessel

The shape of inner surface is shown at different toroidal angle in this chapter. Fig 4.1-1 shows how to define the shape. The other figures show cross sectional shape at different angles. The cross sectional area is larger than that of the cfqs-2b32 reference surface that is the last closed magnetic surface with the aspect ratio of 3.2. It will cover the bundle divertor configuration. The width and the height of the inner surface are both at least 450 mm, which is sufficient for people to work inside.

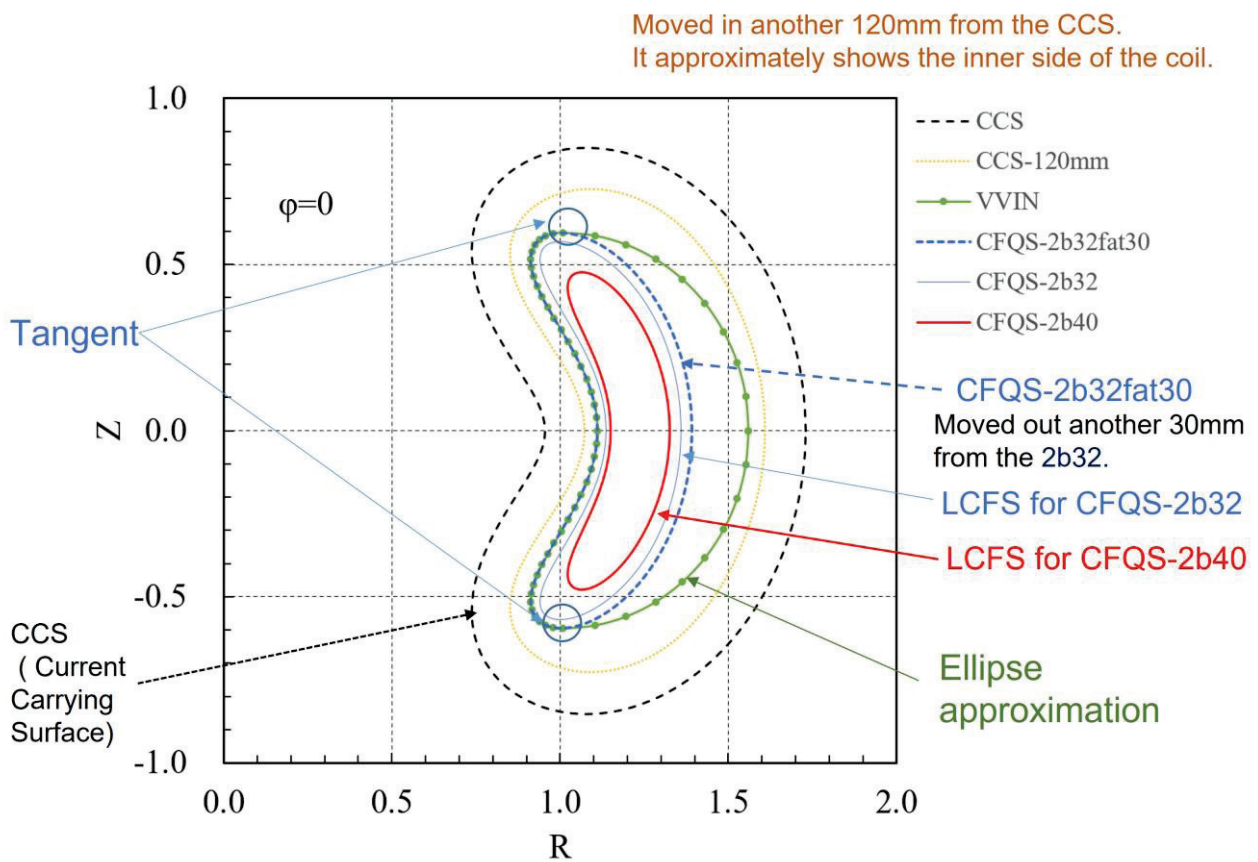


Fig 4.1-1 Drawing with showing how to define the shape of the vacuum vessel.

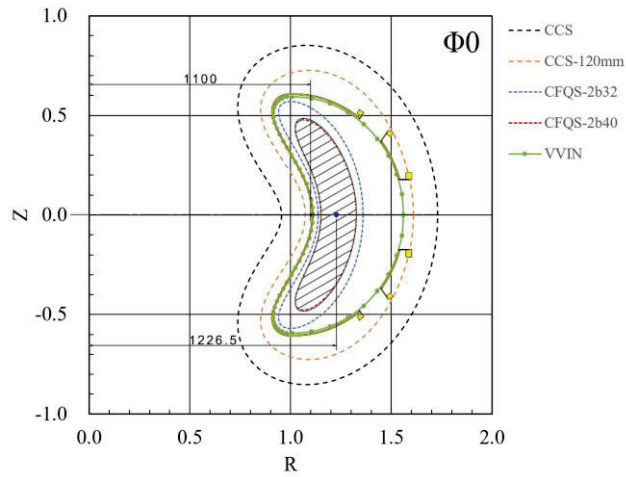


Fig 4.1-2 Shape of main vessel at 0 degrees.

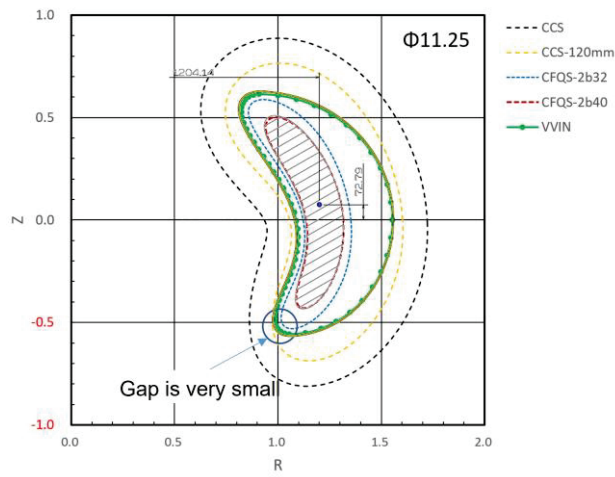


Fig 4.1-3 Shape of main vessel at 11.25 ($1/8 \times 90$) degrees.

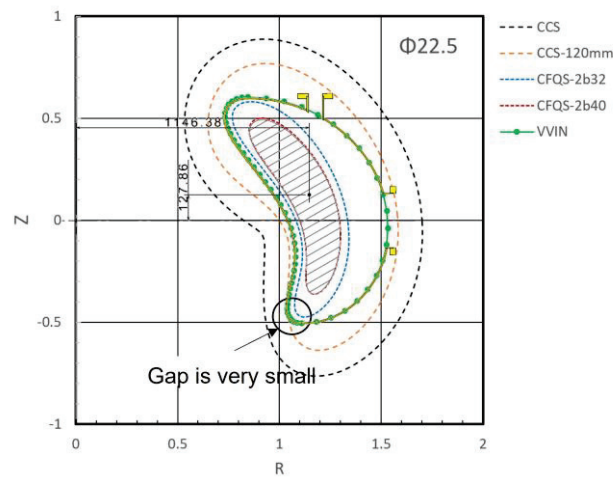


Fig 4.1-4 Shape of main vessel at 22.5 ($2/8 \times 90$) degrees.

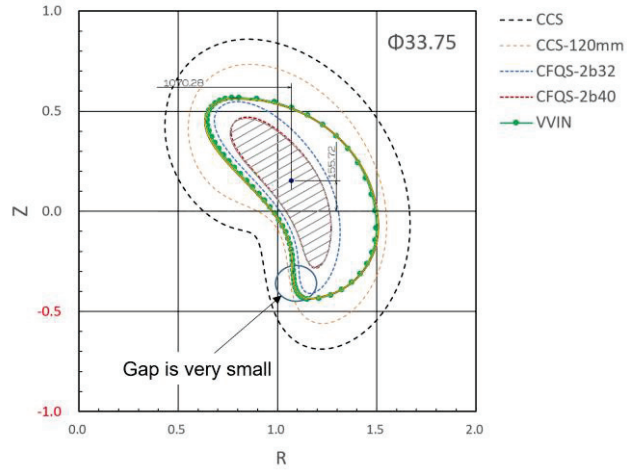


Fig 4.1-5 Shape of main vessel at 33.75 ($3/8 \times 90$) degrees.

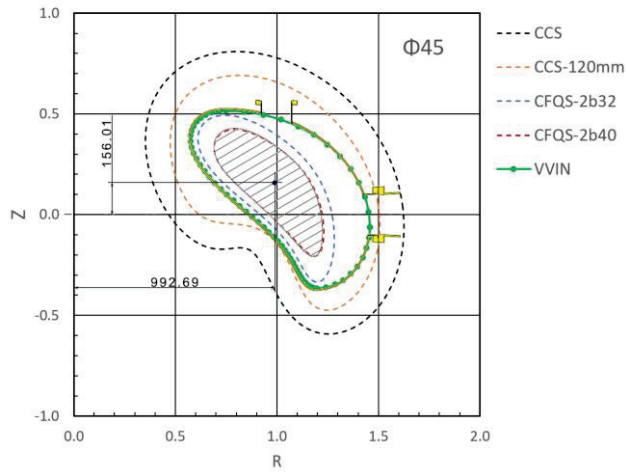


Fig 4.1-6 Shape of main vessel at 45 ($4/8 \times 90$) degrees.

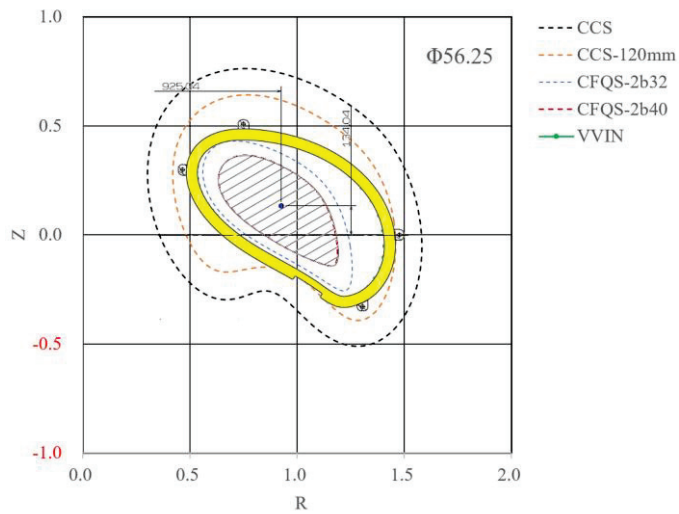


Fig 4.1-7 Shape of main vessel at 56.25 ($5/8 \times 90$) degrees.

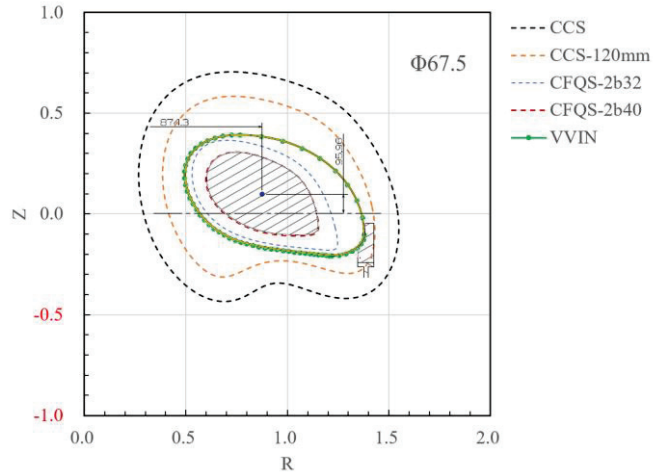


Fig 4.1-8 Shape of main vessel at 67.5 (6/8 × 90) degrees.

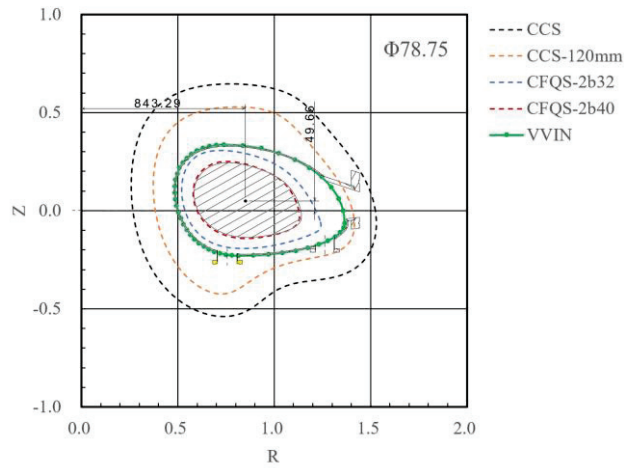


Fig 4.1-9 Shape of main vessel at 78.75 (7/8 × 90) degrees.

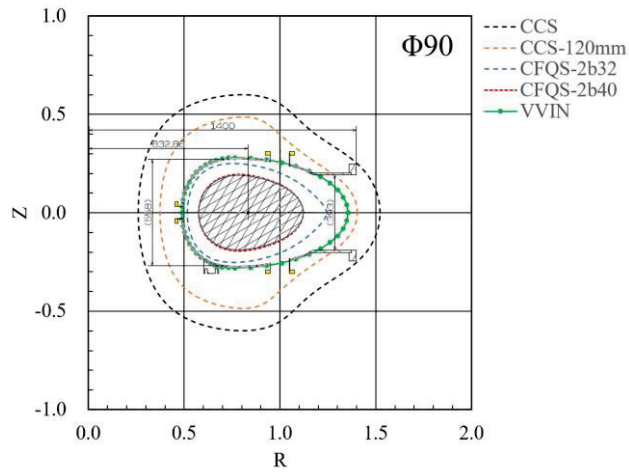


Fig 4.1-10 Shape of main vessel at 90 degrees.

4.2 Shape of the vacuum vessel defined by the Fourier expansion

The shape of the vacuum vessel was defined by the nine planes with a 11.25 degree pitch described in the previous section. Since the shape in the middle of the definition plane is required for the design of the measuring device, the coordinates of the vacuum vessel was expressed by the Fourier series of the following equation with the toroidal periodic number of $N_p=2$.

$$R_{VV}(\theta, \phi) = \sum R_{VVmn} \cos(m\theta - N_p n\phi)$$

$$Z_{VV}(\theta, \phi) = \sum Z_{VVmn} \sin(m\theta - N_p n\phi)$$

The Fourier coefficients of the vacuum vessel were obtained by the fitting technique. The shape of the inner wall of the vacuum vessel expressed in Fourier series is shown in Fig 4.2-1, and the Fourier coefficient is shown in Table 4.2-1.

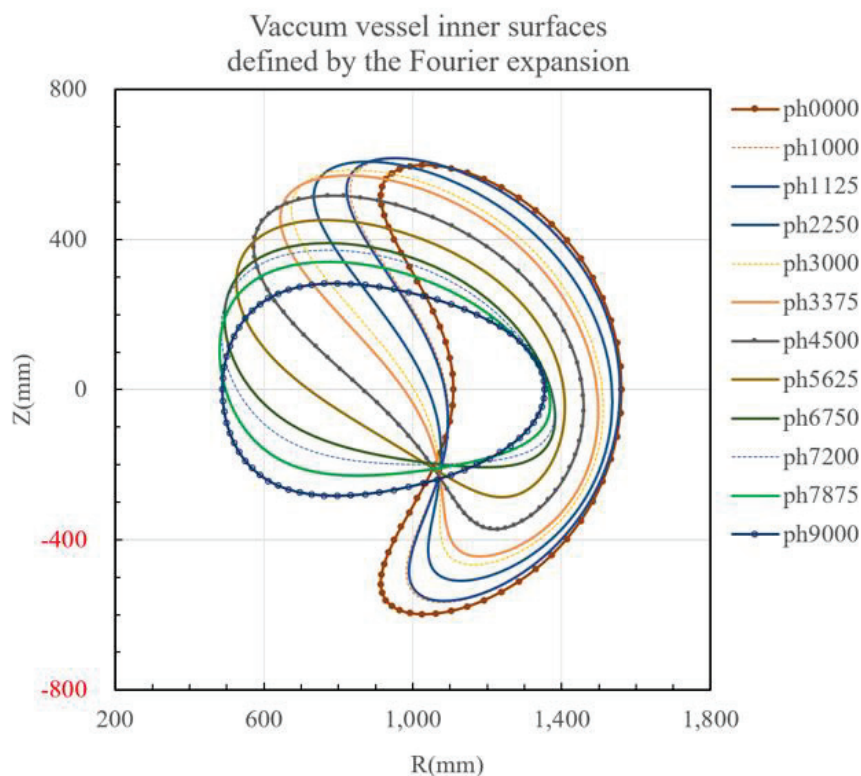


Fig 4.2-1 Inner surface of the vacuum vessel defined by the Fourier expansion of CFQS-VVIN. The ph0000 to ph9000 are the toroidal angles.

Table 4.2-1 Fourier coefficients of R_{vw} , Z_{vw} for the CFQS vacuum vessel with $N_p=2$. Name of the data is CFQS-VVIN.

No	m	n	Rvvmn	Zvvmn	No	m	n	Rvvmn	Zvvmn
1	0	0	1.0288E+00	0.0000E+00	31	3	-3	-2.0327E-04	-3.5711E-04
2	0	1	1.2320E-01	-8.0194E-02	32	3	-2	3.7360E-04	6.7231E-04
3	0	2	-5.9446E-03	1.1979E-02	33	3	-1	5.9290E-04	9.6489E-05
4	0	3	1.7701E-03	-2.9656E-03	34	3	0	-3.0117E-03	2.3752E-03
5	0	4	4.4606E-04	-4.2998E-03	35	3	1	-5.0933E-03	-1.8885E-03
6	0	5	1.4088E-03	-7.5785E-05	36	3	2	-7.1247E-03	4.1531E-03
7	1	-5	3.3737E-03	2.4269E-03	37	3	3	8.3291E-04	5.4984E-04
8	1	-4	-6.0060E-03	-3.0923E-03	38	3	4	1.5480E-03	-2.6492E-03
9	1	-3	7.7172E-03	2.9200E-03	39	3	5	-1.5080E-03	6.0208E-04
10	1	-2	-2.5688E-02	-1.9217E-02	40	4	-5	-2.6041E-05	5.6711E-05
11	1	-1	6.1708E-02	6.2221E-02	41	4	-4	-7.6778E-05	9.0399E-05
12	1	0	3.4249E-01	4.3172E-01	42	4	-3	-5.4953E-05	2.7751E-05
13	1	1	-1.5301E-01	1.0227E-01	43	4	-2	3.6087E-05	-6.5205E-05
14	1	2	1.9211E-02	2.2323E-02	44	4	-1	-1.8630E-04	-9.8974E-05
15	1	3	-9.6336E-03	-1.1164E-02	45	4	0	-5.8879E-04	3.7630E-04
16	1	4	7.6113E-03	6.7501E-03	46	4	1	-8.6959E-05	8.3362E-04
17	1	5	-6.9114E-03	-5.2297E-03	47	4	2	8.3636E-04	-1.6512E-05
18	2	-5	2.6371E-04	7.4712E-04	48	4	3	4.7682E-04	-7.8666E-04
19	2	-4	1.1591E-03	3.9776E-03	49	4	4	-3.2043E-04	3.7849E-04
20	2	-3	-3.0637E-03	-1.7396E-03	50	4	5	8.7689E-05	1.9705E-04
21	2	-2	-5.2165E-03	-1.9762E-03	51	5	-5	-6.6178E-06	6.5772E-06
22	2	-1	1.5203E-02	8.5773E-03	52	5	-4	-5.9262E-06	6.3467E-06
23	2	0	7.9277E-02	2.6113E-02	53	5	-3	-2.5895E-05	7.9294E-06
24	2	1	7.7361E-02	2.2256E-02	54	5	-2	2.7150E-05	-2.0119E-06
25	2	2	2.6689E-02	-7.1380E-03	55	5	-1	1.3339E-05	-3.6589E-05
26	2	3	-9.9115E-03	8.3411E-03	56	5	0	-3.5848E-05	6.2538E-05
27	2	4	3.1837E-03	-3.5510E-03	57	5	1	2.3349E-05	6.4511E-05
28	2	5	1.8954E-04	1.1027E-03	58	5	2	-1.8096E-04	-1.9627E-04
29	3	-5	-1.2095E-03	4.6626E-05	59	5	3	-9.3961E-05	2.0521E-04
30	3	-4	4.0349E-04	4.2148E-04	60	5	4	4.2087E-05	5.7100E-05
					61	5	5	-1.2199E-05	-9.9056E-05

4.3 Port location and the cross-sectional shape of vacuum vessel at the port

The location of each port and the shape of the vacuum vessel near the port are shown in this chapter for convenience in considering the use of each port.

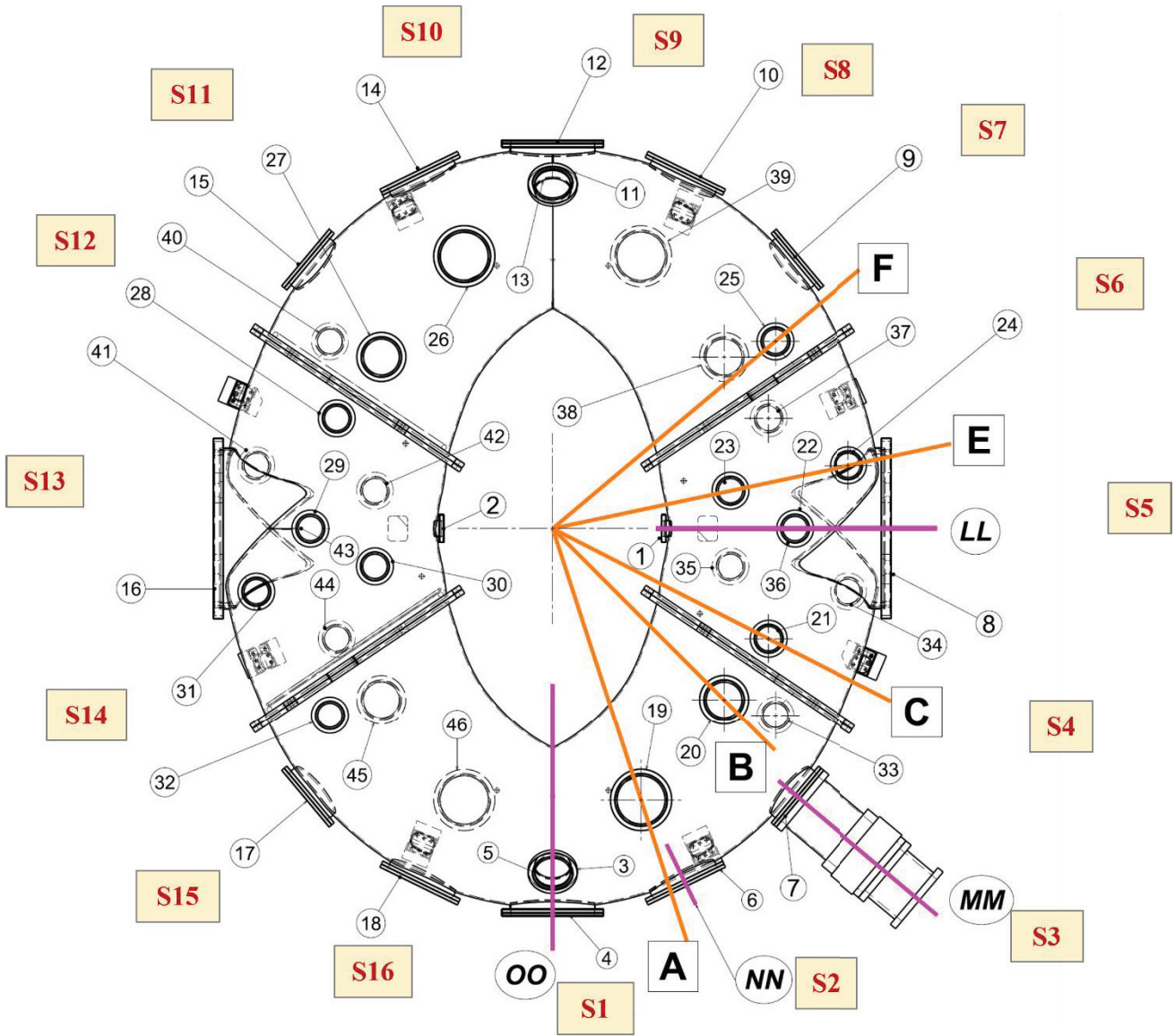


Fig 4.3-1 Position of the cut surface indicating the port arrangement. The S1 to S16 show the section numbers and the (1) to (46) show the port numbers.

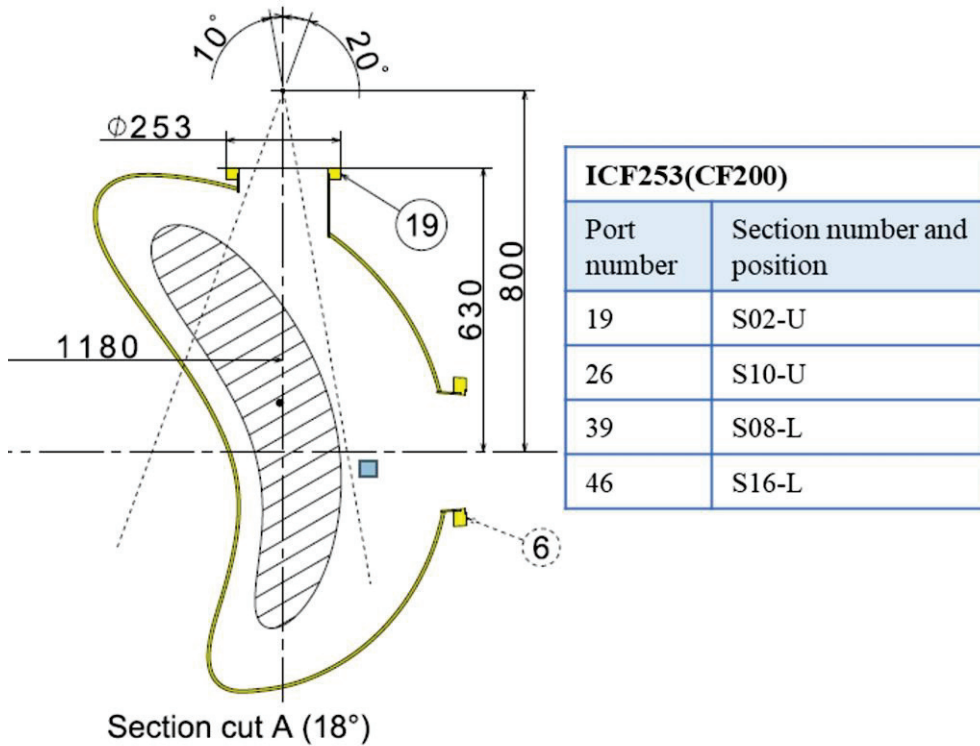


Fig 4.3-2 Port arrangement near the cut surface A. There are 4 ports in the table with the same arrangement. The position of U shows the upper port, L the lower port and O the outside port.

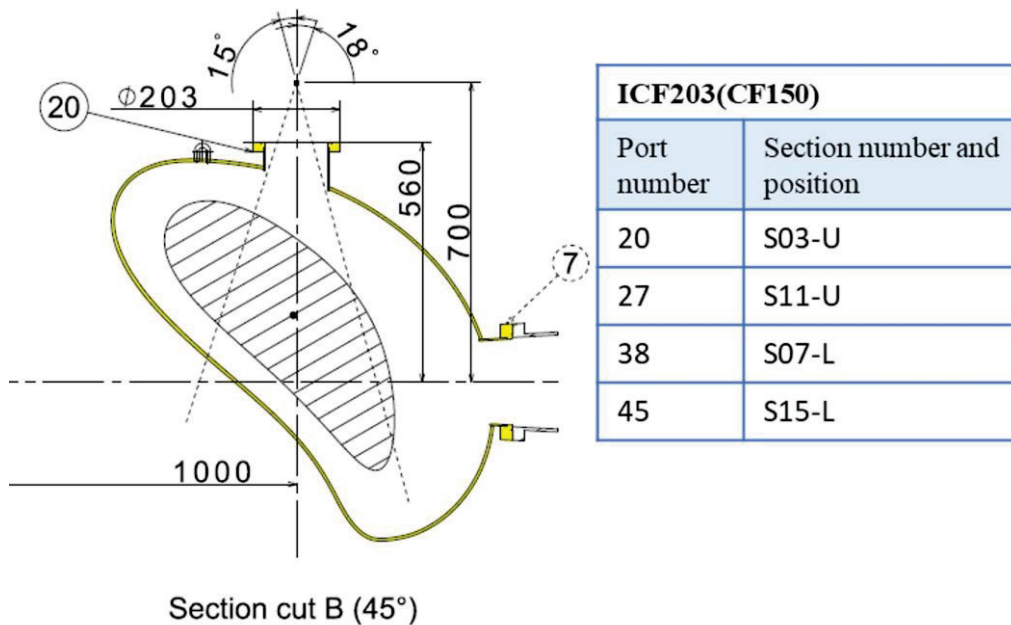


Fig 4.3-3 Port arrangement near the cut surface B. There are 4 ports in the table with the same arrangement. The position of U shows the upper port, L the lower port and O the outside port.

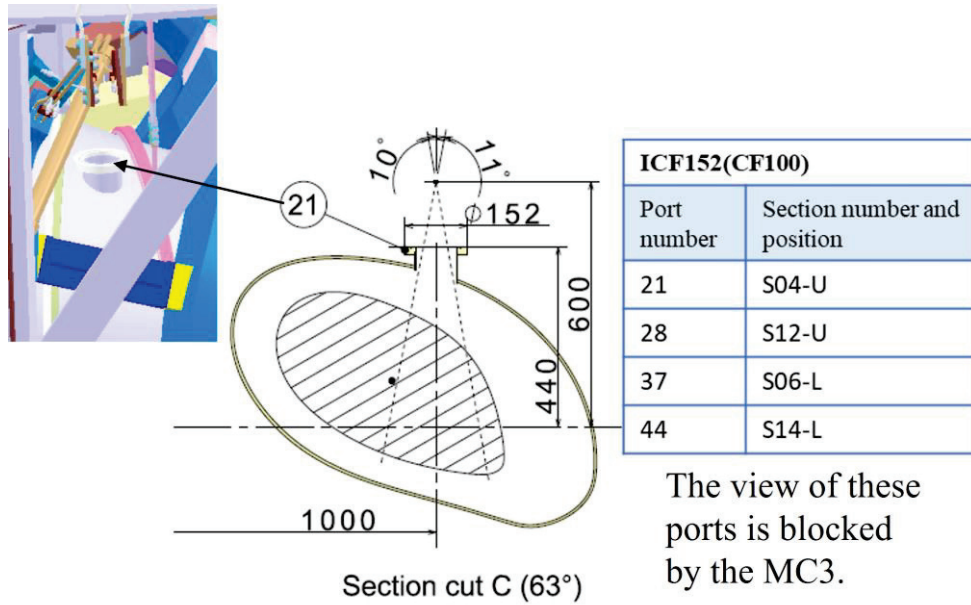


Fig 4.3-4 Port arrangement near the cut surface C. There are 4 ports in the table with the same arrangement. The position of U shows the upper port and L the lower port.

The view of ports 23~42 is blocked by the MC4.

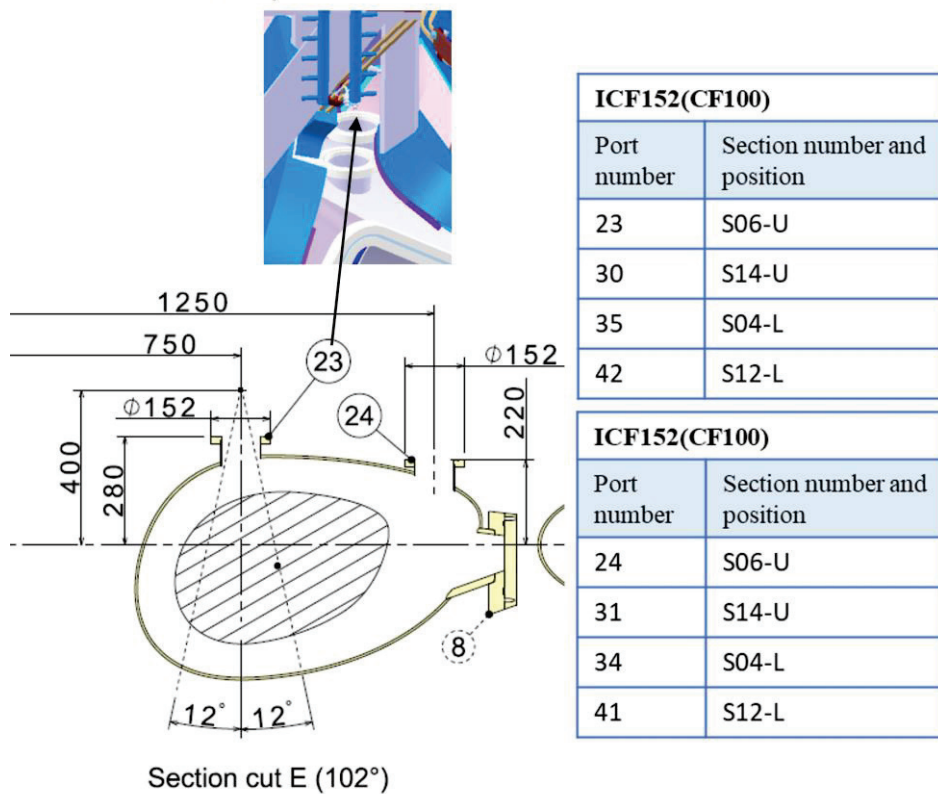
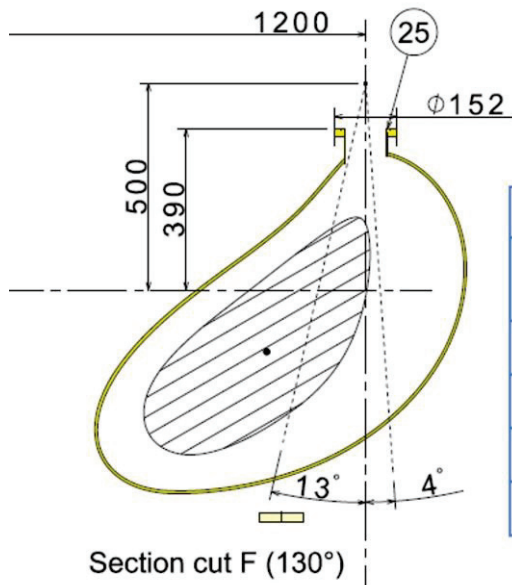
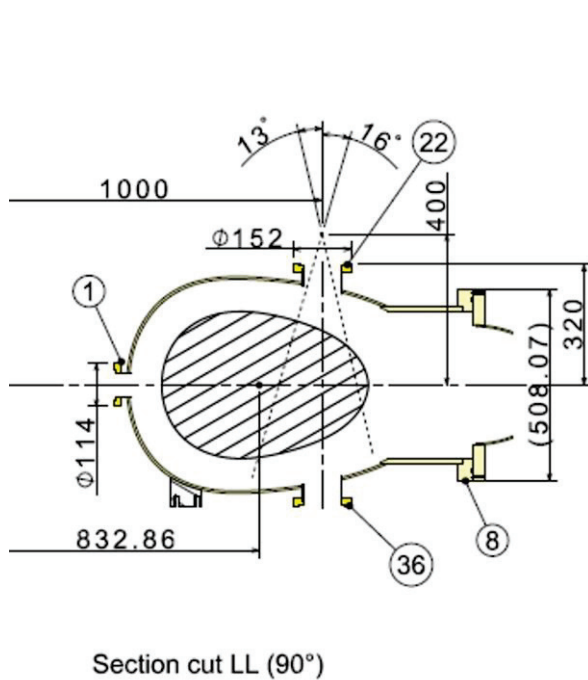


Fig 4.3-5 Port arrangement near the cut surface E. There are 4 ports or 2 ports in the table with the same arrangement. The position of U shows the upper port, L the lower port and O the outside port.



ICF152(CF100)	
Port number	Section number and position
25	S07-U
32	S15-U
33	S03-L
40	S11-L

Fig 4.3-6 Port arrangement near the cut surface F. There are 4 ports in the table with the same arrangement. The position of U shows the upper port and L the lower port.

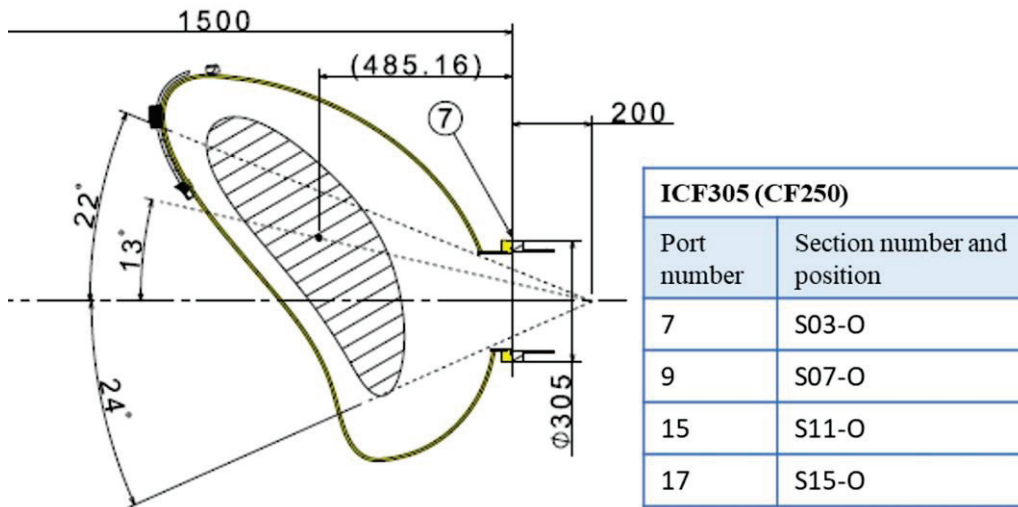


ICF114(CF63)	
Port number	Section number and position
1	S05-I
2	S13-I

ICF152(CF100)	
Port number	Section number and position
22	S05-U
29	S13-U
36	S05-L
43	S13-L

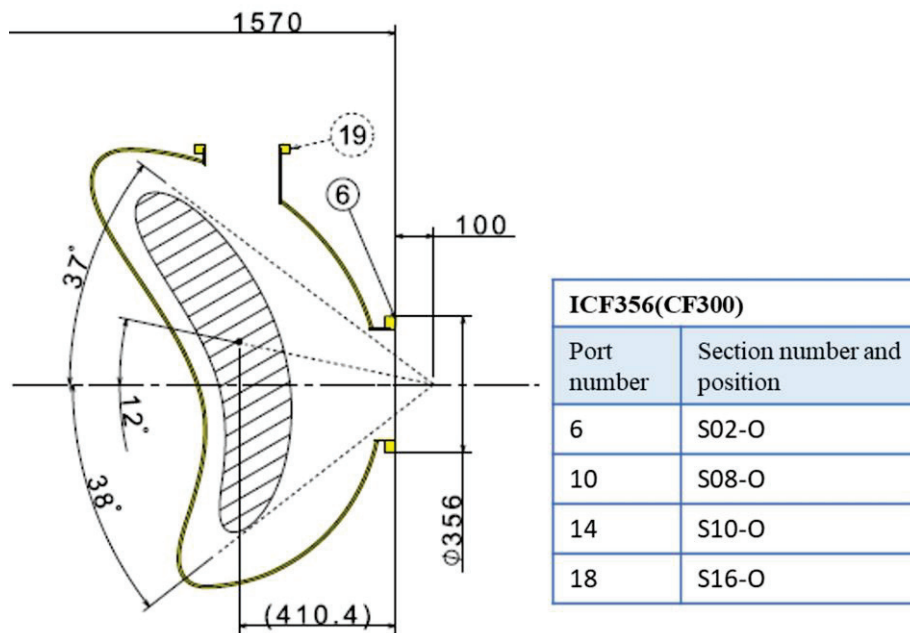
Large rectangular port	
Port number	Section number and position
8	S05-O
16	S13-O

Fig 4.3-7 Port arrangement near the cut surface LL. There are 4 or 2 ports in the table with the same arrangement. The position of U shows the upper port, L the lower port, I the inside port and O the outside port.



Section cut MM (50° -200mm)

Fig 4.3-8 Port arrangement near the cut surface MM. There are 4 ports in the table with the same arrangement. The position of O shows the outside port.



Section cut NN (26° -150mm)

Fig 4.3-9 Port arrangement near the cut surface NN. There are 4 ports in the table with the same arrangement. The position of U shows the upper port, L the lower port and O the outside port.

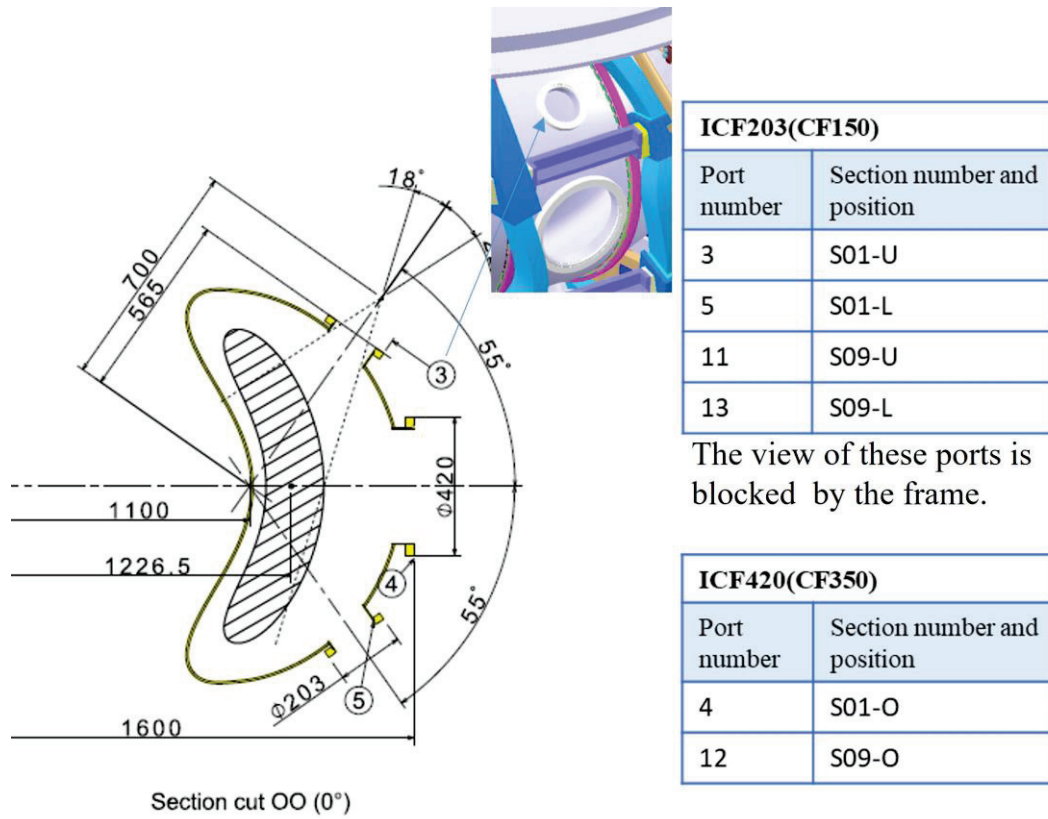


Fig 4.3-10 Port arrangement near the cut surface OO. There are 4 or 2 ports in the table with the same arrangement. The position of U shows the upper port, L the lower port and O the outside port.

4.4 Design of leaf-spring type leg

4.4.1 Summary

To absorb the heat expansion deformation by the baking, the vacuum vessel is supported by eight leaf spring type legs. Since the leaf spring type leg will receive a compressive load, it is necessary to evaluate its buckling and bending stress. This chapter introduces the results of analysis and evaluation by hand calculation.

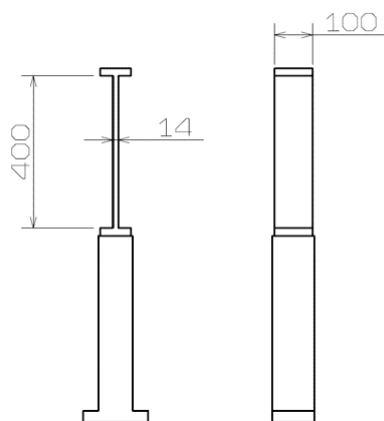


Fig 4.4-1 Design dimension of the leg

4.4.2 Design values

Design values of the leaf spring are as follows. Since the weight of the vacuum vessel is about 4000 kg with extra 1400 kg of additional devices, it is assumed that one leg shares $F=500$ kg. The thermal expansion of the stainless steel is $1.73 \times 10^{-5}/\text{degree}$. The major radius increases by an average of 0.17 % ($=1.73 \times 10^{-5} \times 100$) when the temperature of the vacuum vessel rises 100 degrees during baking. Since the major radius of the CFQS is 1 m, the amount of forced displacement is assumed to be $\delta=2$ mm.

Table 4.4-1 Design values of the leaf spring type leg.

Item	Symbol	Unit	Value
Beam thickness	H	mm	14
Beam width	B	mm	100
Beam length	L	mm	400
Number of legs			8
Material			SUS316L
Design temperature		Degrees C	150
Young's modulus	E	GPa	193
Design allowable stress		MPa	115
Yield stress (150°C)	σ_y	MPa	173
Support load	F_s	N	4903 (500kg)
Forced displacement		mm	2

4.4.3 Buckling load and safety factor

The buckling load is calculated as follows by the formula of the beam fixed at two ends.

$$P_{cr} = \pi^2 EI / (KL)^2$$

$$\sigma_{cr} = \frac{P_{cr}}{A} = \pi^2 E / (KL/r)^2 < \sigma_y$$

where P_{cr} is the Euler's critical load (longitudinal compression load on column) and σ_{cr} is the critical buckling stress. E is the modulus of elasticity of column material (Young's modulus), and I is the minimum area moment of inertia of the cross section of the column, L is the unsupported length of column. K is the column effective length factor and $K = 0.5$ is for the beam fixed at two ends. The value of K may change in the range of 0.5 to 2 at fixed conditions at both ends. In the worst case, the critical load will be 1/16 times, so it is necessary for the design to have a sufficient margin. A is the area cross section and r is the radius of gyration ($r = \sqrt{I/A}$).

Substituting the design values will give us the results in the table. Here, the safety factor 222 is reasonably large enough.

Table 4.4-2 Buckling calculation.

Item	Symbol	Unit	Value
Cross section	A	m ²	0.014 x 0.1 = 0.0014
Moment of inertia of area	I	m ⁴	$I = BH^3/12 = 2.29 \times 10^{-8}$,
Radius of gyration of area	r	m	$r = \sqrt{2.29 \times 10^{-8}/0.0014} = 0.00404$
Effective length factor	K		0.5, (Beam fixed on both ends)
Slenderness ratio	KL/r		$KL/r = (0.5 \times 0.4)/0.00404 = 49.5$
Critical buckling stress	σ_{cr}	Pa	$\sigma_{cr} = \pi^2 \times 193 \times 10^9 / 49.5^2 = 777 \times 10^6$
Buckling load	P_{cr}	N	$P_{cr} = 777 \times 10^6 \times 0.0014 = 1.089 \times 10^6$
Safety factor	<i>Safe</i>		$Safe = P_{cr}/F_s = 1.089 \times 10^6 / 4903 = 222$

4.4.4 Bending stress with the forced displacement

The bending stress of beam fixed at two ends can be obtained by expanding the model fixed at one end.

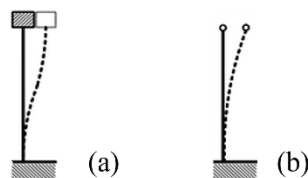


Fig 4.4-2 Bended shape of a beam. (a) a beam fixed at two ends and (b) fixed at one end and other free.

The deflection at the unsupported end of the model (b) in Fig 4.4-2 is calculated as follows.

$$y = \frac{WX^3}{3EI}$$

$$\sigma_b = \frac{M}{Z}$$

$$M = WX$$

where y is the Displacement at the top of the model (b). σ_b is the bending stress at the fixed end of the model (b). W is the load at unsupported end of the model (b). X is the beam length of the model (b), E is the young's modulus, I is the moment of inertia, M is the bending moment at the fixed end of the model (b). Z is the section modulus of the beam = $I/(H/2)$, and H is the thickness of the beam.

The bending stress of the model (a) is equal to a result with

$$y = 0.5 \times \text{the displacement at the top of the model (b),}$$

$$X = 0.5 \times \text{the beam length of the model (b).}$$

Substituting the design values will give us the results in the table. Here, the safety factor 1.65 is reasonably large enough.

Table 4.4-3 Bending stress calculation.

Item	Symbol	Unit	Value
Fixed condition			Beam fixed on both ends
Equivalent displacement	y	m	$0.002/2 = 0.001$
Equivalent beam length	x	m	$0.4/2 = 0.2$
Section modulus	Z	m^3	$I/(H/2) = 2.29 \times 10^{-8}/0.007 = 3.27 \times 10^{-6}$
Load at unsupported end	W	N	$3 \times E \times I \times y / x^3 = 1655$
Bending moment	M	Nm	$W \times x = 331$
Bending stress	σ_b	Pa	$M/Z = 331/3.27 \times 10^{-6} = 1.013 \times 10^8$
Compressive membrane stress	σ_m	Pa	$F_s/A = 4903/0.0014 = 3.502 \times 10^6$
Bending plus membrane stress	$\sigma_b + \sigma_m$	Pa	1.048×10^8
Safety factor			$\sigma_y / (\sigma_b + \sigma_m) = 1.65$

4.5 Eddy current analysis of vacuum vessel

In the CFQS using normal conducting coils, since the energization time of magnetic field coils is limited by the balance between heat generation and cooling performance of coils, the plasma discharge duration is also limited. Hence, the influence of the eddy current generated on the vacuum vessel may be exerted during the plasma discharge.

4.5.1 Time constant of eddy current and its effect on plasma discharge.

The eddy current on the vacuum vessel is induced by the current change of the external coil, such as the MC, the TFC, and PFC. A vacuum vessel in which eddy currents do not flow is preferable because eddy currents disturb the target magnetic field distribution of the external coil, but it is difficult in practice. Therefore, the strategy is to delay the generation of plasma until the induced eddy current decays and its effect can be ignored. To judge whether the strategy is appropriate, the time constant of the eddy current was evaluated by eddy current analysis.

Fig 4.5-1 shows example of the external coil current and the eddy current on the vacuum vessel. The figure below shows the eddy currents when three types of coil current change as the external coil.

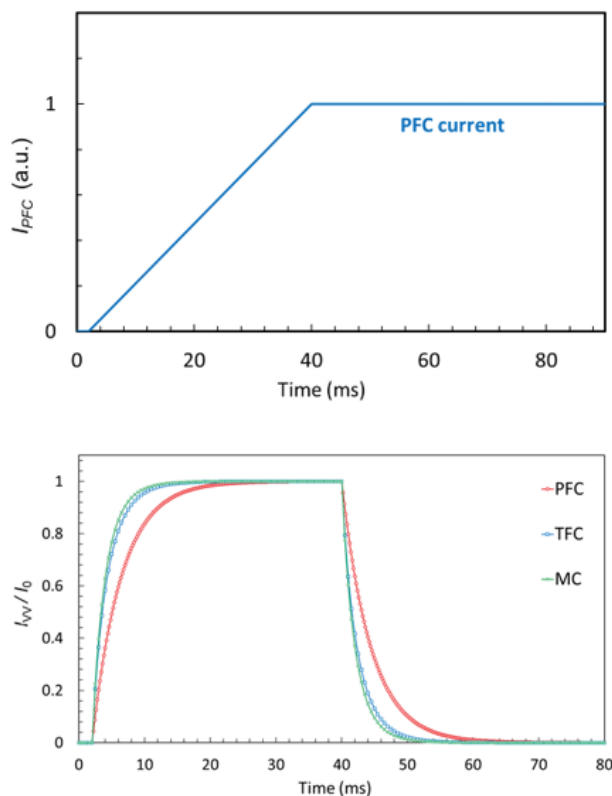


Fig 4.5-1 Example of time-varying waveform of external coil current and total eddy current.

Eddy current is induced on the VV by the current change of the external coils. This relationship can be approximately expressed by the following equivalent circuit equation.

$$L \frac{dI_{VV}}{dt} + RI_{VV} = V = M \frac{dI_{EXT}}{dt} .$$

Where I_{VV} is a total eddy current induced on the VV, I_{EXT} is a current flowing in external coil like the MC, the PFC and TFC. L and R are the inductance and resistance of the VV, respectively, and M is the mutual inductance between the external coil and the VV. Here, when the right-hand side of the equation is constant, that is, when the external coil current increases / decreases at a constant rate, the equation can be analytically solved, and the eddy current is given by the following equation.

$$I_{VV} = I_0 \left(1 - e^{-\frac{t}{\tau}} \right) .$$

Where, I_0 is the maximum value of the eddy current, and τ is the time constant of the eddy current determined by L/R .

Note that the time constant τ does not depend on the current value of the external coil and can be a useful method for evaluating the time to reach flattop or the remaining time of the eddy current. As shown in Fig 4.5-2, when $t = \tau$, the value of the eddy current is approximately 63 % of the maximum value and when $t = 5\tau$, the eddy current is approximately 99 % of the maximum value. Therefore, if the plasma discharge is performed at a time of 5τ or more after the rise of the external coil current, we can consider that the influence of the eddy current is almost eliminated.

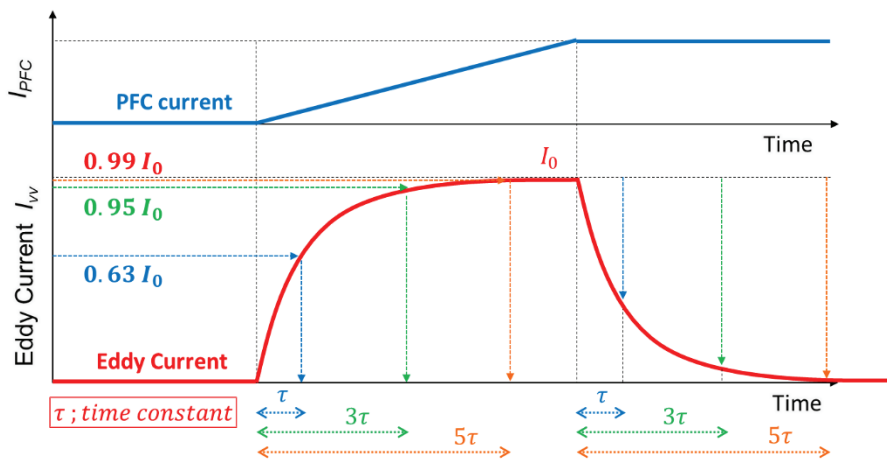


Fig 4.5-2 A time evolution of eddy current due to PFC.

The eddy current induced on the VV by the PFC was calculated by the ANSYS/Maxwell system. The PFC current was set to increase linearly from the time of 2 ms to 40 ms, and then was set to be constant as shown in Fig 4.5-1. Fig 4.5-3 shows the calculation meshes used in the eddy current analysis, in which the transient analysis is required to calculate the eddy current. To accurately evaluate the change in the eddy current, it is necessary to make the time step fine. The time step Δt was set to 0.2 ms in this analysis. A rectangular computational domain was designed to enclose the CFQS VV and the external coils. Also, on its boundaries, the Neumann condition ($\partial H / \partial n = 0$) was applied. To detect the eddy current, fine meshes were arranged in the model. The average element size in the entire model is 36.14 mm (minimum element size is 0.03 mm). The number of elements is 267,454 for the

vacuum vessel, and 501,532 for all elements with the computational domain.

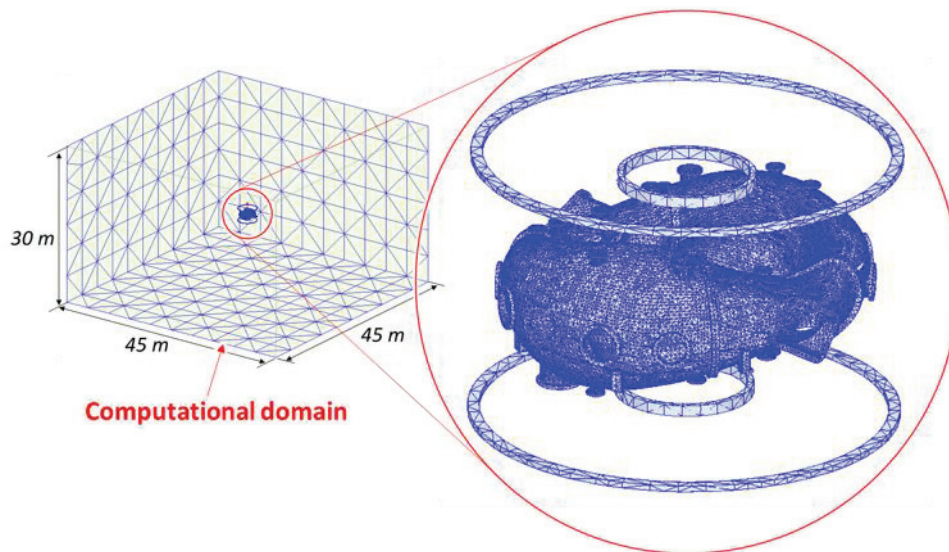


Fig 4.5-3 Computational meshes of vacuum vessel, PFC, and computational domain.

Fig 4.5-4 shows a result of the eddy current density distribution at the time of 40 ms with the PFC current change as an example. The eddy current flows counterclockwise as seen from the top, and a relatively high current density appears near diagnostics ports. This result is consistent with the theoretically expected trend. Similar calculations were performed with the TFC and the MC current change, and the results are shown in Fig 4.5-1 which shows the time evolution of the total eddy current on the vacuum vessel.

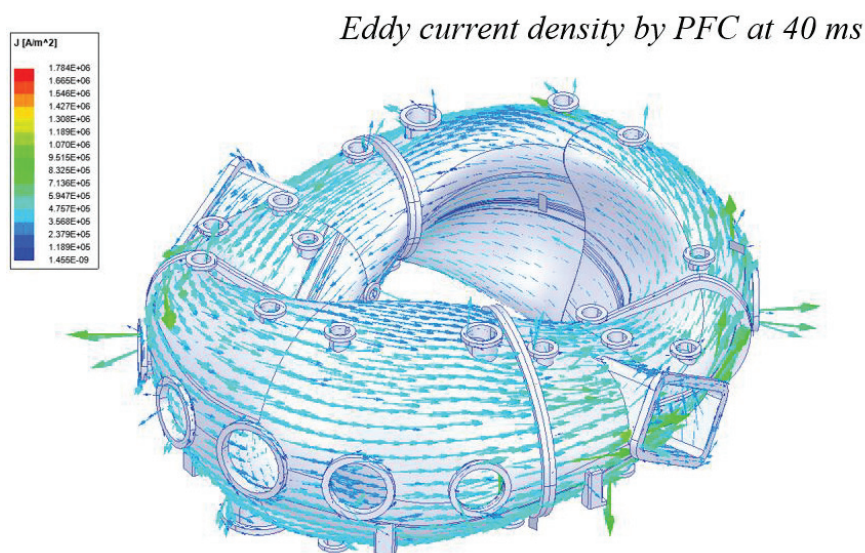


Fig 4.5-4 Distribution of eddy current density on the vacuum vessel with the PFC current change.

To calculate the total eddy current induced on the VV, it is necessary to integrate the current density in a cross-

section perpendicular to the direction in which the eddy current flows. Fig 4.5-5 shows integral cross sections for calculating the total eddy current.

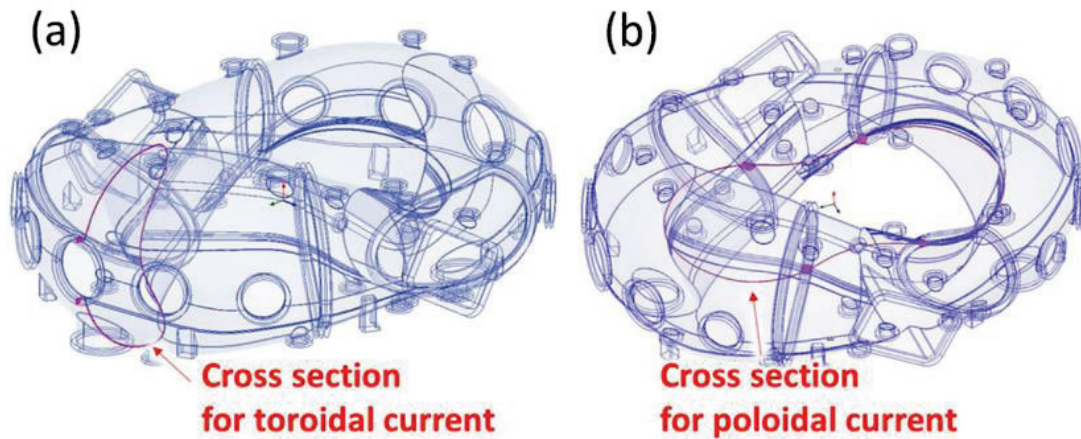
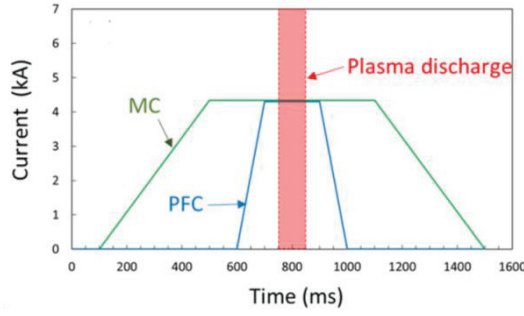
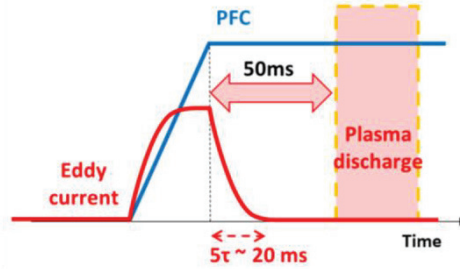


Fig 4.5-5 Cross section to obtain total eddy current. To obtain the total eddy current at each time, the current density was surface-integrated with the cross section indicated by the red line. (a) is for getting the toroidal eddy current induced by the PFC current change, (b) is for getting the poloidal eddy current induced by the TFC or the MC current change

From the current waveform, the time constant τ is approximately 4 ms for the PFC and 2 ms for the MC and the TFC, respectively. Fig 4.5-6 shows a typical current scenario of the MC current and the PFC current in the CFQS experiment. The plasma discharge begins to start 50 ms after the PFC current reaches the flat top. The impact on the plasma discharge is expected to be negligibly small, because the eddy current ($5\tau \sim 20$ ms) is small enough to ignore at the start of plasma discharge.



(a) Coil current waveform



(b) Relationship of the eddy current and the plasma discharge

Fig 4.5-6 Typical scenario of plasma experiment.

Further, the resistance R and the inductance L of the VV are obtained by using the time constant and stored magnetic energy from the result. To obtain a resistance of the VV in the toroidal direction, which is called the one - turn resistance, simple electrical circuit equation is used. Here, the magnetic energy U_M is given by the equation,

$$U_M = \frac{1}{2} L I_{VV}^2 = \frac{1}{2} \int \mathbf{B} \cdot \mathbf{H} dV,$$

where, B and H are integrated over the entire analysis region in ANSYS/Maxwell. Since I_{VV} , U_M , and τ are known, the resistance R and the inductance L can be calculated by the following equations.

$$L = 2U_M / I_{VV}^2,$$

$$R = L / \tau .$$

The resistance and inductance of the CFQS VV in the toroidal direction can be estimated to be 0.4 mΩ and 1.8 μH, respectively, from the eddy current analysis with the PFC current. And those in the poloidal direction are 0.058 mΩ and 0.14 μH, respectively, from the eddy current analysis with the MC current.

In a medium-sized tokamak, a Joule heating is required during experiment. In general, a one-turn voltage of the VV is applied to be about 10 V for the Joule heating. If the one-turn resistance is 0.4 mΩ, a large current as much as several tens of kA flows. In this case, a one-turn break, or a bellow is required to increase the resistance. However, since we do not conduct the Joule heating in the CFQS, there is no need to consider the one-turn break or bellows. This result will contribute to the reduction on the VV construction costs.

4.5.2 EM force on the vacuum vessel

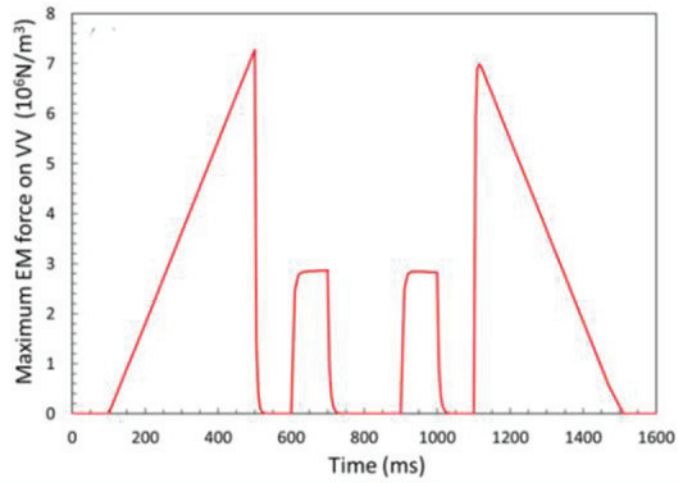
The EM force is generated on the VV by the interaction of the eddy current and mainly magnetic field produced by the MC. The effect of the EM force is evaluated by structural analysis. Major component of the eddy current can be classified into a poloidal current and a toroidal current. The former is mainly induced by the MC current and the latter by the PFC current. The TFC current also induces a poloidal eddy current, but since its magnetomotive force is smaller than that of MC, it will be ignored below.

The typical current scenario of the PFC and the MC as shown in Fig 4.5-6 was assumed in this analysis. The current change rates of the MC and the PFC are 10.75 kA/s and 43 kA/s, respectively. The maximum current of the MC is 4.3 kA with 72 turns. Regarding the PFC, the maximum current is 4.3 kA with 32 turns. The EM force under this current scenario were investigated by using ANSYS Maxwell. The time step Δt was set to 1ms in this analysis.

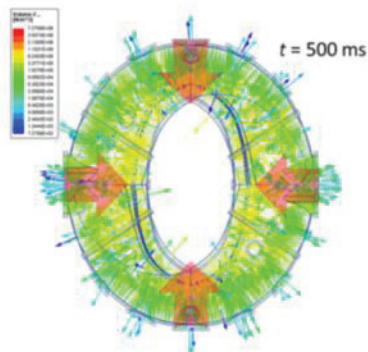
Fig 4.5-7(a) shows the time evolution of the maximum EM force per volume (N/m^3) on the VV under the typical current scenario mentioned above. The EM force increases almost linearly with the rise of the MC current and decreases almost linearly with the fall of the MC current, since the eddy current induced by the MC is almost constant. We find two peaks of the EM force at 500 ms and 1,100 ms. We also found that the directions of the EM force at two peaks are opposite as shown in Fig 4.5-7(b) and (c), at 500 ms is more dangerous since the direction of force the same as the direction of vacuum pressure.

The EM force is generated again with the rise of the PFC current. We find that the EM force by the PFC is smaller than that of the MC.

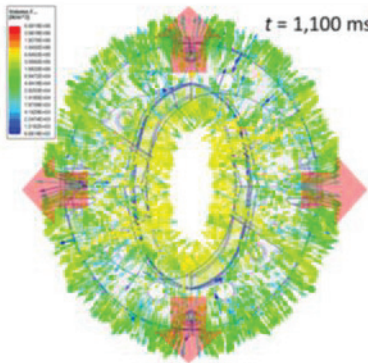
The force in this analysis can be converted into the EM pressure on the VV. The EM pressure is about 0.4 atm in consideration of the thickness of the stainless-steel plate of 6 mm. Although the EM pressure is lower than the atmospheric pressure (1 atm), it is not a negligible value.



(a) Time evolution of maximum EM force



(b) EM force distribution at 500 ms



(c) EM force distribution at 1100 ms

Fig 4.5-7 Time evolution of EM force on the VV under the typical scenario.

4.5.3 Inductive heating of the vacuum vessel

Gases such as nitrogen, oxygen, hydrogen, water vapor, and carbon dioxide are adsorbed on the inner wall of a VV under the atmospheric pressure, and these adsorbed gases are released as outgas from a VV inner wall during the vacuum pumping. Since these outgases hinder the high vacuum pumping process, it is necessary to heat up the entire VV by heaters such as tape-shaped heaters around the outer wall of the VV in general, and to release the adsorbed gas attached to the inner wall. Regarding a baking method for the CFQS VV, usage of an induction heating with an eddy current generated in the VV has been proposed. 16 MCs are connected in a series and an AC is applied to the MC to generate heat by resistance loss of eddy current generated in the VV. We must check the feasibility of adopting the induction heating in the CFQS from the engineering point of view.

In this analysis, the AC analysis is required to calculate the heat generation of the CFQS VV by the induction current induced by the MCs. In general, when an AC flows through a conductor, a skin effect appears in which the current density is high at the surface of the conductor and gradually decreases with distance from the surface. If the skin depth δ is smaller than the thickness of the VV (6 mm), it can be considered that the eddy current concentrates on the VV surface. In this case, since a layered thin and fine mesh is required on the surface of the VV even in the FEA, the skin depth must be considered in advance. Here, skin depth δ can be calculated by the following equation,

$$\delta = \sqrt{\frac{2}{2\pi f \mu_r \mu_0 \sigma}}$$

where f is the AC frequency, μ_r is the relative magnetic permeability, μ_0 is the vacuum magnetic permeability, and σ is the electric conductivity of the VV. When the skin depth is calculated using this equation, for example in the case of $f = 2$ kHz, the skin depth δ is approximately 9 mm. Therefore, since the skin depth is larger than the plate thickness of the VV, we considered that the current concentration due to the skin effect does not occur on the CFQS VV surface.

Fig 4.5-8 shows the heat generation of the CFQS VV with the current value and AC frequency of MC changing was investigated by using ANSYS Maxwell. The Root Mean Square (RMS) value I_{AC} of input current in a conductor was changed from about 7 A to 21 A, and the AC frequency was investigated at 500 Hz, 1 kHz, 1.5 kHz, and 2 kHz. Fig 4.5-9 shows an example of the heat distribution of the VV obtained by this analysis in the case of $f = 1$ kHz and $I_{AC} = 7$ A.

The heat generation is more strongly dependent on the current value than the AC frequency. Here, the heat generation required for baking in the CFQS VV is 25 kW. This value is determined based on the actual value of VV baking system of CHS which has a similar size to the CFQS. In this case, the current required for the CFQS VV baking can be obtained to be about 18 A. The voltage applied in the MC is obtained by this current value I_{AC} and AC resistance ωL as follows.

$$V_{MC} = I_{AC} \cdot \omega L,$$

where ω is the angular frequency represented as $2\pi f$. The inductance L of the MCs arranged in series was calculated to be about 0.3 H by using ANSYS Maxwell. Substituting $I_{AC} = 18 A$, and $f = 1 kHz$, the applied voltage on the MC is obtained to be about 34 kV.

As a result, this voltage value exceeds the operation voltage of DC 2.4 kV. Therefore, we found that the induction heating method could not be adopted in the CFQS. An alternative method should be considered as a next option, for example, the sheathed heater system.

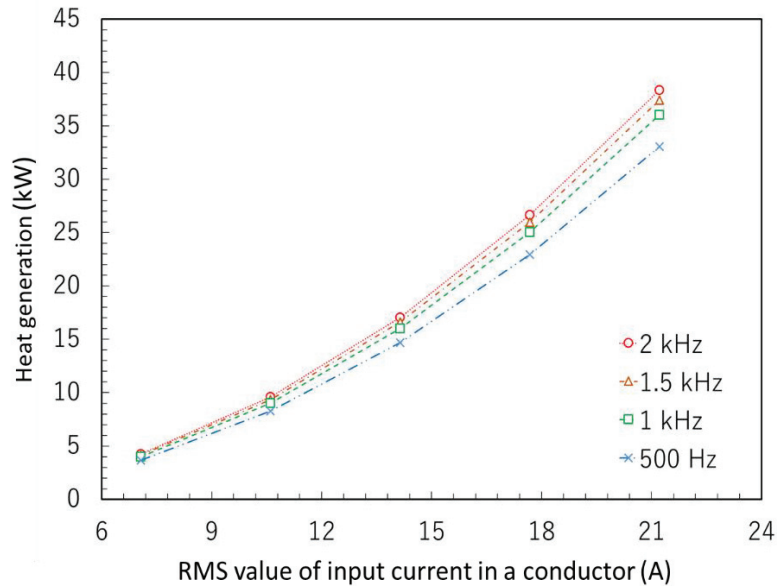


Fig 4.5-8 Heat generation with changing RMS value of input current. Number of MC and turns are 16 and 72, respectively.

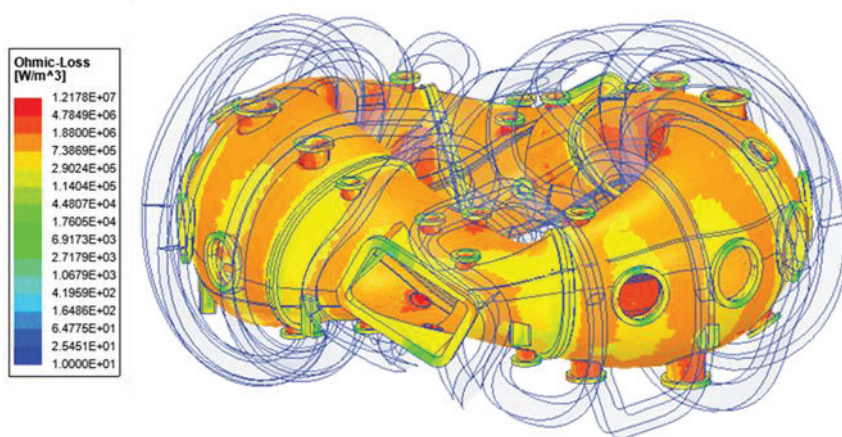


Fig 4.5-9 Distribution of the heat generation. $I_{AC}=7A$, $f=1kHz$. The maximum heat generation in VV is about $1.2 \times 10^7 W/m^3$.

4.6 Structural analysis of vacuum vessel

4.6.1 Stress and displacement in various operating conditions

On plasma operation, the vacuum vessel (VV) is exposed to several loads, such as an atmospheric pressure, a thermal stress, and EM forces of eddy current. The most important of these is the vacuum force, and it is necessary to confirm that the deformation and stress due to that force are within a reasonable range. Due to its complexity of shape, it is hard to predict the mechanical behavior of the VV. Therefore, we have performed structural analyses to validate the reliability of VV with use of the ANSYS/Mechanical.

In the analysis, we had chosen 2 models as shown in Table 4.6-1. The results are summarized in Table 4.6-2. Here, the model for the case 1-0 and 1-1 was created according to the latest design of the vacuum vessel, and the model for the case 2-0 and 2-1 was created in the preliminary simplified design to reduce the computer load during eddy current analysis since the coupled analysis of eddy current and stress requires a huge amount of calculation time. Fig 4.6-1 shows the mesh of the vacuum vessel and Fig 4.6-2 shows the boundary condition and the load for the stress analysis. The vacuum pressure (atmospheric pressure 0.1 MPa) was applied on the outer surface as shown in the blue arrows. The bottom surfaces of eight legs was fixed for constraint condition. Furthermore, gravitational acceleration is applied on the entire vacuum vessel as a self-weight.

By comparing the case 1-0 and 2-0, it was found that there was a variation of 10% in the result depending on the model. In the following, we will discuss the validity of the design on the assumption that there is an error of about 10%.

The stress due to vacuum pressure is up to 96 MPa in case 1-0 of Fig 4.6-5 and up to 100 MPa in case 2-0 of Fig 4.6-8. These values are much less than the design stress of 137 MPa. The location with the maximum stress is near the root of the upper and lower diagnostic port. In this analysis, it was assumed that the port was connected to the vacuum vessel body by full welding. Incomplete welding is likely to be applied for the purpose of cost reduction, so the effects of this will be considered separately.

The deformation due to vacuum pressure up to 0.98 mm in case 1-0 of Fig 4.6-4 and up to 1.22 mm in case 2-0 of Fig 4.6-7. Since the distance between the vacuum vessel and the peripheral equipment is over 5 mm, it is presumed that this deformation is not a problem.

To evaluate thermal deformation during baking, the temperature distribution obtained by the heat transfer analysis in advance, whose result was shown in Fig 4.6-3. For simplicity, the vacuum vessel and bottom surfaces of legs were fixed to 130 °C and 22 °C, respectively.

Fig 4.6-4 and Fig 4.6-5 show comparisons of the stress analysis with and without the baking. As shown in Fig 4.6-5(2), the maximum stress was increased up to 109MPa, which is acceptable. The location at the maximum was near the base of the leaf spring type legs. The maximum displacement of 3.3 mm in Fig 4.6-4(2) was caused by the increase in the major radius due to the temperature rise during baking. This deformation will be unavoidable because it is determined by the thermal expansion coefficient and temperature of the vacuum vessel.

By the coupled analysis function of the ANSYS/Maxwell and the ANSYS/Mechanical, the EM force due to the eddy current at 500 ms as shown in Fig 4.6-6 was applied to the stress analysis model as a distributed load. The body force distribution is locally up to 0.015 N / mm³, but in most places less than 0.002 N / mm³, which is

0.012MPa (0.02 x 6mm) in terms of surface pressure. Since the 0.012 MPa is only 10% of atmospheric pressure, it is estimated that the effect of the eddy current is very small.

Fig 4.6-7 and Fig 4.6-8 show comparisons of the stress analysis with and without the EM force. As shown in these figures, the differences of the stress and the deformation are very small, and the effect of the EM force can be ignored.

Therefore, it was confirmed that the maximum stress is within an elastic deformation range, and there is also no possibility that the vacuum vessel will break due to repeated stress fluctuations.

Table 4.6-1 Condition of the stress analysis.

Name	Model	Main purpose	External pressure and self-weight	Thermal deformation	Distributed load (External)
Case 1-0 (VP)	Latest design with the legs	Validation under the vacuum pressure	0.1 MPa 1G	-	-
Case 1-1 (TD)		Validation at the time of baking	0.1 MPa 1G	108 Degrees (130-22°C)	-
Case 2-0 (VP)	Preliminary simplified design without the legs and the close flange.	Validation of the model.	0.1 MPa 1G	-	-
Case 2-1 (EM)		Validation with EM force	0.1 MPa 1G	-	0.01MPa equivalent

Table 4.6-2 Result of the stress analysis.

Name	Equivalent (Mises) stress (MPa)		Maximum deformation (mm)	Notes
	Maximum	Allowed		
Case 1-0 (VP)	100	137 (Sm at 30°C)	0.98	Large stress and deformation near the base of the port.
Case 1-1 (TD)	109	150 (1.5Sm at 150°C)	3.3	Thermal stress concentrates on the base of the leg.
Case 2-0 (VP)	96	137 (Sm at 30°C)	1.22	There is a deviation of about 5% from the case 1-0 due to the influence of the mesh or the leg.
Case 2-1 (EM)	97	137 (Sm at 30°C)	1.23	The effect of EM force can be ignored.

The Sm is a design stress of SUS316L.

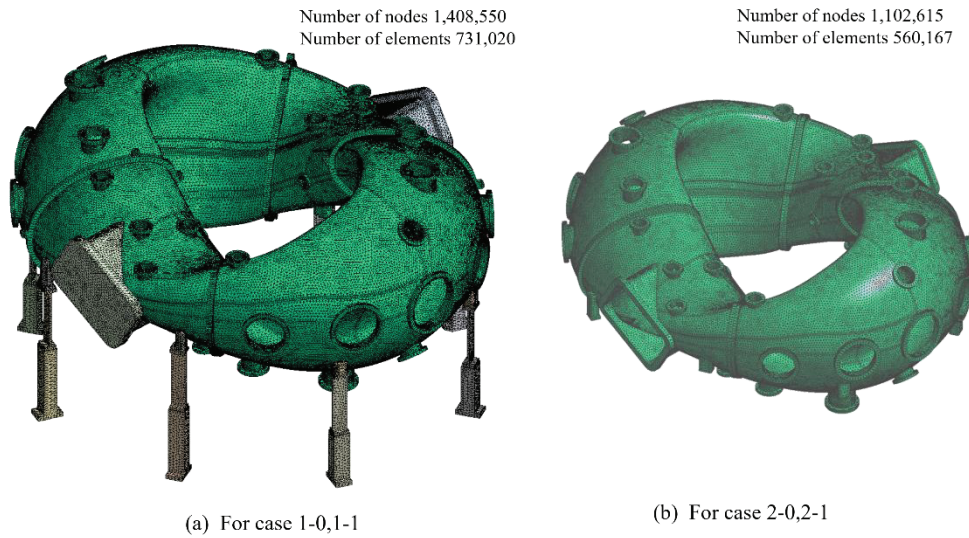


Fig 4.6-1 Mesh of the vacuum vessel for the stress analysis. Since the coupled analysis of eddy current and stress requires a huge amount of calculation time, a preliminary simplified model was used for the case 2-1. There are differences such as ignoring the legs and the rectangular close flange and the thickness of the large flanges at split location is different.

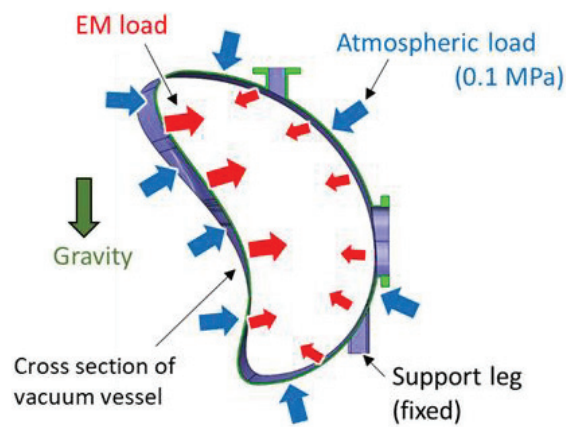


Fig 4.6-2 Boundary conditions for the stress analysis with the EM load and vacuum pressure. The EM load is applied by the eddy current.

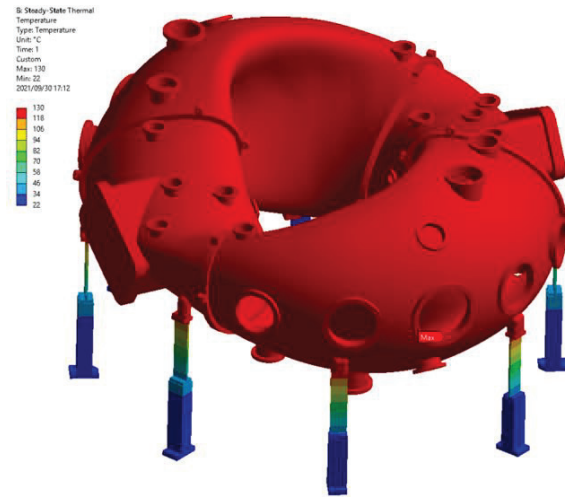


Fig 4.6-3 Temperature distribution that causes thermal deformation for the case 1-1. It was obtained by heat conduction analysis. It is 22 °C at the base of the legs, and 130 °C on the thin plates of the vacuum vessel.

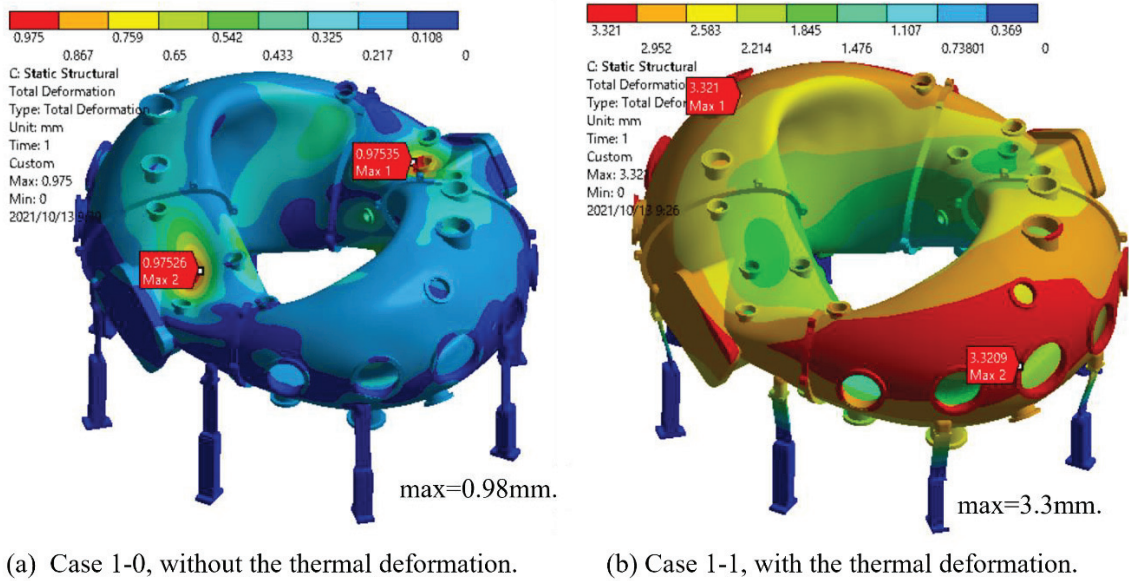


Fig 4.6-4 Changes in the deformation due to the baking.

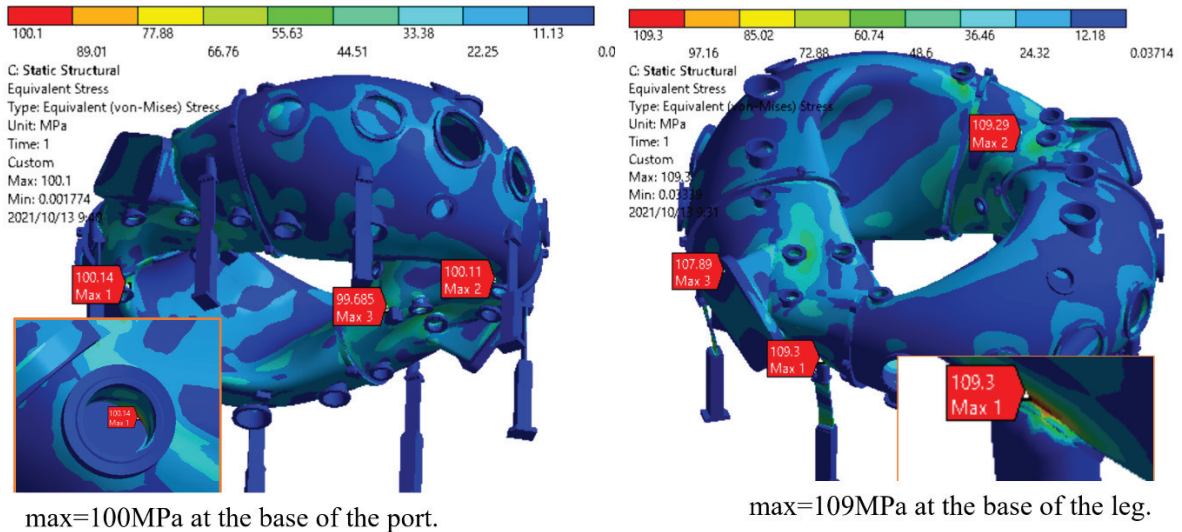


Fig 4.6-5 Changes in the equivalent stress distribution due to the baking. The stress due to the deformation of the thin plate due to vacuum pressure is the largest without the baking, and the stress at the base of the leg due to thermal deformation is the largest with the baking.

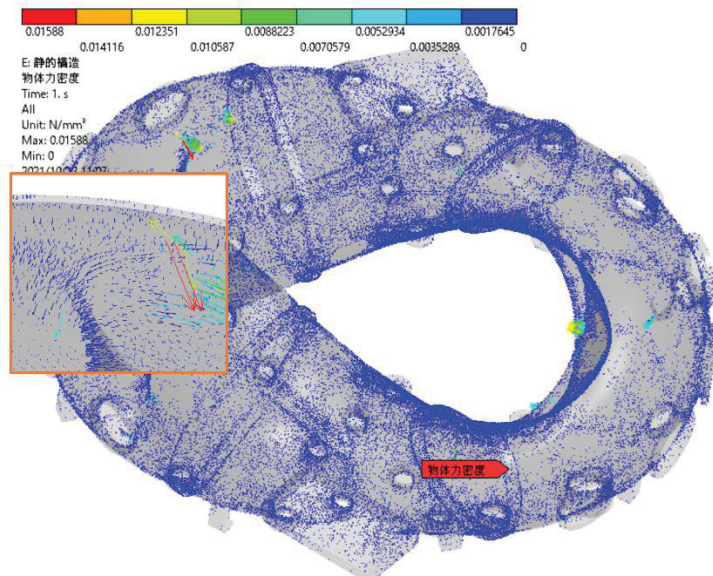
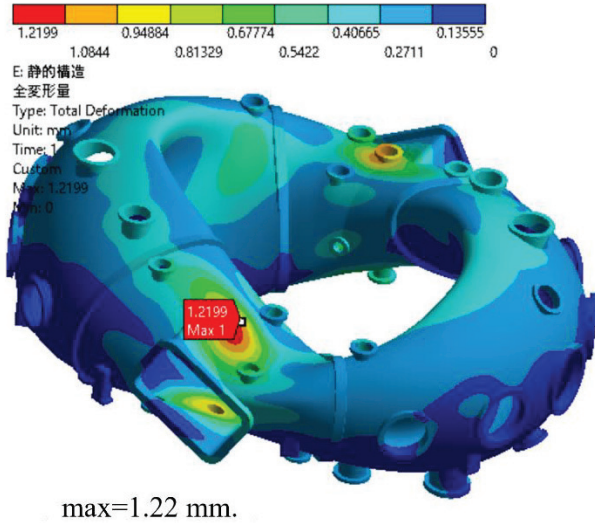
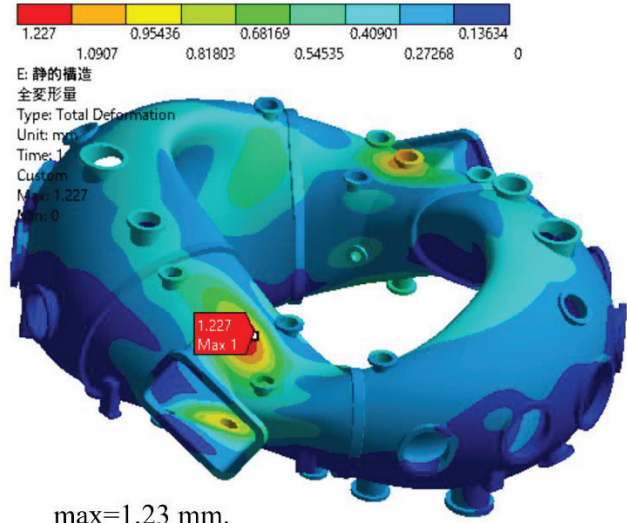


Fig 4.6-6 EM distribution by the eddy current at 500ms.



max=1.22 mm.

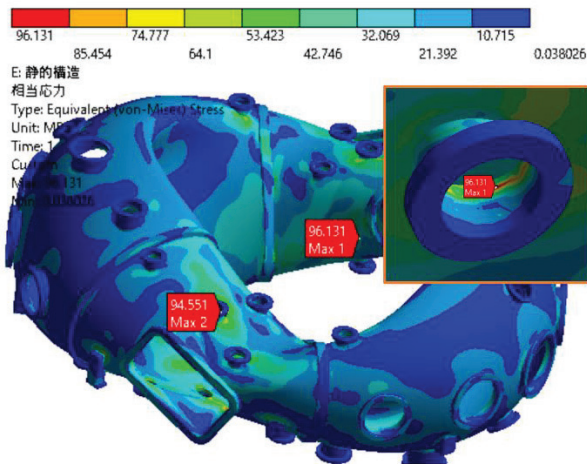
(a) Case 2-0, without the EM force



max=1.23 mm.

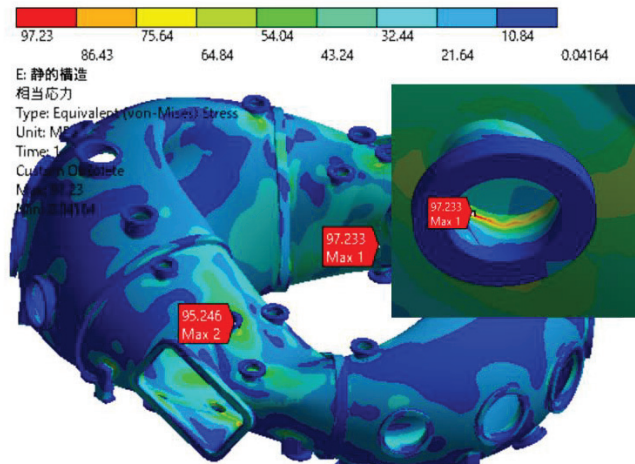
(b) Case 2-1, with the EM force

Fig 4.6-7 Changes in the deformation due to the EM force.



max=96MPa at the base of the port.

(a) Case 2-0, without the EM force



max=97MPa at the base of the port.

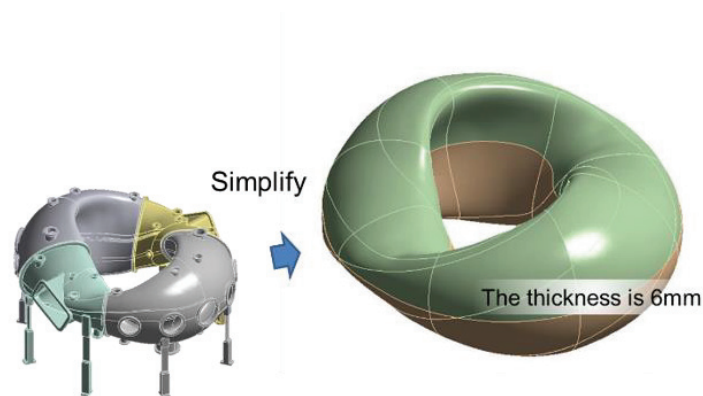
(b) Case 2-1, with the EM force

Fig 4.6-8 Changes in the equivalent stress distribution due to the EM force. The stress is the largest at the base of the port, which is mainly caused by the deformation of the thin plate due to the vacuum pressure. The effect of the EM force is very small.

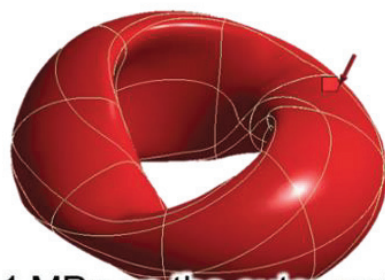
4.6.2 Effect of mesh size in the analysis for the vacuum vessel

A mesh size is one of the most important factors in the FEM since a result of the FEM depends on mesh size significantly. Therefore, we have conducted preliminary analysis with a simplified model and estimated reasonable mesh size for the analysis of the CFQS vacuum vessel (VV). Fig 4.6-9 shows the model and analysis condition. We have investigated how the result changes with mesh refinement.

The results are summarized in Fig 4.6-10. The vertical lines show the maximum deformation and stress, and the horizontal one the number of elements. According to this figure, as the mesh size decreases, the result of solid element shown as red circle seems to converge, and in case of less than 25 mm, it agrees with the result of shell element. From this result, we can assume that the mesh size should be less than 25 mm in the analysis of the VV for the CFQS.



(a) Simplified model



0.1 MPa on the outer surface

(b) Simplified load condition

Fig 4.6-9 Simplified model and the load condition for the vacuum vessel.

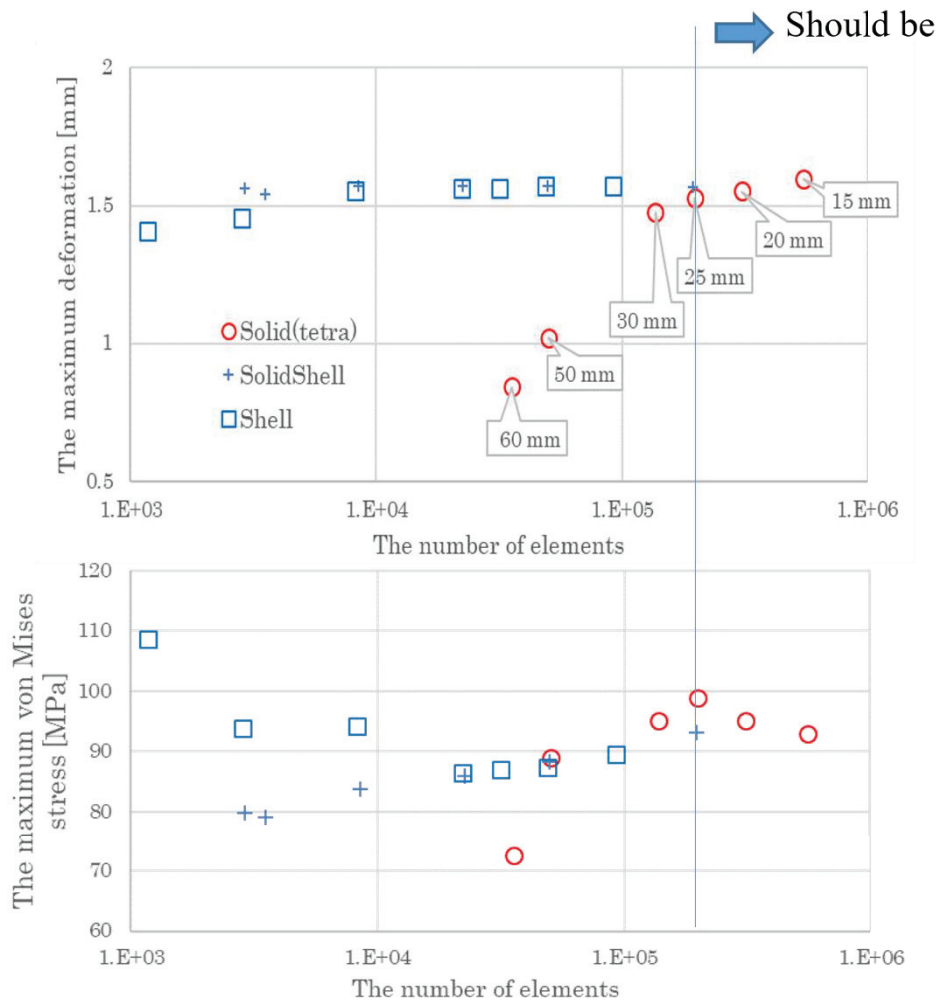


Fig 4.6-10 Relationship between FEM analysis and number of meshes. The results show that the mesh size should be less than 25 mm in the analysis.

4.7 Baking heater for vacuum vessel

4.7.1 Specification of the baking heaters

For baking of the vacuum vessel, we will wind some sheath heaters on the vacuum vessel surface. Total required baking power is estimated approximately 25kW, which is referred by CHS baking system since the volume of the CFQS is almost equivalent to that of CHS.

Baking regions are distinguished 8×2 sections based on 12 TFC and 4 flanges to connect 4 sections as shown in Fig 4.7-1. Each heater is wound separately so as not to leap over them and has its own power system to make it easier to control the temperature. Each baking heater winding route is arranged as shown in the figure.

The heating capacity of each section was set so that the amount of heat per unit mass was almost constant. Diameter of each sheath heater is 4.8 mm and its resistance is 1.55 Ω /m. The heater length was estimated from the 3D-CAD model. It is mounted on the surface of vacuum vessel with an interval of about 100 mm. Table 4.7-1 shows the specification of the baking heaters, such as heater length, required capacity and voltage.

4.7.2 Required length of the baking heater

Since the baking heater is outsourced by specifying the length, it is necessary to evaluate the required length in advance. However, since the shape of the vacuum vessel is complicated and the wiring path of the heater is not simple, it is not easy to evaluate the required length.

It was a little tough to estimate a length of the baking heater. We know creating 3-D model is the best way to estimate the length however it usually takes a lot of times and efforts to create complicated 3-D path in a CAD. In the early stage, we used strings and 3-D printed model to consider a suitable winding route and to estimate the length of baking heater. Following pictures in Fig 4.7-2 show 1/10 scale 3-D printer models with wound strings instead of heaters.

After determining the approximate winding policy using 3-D printer models, the heater route was determined on 3-D CAD. Table 4.7-2 shows a comparison between the heater length estimated by the 3-D printer model with strings and that estimated in 3-D CAD. As you can see from this table, there is no significant difference except for B2. In this region, heater path is modified to some extent.

Table 4.7-1 Specification of baking heaters.

Region	Required capacity [kW]	Heater length [m]	Resistance [Ω]	Maximum voltage [V]	Maximum current [A]	Heating capacity [kW]
A1	0.98	4.8	7.4	110	14.8	1.6
A2	2.42	11.3	17.6	220	12.5	2.8
A3	1.05	4.8	7.4	110	14.9	1.6
B1	1.67	10.1	15.7	220	14.0	3.1
B2	1.63	10.7	16.7	220	13.2	2.9
B3	1.46	11.6	18.0	220	12.2	2.7
B4	1.62	10.9	16.9	220	13.0	2.9
B5	1.67	10.1	15.7	220	14.0	3.1
Sum	12.5	74.3				20.7

Diameter of each sheath heater is 4.8mm and its resistance is 1.55 Ω /m.

Table 4.7-2 Comparison of the heater length estimated.

Region	Heater length [mm]		Difference
	3-D printer model with strings	3-D CAD	
A1	4,750	4,788	-0.8 %
A2	12,000	11,325	6.0 %
A3	-	4,752	-
B1	10,750	10,105	6.4 %
B2	12,200	10,746	13.5 %
B3	12,200	11,621	5.0 %
B4	-	10,883	-
B5	-	10,105	-

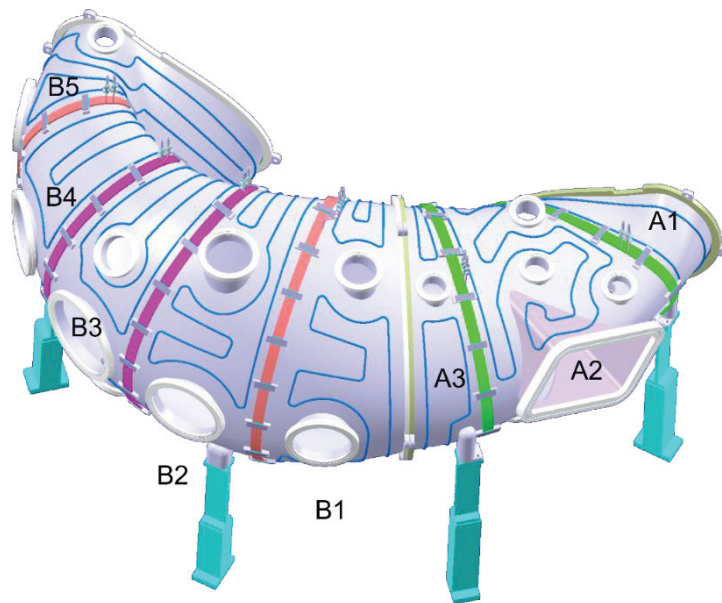


Fig 4.7-1 Baking heater on the vacuum vessel.

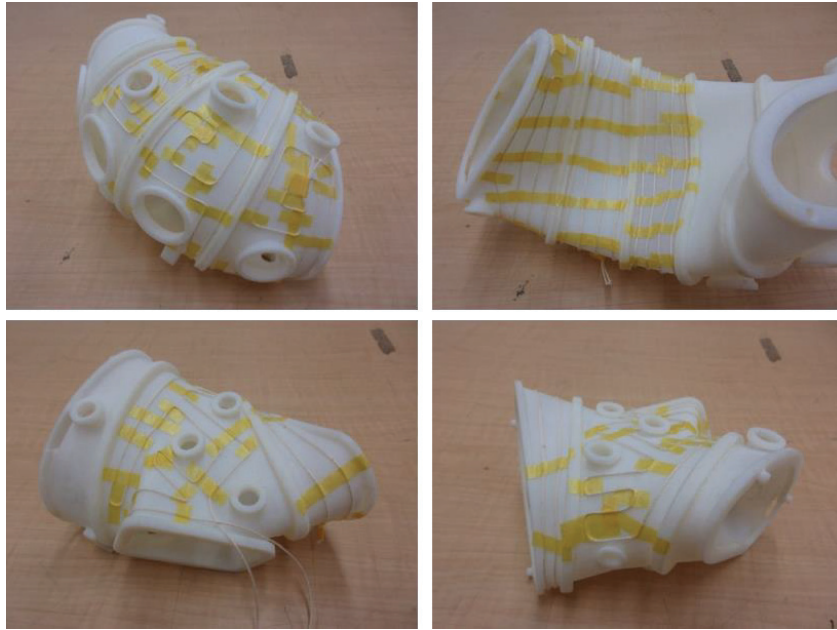


Fig 4.7-2 3-D printed models with wounded strings instead of the heaters.

4.8 Preliminary layout of magnetic measuring elements

In the future, four types of magnetic measuring instruments will be installed in the vacuum vessel to measure instability and energy in the plasma. We designed the installation location and wiring route of the magnetic measuring instrument so that those locations would not be used for other purposes. Fig 4.8-1 shows layout example of the magnetic measuring instruments.

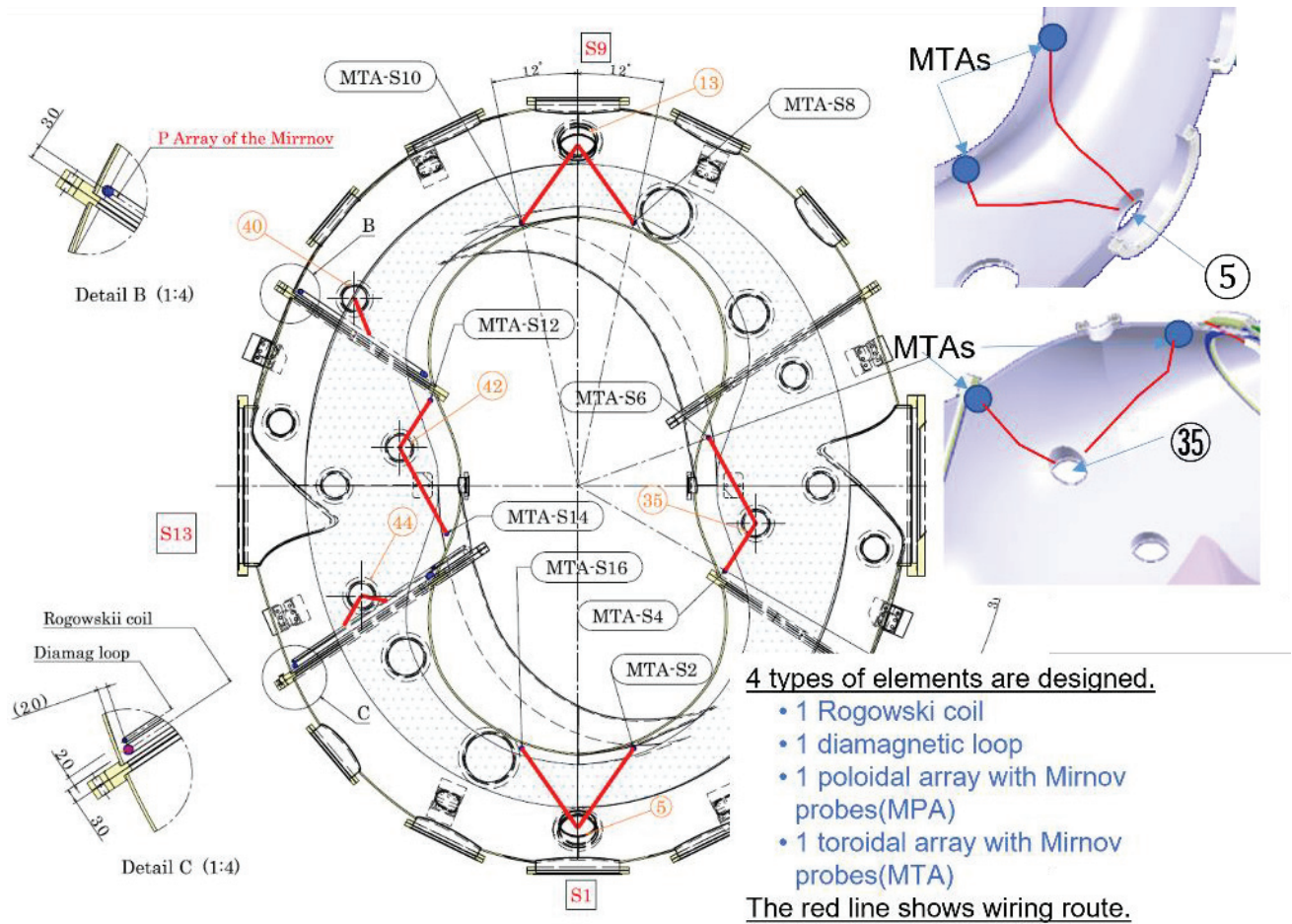


Fig 4.8-1 Magnetic measuring elements

4.9 Preliminary layout of the view ports

To observe the shape and behavior of the plasma, we will provide view ports for seeing the plasma in the tangential direction in the vacuum vessel. However, since the shape of the vacuum vessel is very complicated, it is not easy to secure a field of view in which the plasma can be seen in the tangential direction. Therefore, we searched for a port that could be used as a tangential port by 3D CAD. The results are shown in Fig 4.9-1. It seems that the plasma can be observed from ports # 8, 17 and 18, but the wall of the vacuum vessel may be in the way and the entire plasma cross section cannot be observed. Depending on which part of the plasma we want to observe, we need to adjust the position, tilt, or size of the flange.

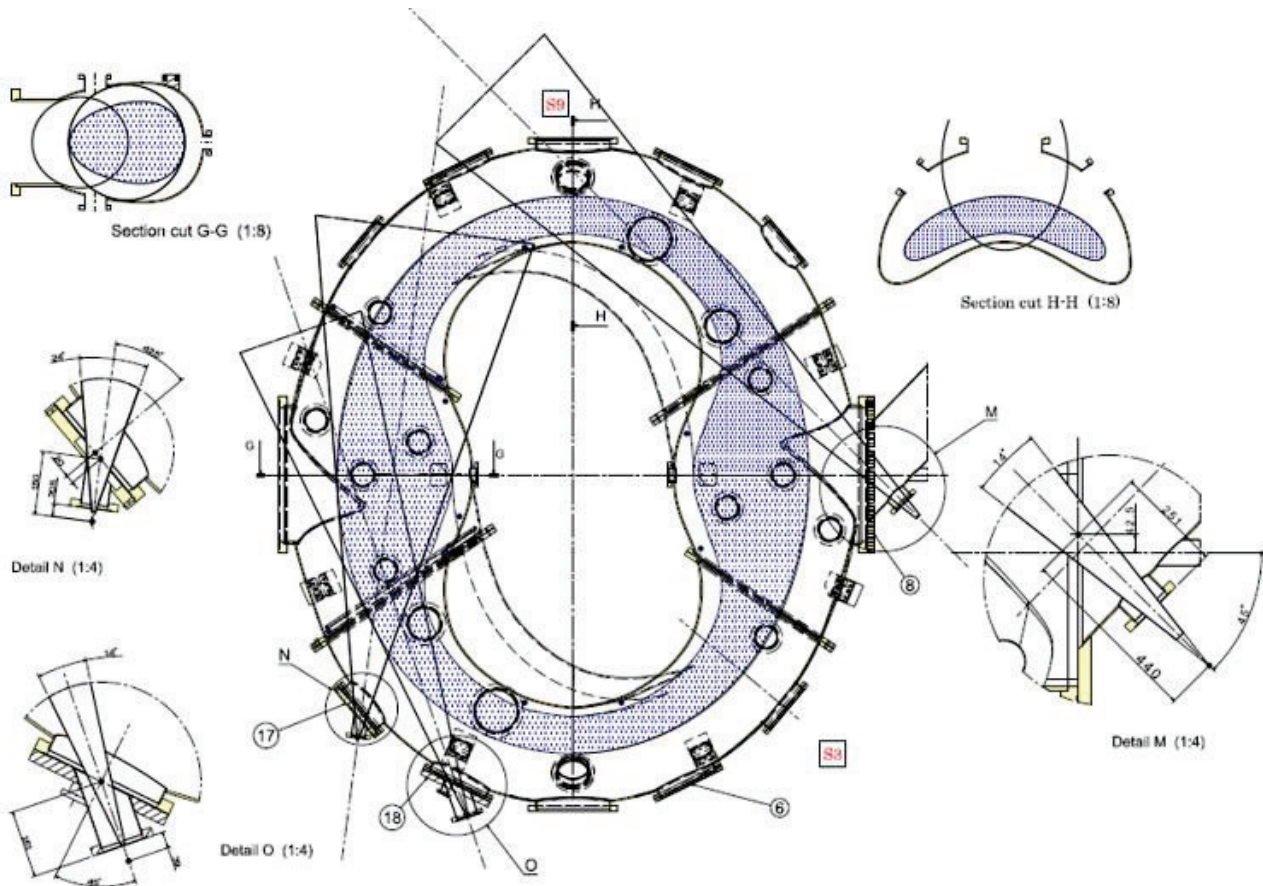


Fig 4.9-1 Tangential view ports

4.10 Preliminary layout of the limiters

we intend to put four sets of the poloidal or rail limiter inside the vacuum vessel for defining the plasma and protecting the wall. Two of them are fixed limiters which will be installed primarily to protect the walls. Others are movable limiters which will be installed for defining the plasma and changing the size of plasma. Fig 4.10-1 shows the layout of the limiters and their conceptual shape.

Although detailed examination is required, it seems possible to install limiters with an outer diameter of about 30 mm x 30 mm in cross section.

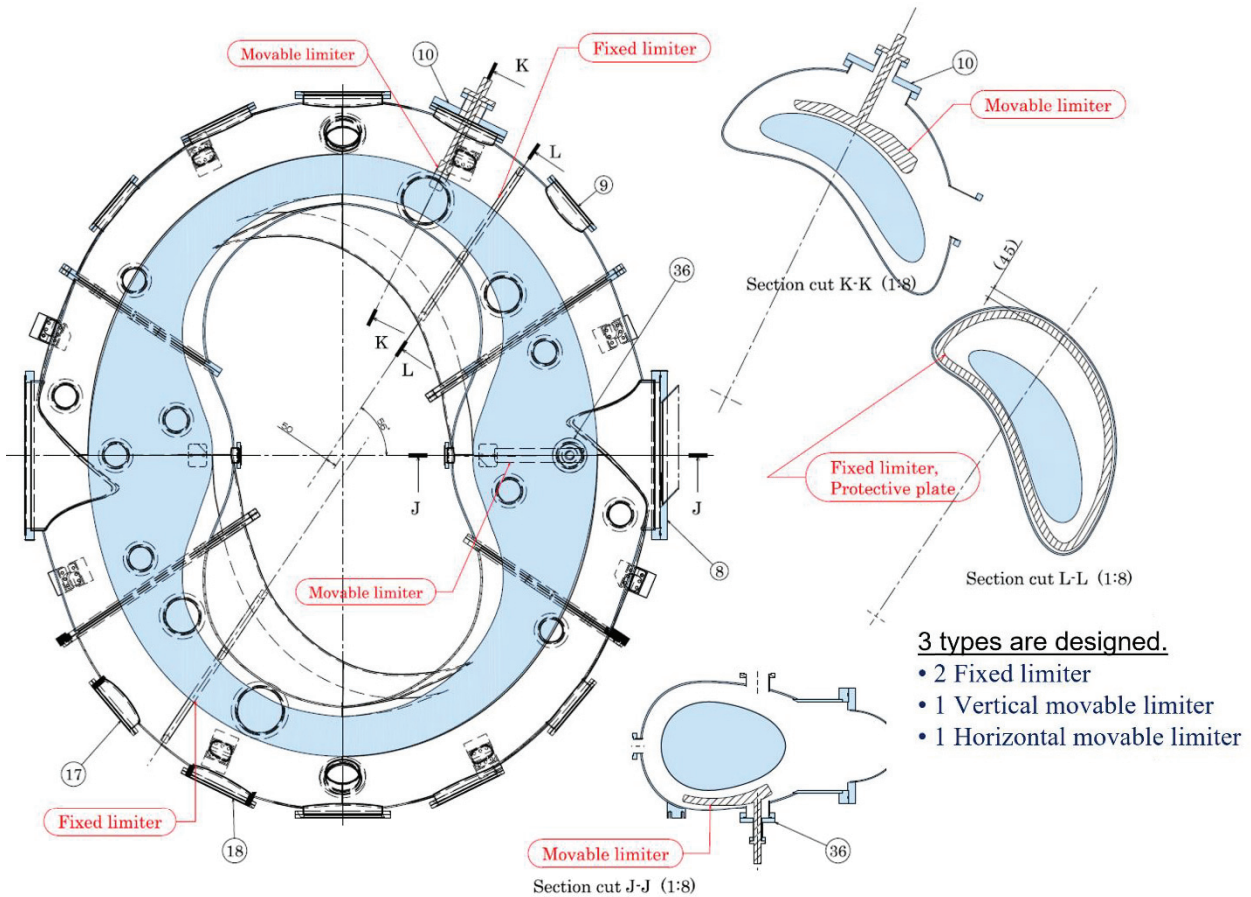


Fig 4.10-1 Limiters

5 Preliminary production flow of the CFQS

5.1 Production flow of vacuum vessel in a factory

We drew up a design plan to carry out manufacturing process of the vacuum vessel and conduct various equilibrium experiments.

Each section of vacuum vessel is manufactured by welding multiple thin plates made by the hot press working and two large flanges to prevent welding deformation as shown in Fig 5.1-1. Fig 5.1-2 shows an example of the bending press mould and the jig for welding and assembly. Fig 5.1-3 shows the example of the divided pieces.

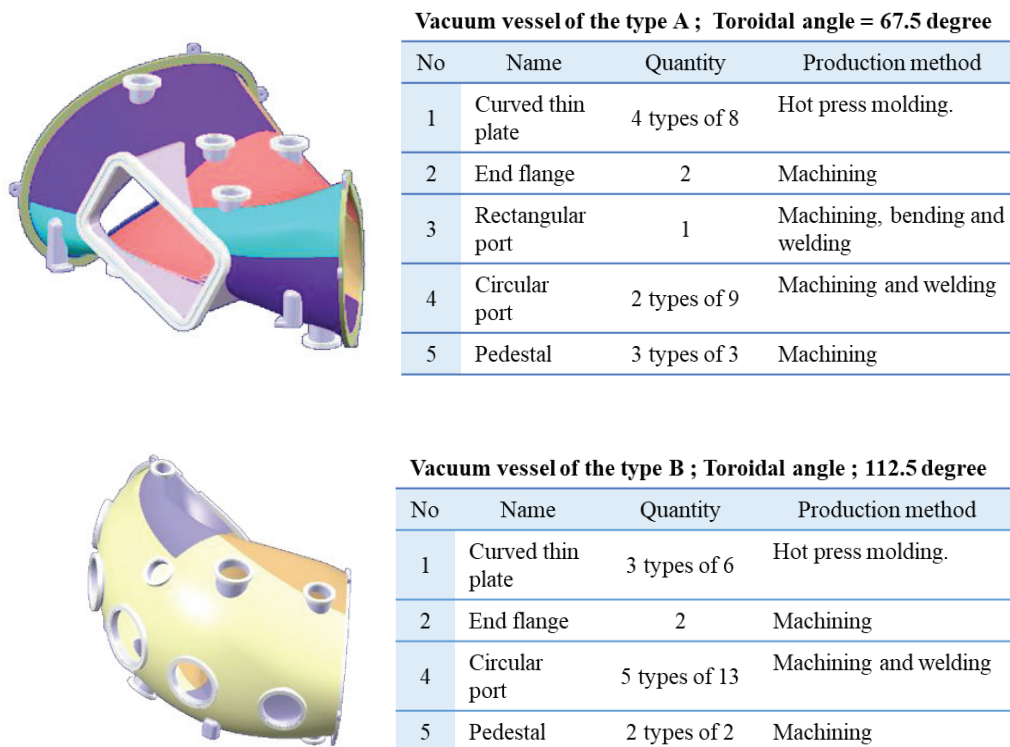


Fig 5.1-1 Material pieces divided plan for vacuum vessel manufacturing. It will be reviewed in the detailed design of the mockup.

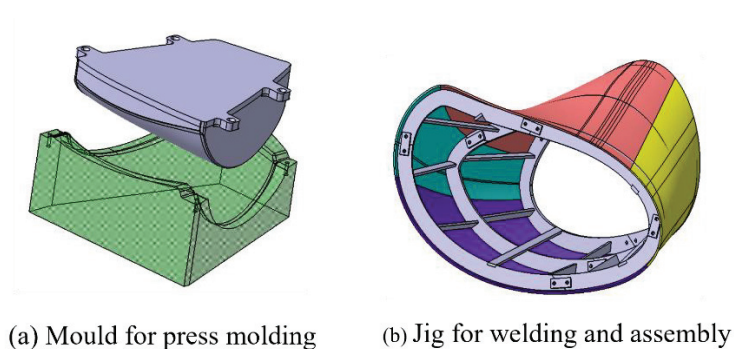


Fig 5.1-2 Example of press mould, and jig for welding and assembly.

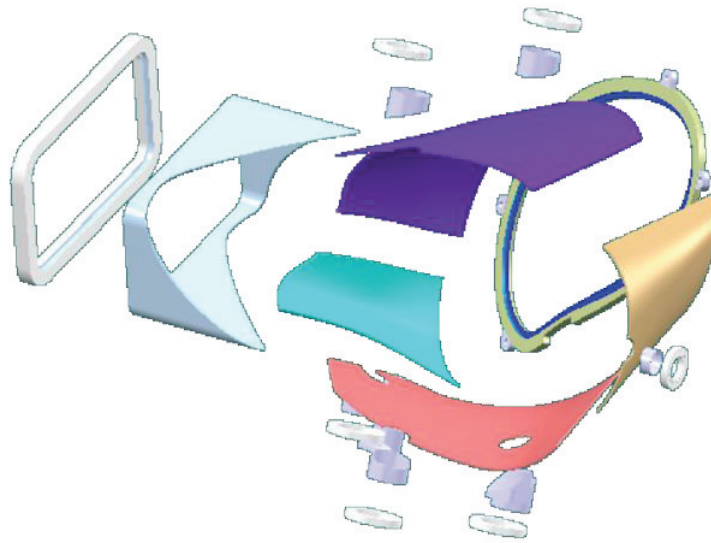
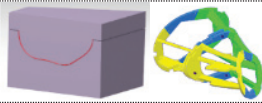
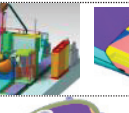
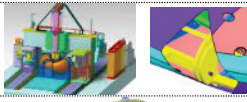
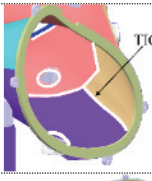


Fig 5.1-3 Half of the divided pieces for the vacuum vessel type A. It will be manufactured by welding 33 pieces in total.

Table 5.1-1 shows the procedure to product one section of the vacuum vessel. The position accuracy of the flange of the measuring port is the most important factor in the quality of the vacuum vessel. To achieve that goal, some machining steps will be inserted in the middle of the production process. Except for the flange surface, large errors will be allowed within the range that does not interfere with other parts in the overall assembly.

Table 5.1-1 Procedure to product one section of the vacuum vessel.

STEP	Contents	Illustration	Target accuracy
1	Purchase the material and the standard parts.		
2	Make the press moulds (7 or 8 mould sets) and the moulds for assembly and welding.		1 mm (Surface)
3	Make the thin curved plates by hot press.		1 mm (Surface)
4	Make the end flanges, and the ports with the flange by machining and welding.		0.5mm (Surface)
5	Correct the deformation of the thin plates based on the mould and cutoff the periphery.		3 mm (Surface)
6	Assemble the curved plates and end flanges on the mould.		
7	Connect the thin plates and end flanges by intermittent welding of the outer surface.		
8	Correct the deformation of the thin plates based on the mould by the point heat quenching or hammering.		
9	Make port holes on the thin curved plates by machining.		0.5 mm (port)
10	Insert the ports into the port holes, connect the ports and the thin plates by intermittent welding of the outer surface, and fix the pedestals for the leg by the welding.		1 mm (port)
11	Measure in 3D at the center of the ports by the laser or something else.		1 mm (port)
12	Remove the mould.		
13	Seal welding from the inside and the PT inspection (Liquid Penetrant Testing).		1 mm (port)
14	Vacuum evacuation test, such as the He leak test, baking test, and displacement measurement.		
15	Machin the surfaces of the end flange just before the overall assembly to improve the accuracy of the weld surface between sectors.		1 mm (Surface)

5.2 Pre-assembly procedure of modular coils and vacuum vessel on site

Before installing the modular coils and the vacuum vessel, it is necessary to pass the vacuum vessel through the coils. The work is planned to be done in a location different from the installation position in the same building. Although this work can be performed in the factory, it is difficult to safely carry the assembled parts together. Therefore, it is planned to transport each part and reassemble them in the laboratory after the defects in the temporary assembly are extracted in the factory. Since this pre-assembly work is complicated and delicate, confirmation of work steps and work training should be conducted in the factory.

Fig 5.2-1 shows the pre-assembly process of the modular coils and the vacuum vessel. In step 1, the vacuum vessel part is fixed with appropriate jigs on the workbench desirable to be composed of a surface plate which is a flat plate used as the main horizontal reference plane for precision inspection. The coil is inserted while rotating it in steps 2, 3, 4 and 5, but since the vacuum vessel has a complicated twisted shape, delicate adjustment work is required to move the coil. It is possible to develop a special transport machine for that work, but to reduce costs, it is also possible to work with an overhead crane and the manual hoist as shown in the figures. Since it is necessary to frequently attach and detach the legs of the vacuum vessel to pass the coil, a jig such as a hydraulic jack will be prepared to facilitate the work. In step 6, the whole is fixed to the upper temporary base and suspended by an overhead crane.

It is considered that the vacuum vessel and the coils can be suspended integrally by assembling in such a procedure. Steps 7 and 8 show a state in which two types of vacuum vessels and coils are suspended.



Fig 5.2-1 Pre-assembly process of the modular coil and vacuum vessel.

6 Power supply for coils

6.1 Current wave form to estimate required power capacity

The required specification of the power supply system for coils is shown in Table 6.1-1. They are estimated by the following procedure.

Table 6.1-1 Required specification of power supply system for coils.

Coil Name	0.09T					1T						
	Operation condition		Specification of power supply			Operation condition				Specification of power supply		
	Imax (A)	Vmax (V)	Imax (V)	Vmax (V)	kVA	Imax (kA)	Vmax (kV)	Pulse (s)	MJ	Imax (kA)	Vmax (kV)	MVA
MC1	391	170	420	210	98.0	4.34	2.151	1.11	11.5	4.5	2.2	11.0
MC2	391	168	420	210	98.0	4.34	2.119	1.11	11.3	4.5	2.2	11.0
MC3	391	162	420	210	98.0	4.34	2.052	1.11	11.0	4.5	2.2	11.0
MC4	391	157	420	210	98.0	4.34	1.982	1.11	10.6	4.5	2.2	11.0
TC10	180	49	210	75	17.5	2	0.467	0.19	0.2	3.2	0.7	2.5
TC32	270	68	315	75	26.3	3	0.643	0.19	0.4	3.2	0.7	2.5
TC70	270	56	315	75	26.3	3	0.53	0.19	0.3	3.2	0.7	2.5
OV	391	108	420	125	58.3	4.34	1.418	0.38	2.6	4.5	1.5	7.5
IV	391	34	420	45	21.0	4.34	0.413	0.38	0.8	4.5	0.5	2.5
Sum					541.3				48.7			61.5

To study the specifications of the coil power supply, the current waveform of each coil was defined. Fig 6.1-1 shows an equivalent circuit and assumed current and voltage waveform. In the actual operation, the waveform of the CFB using the feedback control circuit will be desirable, but here, for simplicity, the waveform of the CVC by the constant voltage power supply for which an analytical solution exists is used.

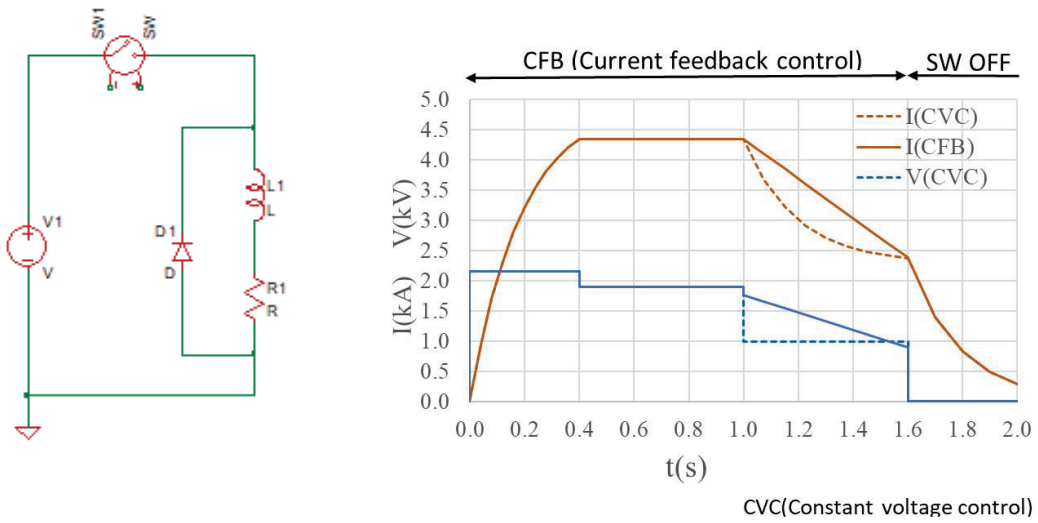


Fig 6.1-1 Equivalent circuit and voltage / current waveform.

The current waveform is represented by a combination of exponential functions.

- Current ramp up phase ($t - t_0 < \Delta t_{up}$)

$$I(t) = \frac{V_{up}}{R} \left\{ 1 - \exp\left(-\frac{t - t_{start}}{\tau}\right) \right\}$$

$$V_{up} = V_{flat} / \left\{ 1 - \exp\left(-\frac{\Delta t_{up} - t_{start}}{\tau}\right) \right\}$$

$\tau = L/R$; Time constant of coil

t_{start} ; Energization start time

- Flat top phase ($t - \Delta t_{up} < \Delta t_{flat}$)

$$I(t) = V_{flat} / R$$

- Decay phase ($t - t_1 = t - \Delta t_{up} - \Delta t_{flat} < \Delta t_{decay}$)

$$I(t) = I(t_1) \exp\left(-\frac{t - t_1}{\tau}\right) + \frac{V_{down}}{R} \left\{ 1 - \exp\left(-\frac{t - t_1}{\tau}\right) \right\}$$

$$t_1 = \Delta t_{up} + \Delta t_{flat}$$

- Shut down phase ($t > t_2 = \Delta t_{up} + \Delta t_{flat} + \Delta t_{decay}$)

$$I(t) = I(t_2) \exp\left(-\frac{t - t_2}{\tau}\right)$$

$$t_2 = \Delta t_{up} + \Delta t_{flat} + \Delta t_{decay}$$

Table 6.1-2 shows parameters to define waveform for each type of coil and Fig 6.1-2 shows typical example of current waveform. Fig 6.1-3 to Fig 6.1-5 show current and voltage waveform for each coil.

Table 6.1-2 Parameters that define the waveform.

Item	Symbol	Unit	MC	PFC	TFC	Plasma
Energization start time	t_{start}	S	0	0.5	0.7	0.73
Current ramp up duration	Δt_{up}	S	0.4	0.1	0.05	0
Flat top duration	Δt_{flat}	S	0.6	0.3	0.15	0.1
Current decay duration	Δt_{decay}	S	0.6	0.0	0.0	0
Flat top (maximum) current	I_{flat}	kA	4.34	4.34	2.17	-
Time constant of coil	τ	s	0.19	0.07~0.08	0.01	-
Voltage at the flat top	V_{flat}	kV	1.8~1.9	0.3~1.0	0.4~0.5	-

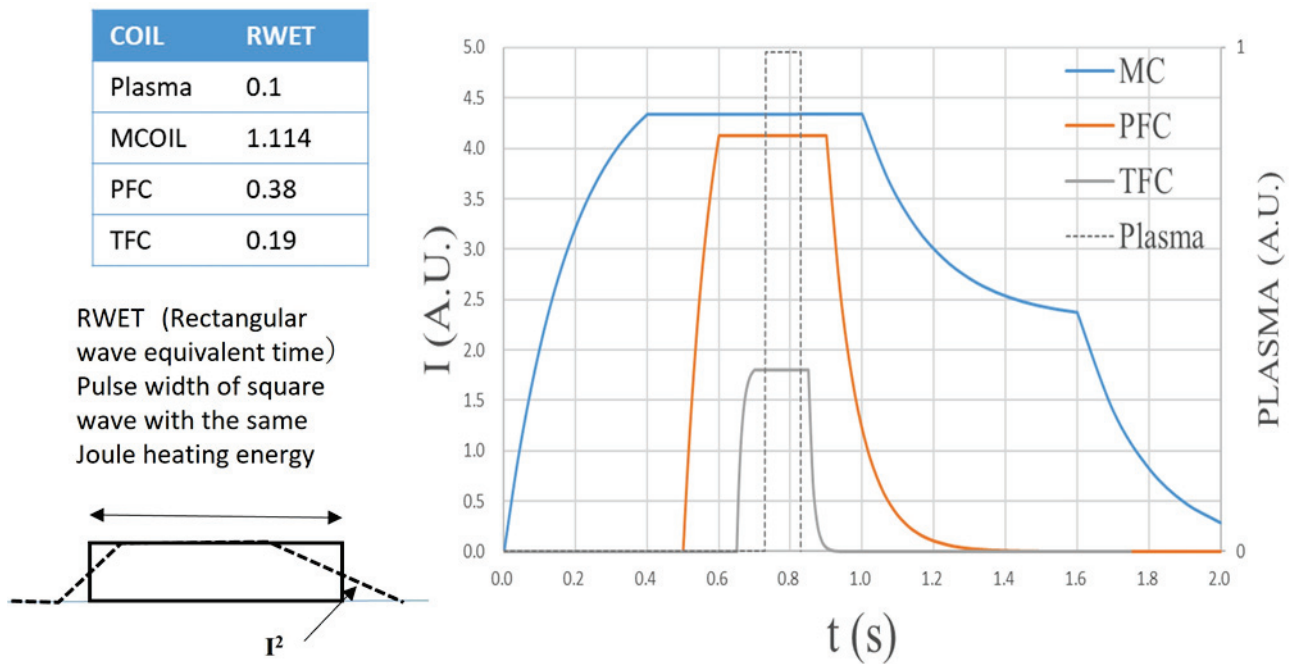


Fig 6.1-2 Defined current waveform for calculation. Exponential function waves were assumed for ease of calculations

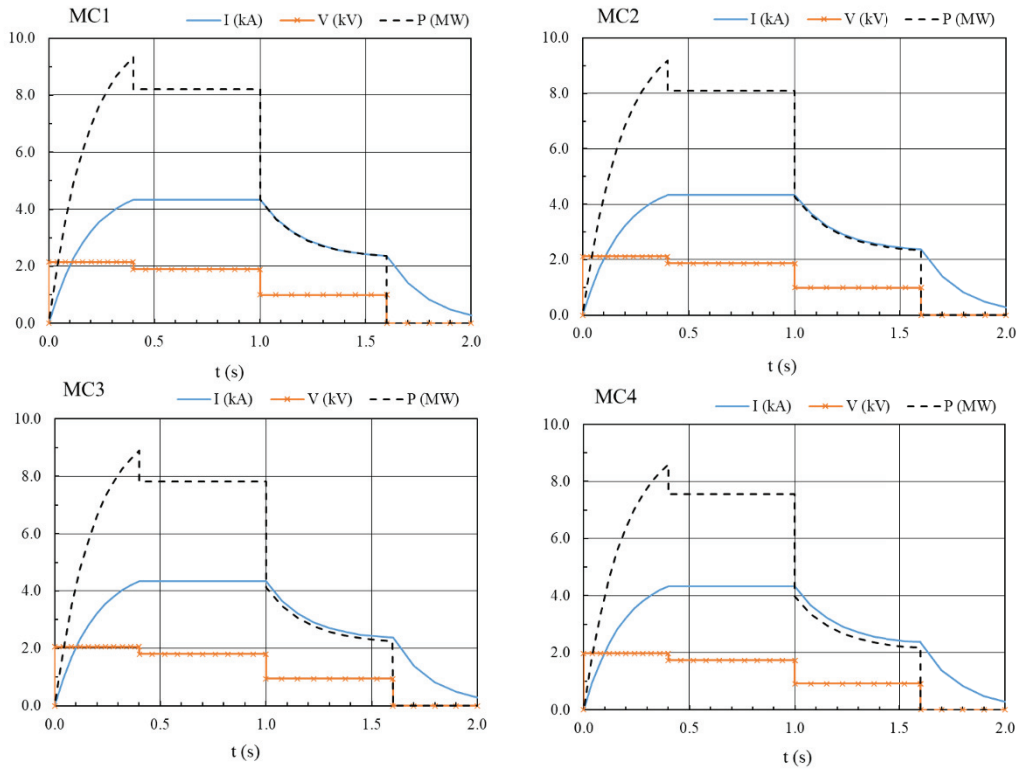


Fig 6.1-3 Current and voltage waveform for the MC power supply.

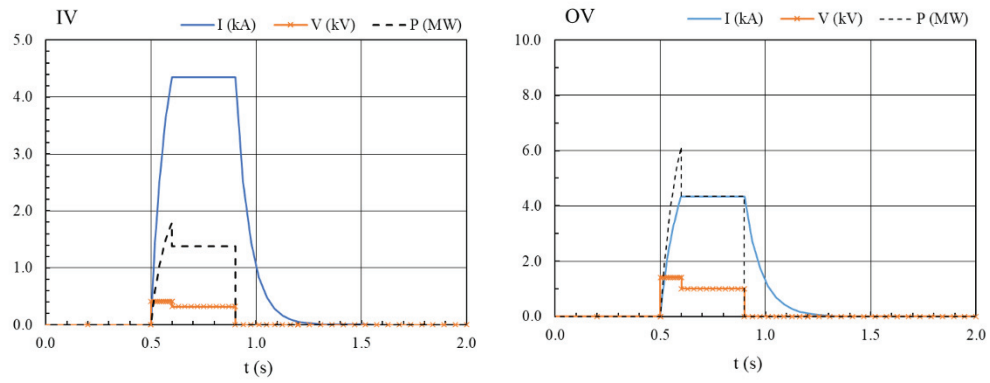


Fig 6.1-4 Current and voltage waveform for the PFC power supply.

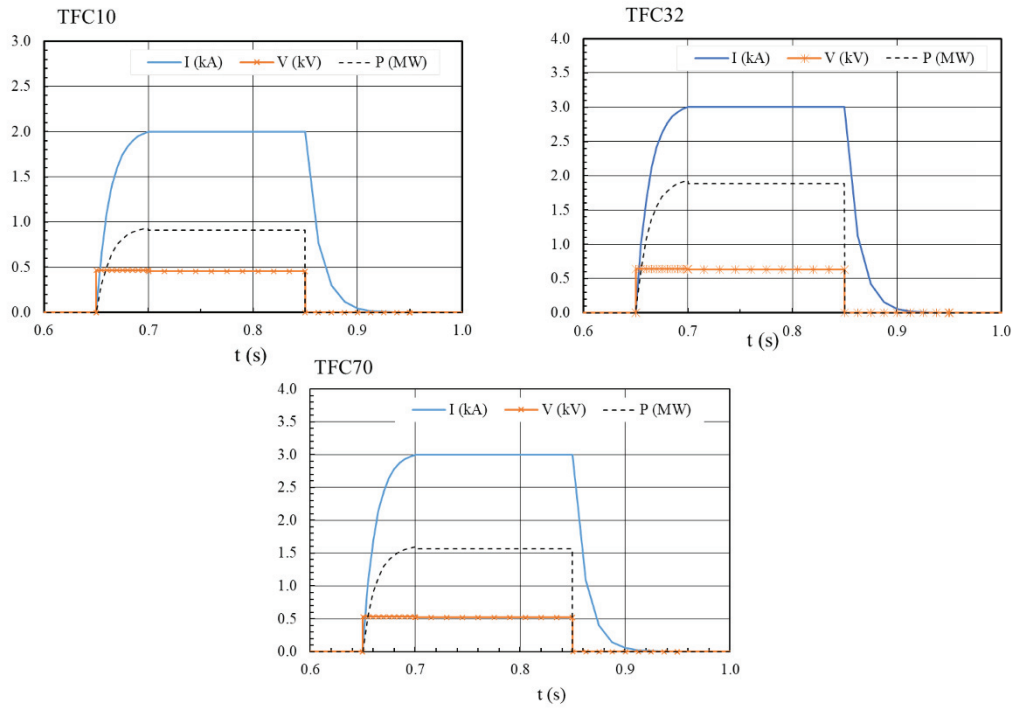


Fig 6.1-5 Current and voltage waveform for the TFC power supply.

6.2 Trial design of coil power supply for 0.09 T operation

Initially, it was planned to execute a 0.1 T experiment using part of the 1.0 T power supplies. However, the experimental plan was changed to a plan to perform 0.09 T operation first to understand the characteristics of the generated magnetic surface. The power supply system for 1.0 T operation has not been determined yet due to its complicated configurations. On the other hands, the design of the power supply system for the 0.09T operation needs to be determined immediately. Therefore, we decided that the power supply system for the 0.09T and the 1T are completely separated. It means that both systems do not share any electrical components.

Fig 6.2-1 shows the preliminary designed circuit diagram of the power supply system for 0.09 T. It mainly consists of four voltage adjusters and four diode rectifiers for the modular coil (MC), and five dc power supplies with thyristor-controlled unit for the TFC and the PFC. Two energy storage stations with 0.5 MVh each will be installed to supply these with a large amount of power equivalent to 600 kVA during the experiment. The charging power will be reduced to 100kW, and the charging time will be 10 hours per one day at night. Since the DC power supply with the thyristor convertor unit for high capacity may be expensive, the power supply with diode rectifiers is adopted for the MC. The DC power supply for the TFC and the PFC will be composed of a thyristor convertor unit which is suitable for high-precision current control.

Based on the circuit diagram, the layout of power supply system for 0.09 T was estimated. The result are shown in Fig 6.2-2. The indoor space for this system is roughly as 10,000 × 4,000 × 2,500H, where the baking system and the low voltage power boards may also be installed. The outdoor space for the energy storage stations is roughly as 13,000 × 2500 × 2,600H. The design is based on the data of products with similar specifications published in the commercial catalog. Re-evaluation according to the specific product design is necessary.

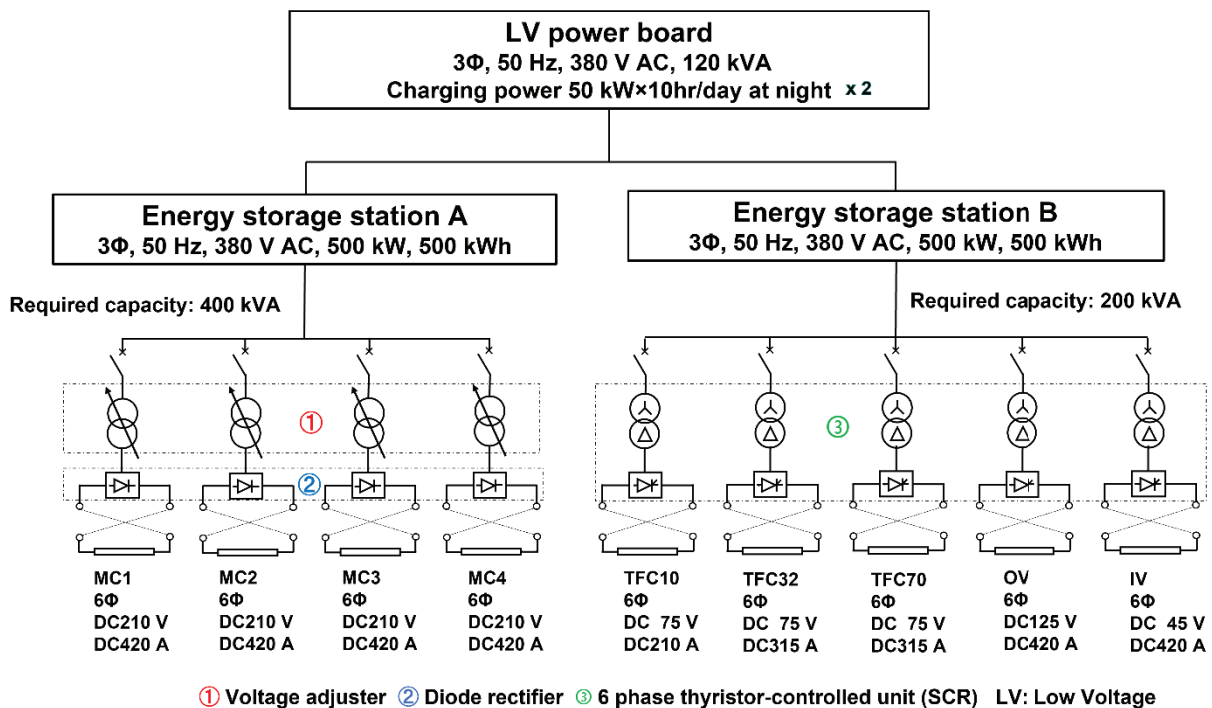


Fig 6.2-1 Circuit diagram of the power supply system for 0.09 T.

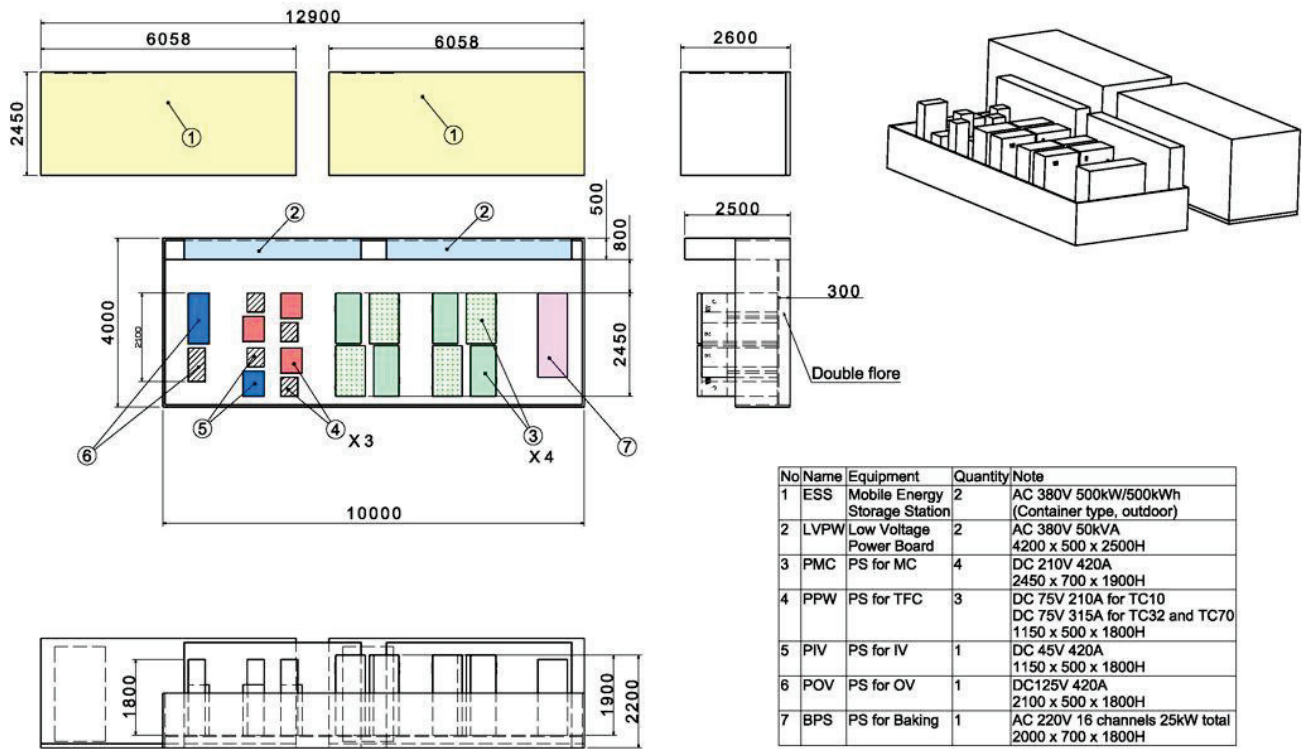


Fig 6.2-2 Layout of the power supply for 0.09T.

6.3 Trial design of coil power supply for 1 T operation

6.3.1 Designed circuit diagram and the layout of MG building

Based on rough estimation, we designed circuit diagram of the power supply system with IM and SG as represented in Fig 6.3-1. The circuit mainly consists of IM, SG, the inverter for IM and SG revolution control, the excitation system for SG, six phase thyristor-control units, and polarity switching circuits. Typical SG with two pole, 50 Hz, 70 MVA rated output, 10 kV of operation voltage is selected by a manufacturer catalog. The static exciting system consisting of an exciting transformer (EXT), an automatic voltage regulator (AVR), and SCR is adopted for SG excitation control. The excitation system has rapid responsiveness for SG voltage control.

Based on the circuit diagram, the layout of power supply system including the MG for 1 T was estimated. The result is shown in Fig 6.3-2. In this plan, the system is divided into two parts. One is a MG system with a synchronous generator and an induction motor, and other is a system with thyristor-controlled transducers and transformers. The space for the system with thyristor-controlled transducers is roughly as 30,000×10,000×3,500H, where it is better to be as close as possible to the CFQS. The space for the MG system is roughly as 20,000×12,000×5,000H. Here, it is presumed that the MG system vibrates the building and generates a large amount of noise. Therefore, it should be installed in a building with noise barriers built on a sturdy foundation, preferably a building different from the CFQS laboratory. The design is based on the data of products with similar specifications published in the commercial catalog. Re-evaluation according to the specific product design is necessary. More details of designs should be proceeded with a manufacturer.

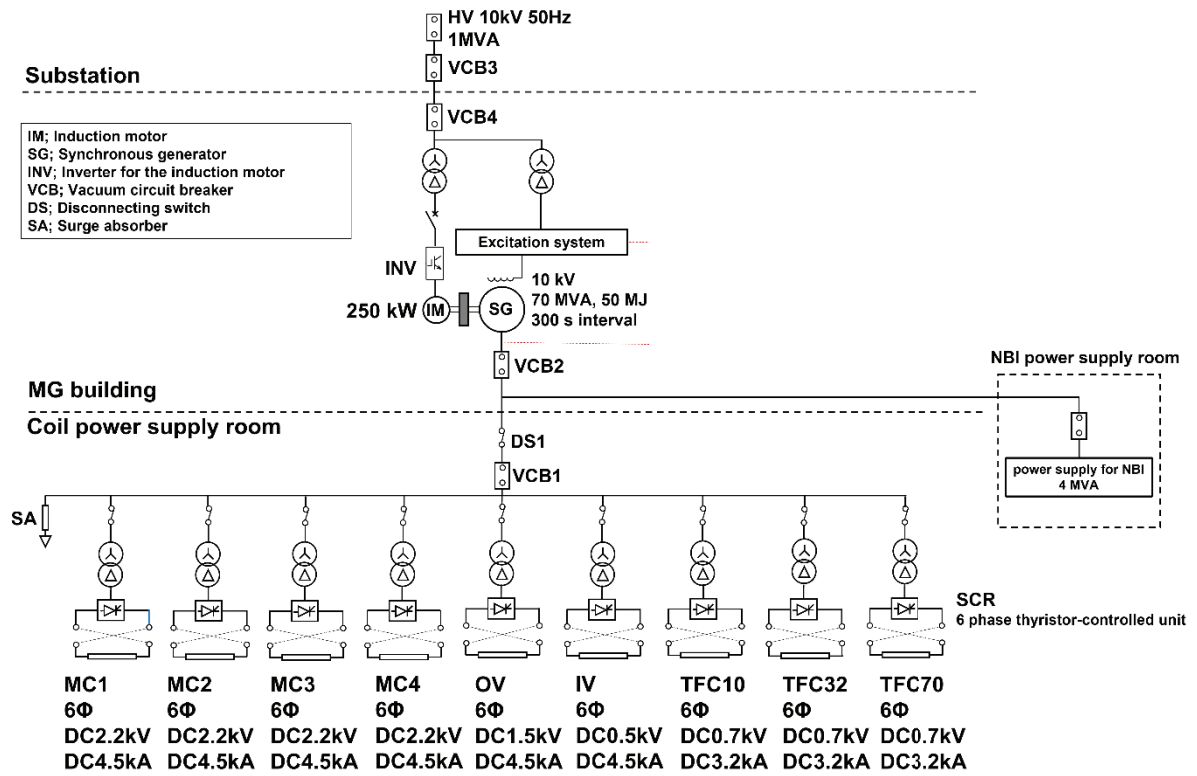


Fig 6.3-1 Designed circuit diagram of power supply system with IM and SG.

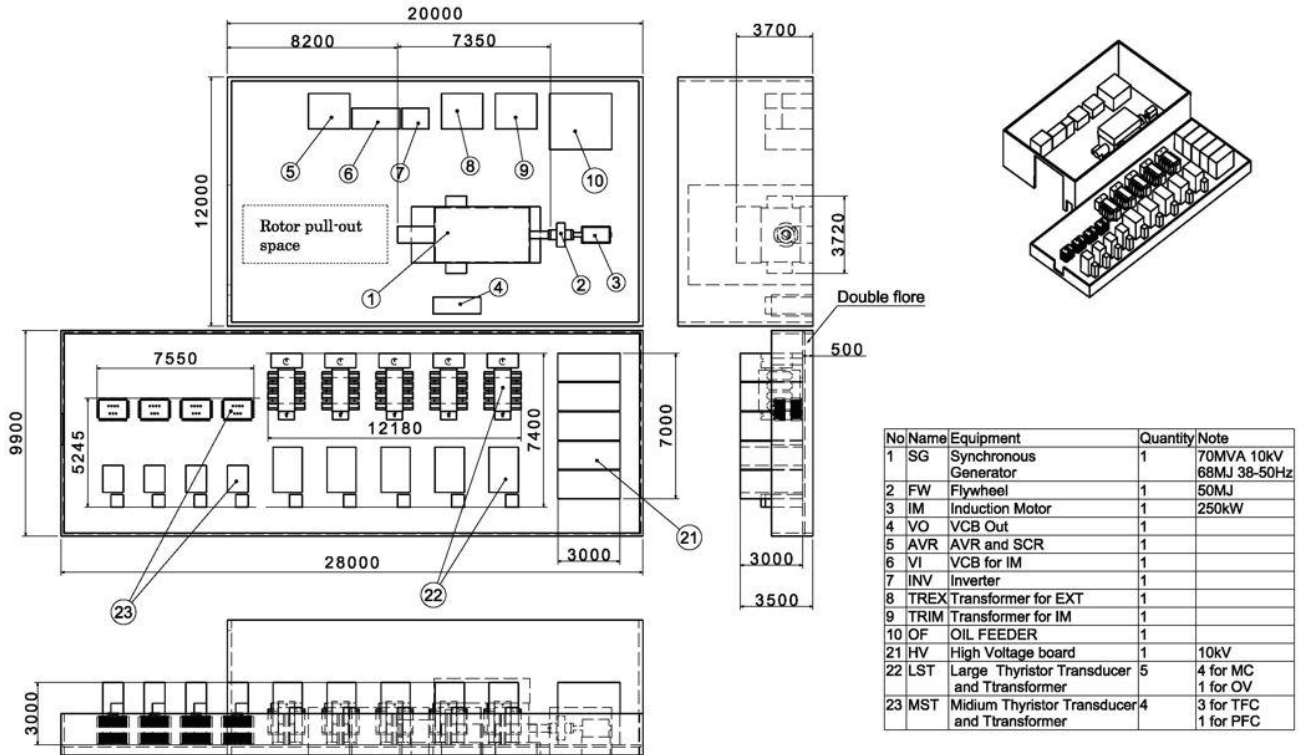


Fig 6.3-2 Layout of the power supply for 1T

6.3.2 Specifications of SG, IM, and a flywheel

Estimation results of specifications of IM, SG and a flywheel are summarized in Table 6.3-1. We have estimated stored energy in SG for CFQS by calculating of inertia moment of SG equipped in NIFS (250 MVA). The formula of inertia moment is followed:

$$J_x = \frac{1}{8} m \cdot D^2 = \frac{\pi}{32} \rho \cdot L \cdot D^4 \text{ [kg} \cdot \text{m}^2], \quad (1)$$

where J_x , m , D , ρ are inertia moment, mass of a rotor, diameter of a rotor and volume density of a rotor made of iron (8000 kg/m³) respectively. The calculated value of J_x of NIFS SG is 289,540 kg m². Based on the calculation result, we estimated the J_x value of CFQS SG by calculating the ratio of rotor size and mass between NIFS SG and CFQS SG. Then, stored energy K_s of CFQS SG is calculated from the following formula:

$$K_s = \frac{1}{2} \times J_{CFQS} \times (2\pi f)^2 \text{ [J]}, \quad (2)$$

where f is frequency with 50 Hz (3000 rpm). J_{CFQS} is inertia moment of CFQS SG with 1386.8 kg m². The calculated value of stored energy for CFQS SG is 68.4 MJ. Given 38 Hz of CFQS SG frequency after kinetic energy transfer to electrical power, only 28.9 MJ which cannot cover the required total energy for coils (40 MJ) is obtained. Therefore, the flywheel compensating stored energy for coil energization should be adopted. Required stored energy of the flywheel at 50 Hz (3000 rpm) is 49.9 MJ. Inertia moment of the flywheel J_{FLY} is $J_{FLY} = 1013.3$ kg m² obtained by Eq. (1). We designed the size of flywheel made of iron with 1150 mm diameter and 750 mm thickness (~6229 kg, 1029.7 kg m²).

We also estimated required operation power for the IM. Given 300 s acceleration time (shot to shot) for number of revolutions of SG rotor and the flywheel from 2280 rpm to 3000 rpm, required torque for the IM is obtained as following formula:

$$T_{IM} = \frac{2\pi \times (J_{CFQS} + J_{FLY})}{60} \times \frac{N_2 - N_1}{600} \text{ [N} \cdot \text{m]}, \quad (3)$$

where N_1 and N_2 show number of revolutions [rpm]. In this case, N_2 is 3000 rpm and N_1 is 2280 rpm. Calculated value of required torque for IM between 2280 rpm to 3000 rpm is 602.9 Nm. On the other side, if SG rotor and the flywheel are accelerated from 0 rpm to 3000 rpm in 1800 s, required torque for IM is 148.7 Nm. Consequently, required maximum mechanical output of IM is 189.5 kW. The value is calculated by

$$P_m = \frac{T_{IM} \times N}{9.545}, \quad (4)$$

where N is number of revolutions. Required input power for IM is estimated around 250 kW because some loss factors such as copper loss, iron loss and windage need to be considered.

Table 6.3-1 Summary of the estimation result of IM and SG specifications.

Component	Parameter	Unit	Value
Generator	Number		1
	Capacity	MVA	70
	Voltage	kV	10
	Power factor	%	90%
	Frequency	Hz	38-50
	Revolution	rpm	2250-3000
	Number of poles	p	2
	Stored energy (Rotor)	MJ	68.4
Motor	Number		1
	Capacity	kW	250
	Voltage	kV	0.44
	Number of poles	p	2
Flywheel	Density	kg/m ³	8000
	Diameter	m	1.15
	Height	m	0.75
	Weight	kg	6,229
	Stored energy	MJ	49.9
	Release energy (Rotor + Flywheel)	MJ	50.0
Accelerating torque	Accelerating time (Shot to Shot)	s	300
	Accelerating time (Start-up)	s	1800
	Torque (Shot to Shot)	Nm	602.8
	Torque (Start-up)	Nm	418.7
	Mechanical output from a Motor (Shot to Shot)	kW	189.5
	Mechanical output from a Motor (Start-up)	kW	131.6

7 Related equipment

7.1 ECH power injection antenna

The requirements for the ECH power injection system from the viewpoint of plasma experiment are to realize local and narrow power deposition and wide beam aiming area. Narrower power deposition by narrower beam at resonance layer requires larger mirrors. However, practically, the power injection system should avoid interference with surrounding structures in CFQS (see Fig 7.1-1), that is, the system should be compact. Thus, the beam waist size and mirror size should be optimized simultaneously. The assigned port for ECH power injection system is O-180 port which has a conflat flange of the CF350. The inner diameter of the CF350 flange opening is 350 mm. As a result of design adjustment and optimization, the circular Gaussian beam parameters, the beam waist size, and beam waist position are determined as 30 mm and $R = 1185$ mm, respectively. Here, R denotes major radial coordinate. Compared with the long radius of ~ 450 mm of the bean-shape plasma at this toroidal position, the beam radius of 30 mm is narrow enough for localized power deposition, while the mirror antenna system can be contained in a mirror vacuum vessel with the CF350 dimension.

A cross-sectional view of the ECH antenna and plasma are shown in Fig 7.1-2. The mirror system consists of 4 mirrors: 2 focusing mirrors and 2 plane mirrors. Counting from the plasma side, the mirrors are named M1, M2, M3, and M4. M1 and M3 are plane mirrors. M1 is steerable mirror for beam direction control, and M2, M3, M4 are fixed. The blue lines represent the Gaussian beam radius which denotes $1/e$ radius of electric field. The red lines show the width of 1.5 times the Gaussian beam radius, and within the red lines, 98.9 % of total power is contained. The mirror corners near the mirror vacuum vessel should be cut to avoid interference with the mirror vacuum vessel as shown in Fig 7.1-3. Beam aiming range of $-450 \text{ mm} < Z < +100 \text{ mm}$ and $-200 \text{ mm} < T < +200 \text{ mm}$ at $R = 1185$ mm is obtained, which is sufficient for electron cyclotron current drive (ECCD) and off-axis heating. Z and T denote vertical and toroidal coordinates, respectively.

As a future work, supporting structure of the mirrors M2, M3, M4 and the steering mechanism of the plane mirror M1 should be designed. Also, supporting structure of mirror vacuum vessel should be designed.

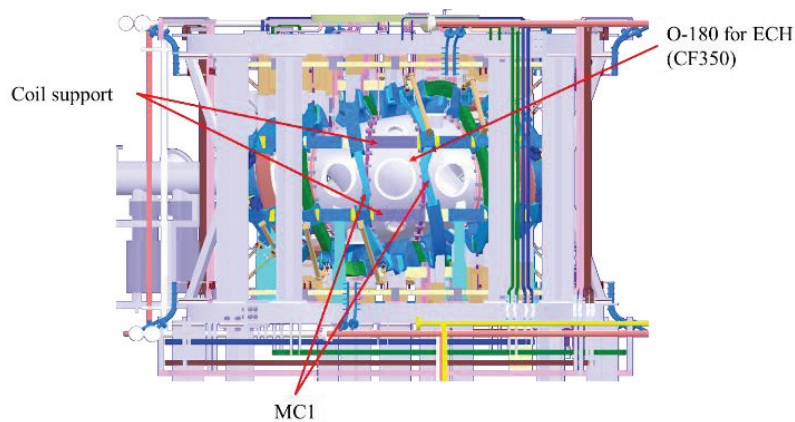


Fig 7.1-1 ECH port and surrounding structures.

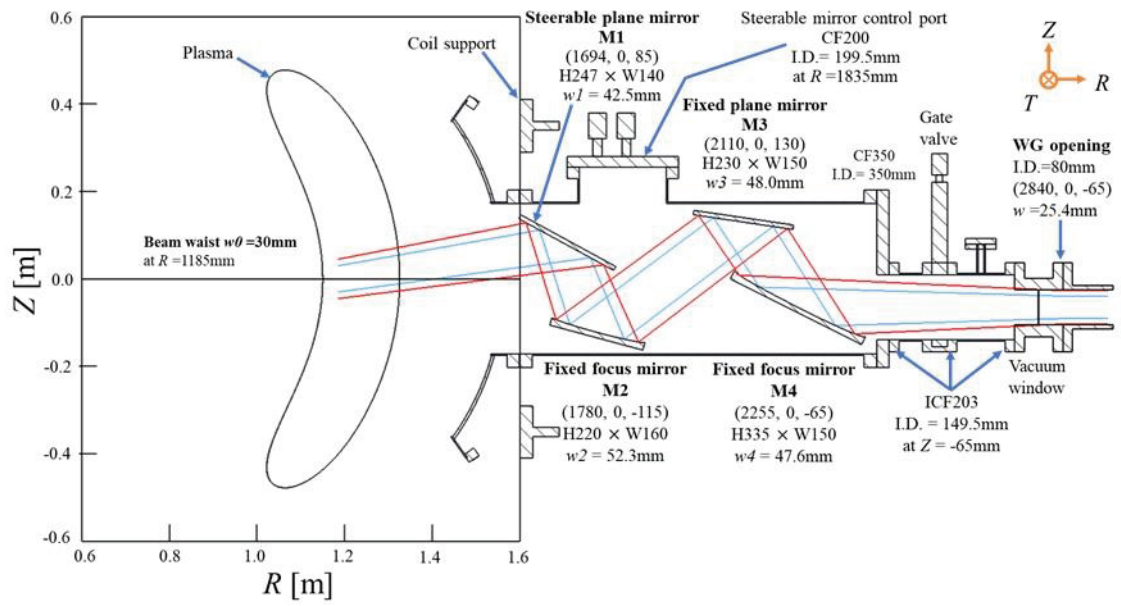


Fig 7.1-2 Design of ECH power injection antenna.

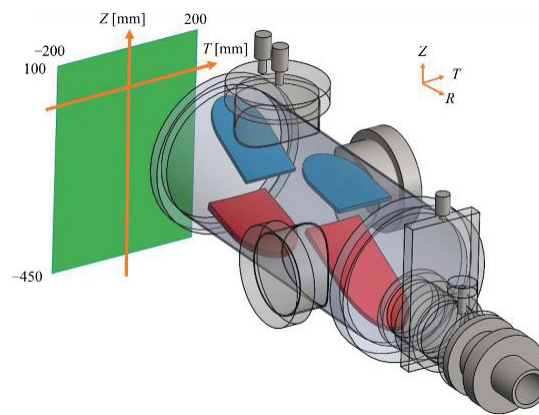


Fig 7.1-3 Beam aiming area and the mirror shapes.

7.2 Vacuum pumping system

Pumping system in CHS will be transferred to the CFQS. As shown in the below figure, rotary pump will be used for rough pumping, then two turbo molecular pumps will get involved.

A rotary pump will be used in vacuum range of 20 to 30 Pa or more to reduce the time reach the work pressure, then will start the two turbo molecular pumps with 1500 l/s of exhaust speed each. The ultimate vacuum pressure will be 1×10^{-7} Pa.

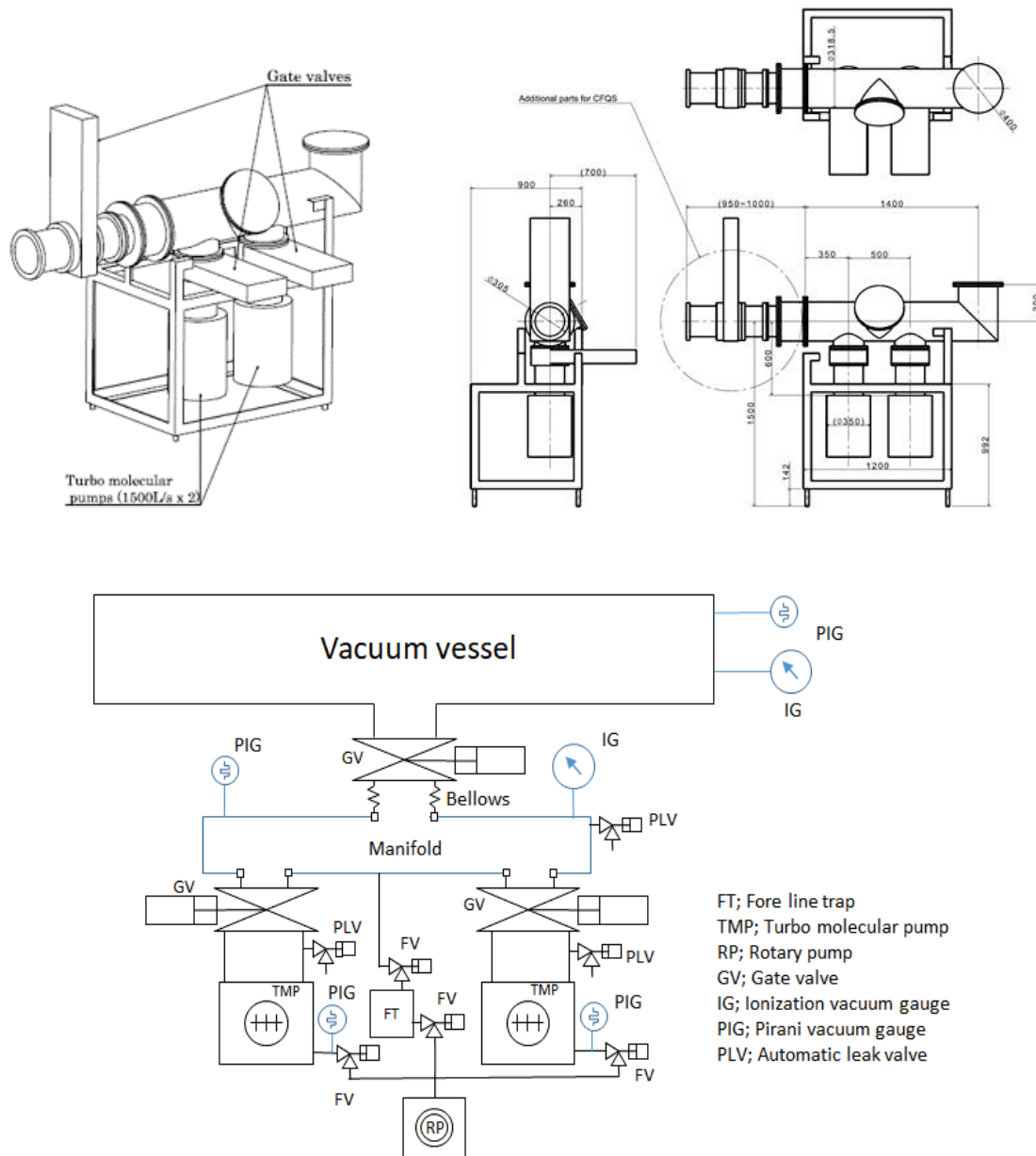


Fig 7.2-1 Sketch of vacuum pumping system.

7.3 Pure water cooling system

Pure water-cooling system is required to cool magnetic coil system, heating system, diagnostic system, and pumping system. And industrial water system to cool the motor generator may be also required. The below figure shows preliminary layout of the pure water cooling system.

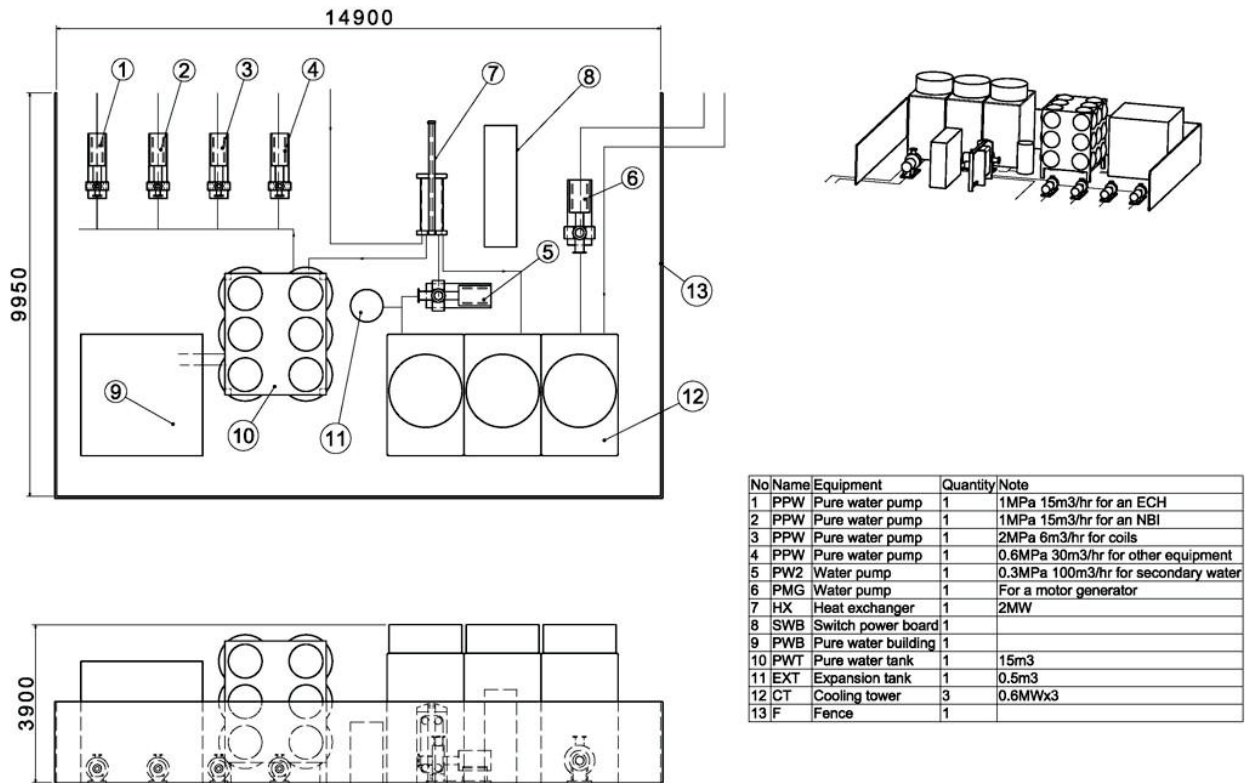


Fig 7.3-1 Preliminary layout of pure water cooling system.

7.4 Baking power supply

Total required baking power for CFQS vacuum vessel (VV) is estimated approximately 25kW. We designed the power supply satisfying the electrical conditions for baking as represented in the below figure. Here, A1 to A3 and B1 to B5 are the names of the baking sections in which the vacuum vessel is divided in the toroidal direction. The heaters on A1 and A3 section are connected in series because these volumes of the A1 and A3 section are relatively small compared with other sections.

The baking power supply mainly consists of AC power regulators (APR) which can change the applied voltage and applied power (up to AC220V, 2.3kW) for each baking heater, a magnet contactor (MC) for emergency shutdown to prevent overheating, molded case circuit breakers (MCCB) for each baking switching and transformer (TR) for insulation. The APR output is controlled by a temperature indication controller (TIC) which monitors surface temperature of VV. Surface temperature is monitored by not only TIC but also the other temperature monitoring system with over 64 measurement spots. The details of the other monitoring system will be designed later. MC is operated to stop baking when any surface temperature of VV exceeds critical value.

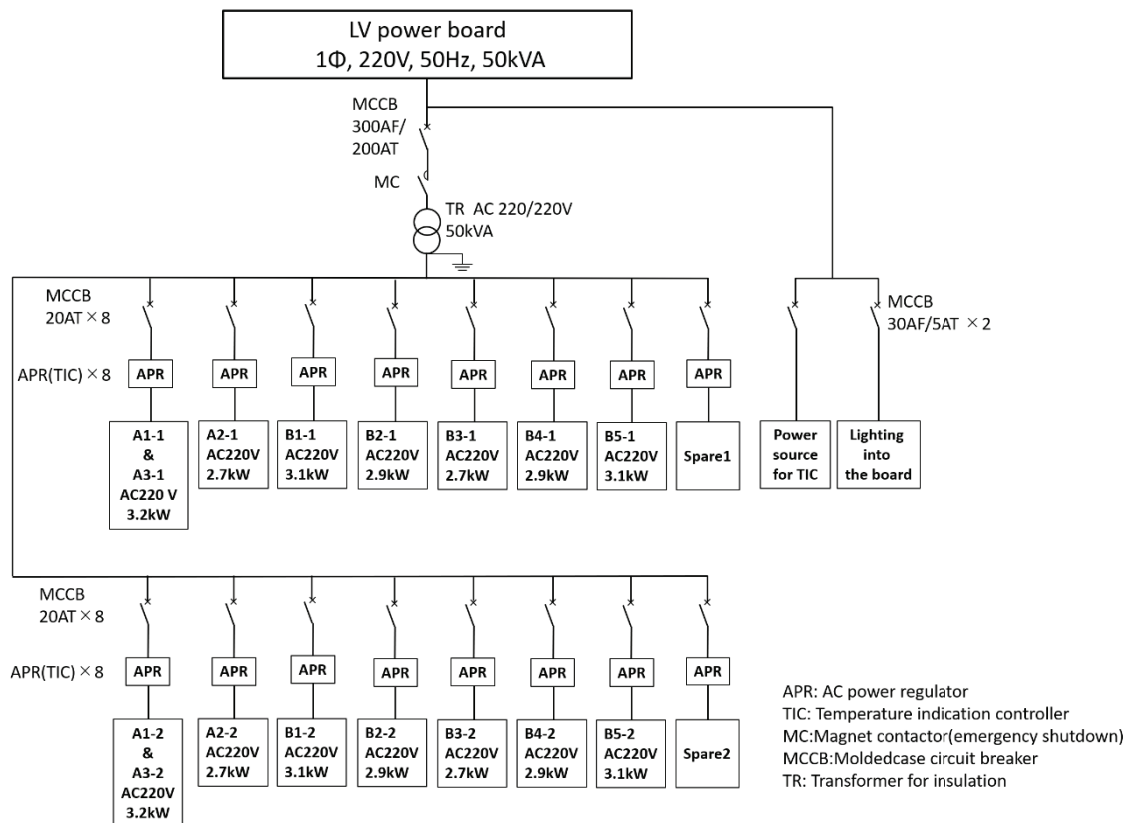


Fig 7.4-1 Designed circuit diagram of the baking system.

NIFS-SWJTU JOINT PROJECT FOR CFQS
~PHYSICS AND ENGINEERING DESIGN~

VER. 4.1

2022. JAN.

APPENDIX-A2 (RD)

~RESERCH AND DEVELOPMENT~

CFQS Team



NIFS; National Institute for Fusion Science

SWJTU; Institute of Fusion Science, School of Physical Science and Technology Southwest Jiaotong University

Hefei Keye; Hefei Keye Electrical Physical Equipment Manufacturing Co., Ltd.

Table of Contents

1	Production and test of a mockup modular coil for the MC4	3
1.1	Summary.....	3
1.2	Conductor and insulation material	4
1.3	Winding manufacture line.....	5
1.4	Design of winding mould	5
1.5	Production process of the MC4 mockup coil.....	7
1.6	Dimension measurement of the MC4 coil	10
1.6.1	Measurement of the winding mould	10
1.6.2	Measurement of the coil on the winding mould after the VPI.....	11
1.6.3	Measurement of the coil without restraint after the heat run test.....	12
1.7	Impulse test.....	14
1.8	Resistance and inductance measurement of the MC4.....	18
1.9	Withstand voltage test for the ground insulation	21
1.10	Airtightness test with nitrogen gas.....	22
1.11	Flow rate dependence of the pressure drop (loss head)	22
1.12	Heat run test.....	24
1.12.1	Summary.....	24
1.12.2	Test result of 1 kA/38 s without cooling water	25
1.12.3	Test result of 1 kA/38 s with cooling water	26
1.12.4	Test result of 500 A/120 s without cooling water	27
1.12.5	Test result of 500 A/120 s with cooling water	28
1.13	Overvoltage test.....	29
2	Plastic model developed by 3-D printer	30
2.1	Plasma.....	30
2.2	Vacuum vessel	31
2.3	Modular coil.....	33
2.4	Assembly of the modular coil, vacuum vessel, and support.	35
2.5	Real scale model of the vacuum vessel.....	36

1 Production and test of a mockup modular coil for the MC4

1.1 Summary

The total number of the CFQS modular coil is 16. The number of MC4 coil is 4, and the MC4 is the most complex coil. So, the M4C mockup coil was manufactured firstly, the manufacturability and the validity of the design were confirmed. Fig 1.1-1 shows the mockup coil and the mould for the VPI process.

An electric current was applied to the coil and the change in coil temperature was measured. Since the experimental results are consistent with the theoretically estimated characteristics, it was confirmed that the coil fabrication was appropriate.



Fig 1.1-1 Picture of the mockup coil

The test results are summarized below.

- (a) The manufacture and test of the MC4 mockup coil was finished.
- (b) The final dimension deviation of the mockup coil was about 3 mm.
- (c) The impulse test results showed that the layer-to-layer insulation was qualified.
- (d) The heat run test showed that the characteristics of temperature changes was as expected theoretically.
- (e) When operating for a long time for discharge cleaning, it is better to increase the flow rate of cooling water to improve the cooling performance. For that purpose, it is necessary to increase the pressure of the cooling water device.
- (f) The withstand voltage of layer insulation was DC10 kV or more. Since it can withstand the operating voltage by itself, it is possible to simplify the ground insulation.
- (g) The withstand voltage of ground insulation was DC 20 kV or more. So, the ground insulation ability is enough and if can be simplified if necessary.

1.2 Conductor and insulation material

The conductor dimension used for the mockup coil is $8.5 \times 8.5 \times \Phi 4$ mm, the layer insulation thickness is 1 mm, and the ground insulation is 3 mm. Eight units Cu conductors have been purchased for the mock-up coil; each unit length is about 100 m. The material of the conductor for the mockup coil is oxygen-free copper and the chemical composition is shown in Table 1.2-1. The Cu content is 99.97 % and oxygen content is 0.0008 %. The mechanical performance of the conductor is shown in Table 1.2-2. The tensile strength is 239 MPa, and elongation is 45 %. The dimension tolerance of the conductor is $8.5 \times 8.5 \times \Phi 4 + 0.08$ mm. Fig 1.2-1 shows the cross section of the conductor.

Table 1.2-1 Chemical composition of the Cu conductor.

化学成分 (%) Chemical Composition	Cu	O							
标准值 Standard Requirement	≥ 99.97	≤ 0.002							
实测值 Test	99.97	0.0008							



Fig 1.2-1 Conductor for the mockup coil

The main material for the insulation is fiber glass tape and polyimide (Kapton) as shown in Fig 1.2-2. The width and thickness of the fiber glass tape and the Kapton are $16 \text{ mm} \times 0.2 \text{ mm}$ and $10 \text{ mm} \times 0.05 \text{ mm}$ respectively for the mockup coil.

Table 1.2-2 Mechanical performance of the Cu conductor.

试验项目 Test	外观·尺寸 Visual & Dimension	抗拉强度 Rm(Mpa) Tensile Strength	延伸率 A(%) Elongation	导电率 (%) Electrical	气压 Pneumatic Pressure	耐击穿电压	钢珠通试
标准值 Standard Requirement		≥ 205	≥ 35	≥ 100	合格		通过
实测值 Test	合格	239	45	100	合格		通过
检验员签章 Inspector:	技术条件 Technical Conditions:		备注 Remark :		上海上大众森科技发展有限公司 SHANGHAI STARKING SCIENCE AND TECHNOLOGY CO., LTD 质保部 Quality Department		



(a) Fiber glass tape
16mm x 0.2mm x 50m
Tensile strength 1920N/25mm



(b) Polyimide (Kapton) tape
10mm x 0.05mm x 2000m
Tensile strength 115MPa

Fig 1.2-2 Insulation materials for the mock-up coil.

1.3 Winding manufacture line

The conceptual design of the coil winding manufacture line for the mockup coil is shown in Fig 1.3-1. It mainly includes rotating platform, winding mould, and clamping, copper conductors, insulation wrapping, and conductor straightening.

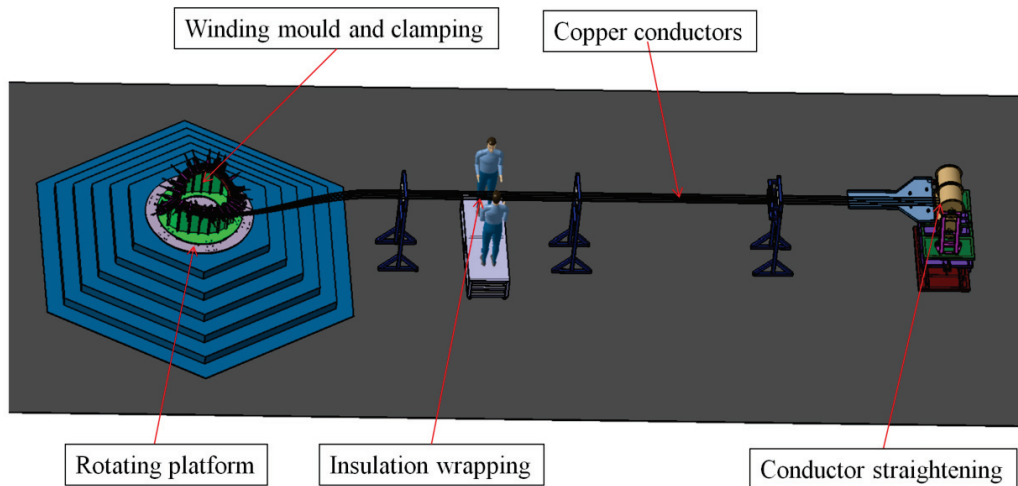


Fig 1.3-1 Conceptual design of the coil winding manufacture line.

1.4 Design of winding mould

The winding mould has been designed based on the MC4 coil profile shape as shown in Fig 1.4-1 and Fig 1.4-2. It consists of a bottom mould, inner plate, outer plate, and top cover plate. Each of the inner plate, outer plate and top cover plate is divided into around ten blocks and can be disassembled and assembled according to the progress.

The usage of the winding mould is divided into 5 stages.

- 1st stage: The bottom mould and inner plate are used for the coil winding with the layer insulation.
- 2nd stage: All blocks are used for the 1st VPI with the the layer insulation.
- 3rd stage: The surface of the all blocks facing the coil is scraped by 3 mm for the ground insulation.
- 4th stage: The coil is wrapped with 3 mm ground insulation without the winding mould.
- 5th stage; All blocks are used for the 2nd VPI with the the ground insulation.

(Attention)

In the production of the mockup coil, the second stage was omitted, and work of the ground insulation was proceeded without VPI, but it was very difficult to insert the coil into the mould for the fifth stage. Reflecting on that, we plan to add a second stage in the actual production.

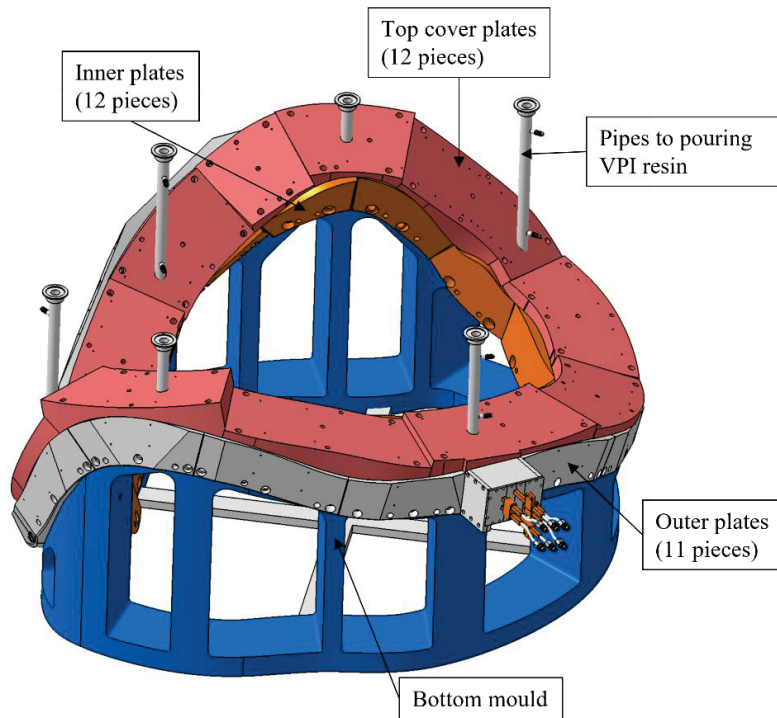


Fig 1.4-1 Winding mould for the MC4 mockup coil with a tank function of the VPI.

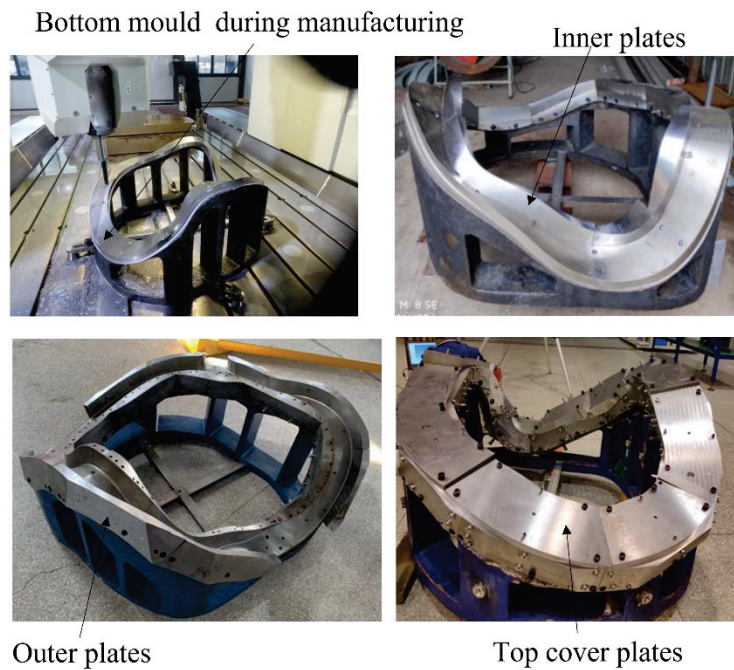


Fig 1.4-2 Pictures of the winding mould.

1.5 Production process of the MC4 mockup coil

The production process of the MC4 mockup coil is shown in Fig 1.5-1, and the main manufacture points is shown in Fig 1.5-2. The typical scenes in each work are summarized in Fig 1.5-1.

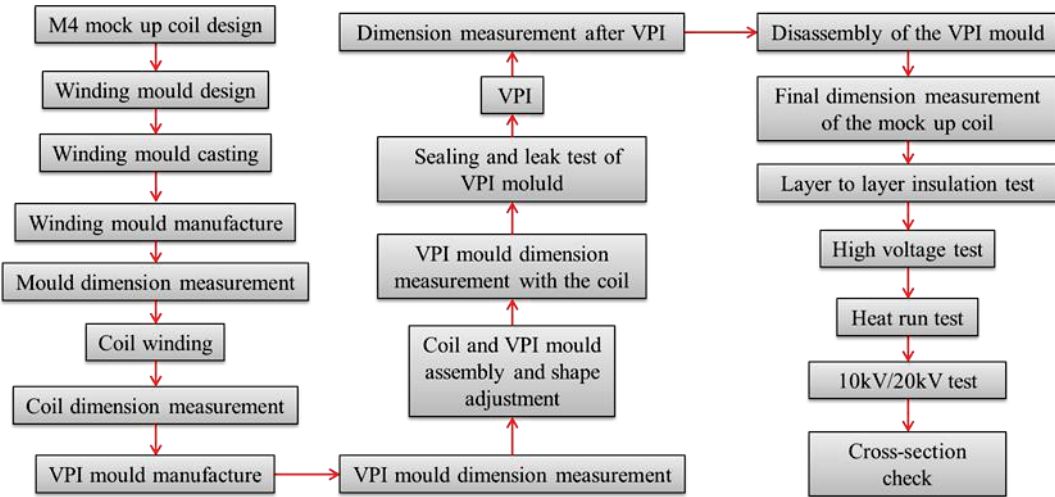


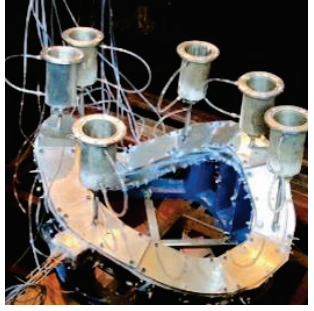
Fig 1.5-1 The production process of the MC4 mockup coil.



Fig 1.5-2 The main production points of the MC4 mockup coil.

Table 1.5-1 Production process of the MC4 mockup coil.

Step	work	Picture
1	Winding preparation. Half of conductor was wound around the cylindrical winding frame.	
2	Bending of a conductor on the mould. The conductor was bent along the winding mould by clamping and hammering.	
3	In the middle of winding work. The conductor was clamped to the winding mould.	
4	In actual production, a VPI dedicated to layer insulation will be added here.	<p style="text-align: center;">---</p>
5	Ground insulation. The conductor was removed from the winding mould and the ground insulating tape was wrapped.	
6	Reinstall the coil with ground insulation into the mould.	

Step	work	Picture
7	Close the winding mould. The coil was returned in the winding mould and the winding frame was closed with the top cover plates.	
8	The gap between the blocks was filled with glue to prevent the resin from leaking.	
9	VPI preparation. Resin tanks and hoses for injecting resin were added.	
10	VPI. All units were installed in a vacuum heating tank and the VPI process was carried out.	
11	Take the mould out of the VPI tank and open the top cover plate.	
12	Take out the top cover plates, inner plates, and outer plates. And clean up the coil by removing hardened excess resin.	
13	Disassemble the coil from the mould. The coil was removed from the winding mould and moved to the test stage.	

1.6 Dimension measurement of the MC4 coil

1.6.1 Measurement of the winding mould

Dimension of the winding mould was measured before the VPI. The result is shown in Fig 1.6-1. The deviation was 0.05~0.52 mm.

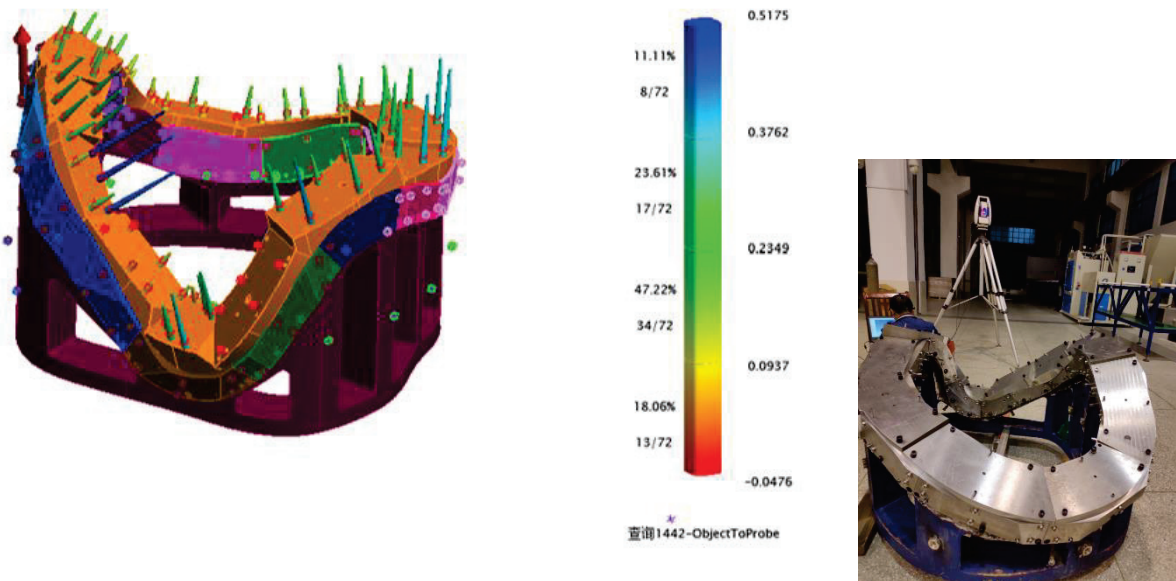


Fig 1.6-1 Result of the dimension measurement of the mould. on the upper surface, at 2019/10/24 and before the VPI. The deviation is -0.05~0.52 mm.

1.6.2 Measurement of the coil on the winding mould after the VPI

Dimension of the MC4 mockup coil was measured on the winding mould after the VPI with ground insulation. Example of the result is shown in Fig 1.6-2. The deviation was as follows:

- ❑ -0.39~0.77 mm on the upper surface,
- ❑ -0.13~-0.98 mm on the outer surface,
- ❑ 0.19~-0.66 mm on the inner surface.

The maximum deviation was about 1 mm which may include a measurement error, and it was found that the coil can be controlled with almost the mould accuracy.

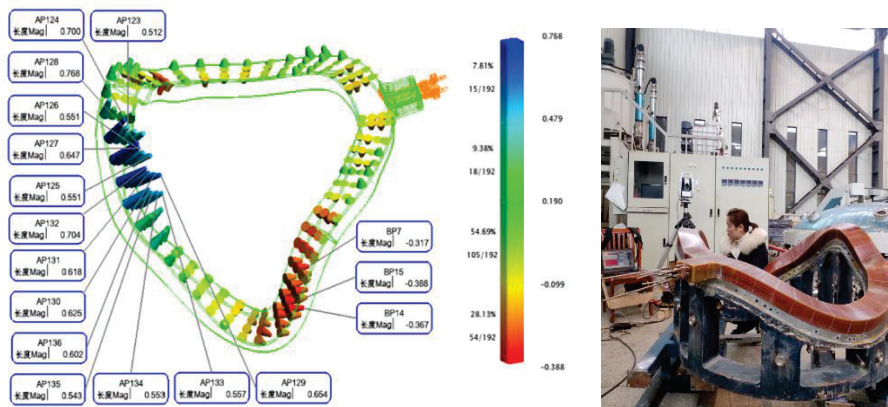


Fig 1.6-2 Example of the dimension measurement of the MC4. Upper surface, on the winding mould, after the VPI, at 2019/12/24 and with ground insulation. The deviation is -0.39~0.77 mm.

1.6.3 Measurement of the coil without restraint after the heat run test

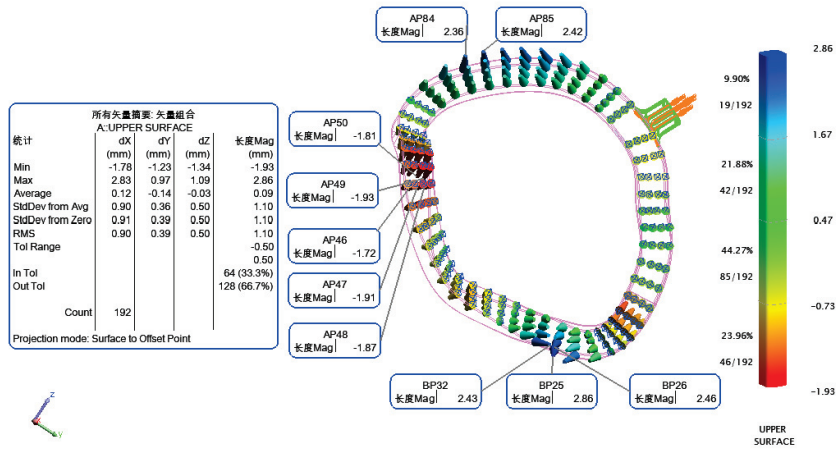
Dimension of the MC4 mockup coil was measured without restraint after heat run test as a final record. The result is shown in Fig 1.6-3 and Fig 1.6-4. The deviation was as follows:

- ❑ -1.93~2.86 mm on the upper surface,
- ❑ -0.72~3.21 mm on the outer surface,
- ❑ -3.26~0.69 mm on the inner surface.

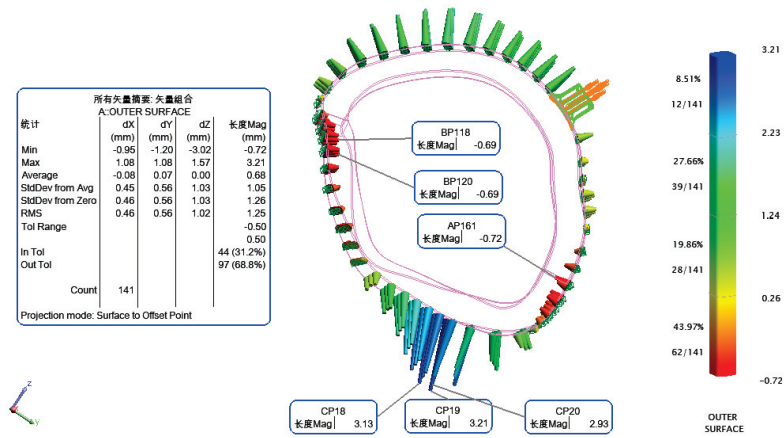
Compare with the result after the VPI, the deviation was about 3 times larger. The reason is not clear, but it is said that it may be the effect of deformation due to removal from the winding mould or the measurement error. In any case, it should be considered that there is a high possibility that a deviation of about 3 mm will occur. Since the standard tolerance of tolerance grades V (very coarse) or C (coarse) is several mm, the deviation of 3 mm is considered reasonable.



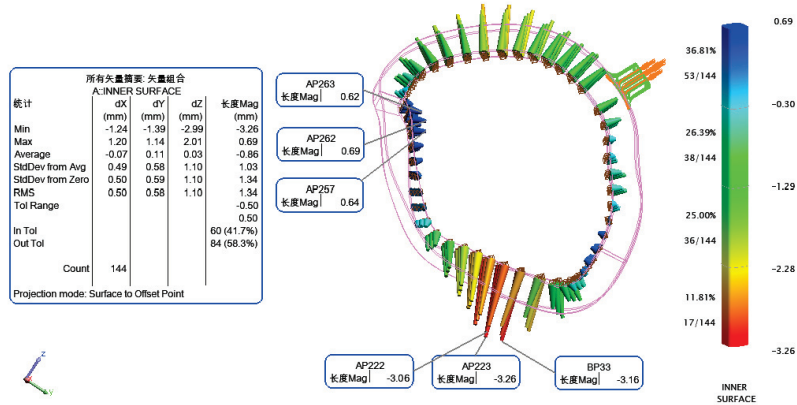
Fig 1.6-3 Scene of the dimension measurement without constraint.



(a) Upper surface, the deviation is -1.93~2.86 mm.



(b) Outer surface, the deviation is -0.72~3.21 mm.



(c) Inner surface, the deviation is -3.26~0.69 mm.

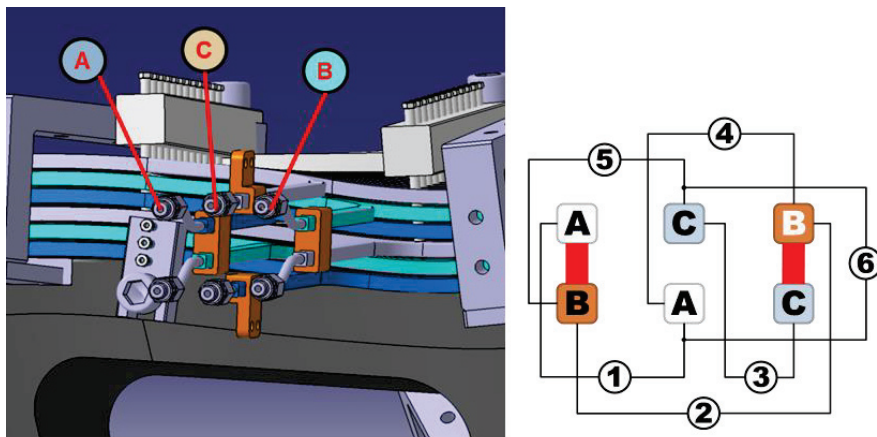
Fig 1.6-4 Result of the dimension measurement of the MC4. Without restraint, after the heat run test, at 2020/07/20 and a final record.

1.7 Impulse test

To inspect the turn-to-turn insulation, the impulse tests were performed as shown in Fig 1.7-1 to Fig 1.7-8. The connecting schematic diagram for the impulse test and example of the waveform are shown in Fig 1.7-1 and Fig 1.7-2. The test process as follow,

- Cut the series connection of the mockup coil, and perform the test of 1, 2, and 3,
- Connect the A and B to perform the test of 4,
- Connect the B and C to perform the test of 5,
- Connect the A, B, and C to perform the test of 6.

In the figure for the waveform of the impulse test, the X axis shows number of sampling time and Y shows voltage. The sampling frequency is 3.12 MSA/s (0.32 μ s/sample) and the number of time points displayed is 6000, which corresponds to 1.92 ms. Time between grids is 0.32 ms. The test results are shown in Fig 1.7-3 to Fig 1.7-8. The waveforms show that the oscillation attenuation trend of all test waveforms are basically same, so the turn-to-turn insulation is qualified.



A mark of ① to ⑥ indicates the name of a test, and a mark of A to B the name of a conductor.

TEST1 is the test of conductor A,
TEST2 is of conductor B,
TEST3 is of conductor C,
TEST4 is of conductor A+B,
TEST5 is of conductor B+C,
and TEST6 is of conductor A+B+C.

Fig 1.7-1 The connecting schematic diagram for the impulse test.

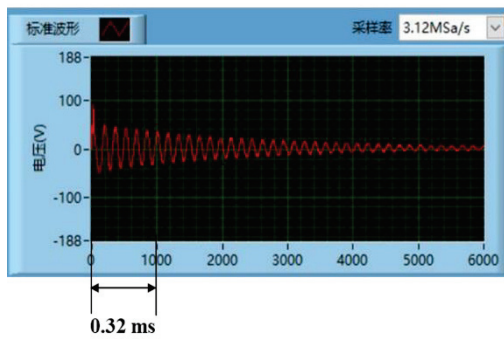


Fig 1.7-2 Scene of the impulse test and example of the waveform. The equipment used is the pulse coil tester of TH2883-1.

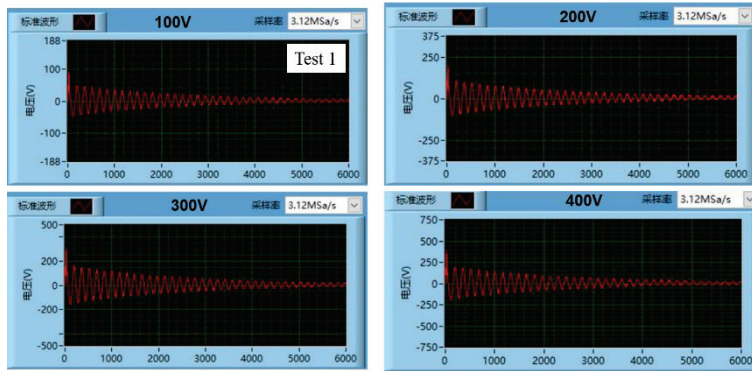


Fig 1.7-3 Test result of the TEST1 (Conductor-A)

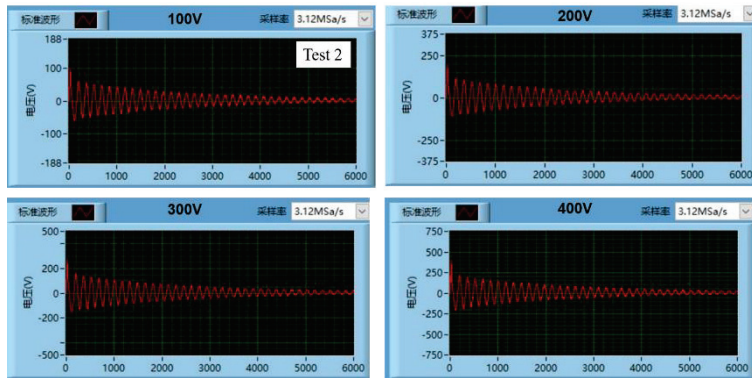


Fig 1.7-4 Impulse test result of the TEST2 (Conductor-B).

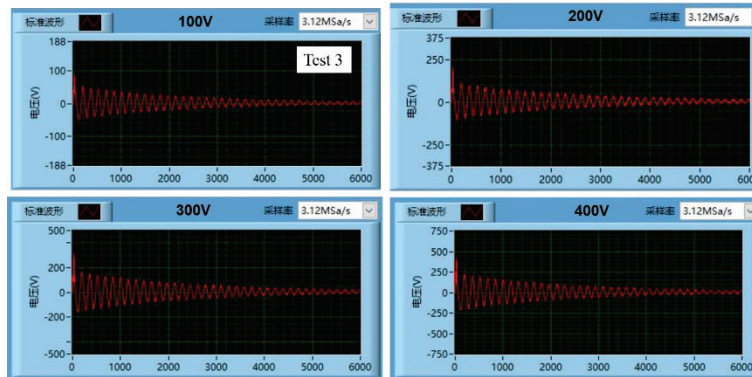


Fig 1.7-5 Impulse test result of the TEST3 (Conductor-C).

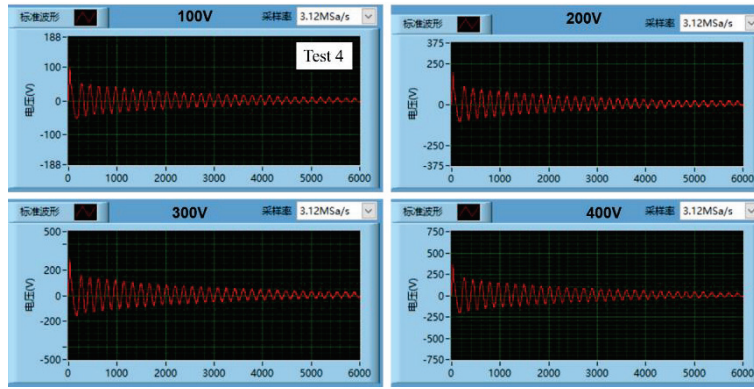


Fig 1.7-6 Impulse test result of the TEST4 (Conductor A+B).

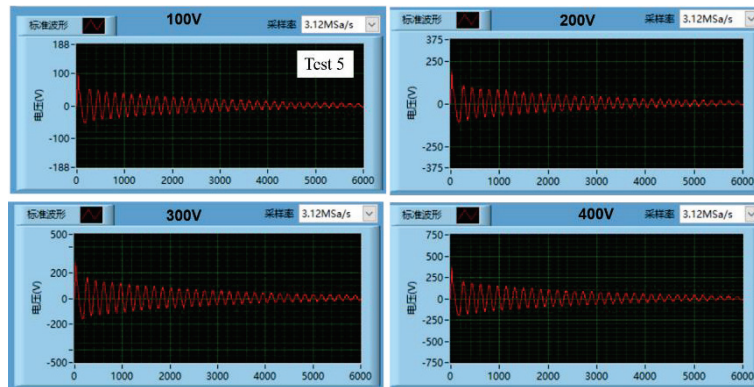


Fig 1.7-7 Impulse test result of the TEST5 (Conductor B+C).

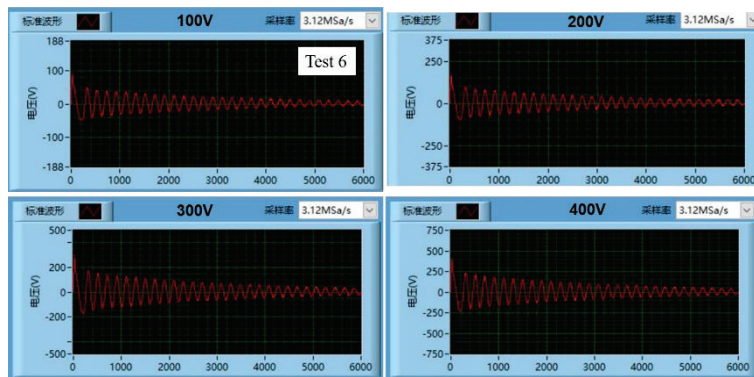


Fig 1.7-8 Impulse test result of the TEST6 (Conductor A+B+C).

1.8 Resistance and inductance measurement of the MC4

To inspect the winding, the resistance and inductance were measured as shown in this chapter. The structure of the measurement points is shown in Fig 1.8-1 and the scene of the inductance measurement is shown in Fig 1.8-2. For measurement, the electrical terminals of the coil and the instrument were connected by measuring wires with a clip. The measurement results are shown in Table 1.8-1, Table 1.8-2, Fig 1.8-3 and Fig 1.8-4. The measured values of this product meet the acceptance criteria.

Table 1.8-1 Result of resistance measurement.

Measurement point	Measured value (mΩ)		Converted value at 20 °C(mΩ)		
	Before the VPI	After the VPI	Before the VPI	After the VPI	Design value
Pancake 1	28.41	27.61	29.34	29.16	28.5
Pancake 2	29.39	27.86	29.32	29.42	28.5
Pancake 3	28.57	28.04	29.51	29.61	28.5
Sum all (1+2+3)	85.43	83.76	88.24	88.45	85.6
Acceptance	81.32~89.88 (±5%)				
Day and environment	2019/11/25 11.9°C 55%	2020/1/15 6.5°C 59%			
Measured current	100 A				
Equipment	DC tester (GD240-100A)				

Table 1.8-2 Result of inductance measurement.

Test frequency (kHz)	Measured value (mH)		Design value (mH)
	Before the VPI	After the VPI	
0.02	10.70	10.71	10.3
0.05	10.70	10.73	10.3
0.3	10.44	10.45	10.3
1.0	10.10	10.10	10.3
Acceptance	9.27 ~ 11.33 (±10%)		
Measurement point	Sum all (1+2+3)		
Day and environment	2019/11/25 11.9°C 55%	2020/1/15 6.5°C 59%	
Equipment	RCL Meter (LCR 8105G)		

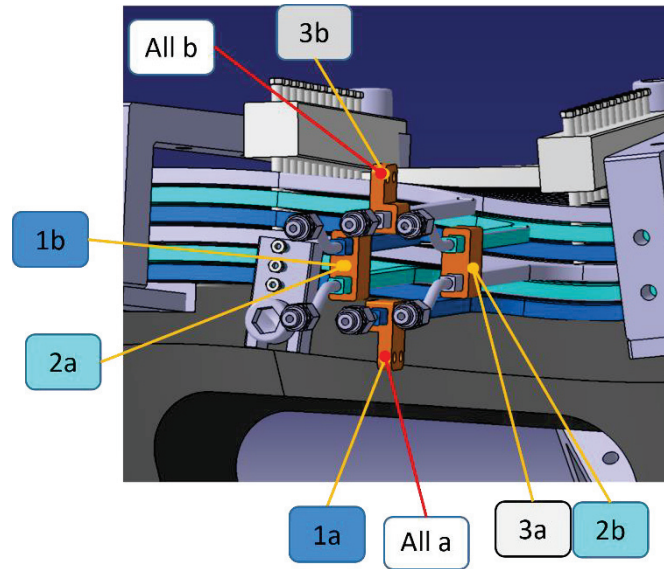


Fig 1.8-1 Schematic diagram of the resistance and inductance measurement.



Fig 1.8-2 Scene of the inductance measurement. To reduce the influence of the magnetic material under the floor, the whole was floated and measured.

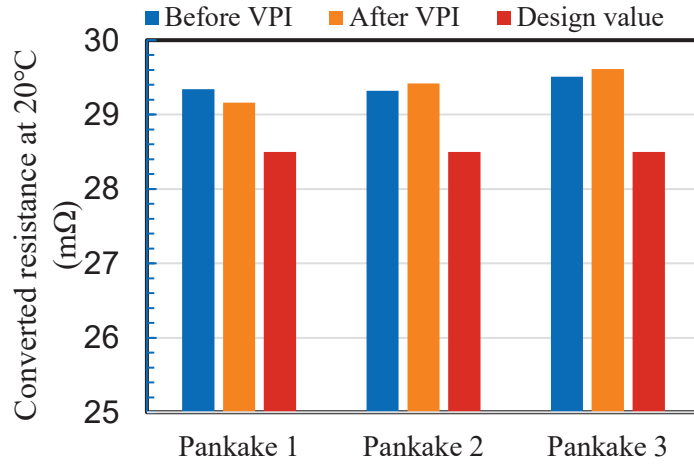


Fig 1.8-3 Result of resistance measurement.

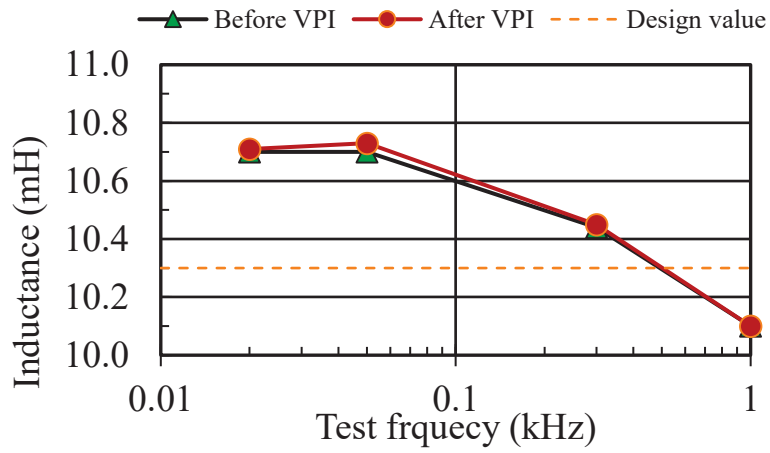


Fig 1.8-4 Result of inductance measurement.

1.9 Withstand voltage test for the ground insulation

To confirm the validity of coil insulation, a test was conducted in which a voltage more than twice the operating voltage was applied between the ground insulation surface and the conductor. The scene of the test is shown in Fig 1.9-1. The test procedure is as follows.

- Wrapping the outer insulation with aluminum foils.
- The high voltage terminal of the equipment is connected to any one of the coil terminals.
- The other ground terminal is connected with the aluminum foil.
- The test voltage is applied for 1 minute.
- The leakage current is measured.

The measurement results are shown in Table 1.9-1. All leakage currents were below the detection sensitivity, and no flashover and breakdown phenomenon were observed. The test result showed that the insulation performance met the required specifications.

Table 1.9-1 Result of the withstand voltage test after the VPI.

Test voltage (DC kV 1min)	Leakage Current (mA)
1.0	0.0
2.0	0.0
2.6	0.0
4.0	0.0
5.0	0.0
7.0	0.0
Acceptance	Less than 0.1 without flashover and breakdown.
Day and environment	2020/1/15 6.5°C 59%
Equipment	High Voltage DC Generator (DHV-100kV/5mA)



Fig 1.9-1 Scene of the withstand voltage test

1.10 Airtightness test with nitrogen gas

The 2.5 MPa pressure was applied in the cooling water channels by nitrogen gas and kept the pressure about 1 hour. There was not any leak of the cooling water channels. The scene of the airtightness test is shown in Fig 1.10-1.



Fig 1.10-1 Scene of the airtightness test at 2020/06/13.

1.11 Flow rate dependence of the pressure drop (loss head)

The pressure drop (loss head) of the cooling channel was measured as shown in this chapter.

Table 1.11-1 Test results of the pressure loss of the MC4.

Cooling channel	Flow rate (l/min)	Pressure (MPa)		
		Inlet	outlet	pressure loss
1	0.5	0.192	0.003	0.189
	0.8	0.375	0.006	0.369
	1.1	0.694	0.01	0.684
	1.3	0.96	0.013	0.947
2	0.5	0.188	0.003	0.185
	0.8	0.392	0.006	0.386
	1.1	0.642	0.009	0.633
	1.3	0.932	0.013	0.919
3	0.5	0.19	0.003	0.187
	0.8	0.39	0.006	0.384
	1.1	0.692	0.01	0.682
	1.3	0.918	0.013	0.905
All Parallel	1.5	0.204	0.017	0.187
	2.4	0.432	0.038	0.394
	3.3	0.764	0.066	0.698
	3.9	1.042	0.099	0.943
	4.2	1.185	0.113	1.072

2020/04/15 at Keye Co.

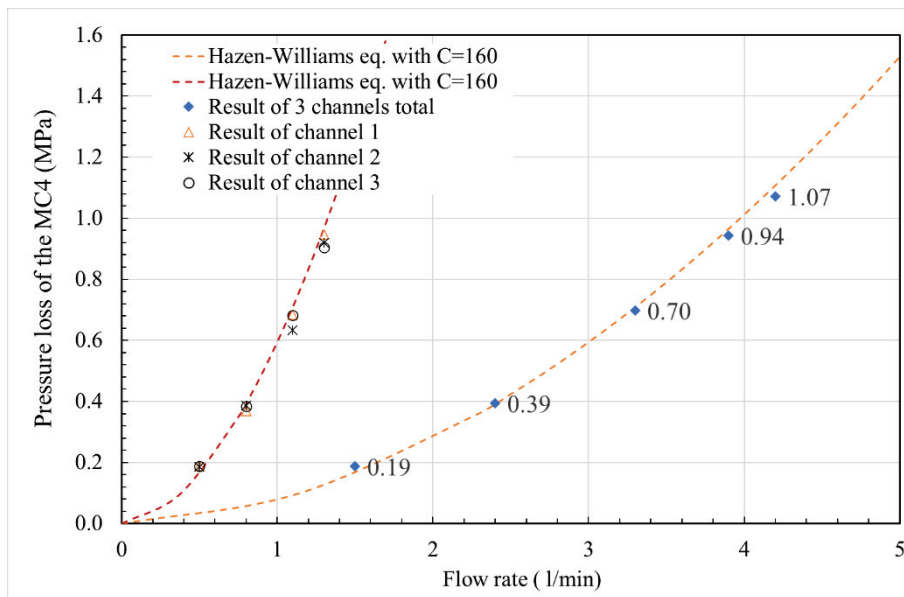


Fig 1.11-1 Flow rate dependence of the pressure loss of the MC4 at 2020/04/15. The broken line indicates a fitted approximation with the Hazen-Williams equation.

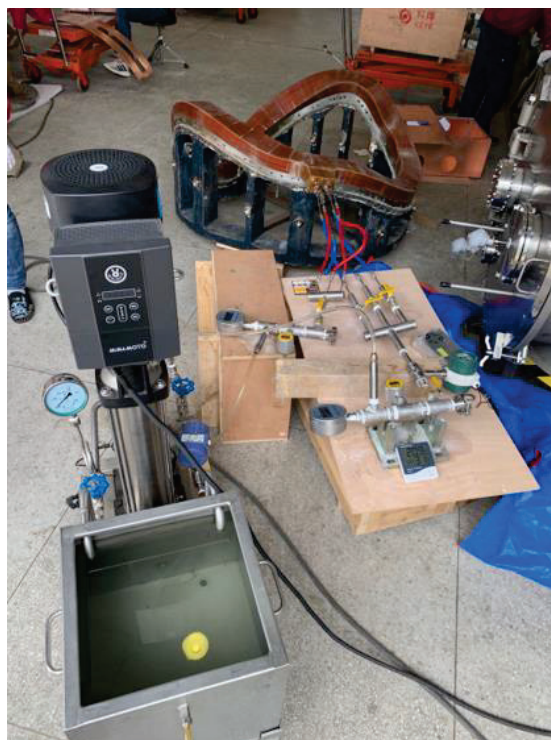


Fig 1.11-2 Scene of the pressure loss measurement

1.12 Heat run test

1.12.1 Summary

To verify the cooling design, the heat run test was performed, the sketch of the heat run test system is shown in Fig 1.12-1 and Fig 1.12-2. The test was performed under 4 kinds of conditions.

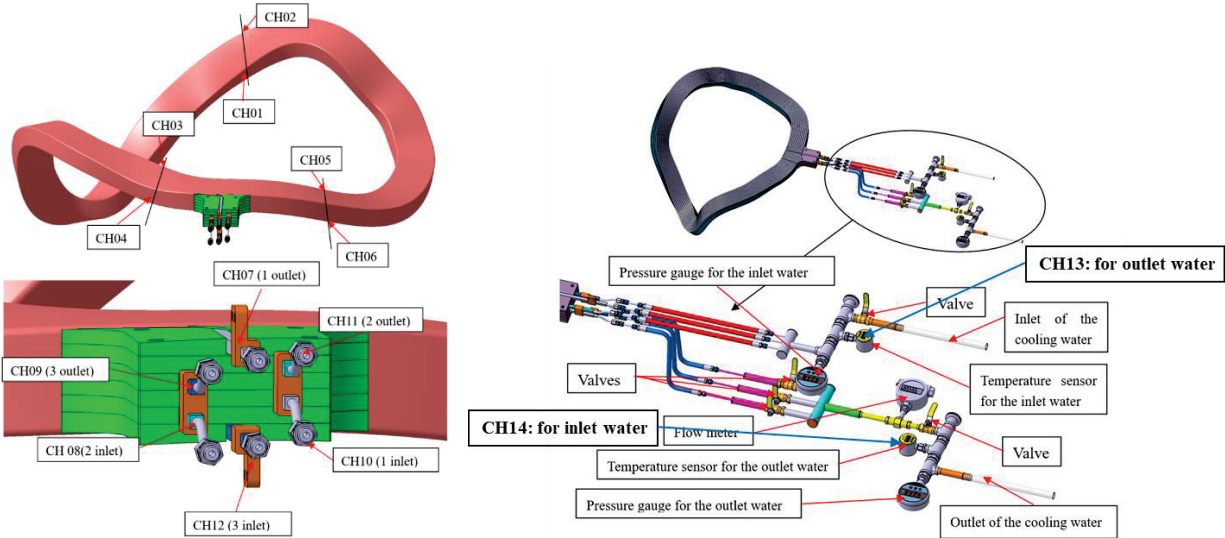


Fig 1.12-1 Sketch of the coil test system and the temperature sensor distribution.

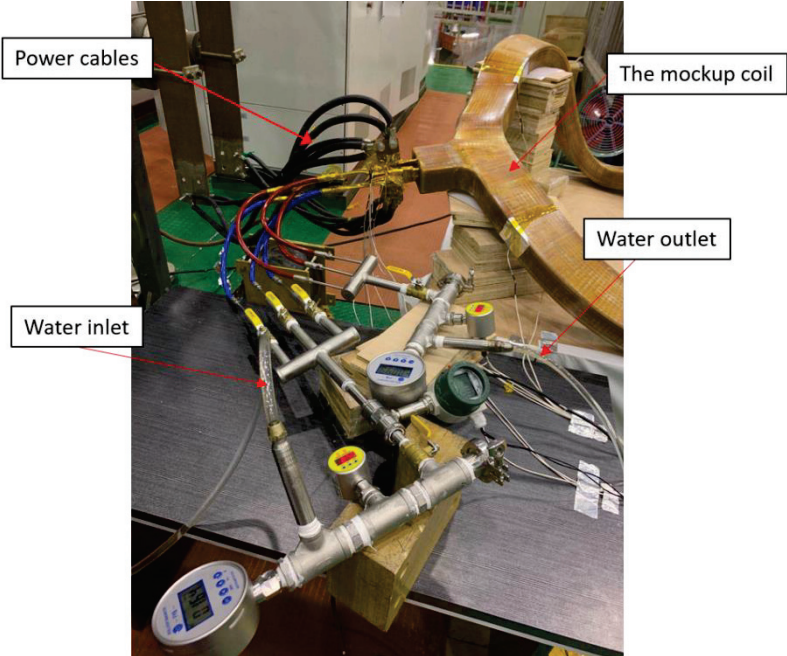


Fig 1.12-2 Heat run test of the MC4 mockup coil.

1.12.2 Test result of 1 kA/38 s without cooling water

- Heat generation of the 1 kA/38s is equivalent to that for the 1.0 T operation (4.34 kA and 2 s).
- Maximum of temperature rise on the insulation surface was 38 °C.
- The temperature on the insulation surface reached its maximum about 2 minutes, which was the time after the current is sut off.
- The temperature drop rate without cooling water was very slow (15 °C /hour).
- It took about half a day to recover and it may be unacceptable.

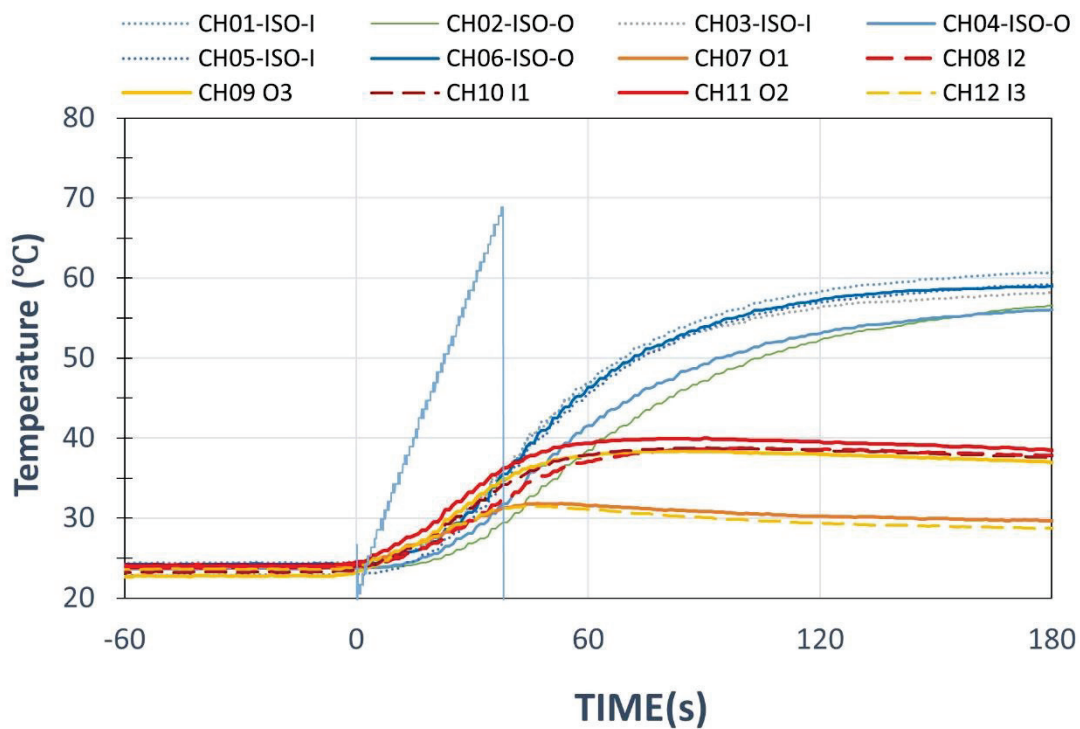
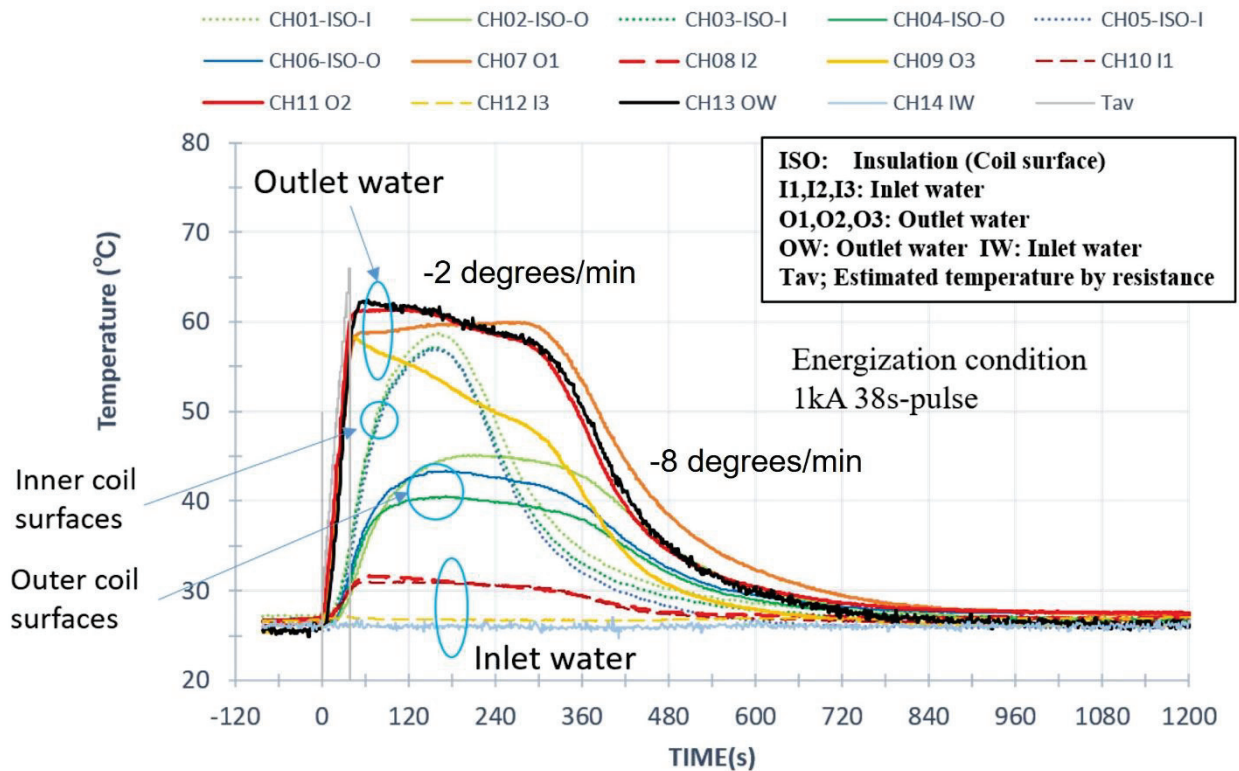


Fig 1.12-3 Temperature rise curve of 1kA/38s without cooling water.

1.12.3 Test result of 1 kA/38 s with cooling water

- Heat generation of the 1 kA/38s is equivalent to that for the 1.0 T operation (4.34 kA and 2 s).
- Maximum temperature rise on the insulation surface was 35 °C. It showed that the temperature rise did not depend on the presence or absence of cooling water.
- The required cooling time was greatly reduces by the water cooling.
- It took about 15 minutes to recover and it may be acceptable.



Note; The temperature change of the cooling water can be classified into two stages of -2 degrees/min and -8 degrees/min. It appears to be related to the time it takes for the water to circulate (a few minutes) and the time delay associated with heating the insulation. Greatly reduces the cooling time with water. It takes about 15 minutes to recover.

Fig 1.12-4 Temperature rise with current of 1 kA/38 s and water cooling of 3.9 L/min.

1.12.4 Test result of 500 A/120 s without cooling water

- The 500 A/120s corresponds to the steady operation condition (434 A).
- Maximum of temperature rise on the insulation surface was 28 °C.
- It took about 3 hours to recover and it may be unacceptable.

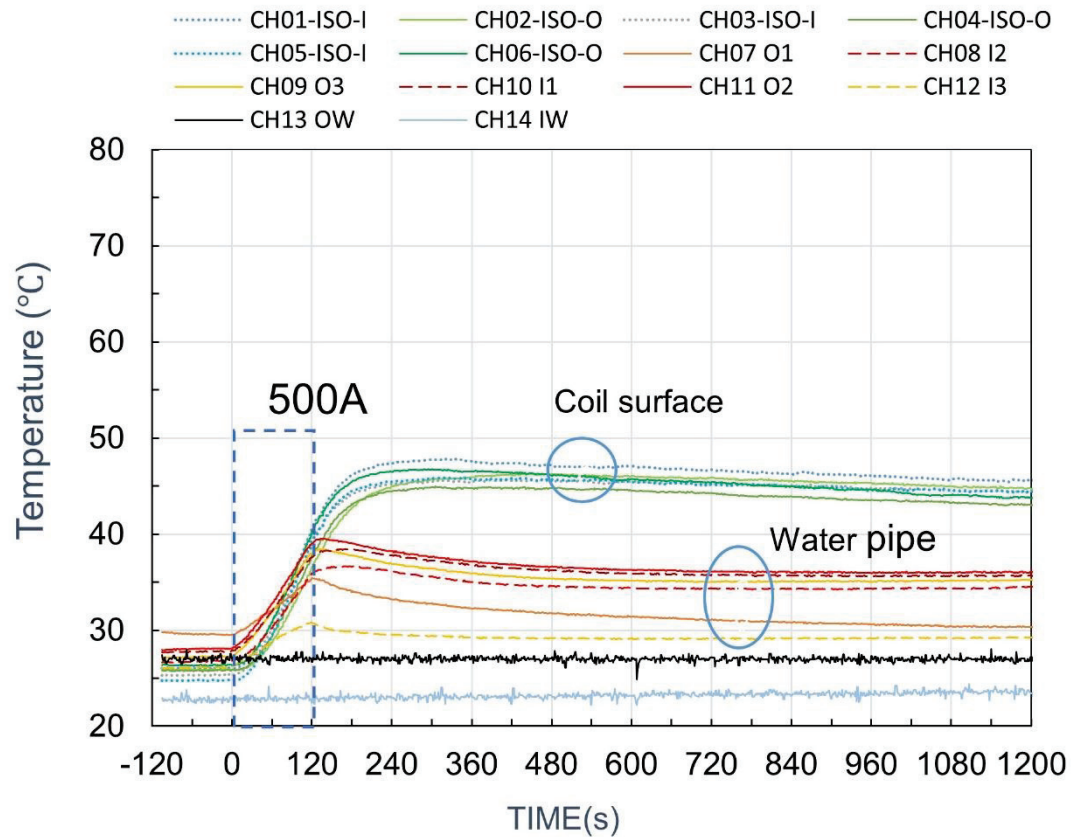


Fig 1.12-5 Temperature rise curve of 500 A/120 s without cooling water.

1.12.5 Test result of 500 A/120 s with cooling water

- The 500A/120s corresponds to the steady operation condition (434 A).
- Maximum of temperature rise on the insulation surface was 28 °C.
- It took about 8 minutes to recover and it may be acceptable.
- The temperature continues to rise after 2 minutes of operation, and it is estimated that the allowable temperature will be reached in about 5 minutes. For continuous operation for 30 minutes or more for discharge cleaning, the cooling water should be increased to saturate at an appropriate temperature.
- It suggests that to improve the cooling effect, the pressure of the cooling water system in the real coil should be increased from 1 MPa to 2 MPa.

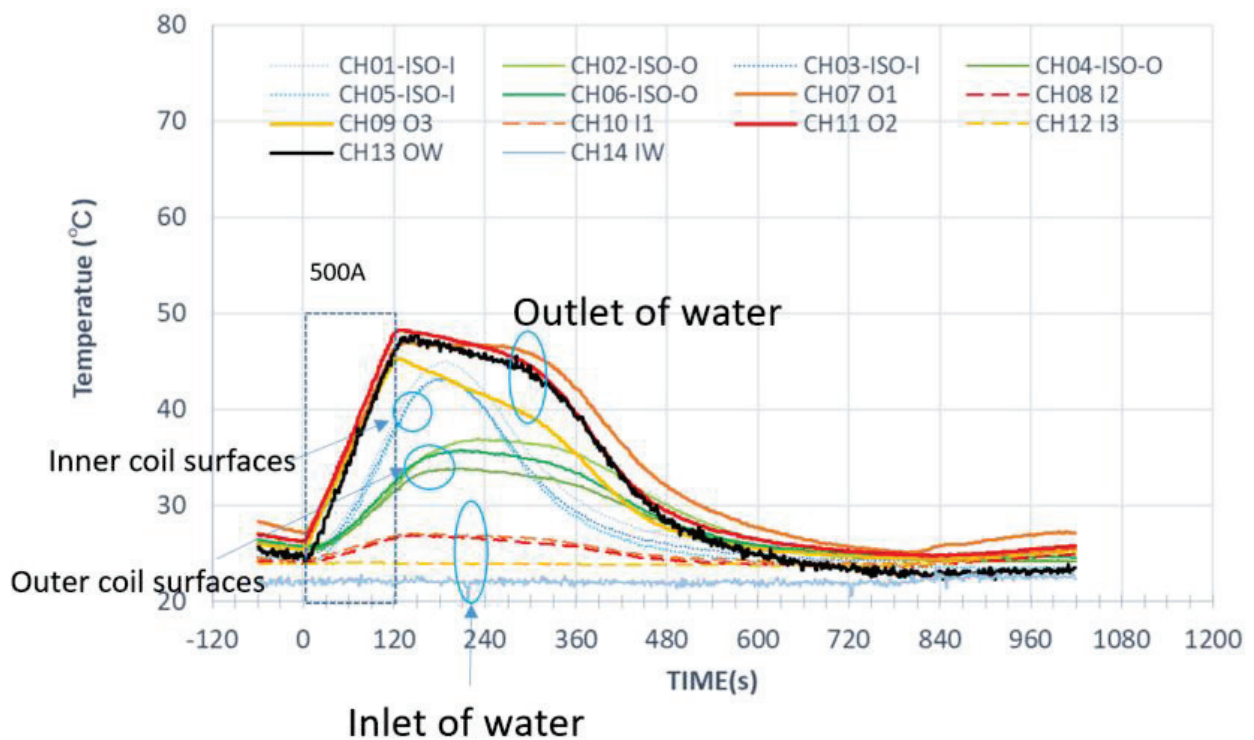


Fig 1.12-6 Temperature rise curve of 500A/120s with 4.2 L/min. cooling water.

1.13 Overvoltage test

To understand the insulation ability, a voltage higher than necessary was applied at the end of a series of tests, and it was confirmed that there was sufficient margin in insulation capacity. Fig 1.13-1 shows the scenes of the test. From this test, it was confirmed that this insulation system has a sufficient margin in the layer and layer insulation capacity.

- Layer to layer insulation test with DC 10 kV

The ground test voltage to confirm the validity of this coil is DC 5.8 kV. If the same insulation performance can be ensured only by the layer insulation, the ground insulation may be simplified more. To confirm that possibility, we planned a test in which a voltage of DC 10 kV was applied between adjacent conductors.

We cut series connection of 3 parallel conductor in the current lead area and apply DC 10 kV between each two conductors of 3 parallel. A high voltage DC generator (DHV-100 kV/5 mA) was used for the DC 10 kV test. Three types of tests were carried out, and it was confirmed whether the leakage current at DC 10 kV was less than 17 μ A (17 μ A between the A and the B, 1 μ A between the B and the C, or the A and the C).

- Ground insulation test with DC 20 kV

If there is sufficient margin, it may be possible to simplify ground insulation. To confirm that possibility, we planned a test in which a voltage of DC 20 kV, which was 3.4 times the required test voltage, was applied between the conductor and the ground. The leakage current at DC 20 kV was not observed.

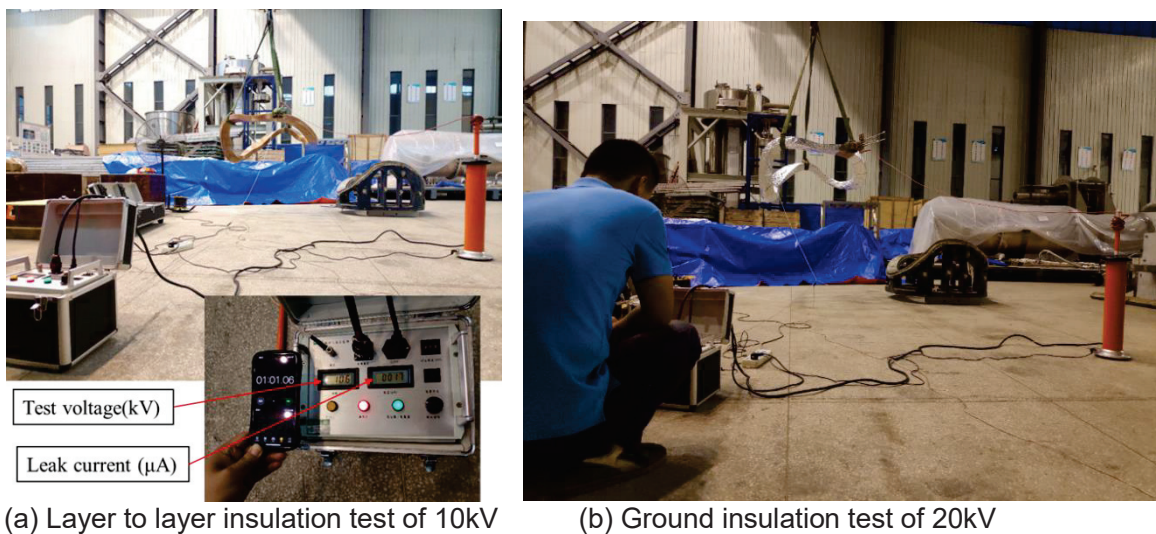


Fig 1.13-1 Scene of the overvoltage test.

2 Plastic model developed by 3-D printer

Various reduced models were developed on the 3-D printer to validate the device fabrication and assembly procedures.

2.1 Plasma

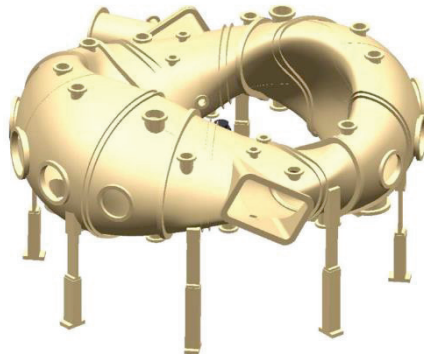


Fig 2.1-1 Last closed surface of the equilibrium.

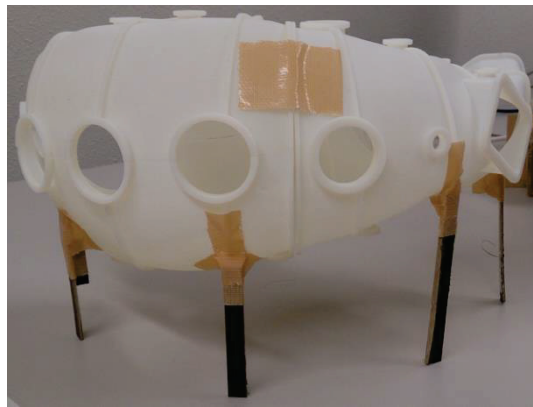


Fig 2.1-2 Data sharing in the project.

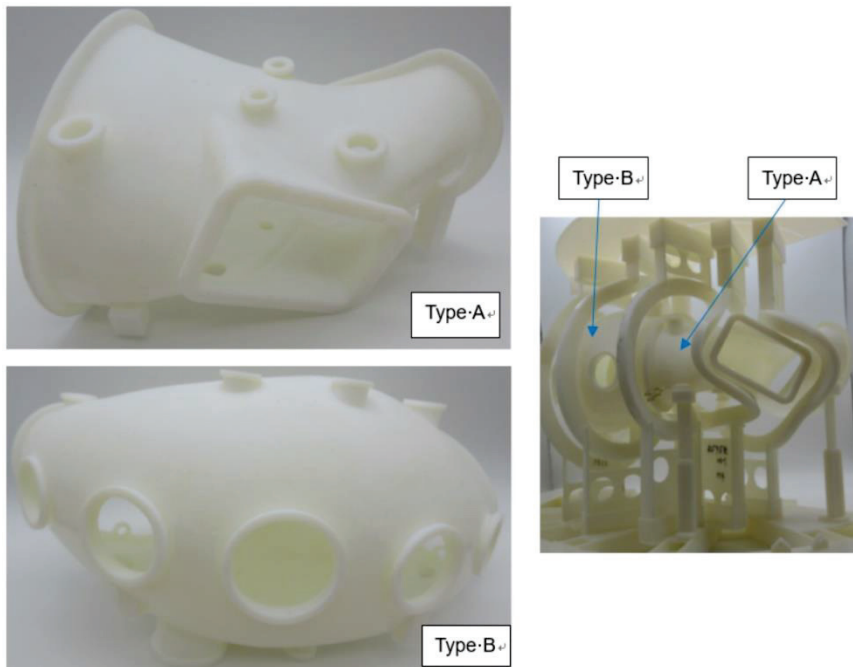
2.2 Vacuum vessel



(a) 3D CAD model of the vacuum vessel



(b) Examination of support legs

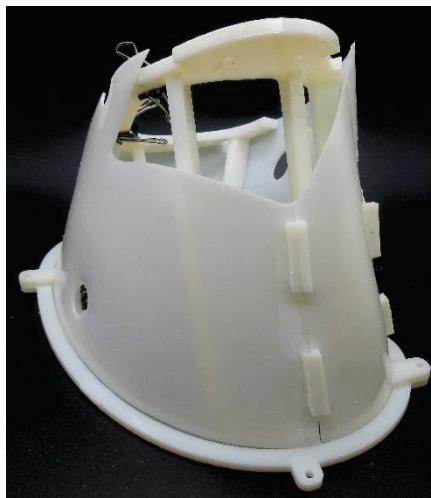


(c) Examination of the shape and assembly problems

Fig 2.2-1 Examination of the vacuum vessel.



(a) Assembly mould



(b) Assembling the pressed plates on the mould



(c) Disassemble the mould after welding plates

Fig 2.2-2 Simulation of production flow for the vacuum vessel.

2.3 Modular coil

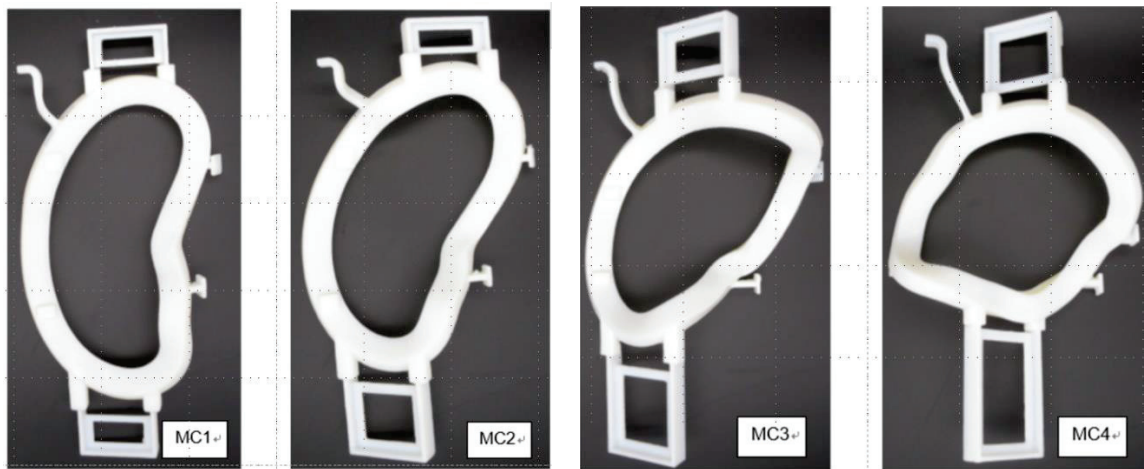


Fig 2.3-1 Preliminary examination of the coil case.

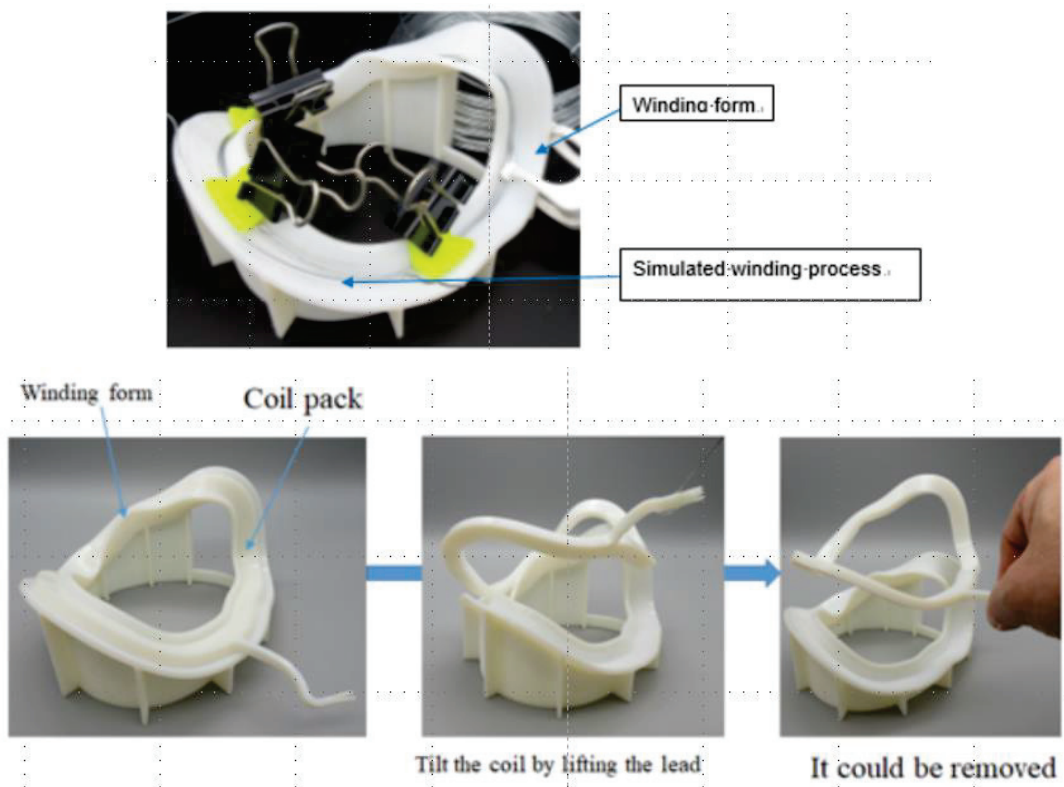


Fig 2.3-2 Simulation of removing the coil pack from the winding mould.



MC1



MC2



MC3



MC4

Fig 2.3-3 Examination of the coil case with the partial cramps.

2.4 Assembly of the modular coil, vacuum vessel, and support.

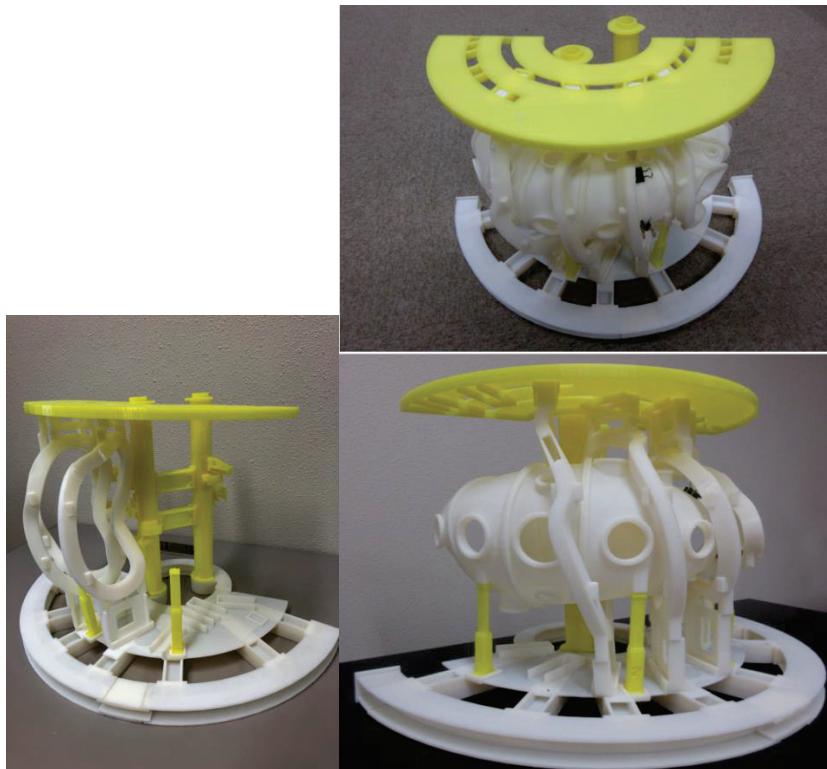


Fig 2.4-1 Assembly of the modular coil and the vacuum vessel.



Fig 2.4-2 Discussion of the structure and the assembly in a meeting

2.5 Real scale model of the vacuum vessel

Real scale model of vacuum vessel type A has been manufactured by 3D printer. Since the size of the vacuum vessel is large, a real scale model cannot be made by 3D printer all at once. Therefore, the type A vacuum vessel has been cut into 16 pieces to print by 3D printer. Each of 16 pieces has been made by 3D printer in Keye company. These 16 pieces are being assembled.

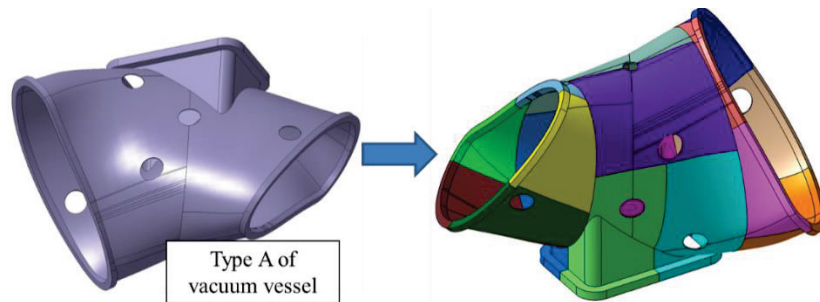


Fig 2.5-1 Type A of vacuum vessel is cut into 16 pieces to print by 3D printer.

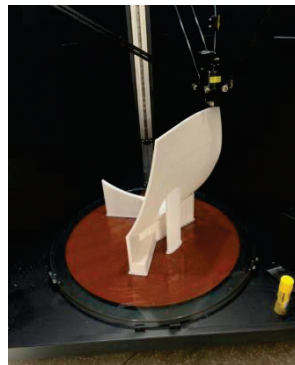


Fig 2.5-2 3D printer to fabricate real scale vacuum chamber model.

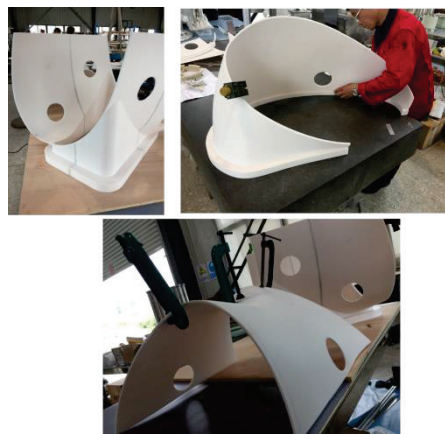


Fig 2.5-3 Pictures of assembled real scale 3D model.

NIFS-SWJTU JOINT PROJECT FOR CFQS
~PHYSICS AND ENGINEERING DESIGN~
VER. 4.1
2022. JAN.

APPENDIX-A3 (DW)

~DRAWING~

CFQS Team



NIFS; National Institute for Fusion Science

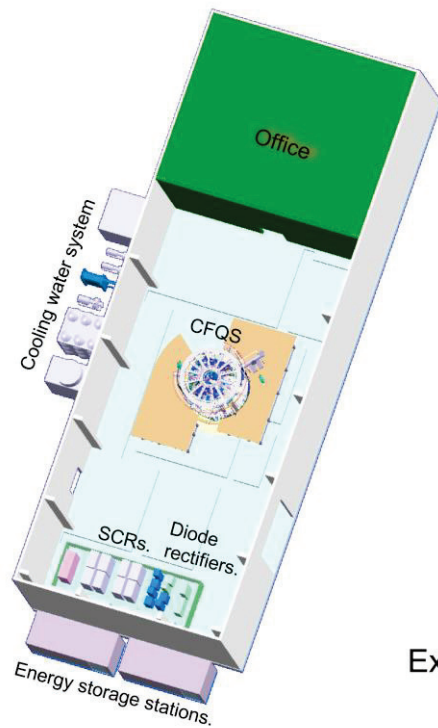
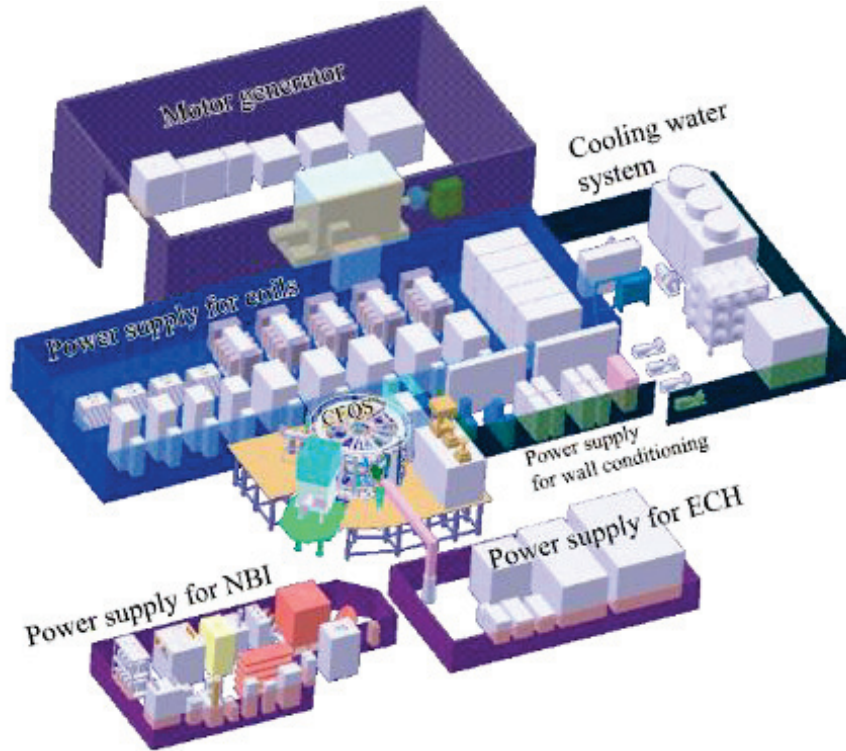
SWJTU; Institute of Fusion Science, School of Physical Science and Technology Southwest Jiaotong University

Hefei Keye; Hefei Keye Electrical Physical Equipment Manufacturing Co., Ltd.

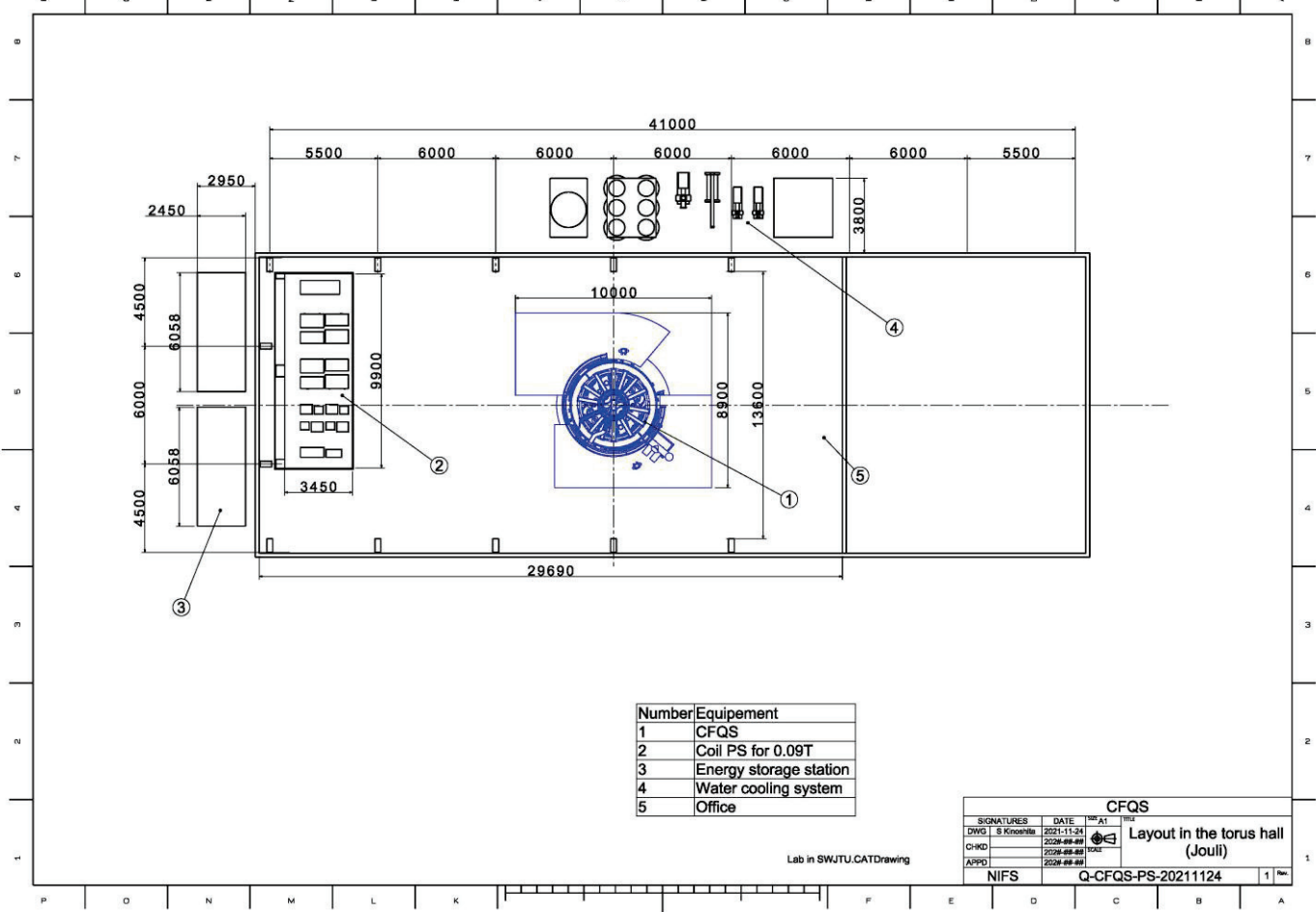
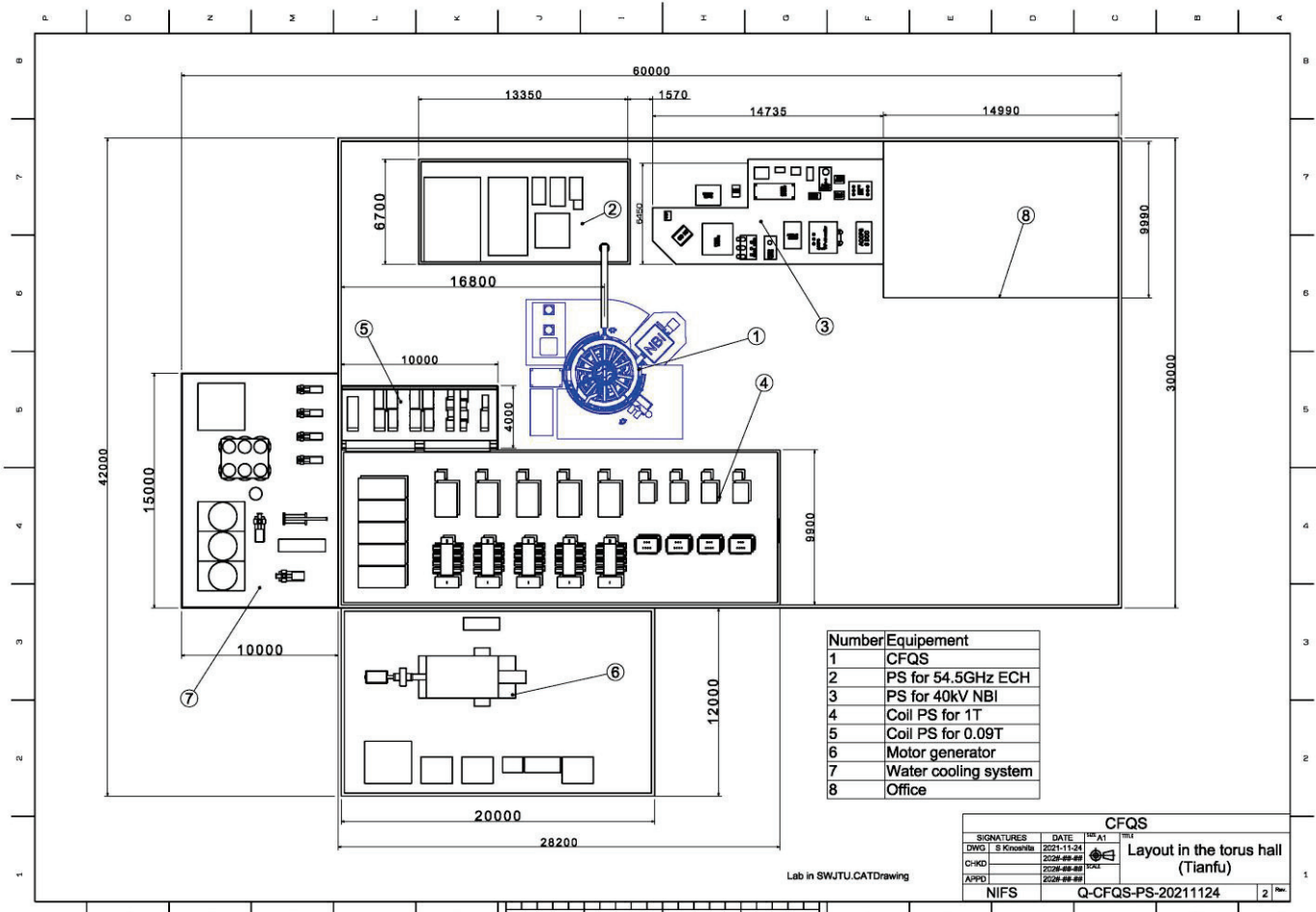
Table of contents

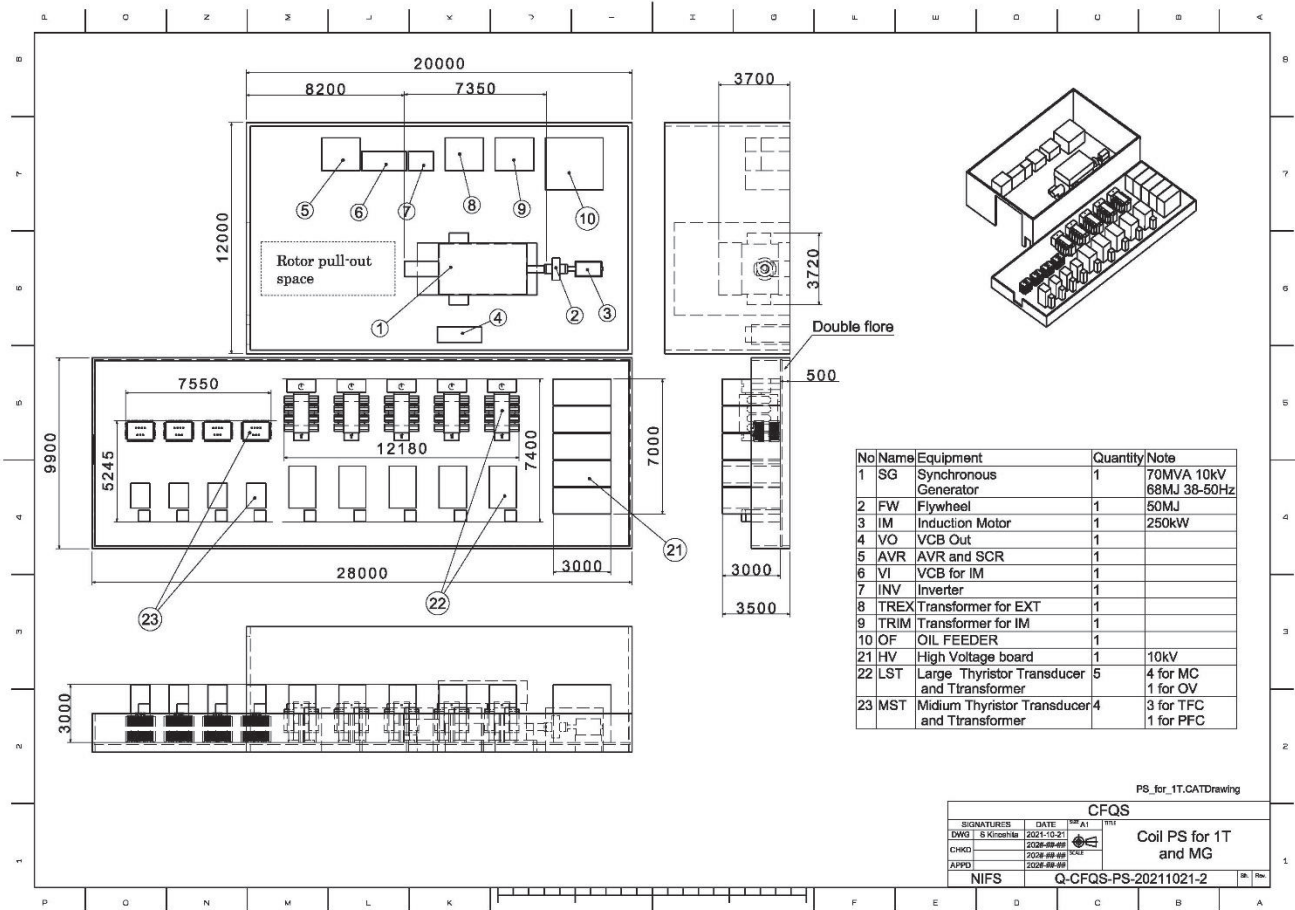
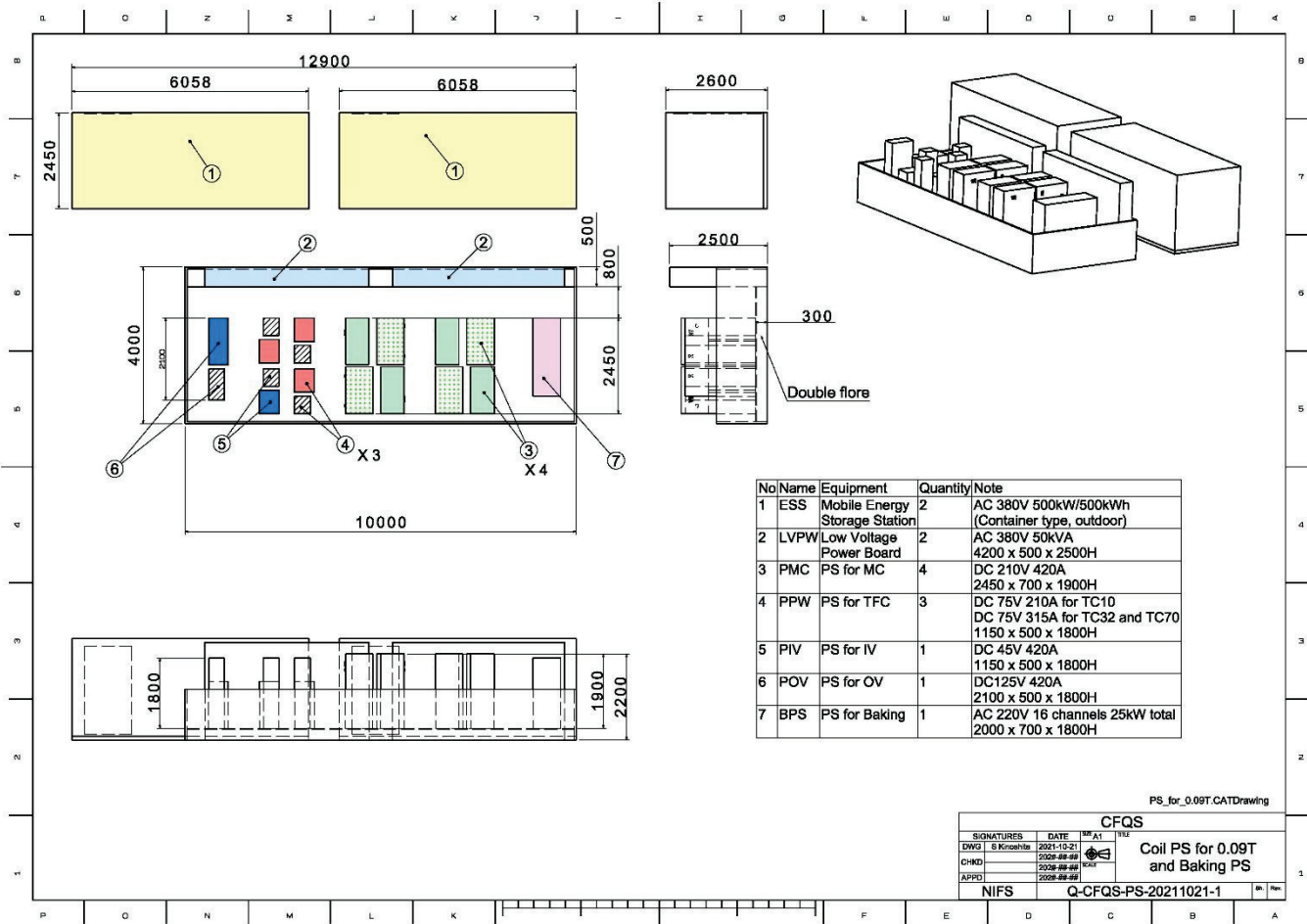
1	CFQS overall view	3
2	Modular coil	6
3	Toroidal field coil.....	12
4	Poloidal field coil	14
5	Vacuum vessel	16
6	External current lead	21
7	Cage type support structure.....	24
8	Cooling water pipe	26

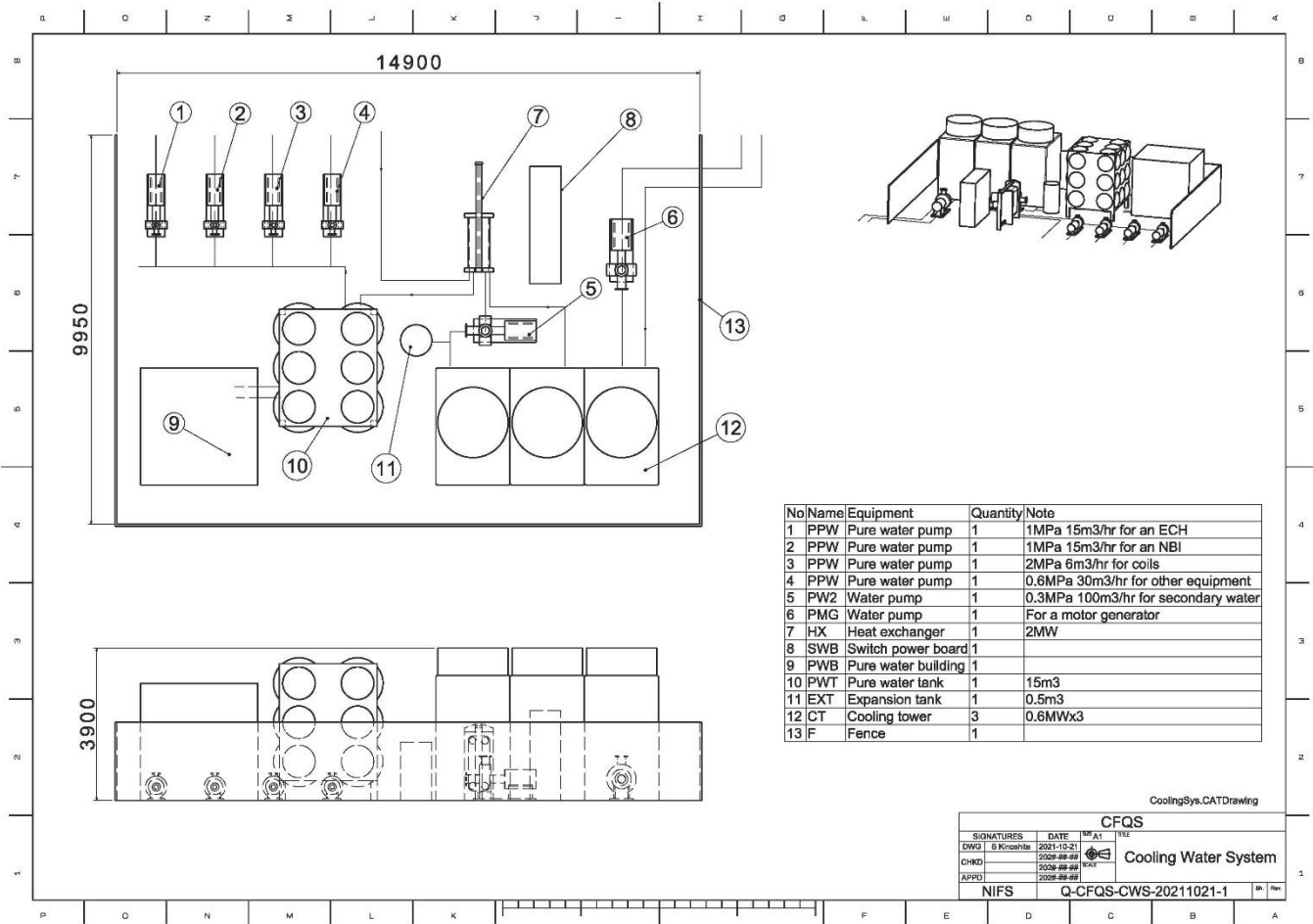
1 CFQS overall view



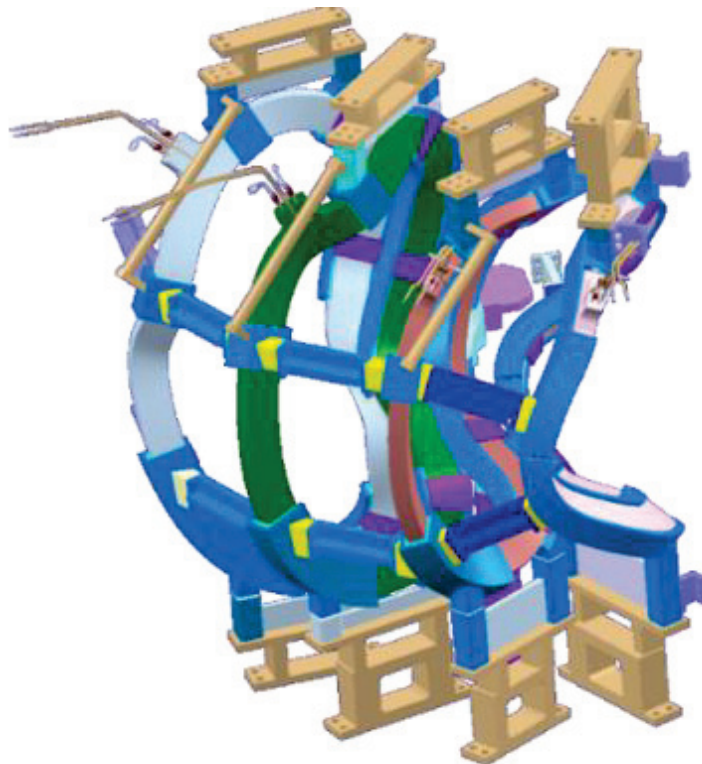
Experimental building in Jiuli campus

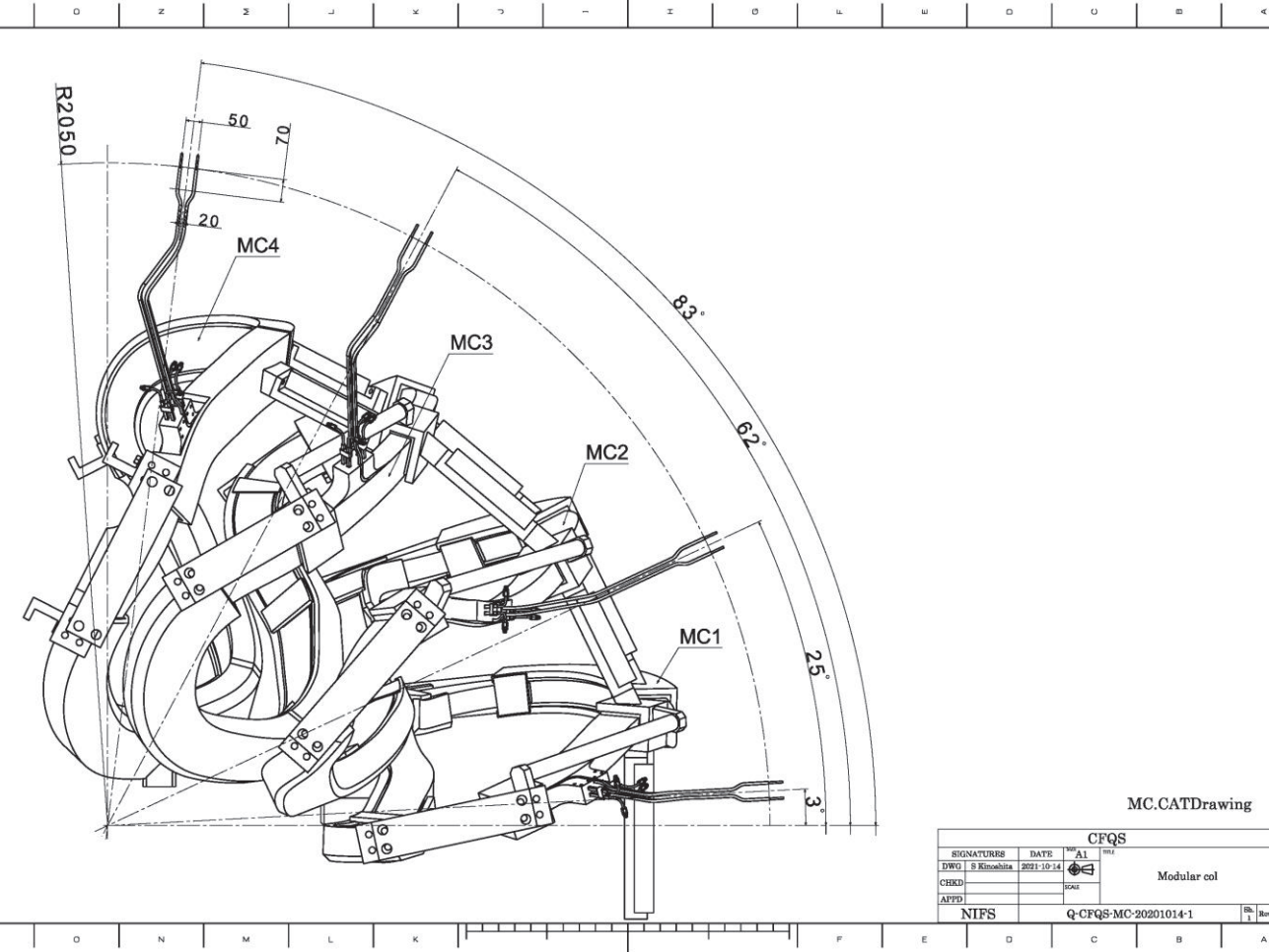
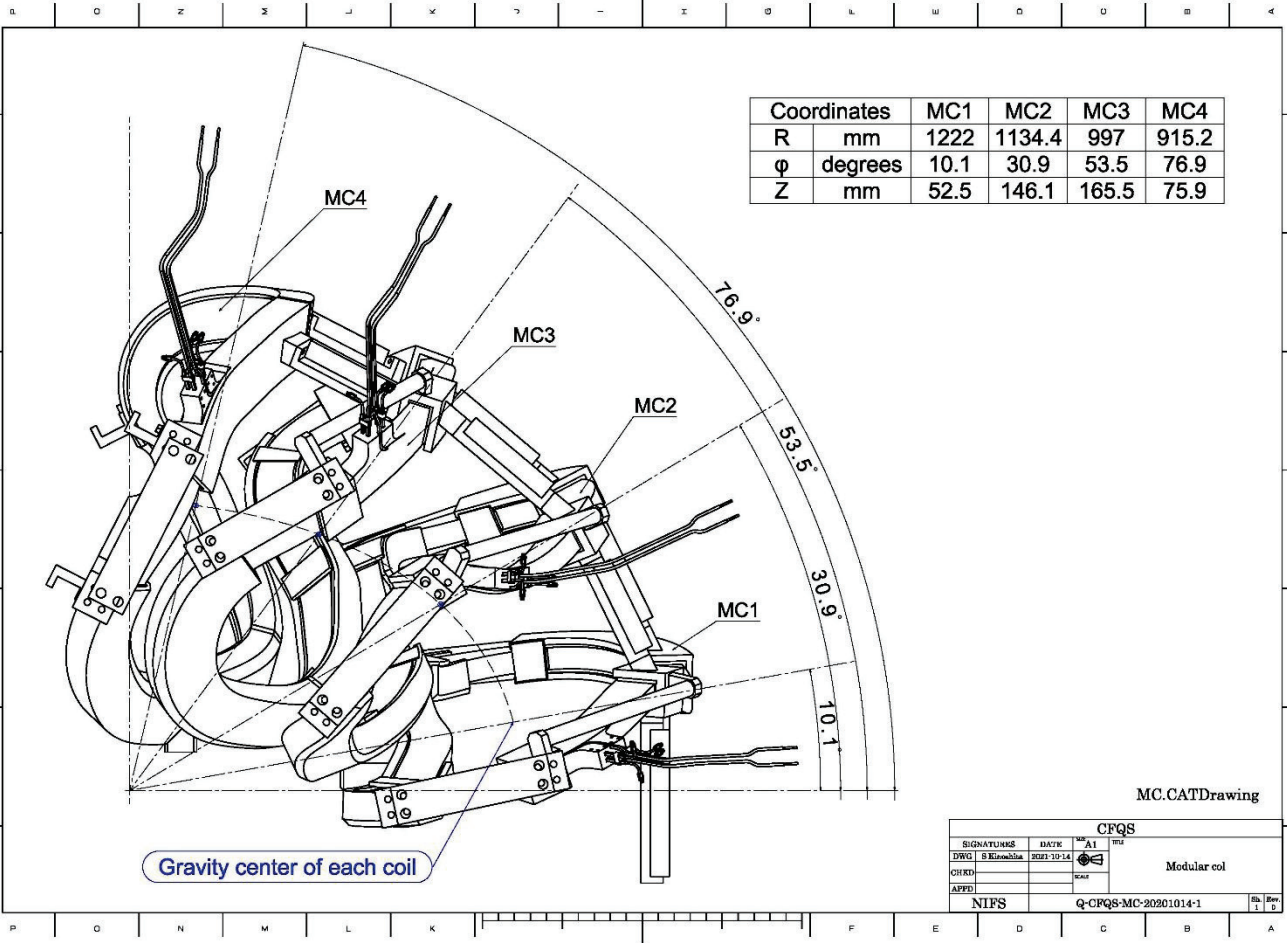


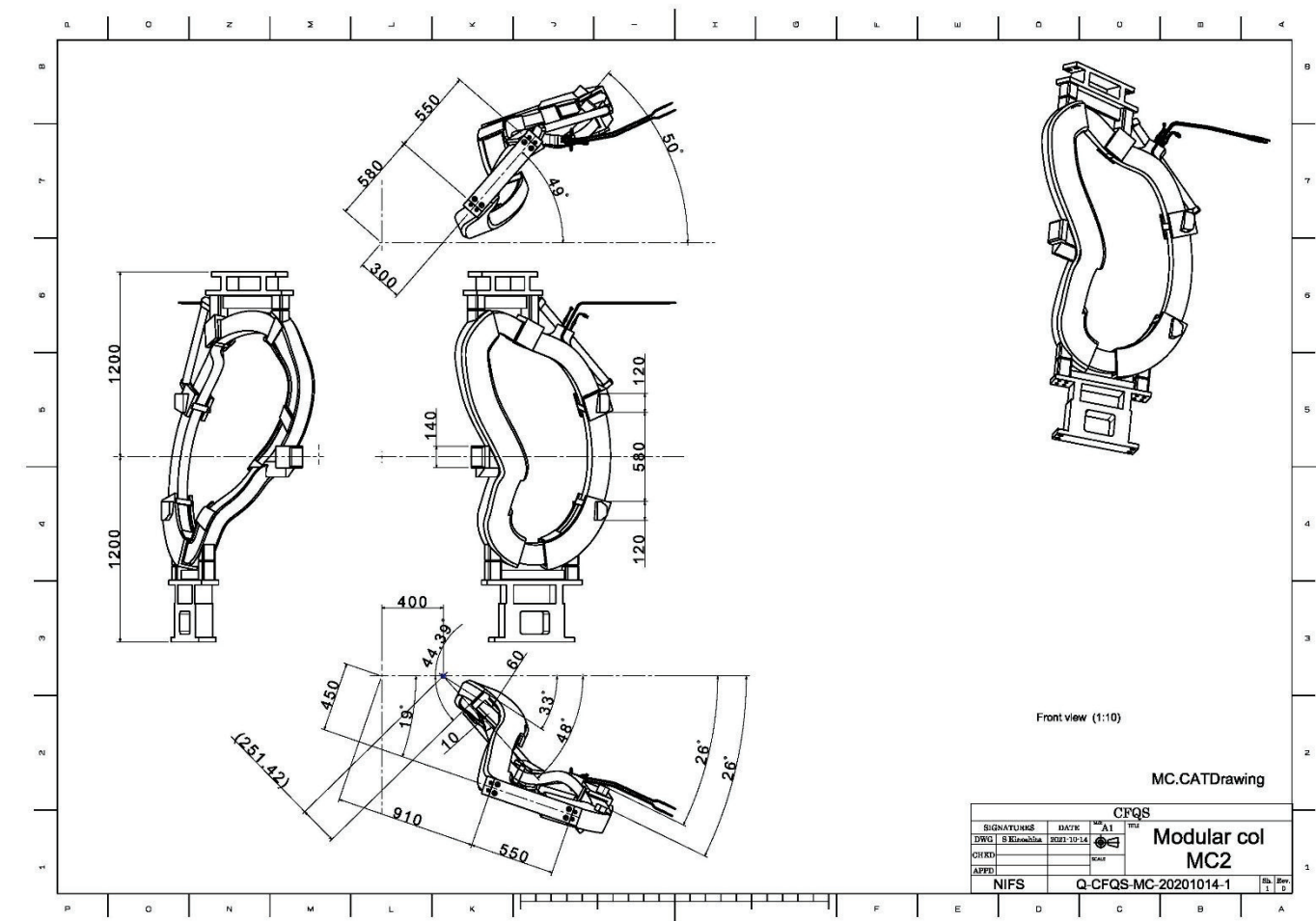
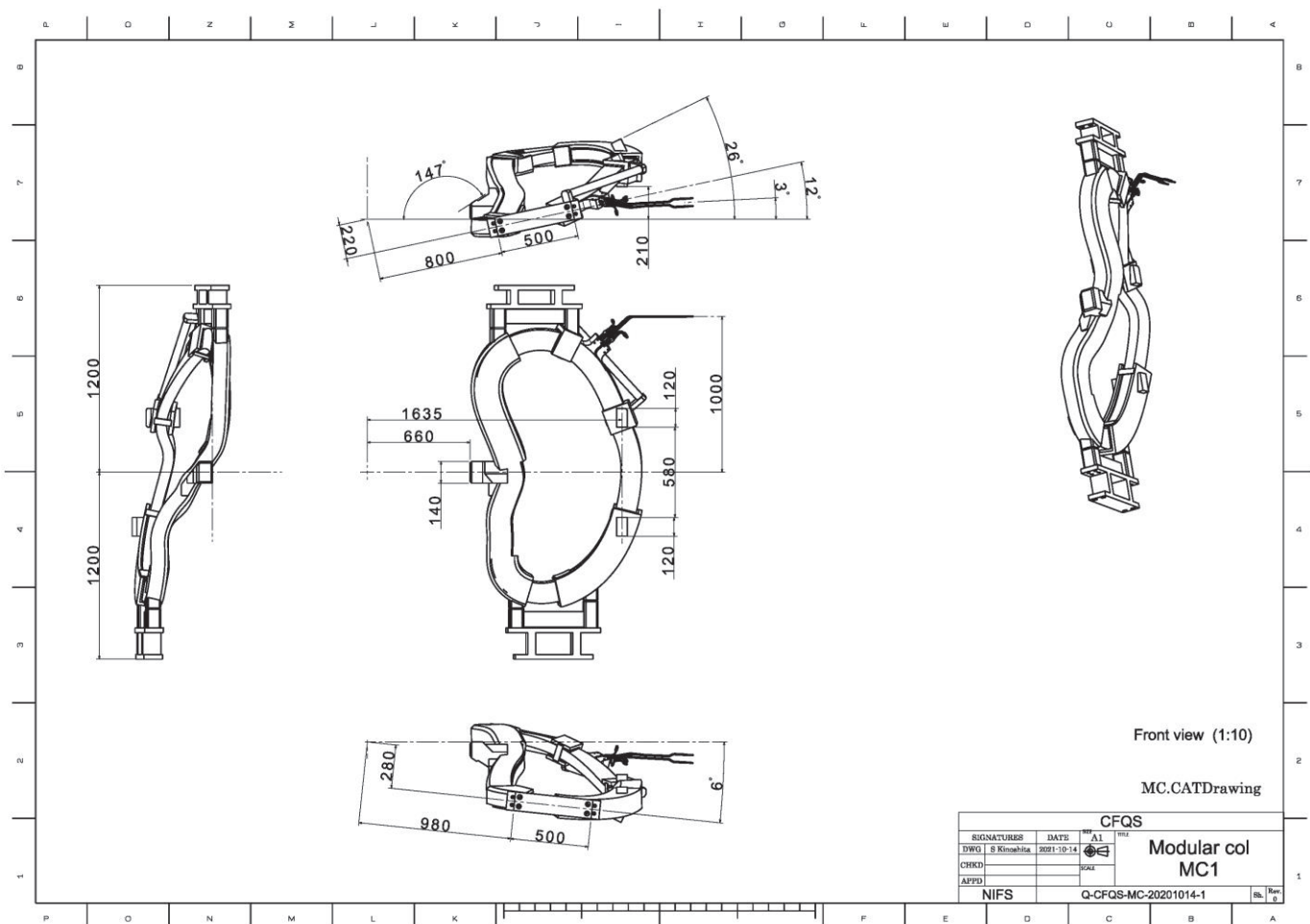


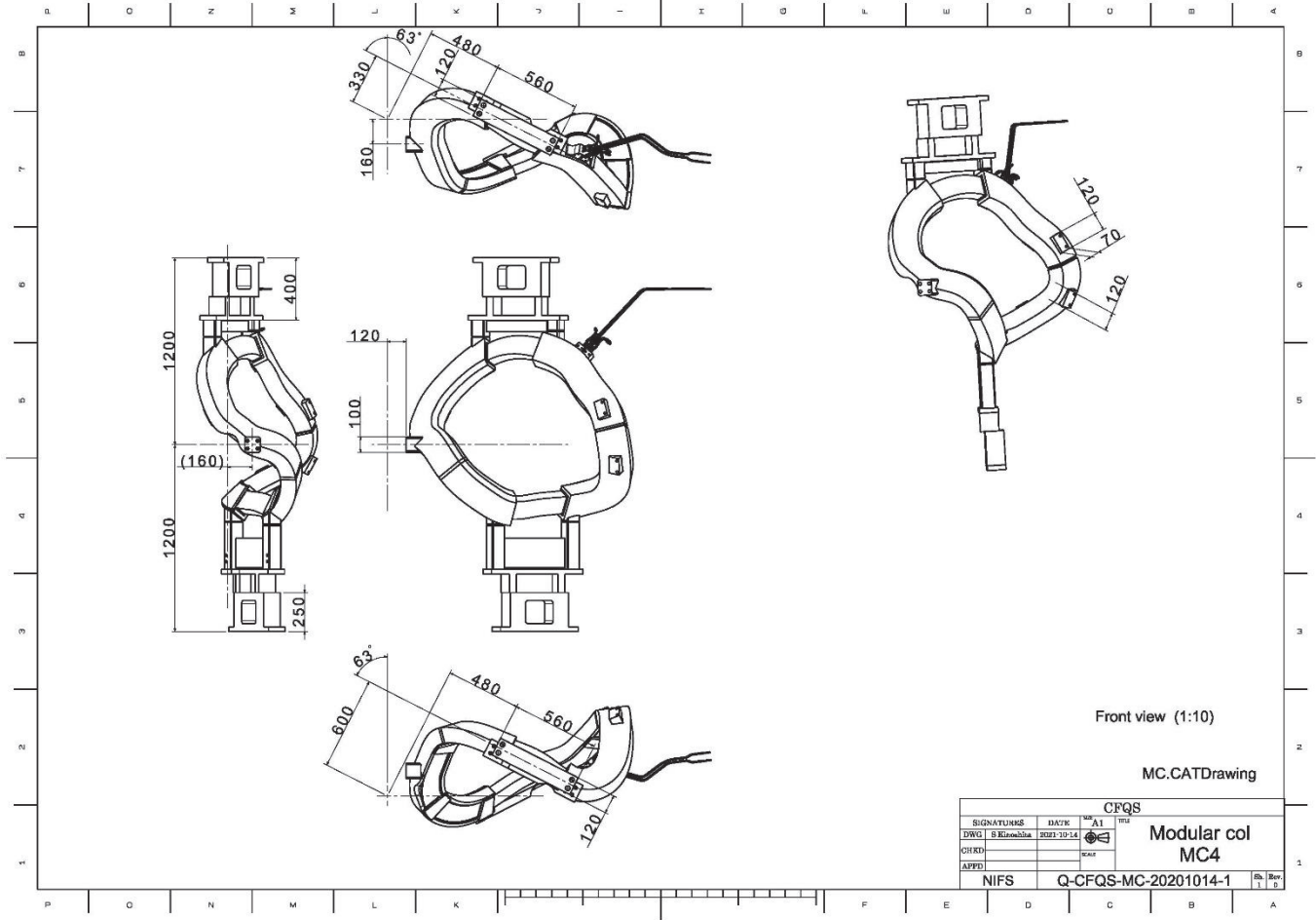
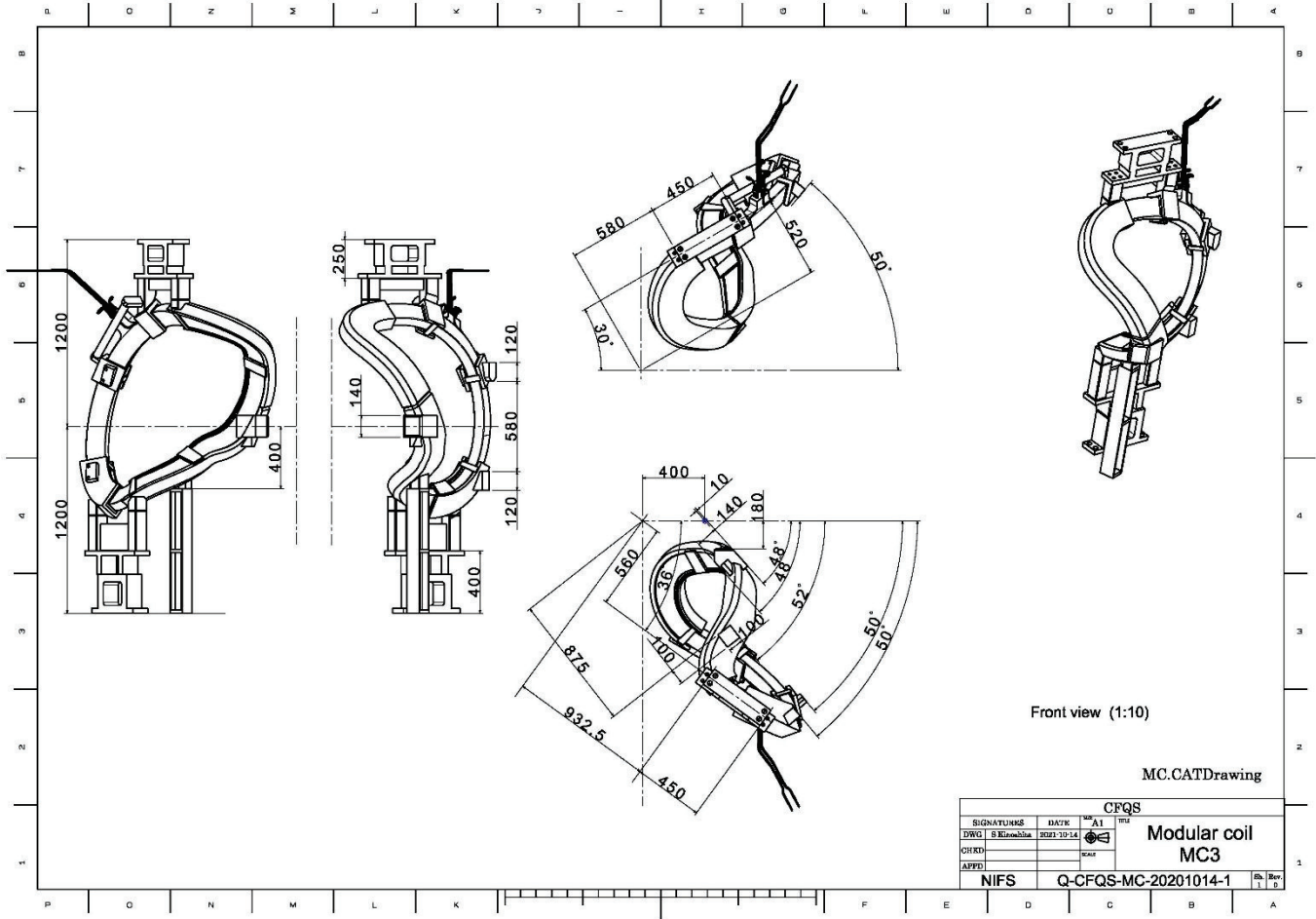


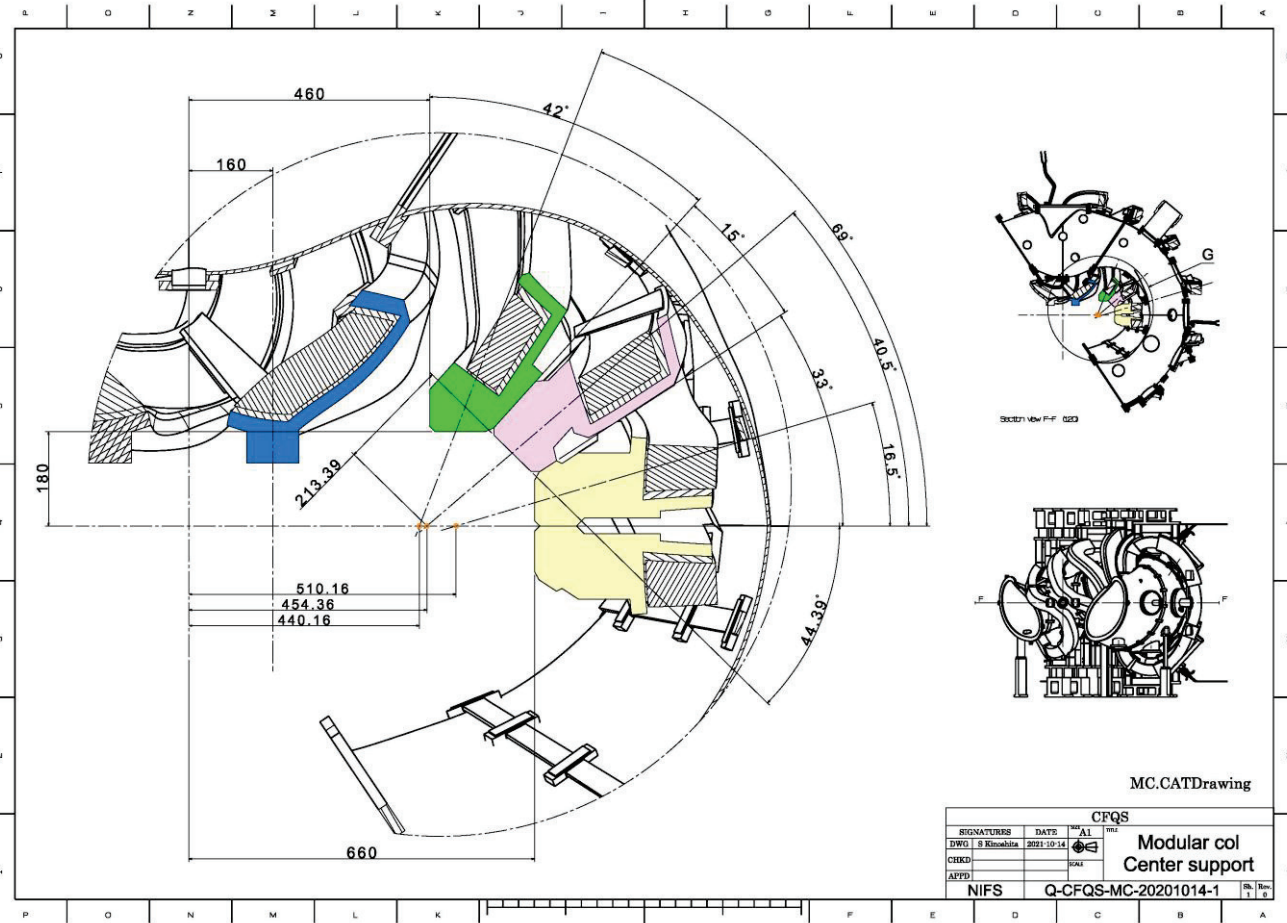
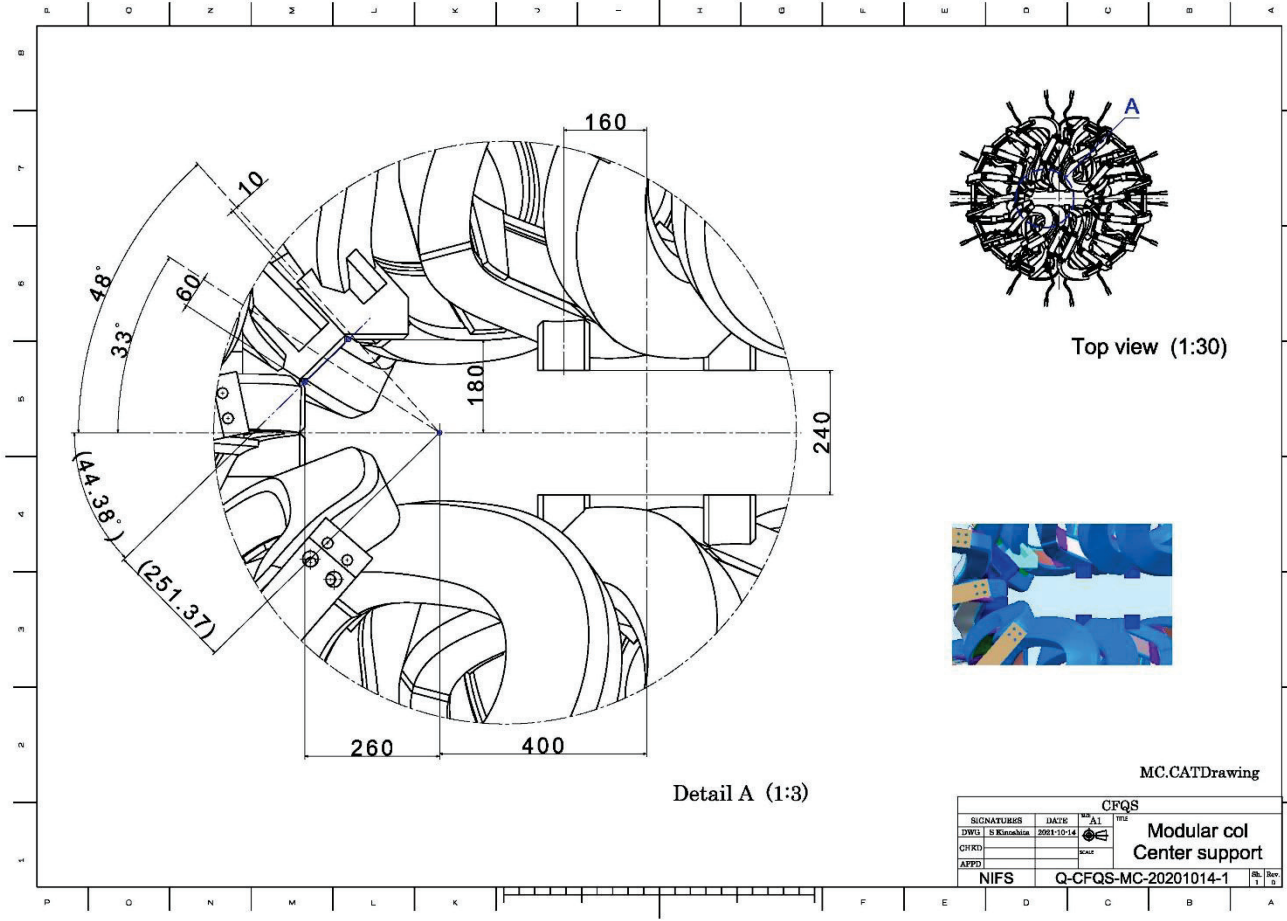
2 Modular coil

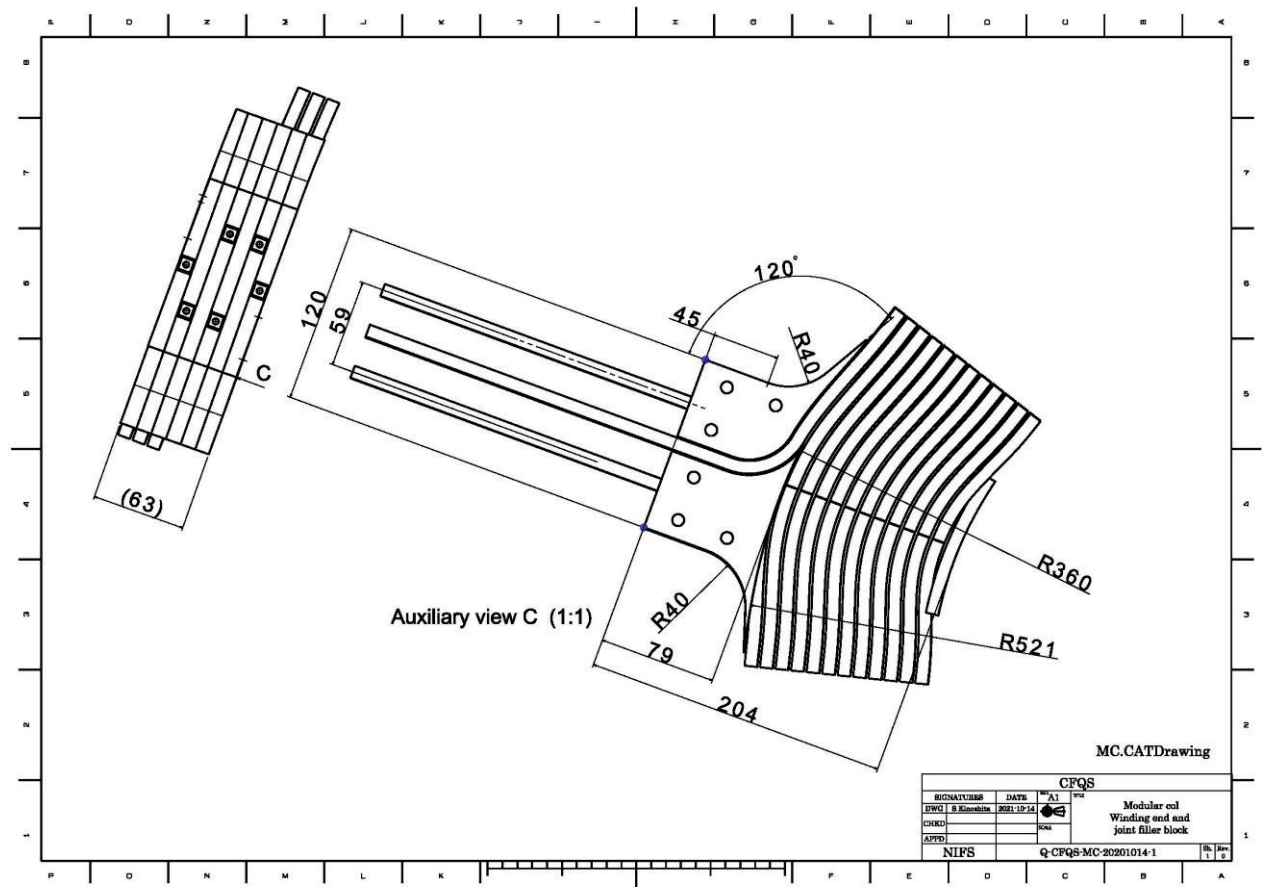
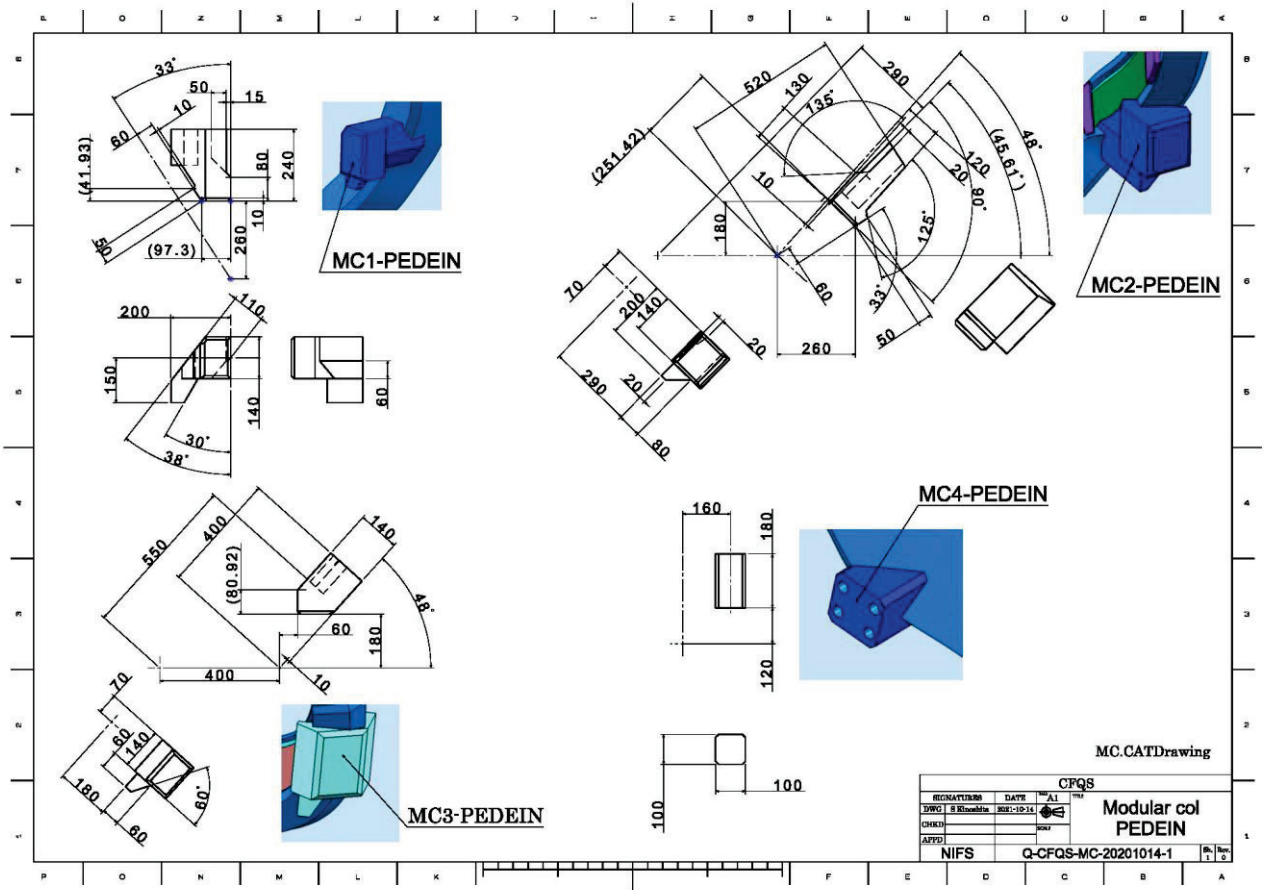




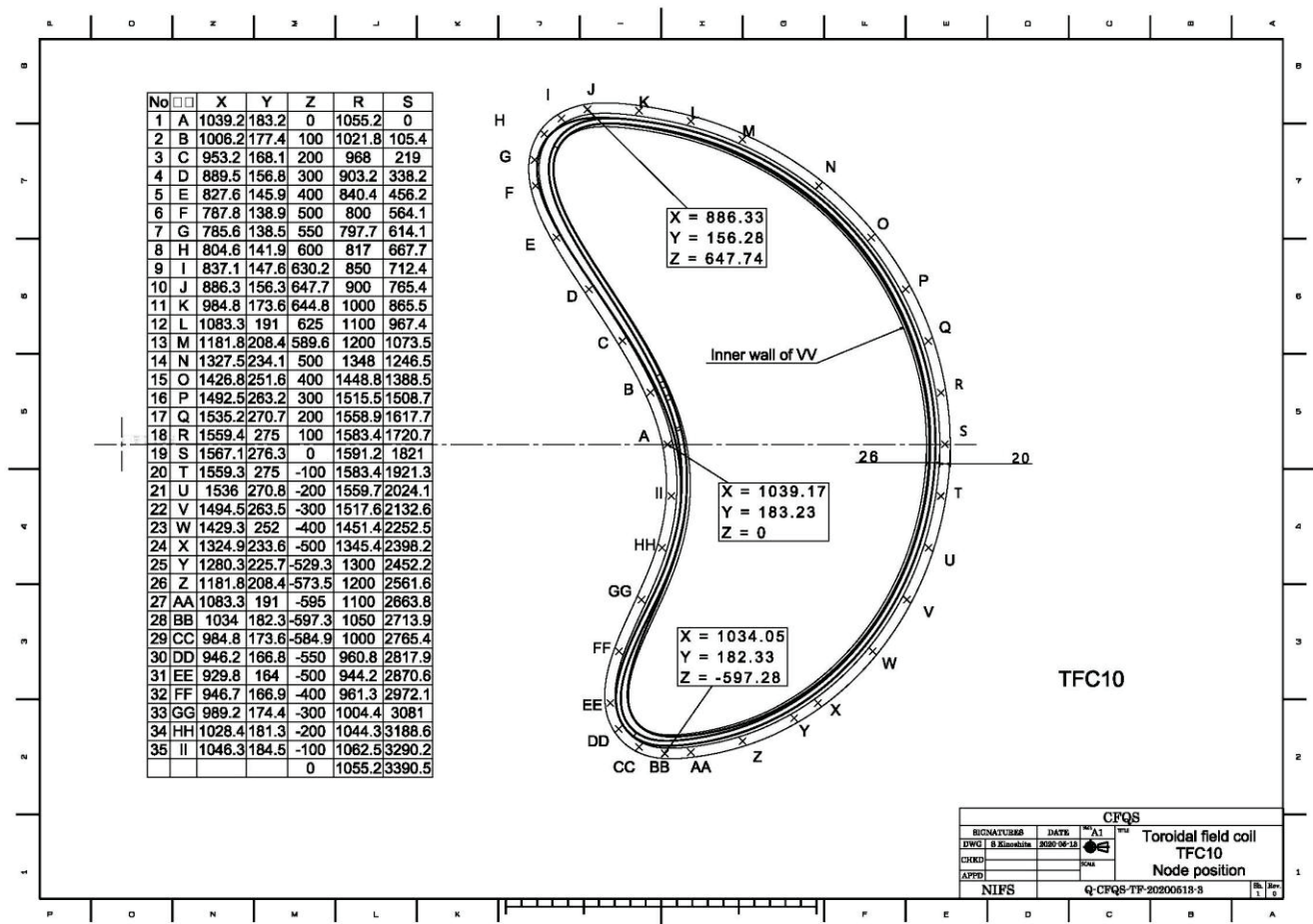
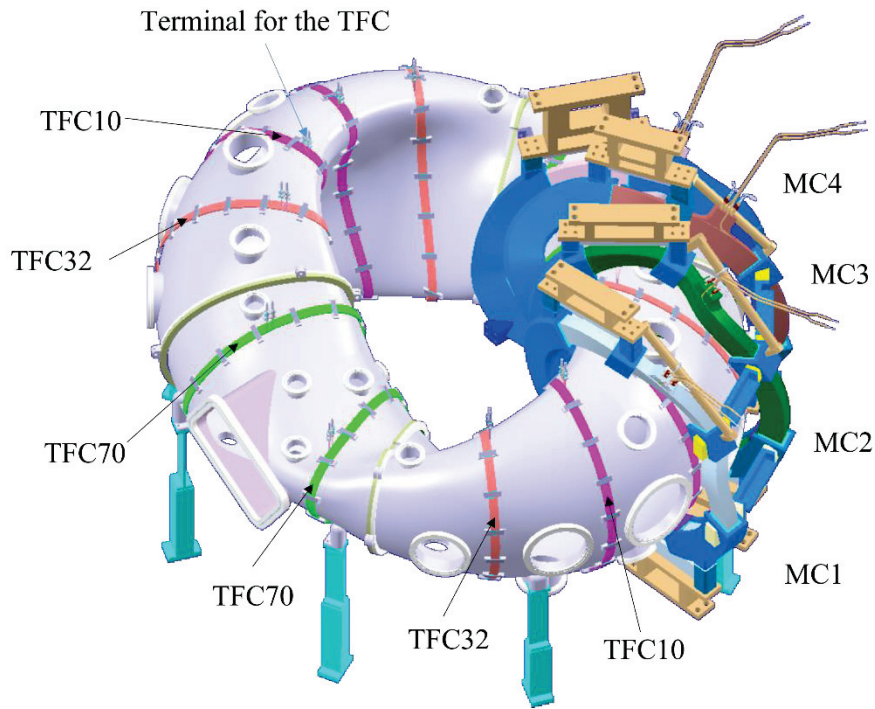




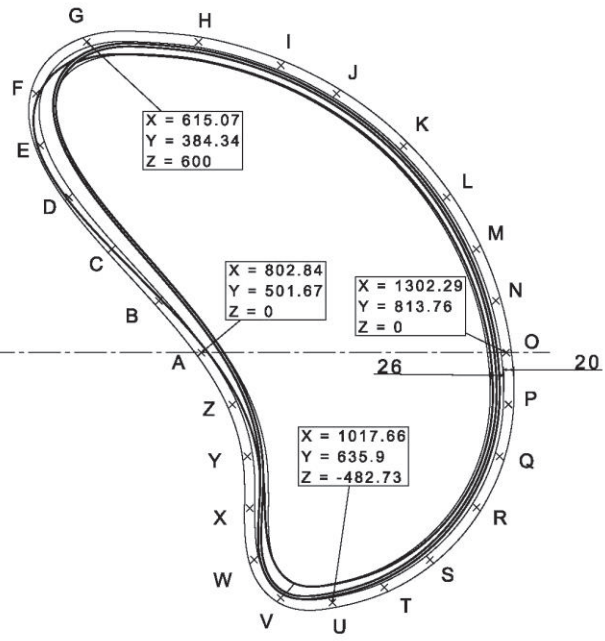




3 Toroidal field coil



NO	X	Y	Z
A	802.84	501.67	0
B	733.1	458.09	100
C	656.12	409.99	200
D	586.03	366.19	300
E	538.99	336.8	400
F	531.85	332.34	500
G	615.07	384.34	600
H	797.83	498.54	600
I	932.85	582.91	554.43
J	1024.29	640.05	500
K	1134.06	708.64	398.97
L	1204.59	752.71	300
M	1253.33	783.17	200
N	1285.05	802.99	-100
O	1302.29	813.76	0
P	1305.96	816.05	-100
Q	1291.49	807.01	-200
R	1253.33	783.17	-298.76
S	1176.96	735.44	-400
T	1102.46	688.9	-453.63
U	1017.66	635.9	-482.73
V	932.85	582.91	-473.75
W	888.93	555.47	-400
X	882.12	551.21	-300
Y	878.45	548.92	-200
Z	853.56	533.37	-100

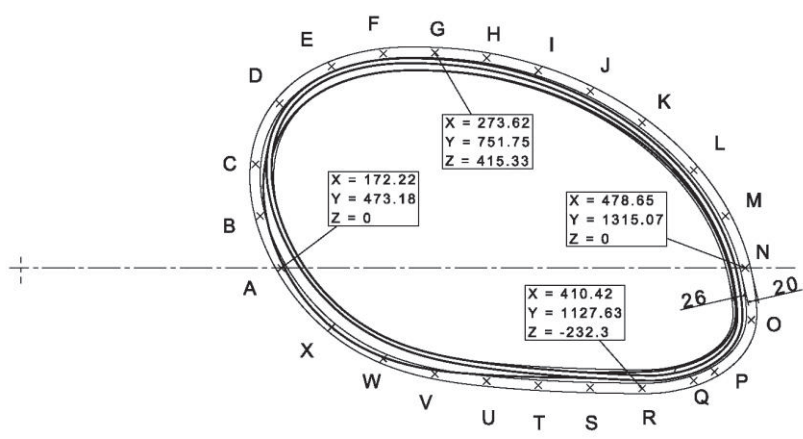


TFC32

CFQS			
SIGNATURE	DATE	NO. A1	REV.
DWG: S Kinoshita	2020-06-12		
CHKD:			
APPD:			
NIFS			Q-CFQS-TF-20200613-3

Toroidal field coil
TFC32
Node position

NO	X	Y	Z
A	172.22	473.18	0
B	158.14	434.48	100
C	155.14	426.24	200
D	171.01	469.85	317.1
E	205.21	563.82	388.71
F	239.41	657.78	413.26
G	273.62	751.75	415.33
H	307.82	845.72	405.06
I	342.02	939.69	380.51
J	376.22	1033.66	340.54
K	410.42	1127.63	280.41
L	444.63	1221.6	188.76
M	465.5	1278.96	100
N	478.65	1315.07	0
O	482.65	1326.07	-100
P	458.38	1259.38	-200
Q	444.63	1221.6	-217.67
R	410.42	1127.63	-232.3
S	376.22	1033.66	-230.75
T	342.02	939.69	-226.4
U	307.82	845.72	-218.49
V	273.62	751.75	-204.41
W	239.41	657.78	-174.84
X	205.21	563.82	-114.77

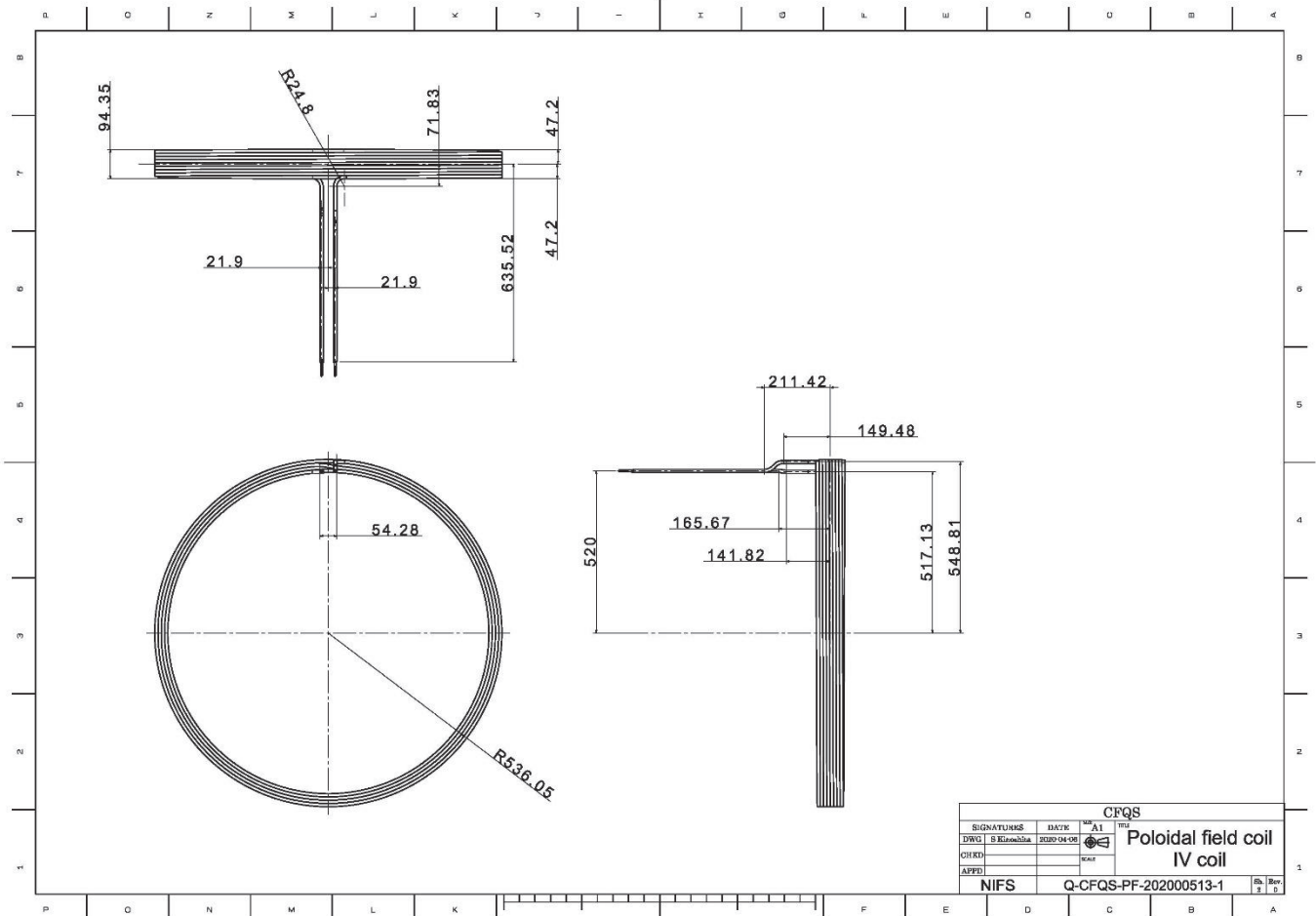
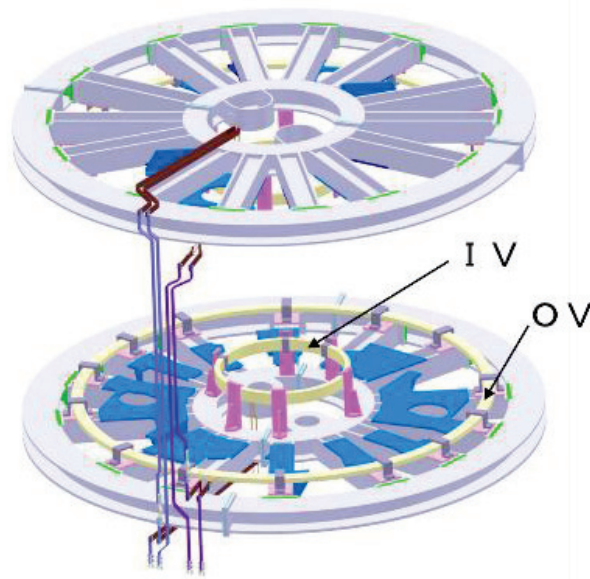


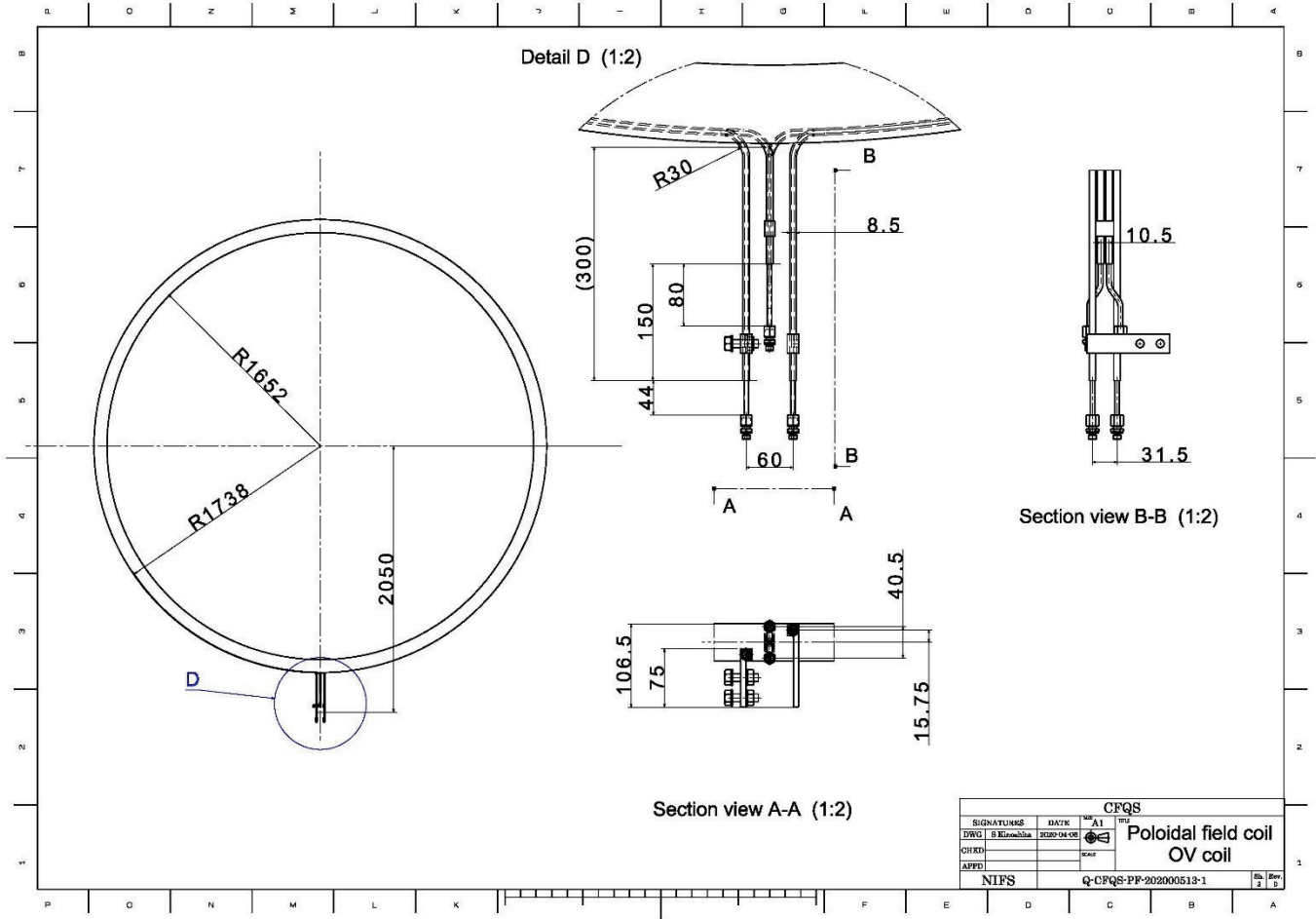
TFC70

CFQS			
SIGNATURE	DATE	NO. A1	REV.
DWG: S Kinoshita	2020-06-12		
CHKD:			
APPD:			
NIFS			Q-CFQS-TF-20200613-3

Toroidal field coil
TFC70
Node position

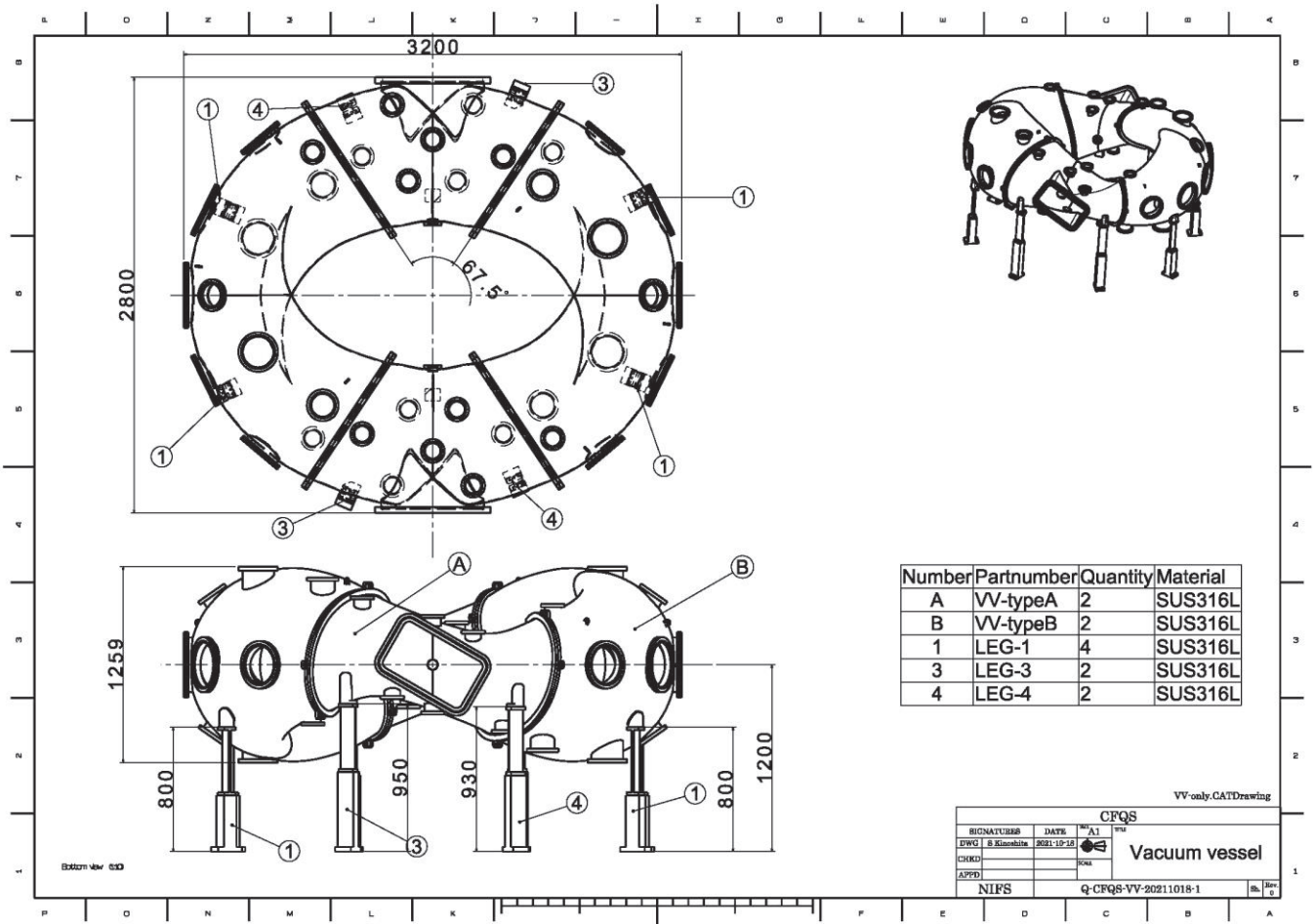
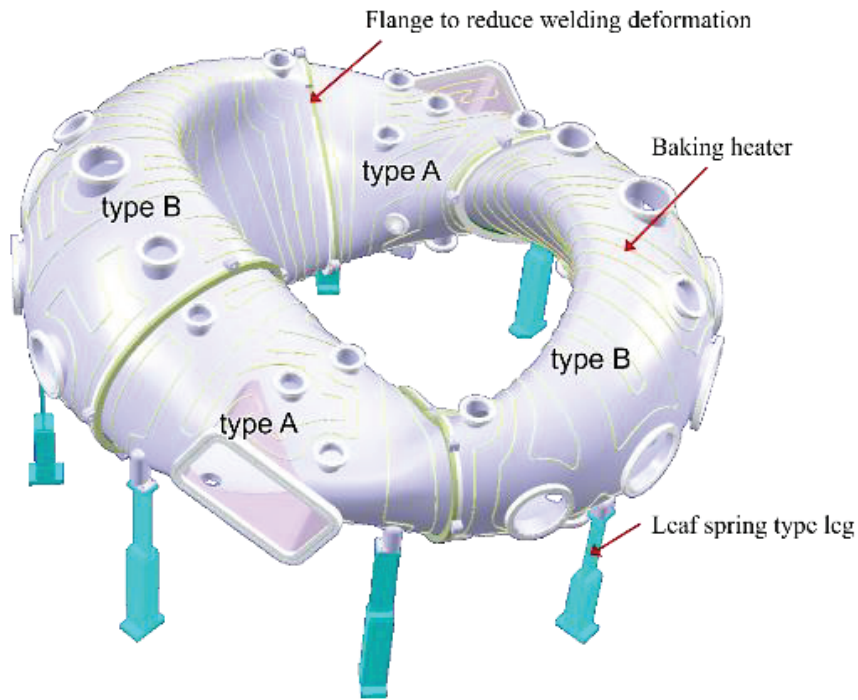
4 Poloidal field coil

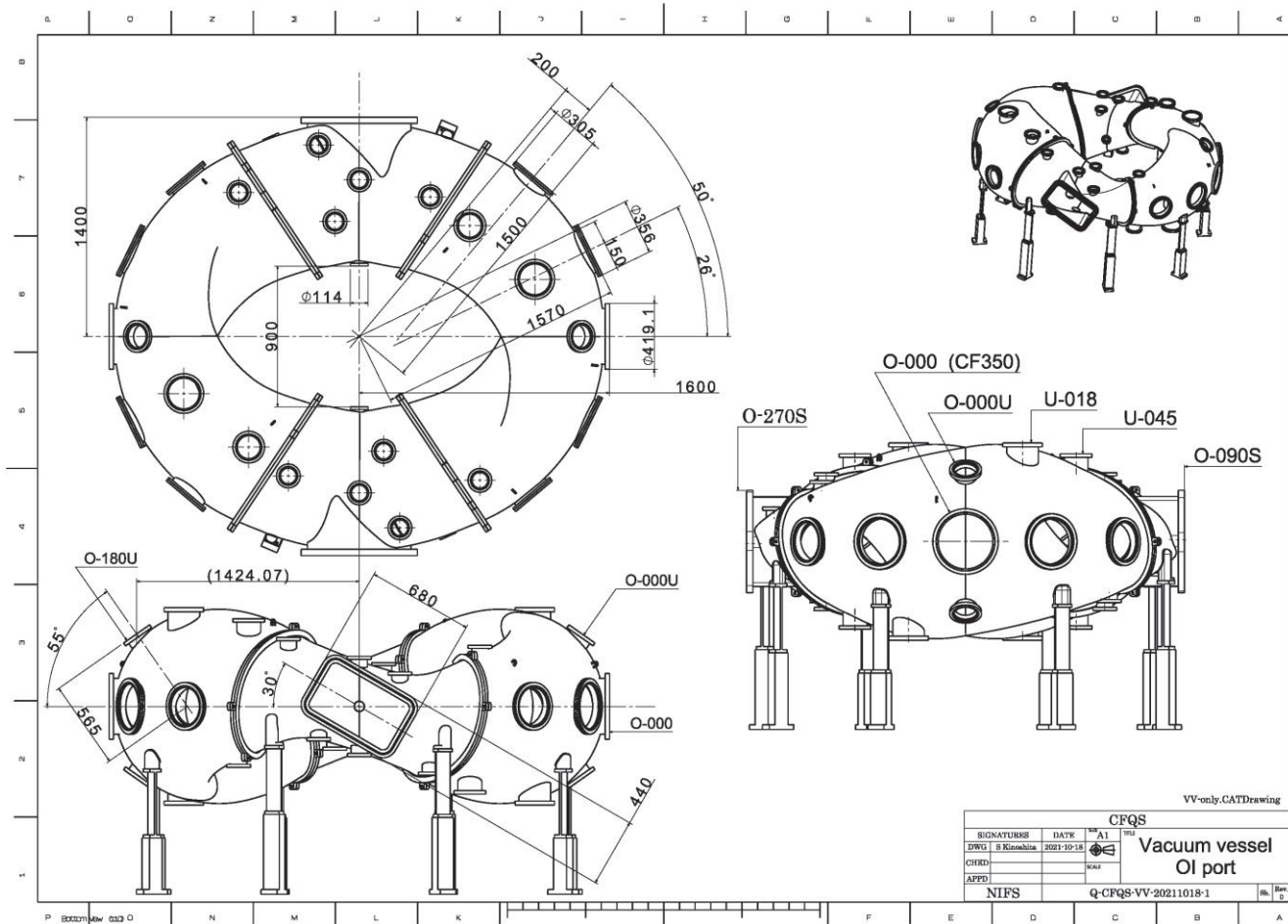
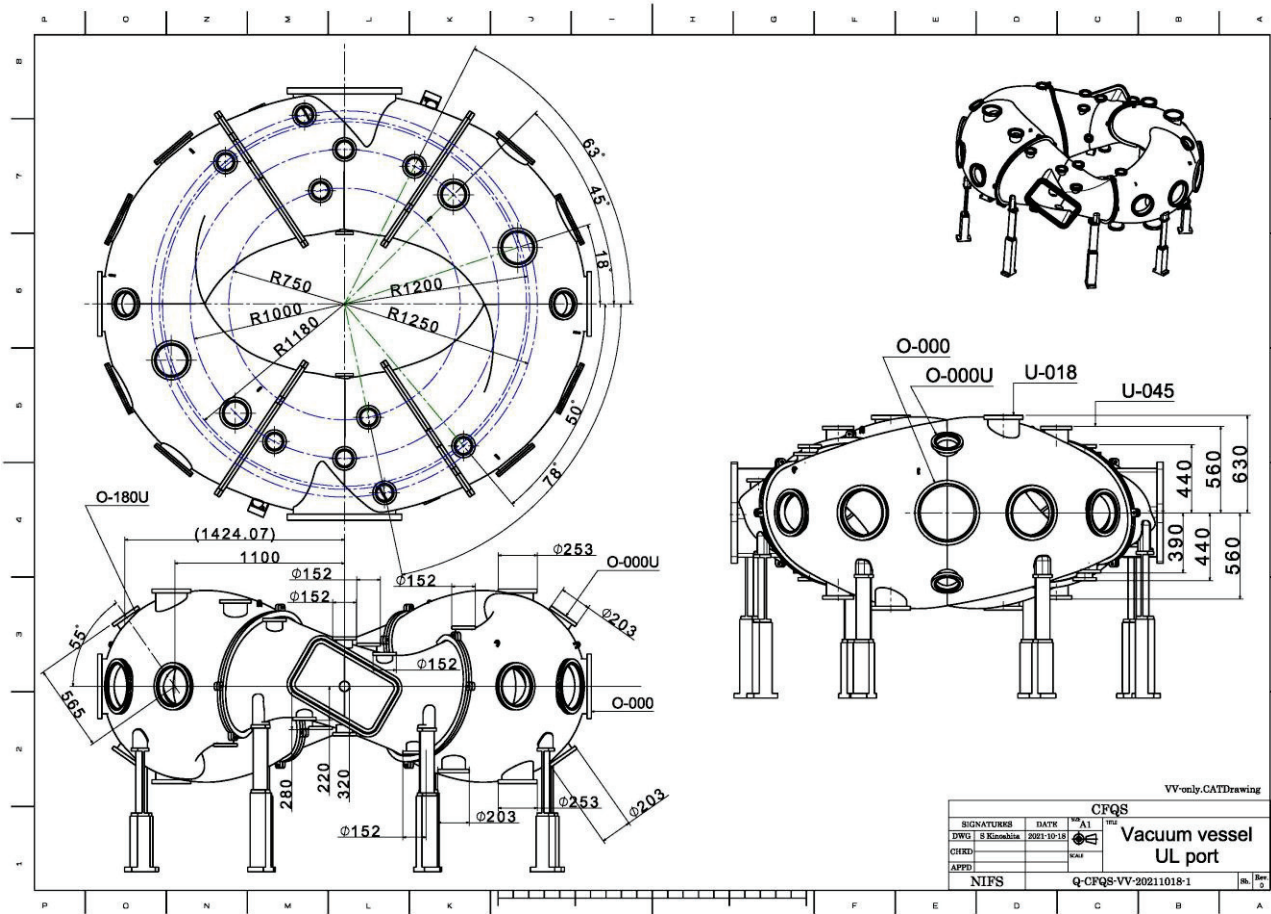


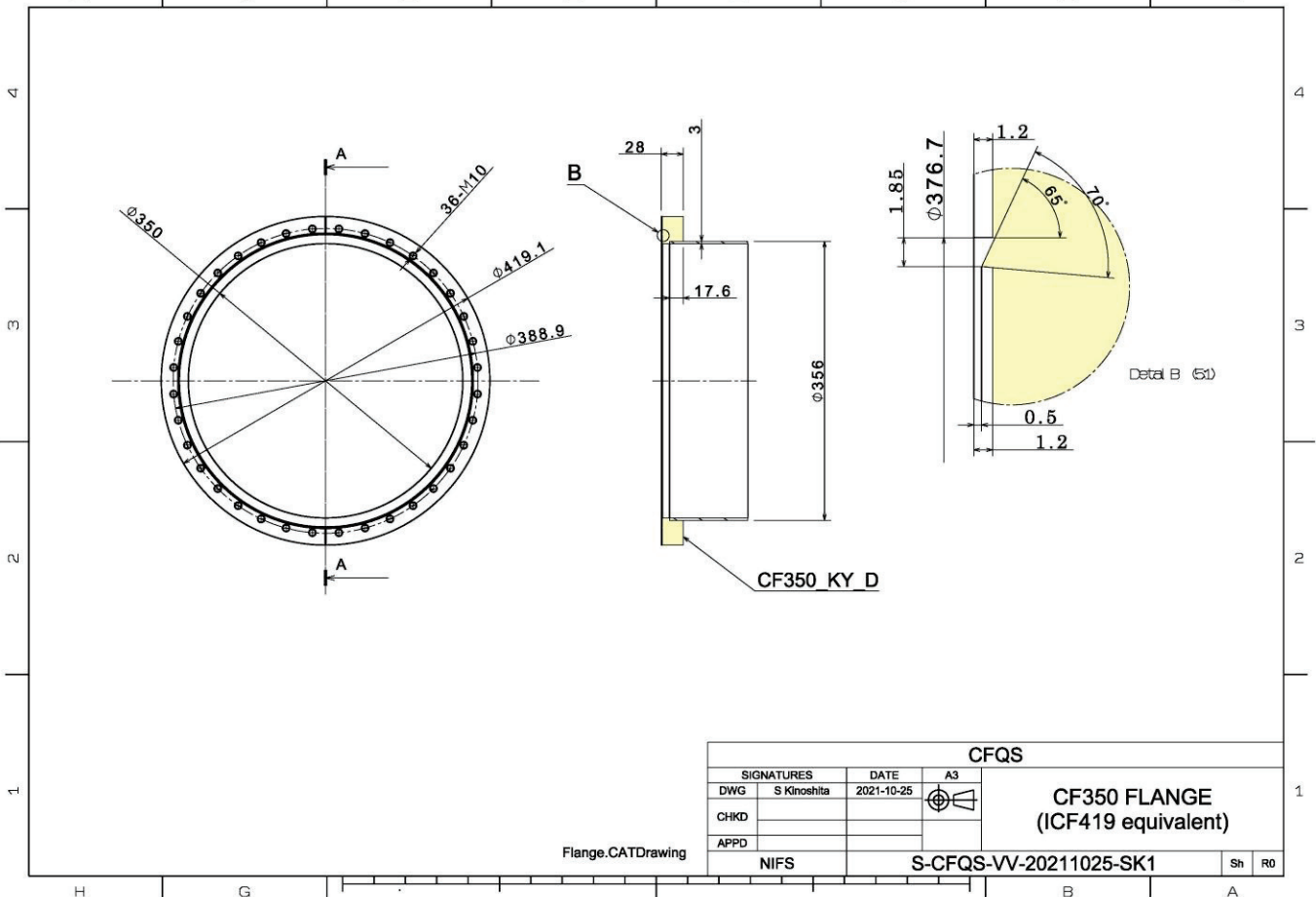
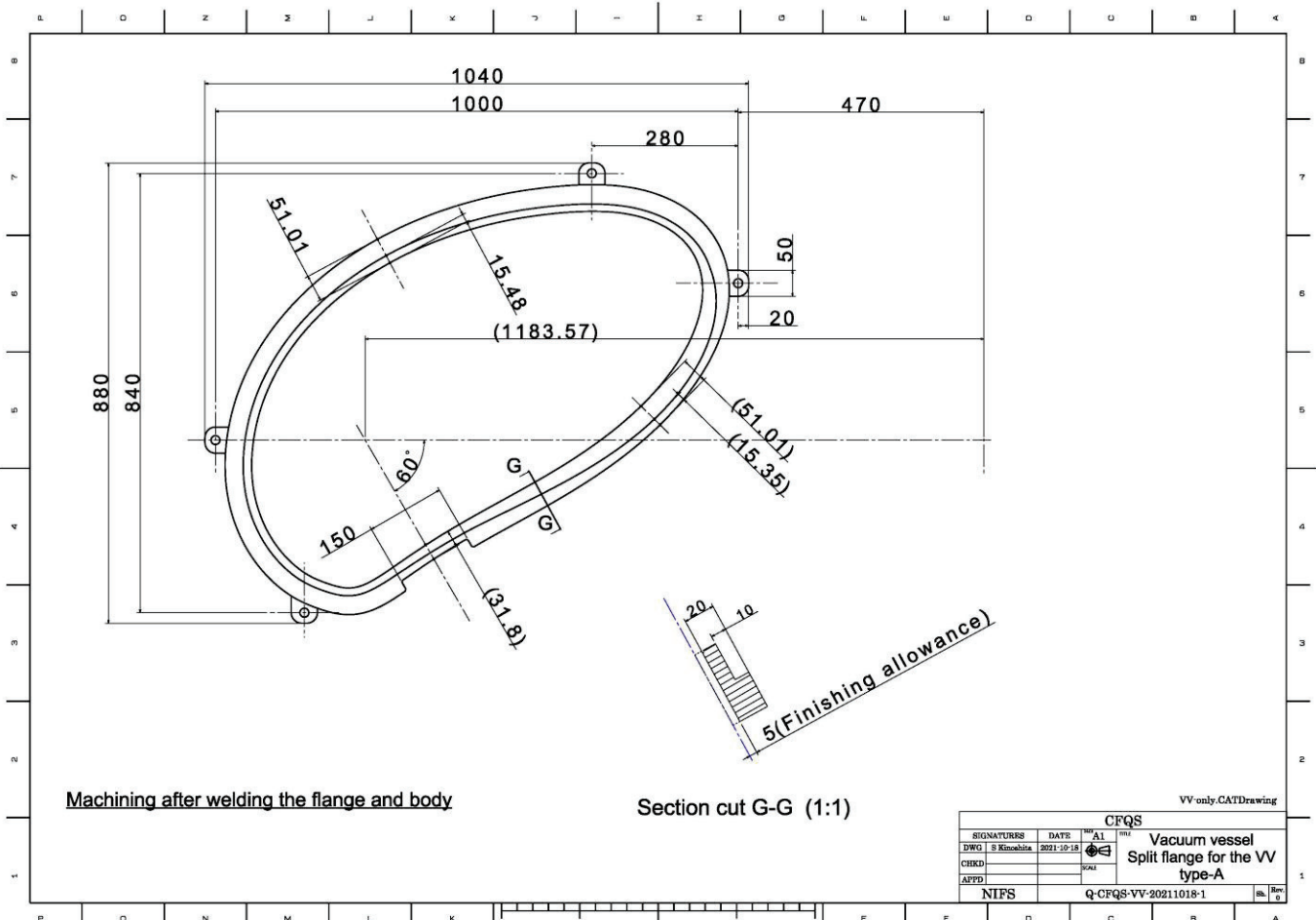


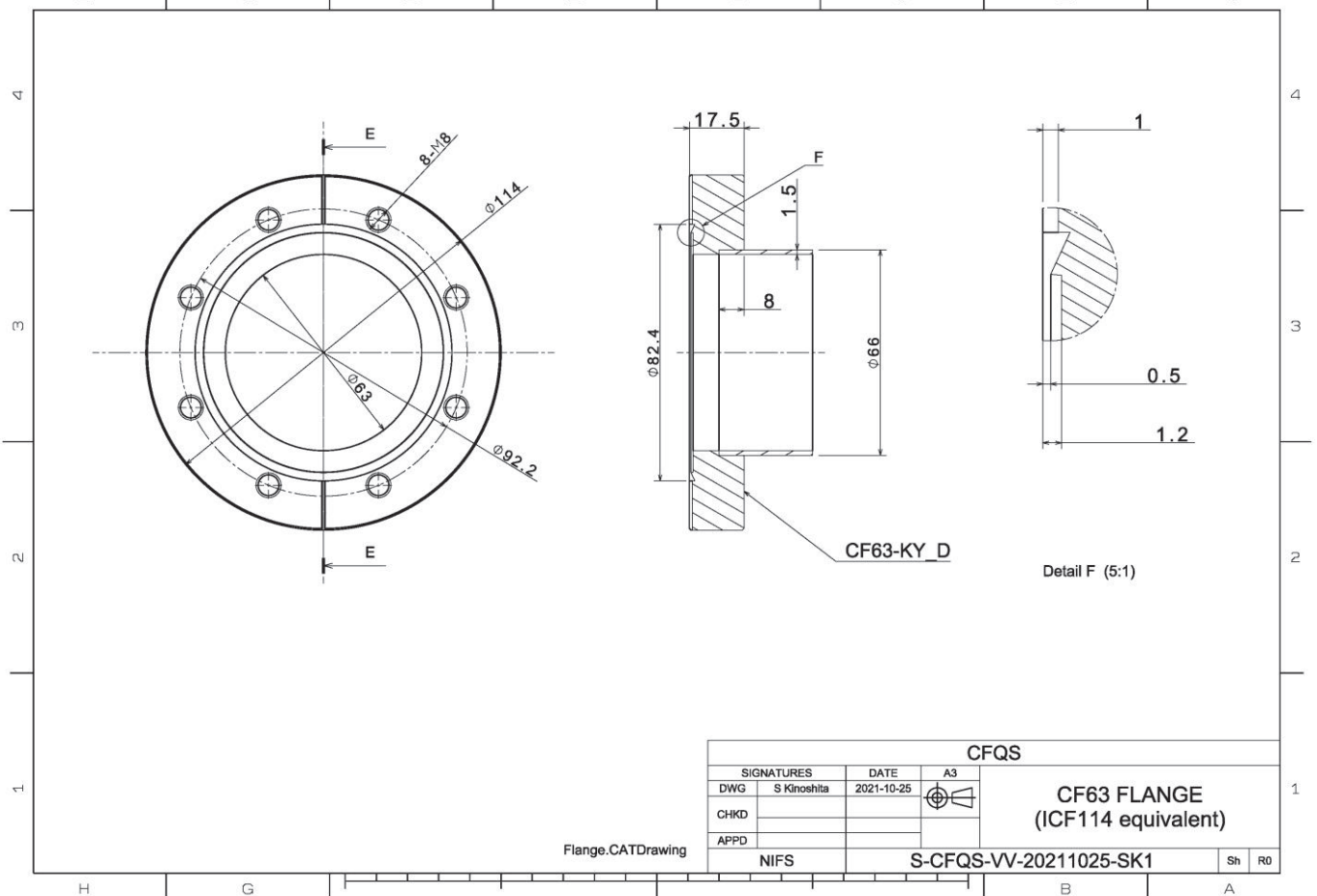
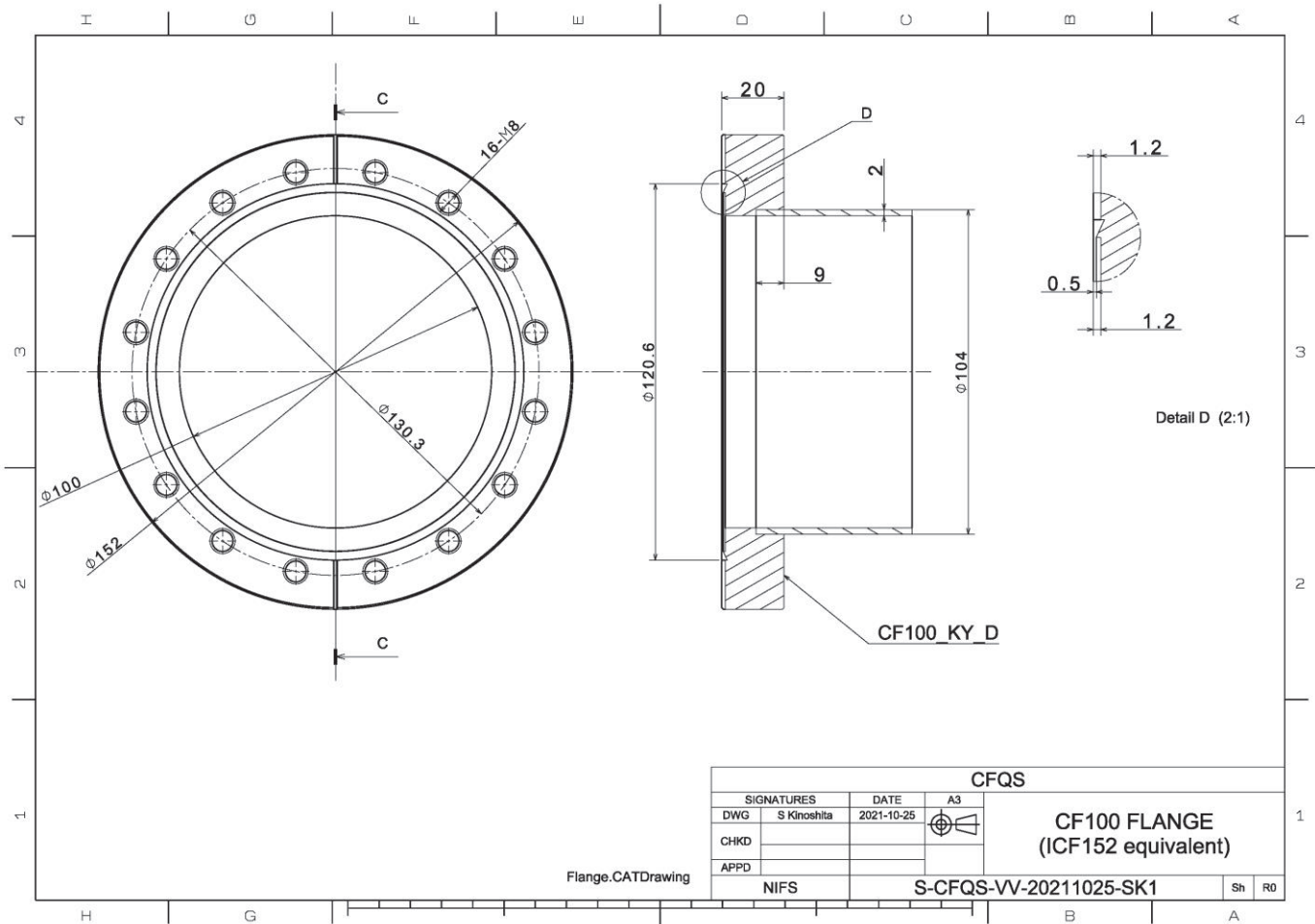
SIGNATURES		DATE	REV	CFQS
DRG	S. Elzschka	2020-04-09	A1	Poloidal field coil OV coil
CHKD				
APFD				
NIFS		Q-CFQS-PP-202000513-1		Sh. Rev. 2 1 D

5 Vacuum vessel

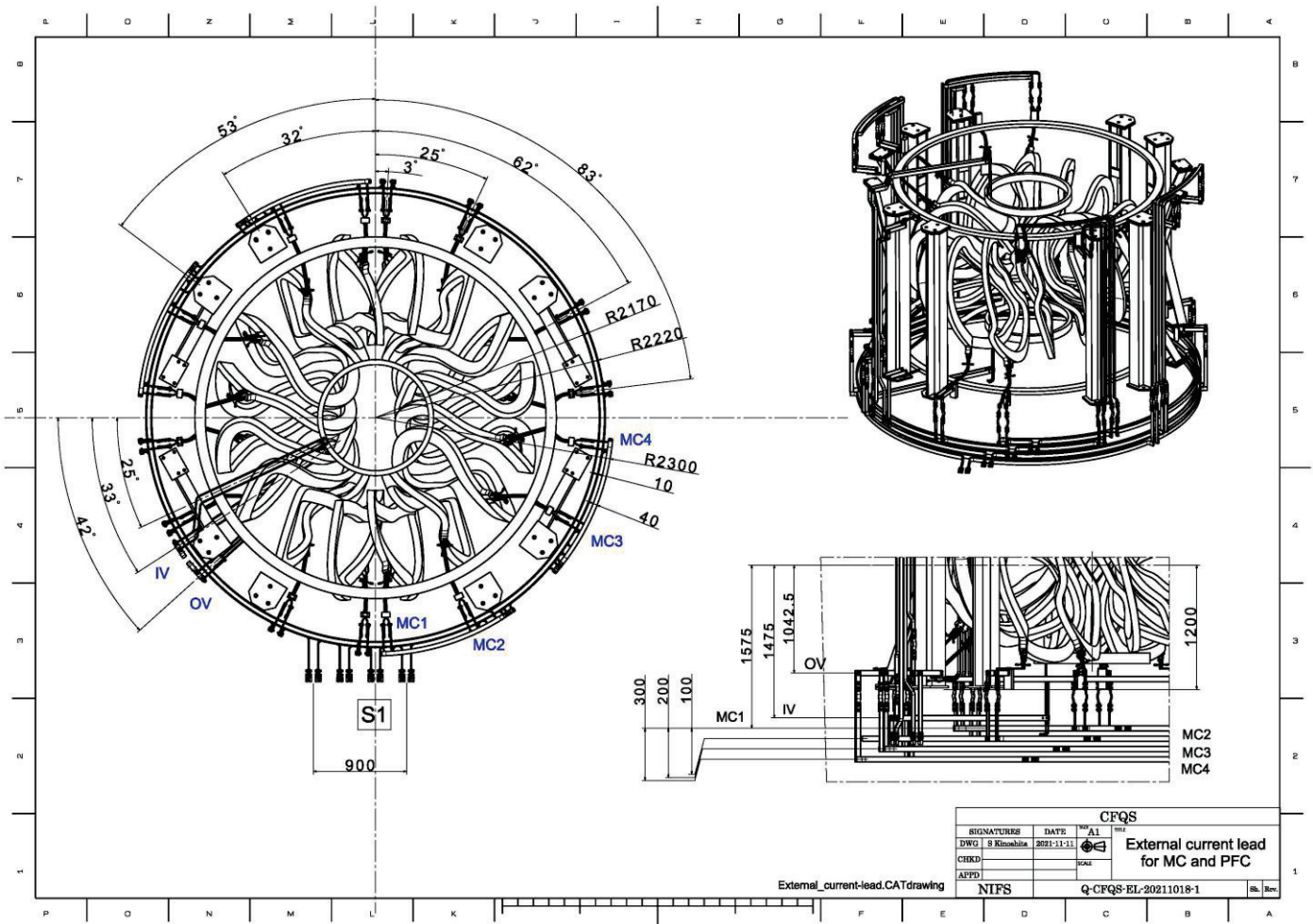
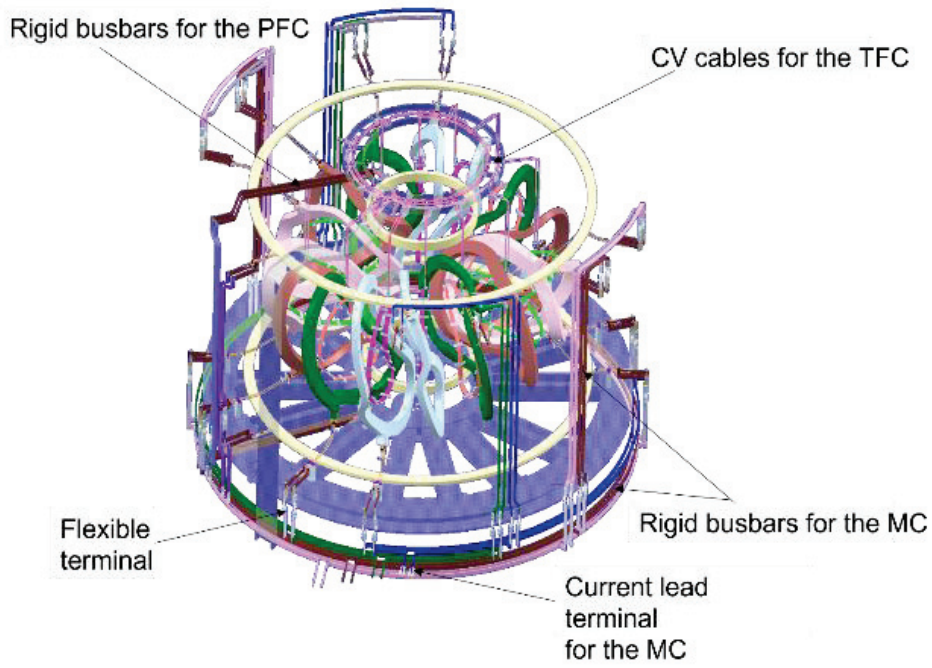


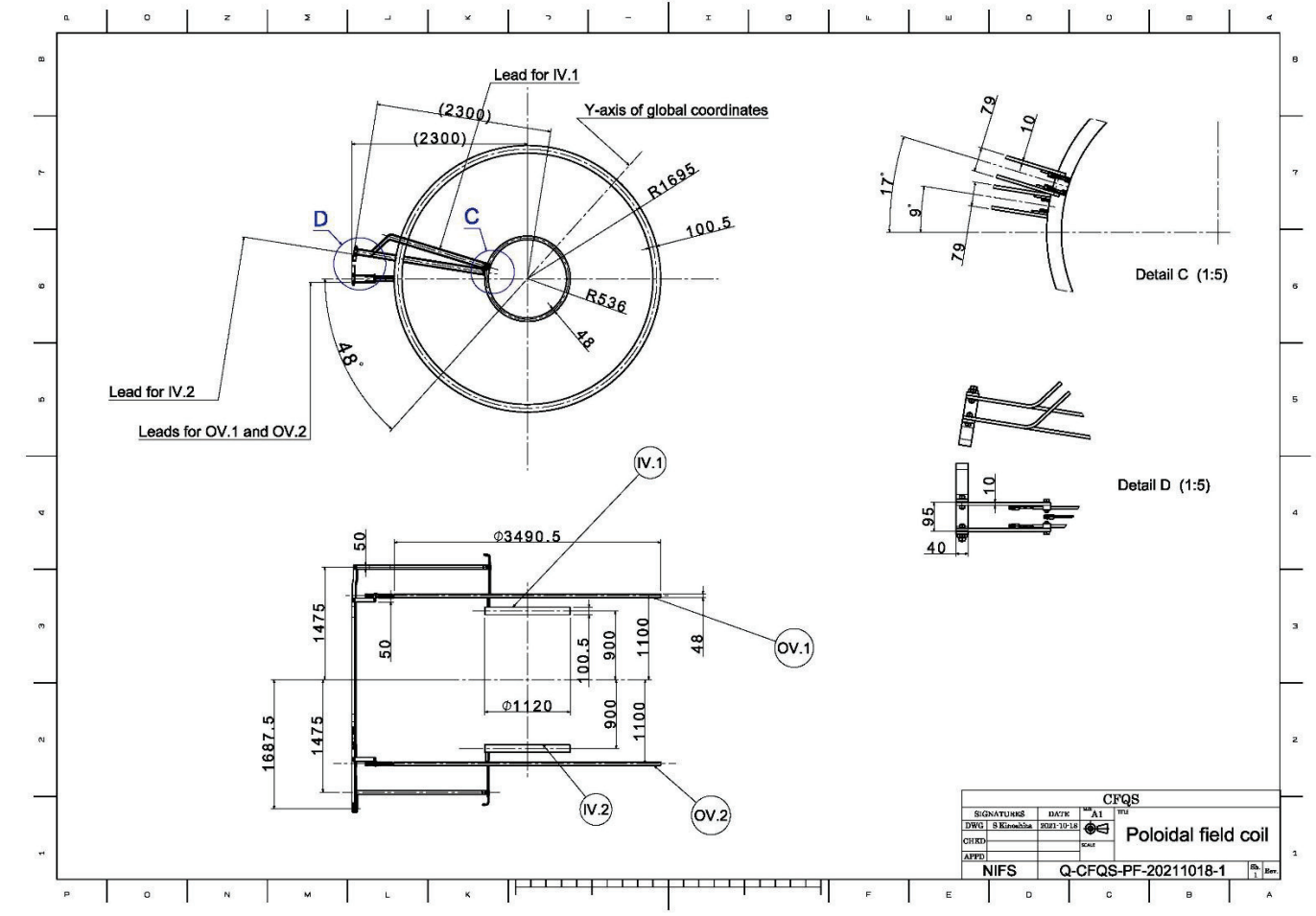
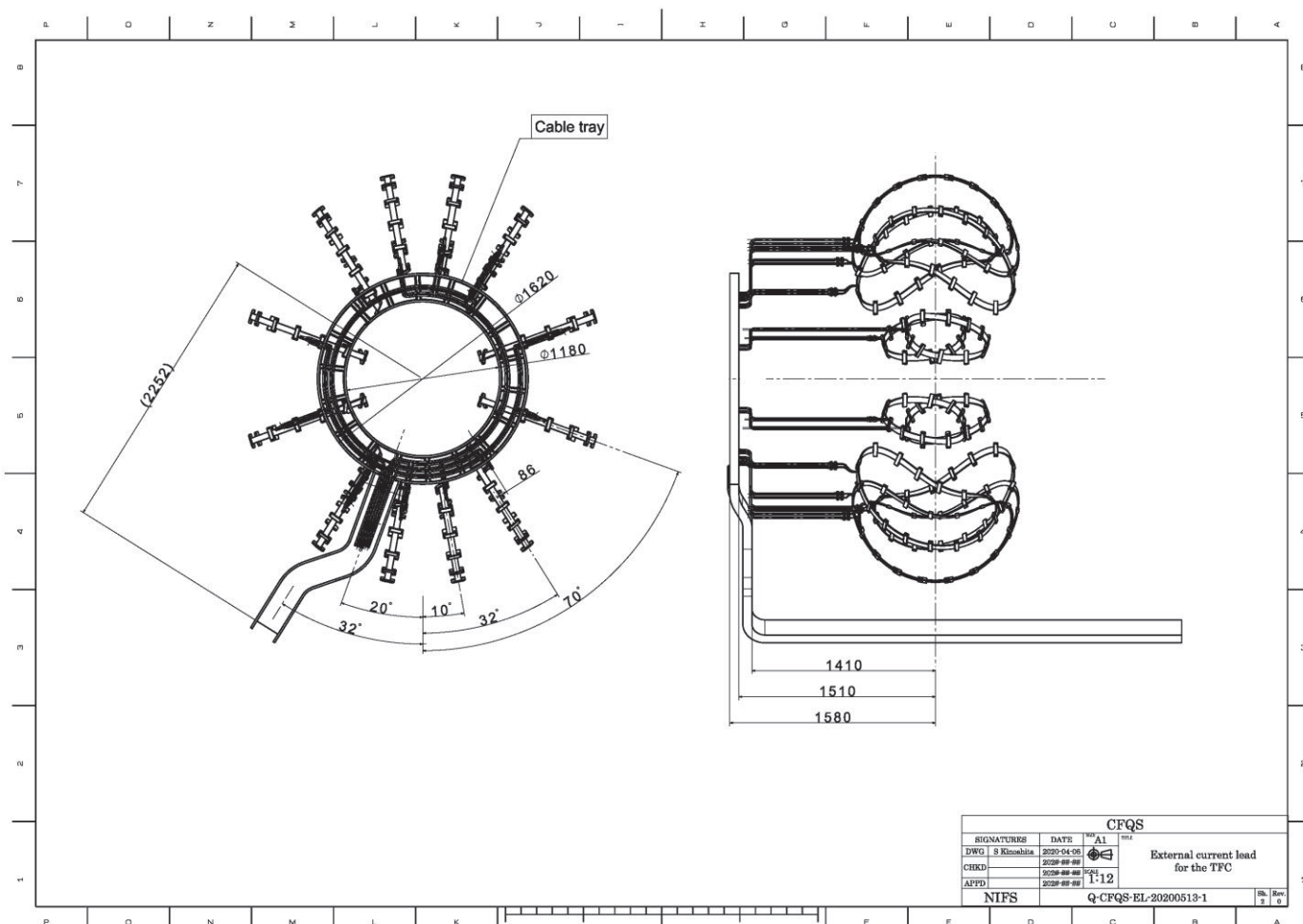




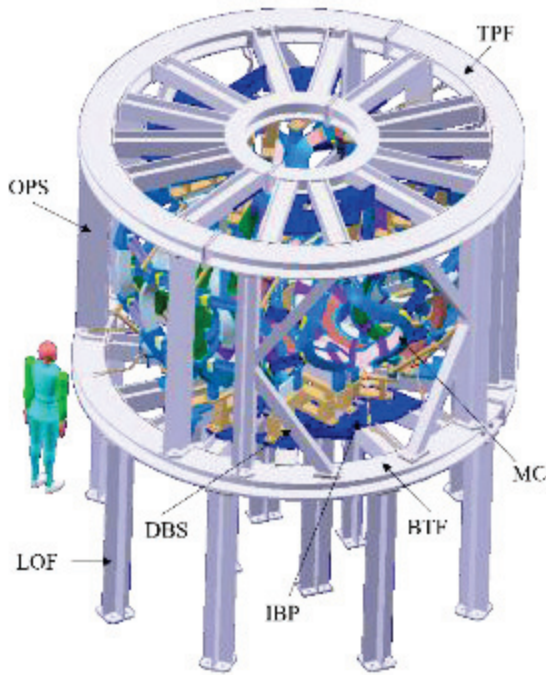


6 External current lead

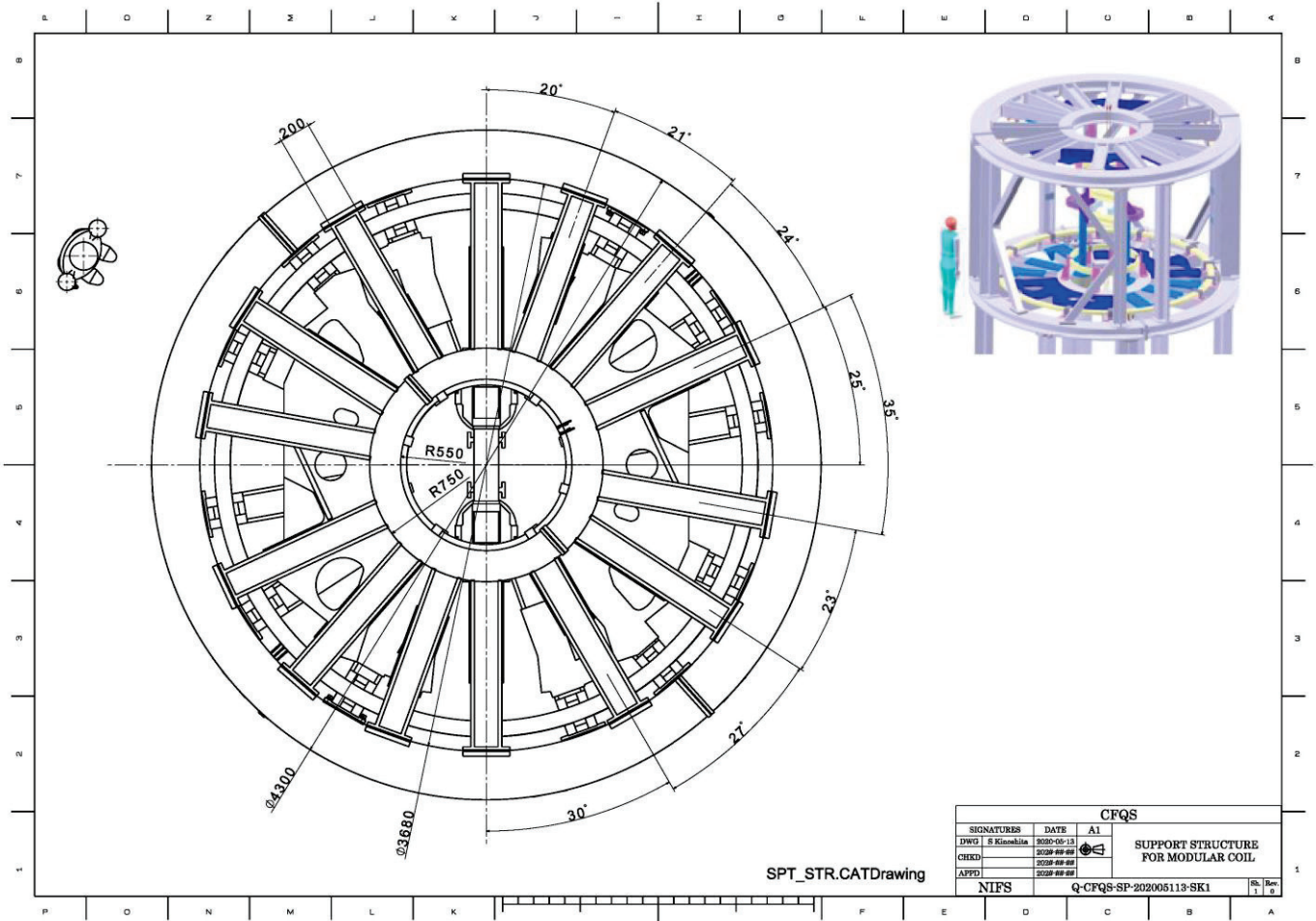




7 Cage type support structure

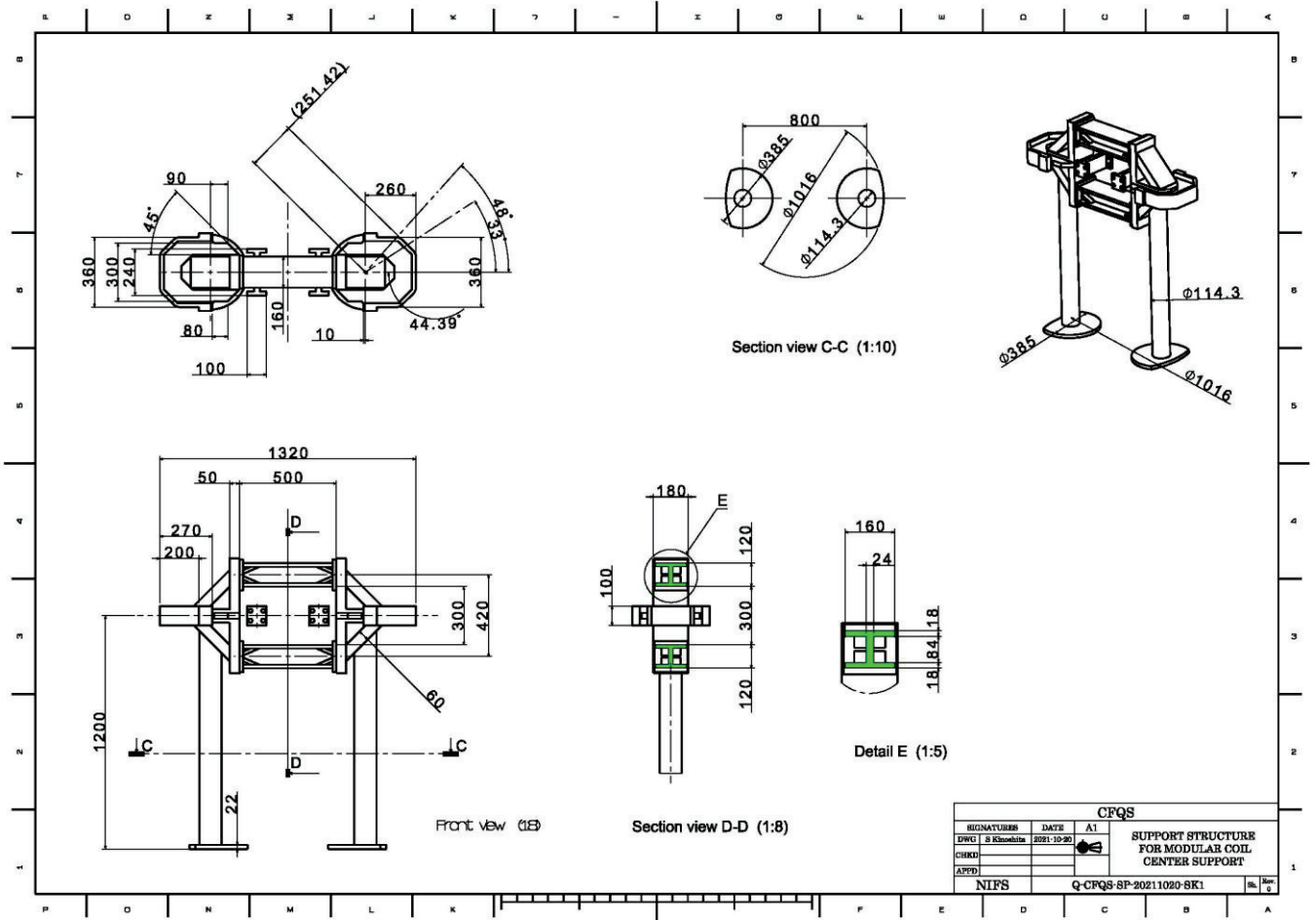
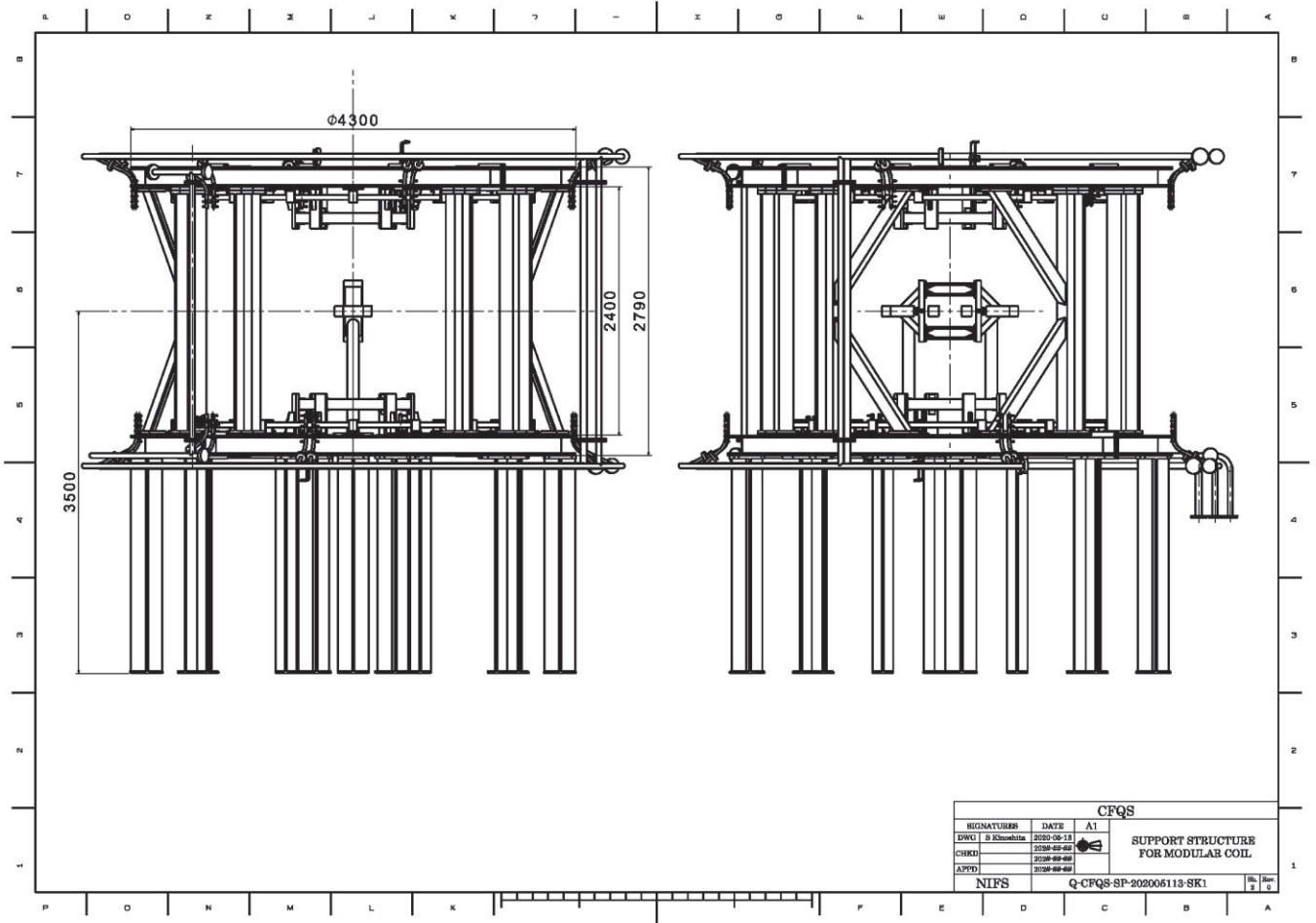


- TPF; Top frame receiving the vertical force and fixing many parts.
- DBS; Diagonal beams prevent the overturning forces rolling coils over.
- LOF; Leg of the CFQS receiving total gravity.
- BTF; Bottom frame receiving the vertical force and fixing many parts.
- IBP; Intermediate base plate as a reference for installing main parts. Their upper surface is necessary to be strictly controlled.
- MC; Modular coil

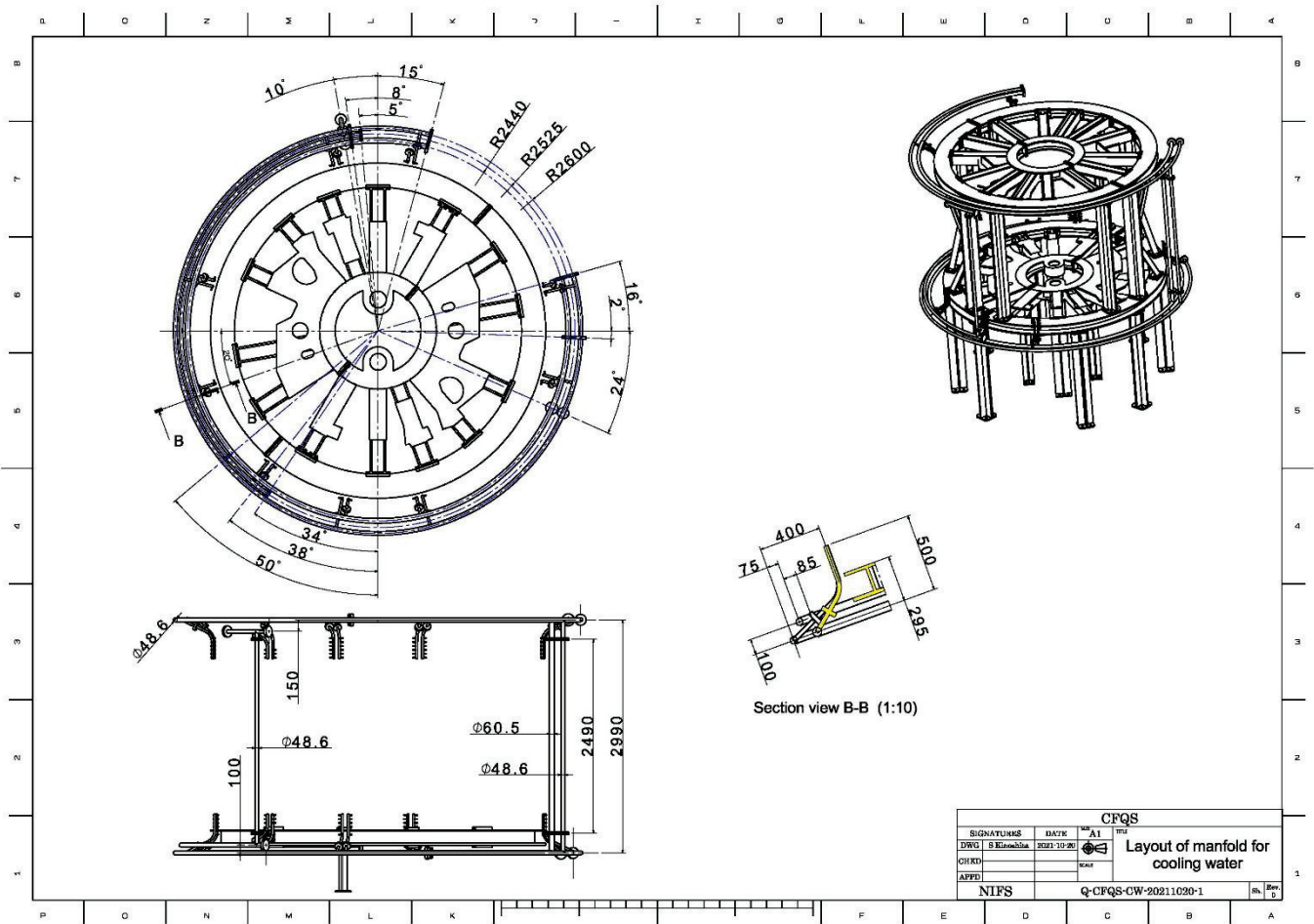
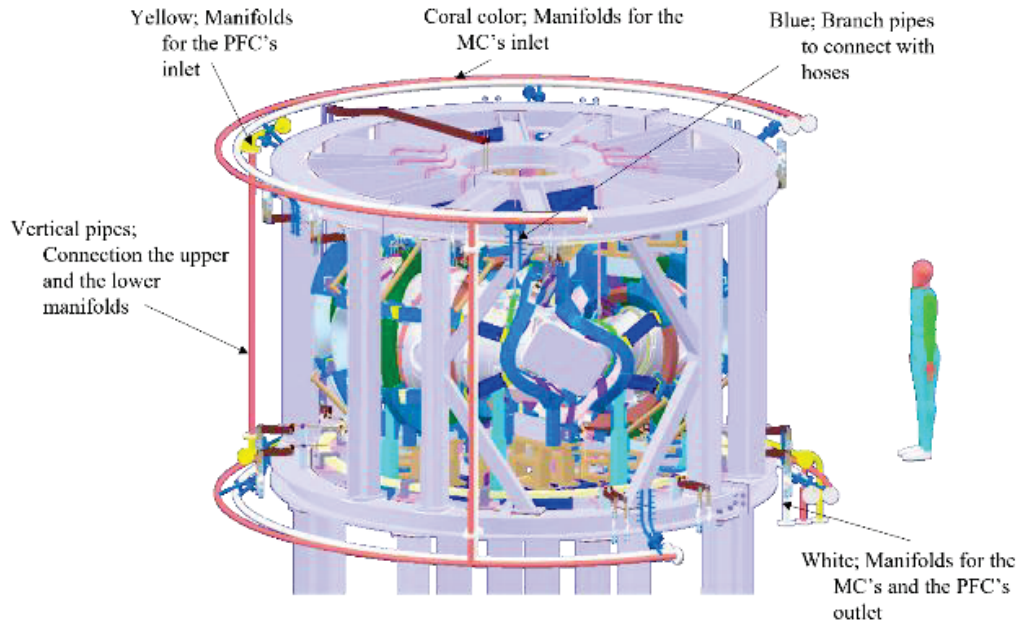


SPT_STR.CATDrawing

SIGNATURES		DATE	A1	CFQS SUPPORT STRUCTURE FOR MODULAR COIL
DWG	S Kinoshita	2020-05-13		
CHEK		2020-05-28		
APPD		2020-05-28		
NIFS		Q-CFQS-SP-202005113-SK1		ISS. Rev 1.1



8 Cooling water pipe



NIFS-SWJTU JOINT PROJECT FOR CFQS
~PHYSICS AND ENGINEERING DESIGN~
VER. 4.1
2022. JAN.

APPENDIX-A4 (ST)

~STANDARD INFORMATION~

CFQS Team



NIFS; National Institute for Fusion Science

SWJTU; Institute of Fusion Science, School of Physical Science and Technology Southwest Jiaotong University

Hefei Keye; Hefei Keye Electrical Physical Equipment Manufacturing Co., Ltd.

Table of contents

1	Design standard	3
1.1	ASME III criterion as a reference.....	3
2	Standard material and parts	4
2.1	Physical property of austenite stainless steel (SUS).....	4
2.2	Physical property of pure copper.....	5
2.3	Gasket or O-ring for vacuum.....	7
2.4	SUS pipe and flange	8
2.5	Electrical cable.....	9
2.6	Solderless terminal.....	10
2.7	Flexible terminal (Standard type)	11
3	Analytical expression.....	12
3.1	Formula of adiabatic temperature rise	12
3.2	Calculation formula and design criteria of lead wires for supplying current to the coil.....	13
4	Comparison of coil power supply system.....	15
4.1	Summary.....	15
4.2	Capacitor bank.....	17
4.3	DC motors.....	18
4.4	Self-excited induction generators (SEIG).....	18
4.5	An induction motor and a synchronous generator	19

1 Design standard

1.1 ASME III criterion as a reference

ASME III defines the following criterion to get allowable limit value of stress. It may be evaluated by the following procedure because it is difficult to distinguish stress components by the FEM calculation.

- $P_m + P_L + P_b + Q < 3 S_m$, absolute requirement everywhere,
- $P_m < S_m$, should be satisfied in major area,
- $P_m + P_b < 1.5 S_m$, local or thermal stress is permitted,
- $P_m + P_b > 1.5 S_m$, may be permitted in extremely limited area,

Here, S_m is a design stress strength obtained by the material properties and P_m, P_L, P_b, Q are stress components obtained by the stress analysis as a von Mises stress. Here technical terms are defined below.

- S_m is a design stress strength that is a reference intensity allowed to load by setting is given as the efficient design. It is obtained from the equation $S_m = \min (2/3 \sigma_y, 1/3 \sigma_u)$, where σ_y is a proof stress or offset yield strength that is a stress changing from elastic deformation to permanent deformation. σ_u is a tensile strength that is a maximum tensile stress appearing in the material before breaking.
- P_m is a primary general membrane stress that is an average value of stress in a cross section. Discontinuities and stress concentration are excluded.
- P_L is a primary local membrane stress that is an average value of stress by discontinuities.
- P_b is a primary bending stress that is a stress component proportional to the distance from the centroid in a cross section. Discontinuities and stress concentration are excluded.
- Q is a secondary stress (bending and membrane stress) that is a self-equilibrium stress generated in discontinuity of structure.

2 Standard material and parts

2.1 Physical property of austenite stainless steel (SUS)

There are slight differences in mechanical properties due to differences in composition. We should choose them according to our purpose.

The SUS 304 is the most distributed and inexpensive. However, as the permeability may increase, caution is required for nuclear fusion. It turns into magnetic material by bending or rolling. It is better not to use it in a magnetic field. We are worried about distorting the magnetic field profile.

The SUS316 and the SUS316L is more stable than the SUS304. The SUS316L is SUS316 with low carbon and has slightly better cold workability and corrosion resistance but it is a little expensive and a little weaker.

Table 2.1-1 Characteristics of typical SUS materials.

	SUS304(JIS G 4303)	SUS316(JIS G 4305)	SUS316L (JIS G 4305)
Material composition	Cr 18-20 % Ni 8-10.5 % Mn less than 2 % C less than 0.08 %	Cr 16-18 % Ni 10-14 % Mo 2-3 % Mn less than 2 % C less than 0.08 %	Cr 16-18 % Ni 12-15 % Mo 2-3 % Mn less than 2 % C less than 0.03 %
Mechanical properties at room temperature (MPa)	$\sigma_y = 205$ $\sigma_u = 520$ $S_m = 129$	$\sigma_y = 205$ $\sigma_u = 520$ $S_m = 129$	$\sigma_y = 175$ $\sigma_u = 480$ $S_m = 114$
Magnetic permeability	$\mu = 1.004 \sim 1.1$ or more	$\mu = 1.004$	$\mu = 1.004$

2.2 Physical property of pure copper

The temperature characteristics of pure copper are important. Particularly in coil design, it is necessary to consider the change in resistivity, so for convenience, an approximate expression is given here.

Table 2.2-1 Physical property of pure copper.

Temperature [K]	Electric resistivity [Ωm]	Specific heat [J/kg K]	Density [kg/m^3]
10	4.00E-10		
80	1.60E-09		
100	3.00E-09		
150	6.50E-09	322	8,990
250	1.25E-08	376	8,950
300	1.55E-08	386	8,880
600	3.55E-08	425	8,780

Ref. JSME Data Book : Heat Transfer 4th Edition, I. Hirata, Journal of the Cryogenic Society of Japan (1970)

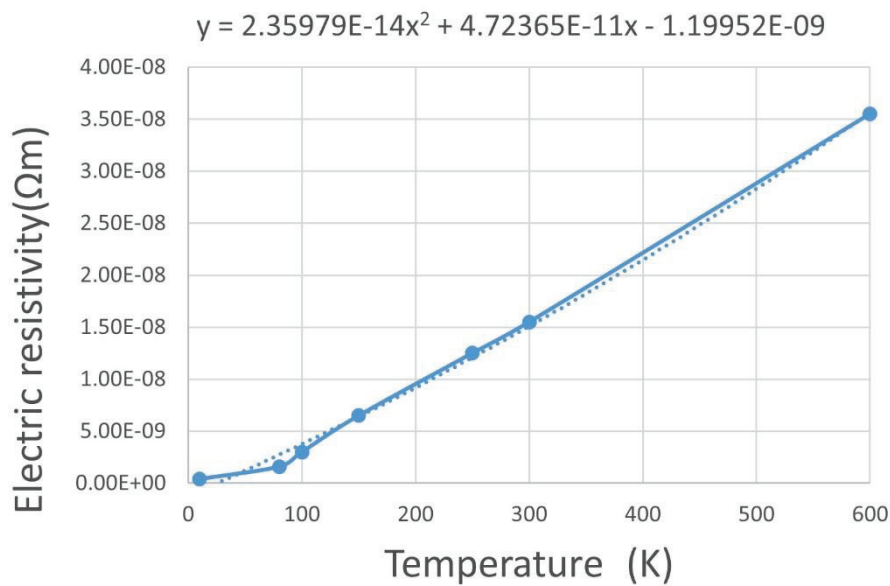


Fig 2.2-1 Temperature characteristics of electrical resistivity by a quadratic function approximation.

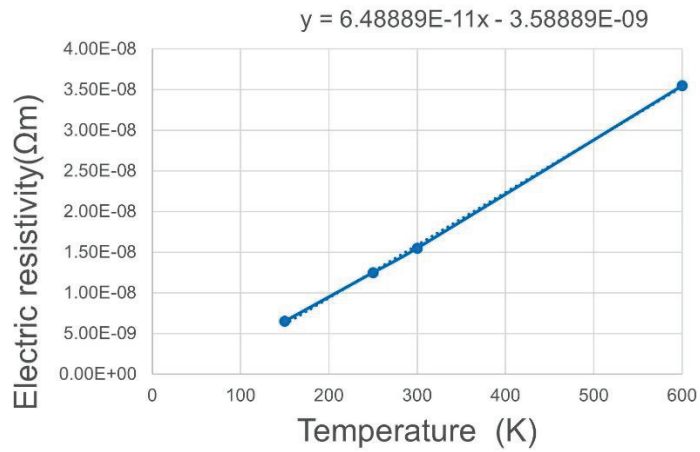


Fig 2.2-2 Temperature characteristics of electrical resistivity by a Linear function approximation.

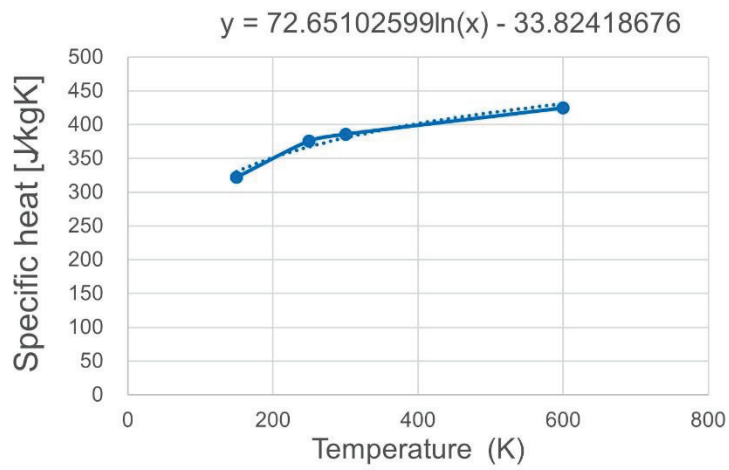


Fig 2.2-3 Temperature characteristics of specific heat.

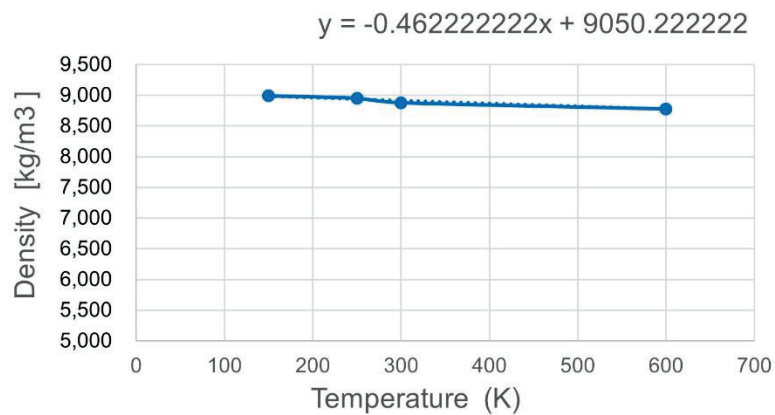


Fig 2.2-4 Temperature characteristics of density.

2.3 Gasket or O-ring for vacuum

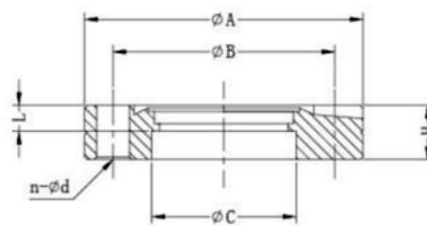
Depending on the operating temperature, it is necessary to select the material of the gasket or O ring properly.

- Nitrile rubber (NBR); -50 ~ 80°C. unusable at baking temperature 100 ~ 150 °C.
- Fluorine rubber (FKM, Viton); -15 ~ 200 °C. may be usable, but worry about low temperature damage due to liquid nitrogen or cryogenic gas that is sometimes used for evacuation.
- Metal gasket; -250 ~ 650 °C. can be used at wide range of temperature.

In the metal gaskets, the conflat flanges is widespread throughout the world. It should be noted that the name and size are slightly different depending on the country and the manufacturer, and there is no compatibility.

Table 2.3-1 Conflat Fixed flanges (example).

Name	O.D (A)	PCD (B)	Thickness (H)	n	d	C	Name of Varian And Anelva (JP)
CF16	33.8	27	7.3	6	4.5	18	ICF34
CF35	69.5	58.7	13	6	6.5	38	ICF70
CF63	113.6	92.2	17.5	8	8.5	66	ICF114
CF100	151.6	130.3	20	16	8.5	104	ICF152
CF150	202.5	181	22	20	8.5	154	ICF203
CF200	253.2	231.8	24.5	24	8.5	205	ICF253
CF250	305	284	24.5	32	8.5	256	ICF305
CF300	355.6	325.7	28.5	32	8.5	306	ICF356
CF350	419.1	388.9	28	36	10.5	356	ICF419



2.4 SUS pipe and flange

Table 2.4-1 SUS pipe and flange.

ND		SUS PIPE								W FLANGE (20K)		
A	B	OD (mm)	Thickness (mm)						JIS	OD (mm)	Thick ness (mm)	JIS
			SCH 5s	SCH 10s	SCH 20s	SCH 40	SCH 80	SCH 120				
6	1/8	10.5	1.0	1.2	1.5	1.7	2.4					
8	1/4	13.8	1.2	1.65	2.0	2.2	3					
10	3/8	17.3	1.2	1.65	2.0	2.3	3.2			90	14	
15	1/2	21.7	1.65	2.1	2.5	2.8	3.7			95	14	
20	3/4	27.2	1.65	2.1	2.5	2.9	3.9			100	16	
25	1	34.0	1.65	2.8	3.0	3.4	4.5			125	16	
32	1-1/4	42.7	1.65	2.8	3.0	3.6	4.9			135	18	
40	1-1/2	48.6	1.65	2.8	3.0	3.7	5.1			140	18	
50	2	60.5	1.65	2.8	3.5	3.9	5.5			155	18	
65	2-1/2	76.3	2.1	3.0	3.5	5.2	7.0			175	20	
80	3	89.1	2.1	3.0	4.0	5.5	7.6			185	22	
90	3-1/2	101.6	2.1	3.0	4.0	5.7	8.1			195	24	
100	4	114.3	2.1	3.0	4.0	6.0	8.6	11.1	13.5	210	24	
125	5	139.8	2.8	3.4	5.0	6.6	9.5	12.7	15.9	250	26	
150	6	165.2	2.8	3.4	5.0	7.1	11.0	14.3	18.2	280	28	
200	8	216.3	2.8	4.0	6.5	8.2	12.7	18.2	23.0	330	30	
250	10	267.4	3.4	4.0	6.5	9.3	15.1	21.4	28.6	400	34	
300	12	318.5	4.0	4.5	6.5	10.3	17.4	25.4	33.3	445	36	
350	14	355.6	4.0	5.0	8.0	11.1				490	40	
400	16	406.4	4.5	5.0	8.0	12.7				560	46	
450	18	457.2	4.5	5.0	8.0	14.3				620	48	
500	20	508.0	5.0	5.5	9.5	15.1				675	50	

ND; Nominal Diameter, OD; Outer Diameter

Unless otherwise specified, the CFQS will use SCH20 for cooling water system and SCH5s for vacuum.

2.5 Electrical cable

Table 2.5-1 Electrical cable.

Type	Twist	Nominal cross section	Finish outer diameter	Conductor outer diameter	Allowable current	Density	Test voltage	Number of strands	Strand diameter		
		mm ²	mm	mm	A	A/mm ²	V		mm		
600 V IV cable HIV cable	Single wire	0.79	2.6	1	16	20.37	1500				
		1.13	2.8	1.2	19	16.80	1500				
		2.01	3.2	1.6	27	13.43	1500				
		3.14	3.6	2	35	11.14	1500				
		5.31	4.6	2.6	48	9.04	1500				
		8.04	5.6	3.2	62	7.71	1500				
		12.57	6.8	4	81	6.45	2000				
	Stranded wire	19.63	8.2	5	107	5.45	2000				
		0.9	2.8	1.2	17	18.89	1500			7	0.4
		1.25	3	1.35	19	15.20	1500			7	0.45
		2	3.4	1.8	27	13.50	1500			7	0.6
		3.5	4.1	2.4	37	10.57	1500			7	0.8
		5.5	5	3	49	8.91	1500			7	1
		8	6	3.6	61	7.63	1500			7	1.2
600 V CV cable	Stranded wire	14	7.6	4.8	88	6.29	2000	7	1.6		
		22	9.2	6	115	5.23	2000	7	2		
		38	11.5	7.8	162	4.26	2500	7	2.6		
		60	14	10	217	3.62	2500	19	2		
		100	17	13	298	2.98	2500	19	2.6		
		150	21	16.1	395	2.63	3000	37	2.3		
		200	23	18.2	469	2.35	3000	37	2.6		
		5.5	8	3	58	10.55	1500	7	1		
		8	8.6	3.6	72	9.00	1500	7	1.2		
		14	9.5	4.4	100	7.14	2000	Circular compression stranded			
22	11	5.5	130	5.91	2000						
38	13	7.3	190	5.00	2500						
60	16	9.3	255	4.25	2500						
100	19	12	355	3.55	2500						
150	23	14.7	455	3.03	3000						
200	26	17	545	2.73	3000						
3300V CV cable	Stranded wire	8	13	3.4	78	9.75	9000				
		14	14	4.4	105	7.50	9000				
		22	15	5.5	140	6.36	9000				
		38	17	7.3	195	5.13	9000				
		60	21	9.3	260	4.33	9000				
		100	23	12	355	3.55	9000				
		150	26	14.7	455	3.03	9000				
200	30	17	540	2.70	9000						
Type	Explanation						Operating temperature				
IV	Wire insulated by Vinyl						Less than 60 °C				
HIV	Heat-proof wire Insulate by Vinyl						Less than 75 °C				
CV	Cross-linked polyethylene insulated Vinyl sheathed						Less than 90 °C				

2.6 Solderless terminal

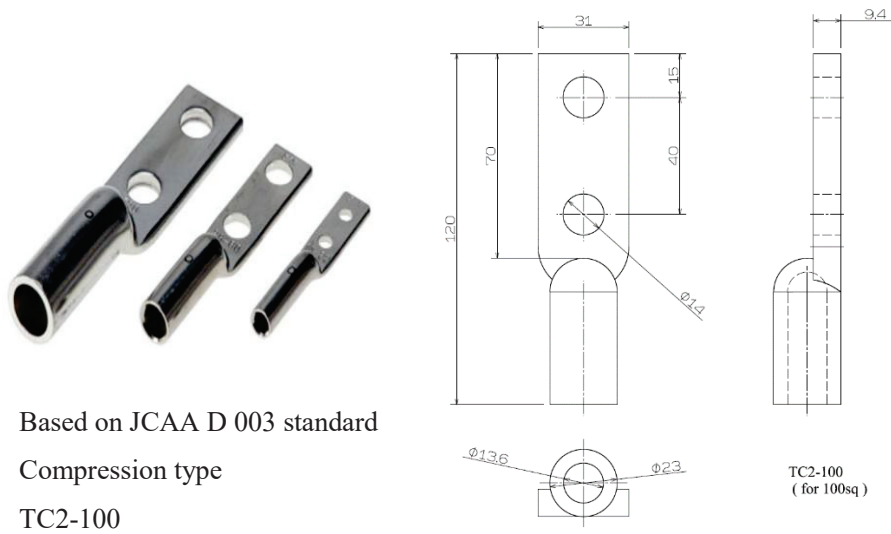


Fig 2.6-1 Compression type solderless terminal TC2-100 for wire 100SQ.

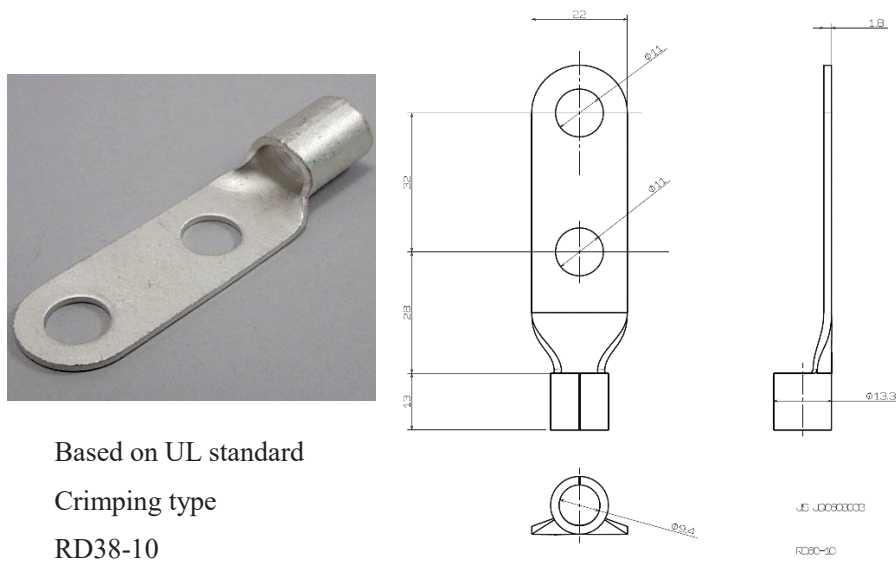


Fig 2.6-2 Crimping type solderless terminal RD38-10 for wire 38SQ.

2.7 Flexible terminal (Standard type)

Many types are on the market for the purpose of absorbing the amount of displacement due to thermal expansion and contraction, absorbing the vibration generated by electrical equipment, and improving workability during assembly. For convenience, representative dimensions of flexible terminals which are likely to be applicable in the CFQS design are shown as an example.

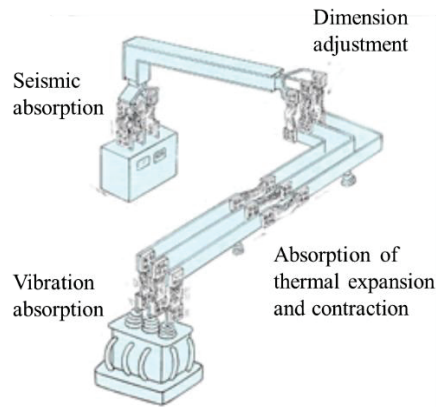


Fig 2.7-1 Application example of flexible terminal.

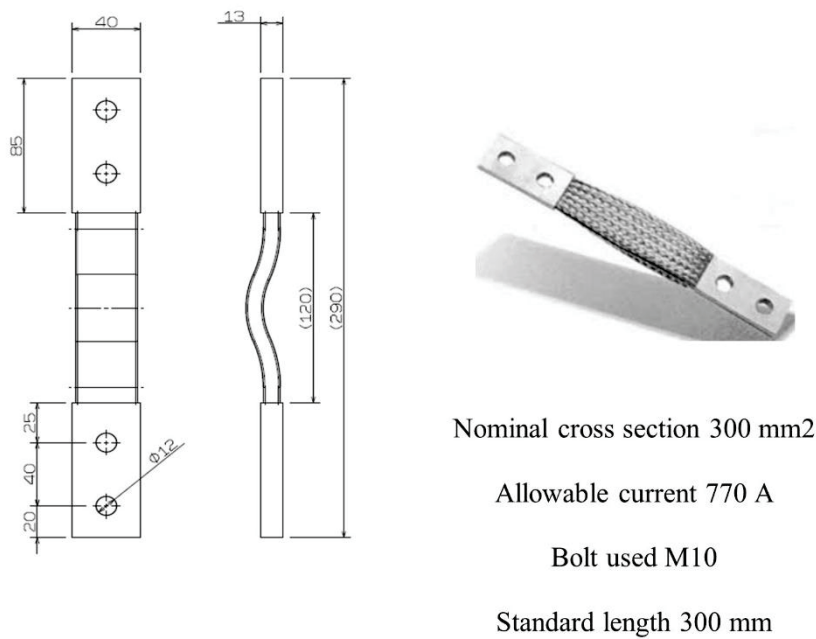


Fig 2.7-2 Example of a standard type of flexible terminal.

3 Analytical expression

3.1 Formula of adiabatic temperature rise

The temperature without cooling during pulse operation of the copper coil can be easily evaluated by the following equation. It almost matches the temperature change in a short time, because the standard thermal time constant is much longer than the pulse length. The temperature change of the conductor is obtained from the thermal equation,

$$C \frac{dT}{dt} = Q_h - Q_c ,$$

$$Q_h = I^2 R = (jS_{cu})^2 \times \rho_e L / S_{cu} = j^2 S_{cu} \rho_e L ,$$

$$Q_c = 0 ,$$

where C is a heat capacity, Q_h is a heating power and Q_c is a cooling power.

- Heat capacity of conductor; $C = mC_p$ [J/K]
- Mass of conductor; $m = LS_{cu}\rho$ [kg]
- Density of conductor; $\rho = 8,911\text{kg/m}^3$ [kg/m³] at room temperature (27 °C)
- Density of conductor; $\rho = 8,888\text{kg/m}^3$ [kg/m³] at 75 °C
- Specific heat of conductor; $C_p = 381$ [J/kgK] at room temperature (27 °C)
- Specific heat of conductor; $C_p = 361$ [J/kgK] at 75 °C
- Resistivity of conductor; $\rho_e = 1.724 \times 10^{-8}$ [Ωm] at room temperature (27 °C)
- Resistivity of conductor; $\rho_e = 1.895 \times 10^{-8}$ [Ωm] at 75 °C

It is as follows when the physical property value of copper is inputted.

$$\frac{dT}{dt} [K/s] = \frac{Q_h}{C} = \frac{j^2 S_{cu} \rho_e L}{LS_{cu} \rho C_p} = j^2 \frac{\rho_e}{\rho C_p} = j^2 [A/mm^2] \times 5.1 \times 10^{-3} \text{ at } 27 \text{ }^\circ\text{C} ,$$

$$\frac{dT}{dt} [K/s] = \frac{Q_h}{C} = \frac{j^2 S_{cu} \rho_e L}{LS_{cu} \rho C_p} = j^2 \frac{\rho_e}{\rho C_p} = j^2 [A/mm^2] \times 5.9 \times 10^{-3} \text{ at } 75 \text{ }^\circ\text{C} .$$

Here, 75 °C is often used as a typical temperature after heating an electric device, and 27 °C = 300K is often used as a typical room temperature before heating an electric device.

3.2 Calculation formula and design criteria of lead wires for supplying current to the coil

We will evaluate the lead support design with simplified analysis model as shown in Fig 3.2-1 to Fig 3.2-3.

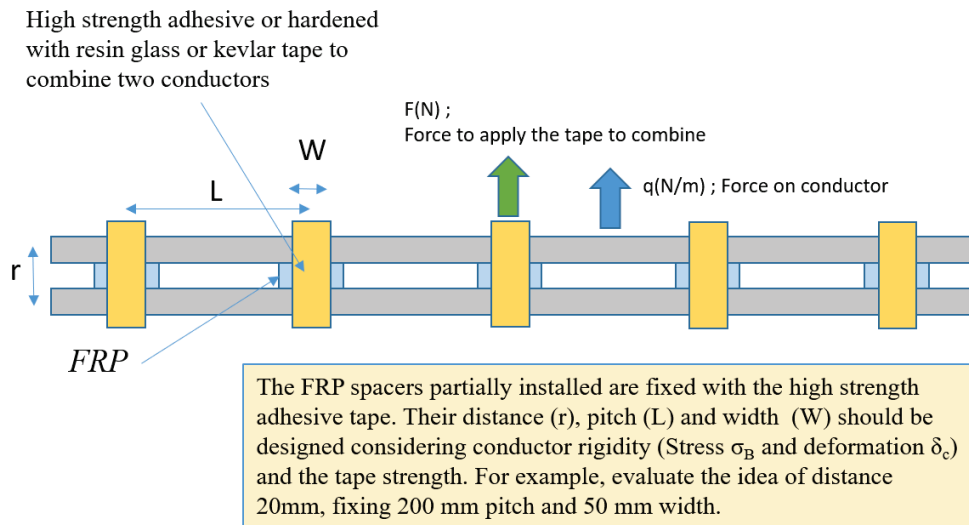


Fig 3.2-1 Simplified analysis model

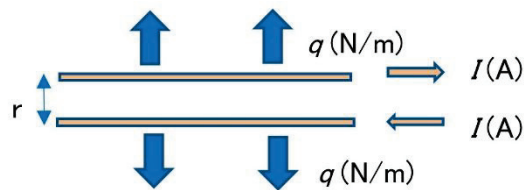


Fig 3.2-2 Definition of repulsive force

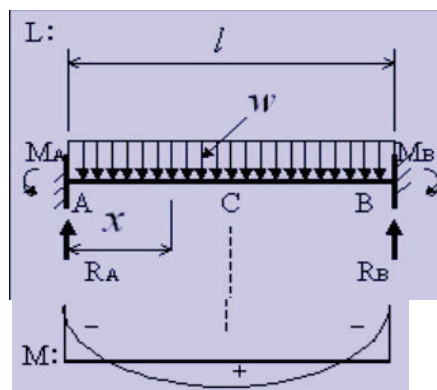


Fig 3.2-3 Deflection and stress distribution of a wire

The lead wire design evaluation formula is as follows.

- Force between parallel straight currents (the repulsive force)

$$q(N/m) = \frac{\mu_0 I^2}{2\pi r}$$

- Maximum stress of the wire with equally distributed load both ends fixed beam

$$\sigma_B(Pa) = \frac{qL^2}{2bh^2} \leq 20 MPa,$$

- Force to apply a part (tape etc.) to combine two wires. The combine part must be designed to endure the force.

$$F(N) = qL,$$

- Deflection of the wire

$$\delta_c(m) = \frac{qL^4}{384EI_x} \leq 2 mm,$$

- Second moment of area (moment of inertia of area) of the wire

$$I_x = \frac{bh^3}{12}.$$

- Lowest natural frequency of the wire

$$f_1 = \frac{4.73^2}{2\pi} \sqrt{\frac{EI_x}{\rho SL^4}} \leq 40 Hz.$$

Where, I (A) is a current, r (m) is a distance between wires, L (m) is the combine part interval, s=b (m) × h (m) is a cross section of wire, E is a longitudinal elastic modulus for the wire, and ρ is a density of the wire. When the wire material is copper of C1020-O,

$$E=100 GPa,$$

$$\rho = 8,960 kg/m^3.$$

4 Comparison of coil power supply system

4.1 Summary

To apply large current to the coil, a short pulse large capacity power supply is required. Since it is difficult to supply such massive electrical power from the commercial power grids directory due to overload (up to 10MVA), a current source with energy storage function should be employed as shown in Fig 4.1-1. Of course, AC/DC SCR control converter or rectifiers and PWM chopper circuit system must be utilized for controlling each coil current. There are mainly four options which may satisfy the electrical conditions.

The comparison is summarized in Table 4.1-1. The IM and SG type may be the most appropriate power storage system. For a reference, Table 4.1-2 shows a capability of the energy stored generators for other fusion devices. Most devices have used the IM and SG type. Discussions for each candidate focusing on capacity, space, cost, and operation control are described as follows.

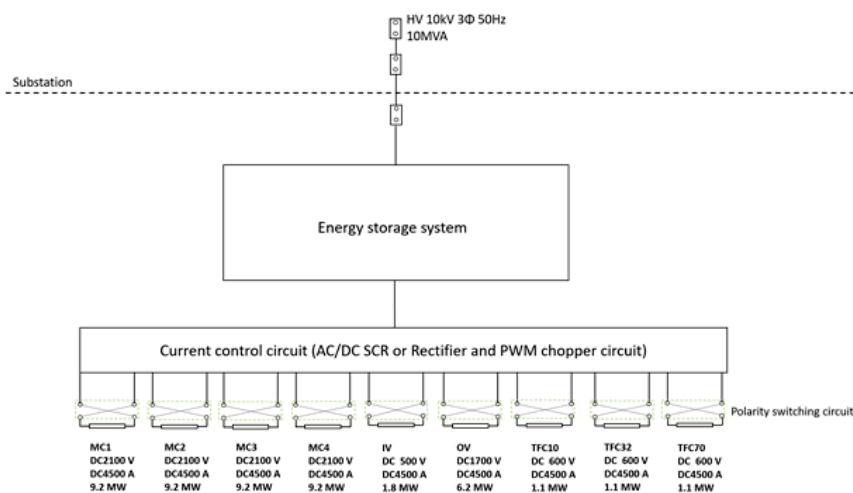


Fig 4.1-1 Configurations of power supply system with a short pulse large capacity.

Table 4.1-1 Comparison of power storage systems.

Power storage candidate	Evaluation	Evaluation reason
Capacitor banks	Impractical	Extremely large number of capacitors (over 600,000) and their installation space is required.
DC motors	Impractical	Large number of motors (over 100) and their installation space is required. Simultaneous operation technique needs to be developed.
Self-excited induction generator (SEIG)	Marginal	There may be no achievement of implementation of power supply with SEIG for large or middle-sized fusion device (over 10MW case). Large number of capacitors with rapid responsiveness switching systems for self-excitation control need to be prepared.
Induction motor and synchronous generator (IM and SG)	Appropriate	It has been utilized for various fusion experimental devices. It can store large amount of electrical energy over 100 MJ and supply power with good controllability.

Table 4.1-2 Power storage systems for fusion device mainly in Japan.

No	Fusion device	Generator		Drive	
		Capacity	Spec	Capacity	Spec
1	TRIAM-1M Kyushu University	125 MVA 60 MJ	3Φ VSYG 6.6 kV 11 kA 67-59 Hz 670-590 rpm	1.4 MW	3Φ IM
2	Heliotron-J Kyoto University	330 MVA 300 MJ	3Φ VSYG 18 kV 10.58 kA 65-50 Hz 650-500 rpm	3.2 MW	3Φ IM
3	JT-60 HMG QST	400 MVA 2.5 GJ	3Φ VSYG 18 kV 12.83 kA 77.6-54.2 Hz 582-406 rpm	15 MW	3Φ IM
4	JT-60 PMG QST	500 MVA 1.3 GJ	3Φ VSYG 18 kV 16 kA 77.6-54.2 Hz 582-406 rpm	7 MW	3Φ IM
5	JT-60 TMG QST	215 MVA 4 GJ	3Φ VSYG 18 kV 6.9 kA 80-56 Hz 600-420 rpm	19 MW	Inverter drive
6	Gamma 10 University of Tsukuba	250 MVA 800 MJ	3Φ VSYG 18 kV 8 kA 77.6-54.3 Hz 582-407 rpm	2.4 MW	3Φ IM
7	LHD and CHS NIFS	250 MVA 1.4 GJ	3Φ VSYG 18 kV 8 kA 93-58 Hz 701-435 rpm	8.5 MW	3Φ IM
8	HL-2A SWIP, Chengdu (CHS Nagoya University)	125 MVA 200 MJ	3Φ HSYG 3 kV 24 kA 120-96 Hz 3600 rpm	2.5 MW	3Φ IM
9	HL-2A SWIP, Chengdu	300 MVA 1.35 GJ	6Φ VSYG 3 kV 29 kA 100-67 Hz 500-335 rpm	8.5 MW	3Φ IM
10	HL-2A SWIP, Chengdu	90 MVA 250 MJ	3Φ HSYG 1650-1488 rpm	2.5 MW	3Φ IM
11	HSX University of Wisconsin - Madison	84 MVA 42 MWp Over 20 MJ	DCM 30 motors 1.68kV 50kA		DCM
12	PLATO Kyushu University	810 kW _{-peak} 2.8 MJ (stored) 384 kJ (release)	3Φ SIM 2 motors 60 Hz-3600 rpm	72 kW	Inverter drive
*	CFQS NSJP	60 MW _{-peak} 50 MJ (released) 120 MJ (stored)	3Φ HSYG 10 kV 50-38 Hz 3000 rpm	250 kW	3Φ IM

$$MVA = kV \times kA \times \sqrt{3}$$

Capacity of the above equipment is excessive for the CFQS.

VSYG; Vertical synchronous generator HSYG; Horizontal synchronous generator
DCM; DC generator and motor SIM; Self-excited induction generator and motor
IM; Induction motor

4.2 Capacitor bank

Fig 4.2-1 shows the power supply system with capacitor banks. This type has been widely adopted for small fusion devices and its configuration is comparatively simple. However, because high voltage capacitors have small energy density per volume, the problem of installation space for capacitors cannot be ignored. Consequently, capacitor bank is impractical for power supply system with 50MJ of the stored energy.

The size of a capacitor depends on its type. Recently, although the energy storage density of a capacitor is greatly increased such as an electrolytic capacitor with small size, it is limited to 500 V or less. The modular coil of the CFQS is required to be applied over DC 1000 V. Thus, there is no choice but to be selected an oil capacitor with extremely large size.

Total required energy for the MC is approximately 45 MJ with 2100 V. Given 3000 V charging voltage of capacitor bank before discharge and 2700 V after discharge, oil capacitors with about 44.4 F capacity is required. Charging voltage for capacitor bank need to be more than 2400 V even after discharge because of discharge current control. The total required capacitor including capacity of the toroidal field coil (TFC) and the poloidal field coil (PFC) is estimated about 46.8 F 210 MJ based on above voltage conditions. If general oil capacitor with 78 μ F, 3510 V rated voltage and size of $0.175 \text{ m} \times 0.620 \text{ m} = 0.11 \text{ m}^2$ is adopted, total required number of capacitors is about 600,000. Therefore, at least 66,000 m^2 space for capacitors is required. It should not be accommodated in the experimental building. Even though given 10 kV charging voltage is applied to capacitor bank, total required capacitance, number of capacitor and space is estimated about 0.9 F, 10,000, respectively.

Moreover, a pulse width modulation (PWM) switching circuit must be installed between the capacitor bank and coils to control the coil current. Since the switching circuit generates ripples, it is necessary to evaluate the power supply by the combination of the capacitors and the switching circuit.

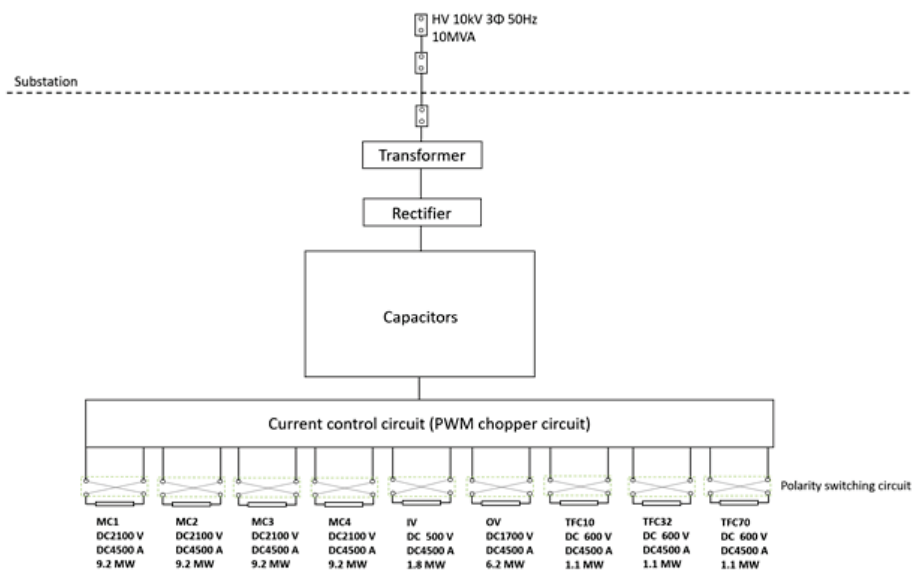


Fig 4.2-1 Power supply system with the capacitor bank.

4.3 DC motors

Fig 4.3-1 shows the power supply system with the DC motors. Since the DC motor is an old technology, procurement of new motors may be difficult. There is no other way but to find for used motors. However, since lifetime of a typical DC motor is limited by a brush, the used motor has relatively high risk of breakdown. Furthermore, over 100 number of DC motors with extremely large installation space may be required to cover the total energy of coils because it is difficult to procurement of over 200 kW used motors. Besides, simultaneous operation control of 100 number of DC motors may be impractical. Thus, the DC motor should be inappropriate for power supply system with 50MJ of the stored energy.

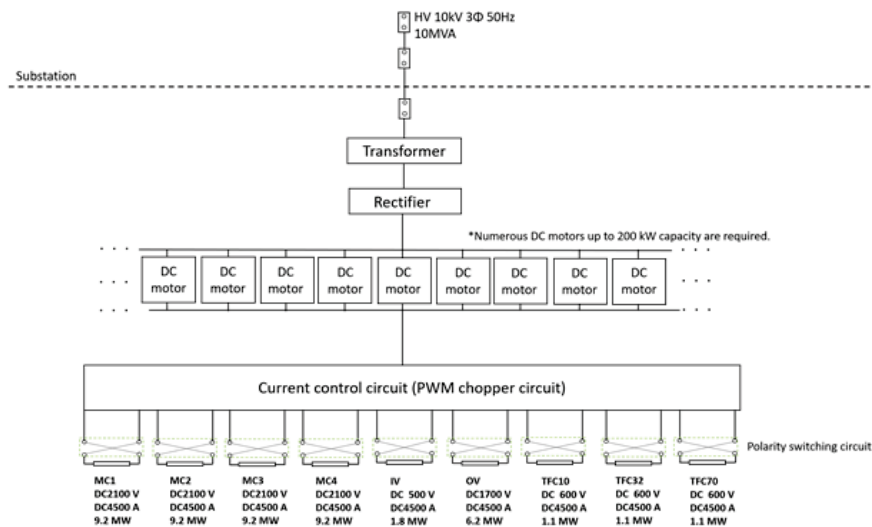


Fig 4.3-1 Power supply system with the DC motors.

4.4 Self-excited induction generators (SEIG)

Fig 4.4-1 shows the power supply system with the SEIG. Murayama et al. adopted this type for power storage system of a small fusion device [Fusion. Eng. Des. **148**, 111270 (2019)]. The system is utilized squirrel cage IM as a motor/generator (MG) instead of SG. The advantage utilizing the IM with squirrel cage casting structure is robustness derived from the simple structure with no wearing parts except for bearings. Moreover, it can generate electricity with capacitor self-excitation phenomena which does not require excitation control system. However, in the case of CFQS, large installation space for the high voltage capacitors with up to 30 MVAR capacity may be required to obtain the suitable output voltage of SEIG. It is difficult to be accommodated in the experimental building.

Furthermore, we need to compensate the voltage drop of SEIG during the coil energization by connecting additional self-exciting capacitors in parallel at the start of the discharge phase. If additional capacitors are connected to SEIG before the discharge phase, output voltage of SEIG is significantly increased and it leads to insulation breakdown and overheat. Therefore, high voltage switching devices with high responsiveness and their control systems should be prepared. There may be no achievement of implementation of power supply with SEIG for large or middle-sized fusion device (over 10 MW case).

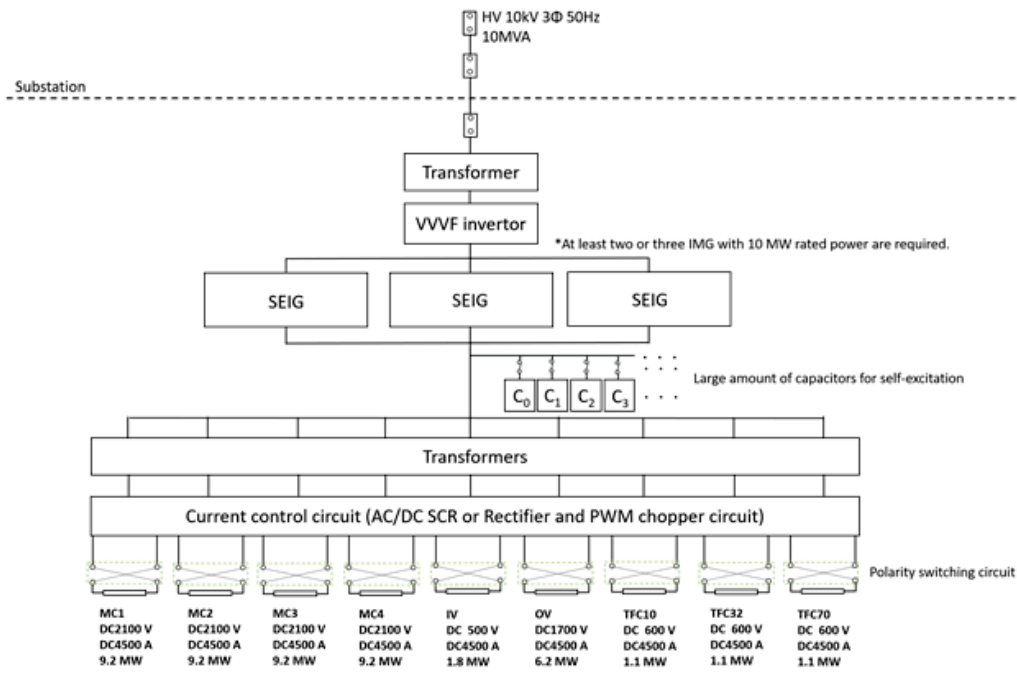


Fig 4.4-1 Power supply system with the self-excited induction generator (SEIG).

4.5 An induction motor and a synchronous generator

IM and SG type as shown in Fig 4.5-1, which has been utilized for various fusion experimental devices may be most suitable as a large power storage system. It can store large amount of electrical energy over 100 MJ and supply power with good controllability.

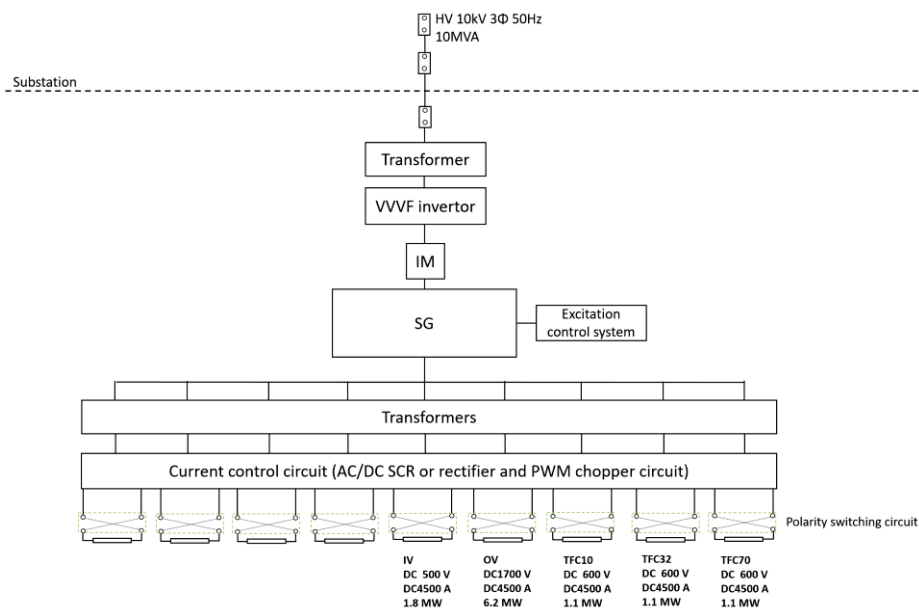


Fig 4.5-1 Power supply system with the induction motor and synchronous generator (IM and SG).

NIFS-SWJTU JOINT PROJECT FOR CFQS
~PHYSICS AND ENGINEERING DESIGN~

VER. 4.1
2022. JAN.

APPENDIX-A5 (PJ)

~RELATED PROJECT~

CFQS Team



NIFS; National Institute for Fusion Science

SWJTU; Institute of Fusion Science, School of Physical Science and Technology Southwest Jiaotong University

Hefei Keye; Hefei Keye Electrical Physical Equipment Manufacturing Co., Ltd.

Table of Contents

1	Compact helical system CHS.....	3
1.1	Layout of torus hall for the CHS.....	3
1.2	Power system for the CHS.....	5
1.3	Vacuum pumping system for the CHS.....	7
1.4	NBI system for the CHS.....	10
1.5	ECRH system for the CHS.....	14
1.6	Power supply to bake vacuum vessel for the CHS.....	18
1.7	Cooling water system for the CHS.....	19
1.8	Plasma diagnostic system for the CHS.....	20
2	Low aspect ratio RFP RELAX.....	21
2.1	Description of RELAX machine.....	21
2.2	3D tomography from soft X-rays through multi-pinhole disk attached to single view port.	21
2.2.1	Principle of 3D tomography.....	21
2.2.2	Numerical trial.....	22
3	Plasma generating device SSHD.....	24
3.1	History of the SSHD.....	24
3.2	Components of the SSHD.....	26
3.3	Plasma measurement with a Langmuir probe.....	28

1 Compact helical system CHS

1.1 Layout of torus hall for the CHS

The CFQS laboratory will be designed with reference to the structure of the development and experiment building with the CHS installed in NIFS. For reference, the layout of the CHS laboratory is shown below.

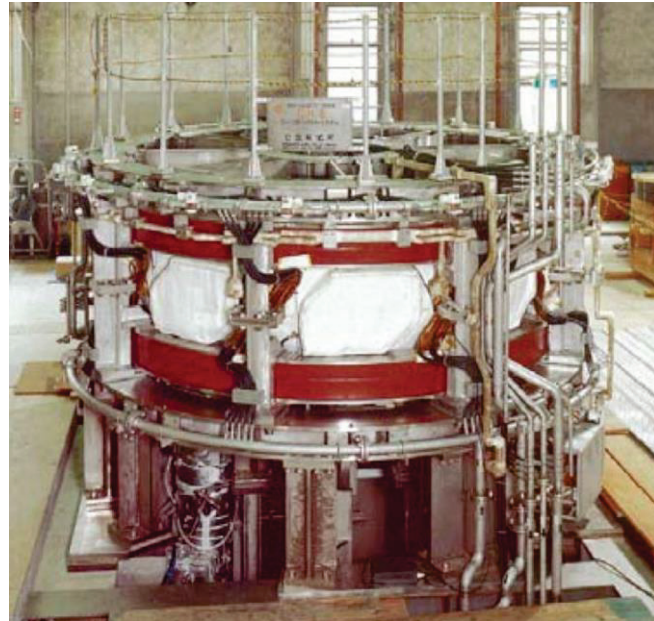


Fig 1.1-1 Body of the CHS (installed in Nagoya University at 1987).

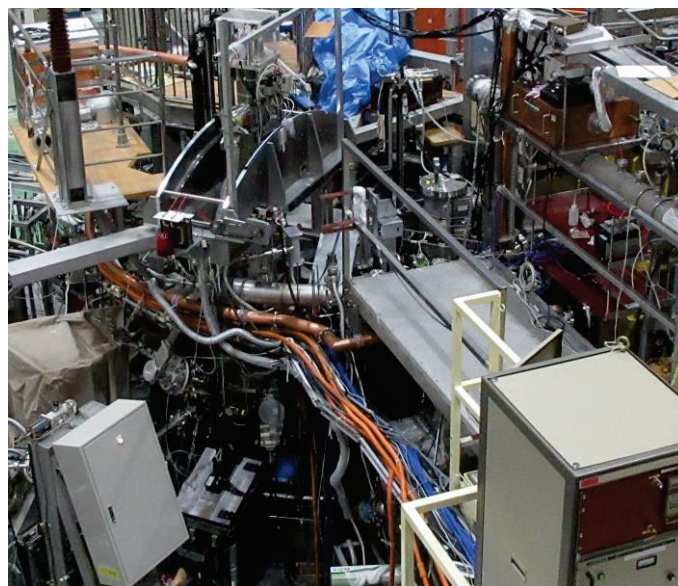


Fig 1.1-2 Body and equipment's of the CHS (installed in NIFS at 2000).

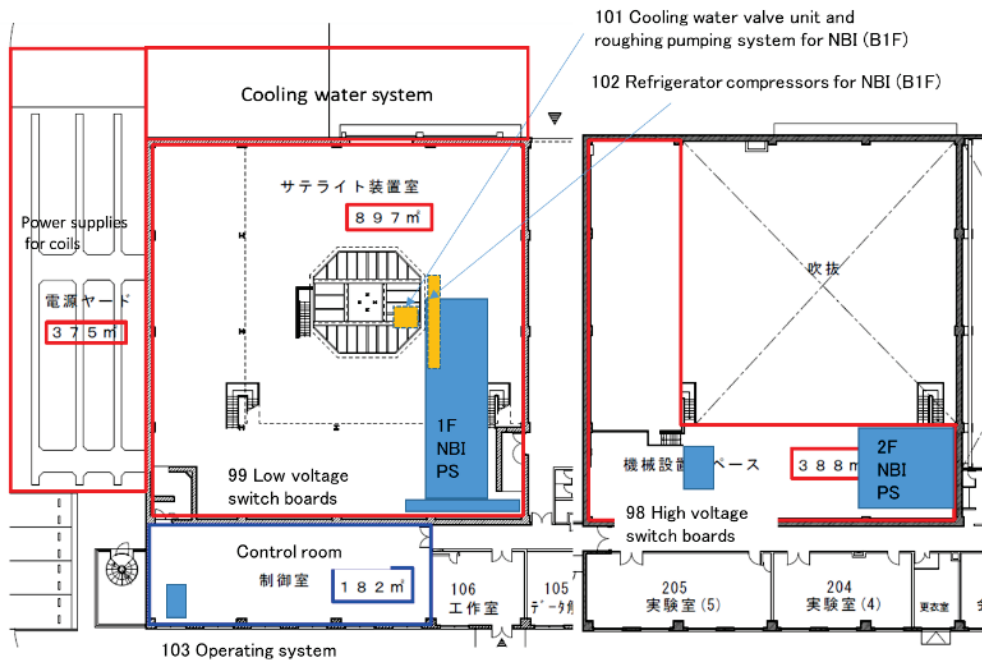


Fig 1.1-3 Layout of torus hall for the CHS in NIFS with the NBI system.

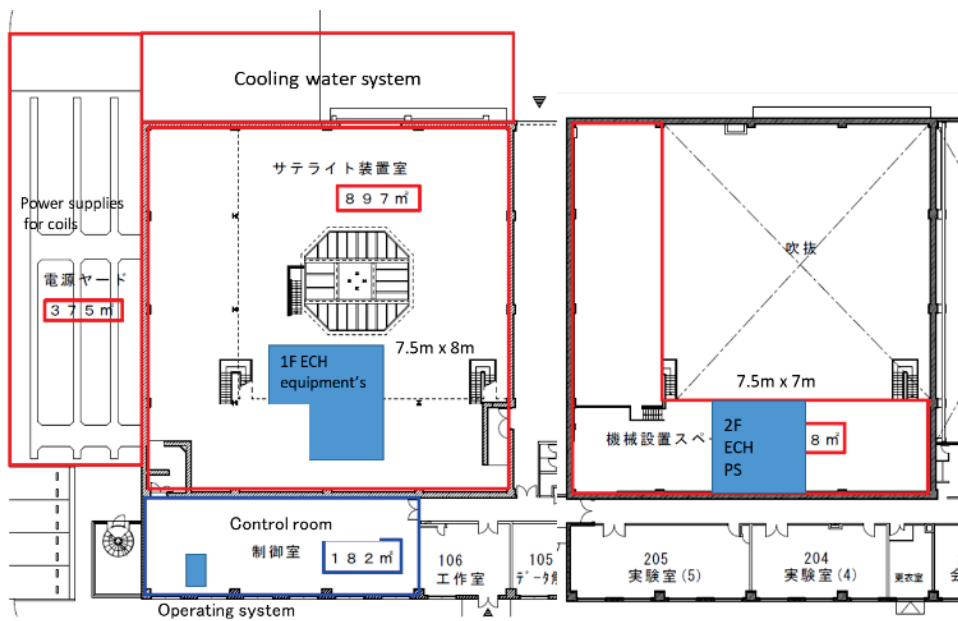


Fig 1.1-4 Layout of torus hall for the CHS in NIFS with the ECRH system.

1.2 Power system for the CHS

It should be noted that the commercial voltage is different in Japan and China as shown in Table 1.2-1. To transfer the CHS equipment to CFQS, transformers will be needed to adjust for voltage differences. Table 1.2-2 shows a list of low-voltage power board related to main equipment relocating from the CHS to the CFQS. It is necessary to prepare a power board to supply these voltages with the CFQS. Fig 1.2-1 shows the one-line diagram of the CHS power supply system.

Table 1.2-1 Difference of power environment.

	Frequency	High voltage	Low voltage 1Φ	Low voltage 3Φ
NIFS	60 (West Japan)	6.6 kV	100 V	200 V
China	50	10 kV	220 V	380 V

Table 1.2-2 Load list of low voltage power board KIT-1A-13 for the CHS in NIFS

Row	No	Voltage(V)	System	Use	Load(kVA)
1	u1	200	ECRH	Charger	24
	u4	200	NBI-2	GTO PS	8
	u5	100	ECRH	1Φ SWB	12
	R1	100	NBI-2	AVP CB	1.6
	R2	100	NBI-2	BLA CB	1.6
	R3	100	NBI-2	TCB	1.6
	L9	100	ECRH	CTRL	1.6
	R9	100	ECRH	LN2	0.8
	2	R1	200	NBI-2	DCL
R2		200	NBI-2	GTO LV	16
R3		200	NBI-2	BMAG	16
R4		200	NBI-2	AVP	4.8
R5		200	NBI-2	SCR CB	4.8
3	L6	200	NBI-2	DCL CB	8
4	L1	200	NBI-2	SB Gas	8
	R1	200	NBI-2	REFCR	8
	L2	200	NBI-2	REFCR	8
	R2	200	NBI-2	REFCR	8
	L3	200	NBI-2	REFCR	8
	R3	200	NBI-2	REFCR	8
	L4	200	NBI-2	REFCR	8
	R4	200	NBI-2	REFCR	8
	L5	200	NBI-2	REFCR	8
	R5	200	NBI-2	AVP	8
5	L5	200	ECRH	COOL OIL	5.28
	B1	200	ECRH	3Φ SWB	35.2

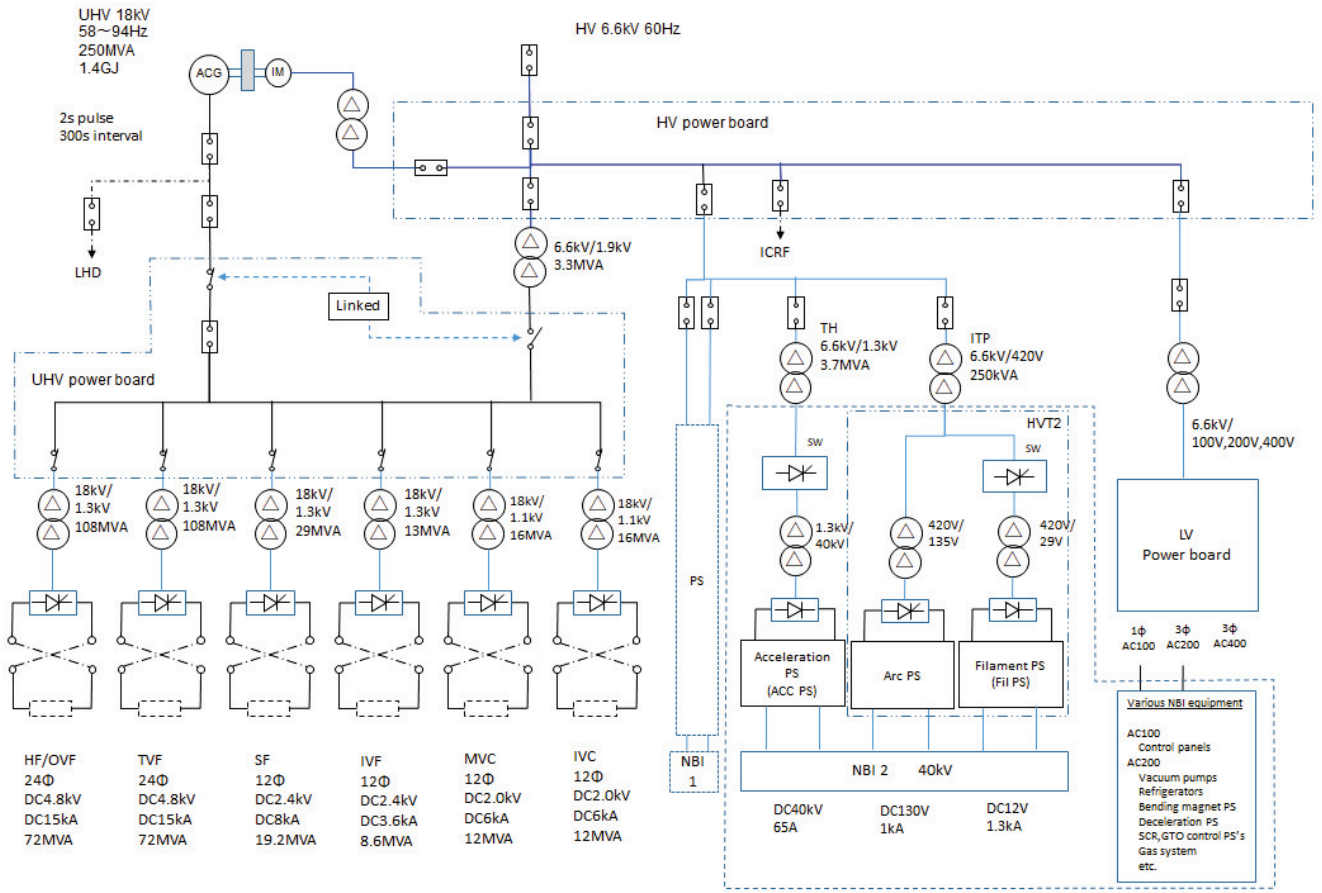


Fig 1.2-1 One line diagram of power supply system for the CHS in NIFS.

1.3 Vacuum pumping system for the CHS

We plan to transfer the vacuum pumping unit for CHS in NIFS to CFQS. Their main specification is shown below. To use this unit with CFQS, modification adding some parts will be required.

Table 1.3-1 Main parameters for the vacuum pumping system for the CHS.

No	Item	Contents
1	Input power supply	AC 220 V, 50/60 Hz, 1Φ/3Φ, 20 A (at startup)
2	Cooling water	8 kgf/cm ² G, 5 ℓ/min or more, 27 °C or less
3	Compressed air	7 kgf/cm ² G, 20 Nm ³ /h
4	Turbo molecular pump (TMP)	Number of units 2 Model; TH1502VW (Osaka Vacuum Ltd.) Exhaust speed; 1500 ℓ/s Ultimate pressure; 1×10 ⁻⁷ Pa Cooling method; water cooling Allowable temperature; 120 °C
5	Rotary pump (RP)	Number of units 1 Model; T2063A (Adixen/Alcatel) Exhaust speed; 1420 ℓ/min(60Hz) 1180 ℓ/min(50Hz)

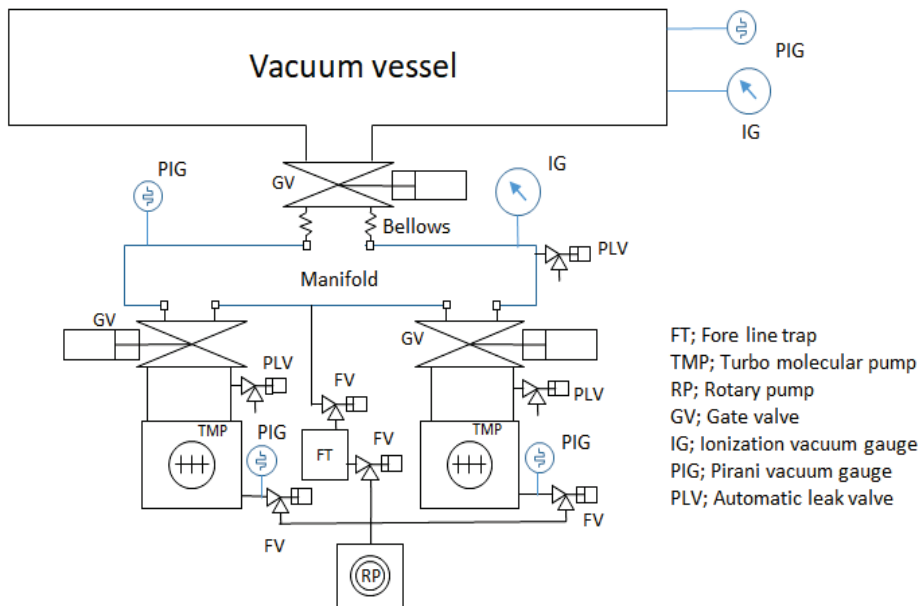


Fig 1.3-1 System diagram of vacuum pumping unit.

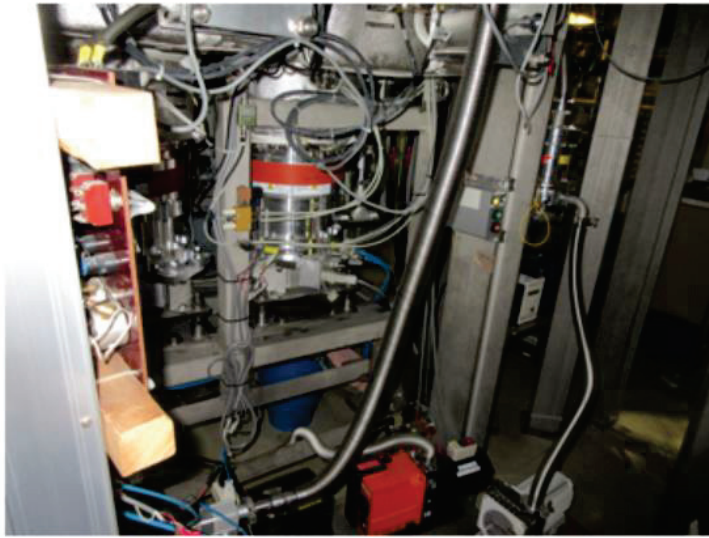
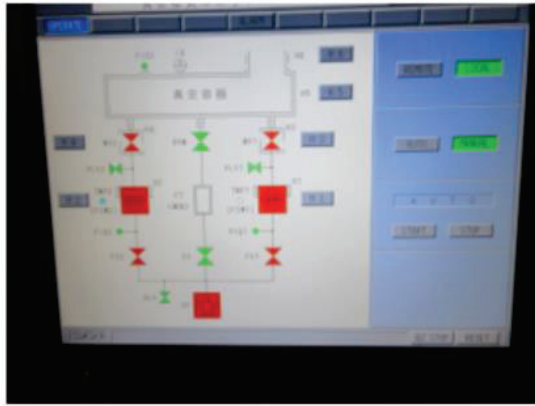


Fig 1.3-3 Picture of vacuum pumping system.

1.4 NBI system for the CHS

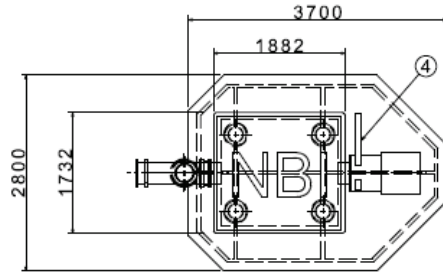
There is a plan to transfer the NBI system from the CHS to the CFQS. A configuration of the NBI and power supply for the CHS is shown below.

Table 1.4-1 Power capacity of the CHS NBI-2 system.

No	Item	Voltage	Output Current	Capacity of input transformer
1	Acceleration power supply	AC6.6 kV/DC 40 KV	65 A	3.7 MVA
2	Arc power supply	AC6.6 kV/DC 135 V	1 kA	250 kVA
3	Filament power supply	AC6.6 kV/DC 12 V	1.32 kA	
4	Deceleration power supply	AC 200 V		26 kVA
5	Bending magnet power supply	AC 200 V		20 kVA
6	Refrigerator for cryogenic pump	AC 200 V		64 kVA
7	Low voltage 1Φ (Others)	AC 100 V		4.8 kVA
8	Low voltage 3Φ (Others)	AC 200 V		50 kVA

Table 1.4-2 Technical specifications of the CHS NBI-2 system.

No	Item	Specification
1	Beam specie	H/D
2	Beam energy	20-40 kV
3	Port-through power	1 MW
4	Beam duration	1 s
5	Ion source	Filament-arc discharge with cusp magnets
6	Beam acceleration area	φ 300 mm
7	Aperture radius	φ 5 mm
8	Current density	250 mA/cm ²
9	Beam optics	Conversing beam via offset aperture
10	Focal length of the beam	3.0 m
11	Beam divergence angle	1 degree
12	Diameter of drift tube	φ 250 mm
13	Neutralization	Gas cell
14	Main vacuum pump	Cryosorption panel (326 m ³ /s)
15	Diagnostics	Calorimetric beam profile measurement



Number	PartNumber	Quantity	Material
1	IonSource	1	
2	Neutrilizer	1	
3	Piping and cables	1	
4	Gate valve	2	SUS
5	Stage for the CFQS	1	SUS
6	Bellows	1	SUS

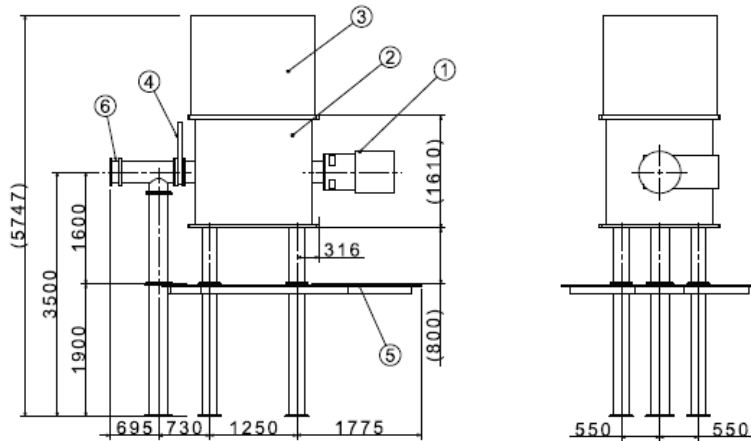


Fig 1.4-1 Ion source of the CHS NBI-2 system.

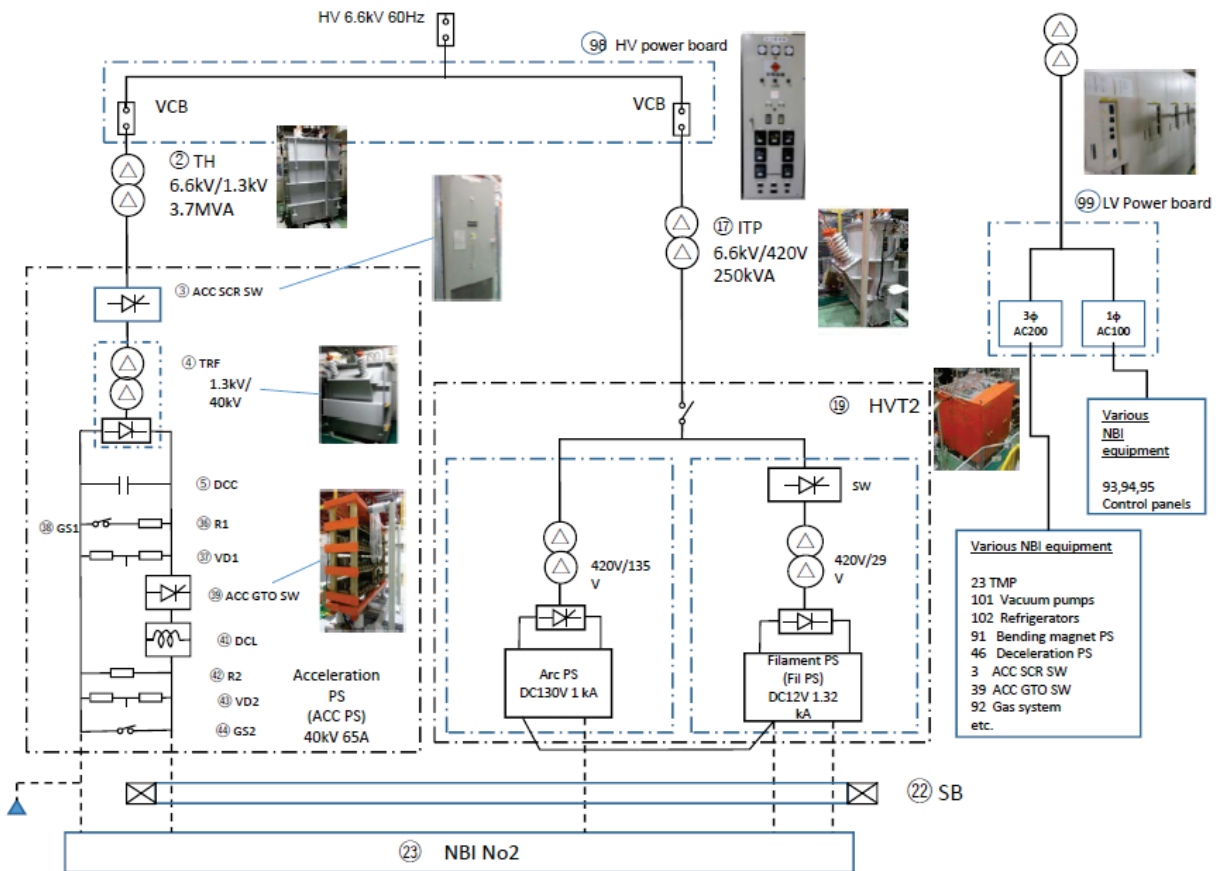


Fig 1.4-2 One-line diagram of the CHS NBI-2 system.

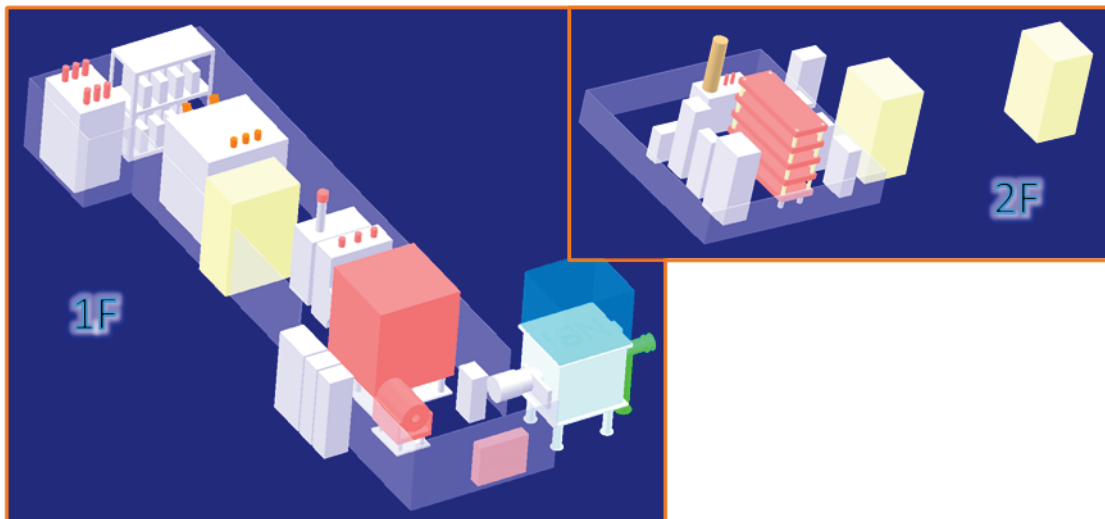
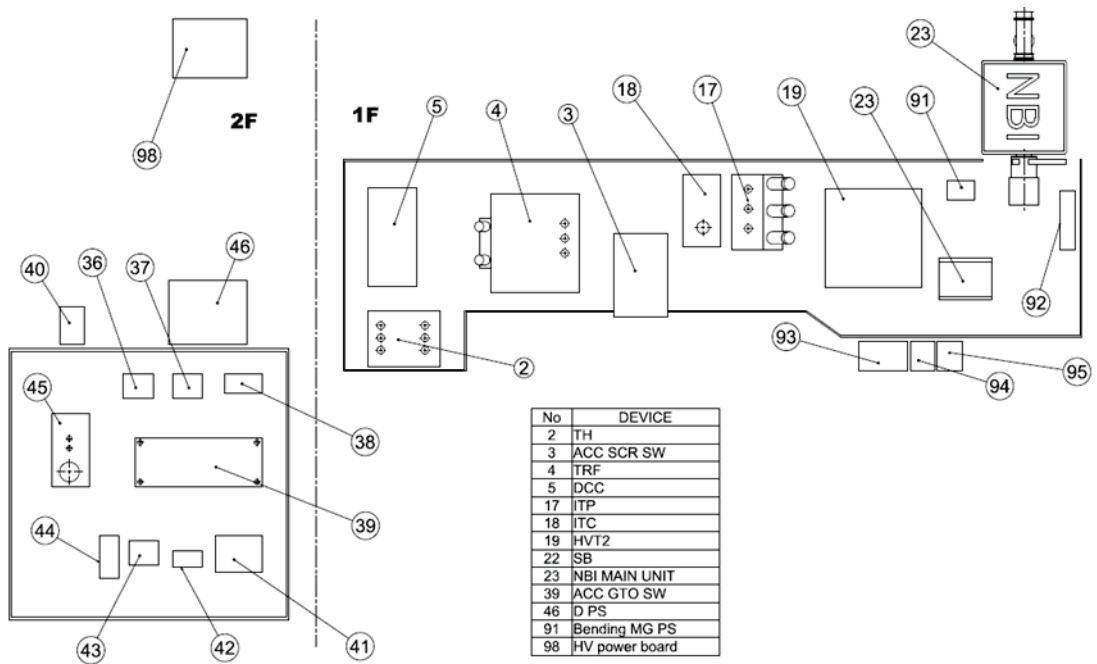


Fig 1.4-3 Layout of the CHS NBI-2 system.

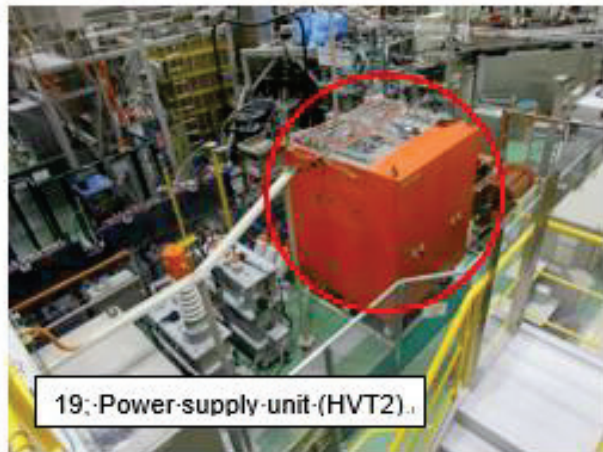


Fig 1.4-4 Picture of main components for the CHS NBI-2 system.

1.5 ECRH system for the CHS

There is a plan to transfer the ECRH system from the CHS to the CFQS. However, many parts are obsolete and have not been in operation for a long time and need to be rebuilt for the CFQS. A configuration of the ECRH and power supply for the CHS is shown below.

Table 1.5-1 Technical specifications of the ECRH for the CHS.

No	Item	Specification
1	Power source	Gyrotron produced by a Russian company, GYCOM
2	Frequency	54.5 GHz
3	Output power	Up to 450 kW
4	Pulse length	0.1 s
5	Resonance condition	1.95 T with fundamental resonance($n=1$) 0.97 T with second harmonic resonance($n=2$)
6	Transmission line	Quasi-optical transmission line (Focusing, plane, polarizer, and 2-D steerable mirrors)
7	Magnet	Super conducting magnet with liquid helium replenishment type. It should be replaced to the new one with dedicated refrigerator.
8	Vacuum window	Sapphire window To minimize power reflection at the vacuum window, the thickness of the window d must satisfy a relation: $d = n \lambda_{in}/2$. Here, n is an integer and λ_{in} is wavelength in the window material.

Table 1.5-2 Power supply of the ECRH for the CHS.

No	Item	Specification
1	Type	High voltage capacitor bank with crowbar circuit
2	Charger	Up to 100 kV DC from 200 V AC
3	Capacitor	86 capacitors with 1.5 μ F each
4	Regulator tube	EIMAC X2062K tetrode tube to supply 70 kV DC. It is very old and must be replaced to new one.
5	Ion pumps	To keep the vacuum condition inside the gyrotron and the regulator tube require DCPS of 3.5 kV
6	Heaters	To generate thermal electron beams, require ACPSs of 150 V
7	Crowbar circuit	High voltage PS used for crowbar-drive works at 8 kV DC
8	Super conducting magnet	SCM requires DCPS of 2 V/33 A

Table 1.5-3 Pure water-cooling system of the ECRH for the CHS.

No	Item	Specification
1	Purpose	Removing heat load on the gyrotron and the regulator tube
2	Cooling collector	100 L/min
3	Cooling body	6 L/min
4	Cooling vacuum window	9 L/min
5	Cooling oil tank	6 L/min
6	Cooling the regulator tube	120 L/min
7	Pressure	0.2 MPa at inlet

Power Supply for Gyrotrons

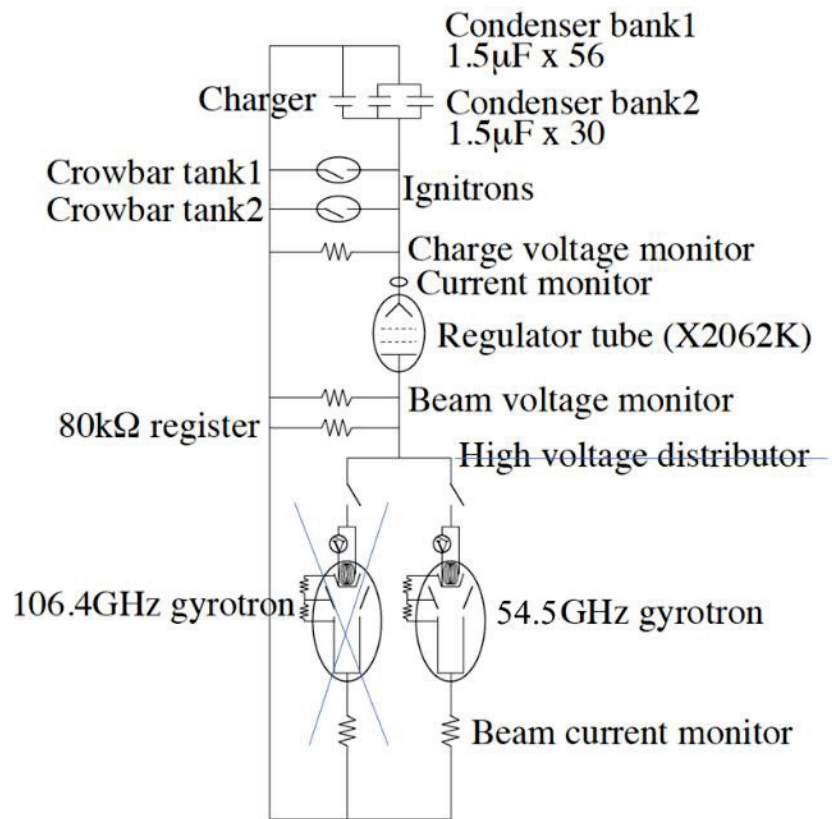


Fig 1.5-1 One-line diagram of the ECRH for the CHS.

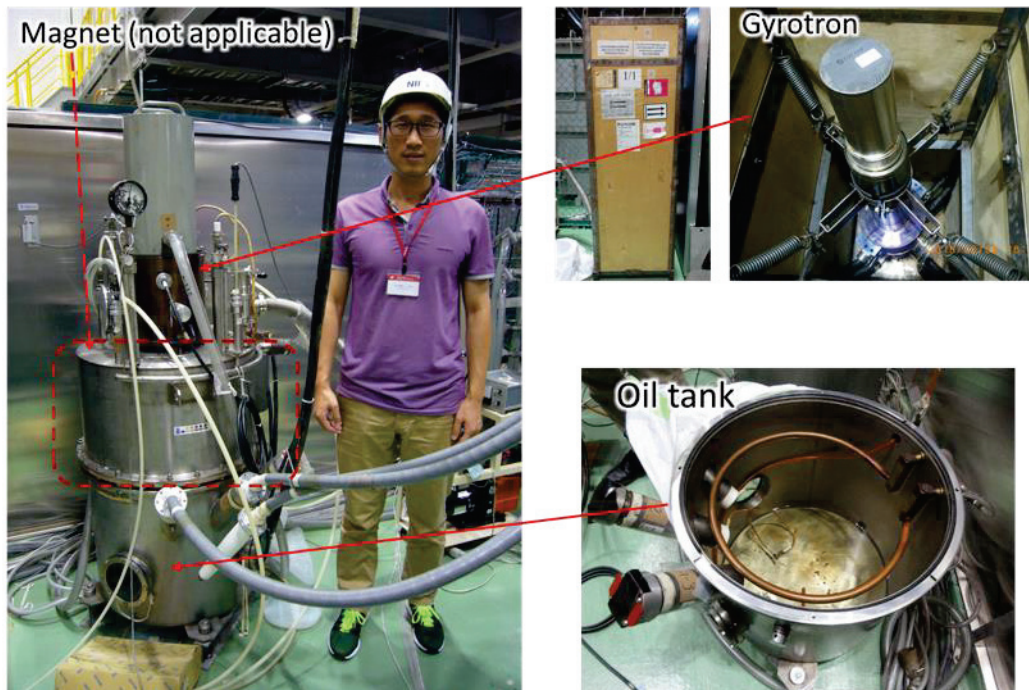


Fig 1.5-2 54.5 GHz gyrotron in the ECRH system for the CHS.

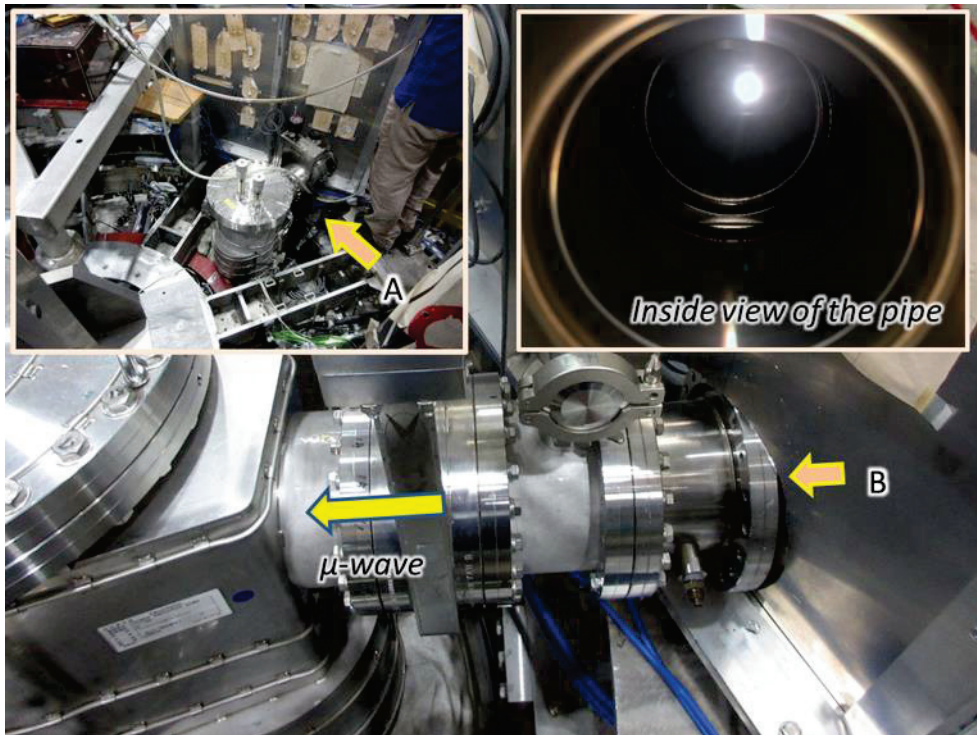


Fig 1.5-3 Sapphire window in the ECRH system for the CHS.

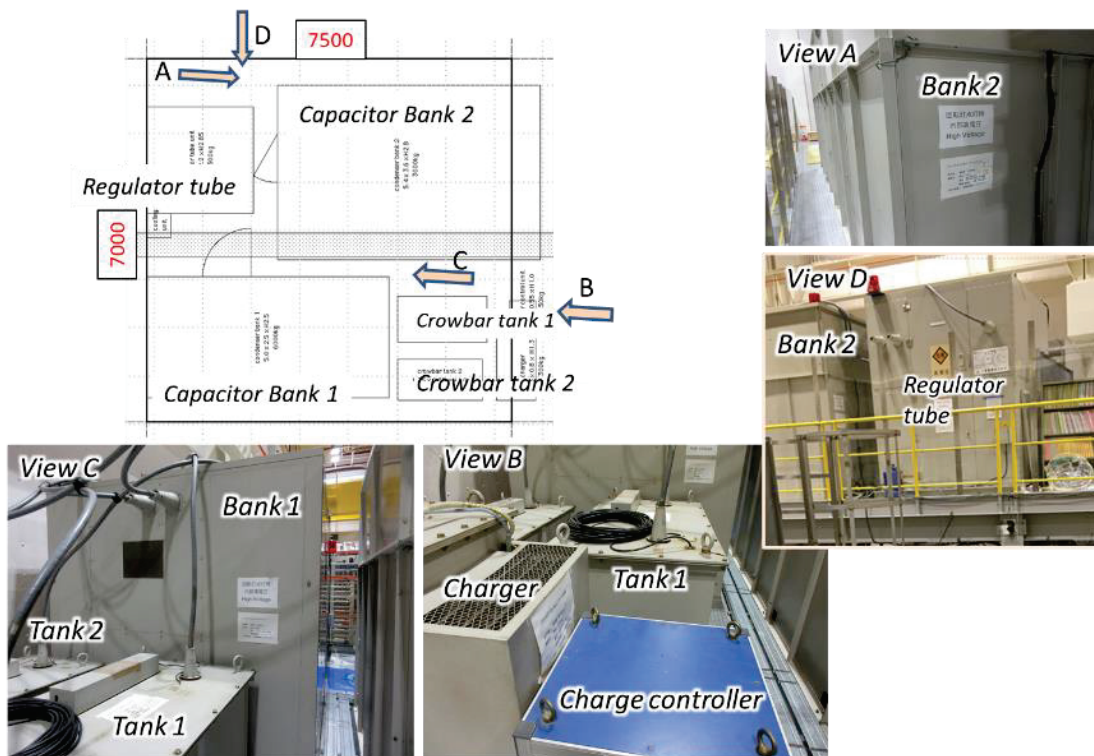


Fig 1.5-4 Power supply for the gyrotron in the ECRH system for the CHS.

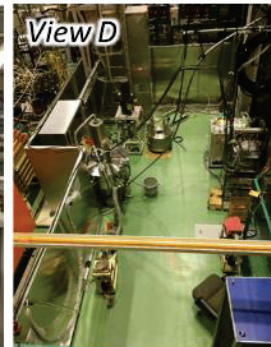
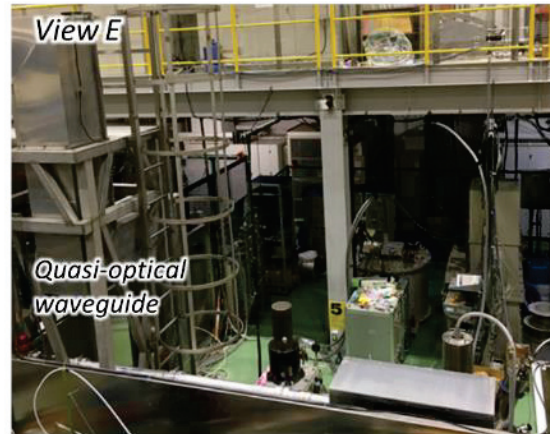
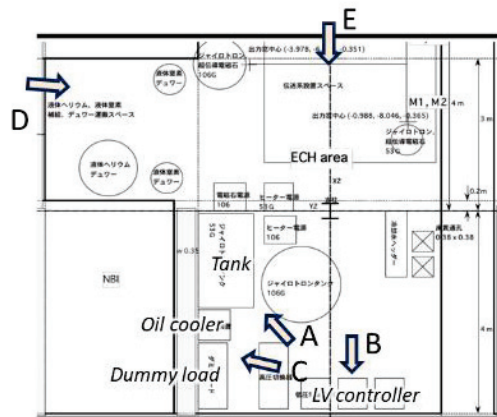


Fig 1.5-5 Some equipment's in the ECRH system for the CHS.

1.6 Power supply to bake vacuum vessel for the CHS.

The following figure shows the configuration of the baking power supply for the CHS. A similar system will be required for the CFQS.



Fig 1.6-1 Power supply to bake the vacuum vessel for the CHS.

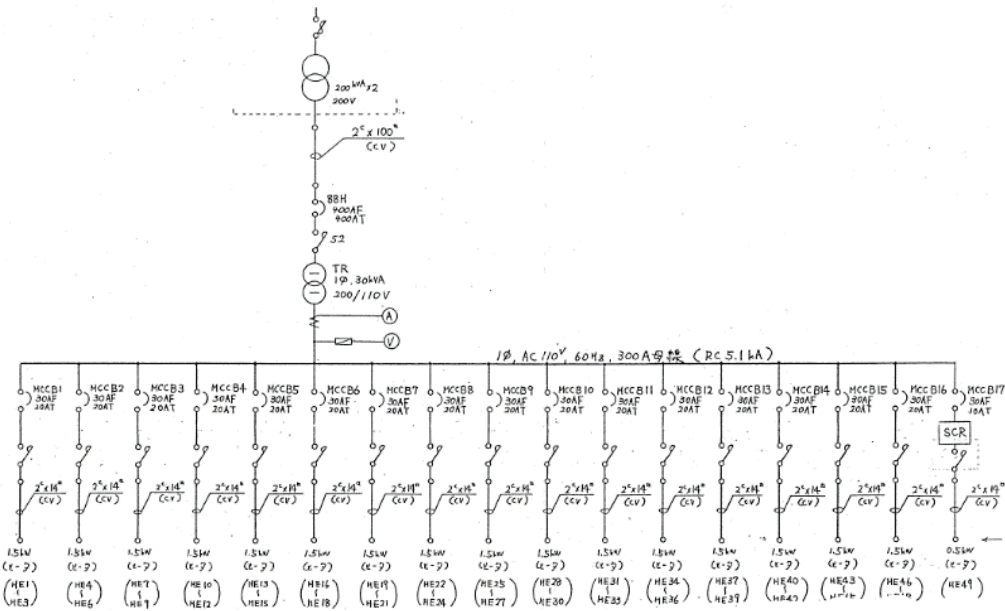


Fig 1.6-2 One line diagram of baking power supply for the CHS.

1.7 Cooling water system for the CHS

The following figure shows the configuration of the water-cooling system for the CHS. The CFQS will also require a similar but smaller system.

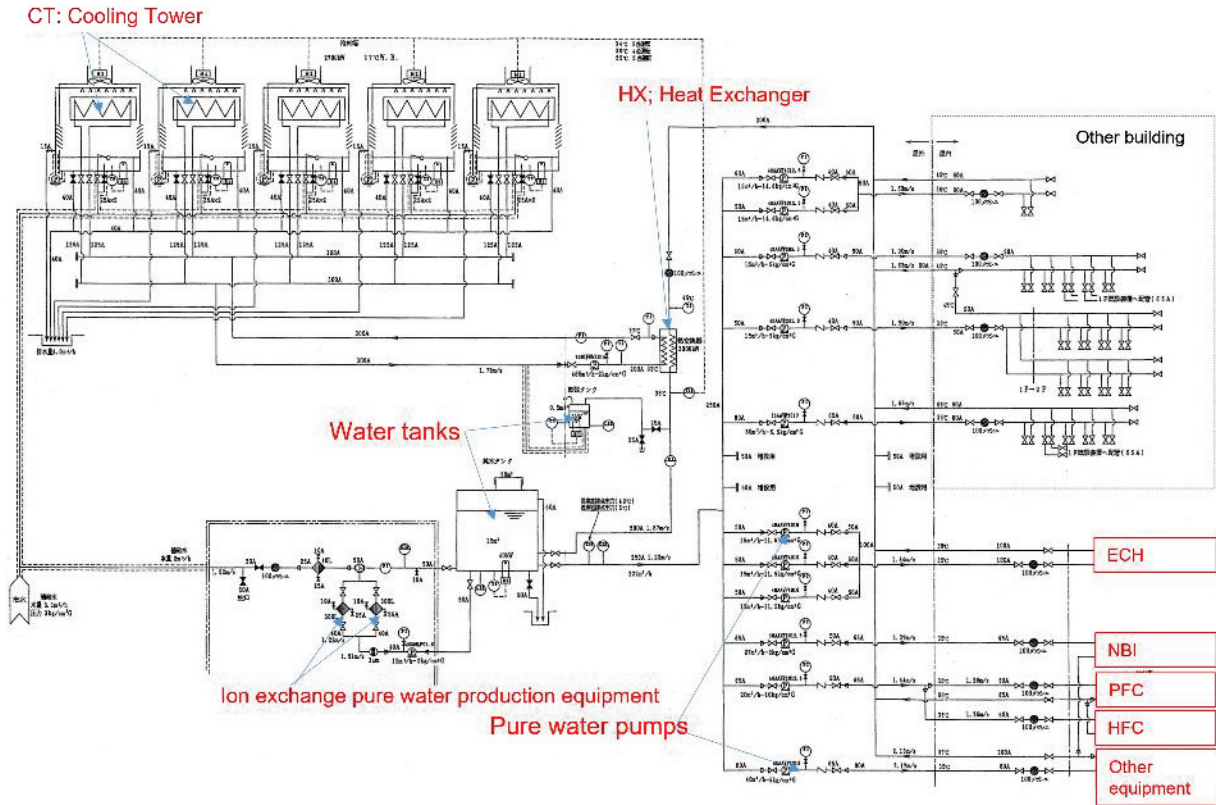


Fig 1.7-1 Cooling water system diagram for the CHS.

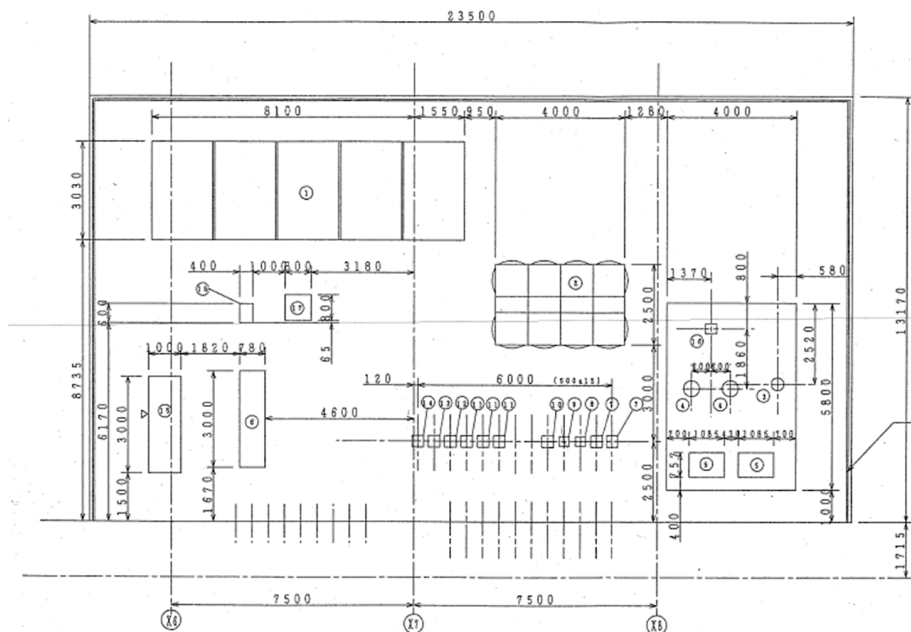


Fig 1.7-2 Layout of cooling water system for the CHS.

1.8 Plasma diagnostic system for the CHS

The following figures show the picture of some plasma diagnostic system for the CHS. Similar systems may be required for the CFQS.

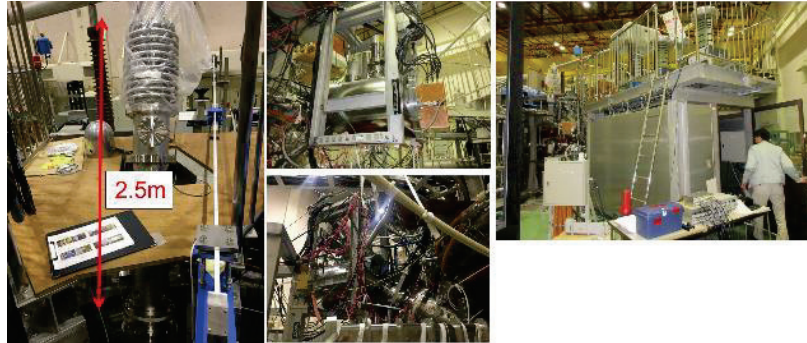


Fig 1.8-1 Heavy ion beam probe to measure turbulence etc. for the CHS.



Fig 1.8-2 Microwave interferometer to measure electron density for the CHS.

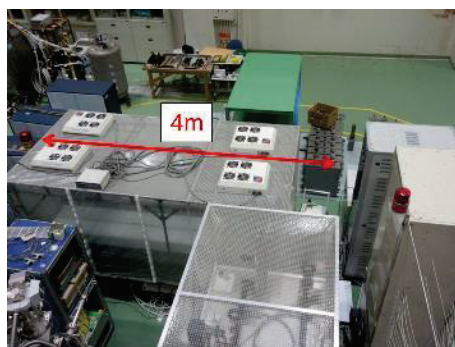


Fig 1.8-3 Thomson scattering system to measure electron temperature for the CHS.

2 Low aspect ratio RFP RELAX

2.1 Description of RELAX machine

The reversed-field pinch (RFP) is one of the magnetic confinement systems for fusion plasma. Recent progress has led to new concepts for the RFP configurations which are free from magnetic chaos caused by the interaction of tearing modes. One is the quasi-single-helicity (QSH) state where single mode grows to dominate a discharge [2-1]. RELAX of Kyoto institute of technology is an RFP machine ($R=0.5$ m/ $a=0.25$ m: $A=R/a=2$) to explore the plasma characteristics in low- A regime [2-2]. In shallow reversal plasmas, the discharge tends to transit between toroidal symmetry state and the QSH state [2-3]. To obtain three-dimensional (3D) structure in such transition, a method of distinguishing the 3D soft X-ray emissivity profile from an image obtained from one view port of limited view area has been developed [2-4].

2.2 3D tomography from soft X-rays through multi-pinhole disk attached to single view port.

2.2.1 Principle of 3D tomography

We propose a new method for obtaining three dimensional (3D) tomography of partial toroidal plasmas without assumptions about the magnetic surfaces using a multi-pinhole disk attached to a single viewport. Fig 2.2-1 shows a schematic of the proposed method. The multi-pinhole disk is a disk with several pinholes. All pinholes of the multi-pinhole disk have a finite parallax. Therefore, X-rays emitted from various locations pass out through pinholes and arrives at the screen emerging as an independent 2D image on the corresponding area of the screen. Dividing the 3D space where the plasma exists in the chamber into many small voxels, the emissivity profile of X-ray $J(x, y, z)$ is denoted as column vector J . Similarly, the image is also divided into small pixels and denoted as a vector I . Using P is a weight coefficient matrix that represents the relationship between pixels and voxels and is determined by the geometric configuration of the device, the obtained image is expressed as $I = PJ$.

Assuming that J consists of a sum of series in terms of orthogonal basis functions as:

$$J = Fs ,$$

where each element of s and each column vector of F corresponds to coefficients and basis vectors, respectively. Conversely, by introducing another matrix A that equal PF , I is consequently expressed by using s as:

$$I = As .$$

By applying an inversion algorithm such as the least square method to an obtained image, the 3D profile of the emissivity of X-rays J can be calculated.

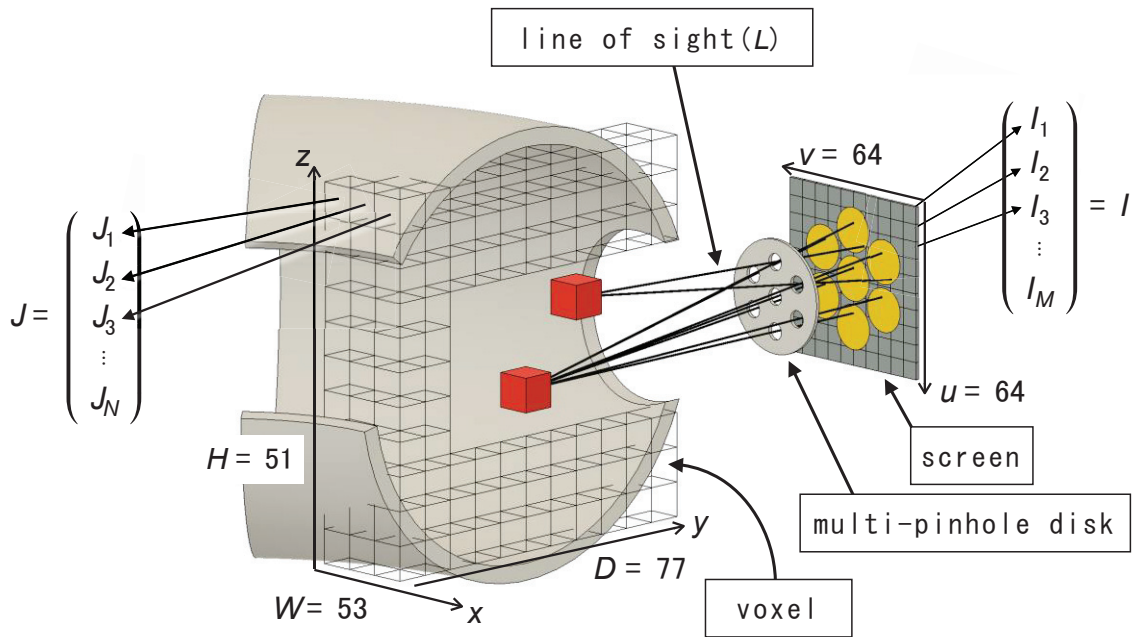


Fig 2.2-1 Schematic of the proposed method for obtaining emissivity profile in a toroidal plasma using a multi-pinhole disk and a screen. The Cartesian (x, y, z) and image (u, v) coordinates are set on the plasma and the screen, respectively. (Reprinted from [2-4])

2.2.2 Numerical trial

We numerically tested whether a test toroidal plasma formed in the RELAX machine could be reconstructed successfully. The test toroidal plasma is asymmetric and has a bean-shaped cross-section with a helical pitch of $\pi/2$ in the toroidal direction, as shown in Fig 2.2-2(a) and (b) and we arrange seven pinholes on the multi-pinhole disk. In this case, the set of seven images in Fig 2.2-2 (c) is the result. By applying the inversion algorithm to the obtained images, $J(x, y, z)$ can be inferred as shown in Fig 2.2-2 (d) and (e). Good agreement is observed between the test plasma and the one inferred in Fig 2.2-2 (a) and (d) as well as between Fig 2.2-2 (b) and (e).

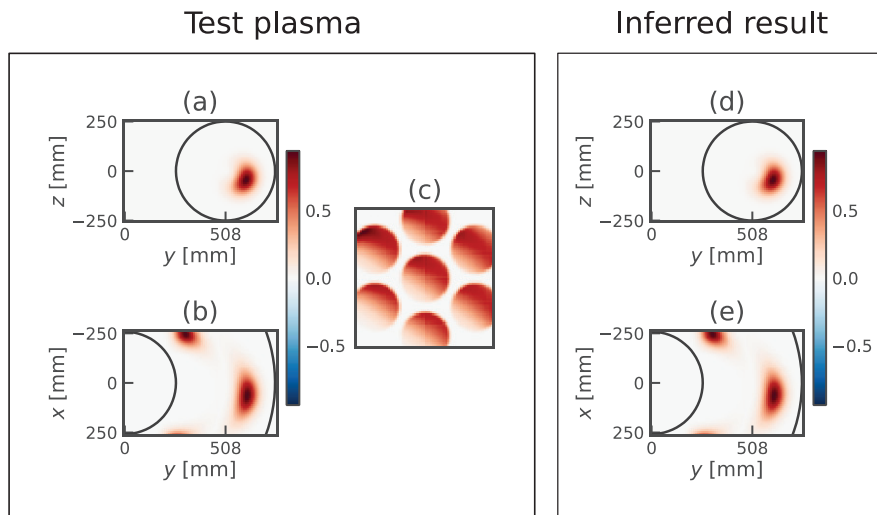


Fig 2.2-2 Comparison of emissivity profile of Test plasma and reconstructed profile. A test spatial profile of emissivity of a toroidal plasma and the seven images obtained in the "Test plasma" window. Conversely, the profile in the "Inferred result" window is a reconstructed result. (Reprinted from [2-4])

References

- [2-1] R. Lorenzini *et al.*, Nat. Phys. **5** (2009) 570.
- [2-2] S. Masamune *et al.*, Proc. of the 26th IAEA Fusion Conference EX/P5-22 (2016).
- [2-3] K. Oki *et al.*, Plasma Fusion Res. **7** (2012) 1402028.
- [2-4] S. Inagaki *et al.*, submitted to Opti. Express.

3 Plasma generating device SSHD

3.1 History of the SSHD

SSHD is a plasma generating device made at Kyoto University in 1980's as an exhibit and educational tool. It was transferred in 2019 from Kyoto University to NIFS and in 2021 from NIFS to SWJTU. It was used to train technical staff with little experience in handling plasma generators.

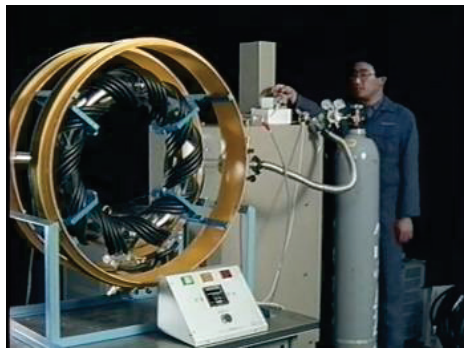


Fig 3.1-1 Demonstration of the SSHD, which was developed for exhibition and education in 1980's at Kyoto University.



Fig 3.1-2 Redevelopment of the SSHD at NIFS. The SSHD was transferred to NIFS in 2019 for the purpose of training technical staff on the handling of plasma equipment.

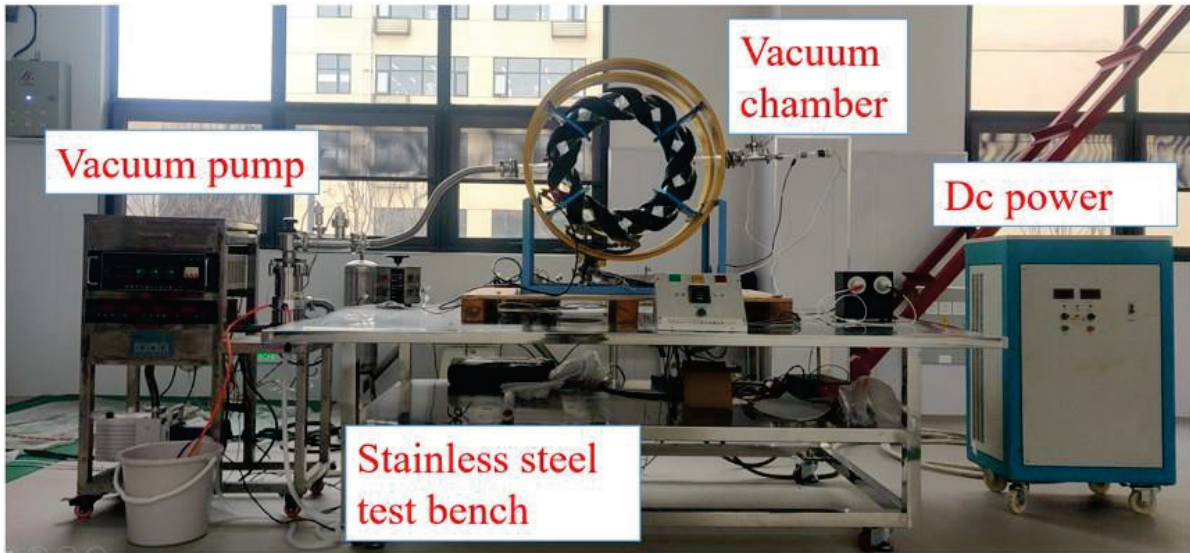


Fig 3.1-3 Redevelopment of the SSHD at SWJTU. The SSHD was transferred to SWJTU in 2021 for the purpose of training technical staff on the handling of plasma equipment.

3.2 Components of the SSHD

Main specifications of the SSHD are summarized in Table 3.2-1. Fig 3.2-1 shows main component of the SSHD, including glass vacuum vessel, coil system, and so on. The glass vacuum vessel is torus-shaped with major radius of 250 mm and minor radius of 50 mm and has two helical coils wound around it. Two poloidal coils are wound on yellow rings. When 450 A is applied to the helical coil system, a toroidal magnetic field is about 0.015 T at the center of the vacuum vessel.

Fig 3.2-2 shows radio frequency (RF) oscillator and Fig 3.2-3 shows Geissler tube and induction coil. After igniting the plasma with a Geissler tube, RF wave with 100 MHz is supplied to maintain the plasma.

Table 3.2-1 Main specifications of the SSHD

Component	No	Item	Value
Vacuum vessel	1	Shape	Torus with a circular cross section
	2	Major radius	250 mm
	3	Minor radius	50 mm
	4	Material	Glass
	5	Vacuum pressure	1×10^{-4} Pa
	6	Vacuum pumping system	Turbo molecular pump (67 l/s)
	7	Exhaust time	10 ~ 30 min
	8	Gas type and filling pressure	Ar and 2×10^{-2} Pa
Helical coil (In series with the poloidal coil)	9	Shape	Helical
	10	Number of coils	$L=2$
	11	Pitch number	$M=5$
	12	Number of turns	4 each
	13	Current	450 A
	14	Voltage	5.1 V (Including the poloidal coil)
	15	Toroidal magnetic field	0.015 T
Poloidal coil	16	Shape	Circular
	17	Number of coils	2
	18	Number of turns	3 each
	19	Current	450 A
RF heating coil (Winding parallel to the helical coil)	20	Shape	Helical
	21	Number of coils	2
	22	Number of turns	2 each
Coil power supply	23	Voltage	8 V max
	24	Current	500 A max
RF power supply	25	Frequency	100 MHz
	26	Power (DC input)	193 W max (770 V, 0.25 mA)

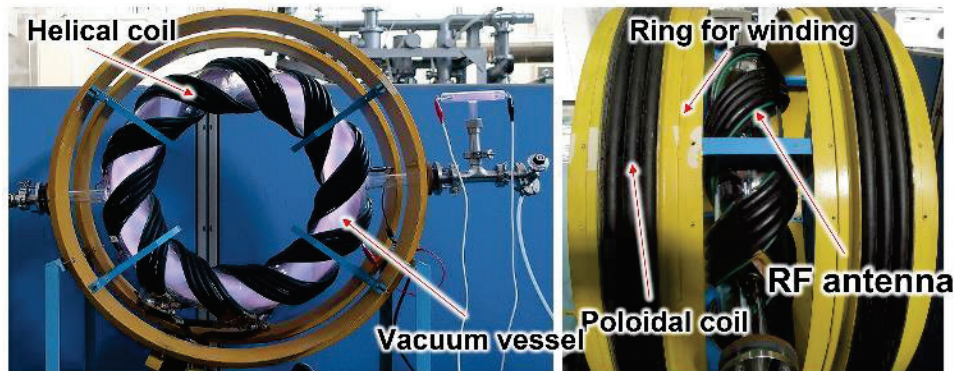
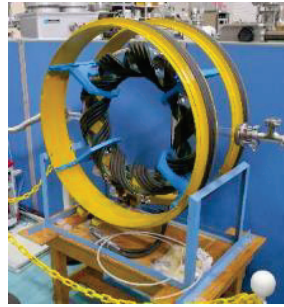


Fig 3.2-1 Vacuum vessel and coil system of the SSHD. The pictures show the helical coil, the vacuum vessel made of glass, the RF antenna, and the poloidal coil.

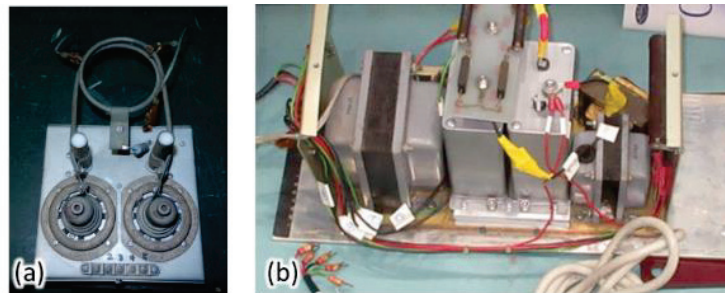


Fig 3.2-2 RF oscillator with 100MHz, which is used to continuously generate plasma. The right picture shows the rectifier circuit, and the left shows the LC resonant circuit for high-frequency oscillation.

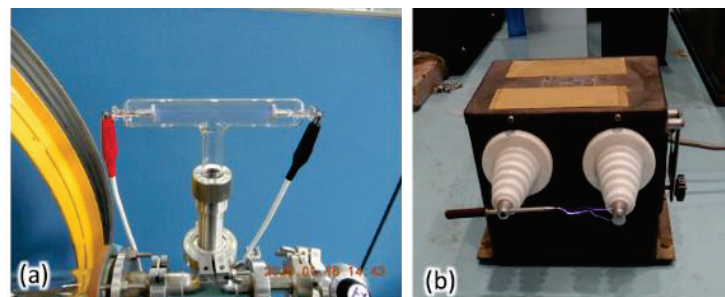


Fig 3.2-3 (a) Geissler tube and (b) induction coil. They are used to ignite plasma.

3.3 Plasma measurement with a Langmuir probe

Plasma experiment with a Langmuir probe was conducted to estimate the plasma parameters. Fig 3.3-1 shows a Langmuir probe, Fig 3.3-2 shows the Langmuir probe inserted into vacuum vessel and plasma. Fig 3.3-3 shows the result of the measurement; electron temperature T_e and electron density n_e for different coil current.

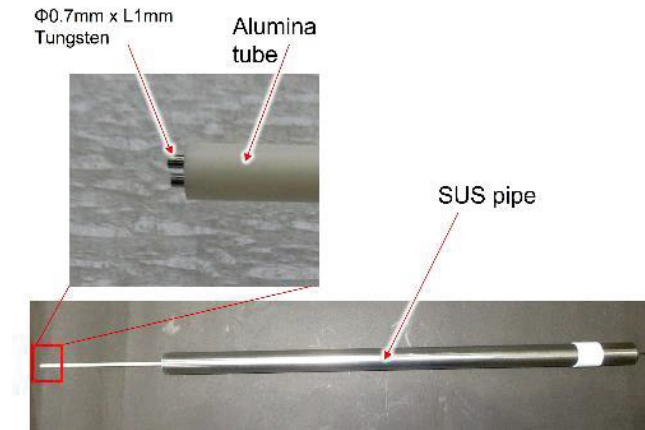


Fig 3.3-1 A Langmuir probe, which was made of two tungsten rods and an alumina sheath. It was used as a single probe with one of two rods.

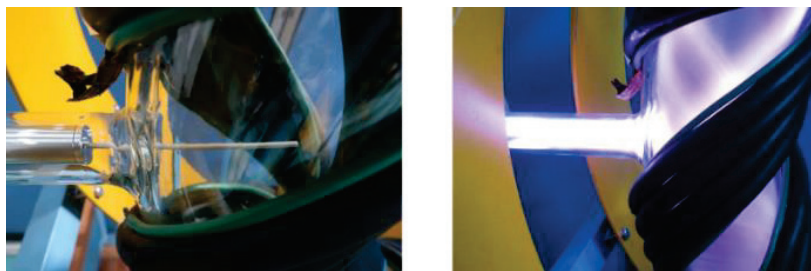


Fig 3.3-2 The Langmuir probe inserted into the vacuum vessel. It is used to estimate the electron temperature and electron density. The left picture shows the tip of the probe and right shows the plasma around the probe.

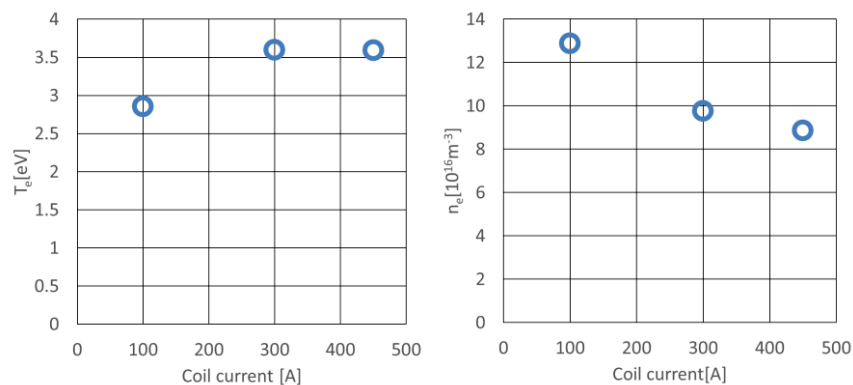


Fig 3.3-3 Electron temperature T_e and electron density n_e for different coil current.

Publication List of NIFS-PROC. Series

- NIFS-PROC-107 Edited by Hiroaki Ito and Tetsuo Ozaki
Recent Progress of Pulsed Power Technology and its Application to High Energy Density Plasma
Nov. 27, 2017
- NIFS-PROC-108 Edited by Yeong-Kook OH, Shigeru MORITA and Liqun HU
Proceeding of A3 Foresight Program Seminar on Critical Physics Issues Specific to Steady State Sustainment of High-Performance Plasmas November 22-25, 2016, Jeju, Korea
Jan. 11, 2018
- NIFS-PROC-109 Edited by Shigeru MORITA, Liqun HU and Yeong-Kook OH
Proceeding of A3 Foresight Program Seminar on Critical Physics Issues Specific to Steady State Sustainment of High Performance Plasmas 11-14 July, 2017, Sapporo, Japan
Jan. 12, 2018
- NIFS-PROC-110 Edited by Jun Hasegawa and Tetsuo Ozaki
Recent Developments of Pulsed Power Technology and Plasma Application Research
Jan. 12, 2018
- NIFS-PROC-111 Edited by Liqun HU, Shigeru MORITA and Yeong-Kook OH
Proceeding of A3 Foresight Program Seminar on Critical Physics Issues Specific to Steady State Sustainment of High Performance Plasmas 12 - 15 December, 2017, Chongqing, China
Jun. 11, 2018
- NIFS-PROC-112 Edited by E. Kikutani (KEK) and S. Kubo (NIFS)
Proceedings of the meeting on Archives in Fields of Natural Sciences in FY 2017
Oct. 18, 2018 (Written in Japanese)
- NIFS-PROC-113 Pulsed Power and High-Density Plasma and its Applications
Edited by Koichi Takaki and Tetsuo Ozaki
Feb. 6, 2019
- NIFS-PROC-114 The 7th Japan-China-Korea Joint Seminar on Atomic and Molecular Processes in Plasma (AMPP2018)
Edited by Daiji Kato, Ling Zhang, and Xiaobin Ding
May 10, 2019
- NIFS-PROC-115 CFQS TEAM
NIFS-SWJTU JOINT PROJECT FOR CFQS -PHYSICS AND ENGINEERING DESIGN-
VER. 2.1 2019. SEP.
Nov. 8, 2019
- NIFS-PROC-116 Satoshi Ohdachi, Editor of the Post-CUP Workshop proceeding
Collected papers at the 2019 Post-CUP Workshop & JSPS-CAS Bilateral Joint Research Projects Workshop,
24th-26th July, 2019, Nagoya, Japan
Feb. 21, 2020
- NIFS-PROC-117 Edited by E. Kikutani (KEK) and S. Kubo (NIFS)
Proceedings of the meetings on Archives in Fields of Natural Sciences in FY2018
June. 9, 2020 (Written in Japanese)
- NIFS-PROC-118 Edited by Tetsuo Ozaki and Sunao Katsuki
New Development of Beam Physics and the Application by New Generation Pulsed Power Technology
June. 29, 2020
National Institute for Fusion Science, National Institutes of Natural Sciences
Institute of Fusion Science, School of Physical Science and Technology, Southwest Jiaotong University
Hefei Keye Electro Physical Equipment Manufacturing Co. Ltd.
- NIFS-PROC-119 Hefei Keye Electro Physical Equipment Manufacturing Co. Ltd.
NIFS-SWJTU JOINT PROJECT FOR CFQS -PHYSICS AND ENGINEERING DESIGN-
VER. 3.1 2020. NOV.
Jan. 25, 2021
- NIFS-PROC-120 Edited by Izumi Tsutsui (KEK) and Shin Kubo (NIFS)
Proceedings of the meetings on Archives in Fields of Natural Sciences in FY2019
Feb. 25, 2021
- NIFS-PROC-121 Edited by Hiroaki Ito and Tetsuo Ozaki
Frontier of Advanced Pulsed Power Technology and its Application to Plasma and Particle Beam
Nov. 08, 2021
- NIFS-PROC-122 National Institute for Fusion Science, National Institutes of Natural Sciences
Institute of Fusion Science, School of Physical Science and Technology, Southwest Jiaotong University
Hefei Keye Electro Physical Equipment Manufacturing Co. Ltd.
NIFS-SWJTU JOINT PROJECT FOR CFQS -PHYSICS AND ENGINEERING DESIGN-
VER. 4.1 2022. JAN.
Feb. 10, 2022